Low Air Gap Magnetic Flux Density, Low Air Gap Electric Field Intensity, Low Loss Coil Design Methodologies for Multi-kW, Large Distance Wireless Power Transfer Systems

by

Guangqi Zhu

A dissertation submitted in partial fulfillment of

the requirements for the degree of

Doctor of Philosophy

(Mechanical Engineering)

at the

UNIVERSITY OF WISCONSIN – MADISON

2018

Date of final oral examination: 12/13/2018

The dissertation is approved by the following members of the Final Oral Committee:

Lorenz, Robert D., Professor, Mechanical Engineering
Jahns, Thomas M., Professor, Electrical and Computer Engineering
Sarlioglu, Bulent, Associate Professor, Engineering Professional Development
Ludois, Daniel C., Assistant Professor, Electrical and Computer Engineering
Zinn, Michael, Associate Professor, Mechanical Engineering

© Copyright by Guangqi Zhu 2018

All Rights Reserved

Abstract

Inductive wireless power transfer (WPT) is being actively investigated as a promising technology to conveniently charge electric vehicles. Existing WPT systems generate large air-gap region magnetic (B) and electric (E) fields to transfer multi-kW of power, which violate typical safety standards. This research focuses on developing general design methodologies to meet the safety requirements by maintaining inherently low air-gap B and E fields while achieving multi-kW, large distance inductive WPT with high power transfer efficiency.

General design variables are identified, and their effects on the air-gap B and E fields, and power transfer efficiency are investigated. A general design methodology based on fast converging analytical models for the estimation of the air-gap B and E fields, and transfer efficiency is developed. Particular winding configurations such as the surface spiral parallel and anti-parallel windings are proposed to achieve high efficiency, low dielectric losses, and reduced spatial voltage stress. A design example is analyzed in detail using both FEA and experiments.

Besides the mutual coupled magnetic flux, the power transfer capability within the safety standard was found to be fundamentally limited by the leakage flux. A combination of new active and passive techniques is developed to mitigate these limitations. In particular, an “I” type shielding design is developed to shape the magnetic flux paths as desired to achieve low air-gap B field and shield the E field without affecting the transfer efficiency. The shielding design is optimized with reduced mass. In addition, the power-scaling law within the field safety limits are developed. Thermal modeling is developed based on the loss distribution analysis.

At the end, the impact of coil misalignment is investigated. Unavoidable misalignment leads to reactive power and change of field distributions. Low loss capacitor and inductor online active tuning techniques are developed to reduce the reactive power, and improve the output power capability. Alternative compensation techniques are investigated to mitigate the variations of the field distributions, and provide an access to tune the field distributions actively.

Acknowledgements

I would like to thank Professor Lorenz, for his guidance and support during the Ph.D. program. The incredible courage and optimism Profess Lorenz are demonstrating, and unbounded enthusiasm will always inspire me in my whole life. Without your spiritual reference as command feedforward, I can't achieve this final goal.

I would like to thank the committer members, Professor Thomas M. Jahns, Professor Bulent Sarlioglu, Professor Daniel C. Ludois, Professor Neil A. Duffie and Professor Michael Zinn for the comments and suggestions on the thesis.

I would like to thank Ted Bohn for his support. The experimental tests would not be possible without his and Algonne National Lab's generous support.

I would like to express appreciation for the opportunity to take classes and conduct research with the Wisconsin Electric Machines and Power Electronics Consortium (WEMPEC). I enjoyed every day studying and living in WEMPEC. It's such a special place that makes me feel in a family. I thank the whole WEMPEC family for making my stay in Madison an enjoyable and unforgattable experience.

I would also like to thank the WEMPEC peers for the stimulating discussions and overshelming support. Thank you for the following, especially Hao Jiang, Apoorva Athavale, Jiejian Dai, Cong Deng, Yang Xu, Huthaifa Flieh, Hung-Yen Ou Yang, Kang Wang, Minhao Sheng, Shang-Chuan Lee, Zhe Chen and all the members of the CAST group from 2013-2018.

At the end, the greatest gratitudes are expressed to my parents, my families, my girlfriend Huilin, and my best partner Jinxin for your long-time confidence in me and conditionless supports. Love you all!!!

Table of Contents

List of Figures

List of Tables

Nomenclature

Symbol	**Description**
L_{tx}, L_p, L_1	Transmitter self-inductance
C_{tx}	Transmitter resonant compensation capacitance
R_{tx}, R_p, R_1	Transmitter equivalent series resistance
N_{tx}	Transmitter number of turns
r_{tx}	Transmitter coil radius
L_{rx}, L_s, L_2	Receiver self-inductance
C_{rx}	Receiver resonant compensation capacitance
R_{rx}, R_s, R_2	Receiver equivalent series resistance
N_{rx}	Receiver number of turns
r_{rx}	Receiver coil radius
r_w	Winding radius
r_{in}	"I" type shield inner radius
r_{out}	"I" type shield outer radius
L_m, M	Mutual inductance between the transmitter and the receiver
d_{ag}	Air-gap distance between the transmitter and the receiver
d_{int}	Inter-turn distance between adjacent turns
$\eta_{coil, max}$	Maximum achievable coil-to-coil efficiency
η_{coil}	Coil-to-coil efficiency
η_{dc}	DC-to-DC efficiency
δ	Skin depth
$\tan\delta$	Dissipation factor or loss tangent
R_{skin}	AC resistance caused by skin effect
R_{AC}	AC resistance caused by skin and proximity effects
R_L	Load resistance
G_p	Proximity factor
B_{agcppk}	Air-gap center plane peak magnetic flux density
$B_{agcppk, r}$	Air-gap center plane radial direction peak magnetic flux density
E_{agcppk}	Air-gap center plane peak electric field intensity
B_{pk}	Peak magnetic flux density
E_{pk}	Peak electric field intensity
H	Magnetic field intensity
k	Coupling coefficient
a	Transfer ratio
Q	Quality factor
μ	Permittivity of a material
σ	Conductivity of a material
f	Operating frequency
f_0	Resonant frequency
ω_0	Angular resonant frequency
X	Reactance

Z	Impedance
P_{in}	Input power
I_{tx}	Transmitter coil current
V_{tx}	Transmitter coil voltage
I_{rx}	Receiver coil current
V_{rx}	Receiver coil voltage
I_L	Load current
K_0	Modified Bessel function of the second kind of order zero
K_1	Modified Bessel function of the second kind of order one
I_0	Modified Bessel function of the first kind of order zero
I_1	Modified Bessel function of the first kind of order one
$\vec{A}$	Magnetic vector potential
Φ	Electric potential
P_{agm}	Air-gap maximum transferrable power within safety limits
P_{mout}	Maximum output power within safety limits

Subscripts

$(\ )_{tx}$, $(\ )_p$	Transmitter
$(\ )_{rx}$, $(\ )_s$	Receiver
$(\ )_x$	x-direction component
$(\ )_y$	y-direction component
$(\ )_z$	z-direction component
$(\ )_r$	r-direction component
$(\ )_\theta$	θ-direction component
$(\ )_{agcppk}$	Air-gap center plane peak

Abbreviations

EV	Electric vehicle
WPT	Wireless power transfer
LCIPT	Loosely coupled inductive power transfer
CPT	Capacitive power transfer
SS	Series primary – series secondary resonant topology
SP	Series primary – parallel secondary resonant topology
PS	Parallel primary – series secondary resonant topology
PP	Parallel primary – parallel secondary resonant topology

ZVS	Zero voltage switching
ZCS	Zero current switching
EMF	Electromagnetic field
MMF	magnetomotive force
FEA	Finite element analysis
SSW	Surface spiral winding
CT	Copper tubing
SSPW	Surface spiral parallel winding
SSAPW	Surface spiral antiparallel winding
RF	Radio frequency
ESR	Equivalent series resistance
ABS	Acrylonitrile butadiene styrene
PC	Polycarbonate
RMS	Root mean square
SAR	Specific absorption rate
AWG	American wire gauge

Introduction

This section provides research motivation, an overview of the research, key research contributions, and a chapter-by-chapter list of the material discussed in this report.

Research Motivation

In the loosely coupled WPT systems applicable to electric vehicles, electromagnetic fields (EMF) between a transmitter coil and a receiver coil may cause severe injuries in adjacent human bodies and animals, such as electrostimulation of nerve and muscle, or thermal heating of tissues. In existing inductive WPT designs, although the magnetic field at a certain distance away from the coils is in compliance with safety regulations, the air-gap center region magnetic flux density is still far above safety limit, which is still a potential threat to human beings and animals. In addition, it can also generate huge eddy current losses if metal parts, like keys and cans, are placed in the air-gap region. Besides that, less attention is paid to the air-gap electric field, which is also very important and increases significantly as the operating frequency increases. There has been found no general design methodologies that focus on the air-gap center region magnetic and electric field safety issues, and power transfer efficiency simultaneously.

The magnetic component design methodologies in the literature focused on improving the coupling coefficient k or the quality factor Q independently to improve the coil-to-coil efficiency, which didn’t capture the fundamental terms that determine the coil-to-coil efficiency. In addition, it turned out that the magnetic component design methodologies in the literature are not scalable to multi-kW level because of the high magnetic and electric fields in the air-gap region. General power scaling laws with the air-gap region magnetic and electric fields satisfying the safety standard are necessary.

In the existing literature, active, passive, and reactive techniques were developed to reduce the leakage magnetic field in the near field outside of the winding. However, these techniques have a negligible effect on the air-gap region magnetic field, the effect on the air-gap region electric field was not investigated. Shielding techniques to reduce the whole air-gap region magnetic and electric fields without affecting the transfer efficiency must be developed.

Unavoidable misalignment between transmitter coil and receiver coil leads to efficiency reduction, reactive power and change of field distributions. The main research focus in existing literature is to maintain the power transfer efficiency. Less attention is paid to the change of field distributions and the reactive power component during misalignment.

Research Overviews

This dissertation develops a multi-kW loosely coupled inductive WPT system general design methodology that can inherently achieve low air-gap magnetic flux density, low air-gap electric field intensity, and high power transfer efficiency simultaneously. Analytical calculation models of the magnetic flux density and electric field intensity over the entire air-gap center plane are developed and evaluated via FEA. The effects of identified general design variables, such as coil radius, number of turns, inter-turn distance, transfer distance, and operating frequency, on the air-gap center plane peak magnetic flux density and peak electric field intensity, and the maximum coil-to-coil efficiency are investigated, general winding design guidelines to meet both magnetic field and electric field safety limits are presented.

Coil geometric solutions that can simultaneously achieve low copper loss, low dielectric losses, and low spatial voltage stress are required for high coil-to-coil efficiency and high power scalability. Previously, WEMPEC created, evaluated, and documented a surface spiral winding (SSW) design methodology to improve the quality factor and the coupling coefficient at MHz operating frequency. Dielectric losses are the limiting factor to further improve coil-to-coil power transfer efficiency. In addition, high spatial voltage stress between the first turn and the end turn limits the power scalability due to voltage breakdown. Further investigations of dielectric material properties and alternative coil geometries are performed in this work.

The dielectric losses are reduced by using low loss materials, by increasing the equivalent dielectric resistance, and by reducing the spatial voltage stress. Through emulating the 3D printed SSW using copper tubing, large spatial inter-turn clearance is achieved to reduce the dielectric losses, the spatial voltage stress, and the proximity effect. Through adding another winding in parallel, the surface spiral parallel winding design is developed to reduce ESR, thereby improving the coil-to-coil efficiency. Through twisting two parallel windings in opposite direction, the surface spiral antiparallel winding design is developed to equalize the spatial voltage stress between adjacent turns while maintaining a low ESR, which improves the power scalability limitation due to voltage breakdown.

In order to understand the limitations of the maximum power transmission capability within given magnetic and electric field limits, the analytical relationship between the air-gap power and the given field limited is derived. The fundamental limitations are identified as magnetic field. An active capacitor tuning method is developed to tune the air-gap magnetic field distribution, which can be used to reduce the mutual coupled magnetic field.

Besides the mutual coupled magnetic field, the power transfer capability within the safety standard was found to be fundamentally limited by the leakage field. Passive methods are developed to reduce the leakage flux. In particular, an “I” type shielding structure is proposed to shape the leakage and mutual flux paths to reduce the leakage field significantly without affecting the mutual coupling and confine the electric field within the shield structure. The shielding structure is optimized with reduced mass while maintaining nearly the same performance. In addition, the power-scaling law within the field safety limits is developed. Thermal modeling is developed based on the loss distribution analysis.

In the last part of this research, the loss distributions in the power converter are analyzed. Low loss capacitor and inductor online active tuning methods are developed to continuously tune the resonant compensation capacitance and inductance online to reduce the reactive power, and improve the output power capability, while maintaining the transfer efficiency and mitigating the change of field distribution during misalignment. Alternative resonant compensation techniques, such as LCC-CCL, are investigated to mitigate the variations of the field distributions during misalignment and provide another access to tune the field distributions actively.

Research Contributions

The primary contribution of this research is a general, scalable design methodology for loosely coupled inductive WPT systems that can inherently achieve low air-gap center plane magnetic flux density and low air-gap center plane electric field intensity within the IEEE C95.1-2005 electrostimulation and tissue heating safety standards, and high power transfer efficiency, even under misalignment conditions. The proposed methodology lays a good foundation for designing inductive WPT systems to charge the electric vehicles safely and efficiently.

Moreover, a surface spiral parallel winding configuration is proposed to reduce the ESR effectively while maintaining the same mutual inductance, thereby improving the coil-to-coil efficiency. A surface spiral antiparallel winding configuration is proposed to equalize the spatial voltage stress between adjacent turns while maintaining a low ESR and the same mutual inductance, which improves the power scalability limitation due to voltage breakdown between adjacent turns and the coil-to-coil efficiency.

In addition, a combination of new active and passive techniques is developed to reduce the axial magnetic flux and the leakage flux simultaneously, thereby reducing the air-gap center plane peak magnetic flux density. In particular, an “I” type shielding design is developed to shape the magnetic flux paths as desired to achieve low air-gap center region magnetic field and shield the electric field without affecting the power transfer efficiency. The shielding structure is optimized with reduced mass. In addition, the power-scaling law within the field safety limits is developed. Thermal modeling is developed based on the loss distribution analysis.

Last but not least, the loss distributions in the power converter are analyzed. Low loss capacitor and inductor online active tuning techniques are developed to continuously tune the resonant compensation capacitance and inductance online to reduce the reactive power, and improve the output power capability, while maintaining the power transfer efficiency and mitigating the change of field distribution during misalignment. Alternative compensation techniques are investigated to provide another access to tune the field distributions actively.

Summary of Chapters

Chapter 1 reviews the state-of-the-art human body safety regulations, winding geometric solutions, shield techniques, air-gap magnetic field and electric field distributions, system equivalent models, and system design methodologies.

Chapter 2 compares winding configurations with respect to power efficiency, and air-gap field distributions, and develops system equivalent circuit model, and analytical models for the inductive WPT system and the air-gap magnetic and electric fields.

Chapter 3 develops the system general design methodology and investigates the effects of identified general design variables, and verified the proposed general design methodology via FEA and experimental test.

Chapter 4 develops an active method and passive methods to reduce the air-gap region magnetic field, and proposes an "I" type shielding structure to reduce both magnetic field and electric field in the whole air-gap region.

Chapter 5 develops the general power scaling laws within the magnetic and electric field safety limits based on available degrees of freedom, and developed optimized shielding design with reduced mass, and develops the thermal modeling based on loss distribution analysis.

Chapter 6 develops capacitor and inductor online active tuning techniques to reduce the reactive power and mitigate the change of field distributions under misalignment. Alternative compensation techniques are investigated to tune the field distributions actively.

Chapter 7 contains the conclusions, and contributions of this research along with the recommended future work.

Chapter 1 State-of-the-Art Review

This chapter reviews the state-of-the-art of wireless power transfer technologies. In the first part of this chapter, a review on the state-of-the-art of far- and near-field wireless power transfer technologies is provided. Human body electromagnetic field (EMF) exposure safety guidelines are investigated in the following section. The review of state-of-the-art system safety problems is identified in the next section. Then modeling and design methodologies for loosely coupled inductive wireless power transfer systems are reviewed. The state-of-the-art review for low loss winding geometries is followed. Identified research opportunities in the wireless power transfer system are addressed in the final section.

1.1 Wireless power transfer systems

When the transfer distance between the transmitter and the receiver is comparable or longer than half of the characteristic lengths (e.g. diameter) of the primary and secondary coils, the system can be treated as a large distance wireless power transfer system. Electric vehicle wireless chargers, implantable biomedical devices wireless chargers, radio frequency (RF) sensors, and radio frequency identification (RFID) are examples of large distance wireless power transfer systems. On the other hand, the transfer distance is short if it is smaller than 0.1 times of the characteristic lengths of the primary and secondary coils. Contactless cellular phone battery chargers, contactless electric toothbrushes, conventional power transformers, DC and AC electric machines are examples of short distance wireless power transfer systems.

The most important difference between short and large distance air-gap WPT systems is the coupling coefficient between the primary coil and the secondary coil. In conventional short air-gap systems, coupling coefficients are generally greater than 0.5, which can be also treated as a strongly coupled system. Widely used transformer design technologies can be applied to strongly coupled systems. However, the coupling coefficients are normally lower than 0.2 for loosely coupled WPT systems. Due to low coupling coefficients, traditional transformer design methodologies, which result in low power transfer efficiency, are not applicable.

The following sections begin with a review of different types of wireless power transfer systems. Transmitting power over large air-gap can be accomplished by two different technologies depending on the operating frequencies: far- and near-field power transfer systems. A review of the definitions of far- and near-field regions is addressed in the subsequent section.

1.1.1 Far- and near-field regions

Based on the distance from a transmitting antenna, the surrounding area of the antenna can be categorized into three sub-regions: reactive near-field region, radiative near-field region, and far-field region as shown in Fig. 1-1 [1].

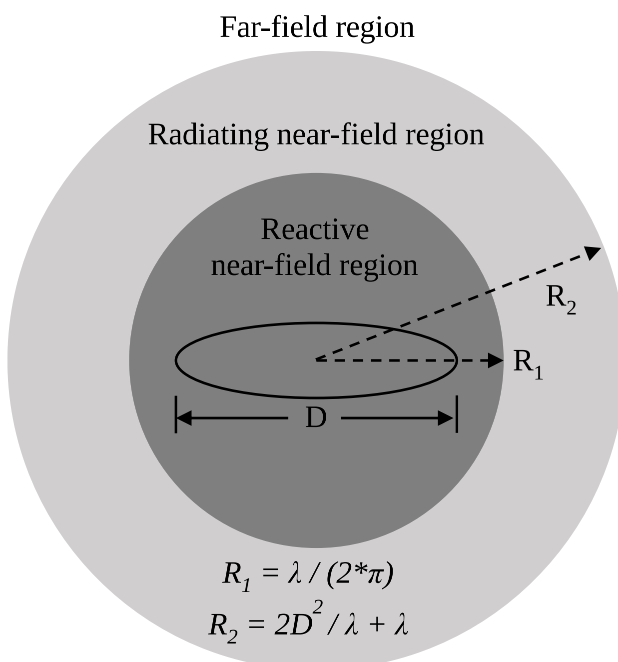

Fig. 1-1. Antenna regions depending on the distance from a transmitting antenna

The reactive near-field region is the zone where the reactive fields and their oscillating energy are predominant [1]. The boundary of this region is $0.62\sqrt{D^3/\lambda}$, where D is the diameter of the antenna, and λ is the wavelength of the electromagnetic fields [1][2]. If D << λ, near-field region boundary is approximated to $\lambda/(2\pi)$. Wavelength λ can be calculated using $\lambda = c / f$, where c is the speed of light, and f is the operating frequency.

Radiating near-field region is a transition area between the reactive near-field region and the far-field region. In this region, the reactive fields do not exist, but radiation fields predominate, and angular field distribution is dependent on the distance from the antenna [1]. The boundary of this region is from $\lambda/(2\pi)$ to $2D^2 / \lambda + \lambda$, where D is the largest dimension of the antenna [3].

Far-field region is the zone that radiating field is predominant and the angular field distribution is independent of the distance from the antenna. In this region, field components are transverse, and the angular distribution is independent of the radial distance. Electromagnetic fields in this area are nearly plane waves. The inner boundary of the far-field region is $2D^2 / \lambda + \lambda$, and the region extends to infinity [3]. In far-field region, the system must be analyzed using antenna theory and Maxwell equations.

Far-field WPT systems can be categorized into two systems depending on the operating principle: directional radiation antenna (microwave antennas) and power beaming by visible light (laser and photovoltaic cells). Near-field WPT systems can also be categorized into two systems depending on the coupling medium: electric field (capacitive) coupling and magnetic field (inductive) coupling. The diagram of classified WPT systems is shown in Fig. 1-2.

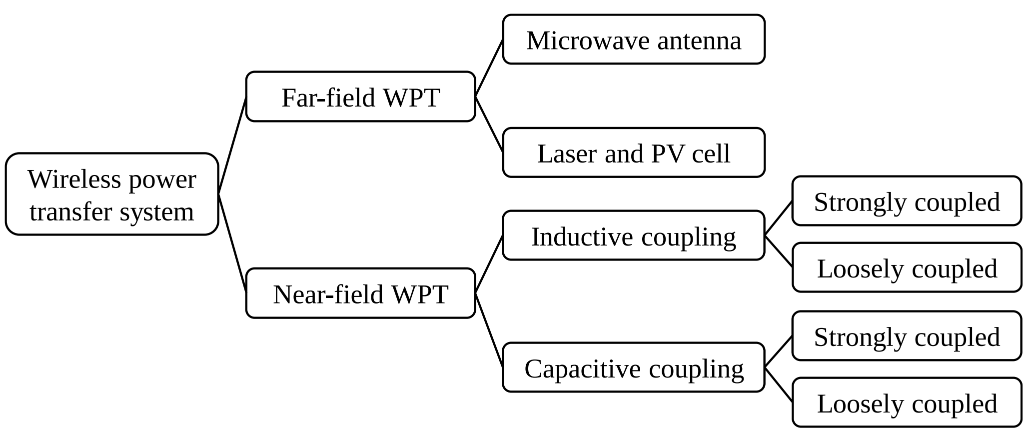

Fig. 1-2. Classification of wireless power transfer systems

1.1.2 Far-field wireless power transfer

Far-field WPT systems deliver power from one or more source antennas to one or more receiver antennas by electromagnetic field radiation. Typically, far-field systems operate at above 300 MHz to achieve high transfer efficiency. The size of $\lambda/4$ or $\lambda/2$ antennas is commonly used for radiation antennas. Since the wavelengths of the systems are comparable with the size of the antennas, Maxwell's equations and wave theories must be applied to analyze the system. Lumped element electric circuit theory cannot be used to analyze far-field systems.

Transmission antennas operating in the range of hundreds of MHz to tens of GHz are called "microwave antennas", and antennas operating over THz are referred as "laser beam antennas". A review on microwave and laser beaming antennas is following in the subsections.

- **Power radiation with microwave antennas**

The operating frequencies of microwave antennas are usually between hundreds of MHz and tens of GHz, thus the wavelengths of the fields are from multi-centimeter to multi-meter. Therefore, the first advantage is that they can transmit power over very large distances. Secondly, compact antennas can be designed due to high operating frequency.

However, radiation antennas have several disadvantages for using in large gap, high efficiency, kW level WPT systems. Firstly, it is difficult to achieve over 90% efficiency from transmitters to receivers, because radiated power is inversely proportional to the square of the distance from the antenna. Secondly, maximum radiation power to far-field is legally limited. A federal government regulation is given for human body safety. The maximum permissible radiated power limit for human body safety in the microwave frequency range in 10 W/m^2 [6][7]. Therefore, high power radiation is strictly limited by human safety issues.

Due to the poor efficiency and the human safety problems, microwave radiation systems typically have been employed in low power and large distance applications, such as RF sensors and RFID cards. High power radiation applications have been investigated only for special purposes, such as military or aerospace projects.

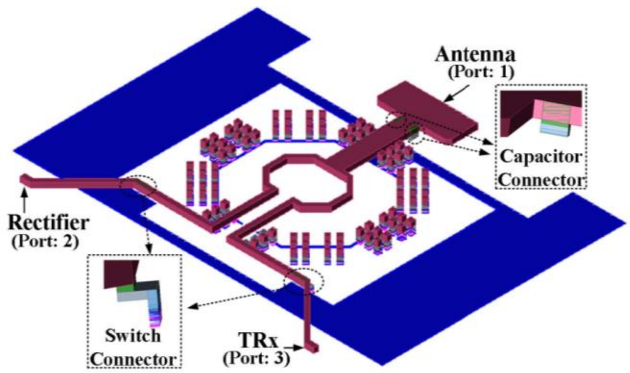

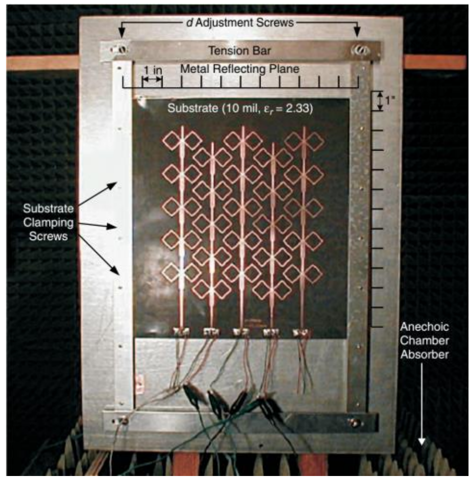

(a) Energy harvesting [4]　　　　(b) Solar power transmission [5]

Fig. 1-3. Pictures of microwave antennas for far-field transfer

It has been shown that high power transfer over a large distance is technically achievable by radiation at GHz frequencies. However, because the power transfer efficiency is lower than 90% and the radiated power is legally limited for human safety, the microwave radiation technique is not suitable for kW rated electric vehicle battery chargers.

- **Power-beaming with visible laser**

When the operating frequency is increased to the THz range, electromagnetic fields become a visible laser. WPT can be achieved by using laser beaming as a transmitter and photovoltaic (PV) cells as receivers [8][9][10]. The wavelength is from a few micrometers to nanometers.

In laser beaming WPT systems, electric energy is converted into optical energy through laser diodes, and then optical energy is beamed to the far-field area, PV cells located in far-field regions convert optical energy to electric energy.

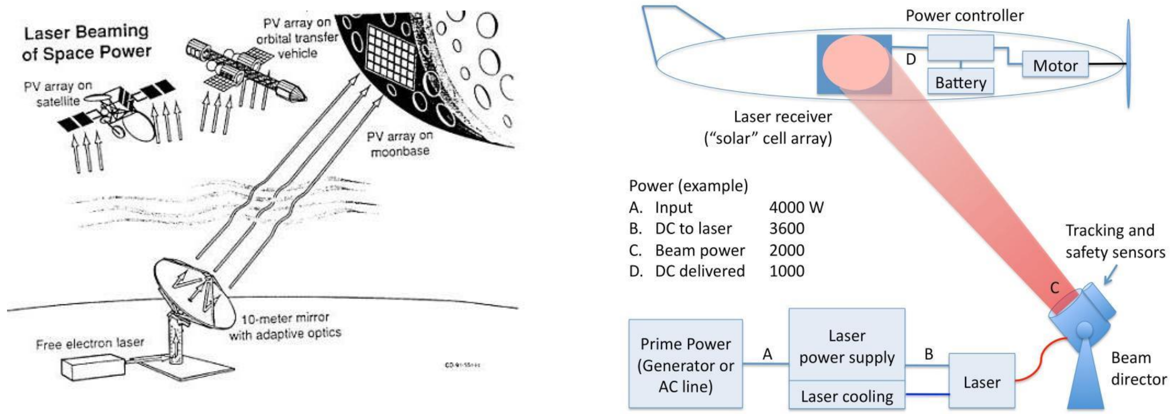

(a) Laser beaming power transfer over space [8] (b) Laser power for UAV [9]

Fig. 1-4. Conceptual diagrams of laser beaming power transfer for far-field

Compared with microwave systems, the laser-beaming systems have advantages as follows: (1) Longer transfer distance can be achieved due to THz operation. (2) The smaller size of transmitters and receivers can be fit into small devices. (3) Laser-beaming system can be used in some special environments where RF interference with other devices is problematic.

However, it has several severe drawbacks to be used in high power and high efficiency systems. Firstly, the energy conversion efficiency between electric energy and optical energy is very low. The efficiency of solid state laser sources was lower than 25% at hundreds of Watts output [11][12]. Flat PV arrays with GaAs or Si have an efficiency of 50% and thin-film arrays made with amorphous Si or CdTe have conversion efficiency less than 20%. Secondly, precise alignment between the transmitter and the receiver is required to maximize transferred power, which means the misalignment tolerance of the system is very poor. Thirdly, like microwave antennas, critical human body hazard problems exist and high power applications are used in special controlled environments such as military or aerospace projects.

In conclusion, kW power level WPT in tens of centimeters using power beaming at THz is technically achievable. However, due to low efficiency and potential hazards to the human body, laser beaming WPT system is not suitable for using as electric vehicle battery chargers.

1.1.3 Near-field wireless power transfer

Near-field WPT systems deliver power from one or more transmitting antennas to one or more receiving antennas by magnetic or electric coupling of the antennas. Receiving antennas are located in the near-field region of transmitting antennas. Their operating frequencies are in the range of 10 kHz to 100 MHz and wavelengths are from 3 m to 30 km.

There are two ways of coupling in near-field WPT: magnetic coupling and electric coupling. Near-field WPT via magnetic field coupling is called “inductive power transfer”. It’s called “capacitive power transfer” if the transmitter and the receiver are electrically coupled. Since the electromagnetic field in the near-field region in non-radiative but reactive, radiation loss is very small. Dominant losses are coming from dielectric losses of insulation materials, hysteresis and eddy current losses of magnetic materials, and Ohmic losses in conductors.

Since the characteristic lengths of transmitters and receivers are less than 1/10 of the wavelength in most typical near-field systems, lumped parameter approximations can be applied to these systems [13].

Inductive WPT system can be approximated by two inductors with mutually coupled inductance as shown in Fig. 1-5 (a), copper losses of the coils are modeled as the equivalent resistance of R_{cond1} and R_{cond2}, radiated power from the transmitter and receiver coils are modeled as R_{rad1} and R_{rad2}.

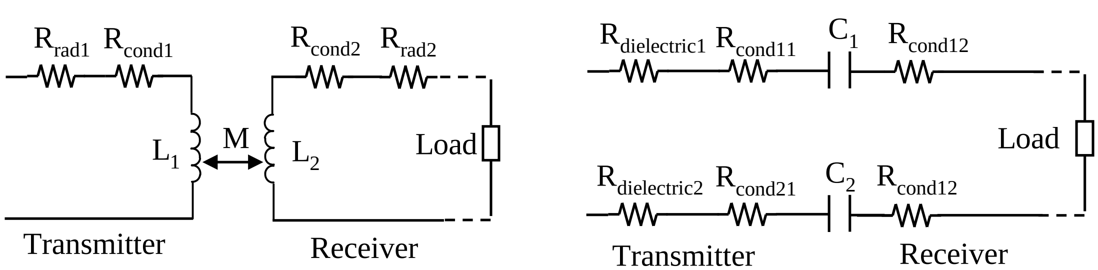

(a) Inductively coupled WPT system (b) Capacitively coupled WPT system

Fig. 1-5. Lumped circuit approximation of near-field WPT systems

Capacitive WPT system can be approximated using two lumped capacitors at forward and return paths as shown in Fig. 1-5 (b), copper losses of the capacitors are modeled as equivalent resistors R_{cond11}, R_{cond12}, R_{cond21}, and R_{cond22}. Dielectric losses of the high permittivity materials of the capacitors are represented as $R_{dielectric1}$ and $R_{dielectric2}$.

The fundamental principle of inductive WPT system is Faraday's law of induction. Oscillating magnetic fields of transmitters induce an electrical potential difference in the receiver, and induced voltage in the receiver winding delivers real power to the load. Strongly coupled and loosely coupled inductive WPT system are introduced in the following subsections.

- **Strongly coupled inductive wireless power transfer**

Strongly coupled inductive WPT system is the most common form of near-field WPT systems. Conventional transformers, DC and AC electric motors, contactless battery charger for electric toothbrushes, and cellular phones are typical strongly coupled inductive power transfer systems [14][15][16][17].

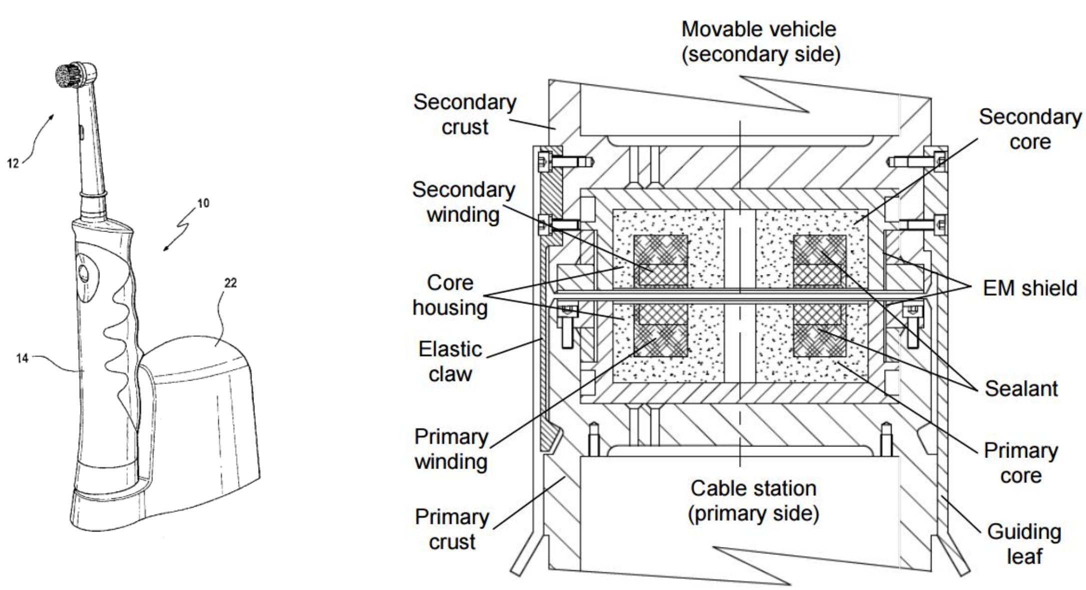

(a) Contactless toothbrush [14] (b) Assembly of the electromagnetic coupler [17]

Fig. 1-6. Examples of strongly coupled systems

In strongly coupled or closely coupled systems, the coupling coefficient is close to unity since magnetic cores are used as a flux guide and the transfer distance is very small compared with the characteristic length of the transmitter and receiver [17]. The leakage inductance is much smaller than mutual inductance. The coupling coefficient can be calculated using

$$k = \frac{M}{\sqrt{L_1 L_2}} \tag{1.1}$$

Where, M is the mutual inductance between transmitter and receiver, L_1 and L_2 are the self-inductances of transmitter and receiver, respectively.

Application of strongly coupled systems have a very broad range of power ratings and the system efficiencies are usually greater than 90% at rated operation condition. However, the efficiency is a strong function of distance and the sizes of transmitter and receiver have to be very large to achieve high coupling coefficient. For example, the diameters of the transmitter and receiver have to be larger than 5 m to be a strongly coupled system at 30 cm transfer distance.

In summary, high power, efficient near-field power transfer can be achieved with strongly coupled systems. They are effective for a few centimeter distances and ineffective for large distance WPT applications.

- **Loosely coupled inductive wireless power transfer**

Compared with strongly coupled inductive WPT system, the coupling coefficients of loosely coupled systems are generally less than 0.2 [18][19][20][21], the mutual inductance is almost negligible compared with the leakage inductance, and the coupling coefficient decreases rapidly as the transfer distance increases. Because of the low coupling coefficient, such systems have very low power transfer efficiency.

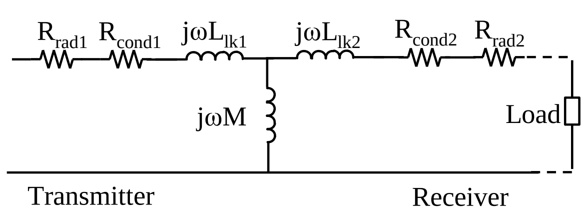

(a) General mutually coupled system

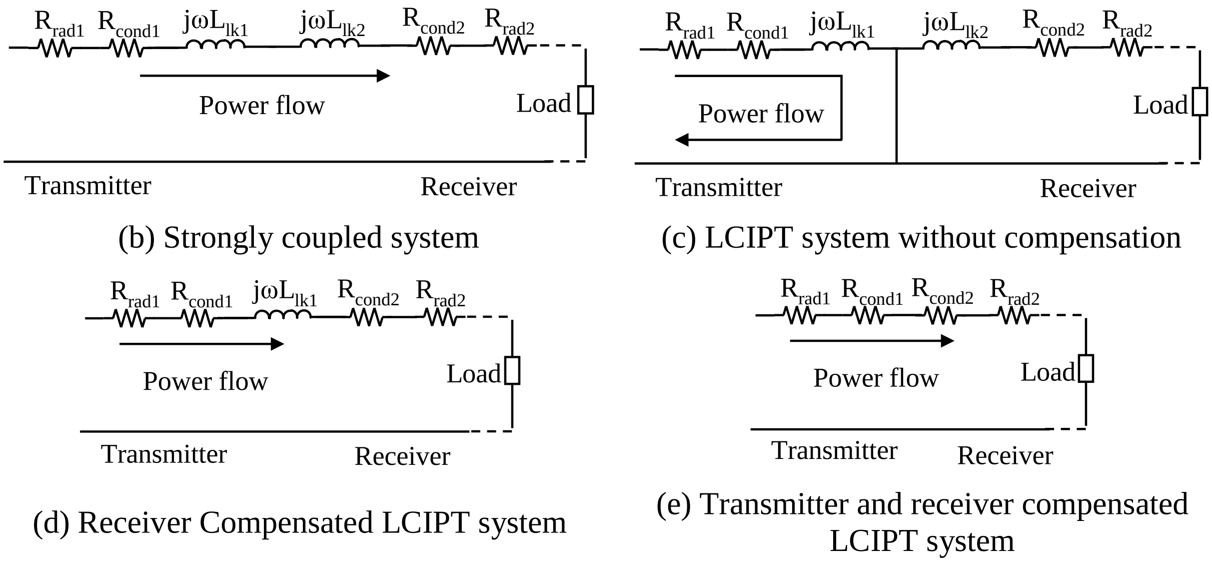

(b) Strongly coupled system

(c) LCIPT system without compensation

(d) Receiver Compensated LCIPT system

(e) Transmitter and receiver compensated LCIPT system

Fig. 1-7. Approximation of near-field inductive power transfer systems

As shown in Fig. 1-7, in the strongly coupled systems, the mutual inductance term can be approximated as an open network because the impedance of the mutual inductance is much larger than the leakage inductance. Therefore, input power from the primary side is transmitted to the secondary side with high efficiency. However, in the loosely coupled systems, the mutual inductance can be treated as a short circuit because the impedance of mutual inductance is much smaller than the impedance of leakage inductance, the transmitted power from the primary side to the secondary side is almost negligible.

In order to improve power transfer efficiency and power capacity, series or parallel resonant tanks can be implemented by adding capacitors in series or in parallel with both/either the transmitter and/or the receiver [22]. This creates a magnetically coupled resonant large air-gap WPT system. If the receiver resonant tank is used, self- and mutual impedance of the receiver is compensated as shown in Fig. 1-7 (d). A large amount of the input power flows to the receiver side due to the receiver compensation. Therefore, the power transfer efficiency can be significantly increased.

However, the large transmitter leakage impedance hinders an additional increase in power capacity of the system in Fig. 1-7 (d). By adding a capacitor to the transmitter coil, the large leakage impedance of the coil is compensated in Fig. 1-7 (e). Since it is resistive at the resonant frequency, the power factor of the system is close to 1 and the power transfer capacity is enhanced even further.

The advantages of loosely coupled resonant inductive WPT systems are that it is good for high power and high efficiency systems, and the system can transmit power over large distances. However, because of large leakage flux, the first drawback of the system is electromagnetic interference (EMI) and electromagnetic compatibility (EMC) issues to adjacent electric devices. Secondly, high reactive power at the transmitter and receiver resonant tank is a problem in terms of system design for high voltage capability. Finally, human body safety issues have to be investigated in such systems because of high reactive energy in the air-gap.

Large air-gap, resonant WPT systems have been investigated not only for small power applications but also for high power applications. Rated power is below tens of Watts, the coupling coefficient is below 0.2, and efficiency is over 80% in many implantable biomedical devices [23]-[26]. On the other side, rated power is multi-kW, and the distance is tens of centimeters, and efficiency is 70~80% in case of electric vehicle chargers [27]-[31].

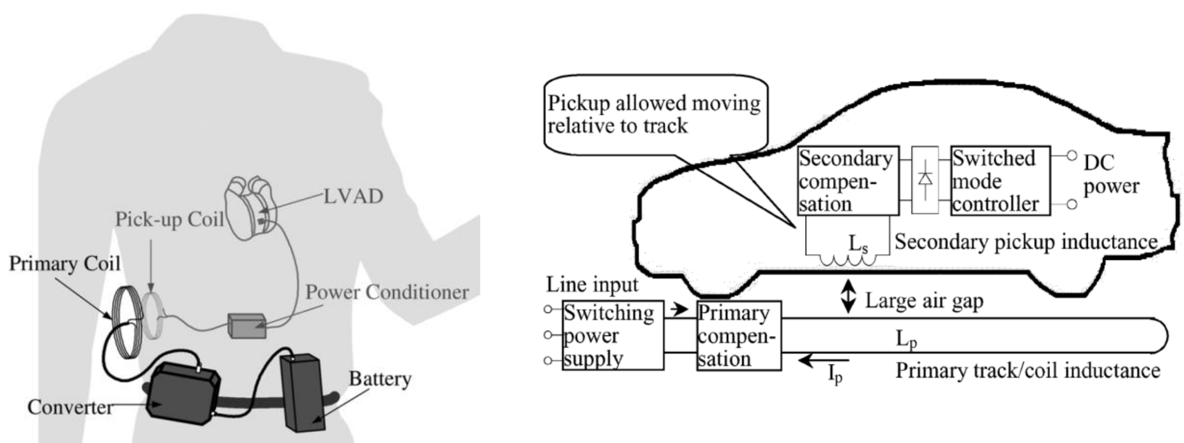

(a) Biomedical devices charger [23] (b) Electric vehicle battery charger [27]

Fig. 1-8. Examples of loosely coupled systems

In summary, loosely coupled resonant systems have been used for tens of centimeters air-gap WPT with 80% efficiency. Therefore, loosely coupled resonant systems are suitable for

20~30 cm, over 90% efficiency, kW power transfer systems. Furthermore, since the transmitters and the receivers are working in the near-field region and the operating frequency is up to tens of MHz, radiated power to the air is negligible. Unlike far-field WPT systems, loosely coupled systems are safe from radiation.

In addition, loosely coupled systems have to be evaluated for EMI/EMC because of large leakage flux. Exceedingly high reactive power of transmitters and receivers has to be considered in the system. Finally, human body safety issues caused by the high leakage flux in the air-gap have to be considered as well.

- **Capacitive wireless power transfer**

Instead of using a magnetic field, capacitive WPT system utilizes electric field coupling between the transmitter and receiver plates [32]-[35]. Fig. 1-9 shows overall system diagram of a capacitive WPT system [32].

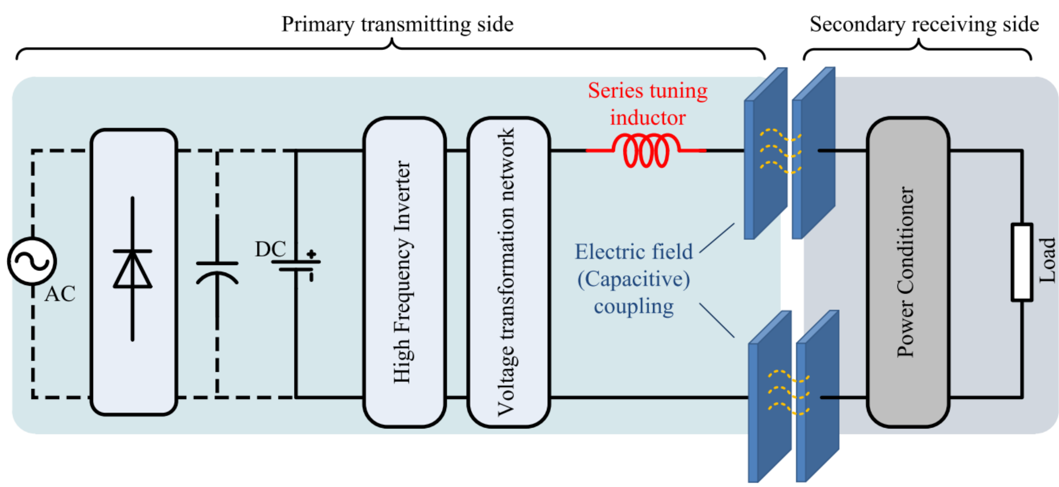

Fig. 1-9. Conceptual diagram of capacitive WPT systems

Advantages of capacitive power transfer systems are, 1) since electric fields are confined in the air-gap, electromagnetic interference (EMI) and electromagnetic compatibility (EMC) problem can be minimized without field shielding [34], 2) unlike a magnetic field coupling system, capacitive power transfer system can transmit power over metal barriers [35].

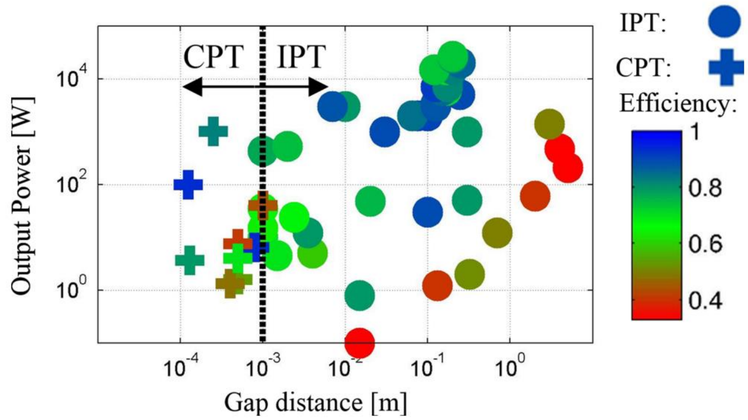

Fig. 1-10. Comparison of IPT and CPT systems output power versus gap distance

Comparison of inductive power transfer (IPT) and capacitive power transfer (CPT) systems power transfer capability versus transmitter to receiver gap distance with efficiency indicated by data point color is shown in Fig. 1-10 [36]. The figure clearly indicates that the IPT techniques are generally applicable in small to large gap regions (i.e., > 1mm), while CPT techniques are applicable in very small to small gap regions (i.e., < 1 mm). It also indicates that both IPT and CPT can achieve ≥ 90% efficiency at kW levels in their respective gap ranges.

One drawback of the capacitive power transfer system is low efficiency in large air-gap applications. In order to achieve over 90% efficiency, electric plates have to be very large. For example, the required plates of capacitive power transfer system in [35] for 90% efficiency are greater than 1 m × 1 m to transmit power over 1 mm gap at 22 kHz. If the operating frequency is increased to 1 MHz, required size of the plates decreased to 16 cm × 16 cm, but the required size of the plates is still very large compared with the 1 mm air-gap. A multiple-plates solution is proposed for large air-gap applications [37], and the power transfer efficiency is 85.87% at 1.88 kW output with a 150 mm air-gap distance, which is far lower than power transfer efficiency (96% [38]) of inductive WPT systems.

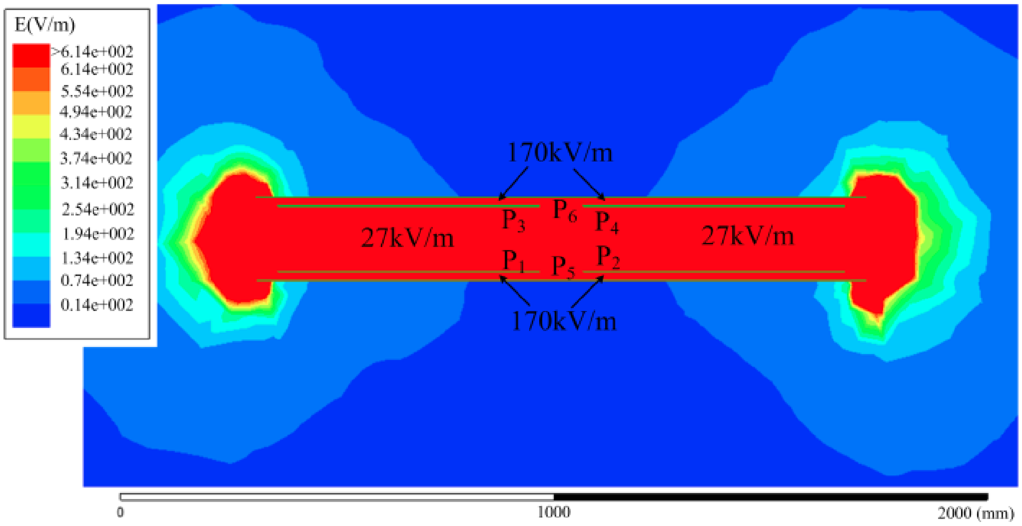

Fig. 1-11. Electric field distribution for a six-plate capacitive coupler transferring 2 kW through 150 mm air-gap at 1 MHz

Furthermore, for large air-gap capacitive power transfer system [37], the electric field within the air-gap, voltage stress between different plates, is higher than tens kV/m for high power application, which is unsafe to human beings and animals in the air-gap region. As shown in Fig. 1-11, when transferring 2 kW through 150 mm air-gap under 1 MHz, the peak electric field in the air-gap is 27kV/m [39]. In addition, capacitive power transfer efficiency is very sensitive to the alignment of the plates [40]. Moreover, the required inductance to achieve resonance is very large in capacitive power transfer systems. Copper and iron losses of the inductor will decrease overall power transfer efficiency severely at MHz frequency, and if the air-core inductors are used, there should be no metal parts around the inductors.

In conclusion, efficient and safe high power transfer system with large air-gap is very hard to achieve with capacitive WPT systems, which are more suitable for small gap, and low power applications.

1.1.4 Summary of wireless power transfer technologies

In this section, properties of various potential technologies for large air-gap wireless systems have been discussed along with their benefits and drawbacks specific to large air-gap, high power transfer system applications.

Far-field transfer technologies are able to transmit kW from a few centimeters to a few kilometers, but the transfer efficiency is usually lower than 50%, and the maximum radiation power is restricted by governments for safety reasons. Hence, far-field WPT systems are not applicable solutions for multi-kW commercial products.

Near-field strongly coupled non-resonant inductive WPT systems are typically used for small air-gap, high power, and over 90% efficiency systems. In order to achieve a strongly coupled system with 30 cm transfer distance, the diameter of a transmitter and a receiver must be bigger than 3 m. For this reason, the strongly coupled WPT systems are not suitable for large air-gap power transfer applications.

Small air-gap capacitive WPT systems have better EMI/EMC performance than inductive WPT systems, large air-gap capacitive systems are hard to achieve high efficiency and the electric field between plates is difficult to reduce within safety limit, therefore, the capacitive systems are more suitable for small gap, and low power applications.

Loosely coupled resonant inductive WPT systems have been used for large distance, kW level applications. The coupling coefficient between a transmitter and a receiver is usually not larger than 0.2. The resonance in the transmitter and the receiver enables the WPT system to achieve high power level and high efficiency with low coupling coefficient.

Therefore, the loosely coupled resonant inductive WPT systems are currently the most relevant technology for the large distance, over 90% efficiency, and multi-kW level applications. However, it should be noted that they still have several challenges:

1) High air-gap magnetic flux density and high air-gap electric field intensity are potentially dangerous to humans and animals
2) Efficiency drop due to misalignment between the transmitter and the receiver
3) Power scaling law considering the magnetic field and electric field safety regulations
4) Magnetic field and electric field distributions under misalignment

5) Electromagnetic interference (EMI/EMC) with adjacent electric devices

1.2 Human body safety regulations for RF magnetic field and electric field exposure

1.2.1 Introduction

Electromagnetic fields generated by WPT system have adverse effects on the human body, such as electrostimulation of nerve and muscle system or thermal heating of tissues [6][7][41]. As the power rating increases, intensive magnetic and electric fields can cause severe injuries in an adjacent human body and system designers must investigate the potential damage.

According to the literature [7], electrostimulation of nerve and muscle system is the major concern at low frequency (below 100 kHz) and tissue heating is critical at high frequency (above 5 MHz). In the transition region (100 kHz to 5 MHz), both effects can cause serious problems. International regulations of maximum permissible exposure (MPE) limit of RF fields to human body exposure are established. Most countries have their own RF field exposure limits. In this section, international and individual countries RF safety regulations are reviewed.

1.2.2 IEEE standard C95.1 - 2005

One of the most generally accepted standards in IEEE (Institute of Electrical and Electronic Engineers) standard C95.1 and its addendums [7]. In this standard, two different kinds of regulations are defined in order to avoid electrostimulation effect at low frequency and thermal heating effect at high frequency.

- **Basic restrictions to avoid electrostimulation**

IEEE C95.1 restricts electric and magnetic fields energy within the biological tissue (*in situ*) for minimum electrostimulation and thermal heating. They are called basic restrictions (BRs). Because it is difficult to measure *in situ* fields in practice, equivalent MPE limits for electric and magnetic fields are listed instead of BRs. MPE limits for the magnetic field from 3 kHz to 5 MHz are shown in Table 1-1.

Table 1-1. MPE for exposure of head and torso, 3 kHz to 5 MHz

Frequency range (kHz)	General public		Persons in controlled environments	
	B_{rms} (mT)	H_{rms} (A/m)	B_{rms} (mT)	H_{rms} (A/m)
3.0 – 3.35	0.687/f	547/f	2.06/f	1640/f
3.35 – 5000	0.205	163	0.615	490

Note: f is expressed in kHz.

The averaging time for the measurement to determine the allowed field levels is 0.2 s. It should be noted that the averaging time is very short, since injuries by electrostimulation are instantaneous.

From 3.35 kHz to 5 MHz that most WPT systems are operating at, allowed magnetic flux density for head and torso is 0.205 mT for the general public, and it is 0.615 mT for the persons in controlled environments. The MPEs for exposure of limbs from 3 kHz to 5 MHz are shown in Table 1-2.

Table 1-2. MPE for exposure of limbs, 3 kHz to 5 MHz

Frequency range (kHz)	General public		Persons in controlled environments	
	B_{rms} (mT)	H_{rms} (A/m)	B_{rms} (mT)	H_{rms} (A/m)
3.0 – 3.35	3.79/f	3016/f	3.79/f	3016/f
3.35 – 5000	1.13	900	1.13	900

Note: f is expressed in kHz.

From 3.35 kHz to 5 MHz that most WPT systems are operating at, allowed magnetic flux density for limbs is 1.13 mT for general public and persons in controlled environments, which is about 5 times higher than the fields allowed for head and torso in general public environment.

- **Basic restrictions to avoid thermal heating**

It has been demonstrated that detrimental temperature increase of whole- and localized body exposure is more important than the electrostimulation of the nerve and muscle systems at high operating frequency for long time operation. Behavioral disruption in rats and non-human primates exposed to RF energy was often associated with a core body temperature increase of about 1 °C above normal [7].

Specific absorption rate (SAR) is the key metric that is directly related to the temperature rise with the dissipated energy in a human body. According to IEEE C95.1, SAR is “The time derivation of the incremental energy (*dW*) absorbed by an incremental mass (*dm*) contained in a volume element (*dV*) of given density (ρ).” The unit of SAR is the Watt per kilogram (W/kg). The SAR can be related to the electric field and to the increase in temperature at a point by (1.2).

$$\mathrm{SAR} = \frac{\mathrm{d}}{\mathrm{dt}}\left(\frac{\mathrm{d}W}{\mathrm{d}m}\right) = \frac{\mathrm{d}}{\mathrm{dt}}\left(\frac{\mathrm{d}W}{\rho \mathrm{d}V}\right) = \frac{\sigma|\mathrm{E}|^2}{\rho} = \mathrm{c}\left.\frac{\Delta T}{\Delta t}\right|_{t=0} \qquad (1.2)$$

Where σ is the tissue conductivity (S/m), ρ is the tissue mass density (kg/m^3), E is the RMS electric field strength in tissue (V/m), ΔT is the change in temperature (°C), Δt is the duration of exposure (s), and c is specific heat capacity (J/kg°C). A SAR of 58.6 W/kg is corresponding to a temperature increase of 1 °C/min of a high-water-content tissue [7]. IEEE C95.1 standard suggests basic restrictions for the whole- and localized body exposure as shown in Table 1-3.

Table 1-3. BRs for frequencies between 100 kHz and 3 GHz

		General public SAR (W/kg)	Persons in controlled environments SAR (W/kg)
Whole-body exposure	Whole-body average (WBA)	0.08	0.4
Localized exposure	Localized (peak spatial-average)	2	10
Localized exposure	Extremities and pinnae	4	20

Note: Localized exposure is averaged over any 10 g of tissue.

Localized exposure SAR restrictions are important in case of a human body is subjected immediately to the air-gap region. For example, if a person put his head in the air-gap region of a WPT system, SAR in the head should be less than 2 W/kg for the general public and 10 W/kg for the persons in controlled environments. Whole-body exposure restrictions are also important if a human body is subjected to uniform electromagnetic fields generated by the system.

Electromagnetic fields of a WPT system were approached to a uniform value if the distance from the system is 5 times larger than the size of the coils. Therefore, whole-body exposure SAR values have to be evaluated for a person at a far distance. Because of the difficulties in measuring whole-body average SAR of tissues, equivalent MPE limits to protect against adverse effects associated with thermal heating are shown in Table 1-4 and Table 1-5.

Table 1-4. MPE for the people in controlled environments

Frequency (MHz)	RMS electric field strength (E, V/m)	RMS magnetic field strength (H, A/m)	RMS power density (S) E-field, H-field (W/m^2)	Averaging time $\|E\|^2$, $\|H\|^2$ or S (min)
0.1 – 1.0	1842	$16.3/f_M$	$(9000, 100\,000/f_M^2)$	6
1.0 – 30	$1842/f_M$	$16.3/f_M$	$(9000/f_M^2, 100\,000/f_M^2)$	6
30 – 100	61.4	$16.3/f_M$	$(10, 100\,000/f_M^2)$	6
100 – 300	61.4	0.163	10	6
300 – 3000	-	-	$f_M/30$	6

Note: f_M is the frequency in MHz.

Table 1-5. MPE for the general public when an RF safety program is unavailable

Frequency (MHz)	RMS electric field strength (E, V/m)	RMS magnetic field strength (H, A/m)	RMS power density (S) E-field, H-field (W/m^2)	Averaging time $\|E\|^2$, $\|H\|^2$ or S (min)	
0.1 – 1.34	614	$16.3/f_M$	$(1000, 100\,000/f_M^2)$	6	6
1.34 – 3	$823.8/f_M$	$16.3/f_M$	$(1800/f_M^2, 100\,000/f_M^2)$	$f_M^2/0.3$	6
3 – 30	$823.8/f_M$	$16.3/f_M$	$(1800/f_M^2, 100\,000/f_M^2)$	30	6
30 – 100	27.5	$158.3/f_M^{1.668}$	$(2, 9\,400\,000/f_M^{3.336})$	30	$0.0636 * f_M^{1.337}$
100 – 400	27.5	0.0729	2	30	30
400 – 2000	-	-	$f_M/200$	30	

Note: f_M is the frequency in MHz. For non-uniform exposures, the mean values of the exposure fields, as obtained by spatially averaging the squares of the flux densities or averaging the power densities over an area equivalent to the vertical cross-section of the human body are compared with the MPEs in the table.

The detrimental effects, SAR and electrostimulation of tissues cannot be tested experimentally, and MPE limits are difficult to be used for near-field WPT systems due to the strong non-uniform fields in the air-gap. Consequently, researchers use full wave finite element analysis (FEA) simulation tools, such as ANSYS HFSS, CST Microwave studio, and SEMCAD etc. in order to get *in situ* magnetic flux density, electric field strength and SARs [42][43][44][45]. Using FEA software, human body safety problems of a large air-gap, multi-kW WPT system will be investigated in the later part of this thesis.

1.2.3 ICNIRP Guidelines - 1998

In 1998, the International Commission on Non-Ionizing Radiation Protection (ICNIRP) published guidelines for electromagnetic fields exposure. The publications on biological effects from exposure to AC fields have been reviewed by UNEP (United Nations Environment Programme) / WHO (World Health Organization) / IRPA (International Radiation Protection Association). Europe countries follow ICNIRP guidelines and the WHO recommends satisfying the guidelines as well.

ICNIRP suggested two types of guidelines: induced current density and SAR. According to literature in the guideline, induced current density is important at low frequency (below 100 kHz), and SAR is important at high frequency (Over 10 MHz).

Table 1-6 shows the basic restrictions for AC fields in order to protect from electrostimulation and heating injuries. It should be noted that from 1 kHz the allowed current density increases as the operating frequency increases for both general public and occupational exposure as shown in Table 1-6 and Fig. 1-12.

Table 1-6. BRs for frequencies up to 10 GHz

Exposure characteristics	Frequency range	Current density for head and trunk (mA/m^2, rms)	Whole-body average SAR (W/kg)	Localized SAR (head and trunk) (W/kg)	Localized SAR (limbs) (W/kg)
Occupational exposure	1 kHz – 100 kHz	f/100	-	-	-
	100 kHz – 10 MHz	f/100	0.4	10	20
	10 MHz – 10 GHz	-	0.4	10	20

General public exposure	1 kHz – 100 kHz	f/500	-	-	-
	100 kHz – 10 MHz	f/500	0.08	2	4
	10 MHz – 10 GHz	-	0.08	2	4

Note: f is the frequency in Hz.

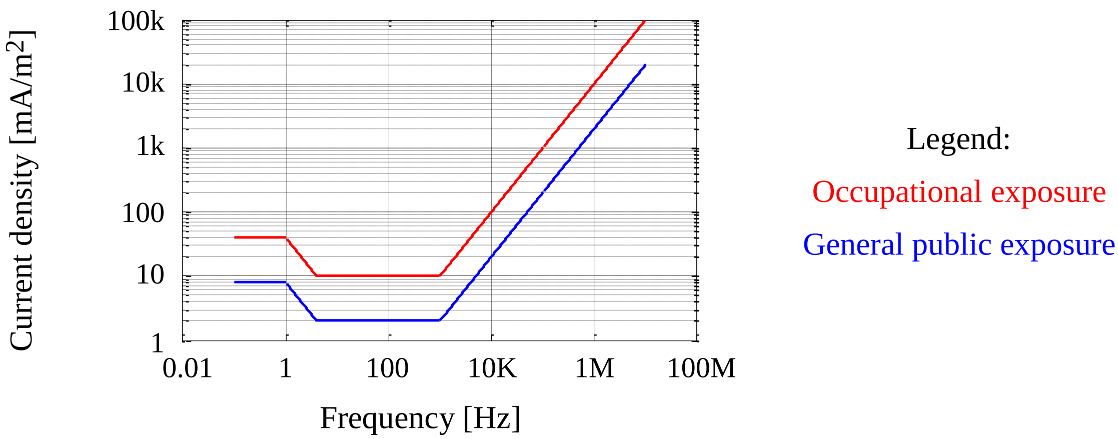

Fig. 1-12. Induced current density limit for head and torso in ICNIRP guidelines

Instead of BRs, electric and magnetic field strength levels are listed in Table 1-7. Compared with IEEE C95.1-2005, SAR limits are the same while induced current limits are established instead of *in situ* electric field limits in IEEE C95.1-2005. In addition, electric field strength and magnetic field strength permissible limits decrease as the frequency increases because the thermal heating problem is more severe at high frequency.

Table 1-7. Reference levels for occupational and general public exposure

Exposure characteristics	Frequency range	Electric field strength (V/m)	Magnetic field strength (A/m)
Occupational exposure	0.82 – 65 kHz	610	24.4
	0.065 – 1 MHz	610	1.6/f
	1 – 10 MHz	610/f	1.6/f
	10 – 400 MHz	61	0.16
General public exposure	0.8 – 3 kHz	250/f	5
	3 – 150 kHz	87	5
	0.15 – 1 MHz	87	0.73/f
	1 – 10 MHz	$87/f^{1/2}$	0.73/f
	10 – 400 MHz	28	0.073

Note: f is the frequency in MHz.

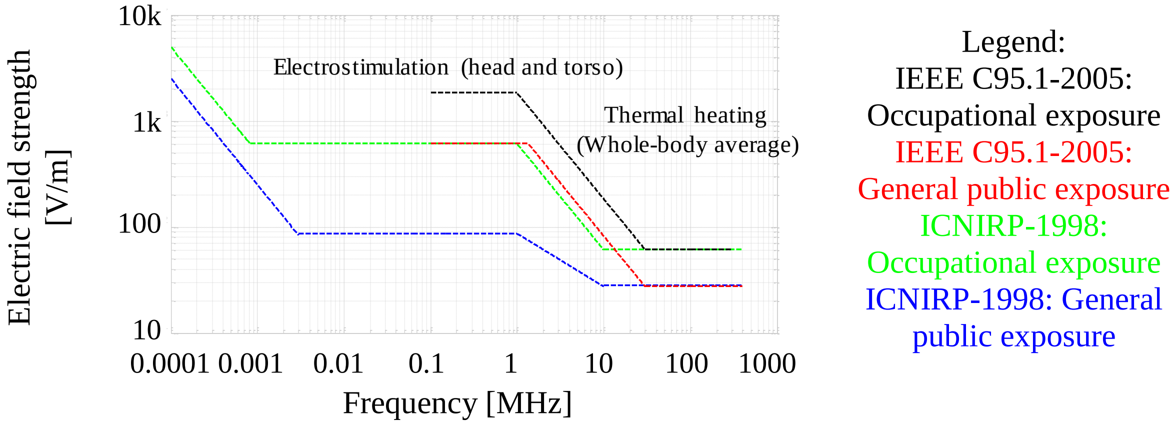

(a) Electric field strength limits

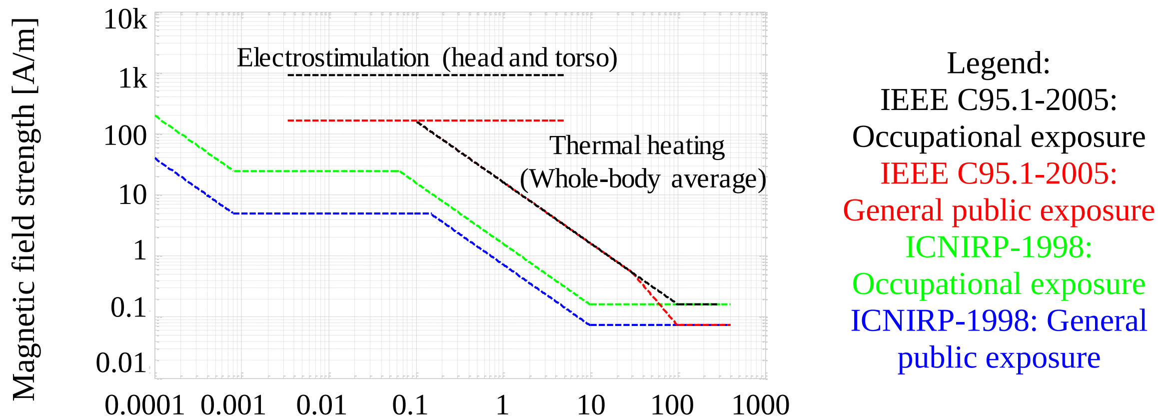

(b) Magnetic field strength limits

Fig. 1-13. RMS maximum permissible exposure limits illustration

It should be noted than ICNIRP 1998 regulation is more conservative than IEEE C95.1-2005 standard for both occupational and general public exposures. For example, when the operating frequency is 3.7 MHz, electric field strength limit, magnetic field strength limit and magnetic flux density of ICNIRP 1998 under occupational exposure condition are 165 V/m, 0.432 A/m and 0.543 µT, respectively, while electric field strength limit, magnetic field strength limit and magnetic flux density of IEEE C95.1-2005 under occupational exposure condition are 498 V/m, 4.405 A/m and 5.533 µT, respectively. However, the basis limits for the IEEE C95.1-2005 standard to protect against established adverse health effects for whole body exposure in human beings is consistent with the ICNIRP guidelines. For localized exposure, the IEEE C95.1-2005 standard uses the recent scientific information to protect against adverse effects in the tissues most sensitive to thermal effects [7].

1.2.4 ICNIRP Guidelines - 2010

In 2010, ICNIRP revised the exposure standard to time-varying electric and magnetic fields from 1 Hz to 100 kHz and increased the reference level significantly.

The reference levels for occupational exposure and general public exposure to the time-varying electric field and magnetic field (unperturbed RMS values) from 1 Hz to 10 MHz in ICNIRP guidelines - 2010 are listed in Table 1-8.

Table 1-8. Reference levels for occupational exposure and general public exposure to time-varying electric and magnetic fields (unperturbed RMS values)

Exposure characteristics	Frequency range	Electric field strength (kV/m)	Magnetic field strength (A/m)
Occupational exposure	1 Hz – 8 Hz	20	$1.63 \times 10^5/f^2$
	8 Hz – 25 Hz	20	$2 \times 10^4/f$
	25 Hz – 300 Hz	$5 \times 10^2/f$	8×10^2
	300 Hz – 3 kHz	$5 \times 10^2/f$	$2.4 \times 10^5/f$
	3 kHz – 10 MHz	1.7×10^{-1}	80
General public exposure	1 Hz – 8 Hz	5	$3.2 \times 10^4/f^2$
	8 Hz – 25 Hz	5	$4 \times 10^3/f$
	25 Hz – 50 Hz	5	1.6×10^2
	50 Hz – 400 Hz	$2.5 \times 10^2/f$	1.6×10^2
	400 Hz – 3 kHz	$2.5 \times 10^2/f$	$6.4 \times 10^4/f$
	3 kHz – 10 MHz	8.3×10^{-2}	21

Note: (1) f in Hz. (2) See separate sections on guidelines for advice on non-sinusoidal and multiple frequency exposures. (3) In the frequency range above 100 kHz, RF specific reference levels need to be considered additionally.

In frequency range above 100 kHz, RF specific reference levels need to be considered additionally, such as the ICNIRP-1998 and the IEEE C95.1-2005 standard, since above 100 kHz, tissues heating should be taken into consideration. The magnetic field and electric safety levels listed in Table 1-8 can only be regarded as the electrostimulation safety limit.

Compared with the IEEE C95.1-2005, the ICNIRP-2010 for 1 Hz to 100 kHz is still conservative. For frequency range above 100 kHz, the ICNIRP organization is still working on it and will release it soon, ICNIRP-1998 should be used for above 100 kHz evaluation.

1.2.5 Summary of human body safety guidelines review

Two widely adopted safety guidelines have been reviewed in this section: IEEE C95.1 and ICNIRP guidelines. The ICNIRP guidelines are widely considered very conservative. The IEEE C95.1 standard uses the more recent scientific information to establish the standard, and there is no health report showing that the IEEE C95.1 standard is not safe, therefore the IEEE C95.1 standard will be used as the safety baseline in the design methodology.

In the literature, the safety of the EV charging systems has been evaluated by means of the simulated and measured magnetic flux density at a certain distance away from the winding. However, it led to an unsafe system because the most dangerous area is the air-gap center region. The flux density in the air-gap center region is much higher, and the field can cause severe injuries to humans and animals. In addition, the electric field was not paid enough attention. It is the high frequency electromagnetic field which contains electric field and magnetic field that transfers power from the transmitter to the receiver. Both the magnetic field and the electric field should meet the safety limits. New system design methodologies are required that satisfy the safety regulations as well as achieve high efficiency and transfer high power.

1.3 Operating principle and field distribution of loosely coupled inductive wireless EV chargers

In this section, research on field distribution of electric vehicle battery chargers with loosely coupled inductive WPT systems is reviewed. EV battery chargers are classified into two categories: stationary and in-motion chargers [29].

1.3.1 Operating principle and field distribution of stationary inductive wireless EV chargers

Stationary inductive wireless EV battery chargers have been widely explored with respect to different power level and air-gap distance, the focus of existing literature is improving the coil-to-coil efficiency and the DC-to-DC efficiency from kW to tens of kW [46]-[83]. Less attention has been paid to the magnetic and electric field distributions in the air-gap center region, which is accessible to human beings and animals.

According to the SAE J2954 [85], foreign object detection (FOD) and living object protection (LOP) systems are required for inductive WPT products, which must ensure the wireless charger is immediately shut down when parts of human body and animals approach the zone where field strengths exceed safety limits. However, bad things could happen if FOD and LOP systems don't work properly considering that the air-gap center region is accessible to humans and animals, and the electrostimulation of nerves and muscle happens instantly.

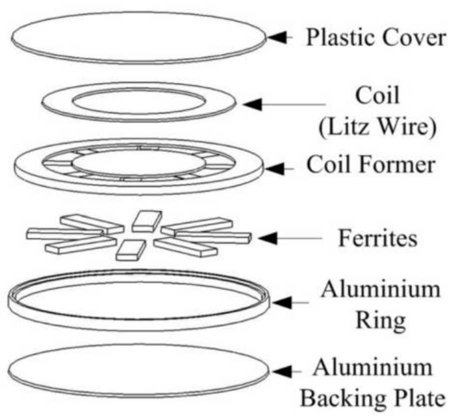

(a) Exploded view of a power pad

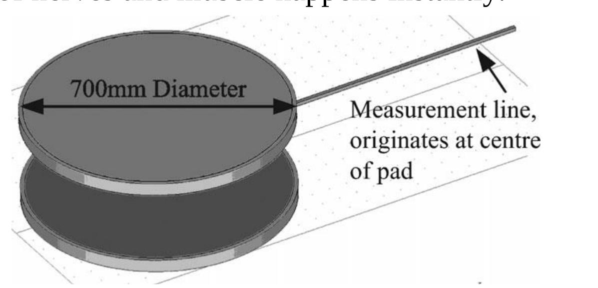

(b) 2 kW pad with an air-gap of 200 mm

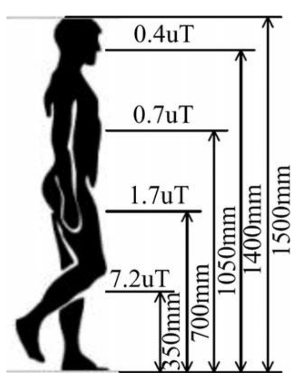

(c) Measured flux density

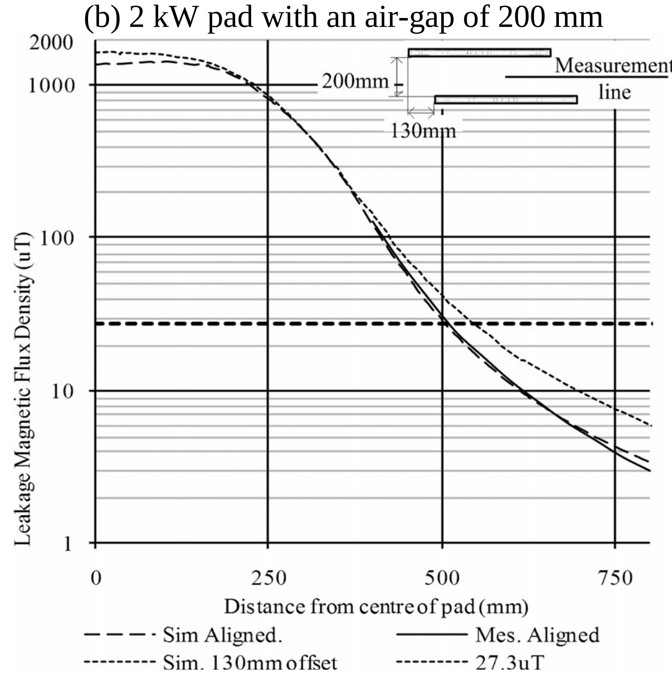

(d) Measured and simulated flux density along measurement line in air-gap center plane

Fig. 1-14. 2 kW WPT system over 200 mm distance using circular pad

Circular pads have been widely used in inductive WPT systems. Covic et al presented a systematic approach to design and optimize circular magnetic structures for lumped inductive WPT systems [52]. A power pad with 700 mm diameter, as shown in Fig. 1-14 (a) and (b), was designed and optimized to transfer 2 kW over 200 mm air-gap at 20 kHz. Measured flux density applying spatial averaging across a female standing 170 mm from the edge of a power pad system transferring 2 kW is shown in Fig. 1-14 (c). Measured and simulated flux densities along a contour midway between aligned and offset pad beginning at the center (measurement line as shown in Fig. 1-14 (c)) are shown in Fig. 1-14 (d). The peak flux density along the measurement line increases slightly (less than 20%) from aligned condition to 130 mm misaligned condition. The authors claimed that the system met the ICNIRP guideline and was safe to use since the spot flux density was 27.3 μT at a distance 500 mm from the center of the pad. However, the peak magnetic flux density in the air-gap center plane, which is accessible to human beings and animals, is above 1000 μT under aligned and misaligned conditions, which is about 4 times higher than the IEEE C95.1 - 2005 electrostimulation safety limit 205 μT. In addition, the electric field distribution in the air-gap was not mentioned. Power scalability limitation under magnetic field and electric field safety limits was also not discussed.

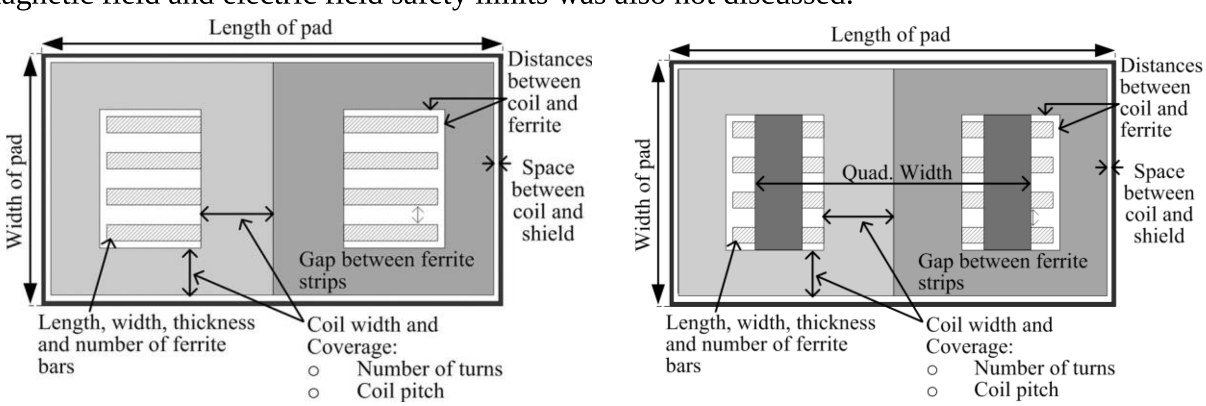

(a) DD pad design variables (b) DDQ pad design variables

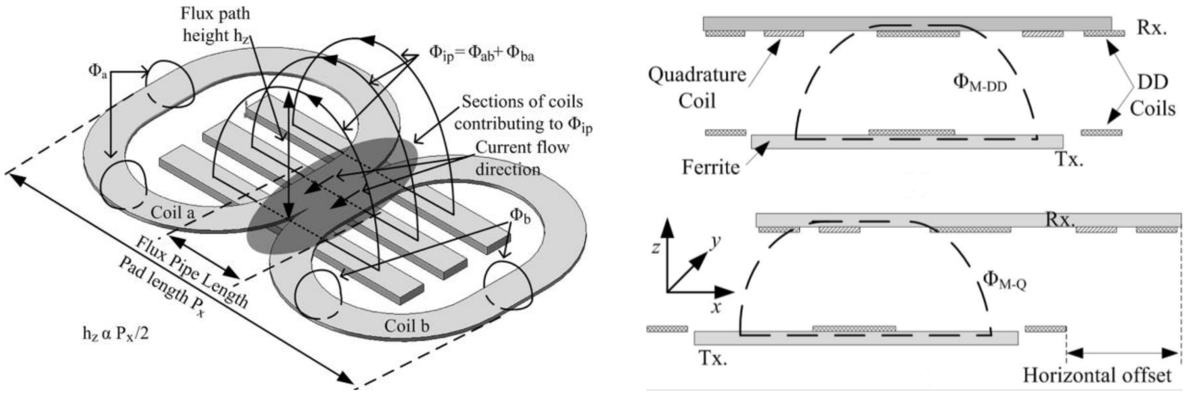

(c) DD pad flux pattern (d) DD pad and DDQ pad coupling modes

Fig. 1-15. DD pad and DDQ pad design variables, flux pattern, coupling modes

Due to the limited design space for electric vehicles and the shape of electric vehicles, polarized couplers, such as double D (DD) pad and double D with a quadrature coil (DDQ) pad shown in Fig. 1-15 (a) and (b), were proposed to improve the mutual coupling and the power transfer efficiency [30][31]. The DD pad forms a “flux pipe” between coil a and coil b, as shown in Fig. 1-15 (c), the height of the intra-pad flux Φ_{ip} is controlled by the adjusting the width of the coils in the shaded area. The fraction of flux Φ_{ip} that couples to the receiver pad is mutual flux as shown in Fig. 1-15 (d). These paths allow good coupling to a similarly shaped receiver because the fundamental height h_z is proportional to half of the pad length. DD receiver coil can only couple horizontal flux components, a quadrature coil is added to the receiver coil to improve the coupling due to horizontal offsets. The coupling modes under aligned and misaligned conditions are plotted in Fig. 1-15 (d).

Charge zones for DD-DDQ and circular pads are shown in Fig. 1-16 (a). Full power can be transferred anywhere within the lightly shaded areas. The charge zones show that DD-DDQ coupler has better misalignment tolerance than circular coupler. The magnetic field distributions transferring 2 kW through 200 mm air-gap at 20 kHz were compared in Fig. 1-16 (b) with 130 mm horizontal misalignment. From circular pad analysis in [52], it is shown that the peak flux densities under aligned and misaligned (130 mm) conditions change within 20%. The air-gap center plane peak flux densities for all proposed pads are above 1 mT, which is at least 4 times higher than the IEEE C95.1-2005 electrostimulation safety limit 205 μT. However, the authors claimed that the systems were safe since the flux density at a distance of 1.5 m from the center is lower than the ICNIRP guidelines. Since the coupling of DD pad is caused by the horizontal flux, there is a null coupling point in the horizontal line if the receiver is also a DD pad. The mutual coupling is determined by the flux path height or the pad length.

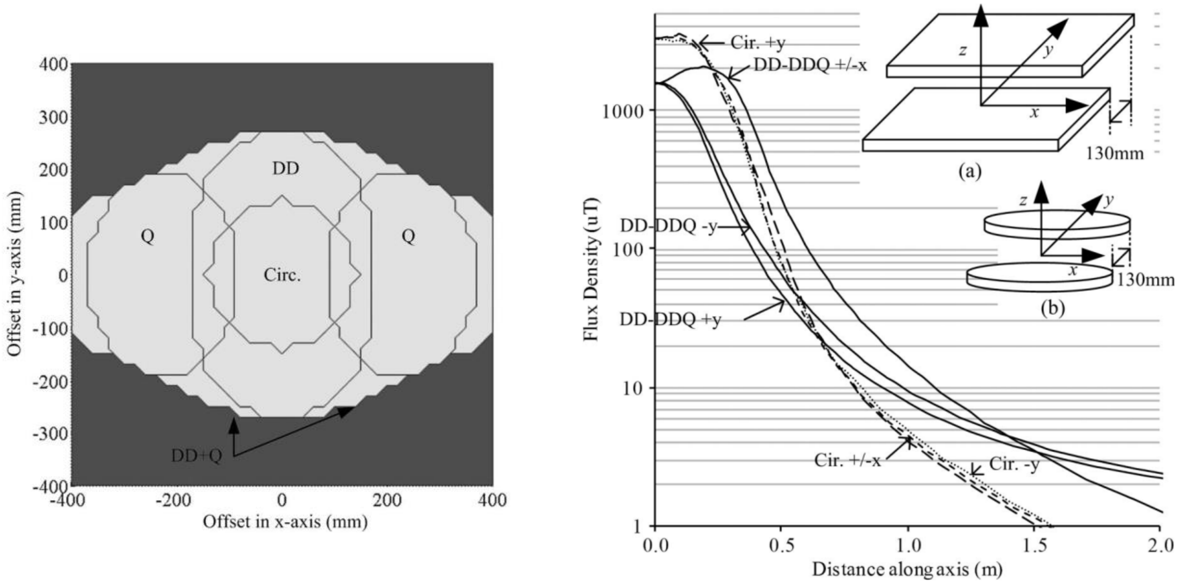

(a) Comparison of charge zones (b) Simulated leakage magnetic flux

Fig. 1-16. Comparison of circular coupler, DD-DDQ coupler charge zones, and simulated leakage magnetic flux

The circular pad generates the vertical field, while the DD pad produces horizontal field, therefore, if a vehicle is equipped with a circular pad as a receiver and parks over a DD pad, the coupling between the transmitter and the receiver will reduce significantly, in addition, the leakage magnetic field will increase hugely. A bipolar pad (BPP) and a tripolar pad (TPP) are proposed to solve this problem [53]-[57].

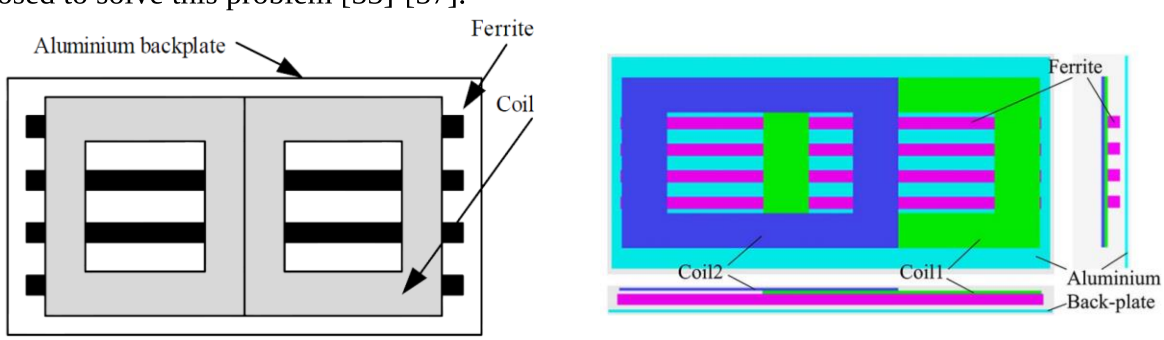

(a) DD pad structure (b) Bipolar pad structure

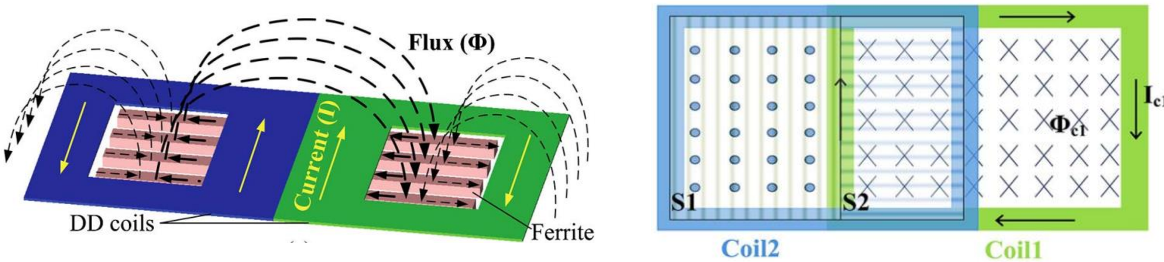

(c) DD pad flux pattern (d) Bipolar pad flux pattern

Fig. 1-17. DD pad and bipolar pad structures and flux patterns

The bipolar pad structure and flux pattern are compared with the DD pad in Fig. 1-17 [54]. Adjusting the overlap area of coil 1 and coil 2 of bipolar pad, the amount of flux, generated by coil 1, that goes through area S2 is equal to the return amount of flux going through area S1, then coil 1 and coil 2 are mutually decoupled, which allows the currents within each coil to be independent in both phase and magnitude and provides a better misalignment tolerance.

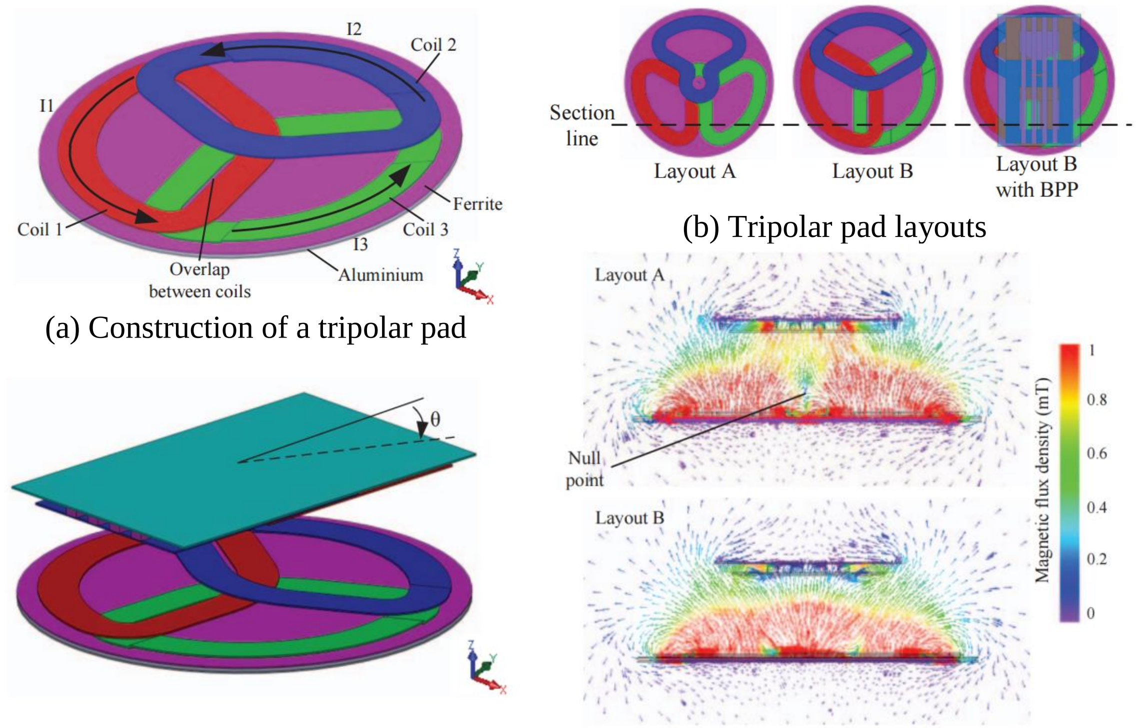

(a) Construction of a tripolar pad

(b) Tripolar pad layouts

(c) Simulation setup for BPP secondary and TPP primary

(d) Field distribution simulation results

Fig. 1-18. Tripolar pad and bipolar pad for inductive power transfer systems

Mutual decoupling among three coils in a tripolar pad was achieved by appropriately adjusting the overlap between the coils so that the net EMF induced in an adjacent coil was as close as possible to zero [55]-[57]. When the secondary coil has rotational misalignments, three mutually decoupled coils can be controlled and driven individually to generate a polarized magnetic field relative to the position of the secondary coil, which helps achieve the rotational tolerances of a non-polarized pad while still taking advantages of a polarized magnetic field.

Both bipolar pad and tripolar pad generate vertical flux, and the mutual coupling is determined by the area enclosed by the pad. They can be treated as an equivalent way to increase the enclosed area to improve the coupling compared with using a single large pad.

The operating frequency was 20 kHz, and Litz-wire was used to build the coil. During simulation and experiment tests, TPP was used as the primary coil and bipolar pad was used as the secondary coil as shown in Fig. 1-18. The air-gap was 200 mm, the evaluation power was 1554 W for layout A and 2040 W for layout B. Three coils in layout A are mutually decoupled to independent control current in each coil, and in layout B are mutually enhanced to increase the power transfer efficiency. The peak magnetic flux density in the air-gap center plane was still above 1 mT. It is claimed that the magnetic flux density 850 mm away from the center of the secondary coil is lower than 27 μT provided by the ICNIRP guidelines [57]. The peak electric field intensity in the air-gap center plane and around the coil was not mentioned.

A double-sided coil, as shown in Fig. 1-19 (a), was proposed for inductive WPT systems [49][58]. It is claimed that the double-sided coils were more beneficial in misalignment tolerance than single-sided coils and the size of the coils for same power level can be reduced using double-sided coils. Because the flux goes through the ferrite like through a pipe, it's also called a flux-pipe coupler. Because of the unwanted leakage flux, aluminum foils were used to shield magnetic flux at the back of the core and increase the coupling coefficient. Ferrite core was added to guide magnetic flux flow, increase coupling coefficient, and reduce required current for same flux level. However, when the shielding is added, the quality factor of a flux-pipe coupler reduces from 260 to 86 [59]. The high shielding loss makes the flux-pipe coupler not a good choice. In addition, when transferring 3 kW over 160 mm air-gap or 200 mm air-gap at 50 kHz, the leakage magnetic flux density, as shown in Fig. 1-19 (d), is at least two times higher than the IEEE C95.1-2005 electrostimulation safety limit at 150 mm away from the center, which means the air-gap center point magnetic flux density will be much higher.

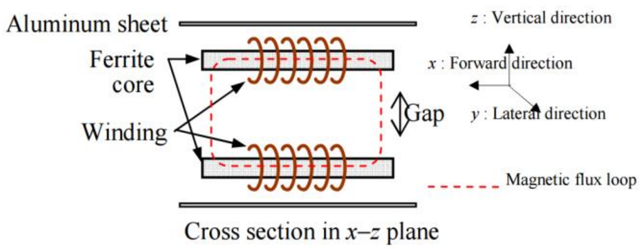

(a) Magnetic flux of the double-sided coils

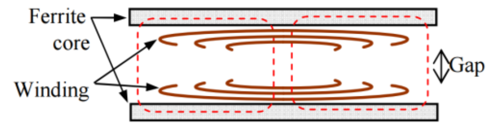

(b) Flux line of single-sided coils


(c) Picture of a prototype

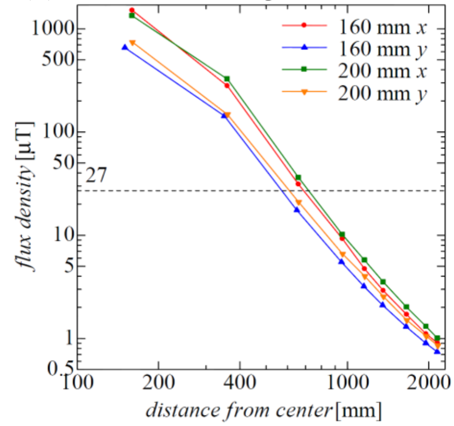

(d) Leakage flux measurement

Fig. 1-19. A double-sided coil flux loop and leakage flux measurement

Due to the limited installation space under the electric vehicle, the receiver coil is usually smaller than the primary coil. In order to evaluate the induced high field strength in the body tissue of humans and living organisms nearby, numerical simulation with human body model and animal model is necessary. A prototype, shown in Fig. 1-20 (a), with a 600 mm diameter primary coil and a 300 mm diameter secondary coil was designed to transfer 3.3 kW through 150 mm air-gap at 85 kHz, the EMF generated by WPT systems was evaluated using a human model and a cat model [60]. A detailed anatomical human model with 14 internal organs as well as a titanium pacemaker provided by DENSO International America, Inc., was used for the numerical simulation. A cat model was used to test the radiation level when this small animal went under the vehicle. The vehicle was also modeled, because the vehicle body, especially its chassis has shielding effect to the magnetic field since the material is metal. The car glasses and all objects inside, which are not metal and far from the radiation source, are neglected.

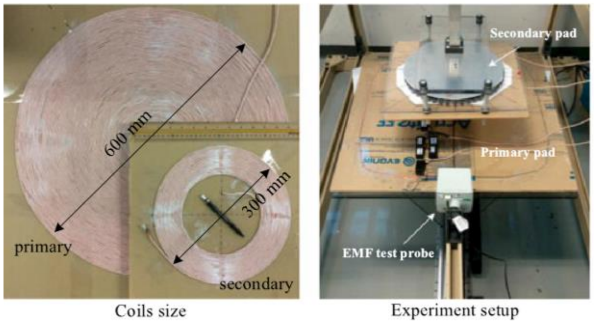

(a) Photo of the test-bed

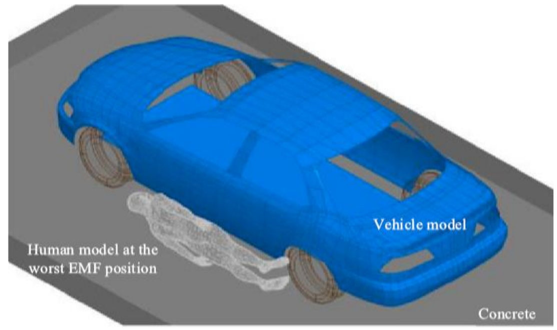

(b) Simulation models for radiation

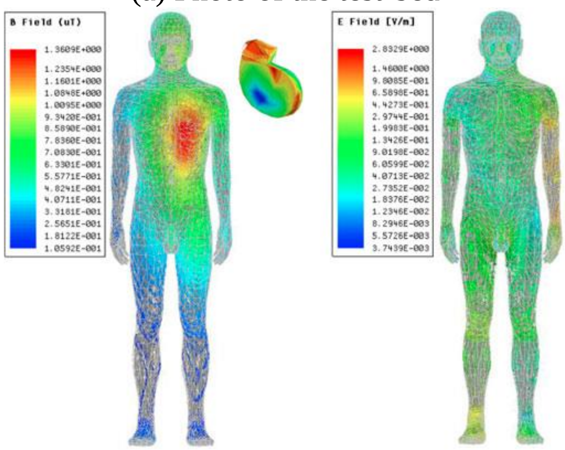

(c) Simulation results of magnetic field and electric field for the worst case

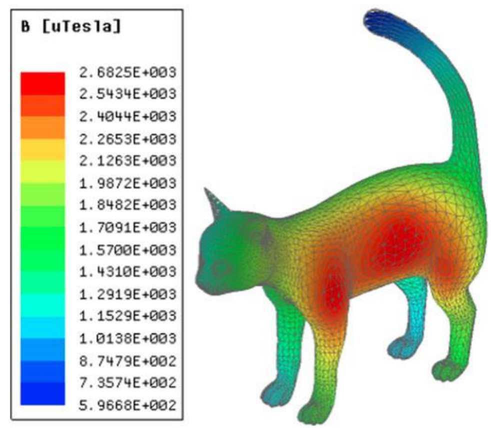

(d) Simulation results of magnetic field for small animals laying inside the air-gap

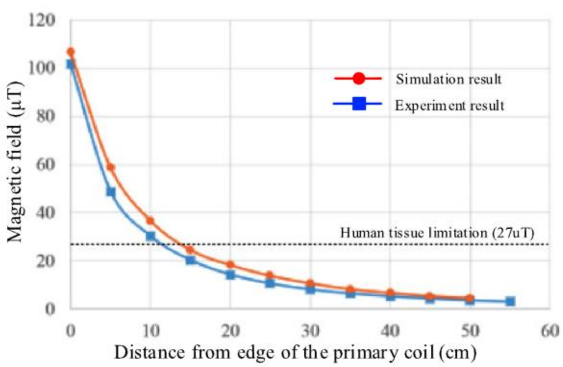

(e) Simulated and measured results of magnetic field

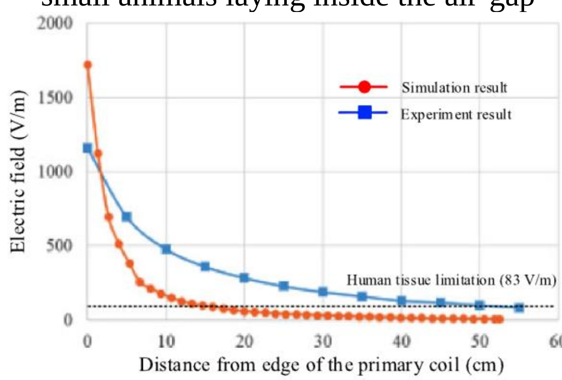

(f) Simulated and measured results of electric field

Fig. 1-20. Test set-up, and results of magnetic field and electric field

It is claimed that the worst case to have the highest level of radiation is the human laying down on his left side, face the vehicle and the radiation source as shown in Fig. 1-20 (b). The simulation results of magnetic field and electric field for the worst case as shown in Fig. 1-20 (c) were lower than the ICNIRP guideline. However, his arms can put under the vehicle chassis, which will have more severe effects and is the much worse case. The peak magnetic flux density in the cat as shown in Fig. 1-20 (d) is 2.68 mT, which is about 10 times higher than the IEEE C95.1 - 2005 electrostimulation safety limit 205 μT. EMF is measured with an electric and magnetic field probe EHP-200 along the line midway between the pad. The line begins from the edge of the primary coil, which is 300 mm from the air-gap center point. The measured and simulated results along this line are shown in Fig. 1-20 (e) and (f). Although the magnetic field with 300 mm away from the center was lower than the IEEE C95.1-2005 electrostimulation magnetic field safety limit 205 μT, the air-gap center plane central point magnetic field was not shown. According to the simulation result for the cat model, it's easy to estimate the air-gap center plane central point magnetic flux density is higher than IEEE C95.1-2005 electrostimulation magnetic field safety limit 205 μT. In addition, the electric field with 300 mm away from the center was higher than the IEEE C95.1-2005 electrostimulation electric field safety limit 614 V/m.

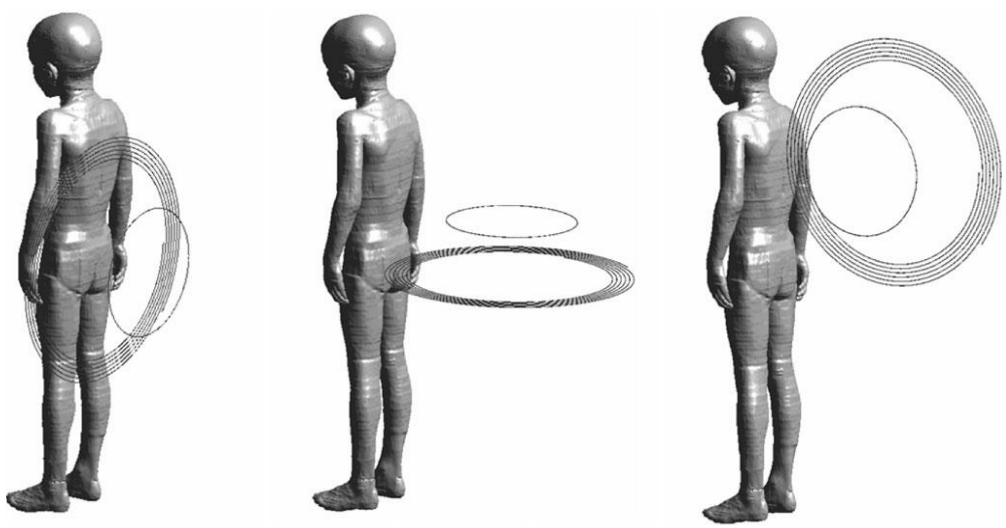

Fig. 1-21. Evaluation positions of human body expose to WPT system

There are also other research works using human body model to evaluate the power limit within the safe magnetic field and electric field levels. On one hand, human body models are not accurate enough to represent all kinds of human beings, like pregnant women and people with different kinds of illness. On the other hand, most of the exposure evaluation and power limit calculation processes placed human body model almost adjacent to the coil, as shown in Fig. 1-21, these evaluation processes are not the case when charging electric vehicles [61]-[78].

Operating at MHz frequency has been proposed to improve the coil-to-coil efficiency and reduce the air-gap center region magnetic flux density [50][79]-[83]. When the input voltage keeps the same, increase the frequency will increase the equivalent input impedance of the system, and then the required current will be reduced. For the same system, when the current is reduced, the flux density will also be reduced based on magnetic field Ampere's law.

Due to the irregularities in the fabrication process and parasitic capacitances between the adjacent turns, conventional Litz-wire is rarely useful in MHz frequency. Surface spiral winding (SSW), shown in Fig. 1-22 (a), was proposed to reduce the skin and proximity effect losses at MHz frequency [50][79]-[83]. SSW twists the copper layer in each turn following a Litz-wire pattern, therefore, it can reduce the proximity effect loss.

A 7-turn SSW with twist factor 1, loop radius 205 mm, cross-sectional radius 25 mm, turn space 2.5 mm, and wall thickness 0.3 mm was built as the transmitter. A single turn copper tubing with loop radius 180 mm, cross-sectional radius 4.75 mm, and wall thickness 1 mm was set as the receiver. The air-gap distance between the transmitter and the receiver was 300 mm. The operating frequency was set at 3.7 MHz.

The magnetic field distribution when transmitting 3 kW was shown in Fig. 1-22 (c), the air-gap center plane peak flux density was around 170 μT, which satisfied the IEEE C95.1-2005 magnetic field electrostimulation safety limit. However, the author didn’t consider the magnetic field tissue heating safety limit, which reduces as the operating frequency increases above 100 kHz. At 100 kHz, the electrostimulation and the tissue heating safety limits are the same.

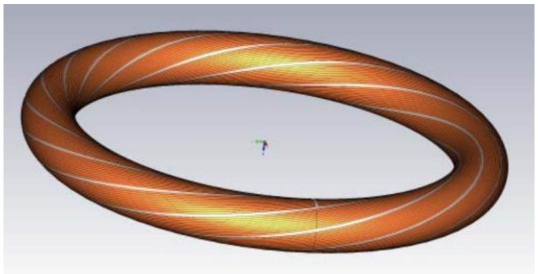

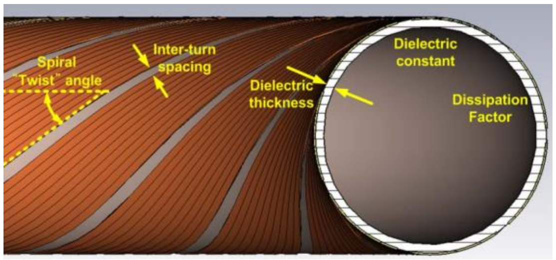

(a) SSW geometry

(b) SSW design variables

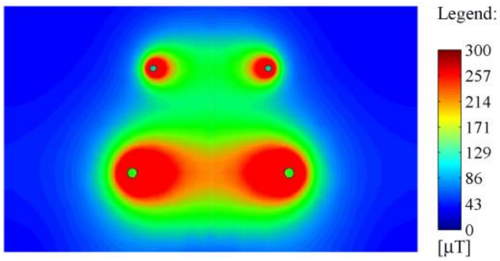

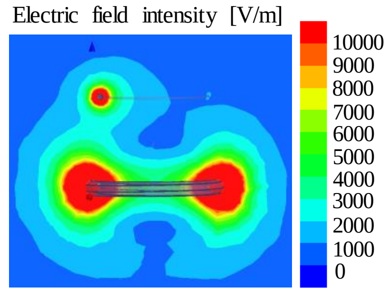

(c) Magnetic field distribution

(d) Electric field distribution

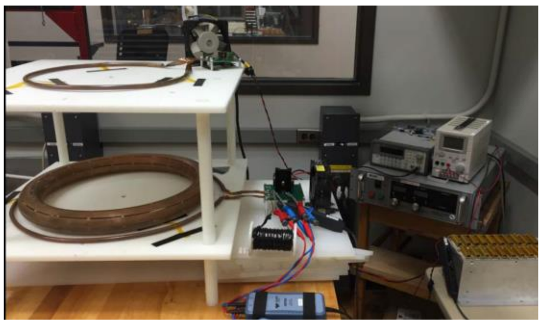

(e) Lab test setup

(f) Voltage breakdown

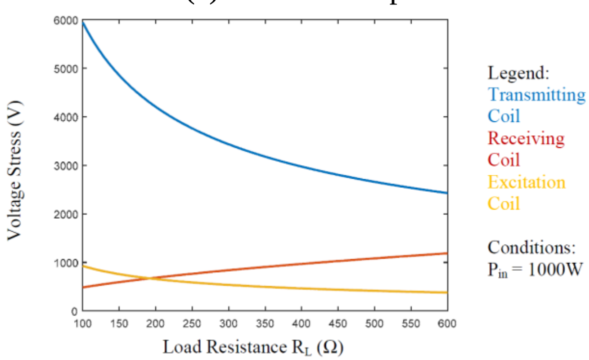

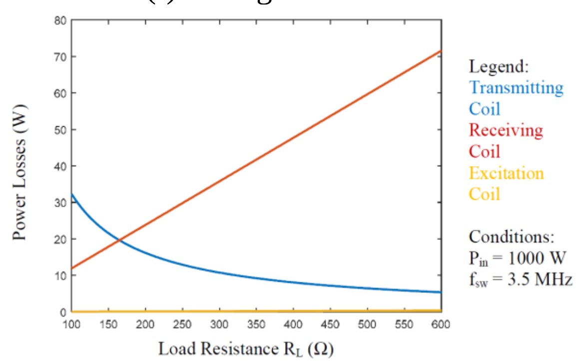

(g) Coil voltage stress vs. load resistance

(h) Coil losses vs. load resistance

Fig. 1-22. A 3.7 MHz WPT system transmitter, field distribution, and properties

In addition, the electric field distribution was not evaluated, which is as important as the magnetic field. The induced electric field distribution is simulated and shown in Fig. 1-22 (d), the peak electric field intensity in the air-gap center plane is above 6000 V/m, which is about 10 times higher than the IEEE C95.1-2005 electric field electrostimulation safety limit 614 V/m. Although the required current to transfer the same amount of power reduces significantly at MHz operating frequency compared with kHz operating frequency, the required voltage increases hugely. An excitation coil as shown in Fig. 1-22 (e) was added to provide the required voltage. According to the experimental tests at 3.5 MHz, the voltage breakdown, shown in Fig. 1-22 (f), did occur in the SSW when transferring 1 kW under the optimal load. The load resistance can be increased to reduce the voltage stress as shown in Fig. 1-22 (g). However, the power transfer efficiency reduces as the load resistance increases as shown in Fig. 1-22 (h), which is a bad solution to push the system to transfer higher power.

Various shielding techniques, such as magnetic shield, passive shield, active shield and reactive shield, were developed to reduce the leakage magnetic field [46][86]-[100]. Since the vehicle body is metal, magnetic shielding above the receiver and below the transmitter is necessary to maintain the coupling and the coil-to-coil power transfer efficiency between the transmitter and the receiver [46]. The optimal geometry of the coils with the ferrite shield for minimizing the magnetic near-fields from the WPT system for EV was developed in [86]. The system was designed to transfer 3 kW over 200 mm air-gap at 20 kHz. The initial coil design and the final coil design are compared in Fig. 1-23 (a) and (b), the horizontal line starting from the air-gap center point is located in the air-gap center plane, the vertical line is 750 mm away from the air-gap center. According to the simulation results showing in Fig. 1-23 (e) and (f), the magnetic near field from the coils can be minimized by making the average winding diameters to be $\sqrt{2}$ times larger than the air-gap length and the ferrite shield diameters to be 3 times larger than the air-gap length, which resulting in over 29.12% reduction of the magnitude of the magnetic near field with negligible loss in the WPT system.

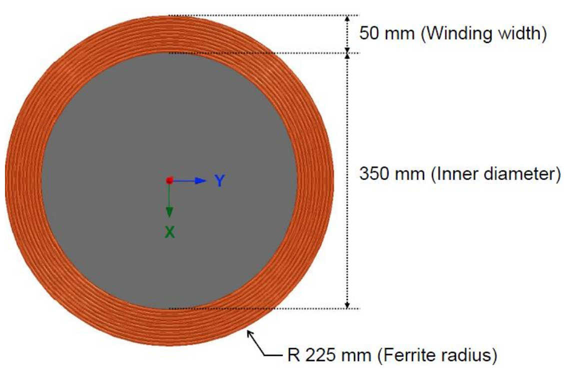

(a) Initial coil design

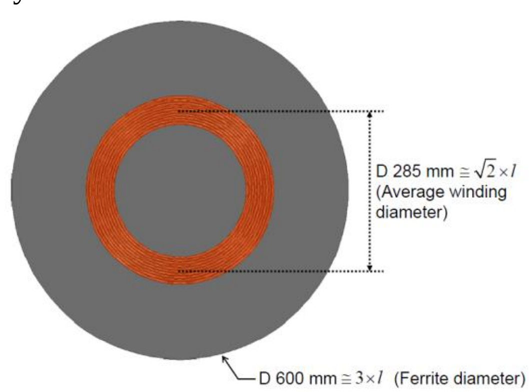

(b) Final coil design

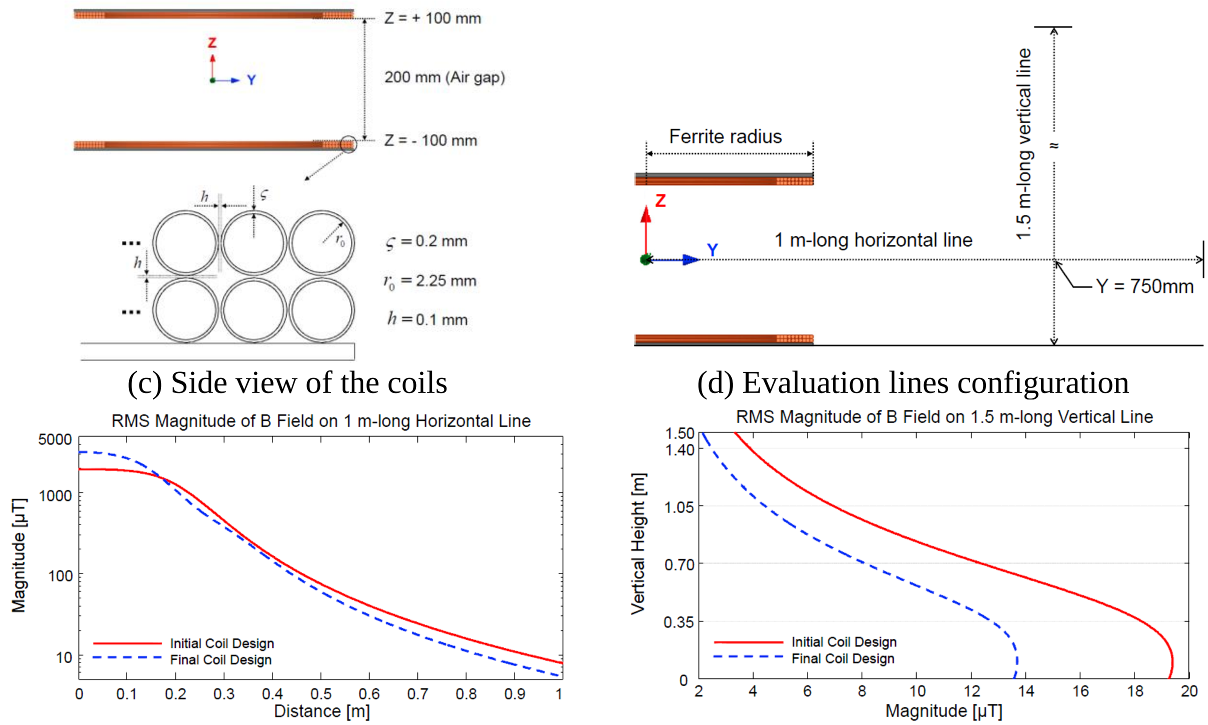

(c) Side view of the coils (d) Evaluation lines configuration

(a) Magnetic field along horizontal line (b) Magnetic field along vertical line

Fig. 1-23. Effects of coil and ferrite geometry on magnetic field

However, the authors didn't consider the increase of the air-gap center plane peak magnetic flux density. In the air-gap center plane central point, the peak magnetic flux densities of both designs are over 2000 μT, which is at least 9 times higher than the IEEE C95.1-2005 magnetic field electrostimulation safety limit 205 μT. After changing to a large ferrite plate, the peak magnetic flux density increases by almost 1000 μT. In addition, the electric field distribution in the air-gap was not considered in both designs.

The passive shield method, shown in Fig. 1-24, uses a metal plate and metallic brush to confine the magnetic field within limited space [87]-[89]. Passive shielding is effective in blocking the magnetic field being emitted from the bottom of the vehicle to the side of the vehicle. However, the passive shield has a physical limitation when used in a WPT system because the shield should fully cover the WPT coils. In addition, the time-varying magnetic field will generate eddy current losses in these shields.

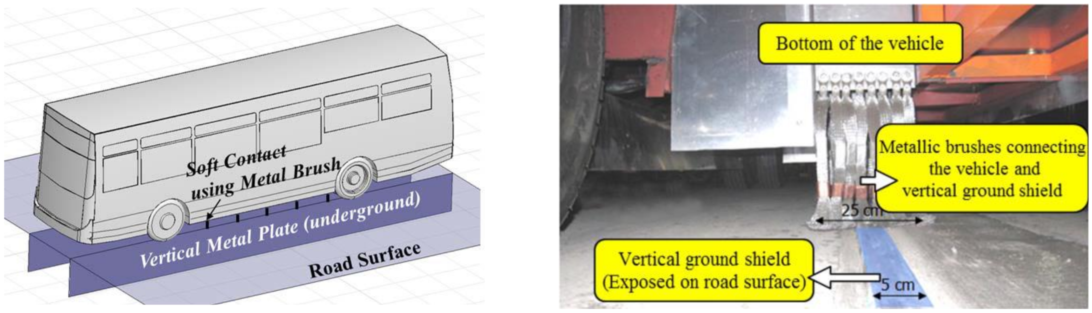

Fig. 1-24. Passive shield methods using metal plate and metal brush

The magnetic field can be canceled by using an active shield. However, the size, weight, and power consumption of the additional power supply for an active shield are additional burdens for the electric vehicle system. In addition, the magnetic field in the air-gap region won't be affected by the active shield.

Reactive shield coil, shown in Fig. 1-25 (a) and (b), was also developed to reduce the magnetic near field [90]-[92]. Through impedance control, the induced magnetic flux generated by the shield coil has the opposite phase with the magnetic flux generated by the WPT coils to reduce the leakage magnetic near field. A WPT system transferring 500 W through 15 cm air-gap at 20 kHz was used to verify the shielding effectiveness. The test setup and simulation results with no shield, single reactive shield coil and double reactive shield coils are shown in Fig. 1-25 (c), (d), (e), (f), (g) and (h). The vertical observation line is 20 cm away from the edge of the electric vehicle. After adding the reactive coils, the magnetic flux density at the observation line was reduced. However, the peak magnetic flux density in the air-gap center plane remained almost the same, which was above 500 μT, 2 times higher than the IEEE C95.1-2005 magnetic field electrostimulation safety limit 205 μT. It would be much higher if the output power increases from 500 W to kW level. In addition, the air-gap center plane electric field intensity was not evaluated.

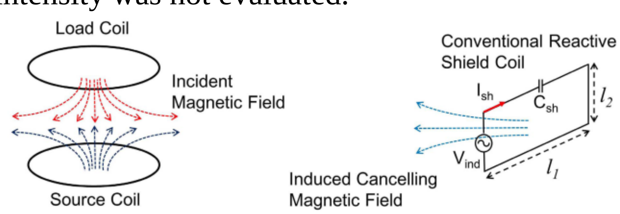

(a) Single reactive shield coil topology

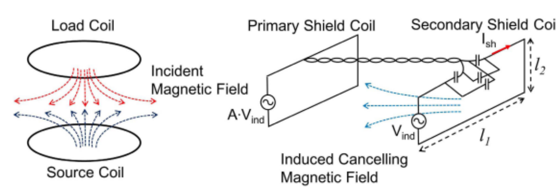

(b) Double reactive shield coils topology

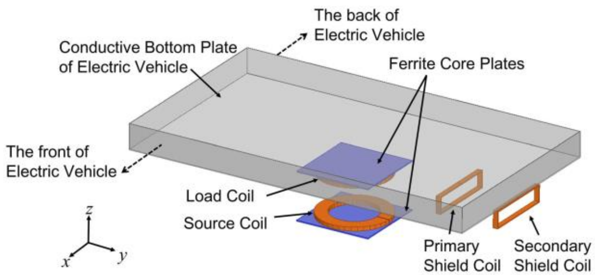

(c) Configuration perspective view

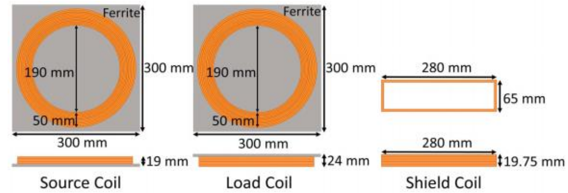

(d) Coil geometrical dimensions

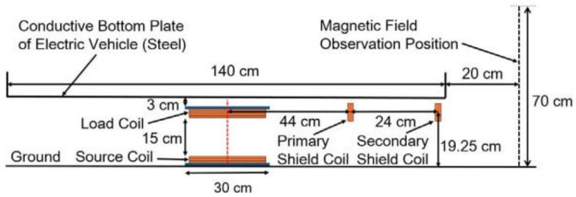

(e) Configuration cross-sectional view

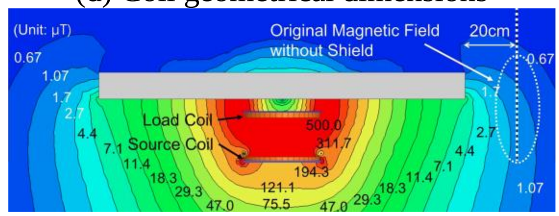

(f) Field distribution with no shield

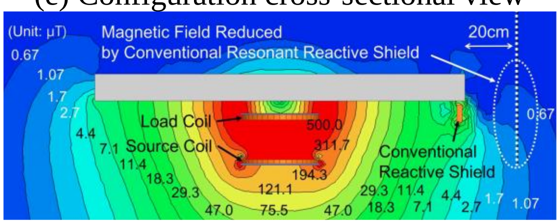

(g) Field distribution with single reactive shield coil

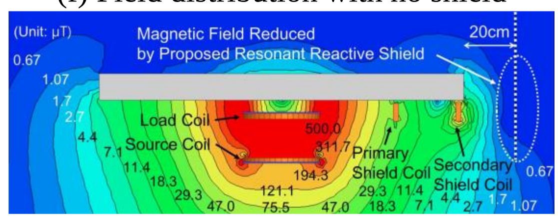

(h) Field distribution with double reactive shield coils

Fig. 1-25. Reactive shield coil topologies and field distributions

Plate shield, ring shield, Litz shield, and revere loop shield, shown in Fig. 1-26 (b) - (e), were compared to reduce the stray magnetic field. The quantified results along the air-gap center plane are shown in Fig. 1-26 (f) [105]. The investigated system transferred 100 W output power through 40 mm air-gap at 100 kHz. The authors said that the stray magnetic field on the side of the coils could be attenuated by 75%. However, the paper did not investigate the effects on air-gap center plane peak magnetic flux density and electric field intensity, and power transfer efficiency. In addition, even though under the best case, the magnetic flux density at 75 mm away from the central point was about 80 µT, when the transferrable power was scaled up to 2.5 kW, the excitation current would increase by 5 times since P is proportional to I^2, which would result in the increase of magnetic flux density by 5 times, then the magnetic flux density at 75 mm away from the central point would be around 400 µT, which is about 1.4 times higher than the IEEE C95.1-2005 safety limit, the peak magnetic flux density along the air-gap center plane would be much higher.

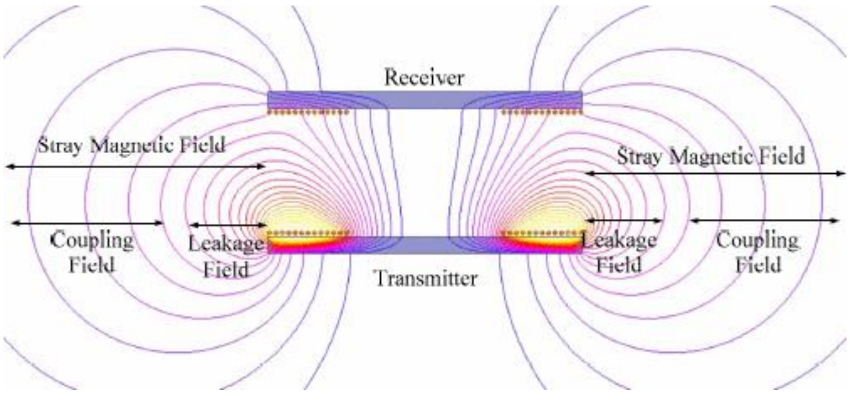

(a) Flux lines of stray magnetic field

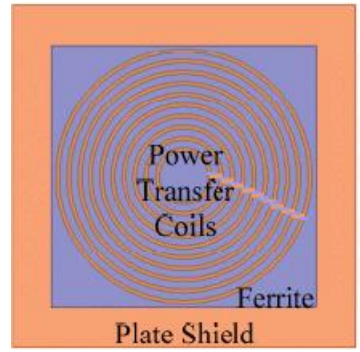

(b) Plate shield

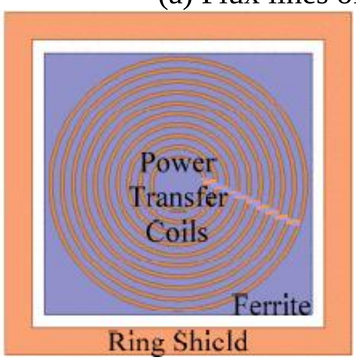

(c) Ring shield

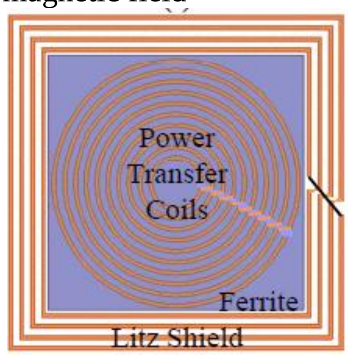

(d) Litz shield

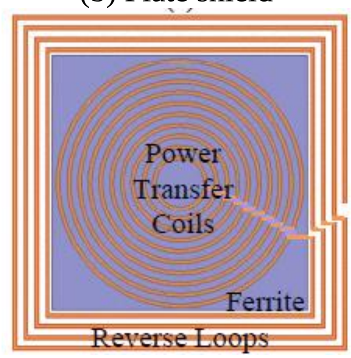

(e) Revere loops shield

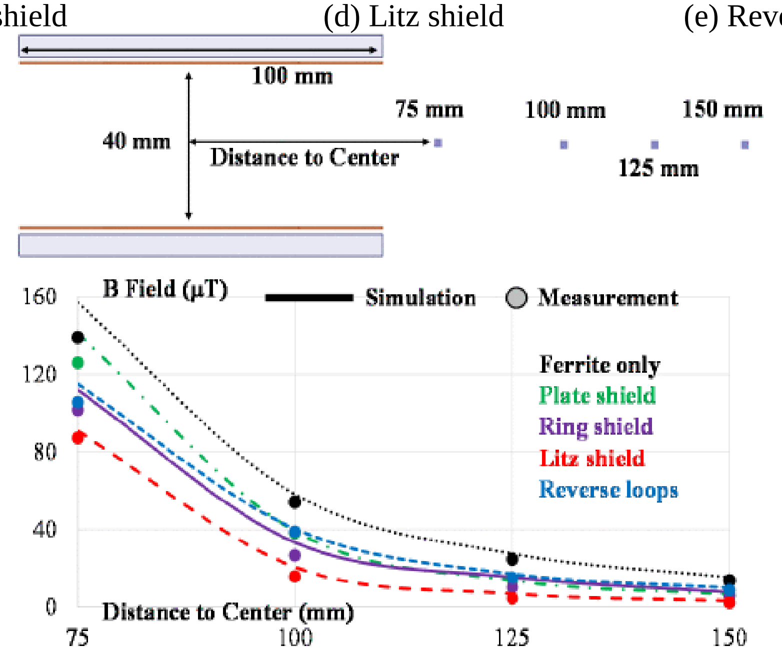

(f) Quantified stray magnetic field along the air-gap center plane

Fig. 1-26. Comparison of different reactive shield structures to reduce stray magnetic field

Phase shift control method was investigated to reduce the stray magnetic field [106]. The magnetic field around the coils is fundamentally a vector combination of the magnetic fields generated by the transmitter and the receiver. Through manipulating the current phase difference, the stray magnetic field can be reduced. The current phase difference was manipulated using a dual-side controlled converter as shown in Fig. 1-27 (c). The evaluated system transferred 100 W through 40 mm air-gap at 100 kHz. According to the results shown in Fig. 1-27 (e) and (f), the stray magnetic field did reduce by controlling the current phase difference. However, the paper didn’t investigate the effects on air-gap center plane peak magnetic flux density, electric field intensity, and power transfer efficiency. When using phase shift control, the converter at the receiver side can’t operate under soft-switching mode, in addition, there will be imaginary power circulating in the resonant tank without delivering to the load.

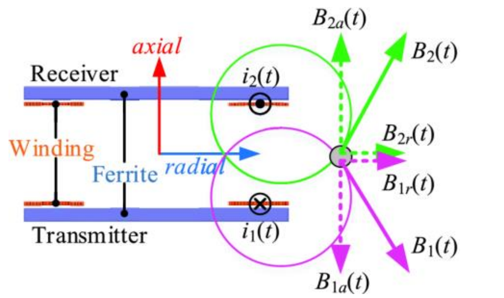

(a) Magnetic field generated by IPT coils

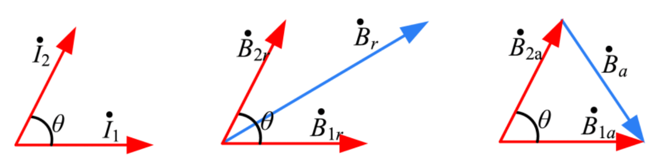

(b) Phasors representing currents and stray magnetic fields

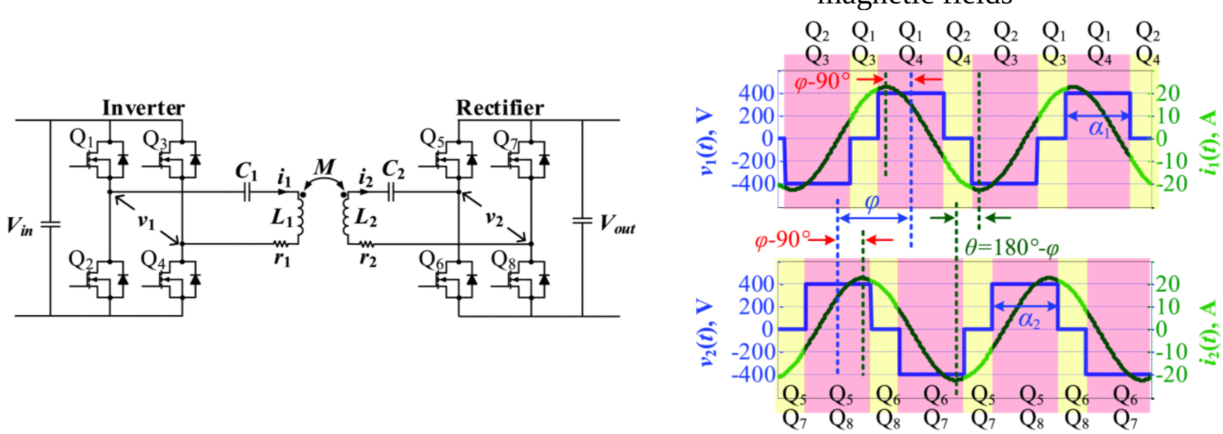

(c) Quantified stray magnetic field along the air-gap center plane

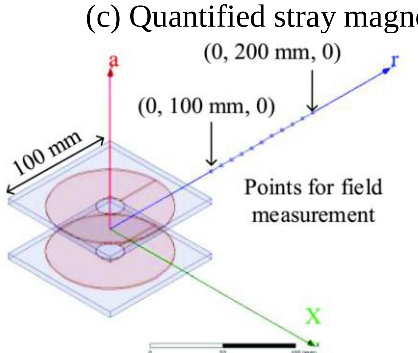

(d) Measurement positions

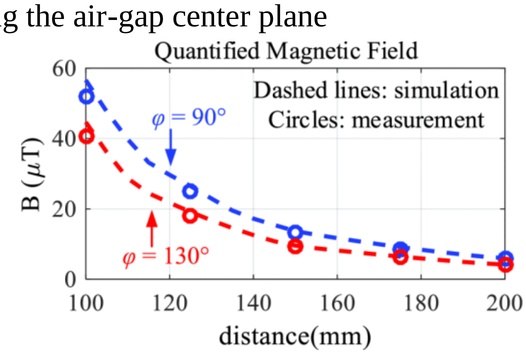

(e) Quantified magnetic field

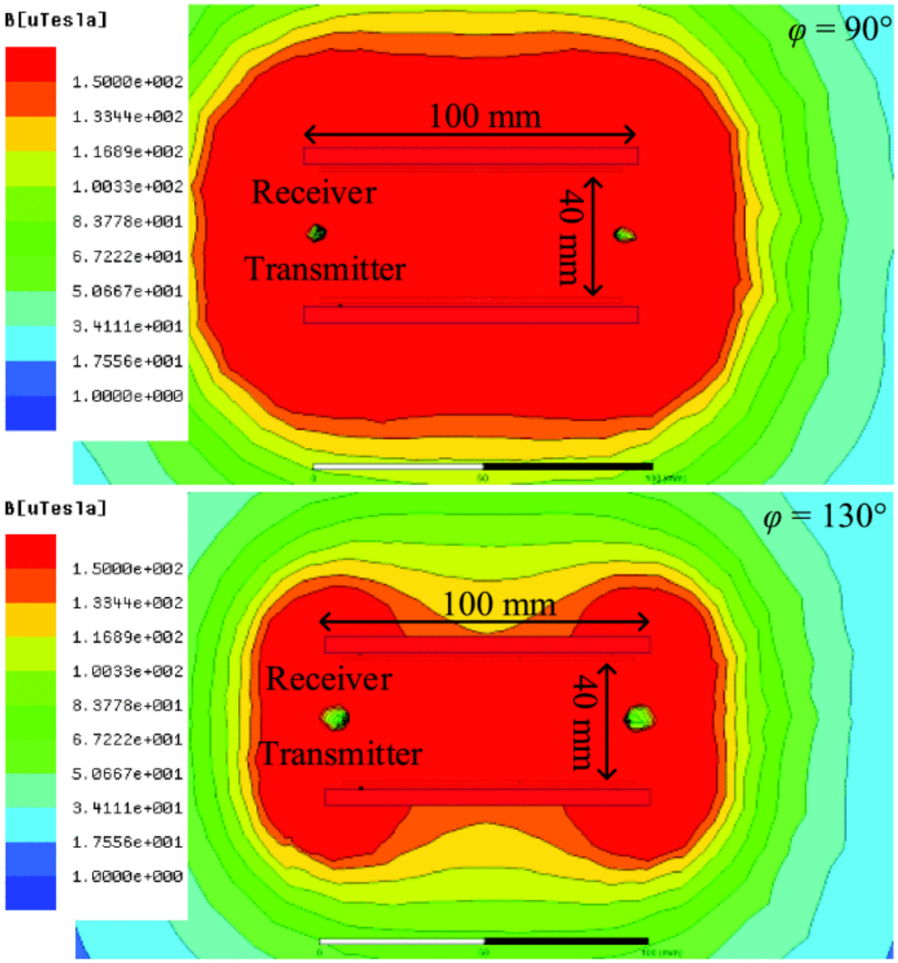

(f) Magnetic field distributions under different current phase differences

Fig. 1-27. Reducing stray magnetic field by phase shift control

There are many companies in the marketplace that provide wireless chargers for buses and vehicles, several selected companies are discussed as follows [107].

IPT Technology from Germany uses their IPT Charge e-Mobility technology provides wireless opportunity charging of hybrid and electric buses equipped with secondary receiver coils. The operating frequency is 15-20 kHz and the transmitting distance are less than 4 cm. Their system is modular for ease of handling and integration and to match the electric bus size. While 60 kW modules are standard for infrastructure transmitters, the bus module size varies with the length of the bus. A 30-kW module is used for buses up to 30 feet long and a 60 or 120 kW module is used for 40-foot buses.

Utah State University spun off the Wireless Advanced Vehicle Electrification (WAVE) startup to commercialize IPT technology for electric buses after developing it within its Electrodynamic Lab. The initial WAVE technology bus demonstration prototype was a campus bus shuttle (Aggie Bus), which modified a 22-foot electric bus to recharge its nickel cadmium (NiCd) battery for 5 minutes every 15 minutes. The Aggie Bus has achieved 90 percent power transfer efficiency for 25 kW at 20 kHz across several inch air gaps during station stops over the road-embedded powered coil.

Bombardier had developed a full suite of e-mobility solutions for electric transit proprietary IPT technology, including a high power (200 kW) rapid IPT charging systems for electric buses. This system requires a smaller and lighter onboard PRIMOVE battery, claimed to have extended life and reduced energy consumptions, which enabling larger passenger loading. Demonstration and implementation of the PRIMOVE IPT for electric buses are underway in Mannheim and Berlin, Germany, and in Bruges, Belgium.

WiTricity from Massachusetts Institute of Technology (MIT) provides IPT products from low power to high power. Their DRIVE 11 evaluation system is an end-to-end reference design for “Park-and-charge” wireless charging of electric and hybrid vehicles. It’s claimed to be able to deliver up to 11 kW of power at efficiency up to 94%, it will be released in 2017.

Eaton Corporation and Momentum Dynamics have also developed high-powered WPT products that support dynamic charging and fast charging of electric buses and trucks. Other WPT technology providers teamed up with electric vehicle manufacturers, such as Fulton Innovations (with its eCoupled charger for Tesla Roadster) and Powermat offering WPT for the GM for the Chevy VOLT.

There are two particular inductive wireless charger products in the marketplace for electric vehicles that need to pay special attention, one is Plugless by Evatran Group Inc., another is Qualcomm Halo by Qualcomm Inc. In both systems, foreign object detection (FOD) and living object protection (LOP) are used to protect human beings and animals. The system adopted automatic detection function and if metallic materials or living objects are detected on parking pad, the charging process will automatically shut down or lockout.

Plugless operates at 20 kHz, the power transfer distance is 100 mm, the primary pad dimension is 559 mm (diameter) × 470 mm (length) × 63.5 mm (height), the secondary pad dimension is 762 mm (length) × 457 mm (width) × 127 mm (height). It has already been used in Tesla Model S, Nissan Leaf, Chevrolet Volt, and Cadillac ELR. The charging input voltage range is 208 – 240 VAC, the rated charging output power is 3.3 kW – 7.2 kW continuous. Idaho national laboratory tested Plugless performance on a 2012 Chevy Volt and released the test report on Jan. 2, 2015 [108]. The test setup is shown Fig. 1-28 (a), the EM filed measurement results are shown in Fig. 1-28 (b). During the test, the input voltage is 208 VAC, the input current RMS is 28 A, the output voltage is 215 VDC, the output current is 13.8 A, the operating frequency is 18 - 20 kHz.

(a) Test setup

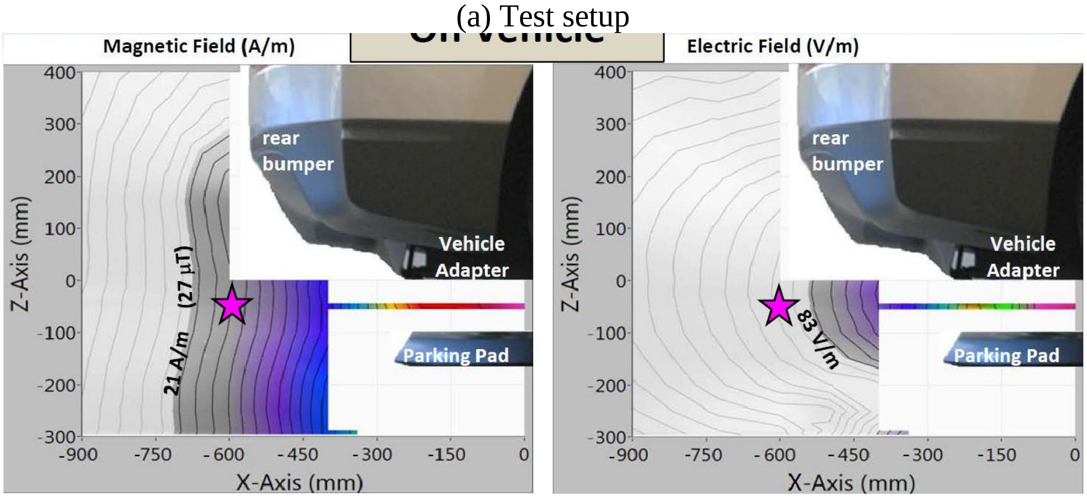

EM Field measurements[2]		EM Field meter position (X,Z)	
Maximum H-field outside vehicle	1490 A/m (1872 μT)	(0,-50)	centered between coils
Maximum E-field outside vehicle	5425 V/m	(0,-50)	centered between coils
H-field below rear bumper	33.6 A/m (42.2 μT)	(-600,-50)	at rear bumper
E-field below rear bumper	57.3 V/m	(-600,-50)	at rear bumper
Maximum H-field inside vehicle	0.5 A/m (0.6 μT)	(0,250)	inside trunk above charge system
Maximum E-field inside vehicle	0.8 V/m	(0,250)	inside trunk above charge system

(b) EM field measurements results

Fig. 1-28. Plugless test setup and test results

The input power from grid side is 3.4 kW, and the output power to charge the battery is 2.8 kW, the test power transfer efficiency from grid input to battery output is 82.3%. However, the centered air-gap magnetic flux density between primary and secondary pads are 1872 μT, which is about 9 times higher than IEEE C95.1-2005 magnetic field safety limit (205 μT), and the centered air-gap electric field strength between primary and secondary coils is 5425 V/m, which is about 9 times higher than IEEE C95.1-2005 electric field safety limit (614 V/m). The air-gap center EM field between the primary coil and the secondary coil is definitely not safe for human beings and animals.

Qualcomm Halo provides four charging power levels: 3.7 kW, 7.4 kW, 11 kW and 22 kW. The operating frequency is 85 kHz, and the claimed power transfer efficiency is 90 %. Halo was used in BMW i3 and i8, and it's going to be used in Mercedes-Benz in 2017. The EM field test results are not released. The pads dimensions and operating modes are shown in Fig. 1-29.

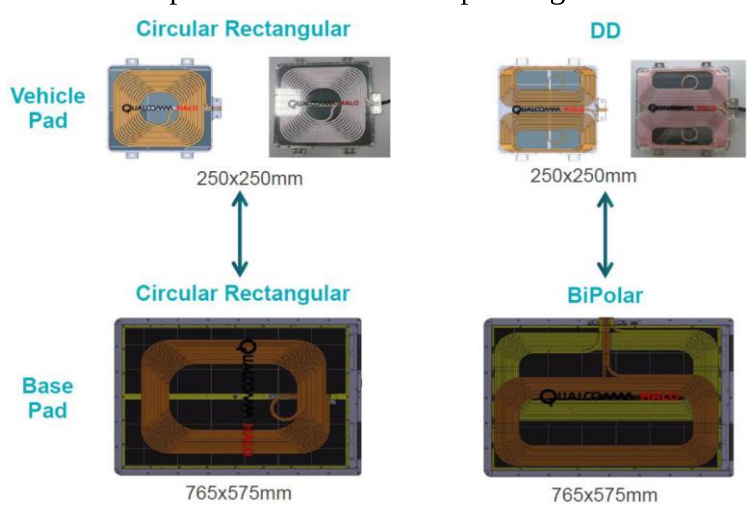

(a) Pad dimensions

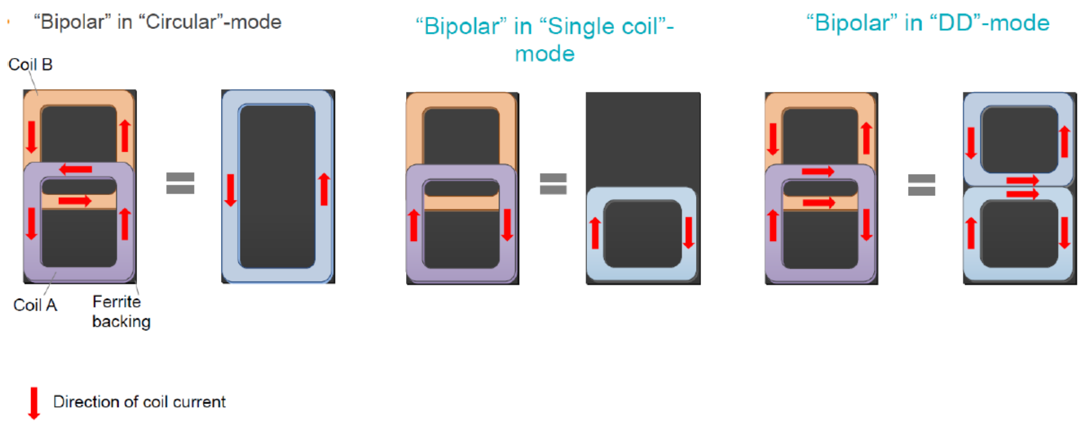

(b) Operating modes

Fig. 1-29. Halo pad dimensions and operating modes

The technology used in Qualcomm Halo are acquired from the HaloIPT team, which is co-founded by John T. Boys from the University of Auckland. Although the EM field measurement results are not released, the simulation and test results for the circular pad, bipolar pad and DD pad in other literature [53]-[57] have already shown that the EM field in the air-gap region is not safe considering the IEEE and ICNIRP standards.

1.3.2 Operating principle and field distribution of in-motion inductive wireless EV chargers

Consider the capacity limit of battery and charge time, battery charging system during in-motion is beneficial to long-distance travel using compact cars and short distance travel using electric buses. An electrified road system is required for the in-motion system. The largest advantage of the system is that the required battery capacity for long distance traveling can be decreased to 30% smaller one compared with the stationary charging system. In-motion charging vehicle is also called on-line electric vehicle (OLEV). For OLEVs, they require charging and discharging multiple times a day, therefore, the power sources should have a long life and fast charging time. Supercapacitors, which have long operating life, extremely high power density, use of environment friendly materials and feature of energy level estimation from terminal voltages, are more suitable to use compared to traditional batteries [109].

There are mainly two kinds of online wireless charger systems based on transmitter types: discrete charging system and continuous charging system. Discrete charging system, as shown in Fig. 1-30 (a), uses multiple small transmitters, all transmitters are the same, the distance between adjacent transmitters is usually large enough so that there is no mutual coupling between adjacent transmitters [110]-[113]. The advantages are: (1) high coupling coefficient and high power transfer efficiency, (2) low magnetic and electric field emissions, (3) flexible to design the total length of powered roadway. The disadvantages are: (1) large pulsations at grid side and receiver side, (2) complexity and a large number of components. The discrete charging system can be treated as multiple stationary charging systems. The field distribution and safety issues are the same the stationary charging systems in the previous section.

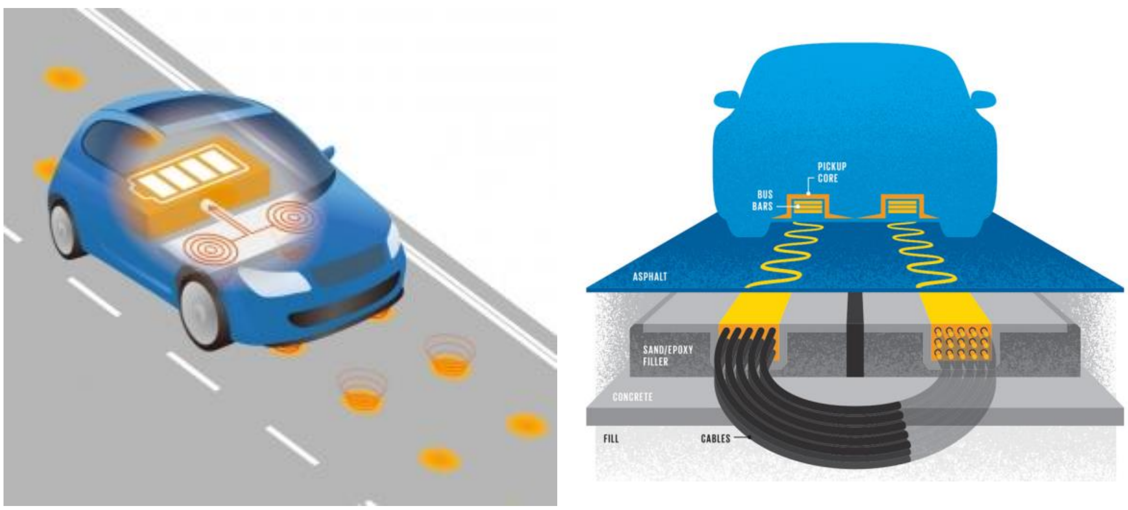

(a) Discrete charging system (b) Continuous charging system

Fig. 1-30. On-line wireless charging systems

Continuous charging system, as shown in Fig. 1-30 (b), uses a long track as the transmitter [114]-[124]. The advantages are: (1) simplicity and a low number of components, (2) continuous charge, no pulsations, (3) support multiple vehicles simultaneously. The disadvantages are: (1) low coupling coefficient and low power transfer efficiency, (2) radiated magnetic and electric fields due to long track. When only one vehicle is driving along the track, the current along the whole track is the same, those sections without a vehicle above the track will have huge leakage magnetic field, which is dangerous to nearby human beings and animals.

Normal transmitter track is U shape track as shown in Fig. 1-30 (b). Other types of transmitter tracks were also proposed to reduce the leakage magnetic field.

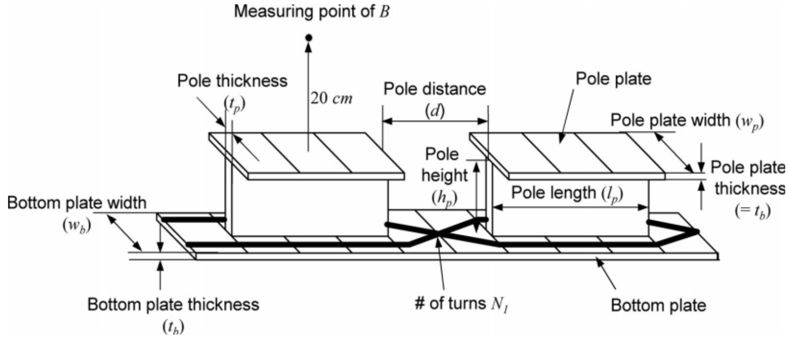

(a) Design parameters of proposed I-type power supply rail

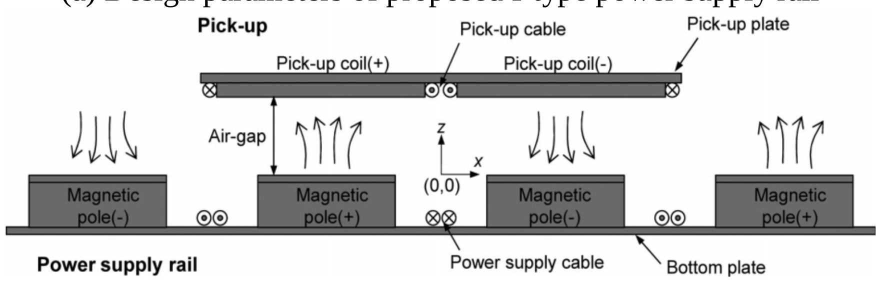

(b) Cross-section of the coils

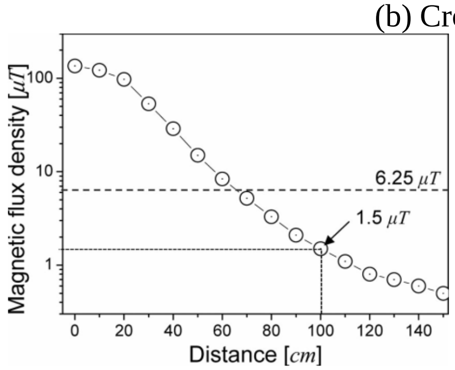

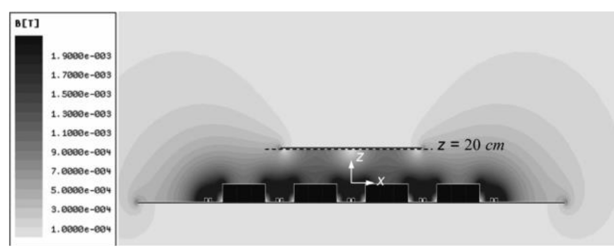

(c) Experimental results of the EMF (d) Magnetic flux density distribution

Fig. 1-31. I-type wireless power supply rail and magnetic field

An I-type wireless power supply rail, shown in Fig. 1-31 (a) and (b), was proposed to reduce the leakage electromagnetic field near the rail [114]. The I-type power supply rail generates alternating polarity magnetic poles along the road. The system was designed to transfer 25 kW through 20 cm air-gap at 20 kHz. The EMF around the rail was measured and shown in Fig. 1-31 (c), the magnetic flux density at a distance of 1 m from the center of the power supply rail lane was 1.5 μT, which was approximately 20 μT for OLEV U type wireless power supply rail [115]. However, according to the side view of the magnetic flux density distribution of the proposed I-type power supply rail with a pickup core, the peak air-gap center plane magnetic flux density was about 1.8 mT. Because the output power is proportional to I^2, while the air-gap magnetic flux density is proportional to I, even though the output power is reduced to 1 kW, the peak air-gap center plane magnetic flux density is still about 0.36 mT, which is 1.5 times higher than the IEEE C95.1-2005 magnetic field electrostimulation safety limit 205 μT. In addition, the air-gap center plane electric field was not considered.

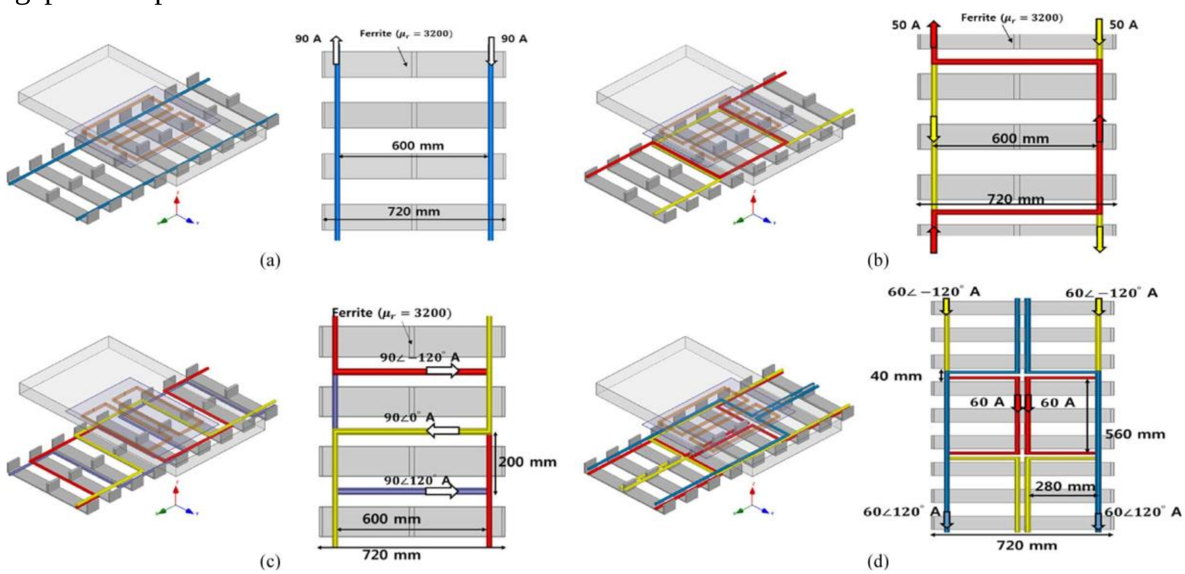

Fig. 1-32. Simulation geometries of four power lines. (a) Straight single line. (b) Meander single line. (c) Conventional three-phase. (d) Proposed three-phase.

A three-phase power line was proposed to reduce the leakage magnetic near-field in [116] and compared with straight single power line, meander single power line, and conventional three-phase power line. Simulation geometries of four power lines are shown in Fig. 1-32. Simulated magnetic field distributions are shown in Fig. 1-33.

A straight single-phase power line is simply a long rectangular loop. It is very simple to design and requires the minimal length of wire for a given power lines. However, the straight single-phase structure is generating the strongest leakage magnetic field compared with the other power-line structure.

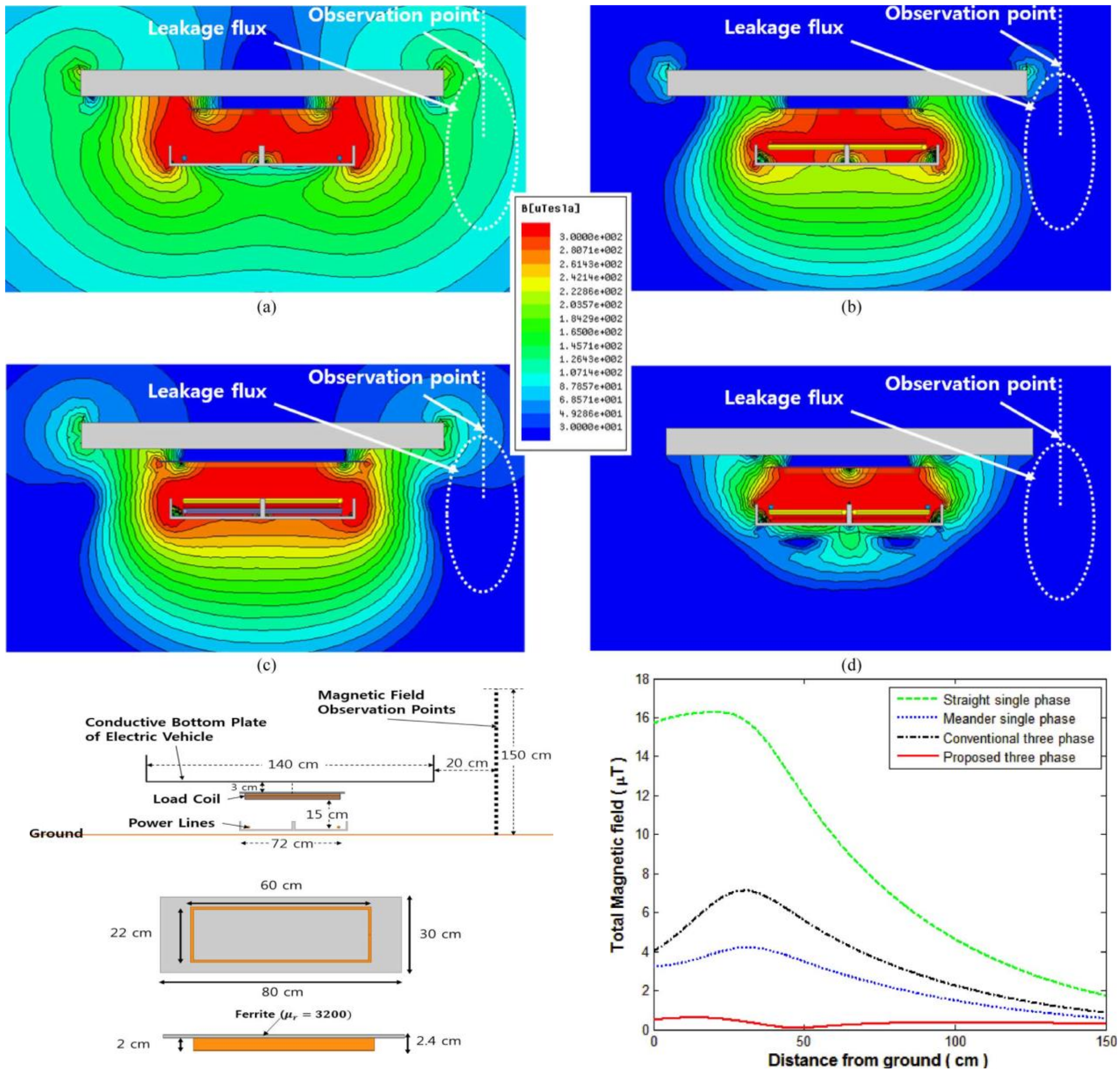

(e) (f)

Fig. 1-33. Side view of magnetic flux density distributions. (a) Straight single-phase. (b) Meander single-phase. (c) Conventional three-phase. (d) Proposed three-phase. (e) Overall setup for simulation side view and geometrical dimension of the pickup coil. (f) Simulated magnetic field at the observation position

In the meander single-phase power line structure, two meander lines are overlaid carrying opposite directions of current, the direction of the current segment in each side alternates at the side part of the power lines. Moreover, the inner part of the power lines increases the mutual inductance between the power lines and receiving coil when the receiving coil is placed at the max position because magnetic pole pairs are aligned. However, the receiving power becomes zero when the magnetic pole pairs are totally misaligned. Thus, it is a disadvantage that the receiving power fluctuates severely when the vehicle is moving along the power lines.

Conventional unipolar three-phase power lines are composed of three overlaid power lines that are terminated to a Y-connection point at the end. Similar to meander single-phase power lines, the three-phase power lines have the characteristic of a meander structure in which the current components in the side part of the power lines are canceling each other when observed at a distance. As the receiving coil is exposed to a magnetic field with three phases that have a 120-degree phase shift, the fluctuation of the receiving power is relatively low when the vehicle is moving along the power lines.

Proposed three-phase power lines consist of six overlaid power lines that are terminated to two Y-connection points at the end. The power lines are symmetrical from their center. Since the current is distributed into two wires in each phase, the side part and the center part of the power lines also cancel each other. It is, therefore, possible to dramatically reduce the leakage magnetic field by using an alternating current and a balancing structure. Similar to the conventional three-phase power lines, the proposed three-phase power lines have a low fluctuation of receiving power when the vehicle is moving along the power lines.

As shown in Fig. 1-33, the straight single-phase power line has the strongest magnetic field. The leakage magnetic flux density at the observation point is highly reduced by using the meander single-phase power line. The proposed three-phase power line has lower leakage field than the conventional three-phase power line. However, the peak magnetic flux density in the air-gap center plane remains almost the same for all four power lines, which is much higher than the IEEE C95.1-2005 safety limits.

A close-packed topology using discrete transmitters was proposed to reduce the receiving power pulsation in discrete charging system [117]. Different from the long track continuous wireless charger topology, the close-packed topology is easy to add more transmitters and extend the powered roadway without redesigning the resonant tanks. Since the transmitters are close-packed, there is mutual coupling between adjacent transmitters, the transmitter size and receiver size are optimized to achieve a high and smooth average coupling coefficient between transmitters and receiver, which ensures the smooth power transfer.

A prototype was built to transfer 1.4 kW through 150 mm air-gap at 85 kHz. The coil arrangements, mutual inductance and field distributions are shown in Fig. 1-34. According to the magnetic field simulation results, the air-gap magnetic flux density between the transmitter and receiver is higher than 387 μT, which is at least 1.5 times higher than the IEEE C95.1-2005 safety limits. The magnetic flux density is lower than 27 μT with 400 mm away from the transmitter vertically. In addition, the electric field distribution was not considered.

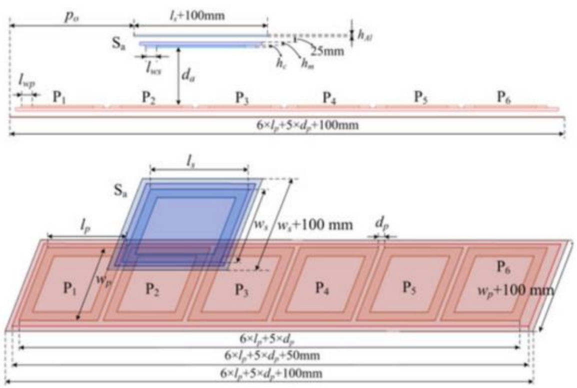

(a) Coil arrangements

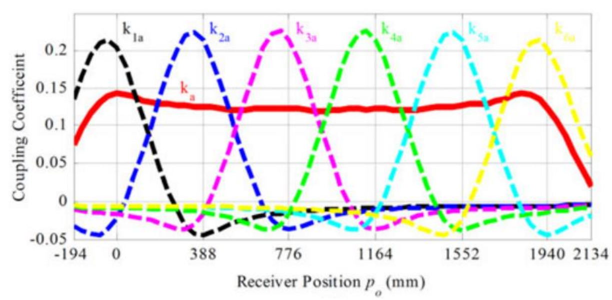

(b) Mutual inductance

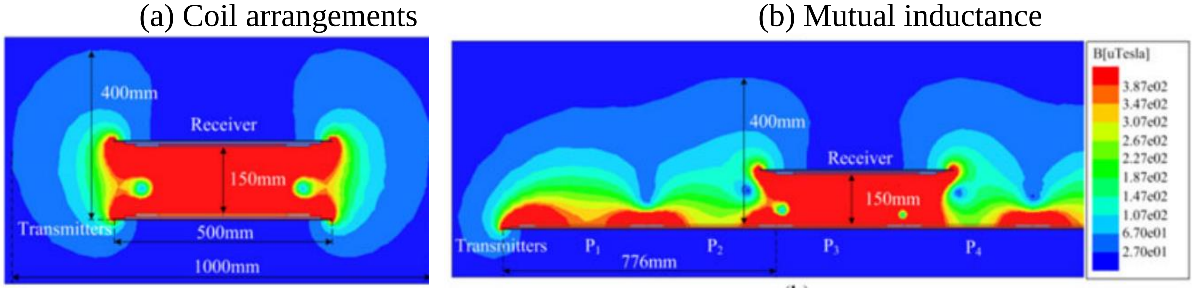

(c) Magnetic field distribution

Fig. 1-34. Close-packed discrete transmitter charging system

A 1 MW inductive power transfer system was developed to supply power to a high-speed train in real time [122]. It consisted of a 128 m U-shape transmitter and four pickups. The operating frequency of the system was 60 kHz to achieve efficient power transfer with a large air-gap. The measured efficiency of the IPT system at the 818-kW output power of the pickups for the 5-cm air-gap was 82.7%.

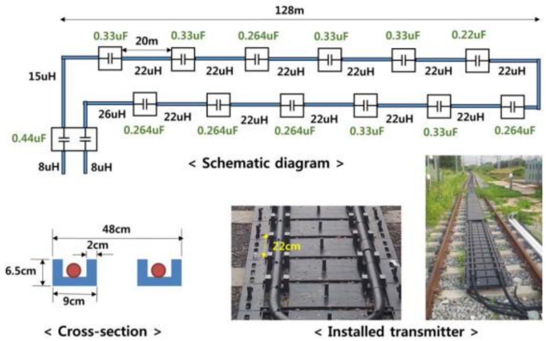

(a) Schematic and photo of transmitter

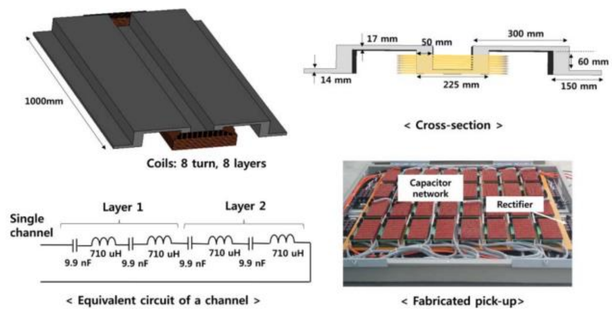

(b) Structure and equivalent circuit

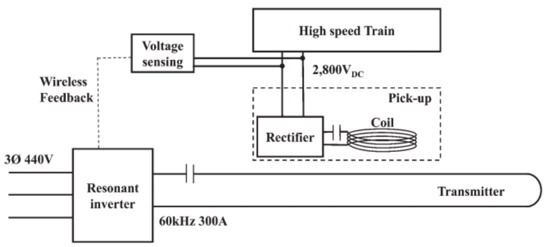

(c) IPT system configuration

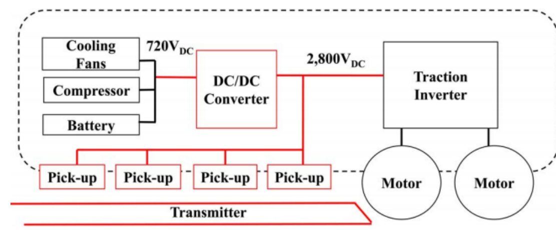

(d) Electric block diagram

Fig. 1-35. 1 MW WPT system for a train

Distributed inductor and capacitor compensation topology was used, which was very helpful to reduce high voltage stresses during resonant operation. Railroad, unlike other vehicles (bus or automobile), has the rail, which is metal that may cause the induced voltage. EMF and induced voltage on the rail were measured using a three-point method according to IEC 62110 [123] under a maximum rated road test (input power of 1 MW). The air-gap flux density was not considered due to low air-gap distance, which was not suitable for automobile application, and the electric field was not considered in the air-gap and around the rail.

1.3.3 Summary and identified research opportunities

In this section, magnetic field distributions of general used stationary and in-motion inductive wireless EV charging couplers, such as circular pad, DD pad, DDQ pad, bipolar pad, tripolar pad, double-sided pad, surface spiral winding, cylindrical winding, U-type power line, I-type power line, single-phase and three-phase power lines, are reviewed. DD pad, DDQ pad, bipolar pad, tripolar pad, and double-sided pad were developed to improve the mutual coupling and misalignment tolerance. Surface spiral winding and cylindrical winding were developed to reduce the air-gap magnetic field. Metal plate and metallic brush are used to shield leakage magnetic near field and electric field. The i-type power line was developed to reduce the leakage magnetic near field. Existing literature discussed air-gap magnetic field and electric field distributions of inductive wireless EV charging couplers are summarized in Table 1-9 with respect to the output power P, the operating frequency f, the air-gap d_{ag}, the air-gap center plane peak magnetic flux density B_{agcppk}, and the air-gap center plane peak electric field intensity E_{agcppk}.

Table 1-9. Summary of inductive wireless EV charging couplers

Ref.	P [kW]	f [kHz]	d_{ag} [mm]	B_{agcppk} [μT]	E_{agcppk} [V/m]	η_{coil} [%]	Institute
[84]	150	60	70	> 6k	NA	90.442 (η_{total})	KAIST, Korea
[86]	3	20	200	> 2k	NA	97.02	
[90][91] [92][96]	0.5	20	150	> 500	NA	90.12 to 97	
[114]	25	20	200	> 1.8k	NA	74 (η_{total})	
[115]	52	20	170	6.25@1.75m	NA	72 (η_{total})	
[116]	I_p = 60A	20	150	>300@edge	NA	NA	
[125]	3	20	200	> 1k	NA	96.1	
[126]	15.6	20	150	> 100k	NA	75	
[129][130]	1.176	20.15	156	> 2k	NA	96.01	
[154]	1.5	20	150	6.28@1.2m	~50	98.4	
[101][102] [103][104]	0.1	100	40	140@0.075m	NA	95.7	VT, US
[105]	0.1	100	40	80@0.075m	NA	94 to 95.7	
[106]	0.1	100	40	40@0.1m	NA	95.4	
[127]	3.3	22	125/150	2.9@0.8m	56.6@0.8m	93/89 (η_{total})	ORNL, US
[60]	3.3	85	150	> 2k	> 1k@0.3m	90 to 97	UM, US
[117]	1.4	85	150	> 387	NA	89.78 (η_{total})	
[128]	3	1000	150	IPT: 205@0.6m	CPT: 614@0.7m	Peak 94.45 (η_{total})	
[150]	0.14	1000	18	IPT > 120	CPT > 10k	61 to 74 (η_{total})	
[144]	3.3	85	200	> 1k	NA	NA	
[58]	3	50	160	> 600	NA	97.1	SU, Japan
	3	50	200	> 1k	NA	95.5	
[131]	3	50	150	> 1k	17.78@3m	97.0	
[132][133] [134]	4.67	20	150	60@0.5m	NA	NA	AU, Denmark
[135]	3.3	15-50	200-300	14@0.6m	NA	NA	UG, US
[136]	22	25	185	> 17k	NA	90.2 to 97.3	USC, US
[137]	3	250	300	4.8k	NA	90	KU, Japan

[155]	2	20	200	> 1k	NA	NA	UA, New Zealand (Use ferrite utilization efficiency as evaluation metrics)
[52]	2	20	200	> 1k	NA	NA	
[30][156]	I_p = 23A	20	125	> 2k	NA	NA	
[31]	2	20	200	> 1k	NA	NA	
[54]	0.26	10	30	> 7k@ I_p = 125A	NA	80 (η_{total})	
[138][157]	I_p = 20A	38.4	150	1.5@0.8m	NA	NA	
[55][56][57]	3.5	20	200	27@0.85m	NA	96	
[139]	0.0449	684	62	> 700	NA	Peak 80 (η_{total})	JLU, China
[140]	3.3	85, 140	100-170	> 450	NA	> 90	IPT, Germany
[141]	3.3	NA	NA	20.84@0.7m	NA	~ 91	SEU, China
[142]	1	85	150	> 2.5k	NA	~ 97.5	TU Delft, the Netherlands
[143]	0.56	85	150	8.8@0.25m	127.8@0.25m	NA	UP, Italy
[94]	8	22	200	> 5.9k	NA	NA	CAS, China
[145]	20	20	200	> 38.4k	NA	NA	TDK, US
[148]	5	150	100	NA	Coil >200k	NA	
[146]	1	8000	300	27@2.72m	83@2.27m	NA	NIT, Japan
[97]	I_p = 5A	40	200	11@0.24	NA	NA	USU, US
[147]	25	393	95-117	NA	>85k	> 60	MIT, US
[149]	I_p = 30A	80	NA	Coil 6.5k	NA	NA	TMU, Japan
[95]	1	27120	116	NA	>140dBV/m	85	FEC, Japan
[151]	1	85	200	> 350	NA	63 to 91 (η_{total})	UL, Italy
[98]	0.191	232	200	4.66@0.6m	NA	93.66	FIU, US
[152]	0.5	20	70	> 5k	NA	NA	
[153]	70	85	200	> 30k	NA	96.89	
[158]	2	20	200	> 800	NA	NA	UHK, China
[80][81]	3	3700	300	~187	~3400	96	UW, US
[83]	1	3500	300	~110	~2000	90 to 96	
[108]	3.4	18-20	100	1872	5425	82.3 (η_{total})	INL, US
[159][160]	5	100	52	~3500	NA	96.5 (η_{total})	ETH Zurich, Switzerland
[160][161]	50	85	160	<27@0.8m	NA	95.8 (η_{total})	

In Table 1-9, 41 unrelated papers investigated the air-gap magnetic field distribution, only 8 papers paid attention to the air-gap electric field distribution. However, none of them satisfies the IEEE C95.1-2005 magnetic field and electric field safety limits simultaneously when transferring multi-kW. Even though designs operating at MHz frequency satisfies the magnetic field electrostimulation safety limit, they didn't meet the electric field safety limit, in addition, they didn't satisfy the magnetic field tissue heating safety limit, which is more important when operating above 100 kHz.

Previous magnetic component designs have focused on improving the power transfer efficiency and misalignment tolerance, and shielding the leakage magnetic near field. However, no research has focused on the loosely coupled inductive WPT system design methodologies to achieve low air-gap magnetic flux density, low air-gap electric field intensity and high transfer efficiency simultaneously when transferring multi-kW. No power scaling law has been developed to meet the safety standards while scaling to multi-kW, and tens of kW. The effect of ferrite shield on magnetic field distribution has been investigated, however, the effect of ferrite shield on electric field distribution has not been investigated. Change of magnetic field distribution due to misalignment have been investigated, however, the effect of misalignment on electric field distribution has not been investigated. In addition, methods to deal with the magnetic and electric field distributions under misalignment have not been developed. Moreover, current magnetic shielding techniques can only shield the magnetic flux above the receiver coil and below the transmitter coil, however, the air-gap magnetic flux density is still very high in the regions adjacent to the coils, there is no shielding technique that has been developed to make the magnetic field distribution uniform in the air-gap region and reduce the air-gap electric field.

1.4 Loosely coupled inductive WPT system modeling for equivalent circuit and electromagnetic field

The equivalent circuit modeling and electromagnetic field calculation of loosely coupled inductive WPT system are required to develop the system design methodologies. Since the transfer distance is much larger than the conventional strongly coupled inductive systems, it is necessary to investigate whether the traditional transformer model is appropriate to analyze the loosely coupled system.

For loosely coupled inductive WPT systems, resonant compensation capacitors are necessary to enhance power capacity and power transfer efficiency. Without the compensations, the systems have almost zero efficiency. Four basic compensation topologies are used in most applications: series-series (SS), series-parallel (SP), parallel-series (PS) and parallel-parallel (PP) resonant circuits. In addition to four basic compensation topologies, LCL and LCC compensation topologies were also proposed to reduce VA rating and improve misalignment tolerance [162]-[166]. Study on the compensation topologies and on the reasons of the topology selection is important in loosely coupled system designs [167][168].

In this section, firstly, lumped circuit model for loosely coupled WPT system is reviewed, then four basic resonant compensation topologies, LCL and LCC compensation topologies, and impedance transformation circuits are reviewed. After that, the electromagnetic calculation methods used in existing literature will be reviewed.

1.4.1 Lumped equivalent circuit model

Depending on the size of coils and the operating frequency, either the distributed or the lumped parameter modeling will be used. According to Inan [13], if the diameter of coils and the transfer distances are smaller than one-tenth of the wavelength, lumped parameter model is suitable for the system analysis. When the operating frequency is 20 MHz, the corresponding wavelength is 15 m, therefore, the maximum length for the diameter of the coil and the power transfer distance should be smaller than 1.5 m in order to use lumped model.

In general, the operating frequency of inductive WPT systems is lower than 20 MHz, and the transfer distance and the size of the coils are shorter than 1.5 m. Therefore, the majority of the inductive WPT system can be modeled with the lumped model instead of a distributed model.

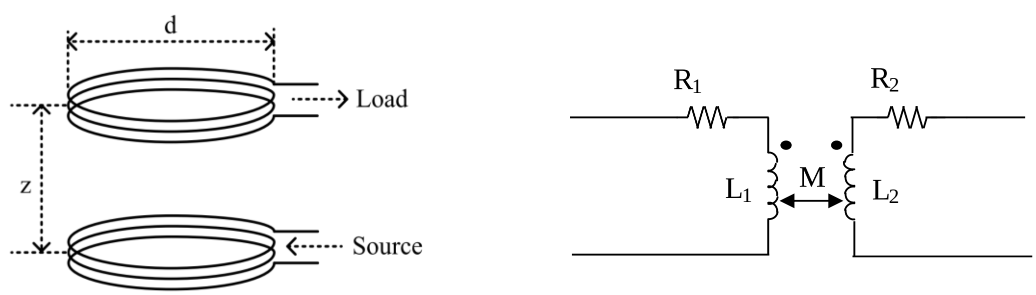

(a) Large air-gap WPT system (b) Equivalent circuit model

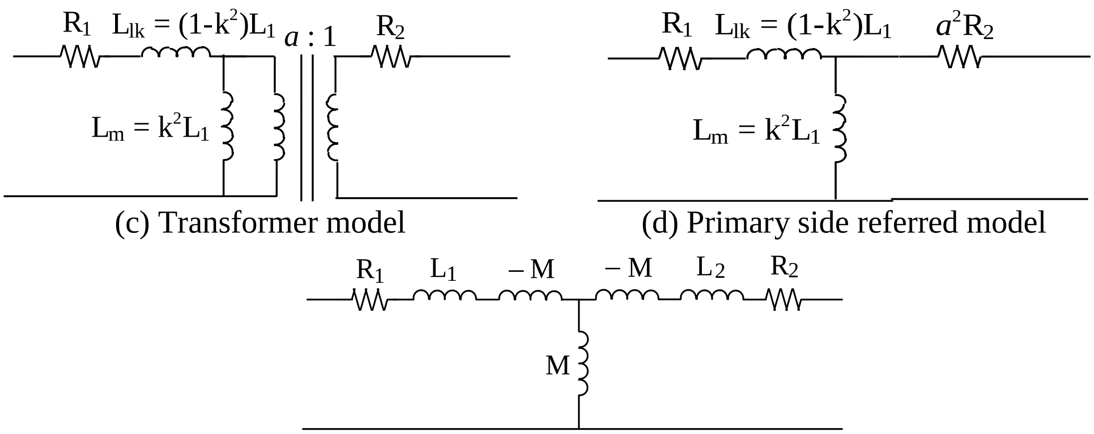

(c) Transformer model (d) Primary side referred model

(e) Transformer T-model

Fig. 1-36. Equivalent lumped element model of inductive transfer system

The lumped model was used for the current carrying loops of 30 cm distance power transfer at 3.7 MHz [80]-[82]. The lumped parameter model was evaluated by analytical, FEA and experimental results. The coupled inductor model in Fig. 1-36 (a) was used for the large air-gap WPT systems. Using the circuit theory [169], the coupled inductor was represeted with equivalent transformer model with the transfer ratio *a* as shown in Fig. 1-36 (c). The transfer ratio *a* of the coupled inductor is defined as

$$a = k\sqrt{\frac{L_1}{L_2}} \tag{1.3}$$

For the convenience of the analysis, the transformer model was referred to the primary side as shown in Fig. 1-36 (d). In order to reduce the calculation effort, the transformer T-model, shown in Fig. 1-36 (e), can also be used to analyze the system.

1.4.2 Compensation topologies in loosely coupled systems

- **SS, SP, PS, and PP compensation topologies**

Resonant compensation topologies are required for loosely coupled inductive WPT system to achieve high power transfer efficiency. The typical SS, SP, PS, and PP compensation topologies are shown in Fig. 1-37.

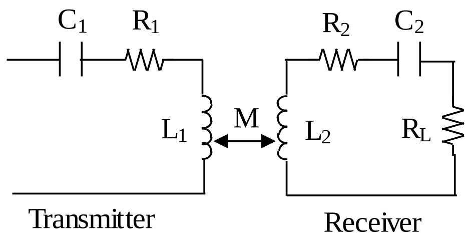

(a) Series-Series compensation topology

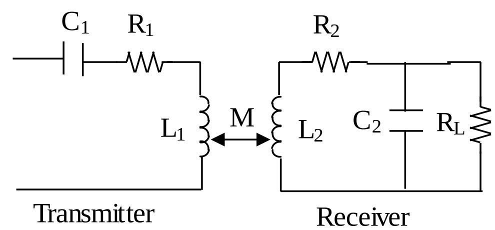

(b) Series-Parallel compensation topology

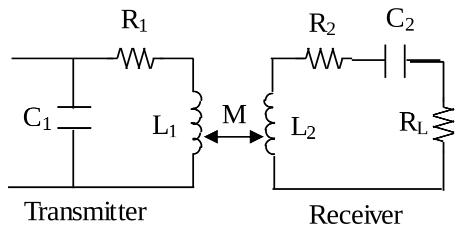

(c) Parallel-Series compensation topology

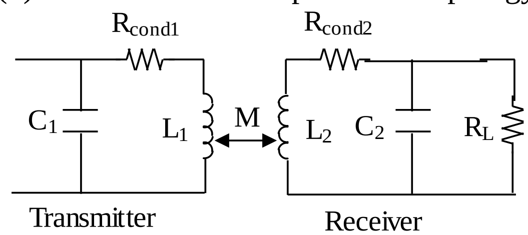

(d) Parallel-Parallel compensation topology

Fig. 1-37. Illustration of the SS, SP, PS, and PP compensation topologies

If the primary side is series compensated, a voltage source converter could be connected directly to the coil. If it is parallel compensated, an inductor is usually inserted to change the converter to a current source. When the primary coil has a constant current, a series compensation at the secondary side makes the output like a voltage source, while a parallel compensation makes the output like a current source [59][170][171].

Charing the battery pack of an electric vehicle is performed in two steps: constant current (CC) mode to bring up the battery pack state-of-charge (SOC), and constant voltage (CV) mode order to meet the upper charge voltage of the battery pack. The compensation topologies that match these modes are well known, with CC mode best implemented with the SS type loaded by a diode rectifier and output filter capacitor, whereas CV mode is generally configured as SP type loaded by a diode rectifier but with an inductor input filter [172][173]. Another thing should be noted is that the equivalent resistance of the battery pack increases slightly in the CC mode, and increases significantly in the CV mode. While there is an optimal load for the inductive WPT system to achieve the maximum coil-to-coil efficiency. It would be beneficial if the WPT system can maintain relatively high efficiency in the whole operating range.

SS and SP systems are preferred for high power applications since the input impedance of the systems is low. Impedance transformation networks are not required typically. Input impedances of PP and PS systems are the maximum at the resonant frequency, therefore, PS and PP systems require an additional series inductor in order to decrease equivalent input impedance and to regulate input current to the resonant circuit. However, additional inductor brings copper loss which will reduce system efficiency, it will also increase converter size and the cost of the system [174]-[176]. The resonant compensation capacitances are calculated as shown below.

Table 1-10. The primary and the secondary compensation capacitance

	Compensation capacitance	
Type	Primary	Secondary
SS	$\dfrac{1}{\omega_0^2 L_1}$	$\dfrac{1}{\omega_0^2 L_2}$
SP	$\dfrac{1}{\omega_0^2 (1 - k^2) L_1}$	$\dfrac{1}{\omega_0^2 L_2}$
PS	$\dfrac{L_1}{\omega_0^2 L_1^2 + \left[R_1 + \dfrac{(a\,\omega_0 L_2)^2}{R_L + R_2}\right]^2}$	$\dfrac{1}{\omega_0^2 L_2}$
PP	$\dfrac{1}{\omega_0^2 (1 - k^2) L_1 + \dfrac{(R_1 + a^2 R_L)^2}{(1 - k^2) L_1}}$	$\dfrac{1}{\omega_0^2 L_2}$

As shown in the above table, the resonant capacitor of SS topology is independent of the coupling factor and load, while the resonant capacitor of SP topology is a function of the coupling coefficient, therefore, the efficiency of SP topology decreases rapidly as the transfer distance increases and the coupling coefficient decreases [177]-[179]. The resonant capacitors of PP and PS systems are a function of the load resistance and the coupling coefficient; hence, the efficiencies of the PP and PS systems are sensitive to the changes of the transfer distance and the load. The dependence of the coil-to-coil efficiency η on the load resistance R_L and the coupling coefficient k for four basic topologies is plotted in Fig. 1-38 [81].

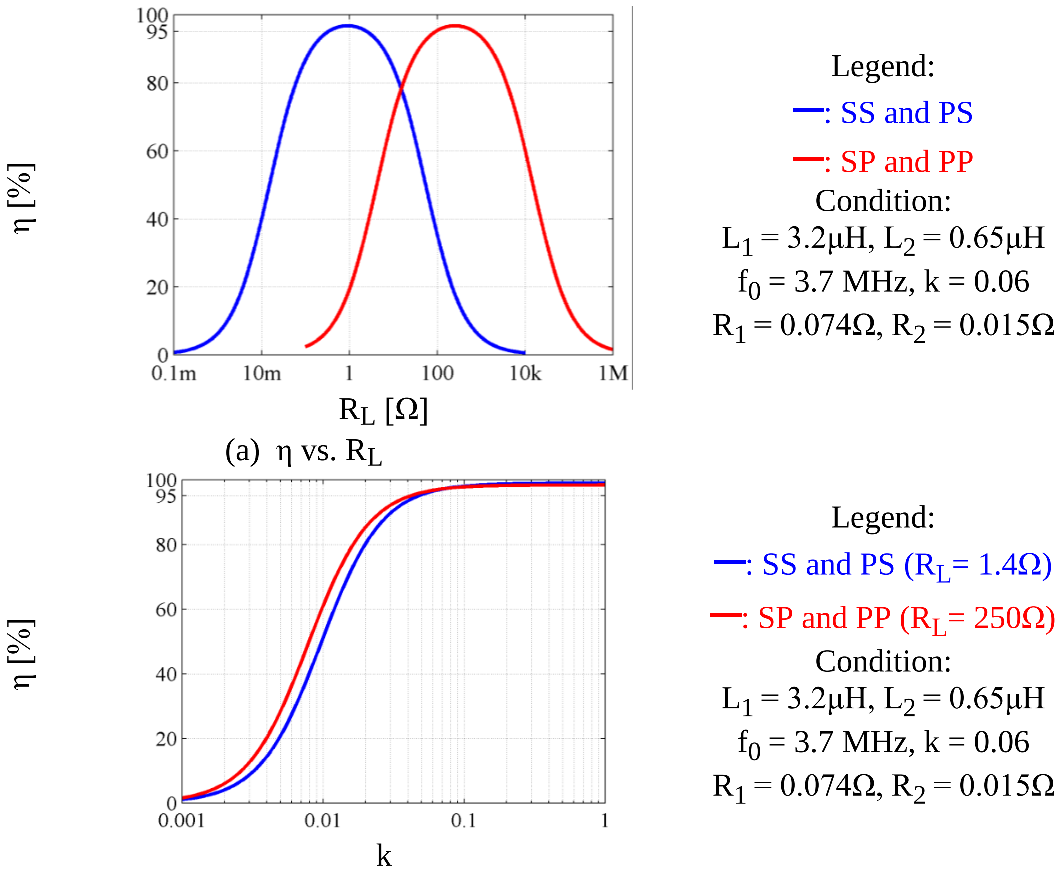

(a) η vs. R_L

(b) η vs. k

Fig. 1-38. Dependence of the coil-to-coil efficiency η on the load resistance R_L and the coupling coefficient k

As shown in Fig. 1-38, the dependences of η on R_L and k are the same for SS and PS topologies, while that are the same for SP and PP topologies. The optimal loads for all four topologies are singular. As the coupling coefficient increases, the coil-to-coil efficiency generally increases. However, one should note that the coil resistances and inductances are not independent of the mutual inductance and coupling coefficient. In addition, the optimal load resistances change with these parameters.

If the load is a voltage source, such as a battery pack in an EV, it is sensitive to the battery voltage. Another problem is that the capacitor can only compensate the coil inductance in the case when the primary and secondary coils are well aligned. When there is a misalignment between the two coils, the output power and efficiency both drop quickly [162][180][181].

Different from four basic compensation topologies, LCL and LCC compensated networks work as a constant current source, which works well for both light and heavy load conditions, and they are not significantly affected by misalignment. In addition, there are a few benefits to have a constant primary coil current. When a coil is designed, the rated current of the coil is determined. A constant current feature can make the coil work at its rated condition easily. For a track form coil at the primary side in dynamic roadway charging, multiple receiving coils could be powered, which also prefers a constant current in the track [164][180][181].

- **LCL compensation topology**

LCL compensation network is formed by adding LC compensation network between the inverter and the transmitting coil. Primary side LCL compensation topology is shown in Fig. 1-39 [162]. The circuit parameters are designed by the following equation to achieve a constant resonant frequency for the topology shown in Fig. 1-39:

$$L_r\, C_p = L_p\, C_p = \frac{1}{\omega_0^2} \tag{1.4}$$

Where ω_0 is the angular resonant frequency, which is only relevant to inductors and capacitors in the system, independent of the coupling coefficient and load conditions.

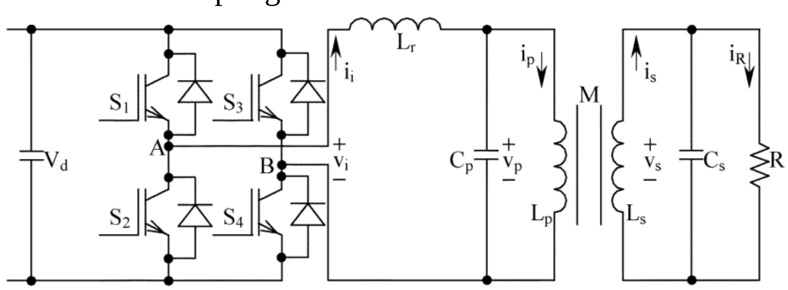

Fig. 1-39. Circuit diagram of an ICPT system driven by an LCL load resonant inverter

The design for an LCL inverter usually requires the same value for the two inductors. However, the coil-to-coil efficiency is still a function of the load resistance and the coupling coefficient the same as the four basic topologies. The inductor L_r changes the voltage source into a current source. The LCL topology can be treated as an extension of the PP topology. The additional inductor L_r will cause additional loss.

- **LCC compensation topology**

Different from LCL compensation topology, a capacitor is put in series with the primary side coil to compensate part of the reactive power in the primary coil, thus, the power rating on L_{f1} can be reduced, the system design flexibility could also be improved. By utilizing an LCC compensation network, a zero-current switching (ZCS) condition could be achieved by tuning the compensation network parameters. Double-sided LCC compensation topology is shown in Fig. 1-40 [180][181].

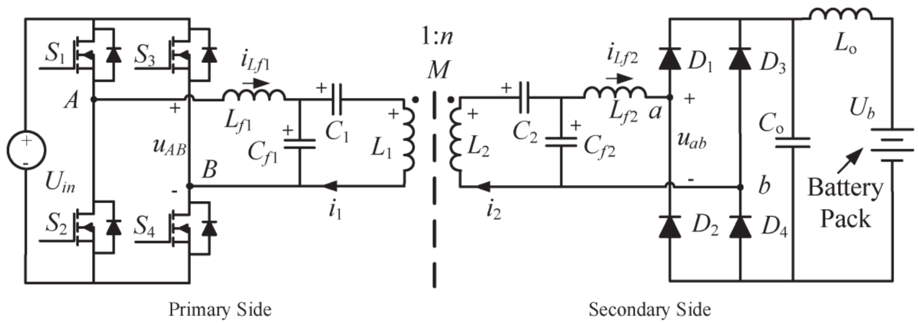

Fig. 1-40. Double-sided LCC compensation topology for WPT

The circuit parameters are designed by the following equations to achieve a constant resonant frequency for the topology shown in Fig. 1-40 [166][182]:

$$L_{f1}\, C_{f1} = \frac{1}{\omega_0^2} \tag{1.5}$$

$$L_{f2}\, C_{f2} = \frac{1}{\omega_0^2} \tag{1.6}$$

$$L_1 - L_{f1} = \frac{1}{\omega_0^2\, C_1} \tag{1.7}$$

$$L_2 - L_{f2} = \frac{1}{\omega_0^2\, C_2} \tag{1.8}$$

Although it looks like that the tuning process is only relevant to inductors and capacitors in the system, independent of coupling coefficient k and load conditions. However, the inductors L_{f1} and L_{f2} depend on the required output power P and the voltages U_{AB} and U_{ab} as shown in the following expression [166]:

$$L_{f1} = L_{f2} = \sqrt{\frac{k\, U_{AB}\, U_{ab}}{\omega_0\, P}\, L_1} \tag{1.9}$$

Which means the system efficiency, tuning capacitors and inductors also depend on the load resistance and the coupling coefficient as other topologies. However, when LCL or LCC compensation topology is used on the secondary side of the inductive coupled WPT system, the reactive power at the secondary side could be compensated to form a unit power factor pickup.

Even though the reactive power at the secondary side can be compensated by using LCL or LCC topology, the reactive power at the primary side can't be compensated when there is a misalignment between the transmitter coil and the receiver coil. Less attention has been paid to reduce the reactive power at the primary side with low loss.

- **Active tuning compensation topologies**

When there is a misalignment or the transfer distance changes, the power transfer efficiency decreases due to the impedance mismatch, which leads to power reflected to the transmitter and reduces the output power capability. Tunable matching networks (TMNs) have been developed to improve the power transfer efficiency.

A TMN is typically implemented as an ideally-lossless, lumped-element reactive network, where some of its reactive elements are realized as variable (tunable) components. The impedance of the tunable components can be controlled externally or dynamically match the load impedance to a desired input impedance at a particular frequency, or over a range of frequencies. Based on the technology employed for realizing the variable reactance elements, conventional TMNs can be classified as either analog (continuously adjustable) or digital (adjustable among a set of discrete values).

The analog TMNs rely on variable reactance elements whose value (at some frequency or over a range of frequencies) can be tuned in an (ideally) continuous manner. For instance, conventional high power RF plasma drives often employ TMNs based on mechanically adjusting physical passive components, such as stepper-motor-adjusted variable-vacuum capacitors [183].

While widespread, this technique is extraordinarily slow. Faster response can be obtained by appropriately adjusting bias conditions of electronic components such as varactors [184] or MEMS-varactors [185]. Nevertheless, power handling with such components is somewhat limited by the relatively high bias voltages required when operating at high power levels [186].

In digital TMNs, on the other hand, tunability is achieved by implementing the variable reactive elements as digitally switched arrays, thus allowing adjustment of the impedance of the variable reactances in discrete steps. The realization of digital TMNs is typically based on CMOS switches [187], MEMS switches [188], PIN diodes [189] or discrete power transistors. MEMS switches are characterized with very low on-state resistance and can operate up to tens of GHz with negligible power consumption. The reliability of MEMS switch-based TMNs, however, is still an issue due to the large control voltages required by MEMS switches. On the other hand, PIN diode and CMOS switch-based TMN realizations offer the capability to handle very high power levels at the expense of some power loss in the switches due to their on-state resistance. Such TMN realizations are particularly favorable for on-die integration. The main drawback of digital TMNs, however, is their limited tuning resolution, and hence, the accuracy with which impedance matching can be achieved with an acceptable number of switched components. In some high power applications where accurate impedance matching is required over a very wide impedance range, such as RF plasma drivers, for example, the use of digital TMNs may be impractical due to the large number of digital switches needed to achieve the required fine tuning resolution. For instance, conventional high-power RF plasma drivers often still employ automatic antenna tuners based on stepper motor-adjusted continuously-variable capacitors as a result of the high requirements for accurate impedance matching and operation over very wide impedance ranges.

The limitations of existing techniques motivate improvement of the capabilities of TMNs to provide more accurate and faster impedance matching (higher tuning bandwidth) over wider impedance range while simultaneously allowing operation at high power levels with minimum loss, including both switching loss and conduction loss.

A four-terminal tunable capacitor is introduced for design of novel resonant filters in power converters [190][191]. The capacitor can be tuned with bias voltage on the auxiliary terminals so that the resonant frequency is kept at the switching frequency. The photo and equivalent circuit of tunable capacitor is shown in Fig. 1-41 (a). When increasing the bias voltage, the effective capacitance will reduce as shown in Fig. 1-41 (c). When the current increases, the effective inductance L_2 will reduce due to saturation, the increased current ripple can be reduced through capacitor active tuning, as shown in Fig. 1-41 (d)(e). However, this kind of capacitor can't be applied to high power applications due to low voltage rating.

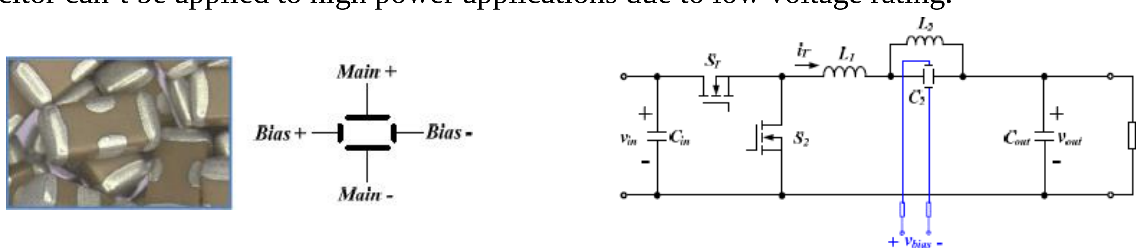

(a) Photo and equivalent circuit of tunable capacitor (b) Buck converter with resonant filter

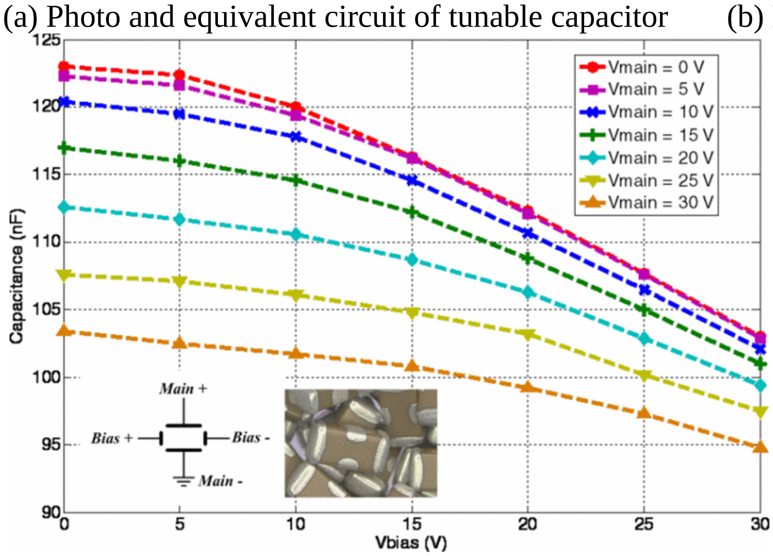

(c) Measured capacitance under various voltage conditions

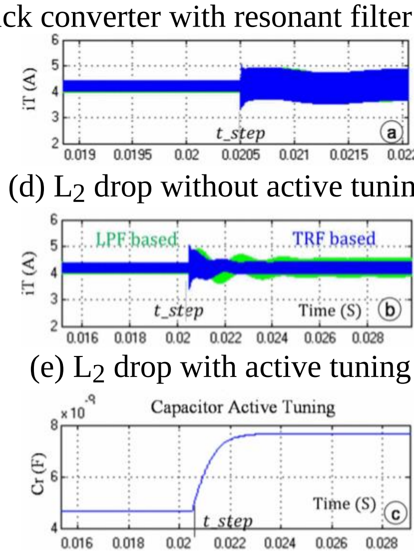

(d) L_2 drop without active tuning

(e) L_2 drop with active tuning

(f) Capacitor value change

Fig. 1-41. Tunable capacitor with bias voltage on the auxiliary terminals

Nonlinear capacitor, such as ceramic capacitor, can also change capacitance by varying DC bias [192]. An auxiliary circuit is required to hold the DC bias and supply the leakage current of the nonlinear capacitor. A double clampled auxiliary circuit with low loss was developed to continuously varying DC bias as shown in Fig. 1-42. Two identical capacitors were implemented in series. When one of these capacitors has DC bias, the other one automatically matches with the inverted DC bias due to ampere second balance.

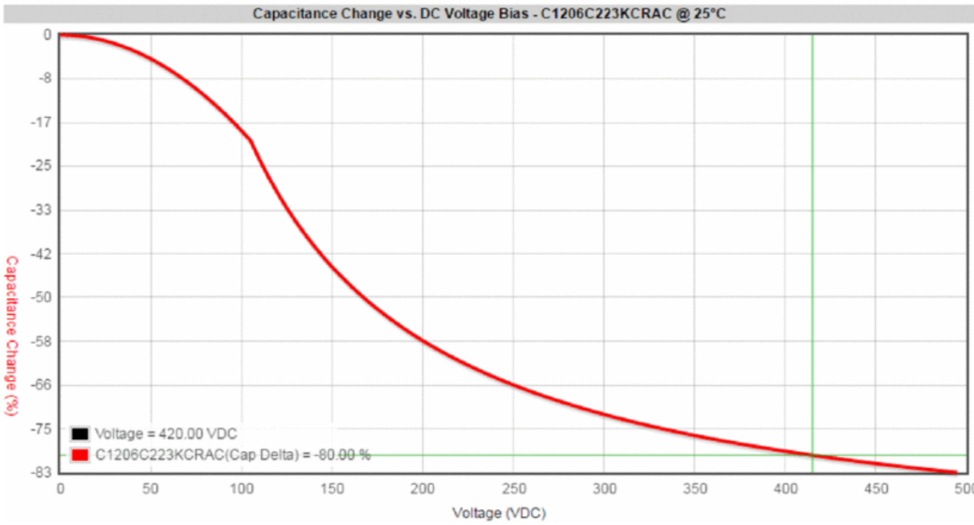

(a) Ceramic capacitance with respect to DC bias

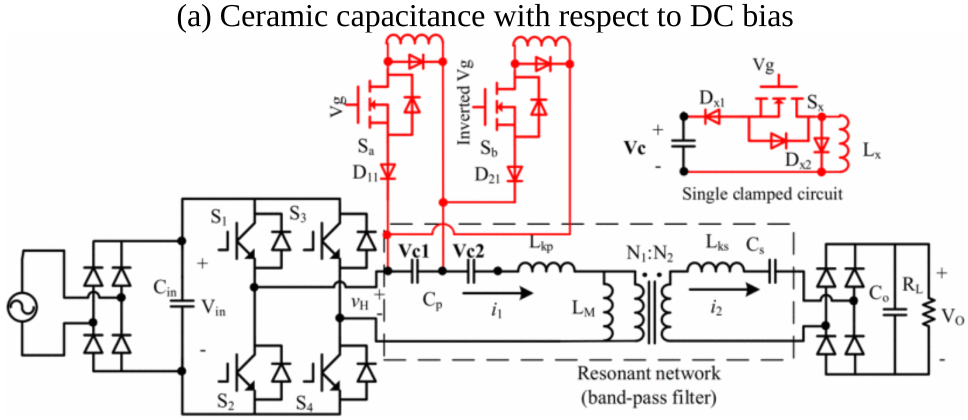

(b) Double clamped auxiliary circuit for capacitor tuning

Fig. 1-42. Ceramic capacitor property and double clamped auxiliary circuit for capacitor tuning

Although it's claimed that this nonlinear capacitor tuning method can be extended to high power applications, special attention must be paid to the control aspect, especially during startup process. In addition, the equivalent-series-resistance (ESR) or dissipation factor of a ceramic capacitor is about 100 times higher than a film capacitor. Moreover, the thermal stability of the ceramic capacitor is worse than that of the film capacitor, a relatively large amount of small capacitors are needed to parallel to reduce the ESR and dissipate the heat.

Capacitor matrix circuit, shown in Fig. 1-43, is used in [193] to maintain high transfer efficiency when the transfer distance changes. However, it can't be scaled to high power due to so many bulky capacitors. In addition, the loss distribution was not analyzed and optimized.

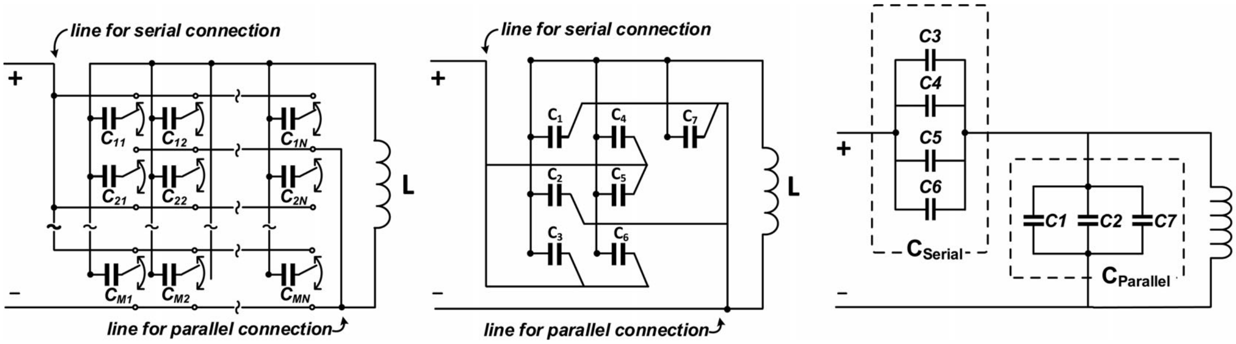

(a) (b) (c)

Fig. 1-43. Capacitor matrix circuit design for impedance matching (a) M x N capacitor matrix circuit. (b) Example of a capacitor matrix with seven capacitors. (c) Equivalent circuit of (b)

Switch-controlled inductor and switch-controlled capacitor have been used to regulate class-E resonant converter [194] and tune impedance matching network [195][196]. Through adjusting the PWM duty cycle to tune the phase shift angle α, the equivalent capacitance or inductance can be manipulated. The topologies and waveforms of full-wave switch-controlled inductor (full-wave SCI) and full-wave switch-controlled capacitor (full-wave SCC) are presented in Fig. 1-44. The relationship between the equivalent inductance L_{SC} (or the equivalent capacitance C_{SC}) and the phase shift angle α can be expressed by

$$\frac{Lsc}{La} \text{ or } \frac{Csc}{Ca} = \frac{\pi}{2\pi - 2\alpha + \sin(2\alpha)} \tag{1.10}$$

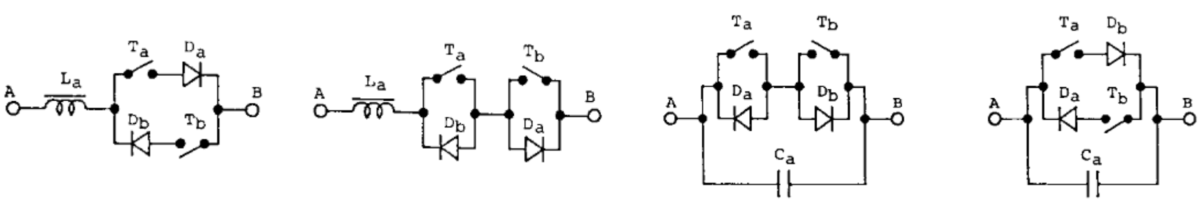

(1) (2) (1) (2)

(a) Full-wave SCI topologies (1) series type and (2) parallel type

(b) Full-wave SCC topologies (1) series type and (2) parallel type

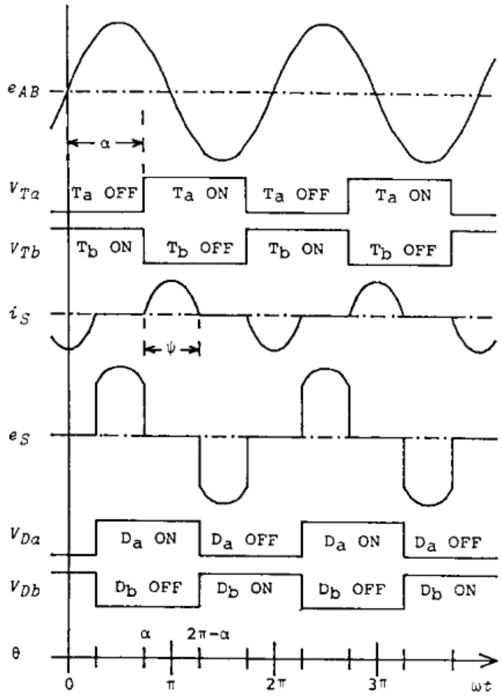

(c) Full-wave SCI waveforms

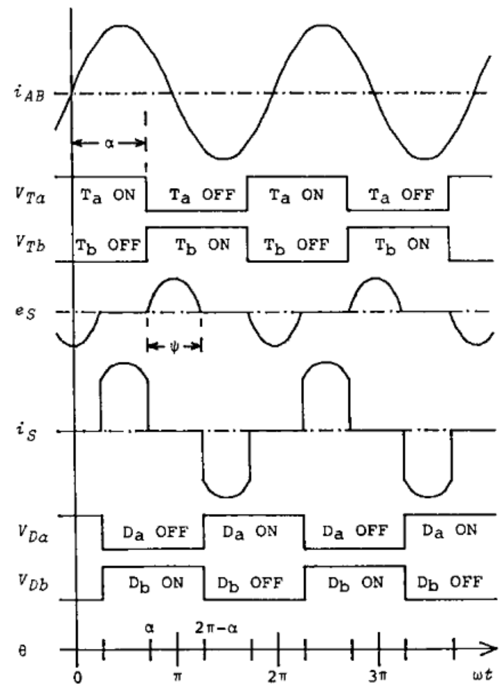

(d) Full-wave SCC waveforms

Fig. 1-44. Topologies and waveforms of full-wave SCI and full-wave SCC

The SCC and SCI provides an access to tune the impedance online. However, the loss distribution has not been fully analyzed, and the low loss SCC and SCI have not been developed. On the other hand, less attention has been paid to use the SCC and SCI in WPT system, the effects on the reactive power and power transfer efficiency has not been analyzed.

- **Control stability conditions**

The coupled resonant system can have one or more zero phase-angle frequencies (ZPF) depending on the loads [197]-[199]. Magnitude and phase plots of an example system are shown in Fig. 1-45 to illustrate zero phase-angle dependency on the load.

There is a single ZPF at the resonant frequency 3.7 MHz when R_L is 8 Ω or 12 Ω. However, the system has three ZPFs when R_L is 4 Ω. Instead of fixed frequency generators, variable frequency controllers which have been widely used for loosely coupled systems are operated by tracking ZPF (resonant frequency) in order to minimize required volt-amp rating of the power generator. However, if there are multiple ZPFs, the variable frequency controllers cannot follow the single tuned frequency, the operating frequency will move back and forth unstably between the three ZPFs, which is called "bifurcation" [19][197][198]. Therefore, estimation of the number of ZPFs is important in evaluating the stability of the system design.

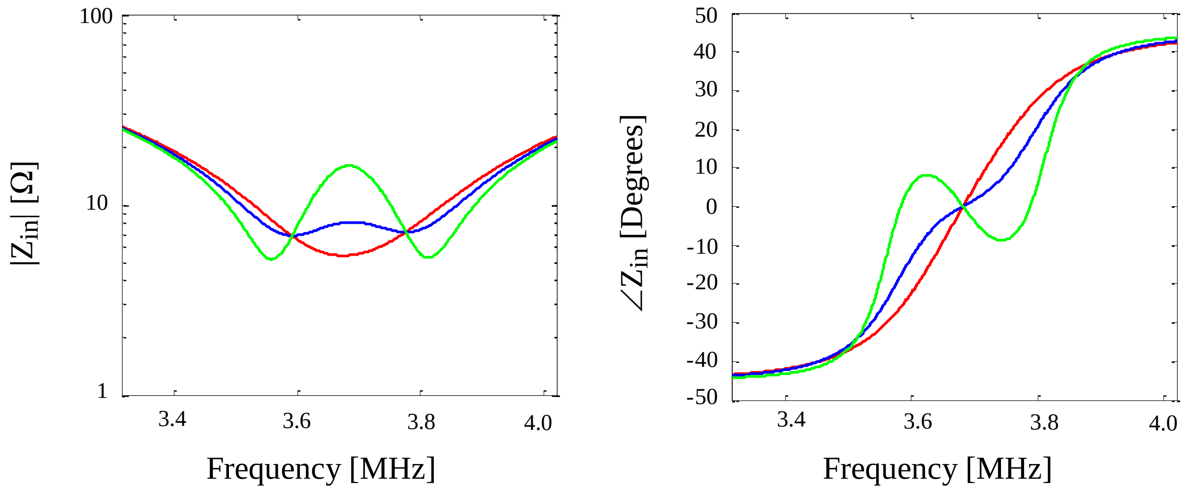

(a) Magnitude of the input impedance (b) Phase of the input impedance

Legend: $R_L = 4\ \Omega$ $R_L = 8\ \Omega$ $R_L = 12\ \Omega$
Test conditions: SS compensated system
$L_p = 7.0693\ \mu H$, $R_p = 0.055\ \Omega$, $L_s = 4.6918\ \mu H$, $R_s = 0.0401\ \Omega$, $M = 0.5971\ \mu H$.

Fig. 1-45. The magnitude and phase plot of the input impedance versus frequency

According to [197], the four compensation topologies have to satisfy the conditions in Table 1-11 in order to have single ZPF at a given load. Q_p and Q_s are the loaded quality factors of the transmitter and the receiver resonant tanks, respectively.

Table 1-11. Stability conditions of the four topologies

	Stability conditions	
SS	$Q_p > \dfrac{4Q_s^3}{4Q_s^2 - 1}$	Where $Q_p = \dfrac{\omega_0 L_1 R_L}{\omega_0^2 M^2}$ and $Q_s = \dfrac{\omega_0 L_2}{R_L}$
PS	$Q_p > Q_s$	
SP	$Q_p > Q_s + \dfrac{1}{Q_s}$	Where $Q_p = \dfrac{\omega_0 L_1 L_2^2}{M^2 R_L}$ and $Q_s = \dfrac{R_L}{\omega_0 L_2}$
PP	$Q_p > Q_s + \dfrac{1}{Q_s}$	

In addition, when different compensation topologies are used, the input impedance of the system will be different, as shown in Fig. 1-46 when LCL compensation topology is used in the primary side for the same system.

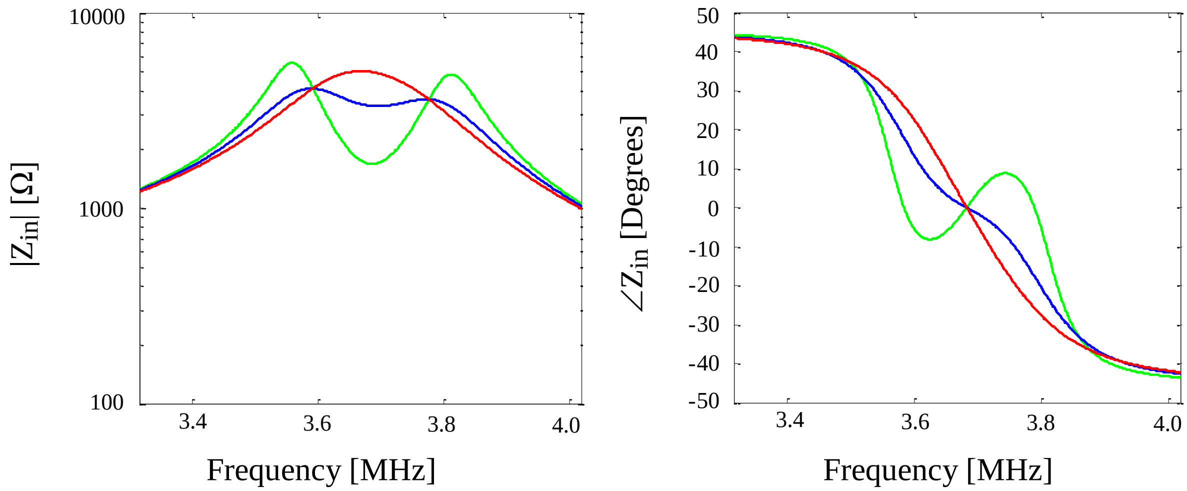

(a) Magnitude of the input impedance (b) Phase of the input impedance

Legend: $R_L = 4\ \Omega$ $R_L = 8\ \Omega$ $R_L = 12\ \Omega$

Test conditions: LCL-Series compensated system

L_p = 7.0693 μH, R_p = 0.055 Ω, L_s = 4.6918 μH, R_s = 0.0401 Ω, M = 0.5971 μH.

Fig. 1-46. The magnitude and phase plot of the input impedance versus frequency

Although R_L remains 12 Ω to achieve one ZPF, the input impedance for LCL system is 5021 Ω, while that of the SS system is 5.406 Ω, which makes the system perform differently when the load changes. There has been a lot of investigation on the effects of different topologies on system efficiency when the load changes or the misalignment occurs, less attention has been paid to the effects of different topologies on the air-gap region magnetic and electric field distributions, especially during misalignment.

1.4.3 Magnetic field and electric field analytical models

Air-gap magnetic field and electric field analytical models are necessary to develop an inductive WPT system general design methodology. Compared with numerical tools, analytical models are efficient and easy to use to find general design guideline. In this subsection, magnetic field and electric field analytical models used in existing literature will be reviewed.

- **Magnetic field analytical model**

The Maxwell-Faraday equation and the Ampère's circuital law with Maxwell's addition as shown in following expressions are the two base equations for the transformation between the AC magnetic field and the AC electric field [200][201]

$$\nabla \times \vec{E} = -\frac{\partial \vec{B}}{\partial t} \tag{1.11}$$

$$\nabla \times \vec{B} = \mu_0 \left(\vec{J} + \varepsilon_0 \frac{\partial \vec{E}}{\partial t} \right) \tag{1.12}$$

According to the magnetic potential theory, the magnetic field $\vec{B}$ of a single current loop with radius R, as shown in Fig. 1-47, can be calculated by the magnetic vector potential $\vec{A}$ using [200][201]:

$$\vec{B} = \nabla \times \vec{A} \tag{1.13}$$

Where, $A_\varphi(r,\ \theta) = \dfrac{\mu_0 I R}{4\pi} \displaystyle\int_{\varphi'=0}^{2\pi} \frac{\cos \varphi'}{\sqrt{R^2 + r^2 - 2 R r \sin \theta \cos \varphi'}} d\varphi'$, r, θ, and φ are spherical coordinates, I is the loop current, s is the distance between the test point and the current element.

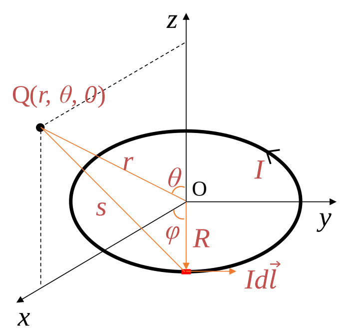

Fig. 1-47. Configuration of a single current loop

The magnetic flux density $\vec{B}$ at the test point can be calculated as

$$\begin{bmatrix} B_r \\ B_\theta \\ B_\varphi \end{bmatrix} = \begin{bmatrix} \dfrac{\hat{r}}{R^2 \sin \theta} & \dfrac{\hat{\theta}}{R \sin \theta} & \dfrac{\hat{\phi}}{R} \\ \dfrac{\partial}{\partial r} & \dfrac{\partial}{\partial \theta} & \dfrac{\partial}{\partial \phi} \\ A_r & r A_\theta & r A_\varphi \sin \theta \end{bmatrix} = \begin{bmatrix} \dfrac{\cos \theta}{r \sin \theta} A_\varphi + \dfrac{1}{r} \dfrac{\partial A_\varphi}{\partial \theta} \\ -\dfrac{1}{r} A_\varphi - \dfrac{\partial A_\varphi}{\partial r} \\ 0 \end{bmatrix} \tag{1.14}$$

The magnetic flux density calculation results in spherical coordinates can be transformed into the Cartesian coordinates using

$$\begin{bmatrix} B_x \\ B_y \\ B_z \end{bmatrix} = \begin{bmatrix} \sin\theta\cos\phi & \cos\theta\cos\phi & -\sin\phi \\ \sin\theta\sin\phi & \cos\theta\sin\phi & \cos\phi \\ \cos\theta & -\sin\theta & 0 \end{bmatrix} \begin{bmatrix} B_r \\ B_\theta \\ B_\varphi \end{bmatrix} \tag{1.15}$$

The magnetic flux density in the Cartesian coordinates can also be expressed using the complete elliptic integrals as follow [202]:

$$\begin{bmatrix} B_x \\ B_y \\ B_z \end{bmatrix} = \begin{bmatrix} \dfrac{C\,x\,z}{2\alpha^2\beta\rho^2}\left[(R^2+s^2)E(k^2)-\alpha^2K(k^2)\right] \\ \dfrac{C\,y\,z}{2\alpha^2\beta\rho^2}\left[(R^2+s^2)E(k^2)-\alpha^2K(k^2)\right] \\ \dfrac{C}{2\alpha^2\beta}\left[(R^2-s^2)E(k^2)+\alpha^2K(k^2)\right] \end{bmatrix} \tag{1.16}$$

Where $\rho^2 = x^2 + y^2$, $s^2 = \rho^2 + z^2$, $\alpha^2 = s^2 + R^2 - 2R\rho$, $\beta^2 = s^2 + R^2 + 2R\rho$, $k^2 = 1 - \alpha^2/\beta^2$, and $C = \mu_0\, I / \pi$. $E(k^2)$ and $K(k^2)$ are the complete elliptic integrals of the first and second kind, respectively.

Only the magnetic flux density generated by the transmitter coil at the air-gap center plane central point is calculated in [81] using

$$B = \frac{\mu_0\, I_1\, R_{lp1}\, N_1}{2\,(R_{lp1}{}^2 + z^2)^{3/2}} \tag{1.17}$$

Where I_1 is the primary coil current, N_1 is the primary coil number of turns, R_{lp1} is the primary coil loop radius, z is the vertical distance between the central point and the primary coil. According to the expression used in [81], the effect of the secondary coil on the magnetic flux density was not considered. The air-gap magnetic flux density should be a vector combination of the magnetic fields generated by both the primary coil and the secondary coil. In addition, the magnetic flux density at the air-gap center plane central point may not the peak one.

In the design methodology for a 300 kW, low flux density, large air-gap, on-line WPT system, the EMF measurement location was located outside of the vehicle as shown in Fig. 1-48, the magnetic flux density at the test location was calculated using [84]

$$B = \frac{\mu_0 I_1 N_1}{2 \pi r_{11}} - \frac{\mu_0 I_1 N_1}{2 \pi r_{12}} + \frac{\mu_0 I_2 N_2}{2 \pi r_{21}} - \frac{\mu_0 I_2 N_2}{2 \pi r_{22}} \tag{1.18}$$

Where r_{11}, r_{12}, r_{21}, and r_{22} are shown in Fig. 1-48 (b), I_1 is the primary coil current, I_2 is the secondary coil current, N_1 is the primary coil number of turns, N_2 is the secondary coil number of turns.

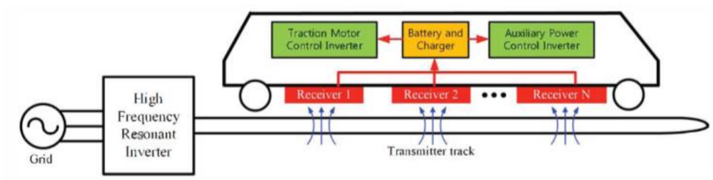

(a) System block diagram of a target on-line WPT system

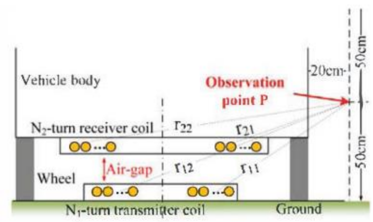

(b) EMF measurement location

Fig. 1-48. System block diagram and EMF measurement location

According to the expression used in [84], the effect of the secondary coil on the magnetic flux density was considered. However, the analytical calculation method was not developed for the air-gap center plane magnetic flux density, which was much higher than the magnetic flux density at the observation point.

The cylindrical coordinates were used in [203] to calculate the magnetic flux density along z- and ρ-direction for a single current loop, however, the center plane magnetic flux density was not calculated, the air-gap magnetic field is a vector combination of the magnetic fields generated by the primary coil and the secondary coil. In addition, the authors didn’t pay attention to the phase delay between the primary coil current and the secondary coil current.

- **Electric field analytical model**

Less attention has been paid to the air-gap electric field distribution for inductive WPT systems. Only numerical tools are used to evaluate the electric field distribution according to the existing literature shown in Table 1-9.

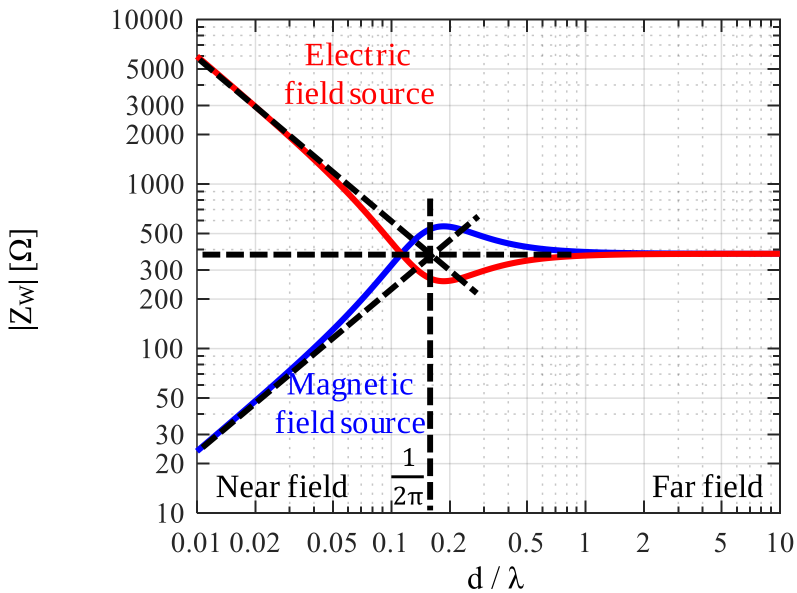

Fig. 1-49. Relationship between wave impedance and distance from source

In far field region, the electric field and the magnetic field have almost constant ratio, which is 377 Ω of free space wave impedance. However, the electromagnetic field between the transmitter and receiver coils and around the electric vehicle can only be treated as near-field region instead of far-field region, since the far field region begins at $\lambda/(2\pi) = c/(2\pi f)$, which is much larger than the vehicle size. In the near-field region, the impedance of free space is defined by the distance away from the source and source type as shown in Fig. 1-49 rather than constant ratio 377 Ω [96][204][205]. In the near-field region, the directions of E and H are not orthogonal as in the far field region. Calculating electric field based on magnetic field and wave impedance may lead to the wrong direction since the distance between the air-gap center plane and the coils (or the measured point distance from the transmitter and receiver) is comparable with the size of the transmitter and receiver, it is difficult to get an accurate wave impedance.

The electric field of a single current loop of radius R and current I, as shown in Fig. 1-47, is evaluated in a region having dimensions which are smaller than or equal to the size of the loop and much smaller than that of the wavelength [205]. The zeroth-order approximation of the vector potential and the Coulomb gauge $\nabla \vec{A} = 0$ was used in the derivation. The electric field intensity E at the test point is expressed in the cylindrical coordinates

$$|E_\varphi(\rho, z)| = \frac{\omega}{c}\frac{2I}{c}\frac{1}{\rho}\left[(R+\rho)^2 + z^2\right]^{1/2}\left[\frac{R^2+\rho^2+z^2}{(R+\rho)^2+z^2}K(k^2) - E(k^2)\right] \tag{1.19}$$

Where $c = 4\pi/\mu_0$, $\rho^2 = x^2 + y^2$, $s^2 = \rho^2 + z^2$, $\alpha^2 = s^2 + R^2 - 2R\rho$, $\beta^2 = s^2 + R^2 + 2R\rho$, $k^2 = 1 - \alpha^2/\beta^2$, $E(k^2)$ and $K(k^2)$ are the complete elliptic integrals of the first and second kind, respectively. Other components of E are zero. However, the authors didn't consider the effect of the excitation terminals, which has the peak voltage difference and electric field intensity.

A circuit in the shape of a ring with a battery of negligible size and a wire of uniform resistance per unit length, as shown in Fig. 1-50, was investigated [206].

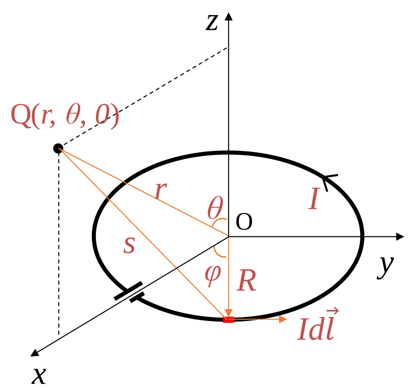

Fig. 1-50. Configuration of a ring with a battery

The electrostatic potential at an arbitrary point in spherical coordinates is given by

$$\Phi(r, \theta, \varphi) = \frac{\lambda}{4\pi\varepsilon_0}\int_{\varphi'=0}^{2\pi}\frac{(\varphi' - \pi)\, d\varphi'}{\sqrt{R^2 + r^2 - 2\, R\, r \sin\theta \cos(\varphi - \varphi')}} \tag{1.20}$$

Where $\lambda = V\, \varepsilon_0\, R \,/\, \ln(R/r_0)$, r_0 is the radius of the wire.

In Cartesian coordinates,

$$\Phi(x, y, z) = \frac{\lambda}{4\pi\varepsilon_0}\int_{\varphi'=0}^{2\pi}\frac{(\varphi' - \pi)\, d\varphi'}{\sqrt{R^2 + x^2 + y^2 + z^2 - 2\, R\, x \cos\varphi' - 2\, R\, y \sin\varphi'}} \tag{1.21}$$

Then the electric field intensity $\vec{E}(x, y, z)$ is given as

$$\vec{E}(x, y, z) = \frac{\lambda}{4\pi\varepsilon_0}\int_{\varphi'=0}^{2\pi} d\varphi' \frac{(\varphi' - \pi)\left[(x - R\cos\varphi')\,\hat{x} + (y - R\sin\varphi')\,\hat{y} + z\,\hat{z}\right]}{(R^2 + x^2 + y^2 + z^2 - 2\, R\, x\cos\varphi' - 2\, R\, y \sin\varphi')^{3/2}} \tag{1.22}$$

The above equation captures the effect of the terminal excitation. None of the existing literature proposed an analytical model for the air-gap center plane electric field intensity.

1.4.4 Summary and identified research opportunities

In this section, the lumped equivalent circuit model for the loosely coupled WPT system is reviewed, the transformer model is valid according to existing literature. Four basic compensation topologies and their properties have been investigated. LCL and LCC topologies can be regarded as the extension of PP resonant topology. All of the resonant topologies are affected by the load resistance and mutual coupling. The resonant compensation inductors and capacitors are designed based on coil lumped parameters. However, no research has systematically investigated the effect of circuit topologies for inductive WPT systems on air-gap magnetic and electric field distributions under aligned and misaligned conditions.

TMNs have been developed to manipulate the system impedance. However, the loss distribution has not been fully analyzed, and the low loss SCC and SCI have not been developed. On the other hand, less attention has been paid to use the SCC and SCI in WPT system, the effects on the reactive power and power transfer efficiency has not been analyzed.

The magnetic field and electric field analytical calculation methods for a single current loop have been developed. The analytical model for the magnetic flux density in the air-gap center plane central point has been developed. The static electric field analytical calculation methods for a single current loop with a battery excitation have been developed. However, no methodology has been developed to analytically calculate the magnetic field and electric field in loosely coupled inductive WPT system air-gap center plane, which is necessary to develop a general design methodology that can inherently achieve low air-gap magnetic flux density and low air-gap electric field intensity when transferring multi-kW. In addition, power converter design and coil design are generally separated. A general system design methodology including power converter design and coil design simultaneously must be developed.

1.5 Loosely coupled WPT system design methodologies

There has been much research on design procedures for strongly coupled power transfer systems, using magnetic core transformers and inductors [200]. However, design methodologies for the loosely coupled WPT winding have not been widely discussed in the literature. In this section, loosely coupled WPT winding design methodologies in low power (below 1 kW) and high power (over 1 kW) applications are reviewed. Advantages and disadvantages of the design methodologies in the literature are discussed as well.

1.5.1 WPT system design methodologies for low power (below 1 kW) applications

- **Implantable biomedical devices design methodologies**

Implantable medical devices have widely used wireless power technology to reduce the risk of battery corruption and potential surgery for battery replacement.

RamRakhyani et al proposed a design and optimization methodology of resonant implantable devices to achieve maximum power transfer efficiency with given space and distance [24]. A four-coil system was adopted to improve the power transfer efficiency as shown in Fig. 1-51 (a), (b) and (c).

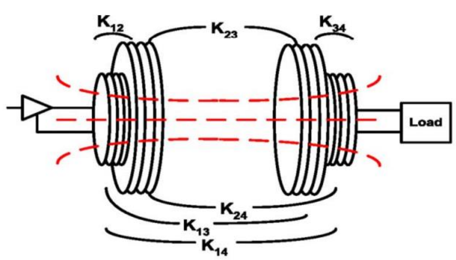

(a) Illustration of the four-coil power transfer system

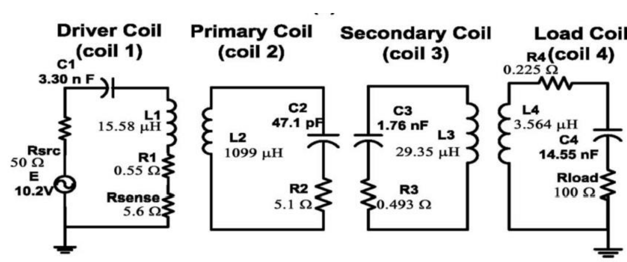

(b) Circuit of the four-coil system

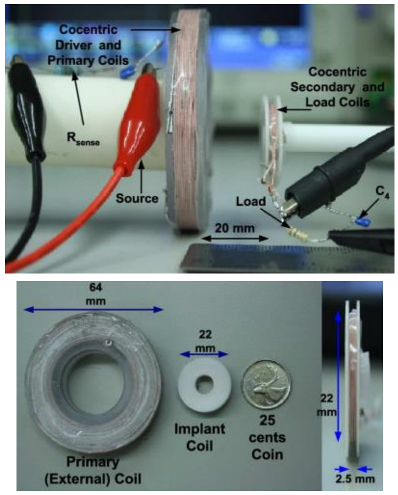

(c) Photo of the four-coil system

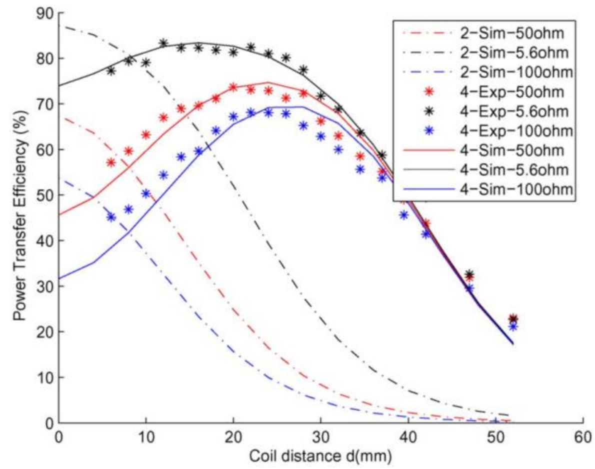

(d) Efficiency dependence on coil distance

Fig. 1-51. Diagrams and efficiency of a four-coil WPT system

Power transfer efficiency of a two-coil (source and load coils) system is a strong function of the Q-factor of source and load coils, but the source coil's Q-factor is limited by the source series resistance, and the load coil's Q-factor is limited by the load resistance. In a four-coil system, the effect of the low Q-factor and the low coupling between the source and load coils can be compensated by using intermediate high-Q-factor coils [24][199]. The paper demonstrated non-monotonic dependency of power transfer efficiency of a four-coil system on transfer distance as shown in Fig. 1-51 (d). In the figure, two-coil system efficiency decreased monotonically as the distance increased while the four-coil system efficiency was convex. There were specific distances resulting in peak power transfer efficiency. Driver, primary, secondary, and load coils are the components to be designed. The design procedure is shown in Fig. 1-52.

It is assumed that the maximum outer diameters of the coils (D_{out}), transfer distances, coil thickness, and load resistance are given by applications. Three design parameters are left to be determined: the operating frequency, the number of winding layers (N_a) and the number of turns per layers (N_t) of coils. In the first step. The optimum value of D_{out} is determined as $D_{out} = 2\sqrt{2}\times d$ in order to maximize magnetic field in the air-gap. And then, N_a and N_t are changed incrementally until the efficiency is maximized. Using this design methodology, 82% efficiency was achieved experimentally with 20 mm transfer distance and 200 mW output power.

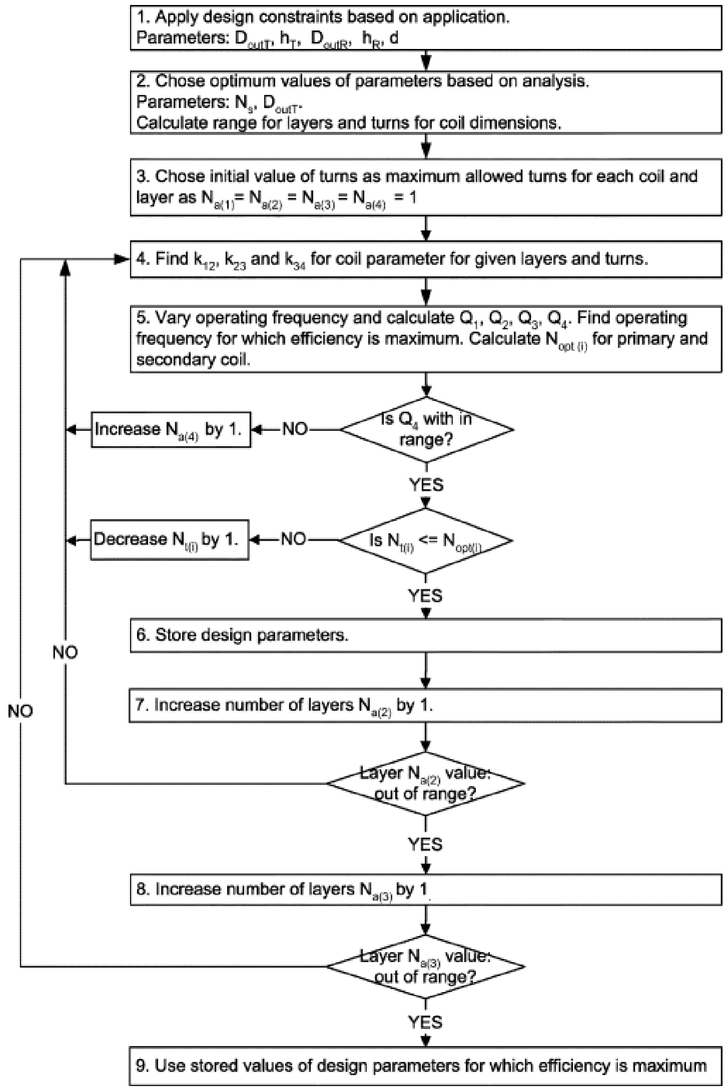

Fig. 1-52. Design methodology of the four-coil implantable biomedical device

Over 80% efficiency system is achieved and the relationship between N_a and N_t on efficiency is considered in the proposed methodology. However, since the major focus of the paper is improving the efficiency, volt-amp rating of transmitters and receivers are not considered in the design process. Moreover, potential safety issue is not addressed.

Kendir et al proposed a design methodology for implantable inductive power link including safety considerations of the devices [174]. In the design process, load power, voltage, coil dimension, distance between the coils, operating frequency, and maximum available DC voltage are assumed to be given.

The design methodology started with single turn inductance and coupling coefficient calculation of the coils based on the given maximum dimensions. Since the coupling coefficient between the transmitter and the receiver is not a function of the number of turns of the coils but a function of distance and diameter of the coils, coupling coefficient is determined in the first step.

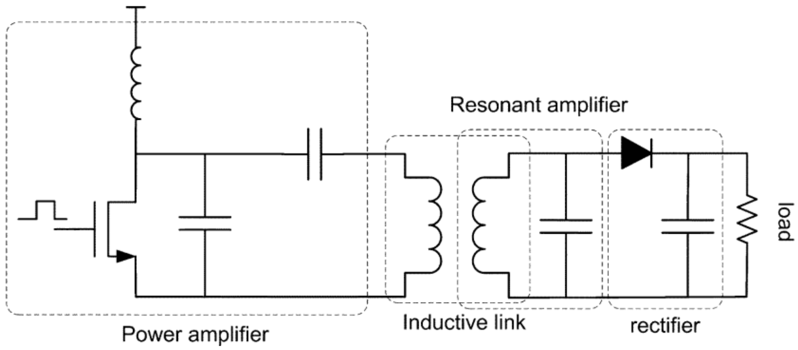

Fig. 1-53. System overview of inductive link using class E amplifier

Then, the receiver inductance selection is followed. Coil loss and H-field dependence on the receiver inductance is the key metric in decision. In the paper, H-field of the receiver is considered more important than the transmitter because the receiver is implanted in a body.

In step three, the total power delivered from the primary side to the secondary side is calculated by adding secondary side losses (coil loss and rectifier loss) and load power. The primary side power loss, the primary side current and the required DC voltage dependence on primary side inductance is calculated. Optimal primary inductance is selected. Then the optimal number of turns of the coils can be decided.

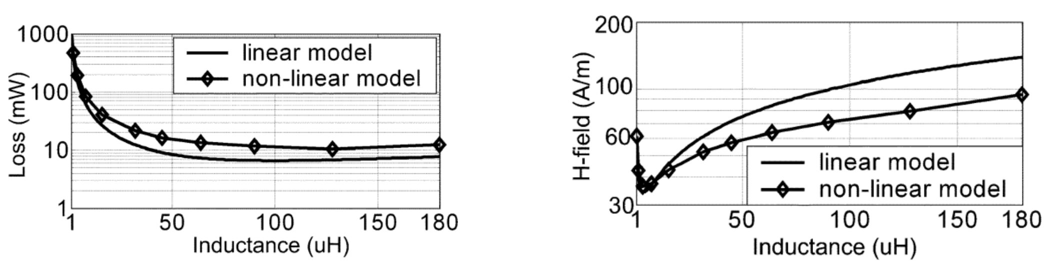

(a) Secondary coil loss vs. its inductance (b) H-field vs. secondary inductance

Fig. 1-54. Loss and H-field dependence on secondary coil inductance

Based on the proposed methodology, 250 mW power transfer system over 7 mm distance was designed and experimentally evaluated. 80% efficiency was achieved.

- **Laptop computer battery charger design methodology**

Meyer et al proposed a design methodology for wireless laptop battery chargers [176]. Since the target is a laptop computer, primary and secondary windings are implemented on a PCB layout to keep the laptop profile thin. A parallel-series resonant circuit topology is adopted.

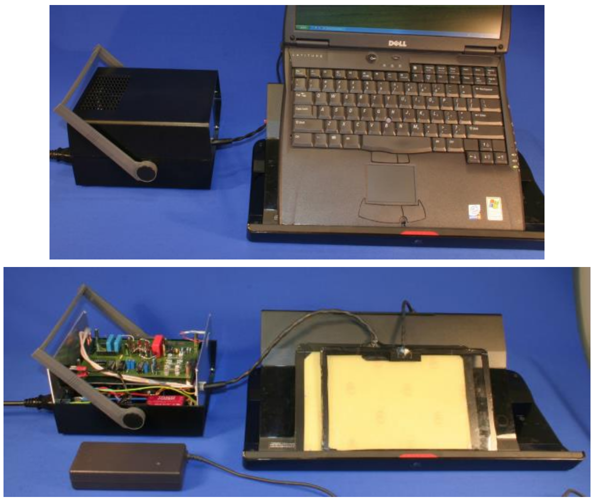

(a) Photos of the system

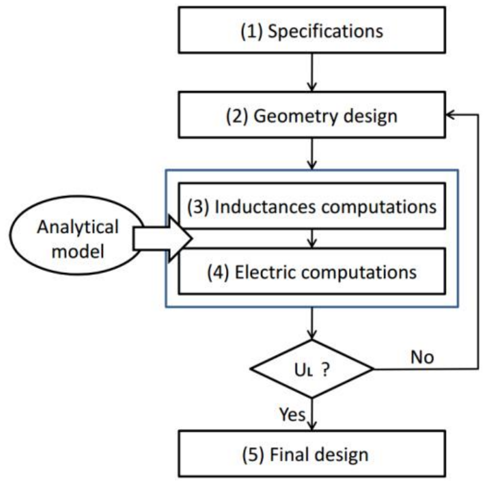

(b) Flowchart of the proposed methodology

Fig. 1-55. Laptop battery wireless charging system

Photos of the system are shown in Fig. 1-55 (a). The coil dimensions (220 mm × 140 mm) are much bigger than the transfer distance (15 mm). Therefore, the system is not loosely coupled. However, the design methodology of such system is similar to the design methodologies of the other small power applications because it is using a coreless inductor, hundreds of kHz, and parallel-series resonant circuit to transmit power.

The proposed design methodology is shown in Fig. 1-55 (b). In the first step, the design specifications of the maximum size of the coils, distance, supply voltage, load resistance, and load voltage are defined. Required transmitted power to the load is 80 W, load resistance is 7 Ω, transmitter coil voltage of 355 V_{rms}, and load voltage of 24 V_{dc}.

With the given specifications, the number of turns and size of the coils are chosen in the first two steps. Inductances and resistances are calculated analytically in the following step. Voltages and currents are calculated using these parameters. If the calculated load voltage is higher than the specification, 24 V, the iterative process is ended. The proposed design methodology is evaluated with experimental results.

However, the paper didn't mention about electromagnetic field around the laptop. Since people are often around the laptop to use it when it is on charge, it is necessary to ensure that the electromagnetic field around the laptop is within safety limit.

Ahn et al proposed a quadruple winding topology to reduce the electromagnetic field of WPT system for laptop applications [208]. Compared with single coil configuration, the quadruple coils have options to choose the directions of the currents of the adjacent coils. The direction of the current in adjacent coils should be opposite to maximize the effectiveness of magnetic field cancellation outside of the coil. The quadruple coil dimension, current directions, and simulation results are shown in Fig. 1-56.

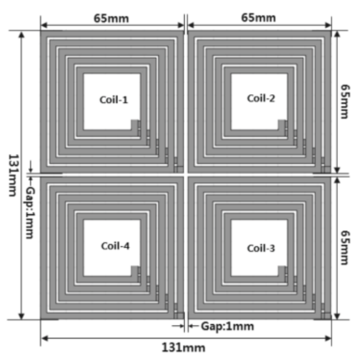

(a) Quadruple coil dimensions

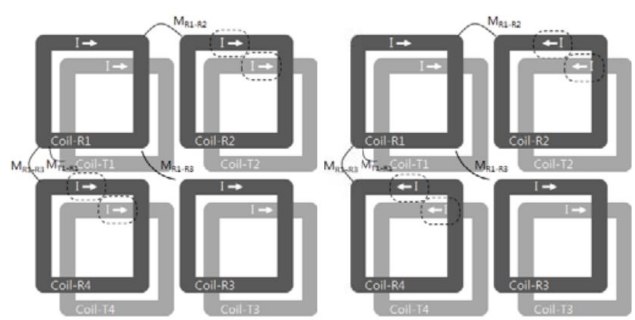

(b) Current directions in the coil

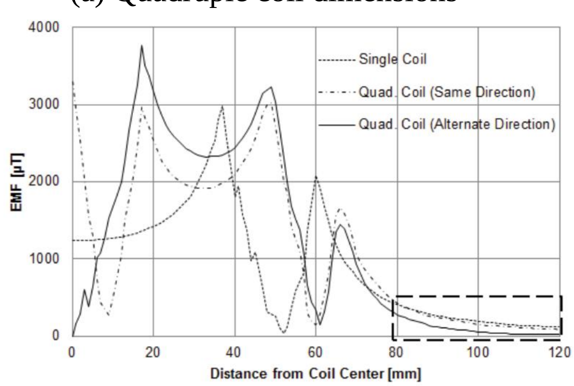

(c) Simulated EMF over the whole region

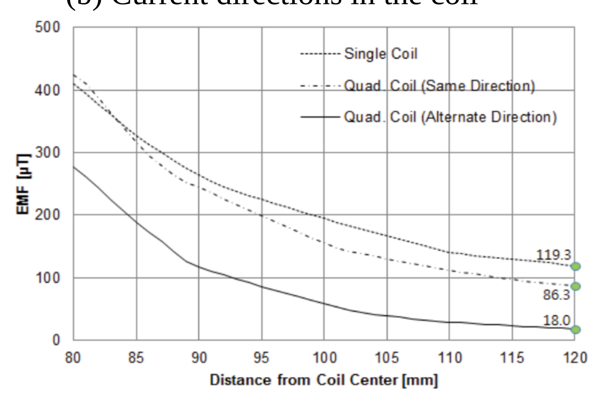

(d) Simulated EMF over magnified region

Fig. 1-56. Quadruple coil dimensions, coil current directions and simulation results

As shown in Fig. 1-56 (d), the quadruple coils decreased faster compared with the single coil and the flux density at 120 mm distance from coil center is 18 μT, which is lower than the safety limit. However, as the simulation results shown in Fig. 1-56 (c), the flux density within the air-gap of the proposed quadruple coils is the highest one, which is much higher than the safety limit, and it is possible that people put their hands to the air-gap region during operation, which would cause severe injury to users.

- **Loosely coupled planar WPT system design methodology (300 W, 10 mm)**

In 2009, Low et al proposed a design approach for a loosely coupled planar WPT system in order to transmit 300 W over 10 mm distance [20]. A parallel-parallel resonant circuit is adopted with an impedance transformation network. The proposed approach is started with design constraints of the coil dimensions. The size of the transmitter was set as 21 cm × 21 cm, and the number of turns was 10. The size of the receiver was set as 13 cm × 13 cm, and the number of turns was 5. AWG 16 magnetic wires are used to fabricate the coils. However, it is not clearly explained how the authors determined the number of turns, the length of the edges, and the cross-section area of the wire used in the coils.

In the first step, operating frequency of the resonant system is determined. The authors understood that higher operating frequency enhances the power transfer efficiency in the broader range of load resistance variation. Operating frequency of 134 kHz is selected. Then the receiver compensation capacitance is selected as 113 nF. After that, the impedance transformation network's L and C values were determined as L_{out} = 100μH and C_{out} = 68nF. At last, the transmitter compensation capacitor value is selected as 105 nF to ensure proper phase response of the input impedance. The authors claimed that phase of the input impedance is important in a sudden unloading case. The proposed methodology is evaluated with an experimental setup. The output power of the system was 295 W at efficiency of 77% with forced air cooling.

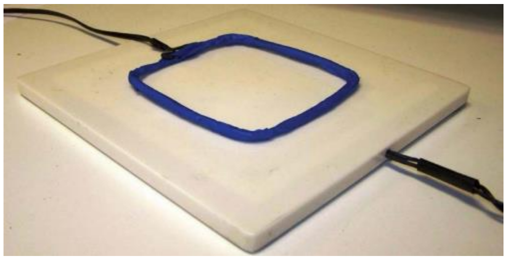

(a) Photo of transmitter and receiver coil

(b) Photo of dual-channel class E amplifier

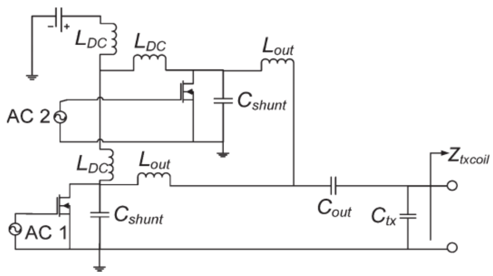

(c) Schematic of dual-channel class E amplifier

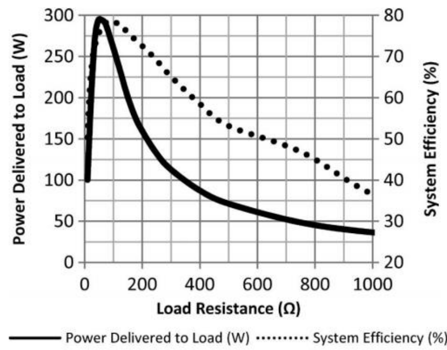

(d) Efficiency dependence on load

Fig. 1-57. 300 W power transfer system over 10 mm distance

The overall power transfer efficiency was too low to be used in commercial electronics. The paper would be improved by adding how the overall efficiency of the systems can be affected by using other resonant circuits such as series-series or series-parallel, etc. Furthermore, VA ratings, human body safety, EMI/EMC effects have to be considered as well.

Pareto fronts of coils’ efficiency versus stray magnetic field was used for a synergetic optimization and winding design for a 100 W inductive WPT system [101][104]. The fronts were derived from finite-element simulation (FES). The procedure for building the simulation model in FES included selecting ferrite width, gap, and misalignment for coils’ structure in Fig. 1-58 (a). Then physical parameters coil radii and number of turns were swept. Two simulations were needed for each set of physical parameters. The first simulation was to derive the self- and mutual inductances, and ESRs, winding currents, and coil-to-coil efficiency. The second simulation was to derive the stray magnetic field in the measurement point. Pareto fronts of coils’ efficiency versus stray magnetic field was derived with the simulations of all sets of physical parameters. The design flowchart is shown in Fig. 1-58 (c). By plotting all the simulation results on a 2-dimensional plot with x-axis to be stray magnetic field and y-axis to be coil-to-coil efficiency, the Pareto front can be derived and is located on the upper left as shown in Fig. 1-58 (d), all the points located on the front can be considered as optimized structures.

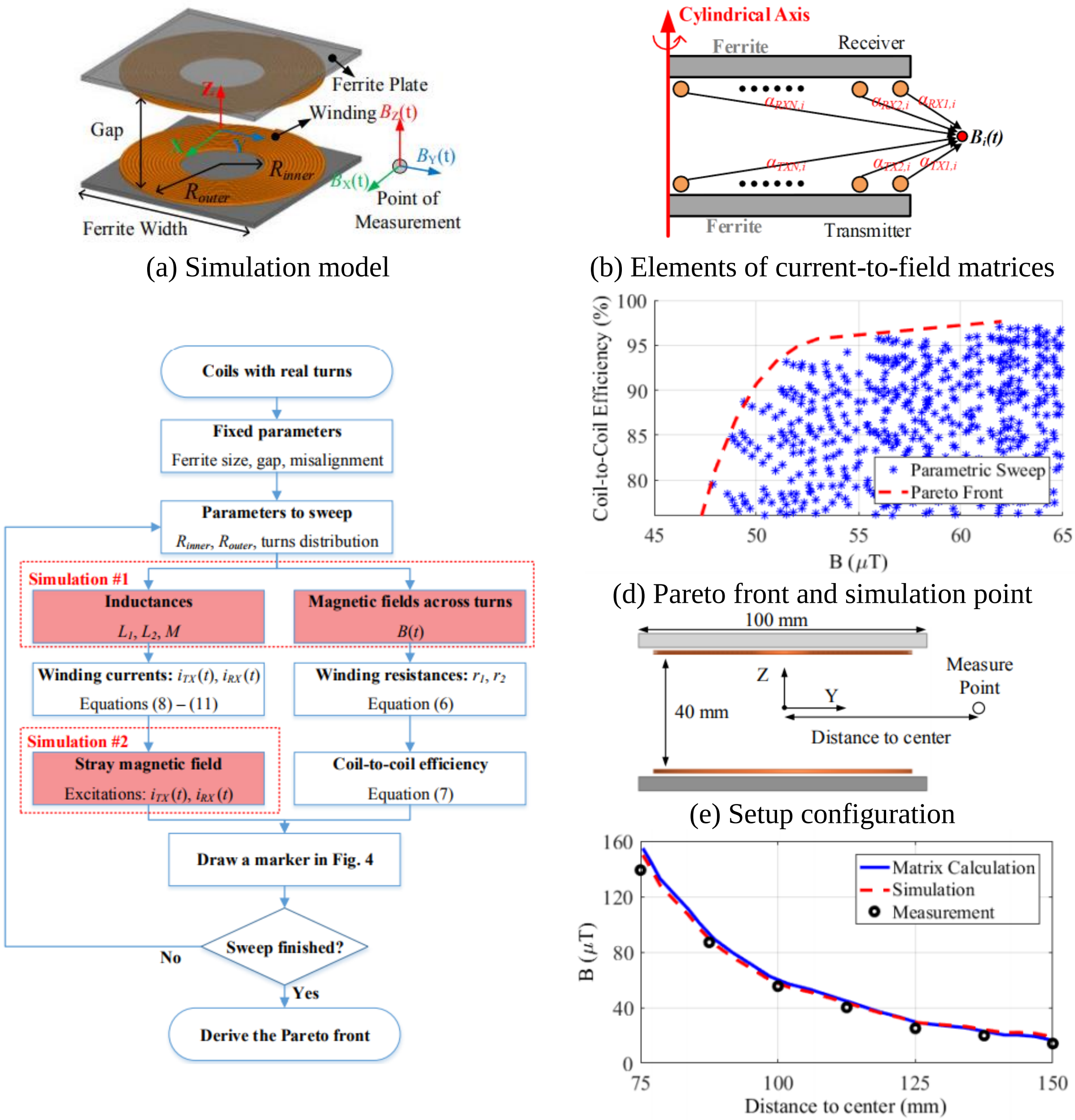

(a) Simulation model

(b) Elements of current-to-field matrices

(d) Pareto front and simulation point

(e) Setup configuration

(c) Design flowchart

(f) Magnetic field results

Fig. 1-58. 100 W inductive WPT system design using Pareto fronts

In the pateto front design methodology, only the magnetic flux density at the air-gap center plane measurement point is included as

$$B_i(t) = B_{TX,i}(t) + B_{RX,i}(t) = \sqrt{2}(\alpha_{TX,i} \bullet I_{TX})\sin(\omega_s\, t) + \sqrt{2}(\alpha_{RX,i} \bullet I_{RX})\sin(\omega_s\, t + \theta) \quad (1.23)$$

Which is definitely not the air-gap center plane peak magnetic flux density. In addition, this design methodology can't be scaled to transfer kW power. At 75 mm away from the central point, B = 140 μT when transferring 100 W, when the output power is scaled to 2.5 kW, the required excitation current will increase 5 times, which will make B increase from 140 μT to 700 μT, which is about 3 times higher than the IEEE C95.1-2005 magnetic field safety limit. Besides that, the air-gap electric field distribution is not considered.

1.5.2 WPT system design methodologies for high power (over 1 kW) applications

- **Vehicle battery charger design methodologies**

In [28] and [47], Villa et al investigated a WPT system for an electric vehicle battery charger. In Fig. 1-59, an overview diagram of the EV battery charging system and its implemented winding geometries are shown.

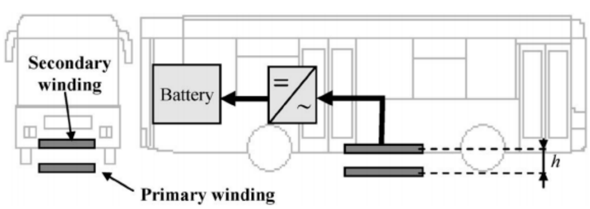

(a) System overview

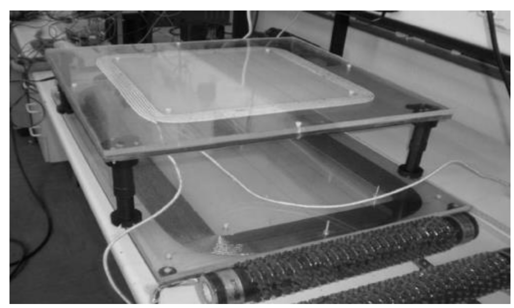

(b) Photo of implemented system

Fig. 1-59. Loosely coupled WPT system for EV battery charger

A design flowchart is proposed to design a 200 kW EV battery charger with 20 cm transfer distance as shown in Fig. 1-60. Winding dimensions, maximum operating frequencies, supply voltage, output power, and desired load voltage are assumed to be given by the target application. The number of turns (N_1, N_2), cross-sectional area (S_1, S_2) of the transmitter and receiver, and operating frequency are the parameters to be determined. The proposed design methodology starts with self- and mutual inductance calculations of single winding coils. In the second step, transferred power over the load is calculated with each of the combination of (N_1,

N_2). In step three, calculated P_2 and desired output power P_{load} are compared. If P_2 is greater than P_{load}, the operating frequency will be changed until $P_2 \leq P_{load}$. If the calculated current density δ_1 and δ_2 of the coils are smaller than the allowable current density of wires, it becomes a design candidate to achieve final design.

The final design is picked if the derived circuit satisfies following six requirements.

(1) $P_L(N_1, N_2) = P_{load}$ (Calculated output power with N_1-turn transmitter and N_2-turn receiver must equal to the given output power requirement.)

(2) $V_L(N_1, N_2) = V_{load}$ (Calculated output voltage with N_1-turn transmitter and N_2-turn receiver must equal to the given output voltage requirement.)

(3) $f_{op}(N_1, N_2) \leq f_{max}$ (Calculated operating frequency with N_1-turn transmitter and N_2-turn receiver must smaller than the maximum allowed operating frequency.)

(4) $Q_p(N_1, N_2) > Q_s(N_1, N_2)$ (Calculated loaded quality factor of the transmitter has to be greater than the loaded quality factor of the receiver for stable operation.)

(5) $\delta_1(N_1, N_2) \leq \delta_{1max}(N_1, N_2)$ (Calculated current density of transmitter winding has to be smaller than allowed maximum current density.)

(6) $\delta_2(N_1, N_2) \leq \delta_{2max}(N_1, N_2)$ (Calculated current density of receiver winding has to be smaller than allowed maximum current density.)

The virtue of the paper is that it compared electrical parameters and required copper mass of four different topologies: Series-series (SS), series-parallel (SP), parallel-series (PS), and parallel-parallel (PP) resonant circuits. SS requires minimum copper mass while PS requires the largest amount of copper, since the maximum allowed current density is the same, and from the optimized design results for the 200 kW system, primary winding current requirement of PS system is 2412 A, while primary winding current requirement of SS system is 370 A. The paper concluded that series primary is preferred than parallel primary resonant circuit for high power applications because of high current requirements of parallel primary circuits (PS or PP). Based on the proposed design methodology, a WPT system over 15 cm distance, 2 kW, at 20 kHz prototype was implemented and evaluated experimentally. Measured efficiency of the system was 82% at 2020W and 20.1 kHz power transfer.

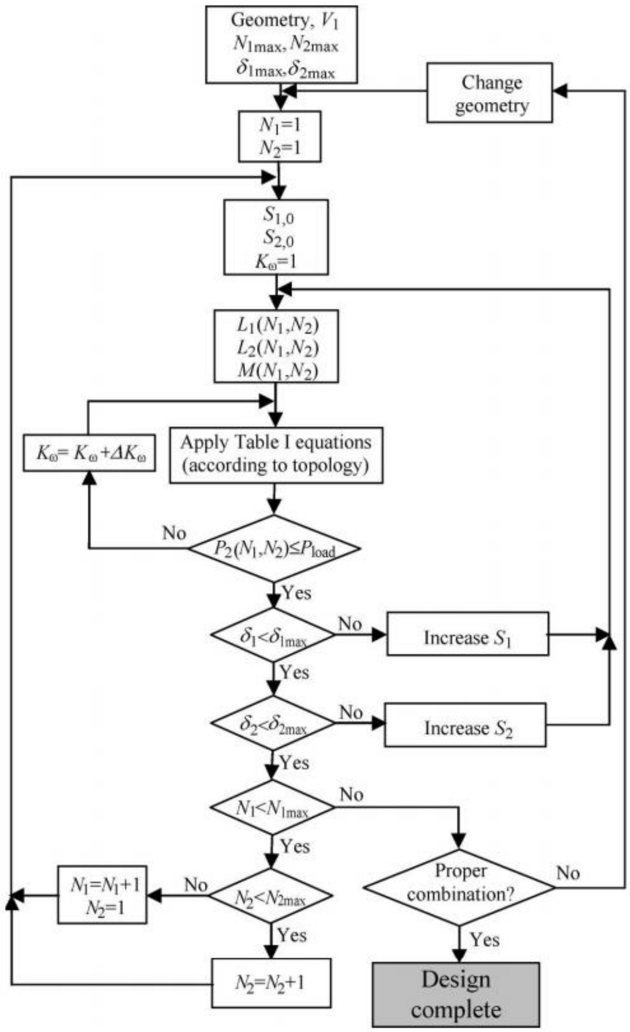

Fig. 1-60. Design flowchart of electric vehicle battery charger

However, it should be noted that the paper did not explore the volt-amp rating variations of coils. Since the power rating of the target applications is kW range, volt-amp (VA) rating of the system changes drastically depending upon the circuit parameters. For example, the VA rating of SS system in the paper is 1.7 MVA while it is 2.1 MVA for SP system to transmit 200 kW real power. Therefore, a deliberate consideration of VA rating dependence on parameters is required to minimize the system volt-amp ratings.

Moreover, the paper would be improved if the authors considered the safety issues since the transmitted power is in kW range and the operating frequency is in kHz range. In the low frequency operation, electrostimulation of muscles and nerves by induced current is critical due to safety concern. Therefore, the induced current in the human body should be estimated and evaluated in the design process.

Stielau et al discussed loosely coupled inductive power transfer topologies and a design methodology in [22]. According to the authors, series compensation in the secondary side has the characteristic of a voltage source, while parallel compensation behaves as a current source. Series compensations were appropriate for variable speed AC motor drives, while parallel secondary circuits were more suitable for battery chargers. On the primary side, series compensation is more attractive for applications that need low input voltage but high coil voltage, because series compensation functions as a voltage amplifier on the primary side. In contrast, parallel compensation is appropriate for applications that need low source current but high primary coil current. Parallel compensation works as a current amplifier in the primary side.

The authors assumed that the operating frequency of target systems is given. Proposed iterative design steps are started with a selection of an experience-based initial circuit topology. In the second step, the primary current is determined. In the following step, the product of $V_{oc} \times I_{sc}$ is calculated using the chosen primary current i_p. V_{oc} is the open circuit voltage, and I_{sc} is the short circuit current. $V_{oc} \times I_{sc}$ is related to the maximum power transfer capacity of an uncompensated secondary. Therefore, using this value, it is decided whether the secondary compensation is necessary or not. In step four, the secondary side compensation is determined. The secondary side VA ratings are calculated and adjusted until the VA ratings of the primary side is greater than the required VA ratings. In the final step, loaded quality factors of the primary (Q_p) and the secondary (Q_s) is compared. If $Q_p >> Q_s$, control stability is assured, and the design process is ended. The design flowchart is shown in Fig. 1-61.

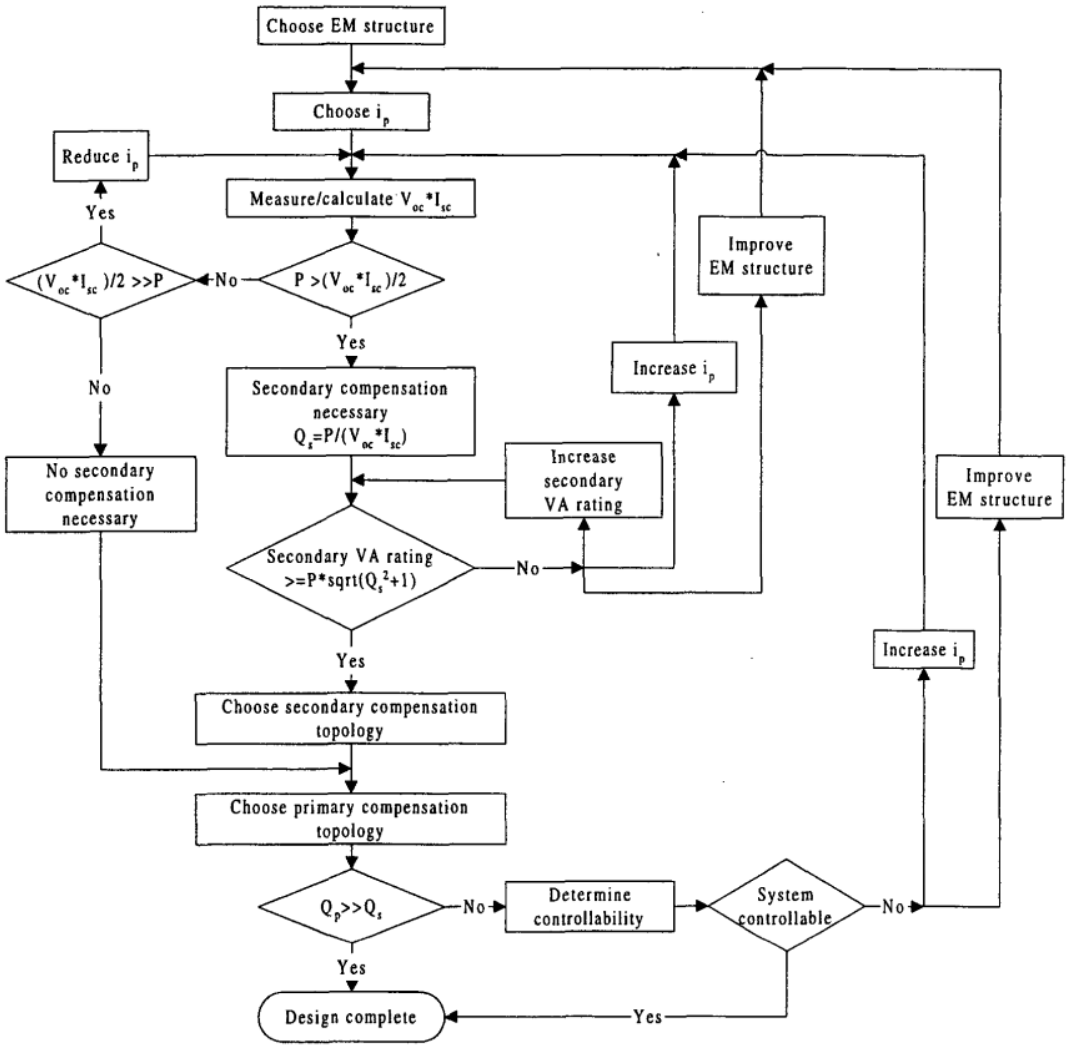

Fig. 1-61. Design flowchart of a loosely coupled wireless EV battery charger

It is excellent that the paper investigated on not only the characteristics of series and parallel compensation networks but also the design methodology of a high power system. Using the proposed methodology, the designed system can satisfy the stability condition and provide the required output power. However, the authors did not clearly explain how to choose the initial circuit parameters in the first step of the design methodology. It was an experience-based selection. Furthermore, the paper did not explore how to achieve minimum volt-amp rated systems, which would affect the air-gap magnetic and electric field distributions. The authors understood that reactive power of a loosely coupled system can be 50 times larger than the real power depending on circuit parameters, but minimizing the VA rating of the system was not discussed. The paper also did not consider safety issues in the design procedure, even though the safety issues become increasingly important as the transferred power and the distance increase.

Lee et al proposed a circuit design methodology to consider efficiency, VA rating, stability, and magnetic field safety issues simultaneously and used an objective function with different weighting coefficients based on design requirement to select an optimal design [80][81]. Consider input impedances, misalignment performance and load conditions, SS and SP systems are preferred in the stationary charger application.

A design space of the SP resonant WPT system was developed as shown in Fig. 1-62 based on the assumptions that P_{in}, $|V_{L2}|$, R_L and k are given, $|V_{L1}|$ should not exceed V_{L1max}, and I_{L1}, I_{L2} should not exceed I_{L1max}, I_{L2max}, respectively.

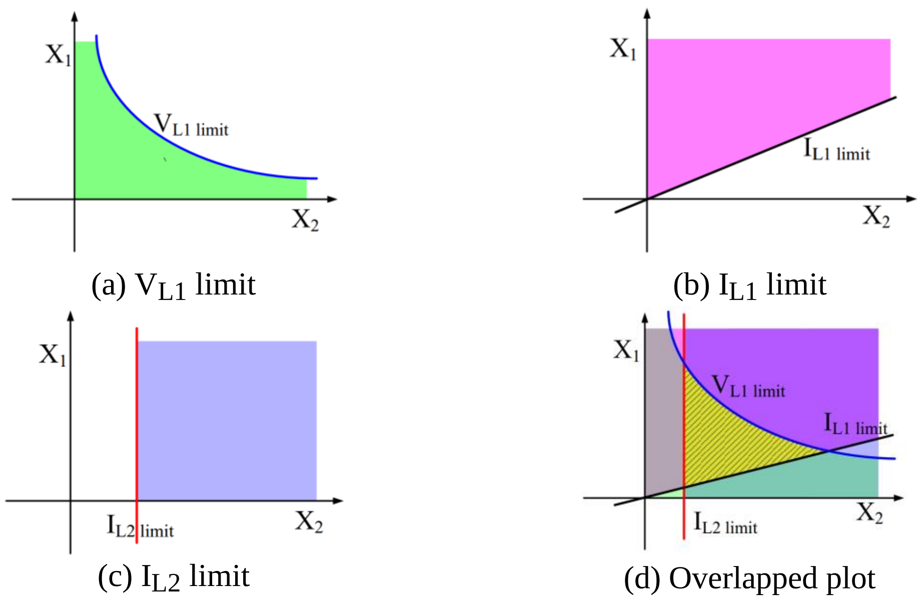

Fig. 1-62. The design space for SP system

The design flowchart is shown in Fig. 1-63. The design space was divided into finite design elements as starting point, based on the impedances of transmitter and receiver coils, firstly, the radius of transmitter coil was initialized as the largest achievable value depending on design space and turn number was set as 1, then the inductance and operating frequency could be calculated based on the given dimension and impedance. After the operating frequency was determined, the receiver coil inductance and dimension could be calculated based on its impedance. At last, coupling coefficient, efficient and flux density are calculated. The transmitter turn number and radius iteration loops would help sweep along all possible designs.

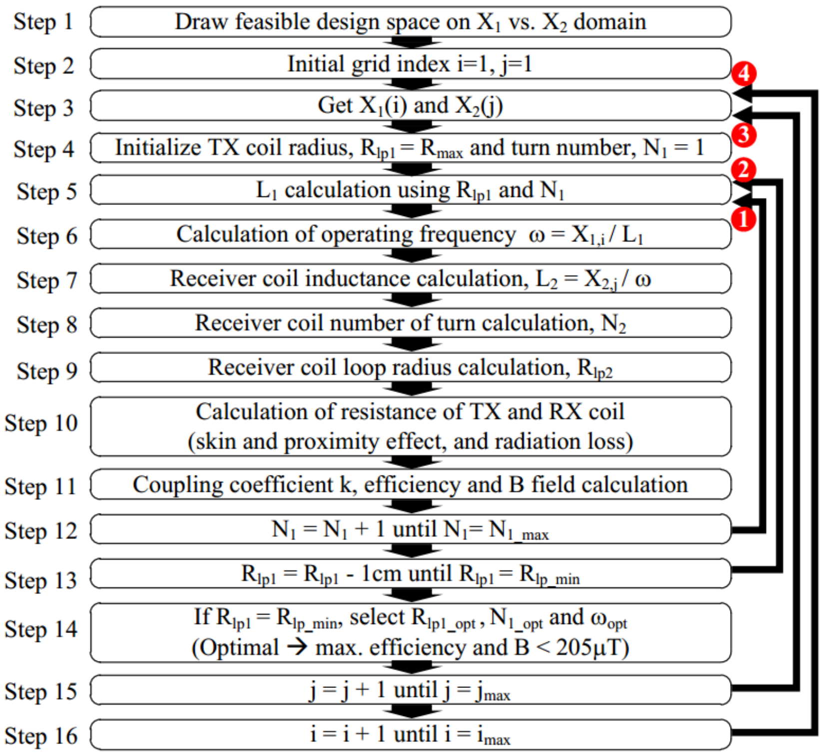

Fig. 1-63. Optimum geometry calculation in feasible design space

Following the design flowchart, the operating frequency, flux density, VA rating, and efficiency distributions over the design space could be plotted in corresponding to transmitter and receiver coil turn numbers and radius. In order to find an optimal design, an objective function with weighting coefficients was proposed to balance all considerations.

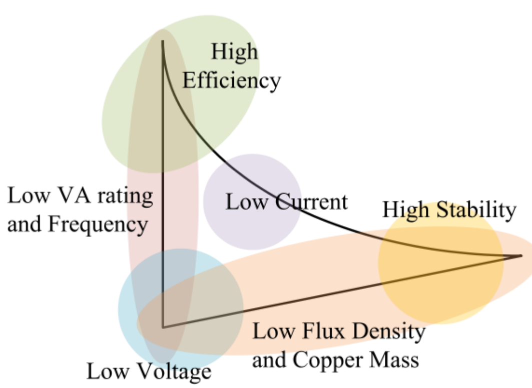

Fig. 1-64. SP LCIPT system performance trade-offs

The performance of the WPT systems has trade-offs depending on the selection of transmitter and receiver impedances as shown in Fig. 1-64. The optimal design point can be changed depending on the weighting of design requirements. The way of determining the weighting coefficient is the designer's decision about the importance of the individual terms.

The benefit of the proposed design methodology is that it considers power transfer efficiency, quality factor, copper mass, VA rating, air-gap center plane central point magnetic flux density, output voltage level, output current level, and control stability simultaneously using an objective function with different weighting coefficients. However, during the design process, the author didn't consider the high spatial voltage stress between the first turn and the end turn, which limits the power scalability, magnetic field tissue heating safety limit and electric field in the air-gap center region, which is equally important as magnetic field. In addition, only the magnetic field generated by the primary coil was considered in the design methodology, and the peak flux density may be not located in the air-gap center plane central point. Moreover, the design process is a sweep process along the impedance range of the primary coil and the secondary coil, the operating frequency is calculated from the impedance and analytical inductance regardless of the effect of parasitic capacitance. Due to the existence of parasitic capacitance, the equivalent impedance won't be equal to ω L.

Lee et al proposed a design methodology for a 300 kW, low flux density, large air-gap, online WPT for train applications [84]. The authors adopted a transmitter track and multiple-receiver topology as shown in Fig. 1-65, and SS compensation network is used.

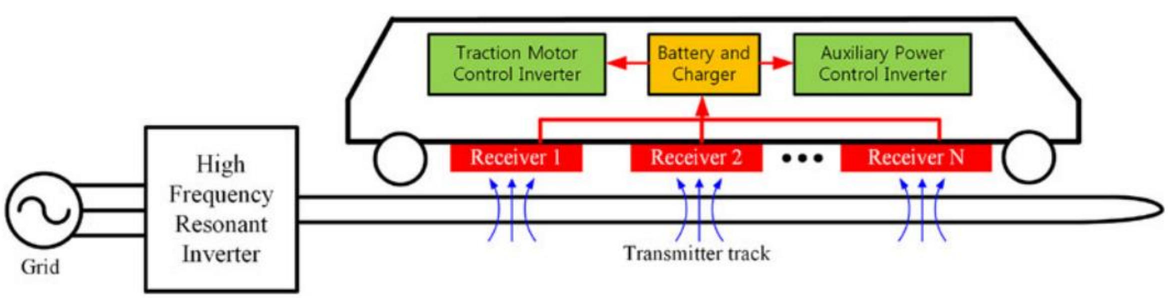

Fig. 1-65. Overall system block diagram of a target online WPT system

The design flowchart is shown in Fig. 1-66. Several assumptions have been made for the proposed design methodology. The operating frequency was assumed to be 60 kHz for high power WPT system in South Korea, width of a target vehicle was assumed as a given value 2.4 m, required air-gap distance was assumed to be given as 7 cm, length of required transmitter track was given as 10 m, and the rated output dc voltage was assumed to be given as 750 V.

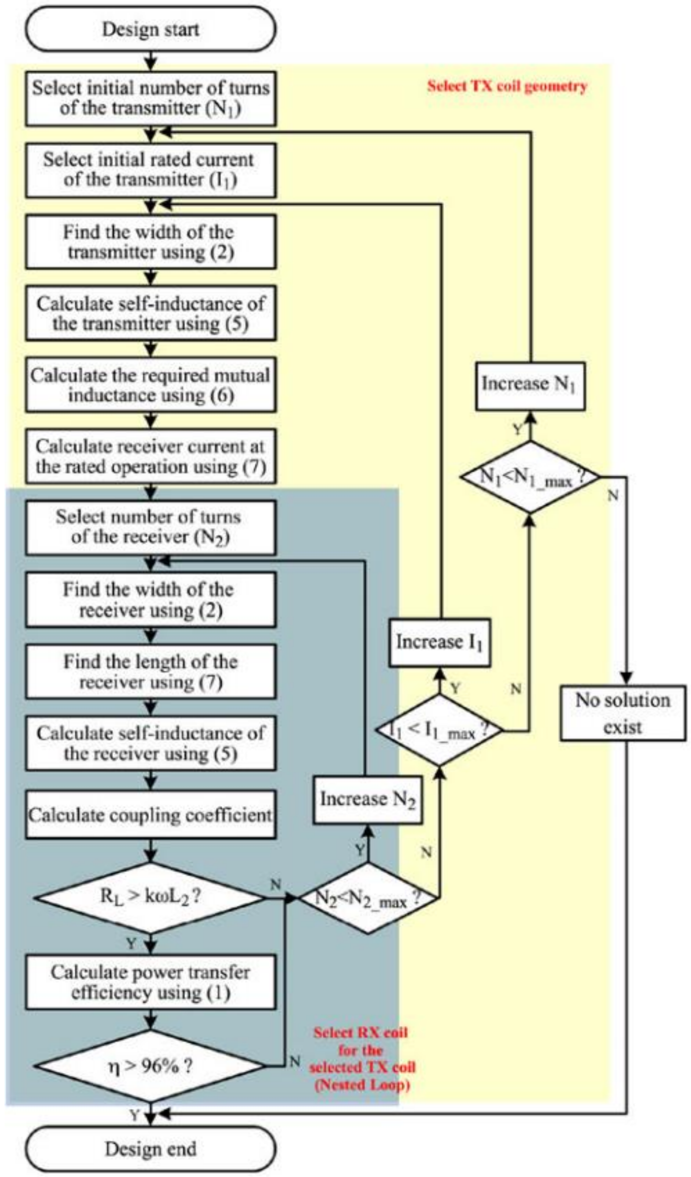

Fig. 1-66. Design flowchart of a 300 kW online WPT system

In the design flowchart, the geometry of the transmitter coil is determined in the first part, and then, the geometry of the receiver coil is selected in the second part. For the transmitter coil design, number of turns and rated operation current are independent variables, the width of the coil is a dependent one. If the number of turns and the rated current are chosen, a maximum width of the transmitter must satisfy international safety guidelines. For the transmitter coil, the rated current of the receiver is a given parameter, the number of turns and the width of the receive winding are dependent on each other to satisfy the safety guideline. Since the magnetic field is cross-coupled with the transmitter and the receiver, the iteration process needs to satisfy both limitations. The control stability criterion was used to avoid zero-phase bifurcation. The efficiency was used at the end to improve the iteration result with high power transfer efficiency. It should be noted that the receiver coil was designed based on selected transmitter coil. The experiment results showed that the measured total efficiency was over 90% at 150-kW transfer and the losses of the transmitter and receiver coils dominated the total losses.

The advantage of the proposed design methodology is that it considers power transfer efficiency, magnetic field distribution, output power level, output voltage level, and control stability simultaneously as design selection criteria. The magnetic flux density distribution at the horizontal distance of 20 cm from the vehicle body (1.4 m distance from the center of the WPT system), as shown in Fig. 1-48, was lower than the safety limit. However, the electric field was not evaluated, which is equally important as magnetic field. In addition, the power transfer distance is 7 cm, and it is not suitable to be used in electric vehicles, and the flux density within the air-gap should also be evaluated.

Miller et al [173] gave important insights into WPT operation in terms of k and ω through investigation of the resonant network associated with the coupler. Although small receiving coils are preferable on the vehicle, and popular perception is that the loss in coupling coefficient can be made up by using high Q obtained in part by increased operating frequency, Miller et al proposed that low k cannot be compensated with higher ω or higher Q, weight and cost benefits are unlikely when the secondary receiver coil on the vehicle is too small, and it’s painful to improve power transfer efficiency. Equivalent primary coil radius and secondary coil radius is recommended. However, he insisted that operating at 21 kHz region is better than operating at a higher frequency, the effect of operating frequency on magnetic and electric field distributions was not investigated. A general system design methodology was not proposed.

1.5.3 Summary and identified research opportunities

In the literature, LCIPT system design methodologies have been investigated in diverse power level applications. The design methodologies for implantable biomedical devices (mW level), laptop battery chargers (W level), electric vehicle battery chargers (kW level), and online train charging (MW level) has been reviewed.

Previous design methodologies began with the transmitter coil and the receiver coil geometry initialization. The initial estimation of the number of turns, loop radius, and other geometric factors of the coils are decided in the first step, and the geometry iterations of the coils are continued until the power transfer efficiency, copper mass, current ampacity, secondary side voltages satisfy the desired values. The magnetic flux density only at the air-gap center plane central point generated by the primary coil was considered in the SSW design methodology, which didn't consider air-gap electric field intensity and could only satisfy magnetic field electrostimulation safety limit at MHz frequency. There is no design methodology that has considered the following requirements simultaneously in the design procedures.

1) The human body safety to RF field exposure including both magnetic field and electric field in the air-gap center region
2) System analytical modeling from the front side to the end side, including inverter, coil, and rectifier
3) DC-to-DC power transfer efficiency including inverter efficiency, coil-to-coil efficiency, and rectifier efficiency
4) Voltage-current ratings of coils, capacitors, and power semiconductors
5) Coil spatial voltage stress between adjacent turns

Therefore, a new general design methodology which results in low air-gap magnetic flux density, low air-gap electric field intensity, high power transfer efficiency, low spatial voltage stress, and low voltage-current ratings is required.

1.6 Loosely coupled WPT system magnetic component design

In this section, the literature of magnetic component designs for high power EV chargers are reviewed. At first, different coil geometries are compared with respect to mutual coupling and performance under misalignment. Then, magnetic component loss distributions are analyzed. After that, mutual inductance calculation methods for different coil geometries are investigated. In the end, power scalability limitations of these geometries are identified.

1.6.1 Comparison of mutual coupling and misalignment tolerance

Operating frequencies of the majority of the state-of-the-art wireless EV chargers are in 10 kHz to 15 MHz. Some designers operated their systems at tens of kHz frequencies for the ease of the power converter design while the other designers operated at a few MHz frequencies for human body safety consideration and high efficiency [80].

(a) The photo of pot core in [179]

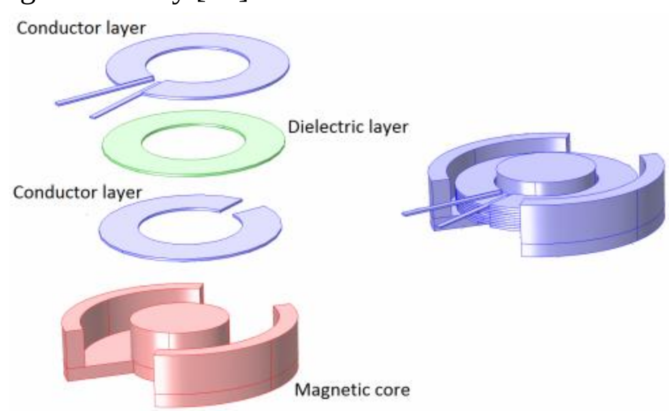

(b) The pot core in [211]

Fig. 1-67. Pot core geometry of kHz frequency WPT systems

In kHz frequency operation, various configurations have been presented for the power transfer. Li et al [17], Moradewicz et al [179], Nakao et al [209], Laouamer et al [210], and Sullivan et al [211] used pot ferrite core and Litz-wire for contactless power chargers to transfer power through a few mm distances. The pot cores are preferred to confine the magnetic flux in the core itself and to increase the coupling coefficient. The Litz-wire windings are preferred to increase the quality factor and to enhance the efficiency. The disadvantages are that the core is expensive, and the misalignment tolerance is very poor due to the confined magnetic flux.

Instead of using the full-size pot and disc cores, Budhia et al [52] optimized circular planar magnetic components with multiple ferrite bars, as shown in Fig. 1-68, to transfer 2 kW over 20 cm air-gap. The aluminum ring and backing plate are used for shielding purpose. The paper investigated the families of circular pad designs to optimize the pad in terms of tolerance in misalignment and high utilization of ferrite material. Dimensions of the ferrite bars and the coils are the design factors to be optimized.

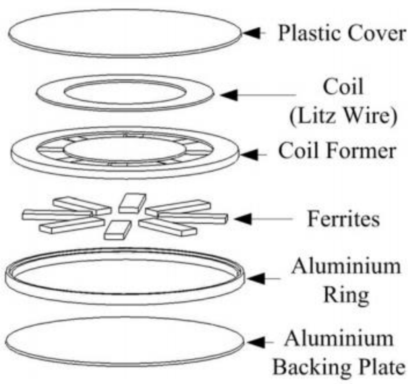

(a) Pad geometry

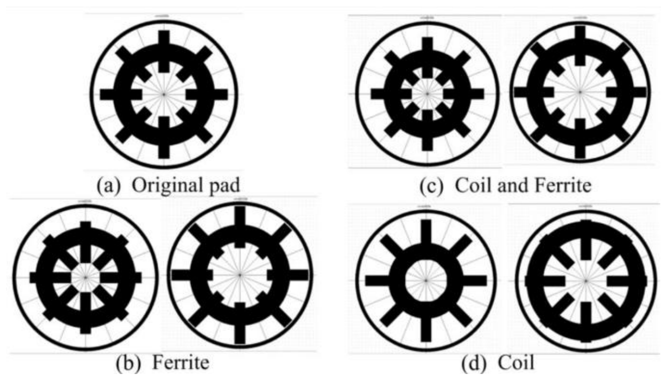

(b) Various bar and coil configuration

Pad Topology	(a)	(b)	(c)	(d)	(e)
	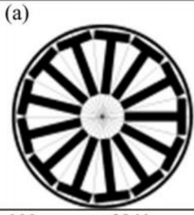	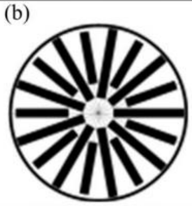	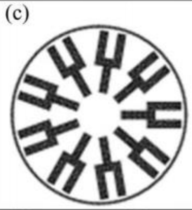	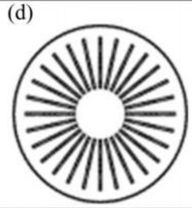	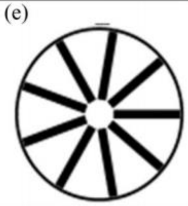
P_{su} at given Separation (VA)	100mm 3841 150mm 1236 200mm 435	100mm 3832 150mm 1212 200mm 420	100mm 3479 150mm 1102 200mm 383	100mm 2825 150mm 868 200mm 293	100mm 2480 150mm 775 200mm 264
No. of bars	32.5	31.5	33	21	18
Use (VA/cm^3)	3.34	3.44	2.98	3.80	3.89

(c) Various pad topologies

Fig. 1-68. Optimization of the ferrite bar pads

According to FEA simulation, the length of the ferrite bars has the most significant impact on transferring power to the receiver while its thickness has the less impact. As the length of the bars increases the power transferred to the receiver is maximized by achieving longest flux paths in the air-gap. As the width of the bars increase, transferred power is increased linearly up to a certain extent because of the enhanced coupling. Over the specific width, transferred power is not increased linearly with the width and the ferrite utilization factor is decreased. From the FEA analysis, the transferred power to the receiver is maximized with longer and narrower ferrite bars while the Litz-wire coil is aligned on the center of the bars. Not only the basic umbrella-rib-style layout, diverse layouts are investigated with additional ferrite bars as shown in Fig. 1-68 (c). The paper chose the second geometry in Fig. 1-68 (c) as an optimal one due to the combination of long and narrow ferrite blocks to achieve the best ferrite utilization, the long one provides favorable magnetic paths that increase flux density above the pad, while the narrow one enables flux around the coil to be guided more effectively.

According to FEA results, maximum horizontal misalignment tolerance of the circular pads is about 40% of the pad diameter, because a power null occurs due to flux cancellation when the receiver is offset from the transmitter at approximately 40% of the pad diameter. The final design has the diameter of 70 cm with a full power diameter of 26 cm with 21 cm air-gap.

Budhia et al proposed a polarized magnetic coupler in order to increase the coupling between the transmitter and the receiver, and to enhance tolerance on specific directional misalignment [30][31]. Unlike the circular pad design, two coils are used in the new polarized design (double D pad, DD) as shown in Fig. 1-69.

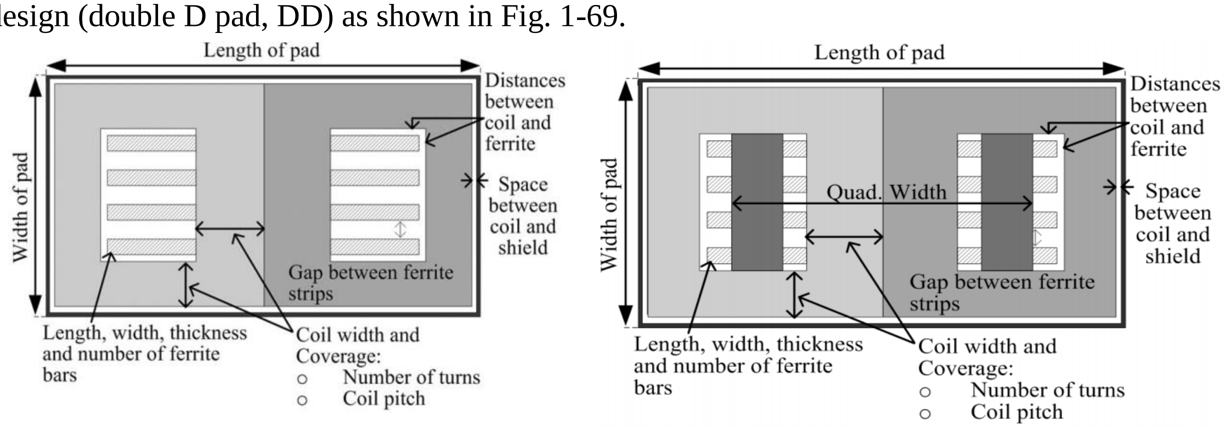

(a) DD pad (b) DDQ pad

Fig. 1-69. Configuration of the DD and DDQ pad

By placing two D-shape coils side by side on the ferrite bars, the generated magnetic flux is concentrated in the center of the pad which is resulting in higher coupling and low leakage flux. Since the coupling of DD pad is caused by the horizontal flux, there is a null coupling point in the horizontal line if the receiver is also a DD pad. Additional rectangular coil is attached below the receiver DD pad to form a double D quadrature (DDQ) pad and the quadrature coil is effective in horizontal misalignment, because the quadrature coil can couple vertical flux components. The DD and DDQ pad geometries (coil and ferrite bar lengths and widths) are optimized to achieve maximum coupling coefficient in a given distance by means of FEA. The transmitted power to the receiver by x- and y directional misalignment is shown in Fig. 1-70.

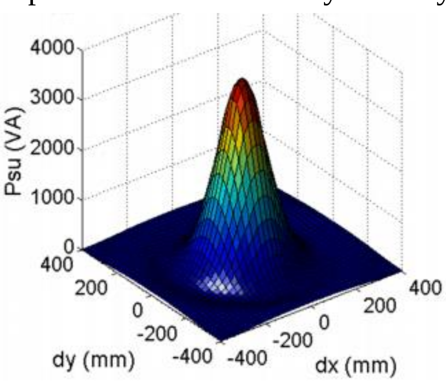

(a) Circular transmitter to circular receiver

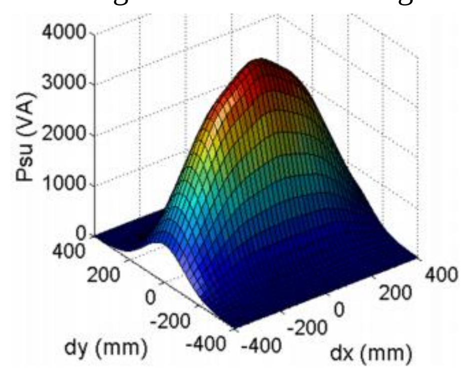

(b) Circular transmitter to DD receiver

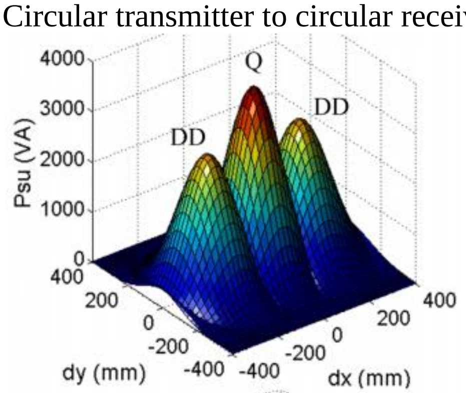

(c) Circular transmitter to DDQ receiver

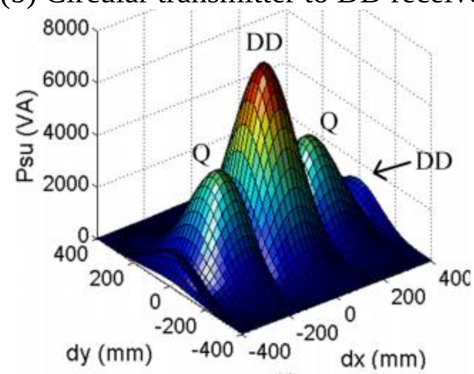

(d) DD transmitter to DDQ receiver

Fig. 1-70. Transferred power dependence on horizontal misalignment

As shown in Fig. 1-70, peak transferred power and misalignment tolerance of DD pads is enhanced significantly compared to the circular pads especially in the x-direction (elongated axis) mainly because the size of DD pad along x-direction is much larger. The misalignment tolerance of DDQ pad is better than DD pad since additional Q pad increases the coupling coefficient between transmitter and receiver coils.

The circular pad generates the vertical field, while the DD pad produces horizontal field, therefore, if a vehicle is equipped with a circular pad as a receiver and parks over a DD pad, the coupling between the transmitter and the receiver will reduce significantly, in addition, the leakage magnetic field will increase hugely. A bipolar pad (BPP) and a tripolar pad (TPP) are proposed to solve this problem [53]-[57].

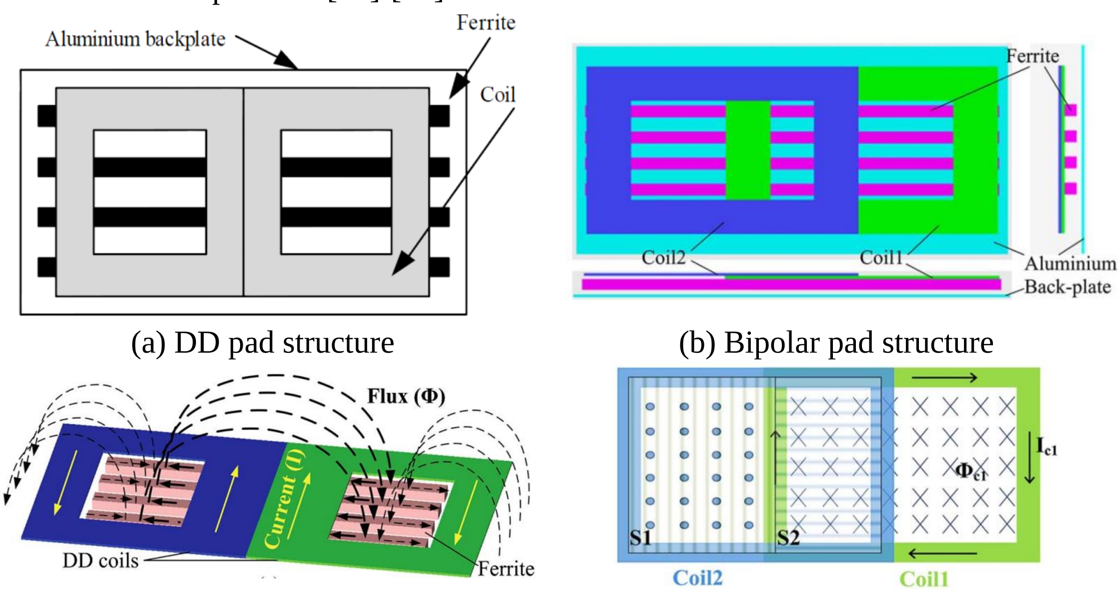

(a) DD pad structure (b) Bipolar pad structure

(c) DD pad flux pattern (d) Bipolar pad flux pattern

Fig. 1-71. DD pad and bipolar pad structures and flux patterns

The bipolar pad structure and flux pattern are compared with the DD pad in Fig. 1-71 [54]. Adjusting the overlap area of coil 1 and coil 2, the amount of flux, generated by coil 1, that goes through area S2 is equal to the return amount of flux going through area S1, then coil 1 and coil 2 are mutually decoupled, which allows the currents within each coil to be independent in both phase and magnitude and provides a better misalignment tolerance.

Mutual decoupling among three coils in a tripolar pad was achieved by appropriately adjusting the overlap between the coils so that the net EMF induced in an adjacent coil was as close as possible to zero [55]-[57]. When the secondary coil has rotational misalignments, three mutually decoupled coils can be controlled and driven individually to generate a polarized magnetic field relative to the position of the secondary coil, which helps achieve the rotational tolerances of a non-polarized pad while still taking advantages of a polarized magnetic field. Three coils in layout A are mutually decoupled to independent control current in each coil, and in layout B are mutually enhanced to increase the power transfer efficiency.

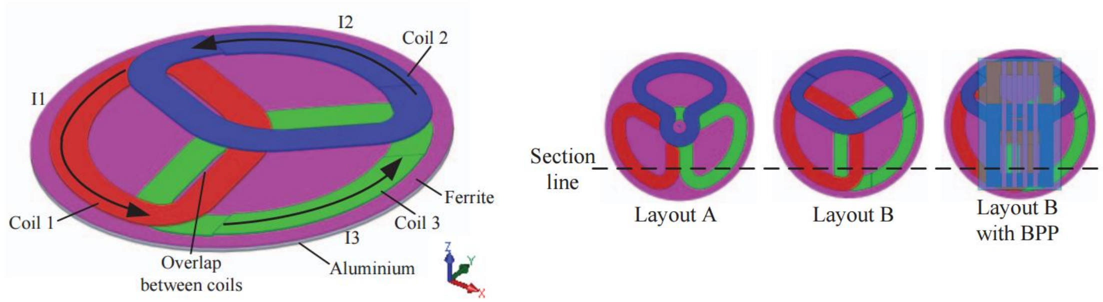

(a) Construction of a tripolar pad (b) Tripolar pad layouts

Fig. 1-72. Tripolar pad for inductive power transfer systems

Both bipolar and tripolar pads generate vertical flux, and the coupling coefficient is determined by the area enclosed by the pad. They can be treated as an equivalent way to increase the enclosed area to improve the coupling factor compared with using a single large pad.

In addition to the single-sided windings, researchers investigated double-sided windings with rectangular magnetic core designs as well [49][58]. The paper insisted that the double-sided winding enables 0.5x transmitter and receiver size for the same coupling coefficient. The proposed double-sided winding geometry in [49] is shown in Fig. 1-73.

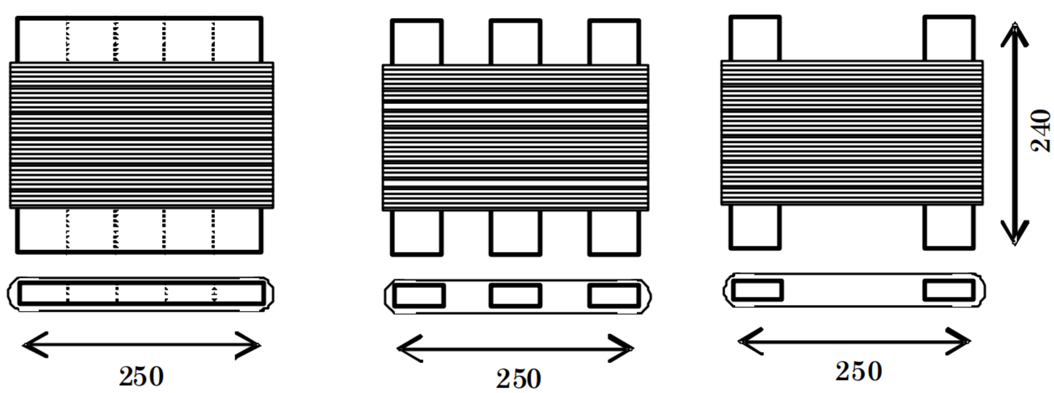

(a) Rectangular core (b) Three I-core (c) Two I-core

Fig. 1-73. Double-sided windings design (unit: mm)

The paper investigated the effect of the number of split cores to the coupling coefficient and power transfer efficiency, in order to optimize the required amount of the core material and cost. With the same copper winding size, the three I-core geometry has comparable efficiency and power level with the rectangular winding geometry. Since the magnetic material is helpful to improve the coupling coefficient, then the power transfer efficiency could be improved. Therefore, the geometry with more magnetic material has the highest power transfer efficiency. It is claimed that the double-sided coils were more beneficial in misalignment tolerance than single-sided coils and the size of the coils for same power level can be reduced using double-sided coils. Because of the unwanted leakage flux, aluminum foils were used to shield magnetic flux at the back of the core and increase the coupling coefficient. However, when the shielding is added, the quality factor of a flux-pipe coupler reduces from 260 to 86. The high shielding loss makes this coupler not a good choice [59].

Only a few resonant inductive WPT systems are operated at MHz frequencies. Lee et al [50][79]-[83] operated the system at 3.7 MHz in order to increase the efficiency with low magnetic flux density. Kurs et al [199] transmitted power at 10 MHz in order to increase the transfer distance. The magnetic component designs in the papers did not use any kind of magnetic cores because of the huge iron loss in the core at MHz frequencies. Air-core coils are typically used. Therefore, copper and dielectric losses play a major role in the total loss of a system in MHz. In some papers, the Litz-wire is used to decrease copper loss in MHz frequency. However, Litz-wire is not a viable solution for kW, MHz operations because of the irregularities in the fabrication process and parasitic capacitances between the adjacent turns. Therefore, copper tubing or silver-plated copper wires have been used for an air-core inductor. Helical or spiral winding geometries are used for the inductor. However, there is not enough research in minimizing losses in MHz frequencies. Typically, large turn spacing coils are used to decrease proximity effect loss in the coils. Two identical helical or spiral coils with copper tubing are fabricated as a transmitter and a receiver in [199][213]. In order to decrease the proximity effect loss and increase the power transfer efficiency, the turn spacing of the coils is very large compared to the tubing diameter.

Instead of using conventional helical or spiral winding, Lee et al [50][79]-[83] proposed the surface spiral winding (SSW) layout, shown in Fig. 1-74 (a) and (b), in order to minimize skin and proximity effect losses of the copper winding at MHz frequencies. With the new layout, compact and high efficiency system is achieved. According to Lee et al [80], the design methodology of the SSW for maximum Q factor is investigated by means of 2D FEA. The Q factor of a SSW is maximized when the following three conditions are met: (1) Wall thickness of the winding is equal to 1.7x skin depth. (2) Large loop radius and less number of turns in case of equal self-inductance coils. (3) Cross-sectional radius of the winding is equal to 0.1x loop radius.

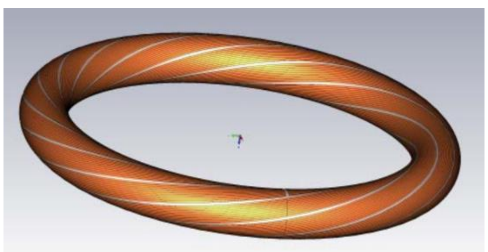

(a) SSW geometry

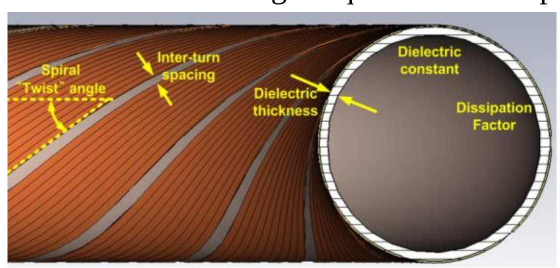

(b) SSW design variables

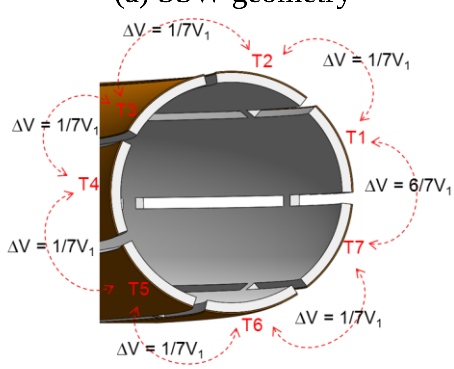

(c) SSW spatial voltage distribution

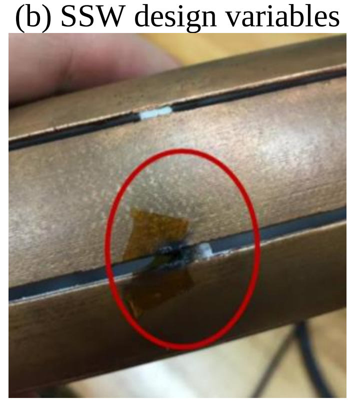

(d) Voltage breakdown when transferring 1 kW

Fig. 1-74. Surface spiral winding geometry, voltage distribution, and breakdown

However, during the design process, the design methodology didn't include the effect of spatial voltage stress over adjacent turns and dielectric losses systematically. The spatial voltage distribution is shown in Fig. 1-74 (c), the highest spatial voltage stress is located between the first turn and the end turn; since it is the spatial voltage stress between adjacent turns that causes the dielectric losses, the main dielectric losses are also located between the first turn and the end turn. In addition, the gap between the first turn and the end turn is the first region that voltage breakdown would happen when pushing to transfer high power. During the SSW experimental test, the voltage breakdown happens instantly between the first turn and the end turn when pushing to transfer 1 kW from the transmitter to the receiver as shown in Fig. 1-74 (d) [83].

- **Comparison of coupling coefficient**

Typical shapes of inductive WPT coils include circular, square, and rectangular structures as shown in Fig. 1-75 (a)-(c) [229]. The DD coil proposed in [31] is represented as the segmented coil as shown in Fig. 1-75 (d).

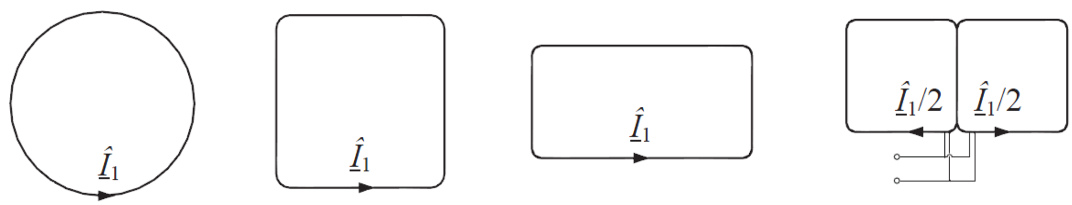

(a) Circular coil (b) Square coil (c) Rectangular coil (d) Segmented (DD) coil

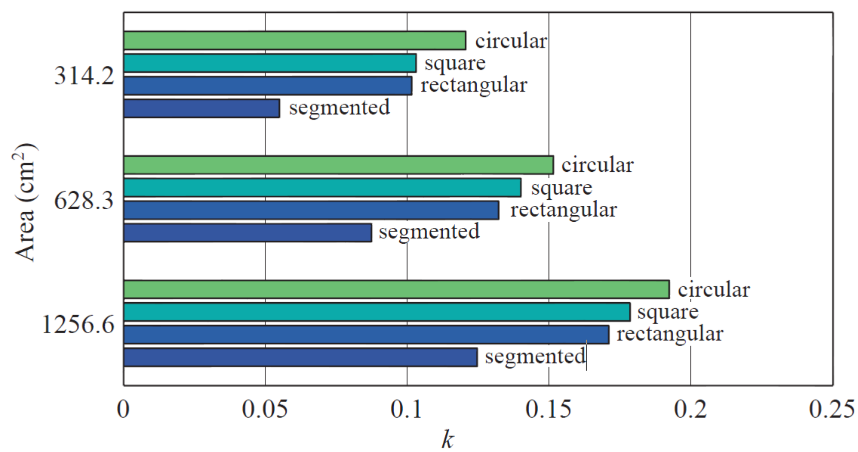

(e) Comparison of the coupling coefficient k

Fig. 1-75. Schematic and coupling coefficient of the simulated inductor shapes

For all models, a small conductor diameter of d_W = 1 mm was used, and the number of turns was set as 1 for both the primary coil and the secondary coil, i.e., the winding was concentrated at the outer edge of the coil, in order to minimize any effects resulting from a finite size of the winding. The air-gap was set as 70 mm. The radius of the circular coil was set to 100 mm, 141.4 mm, and 200 mm. The three resulting coil areas were taken as a reference for the other models, which were designed to have the same area. The rectangular coil and the segmented coil were designed with a width to length ratio of 1/2. The coupling coefficients are compared and shown in Fig. 1-75 (e).

The magnetic coupling obtained with a circular coil is higher than that of the square and the rectangular coil. It is claimed that it can be explained by the distortion of the field distribution around the corners of those shapes [229]. However, when the aspect ratio of the rectangular coil keeps increase, its mutual coupling will further reduce due to leakage magnetic field. The segmented coil achieves a magnetic coupling that approximately corresponds to that of a rectangular coil with only half the size, which is actually the mutual coupling of a circular coil or a square coil with only half the size.

A comprehensive comparison of the coupling factor with respect to various coil geometries was investigated [214][215]. The evaluated coil geometries are shown in Fig. 1-76 (a)-(p). The geometries with a compensation winding have an outer winding with an opposed direction of current to the inner windings. The triangular geometry is made of two triangles in mirror symmetry. All other geometries were designed based the circular geometry with same area and number of turns. The coil diameter of the circular geometry is 550 mm, the coil cross-section is 50 mm^2, the number of turns is set as 5, and the distance between adjacent turns is 20 mm. The coupling factors are compared in Fig. 1-76 (q) under different air-gaps.

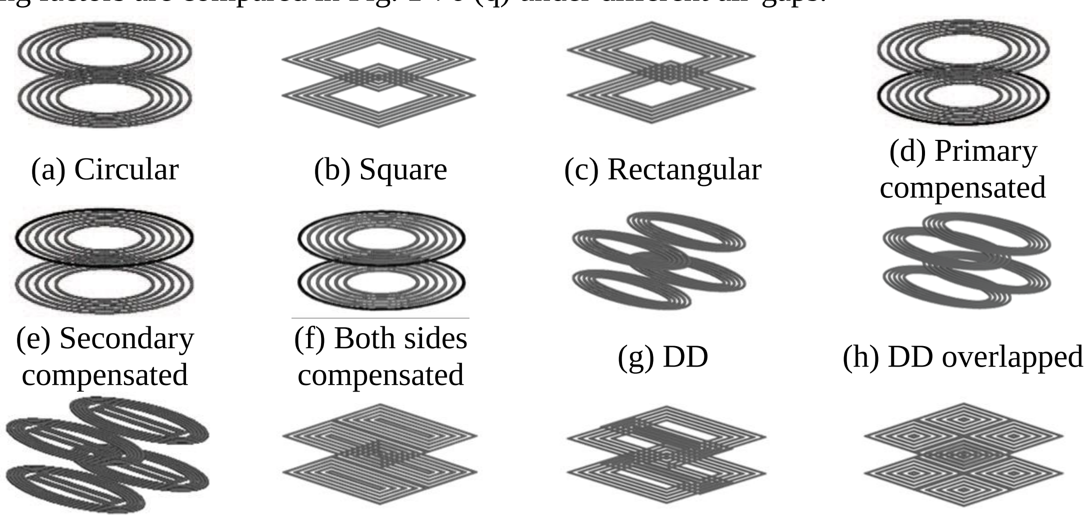

(a) Circular (b) Square (c) Rectangular (d) Primary compensated

(e) Secondary compensated (f) Both sides compensated (g) DD (h) DD overlapped

(i) DDQ (j) Two squares (k) Two squares (l) Four squares overlapped

(m) Four squares overlapped (n) Triangular (o) Circular quartered (p) Circular quartered overlapped

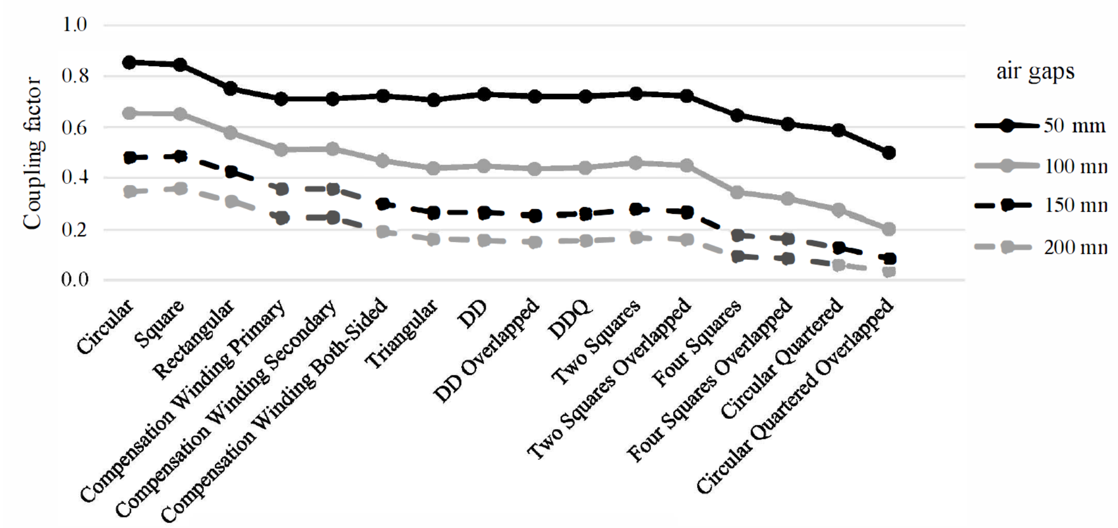

(q) Comparison of the coupling factor

Fig. 1-76. Schematic and coupling coefficient of various coil geometries

As shown in Fig. 1-76 (q), the circular coil can achieve the highest mutual coupling, the square coil is slightly lower due to the magnetic field distortion at the corners.

The self-inductance and coupling coefficient of the surface spiral winding (SSW) and planar spiral winding (PSW) are compared in Fig. 1-77 [81].

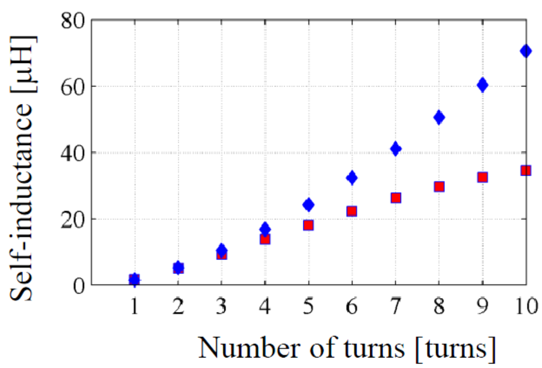

(a) Self-inductance vs. number of turns

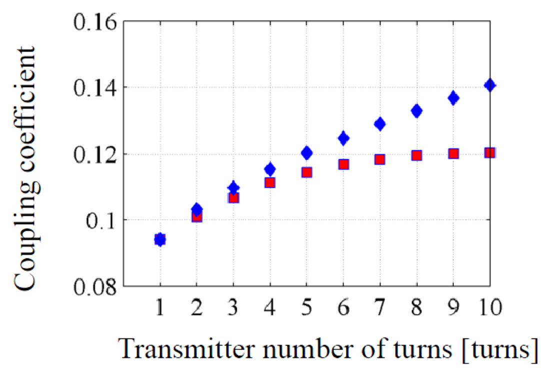

(b) Coupling coefficient vs. number of turns

Legend: SSW, PSW.

Condition: Transmitter and receiver outer loop radius 30cm, receiver number of turn 1. Cross-sectional radii: SSW 16mm, PSW 2 mm. Inter-turn spacing 0.3 mm.

Fig. 1-77. Comparison of self-inductance and coupling coefficient of SSW and PSW

As shown in Fig. 1-77, SSW typically has higher coupling coefficient compared to the PSW, since each turn of the SSW has the same loop radius.

In summary, under aligned conditions, planar circular geometry can achieve the highest mutual coupling compared with other geometries. Rectangular shape geometries, such as the rectangular pad, the DD pad, the bipolar pad and the DDQ pad, and the double-sided coil have higher lateral misalignment tolerance along the length direction, while the lateral misalignment tolerance along the width direction is almost the same as the circular coil, which means the improvement in misalignment tolerance along the length direction is mainly due to the increment of area along the elongated direction. The bipolar pad and tripolar pad are mutually decoupled, which is an equivalent way to increase the area enclosed by the coil. SSW can achieve higher mutual coupling than the PSW since the diameter of each turn maintains the same.

1.6.2 Mutual inductance calculation under aligned and misaligned conditions

Most of the transmitter and the receiver designs are based on perfectly aligned cases. System analysis and design with the coupling coefficient of coaxially aligned coils is a good starting point. However, misalignment between the transmitter and the receiver is unavoidable in the real worlds, maximum allowable misalignment of a system has to be investigated for efficient power transfer.

Because analytical calculation of the coupling coefficient of arbitrary misaligned coils required solving the double integral of Neumann's formula [216], only a few researchers used analytical methods. The double integral of Neumann's formula results in the first and second kind of complete elliptic integrals [26][217]. As of the complexity of analytical methods, empirical or numerical methods have been used as well, though they are limited to special geometries and massive numerical integration.

Noureddine [217] and Babic [218] et al calculated the mutual inductance of lateral and angular misaligned coils by means of numerical integration. Flack et al [219], Hochmair [220], and Kim et al [221] have considered lateral misalignment of the coils by means of experimental and numerical analysis. In contrast, Soma et al [26] and Galbraith et al [222] have investigated mutual inductance dependence on lateral and angular misalignments using simplified analytical method and empirical corrections. The major limitation of such analytical method is calculation precision in case of the large air-gap WPT systems. The proposed method was valid until the lateral misalignment distance is smaller than the radius of a receiver coil. Furthermore, the estimation error became bigger as the misalignment distance increases.

Fotopoulou et al proposed a semi-analytical method in [21]. Instead of complex integration, the paper assumed that the spatial distribution of magnetic field in the receiver loop is uniform because the coils are loosely coupled ($k < 0.001$). In the paper, flux linkage calculation was independent of the spatial distribution. However, the paper did not quantitatively explore the error in net flux linkage calculation coming from the approximation. In a far-field transfer such assumption does not make sever error, because the electromagnetic field in the far-field area is planar [1]. However, in a near-field area, especially loosely coupled systems ($0.001 < k < 0.01$) may have a severe error because of the non-uniform distribution of E and H fields.

- **Mutual inductance calculation for perfectly aligned coils**

Mutual inductance calculation of two coaxial coils was investigated for more than 100 years since the era of Maxwell. According to Maxwell, the mutual inductance of two coaxial filaments can be calculated using following expression [223]

$$M = -\mu_0(\pi ab)\int_0^{\infty} J_1(kb)J_1(ka)e^{-kz}\,dk \tag{1.24}$$

Where a and b are the radii of the filaments, J_1 is a Bessel function of the first kind. The exact integration of above expression in elliptic integrals is shown below

$$M = \frac{2\mu_0}{\gamma}(ab)^{1/2}\left[\left(1 - \frac{\gamma^2}{2}\right)K(\gamma) - E(\gamma)\right] \tag{1.25}$$

Where $K(\gamma)$ and $E(\gamma)$ are complete elliptic integrals of the first and second kind, respectively, and $\gamma = \sqrt{4ab / [(a+b)^2 + z^2]}$.

Hurley et al calculated the mutual inductance of two planar multi-turn coils by an analytical method in [224]. The mutual inductance of planar coils in the air follows

$$M = \frac{\mu_0 \pi}{h_1 h_2 \ln\left(\frac{r_2}{r_1}\right) \ln\left(\frac{a_2}{a_1}\right)} \int_0^{\infty} S(kr_2, kr_1) S(ka_2, ka_1) Q(kh_2, kh_1) e^{-k|z|} \, dk \tag{1.26}$$

Where r_1, r_2 and a_1, a_2 are inner and outer radii of the coil 1 and coil 2, respectively, and $Q(kx, ky) = \frac{2}{k_2}\left[\cosh\left(k\,\frac{x+y}{2}\right) - \cosh\left(k\,\frac{x-y}{2}\right)\right]$ if $z > \frac{h_1 + h_2}{2}$, and when z = 0, x = y = h, $Q(kx, ky) = \frac{2}{k}\left(h + \frac{e^{-kh} - 1}{k}\right)$, $S(kx, ky) = \frac{J_0(kx) - J_0(ky)}{k}$.

Miller demonstrated self- and mutual inductance calculation of single-layer solenoids [225]. The self-inductance of a solenoid can be calculated by

$$L = \frac{\mu_0 N^2 a^2}{3c}\left\{\frac{dc}{a^2}\,[F(k) - E(k)] + \frac{4d}{c}\,E(k) - \frac{8a}{c}\right\} \tag{1.27}$$

Where a, c, and N are radius, axial length, and the number of turns of the solenoid, respectively. $d = \sqrt{4a^2 + c^2}$ and k = 2a/d. K(k) and E(k) are complete elliptic integrals of the first and second kind, respectively.

The paper addressed the mutual inductance of two solenoids as well. The mutual inductance equation was the same with (1.23), because the axial lengths of the coils were not considered in the paper.

- **Mutual inductance calculation for coils with lateral misalignment**

Fotopoulou et al determined the magnetic field intensity at the center of laterally misaligned receiver winding when the transmitter is a multi-turn solenoid, circular spiral coil or square spiral coil [21].

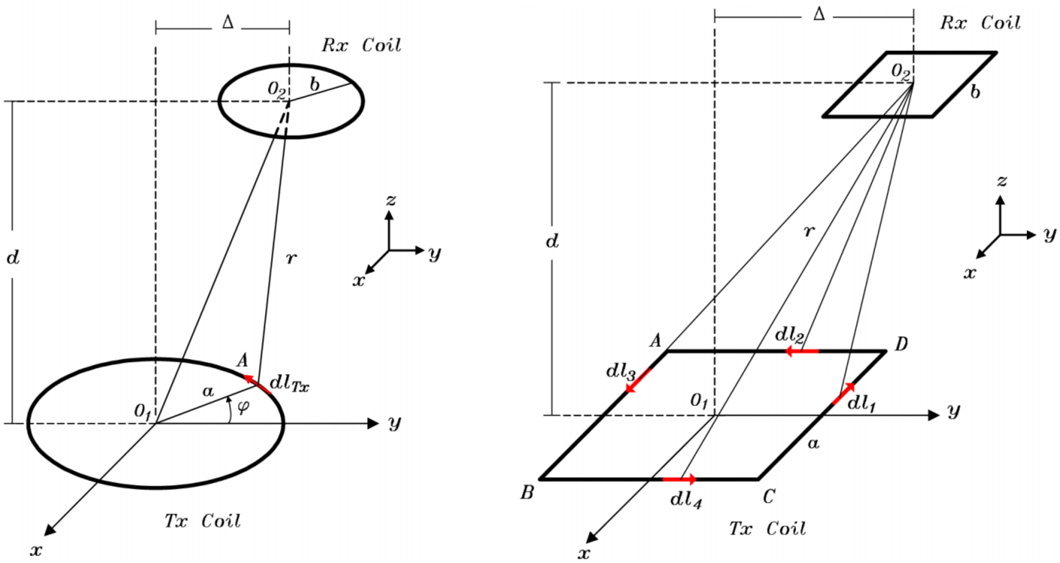

(a) Circular winding (b) Square winding

Fig. 1-78. Laterally misaligned coils

In case of solenoid and circular spiral coils, the z-component of the magnetic field intensity at the center of the receiver winding can be calculated by

$$H_z = \frac{I \times N}{2\pi\Delta}\left(\frac{m}{4a\Delta}\right)^{1/2}\left[\Delta K(m) + \frac{am - (2-m)\Delta}{2-2m}E(m)\right] \text{(solenoid)}$$

$$H_z = \frac{I}{2\pi\Delta}\sum_{i=1}^{n}\left(\frac{m_i}{4a_i\Delta}\right)^{1/2}\left[\Delta K(m_i) + \frac{a_i m_i - (2-m_i)\Delta}{2-2m_i}E(m_i)\right] \text{(circular spiral)} \tag{1.28}$$

Where $m = \dfrac{4a\Delta}{(a+\Delta)^2 + d^2}$, $m_i = \dfrac{4a_i\Delta}{(a_i+\Delta)^2 + d^2}$, I is the current of the transmitter coil, N is the number of turns, a is the transmitter radius, d and Δ are the vertical and lateral distances in the coils. K(m) and E(m) are the complete elliptic integral of the first and second kind, respectively.

By assuming that H_z is spatially uniform in the receiver coil surface, the paper obtained simplified expression of the induced voltage.

$$V_{ind} = -\frac{\partial}{\partial t}\int_S \mu_0 H_z \, dS = j\omega S_{eff} \mu_0 H_z \tag{1.29}$$

Where S_{eff} is the effective area of the receiver coil. The paper discussed efficiency dependence on lateral and angular misalignment with the induced voltage at the secondary coil. However, as mentioned earlier, the paper did not explore the calculation error caused by the approximation.

Soma et al [26] proposed an approximate mutual inductance calculation method of misaligned coils. Because of the tedious integral procedure, the paper estimated mutual inductance by empirical approximation of the integrals.

$$M_L(\min) = \frac{\mu_0 ab}{\sqrt{a(b+\Delta)}}\, G(r_{\min}) \text{ and } M_L(\max) = \frac{\mu_0 ab}{\sqrt{a(b-\Delta)}}\, G(r_{\max}) \qquad (1.30)$$

Where $G(r) = \left(\frac{2}{r} - r\right) K(r) - \frac{2}{r} E(r)$, $r_{\min} = \frac{4a(b-\Delta)}{(a+b-\Delta)^2 + d^2}$ and $r_{\max} = \frac{4a(b+\Delta)}{(a+b+\Delta)^2 + d^2}$.

The calculated approximate mutual inductance dependence on lateral misalignment with exact values is shown in Fig. 1-79 (a). As the lateral misalignment increases to the same value with the inter-coil distance, 5 mm, the mutual inductance decreased from 0.9 nH to 0.65 nH. $M_{L2} = \frac{M_L(\min) + M_L(\max)}{2}$ was close to the exact value in case of lateral misalignment.

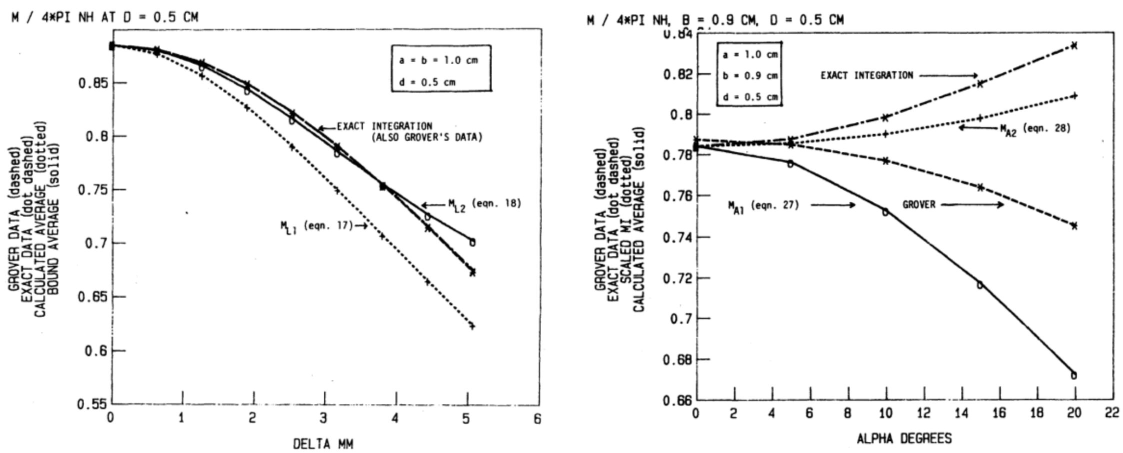

(a) Lateral misalignments (b) Angular misalignments

Fig. 1-79. Mutual inductance dependence on misalignments

Unlike the simplified expressions, an exact analytical solution of the mutual impedance of sandwich structure, laterally misaligned coils have been investigated by Su et al in 2009 [226].

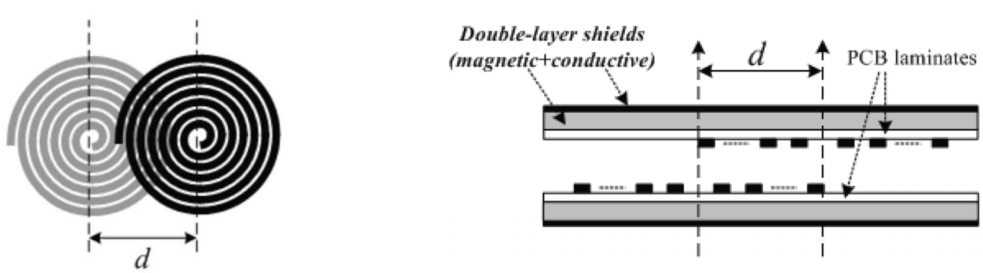

(a) Top view without shields (b) Cross-sectional view

Fig. 1-80. Laterally misaligned sandwich structure coils

Calculated mutual impedance Z of the laterally misaligned sandwich coil follows

$$Z = j\omega M + Z_{nc}^{f} \tag{1.31}$$

Where $M = \mu_0 R_p R_s \int_0^{\infty}\left[\int_0^{\pi} \frac{R_s - d\cos\varphi}{r} J_1(kR_p)\, J_1(kr)\, e^{-k|d_2 - d_1|}\, d\varphi\right] dk$, $Z_{nc}^{f} = j\omega \times \mu_0 R_p R_s \int_0^{\infty}\left[\int_0^{\pi} \frac{R_s - d\cos\varphi}{r} J_1(kR_p) J_1(kr)[f(\lambda) + g(\lambda)]\, d\varphi\right] dk$, J_1 is a Bessel function of the first kind, R_p and R_s are the radii of the coils, d is the lateral misalignment, d_1 and d_2 are the vertical distance of the coils from the bottom substrate.

Although the paper developed the exact analytic expressions for lateral misalignments, it is very difficult to use for system design because of the tedious double integral of the Bessel functions and its multiplications.

Kim et al [221] and Akyel et al [227] adopted numerical methods to calculate the mutual inductance of laterally misaligned coils. The coil was divided into small elements and the total mutual inductance was added together by small elements.

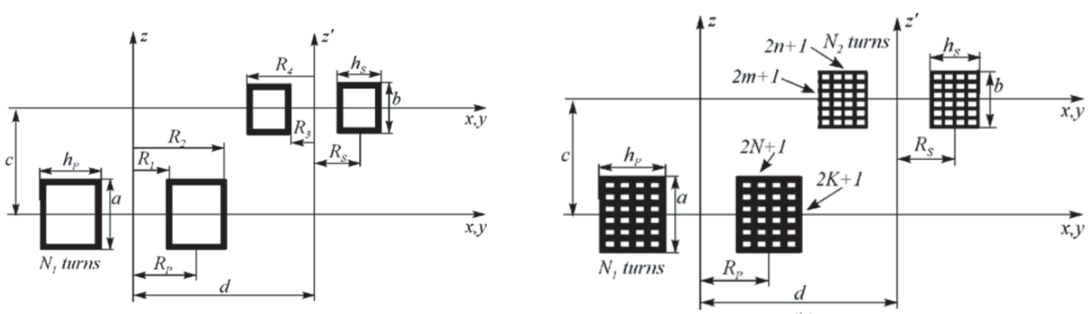

(a) Side view of two filaments (b) Mesh configuration

Fig. 1-81. Laterally misaligned coils for numerical calculation

Since the mesh size is critical to the accuracy of the calculation, fine mesh configuration is required in general. The numerical method requires large memory and time for calculation.

- **Mutual inductance calculation for coils with angular misalignment**

For the angular misalignment, Fotopoulou et al calculated the normal component of magnetic field intensity by a dot product of H_z and the normal unit vector of the inclined surface [21]. Then, the paper again assumed that the H-field distribution in the receiver coil surface is uniform with the value at the center of the coil.

Babic et al [218] proposed numerical integration method of an angular misalignment configuration. The coil was divided into small elements as shown in Fig. 1-82 and the total mutual inductance was added together by small elements.

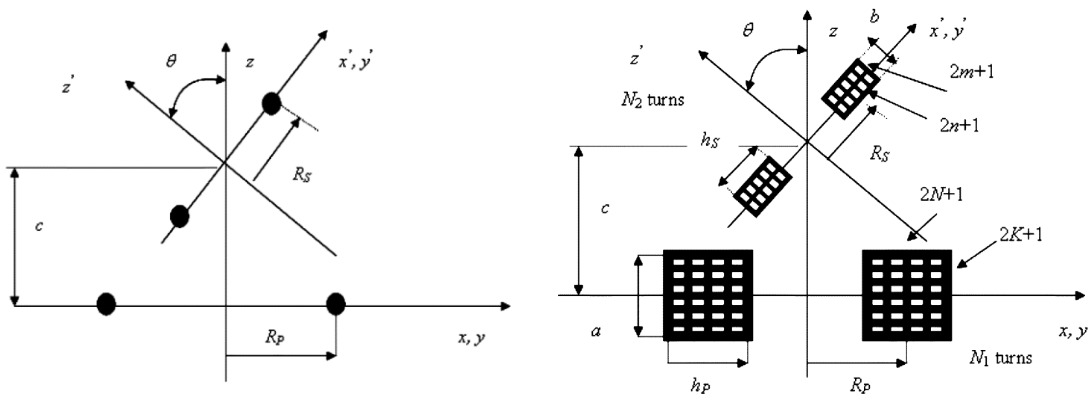

(a) Side view of two filaments (b) Mesh configuration

Fig. 1-82. Angular misaligned coils for numerical calculation

The mutual inductance of two angular misaligned filaments can be calculated by

$$M = \frac{\mu_0}{\pi}\sqrt{R_p R_s}\cos\theta \int_0^{\pi} \frac{\Psi(k)}{\sqrt{V^3}}\, d\phi \tag{1.32}$$

Where R_p and R_s are the radii of the filaments, c is the center to center distance, and $V = \sqrt{1 - \cos^2\phi \sin^2\theta}$, $k^2 = \frac{4\alpha V}{1 + \alpha^2 + \beta^2 + 2\alpha\beta\cos\phi\sin\theta + 2\alpha V}$, $\alpha = R_s/R_p$, $\beta = c/R_p$, $\Psi(k) = K(k)\left(\frac{2}{k} - k\right) - E(k)\frac{2}{k}$.

Fine mesh configuration is required in general to get a high accuracy calculation result. Numerical integration method is appropriate for high accuracy mutual inductance calculation of complicated cross-sectional shape coils.

Because it is very difficult to get a closed expression of (1.22), Soma et al [26] attempted to obtain an approximated value of (1.22) for the design purpose. The mutual inductance of angularly misaligned coils was followed

$$M = \frac{\mu_0 \sqrt{R_p R_s}}{\pi \sqrt{\cos\alpha}} \int_0^{\pi} \left(\frac{\cos\lambda}{\cos\phi}\right)^{3/2} d\phi \tag{1.33}$$

Where α is the inclined angle, θ and ϕ are the displacement angles of the source and observing elements of the transmitter and receiver filaments in their local coordinates as shown in Fig. 1-83. G(r) is given in (1.20), and the definition of $\tan(\lambda)$ is $\frac{\sin\phi}{\cos\phi \cos\alpha}$.

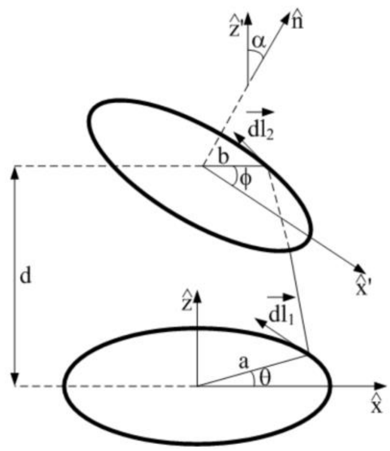

Fig. 1-83. Configuration of angular misalignment

The paper got an approximate value of (1.23) as (1.24) with an empirical assumption that the misalignment is less than 25-degree.

$$M = \frac{M_i}{\sqrt{\cos\alpha}} \tag{1.34}$$

Where M_i is the mutual inductance of the coaxial coils ($\alpha = 0$). Calculated mutual inductance is plotted in Fig. 1-79 (b).

- **Mutual inductance calculation for coils with general misalignment**

In general, lateral and angular misalignment happen concurrently. Therefore, the integrals in H-field calculation are extremely complicated for the general case. The configuration of general misalignment is shown in Fig. 1-84.

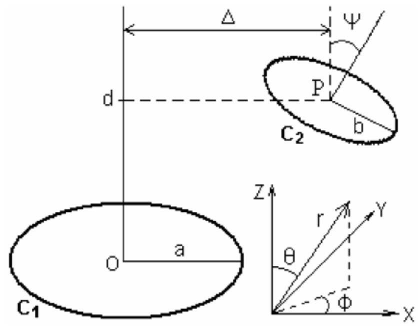

Fig. 1-84. Configuration of general misalignment

Noreddine et al developed a general expression for the mutual inductance of misaligned coils as [217]

$$M = \frac{\mu_0}{2\pi} b \sqrt{a} \int_0^{2\pi} \frac{G(k)}{V_\varphi^{3/2}} (\Delta\cos\varphi + b\cos\psi)\, d\varphi \tag{1.35}$$

Where G(k) is given in (1.20), a and b are the radii of the coils, Δ and d are the lateral and vertical distances of the coils, ψ is the misalignment angle, k and b_φ are defined as $k = \sqrt{\frac{4ab_\varphi}{(a + b_\varphi)^2 + (d - b\sin\psi\cos\varphi)^2}}$, $b_\varphi = \sqrt{(\Delta + b\cos\psi\cos\varphi)^2 + (b\sin\varphi)^2}$.

It is obvious that the closed form solution for (1.25) is impossible to develop. The paper calculated the mutual inductance using numerical integration method.

Instead of the incorporated analysis in [217], Soma et al [26] demonstrated that the lateral and angular misalignments effect on mutual inductance can be considered independently in the approximated calculation. The approximated mutual inductance of general misalignment case can be calculated by

$$M_1 = \frac{M_{L1}}{\sqrt{\cos\alpha}}, \quad M_2 = \frac{M_{L2}}{\sqrt{\cos\alpha}} \tag{1.36}$$

Where $M_{L1} = \frac{\mu_0 ab}{\sqrt{a(b+\Delta)}} G(r_{max})$, $M_{L2} = \frac{M_L(min) + M_L(max)}{2}$, α is the misalignment angle, $M_L(min)$ and $M_L(max)$ are defined in (1.28).

In summary, the literatures have developed enough methods to calculate the mutual inductance and coupling coefficient, which is necessary to develop a general design methodology for loosely coupled inductive WPT systems achieving given requirements under aligned and misaligned conditions.

1.6.3 Magnetic component loss distributions

Losses of the magnetic components are: iron loss, copper loss, radiation loss, and dielectric loss. An inductor with a magnetic core is generally used in WPT systems for electric vehicles. Loss distributions of inductive WPT coils are investigated in this section.

- **Iron loss**

Soft magnetic materials are generally used in inductive WPT coils to shield magnetic flux and increase mutual coupling between the transmitter and the receiver. Applications and performance ranges of typical soft magnetic materials and their development objectives are shown in Fig. 1-85 [228].

Operating flux density (T): contributor to 1k 10k 100k 1M downsizing and electric power capacity

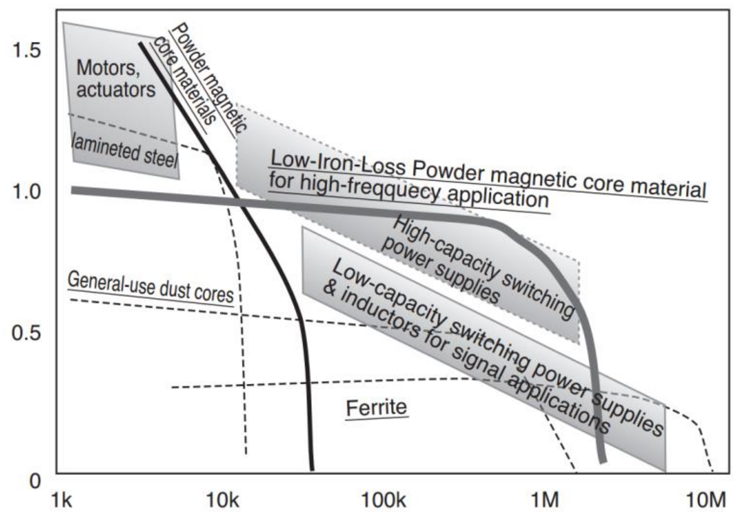

Switching frequency (Hz): contributor to conversion efficiency

Fig. 1-85. Applications and performance ranges of typical soft magnetic materials and their development objectives

For inductive WPT application, the magnetic flux density near the transmitter coils and the receiver coils is normally lower than 0.1 T. In addition, the operating frequency range for inductive WPT system is from kHz to MHz. Ferrite material is a good option compared to other soft magnet materials. Under the sinusoidal excitation, the losses per unit volume P_c can be calculated using the Steinmetz equation [229]

$$P_c = \kappa\, f_0^{\alpha}\, B^{\beta} \tag{1.37}$$

Where κ, α and β are the Steinmetz coefficients of the core material, f is the operating frequency, B is the peak flux density.

According to the application note [230] provided by Ferroxcube, several ferrites that are suitable for high frequency operation are provided with the methods to calculate the core losses, such as 3C94 for the frequency range 20 kHz to 400 kHz, 3F3 for the frequency range 100 kHz to 1000 kHz, and 3F4 for the frequency range 500 kHz to 3000 kHz. Core loss density can be approximated [231] by the following formula:

$$P_c = C_m\, f^{\,x}\, B^{y} \left(ct_0 - ct_1 T + ct_2 T^2\right) \ [\mathrm{mW/cm^3}] \tag{1.38}$$

Where f is the operating frequency (f in Hz), B is the peak flux density (B in T), T is the temperature (T in °C), C_m, x, y, ct_0, ct_1, and ct_2 are parameters which have been found by curve fitting of the measured power loss data. The fit parameters are listed for several Ferroxcube power ferrites as shown in Fig. 1-86 from the application note.

ferrite	f (kHz)	Cm	x	y	ct_2	ct_1	ct_0
3C30	20-100	$7.13.10^{-3}$	1.42	3.02	$3.65.10^{-4}$	$6.65.10^{-2}$	4
	100-200	$7.13.10^{-3}$	1.42	3.02	4.10^{-4}	$6.8\ .10^{-2}$	3.8
3C90	20-200	$3.2.10^{-3}$	1.46	2.75	$1.65.10^{-4}$	$3.1.10^{-2}$	2.45
3C94	20-200	$2.37.10^{-3}$	1.46	2.75	$1.65.10^{-4}$	$3.1.10^{-2}$	2.45
	200-400	2.10^{-9}	2.6	2.75	$1.65.10^{-4}$	$3.1.10^{-2}$	2.45
3F3	100-300	$0.25.10^{-3}$	1.63	2.45	$0.79.10^{-4}$	$1.05.10^{-2}$	1.26
	300-500	2.10^{-5}	1.8	2.5	$0.77.10^{-4}$	$1.05.10^{-2}$	1.28
	500-1000	$3.6.10^{-9}$	2.4	2.25	$0.67.10^{-4}$	$0.81.10^{-2}$	1.14
3F4	500-1000	12.10^{-4}	1.75	2.9	$0.95.10^{-4}$	$1.1.10^{-2}$	1.15
	1000-3000	$1.1.10^{-11}$	2.8	2.4	$0.34.10^{-4}$	$0.01.10^{-2}$	0.67

Fig. 1-86. Fit parameters to calculate the power loss density

3C94 is taken as an example to calculate the core loss under 100 kHz. The ferrite plate that uses to shield the magnetic flux generally has the same diameter as the coils. Assume the diameter is 1200 mm and the thickness of the ferrite plate is 5 mm, the average peak flux density over the entire ferrite plate is 0.01 T, the average temperature is 40 °C. According to previous approximation formula and listed parameters, the total core loss in each ferrite plate can be calculated as

$$P_{core} = P_c \times \text{Volume} = 1.25\ [\text{W}] \tag{1.39}$$

Therefore, compared with copper loss and the dielectric loss, the total core losses are negligible. However, the magnetic material is necessary for magnetic flux shielding.

- **Skin- and proximity effect losses of air-core windings**

It is well-known that skin- and proximity effects have a significant impact on the current distribution and equivalent series resistance of an inductor at AC operation [232]-[238]. The skin effect is a phenomenon in which the current density in a conductor tends to concentrate to the surface of the conductor and thus increase power loss as the operating frequency increases. The high current density area of the conductor caused by the skin effect is called *skin depth* which is defined in (1.27)

$$\delta = \frac{1}{\sqrt{\pi f \mu \sigma}} \tag{1.40}$$

Where f is the operating frequency, μ and σ is the permittivity and the conductivity of the conductor, respectively. The skin depth gets narrower as the operating frequency increases.

The proximity effect is caused by the current in an adjacent conductor. The current in the adjacent conductor generates a time-varying magnetic field and induces an internal circulating current in the conductor. Both the skin- and proximity effect cause non-uniform distribution of current in the conductor and higher copper loss at higher operating frequency [239]-[243].

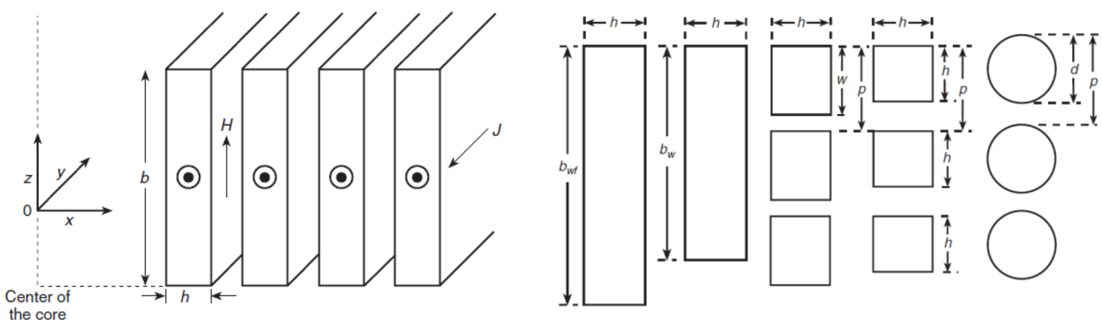

(a) Foil winding configuration (b) Equivalent cross-section

Fig. 1-87. Configuration of foil winding and equivalent cross-section

There are generally two methods to calculate AC resistances caused by skin- and proximity effect: Dowell method and Ferreira method. Dowell method is derived based on the rectangular conductor assumption and Ferreira method is derived based on circular conductor assumption. For a foil winding shown in Fig. 1-87 (a), the winding AC resistance with a sinusoidal inductor current excitation is

$$\text{(Dowell Method) } R_w = F_D\, R_{wDC}$$
$$= \frac{\rho_w L_w}{bh}\left(\frac{h}{\delta_w}\right)\left[\frac{\sinh\left(\frac{2h}{\delta_w}\right)+\sin\left(\frac{2h}{\delta_w}\right)}{\cosh\left(\frac{2h}{\delta_w}\right)-\cos\left(\frac{2h}{\delta_w}\right)}+\frac{2(N_l^2-1)}{3}\,\frac{\sinh\left(\frac{h}{\delta_w}\right)-\sin\left(\frac{h}{\delta_w}\right)}{\cosh\left(\frac{h}{\delta_w}\right)+\cos\left(\frac{h}{\delta_w}\right)}\right] \tag{1.41}$$

$$\text{(Ferreira Method) } R_w = F_F\, R_{wDC} =$$
$$\frac{\rho_w L_w}{bh}\,\frac{\gamma}{2}\left[\frac{bei'(\gamma)ber(\gamma)-ber'(\gamma)bei(\gamma)}{bei'^2(\gamma)+ber'^2(\gamma)}-2\pi(2N_l-1)^2\frac{ber'(\gamma)ber_2(\gamma)+bei'(\gamma)bei_2(\gamma)}{bei^2(\gamma)+ber^2(\gamma)}\right]$$

Where ρ_w is resistivity, L_w is foil winding length, b is foil winding width, h is foil winding height, δ_w is skin depth, $\gamma = \frac{d}{\sqrt{2}\,\delta_w}$, d is equivalent diameter, *bei* and *ber* are the real and imaginary parts of Bessel functions and prime in the above equation is the first derivative, with respect to γ, ber_2 and bei_2 are second order Kelvin's equation, N_l is number of layers, R_{wDC} is foil winding DC resistance.

Because the proximity effect is perpendicular to the skin effect [240][241], the AC resistance shown in above expressions can be treated as a sum of skin effect resistance (first part) and proximity effect resistance (second part). The relationship between F_D and h/δ_w is plotted in Fig. 1-88.

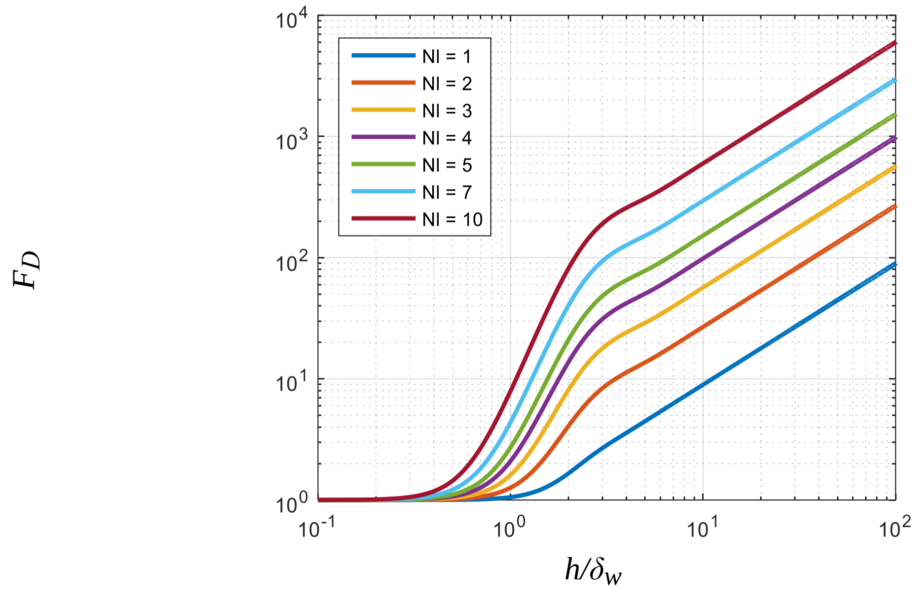

Fig. 1-88. Relationship between F_D and h/δ_w

As shown in Fig. 1-88, when the thickness of the foiling winding h is much smaller than (0.1x) the skin depth δ_w, the conductor will force the current distribution to be uniform, high frequency effects, like skin effect and proximity effect, are reduced almost zero, therefore, the total resistance is almost the same as the DC resistance. However, when the thickness of the foil winding h is much larger than (10x) the skin depth δ_w, the AC resistance increases sharply because of skin effect and proximity effect, and AC resistance caused by proximity effect is more severe than skin effect.

For Dowell method, when the foil winding is transformed into equivalent rectangular or square winding or circular winding, equation in (1.28) didn't consider the gap between adjacent equivalent rectangular windings, the formulas were improved as shown in (1.29)

$$\text{(Dowell Method) } R_w = F_D^{'}\ R_{wDC}$$
$$= \frac{\rho_w L_w}{bh}\left(\frac{h}{\delta_w}\right)\sqrt{\eta}\left[\frac{\sinh(2A)+\sin(2A)}{\cosh(2A)-\cos(2A)} + \frac{2(N_l^2-1)}{3}\,\frac{\sinh(A)-\sin(A)}{\cosh(A)+\cos(A)}\right] \tag{1.42}$$

Where $A = \frac{h}{\delta_w}\sqrt{\frac{w}{p}} = \frac{h}{\delta_w}\sqrt{\eta}$, w and p are shown in Fig. 1-87.

The Ferreira method, which is based on the exact Bessel-function solution for the eddy current in an isolated conducting cylinder subjected to a time-varying magnetic field, is found to be most accurate for loosely packed windings, whereas the Dowell Method, which approximates winding layers comprising multiple turns of round wire with a rectangular conducting sheet, is most accurate for closely-packed windings [242].

Windings used in WPT systems mostly are loosely packed to reduce proximity effect, therefore, Ferreira method is better to be used to calculate the equivalent AC resistances. However, both Dowell and Ferreira methods didn't consider the number of turns in each layer and the distance between each layer, the analytical calculation results are not accurate.

Another way to calculate AC resistance is Smith method [232] as shown in Fig. 1-89. Because the proximity effect is perpendicular to the skin effect, net resistance of a conductor with AC current flowing could be represented as a sum of resistance caused by skin effect and resistance due to proximity effect. It should be noted that the proximity factor adds larger loss as the number of turns increases and the turn-spacing decreases.

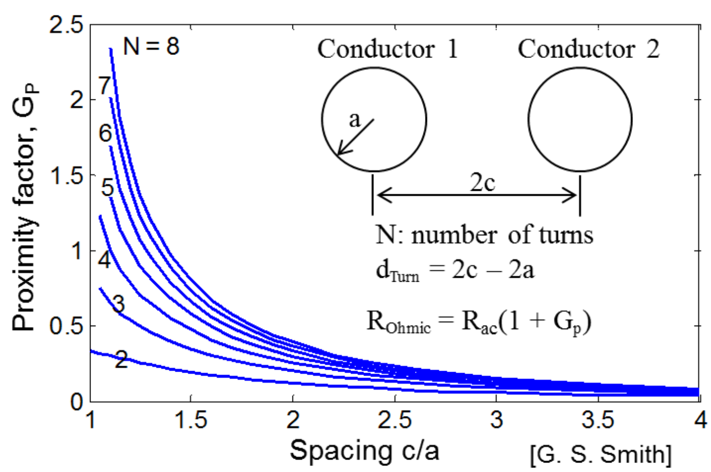

Fig. 1-89. Proximity effect factor dependence on turn-spacing

The proximity factor shown in Fig. 1-89 is calculated based on experimental tests for planar spiral winding, which ensure the AC resistance calculation accuracy. However, the Smith method may be not accurate when calculating other geometries. In addition, when the number of turns is higher than 8, the Smith method is not applicable. It can be extended to higher number of turns through FEA simulation.

It is common to use Litz-wire in high frequency to reduce the high frequency losses. The skin- and proximity effect losses of magnetic components can be minimized by using the Litz-wire which is consisted with a large number of strands of copper wire that are insulated from each other. By decreasing the size of the individual strand, Litz-wire can achieve unity skin effect factor. Each strand is transposed in the azimuthal and radial direction in order to possess all potential positions of the other strands. By the transposition, all the strands experience equal average magnetic field which is resulting in equal current density in the strands [244]-[247].

The calculation of AC resistance of an inductor with Litz-wire has been investigated by many researchers. Acero et al developed closed-form equations for the calculation of Litz-wire resistances [247]. The paper classified the losses of Litz-wire windings into three categories: skin effect loss of the strands, proximity effect loss between the strands in a single turn wire, and proximity effect loss by the adjacent turns. The skin effect resistance per unit length of n_0 strand Litz-wire windings is followed.

$$R_{skin} = \frac{1}{n_0}\frac{\xi}{2\pi r_0 \sigma}\frac{ber(\xi\, r_0)\, bei'(\xi\, r_0) - ber'(\xi\, r_0) bei(\xi\, r_0)}{ber'^2(\xi\, r_0) + bei'^2(\xi\, r_0)} \tag{1.43}$$

Where r_0 is the radius of a single strand, $\xi = \sqrt{\mu\sigma\omega}$, and *bei*, *ber*, *bei'* and *ber'* are Kevin functions and their derivatives. The proximity effect loss in stands of a single turn Litz-wire (internal proximity loss) can be calculated by

$$R_{prox\_internal} = n_0 \frac{-\xi\, r_0}{3\pi r_c^2 \sigma}\frac{ber_2(\xi\, r_0)\, ber'(\xi\, r_0) + bei'(\xi\, r_0) bei_2(\xi\, r_0)}{ber^2(\xi\, r_0) + bei^2(\xi\, r_0)} \tag{1.44}$$

Where r_c is the radius of strand bundle, and ber_2 and bei_2 are Kelvin functions [247]. The proximity effect loss in a turn because of the adjacent turns (external proximity loss) is

$$R_{prox\_external} = n_0 \frac{-2\pi^2 \xi r_0}{\sigma}\frac{ber_2(\xi\, r_0)\, ber'(\xi\, r_0) + bei'(\xi\, r_0) bei_2(\xi\, r_0)}{ber^2(\xi\, r_0) + bei^2(\xi\, r_0)} \sum_{i=1}^{n} a_i \langle H_i^2 \rangle \tag{1.45}$$

Where $\langle H_i^2 \rangle$ is the squared average of the external magnetic field of i^{th} turn, and a_i is the loop radius of the i^{th} turn. Then the total resistance of a spiral inductor with N turns of Litz-wire is

$$R_{tot} = R_{skin} + R_{prox\_internal} + R_{prox\_external} \tag{1.46}$$

In theory, the transposition of strands enables the AC resistance of a Litz-wire to be equal to the DC resistance at any frequencies. However, in practice, the Litz-wires are effective at 500 kHz or lower frequencies because of the irregularities in stranding and in capacity of the strands. It is less effective as the frequency increases, and it is rarely useful at frequencies over 1 MHz [248].

Using (1.30) – (1.33), the AC resistance of a spiral inductor built with a commercial Litz-wire is calculated. The total number of the individual strands is 4500 and the strand AWG of the Litz-wire is 48 and the bundle AWG is 12. The tested Litz-wire is designed for 1.4 to 2.8 MHz operation and it is the highest available frequency of the Litz-wires [249].

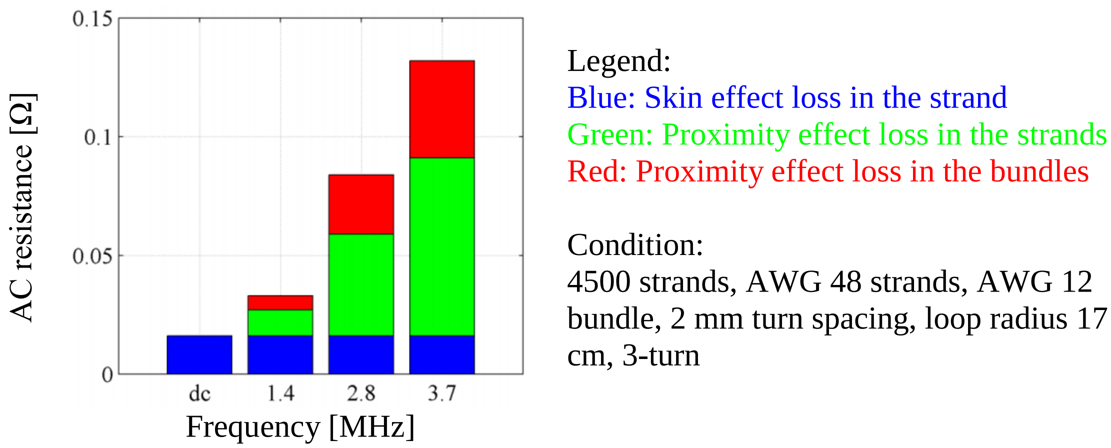

Fig. 1-90. The AC resistance of the Litz-wire

As shown in Fig. 1-90, the skin effect loss in the strands at MHz operation is close to DC resistance because the diameter of the individual strands is smaller than the skin depth. However, the total resistance of the inductor is increased to two times larger value as the frequency increases from 1.4 MHz to 2.8 MHz. The skin effect loss in the strands is almost the same but the proximity effect losses in the strands and bundles are the major issues in the inductor resistance.

As the operating frequency increases to 3.7 MHz, the proximity effect losses in the strands and the bundles become more serious.

The AC resistance of the Litz-wire is compared with the spiral inductor made of copper tubing in Fig. 1-91.

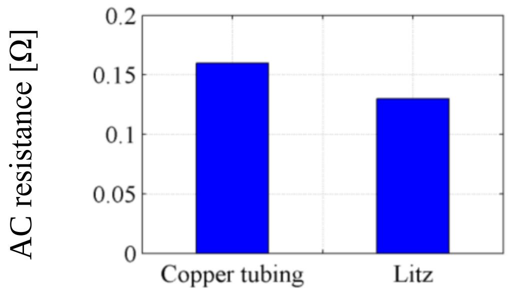

Condition:
Frequency: 3.7 MHz, loop radius: 17 cm, turn spacing: 2mm, number of turns: 3
Litz-wire: 4500 strands, AWG 48 strands, AWG 12 bundle
Copper tubing: 1 cm diameter, 1 mm wall thickness

Fig. 1-91. The AC resistance comparison of the Litz-wire and copper tubing

As shown in above figure, the Litz-wire is slightly helpful in decreasing the loss of the spiral inductor compared to the copper tubing and it is much more expansive than commercial copper tubing. Therefore, it can be concluded that the Litz-wire is definitely not the best solution for MHz frequency operation.

SSW twisted each turn using Litz-wire pattern and could significantly reduce the proximity effect loss. The AC resistance simulation results of conventional PSW and SSW are compared in Fig. 1-92.

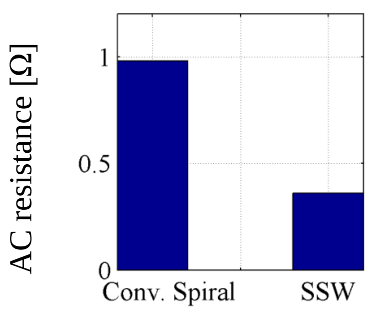

Test conditions:
Frequency: 3.7 MHz
Conventional spiral winding:
Seven-turn, Loop radius: 200 mm, Cross-sectional radius: 10 mm, Inter-turn spacing: 2.5 mm,
Surface spiral winding:
Seven-turn, Loop radius: 200 mm, Cross-sectional radius: 25 mm, Inter-turn spacing: 2.5 mm,

Fig. 1-92. Simulated AC resistance of conventional spiral coil and SSW coil

As shown in Fig. 1-92, SSW can reduce the AC resistance by more than 50% compared with the PSW. However, proposed SSW consumes air-gap space to twist each turn. In addition, the high spatial voltage stress between adjacent turns due to small inter-turn spacing limits power scalability and causes dielectric losses, which have a significant effect on power scalability and coil-to-coil power transfer efficiency. According to the test results, voltage breakdown did occur when transferring 1 kW under 3.5 MHz.

- **Radiation losses**

Any current carrying loop radiates electric and magnetic fields to the far-field area and its radiation effectiveness is represented by radiation resistance [1]. The radiation resistance of N-turn coil can be calculated by

$$R_r = \eta \left(\frac{2\pi}{3}\right)\left(\frac{kS}{\lambda}\right)^2 N^2 \approx 31171\, N^2 \left(\frac{S^2}{\lambda^4}\right) = 31171 \left(\frac{N^2}{c^4}\right) S^2 f^4 \text{ (in the air)} \quad (1.47)$$

Where η is the intrinsic impedance of radiation medium (in air η = 377), c is the speed of light (3×10^8 m/s), $k = \frac{2\pi}{\lambda}$ is the wave number, $S = \pi a^2$ is the area, N is number of turns, and λ is the wavelength. It should be noted that the operating frequency and the size of the coil are critical in radiation. As an example, radiation resistance versus frequency of a single turn, 40 cm radius circular coil is plotted in Fig. 1-93.

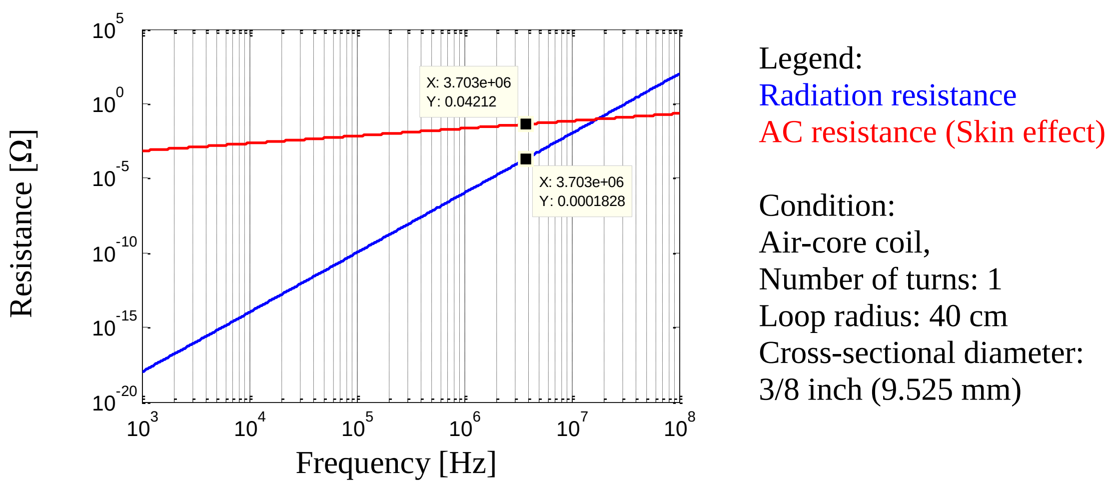

Fig. 1-93. Resistance versus frequency

The Ohmic resistance due to skin effect of the coil is plotted as well in Fig. 1-93. As compared in the figure, radiation resistance is greater than the Ohmic resistance when the operating frequency is higher than 20 MHz. In the dominant frequency range of near-field WPT systems, 10 kHz to 10 MHz, radiation resistance has a trivial impact on the power transfer efficiency. Such poor radiator is called “electrically small” loop. The radiation resistance of the electrically small loops is usually very small. Therefore, radiation loss of a coil will not be discussed anymore in this research.

- **Dielectric losses**

Dielectric materials such as plastics, glasses, and woods etc., can be used for inductors in order to support or package the inductor or to maintain the coil geometry and turn spacing. However, such dielectrics generate additional losses in time-varying electric fields because of its non-zero conductivity and the complex permittivity [13]. The general permittivity of a dielectric material has real and imaginary part as shown below

$$\varepsilon = \varepsilon' - j\,\varepsilon'' \tag{1.48}$$

Maxwell's equation for the steady magnetic field can be rewritten as

$$\nabla\times\mathbf{H} = \mathbf{J}_{tot} = \mathbf{J} + j\omega\mathbf{D} = \sigma\mathbf{E} + j\omega(\varepsilon' - j\,\varepsilon'')\mathbf{E} = (\sigma + \omega\,\varepsilon'')\mathbf{E} + j\omega\varepsilon'\,\mathbf{E} \tag{1.49}$$

Where σ is the volume conductivity of the material, ω is the angular frequency. The equivalent permittivity of a material can be calculated from $\mathbf{J}_{tot} = j\omega\varepsilon_{eq}\mathbf{E}$,

$$\varepsilon_{eq} = \varepsilon' - j\,(\varepsilon'' + \frac{\sigma}{\omega}) \tag{1.50}$$

Then, the Ohmic loss per unit volume of a dielectric material can be calculated using [197]

$$\frac{dP_{loss}}{dV} = \frac{1}{2}\,\mathrm{Re}[\mathbf{J}_{tot}\cdot\mathbf{E}^*] = \frac{1}{2}(\sigma + \omega\,\varepsilon'')\,|\mathbf{E}|^2 \tag{1.51}$$

In order to quantify the loss characteristic of a material, the loss tangent is defined as the ratio of the lossy (imaginary) part to the lossless (real) part of the equivalent permittivity.

$$\tan\delta = \frac{\sigma + \omega\,\varepsilon''}{\omega\,\varepsilon'} \tag{1.52}$$

The material with high $\tan\delta$ is lossy, such as wood (0.02 @ 1MHz) and nylon (0.0218 @ 1MHz). Ceramics, glasses, polypropylene, and polystyrene, etc. have 0.001 or lower $\tan\delta$ at high frequencies. The dielectric loss per unit volume of a material follows [250].

$$W_{vol} = \frac{\text{Power loss}}{\text{Volume}} = \omega\,E^2\,\varepsilon_0\,\varepsilon_r\,(\tan\delta) \tag{1.53}$$

In the first version of SSW coil, ABS-like dielectric material, Somos-Next, was used to build the dielectric substrate, the peak coil-to-coil power transfer efficiency was 62% due to high dielectric losses, which was much lower than the expected efficiency from the theoretical and FEA results as shown in Fig. 1-94.

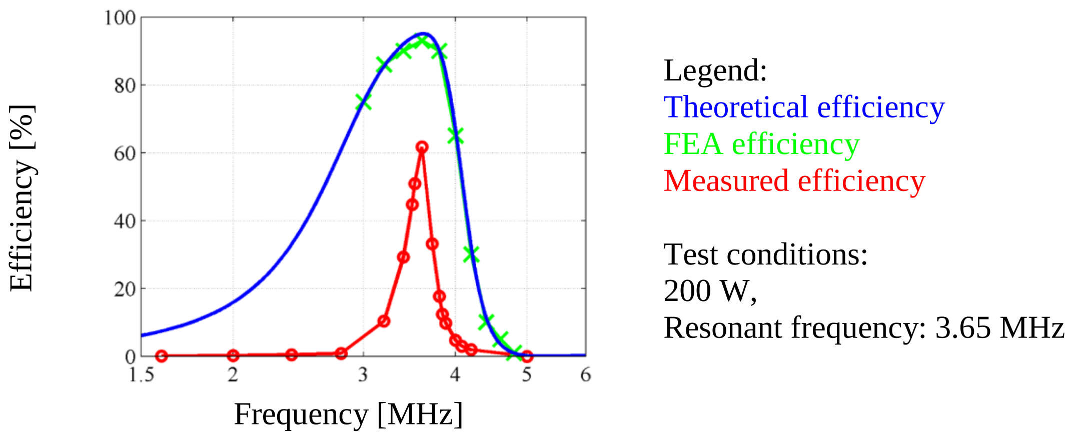

Fig. 1-94. Comparison of SSW coil-to-coil power transfer efficiency

In the second version of SSW coil, Polycarbonate (PC) was used to build the dielectric substrate by 3D-printing technique. Compared with Somos-Next ($\tan\delta = 0.02$ @ 4MHz), PC ($\tan\delta = 0.0063$ @ 4MHz) has much lower dissipation factor, and the measured peak coil-to-coil efficiency was 96%.

However, the dielectric losses in SSW are still a limiting factor to further improve the coil-to-coil power transfer efficiency. The dielectric losses are mainly located in the region between the first turn and the end turn due to high spatial voltage stress. Alternative coil geometries with low spatial voltage stress and low dielectric losses are required.

1.6.4 Methods to improve the coil-to-coil efficiency

According to the loss distribution analysis in the previous section, if the radiation loss and the foreign object loss are neglected, the coil-to-coil efficiency can be calculated by

$$\eta = \frac{P_{load}}{P_{loss\_tx} + P_{loss\_rx} + P_{load}} = \frac{|I_L|^2 R_L}{|I_{tx}|^2 R_{tx} + |I_{rx}|^2 R_{rx} + |I_L|^2 R_L} \tag{1.54}$$

The maximum achievable coil-to-coil efficiency $\eta_{coil,\ max}$ in a two-coil system can be simplified as [59]

$$\eta_{coil,\ max} = \frac{k^2 Q_{tx} Q_{rx}}{\left[1 + \sqrt{1 + k^2 Q_{tx} Q_{rx}}\right]^2} \tag{1.55}$$

Where, k is the coupling coefficient between the transmitter and the receiver, $Q_{tx} = \frac{\omega\, L_{tx}}{R_{tx}}$ is the transmitter coil quality factor, $Q_{rx} = \frac{\omega\, L_{rx}}{R_{rx}}$ is the receiver coil quality factor.

In the existing literature to improve the coil-to-coil efficiency, k and Q are usually treated as independent variables.

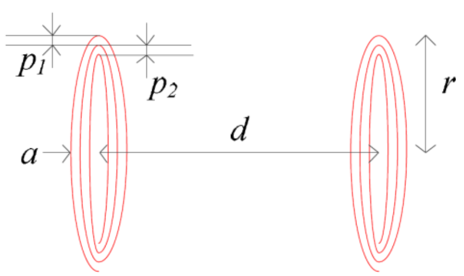

(a) Test setup

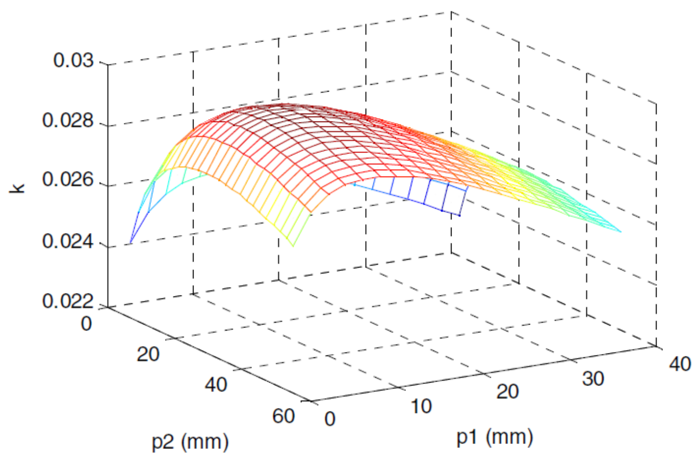

(b) Effect of pitches on coupling coefficient

Fig. 1-95. Adjusting pitches to achieve high coupling coefficient

On the one hand, it is believed that improving k can increase the highest possible efficiency [251]. The inter-turn distances (or the pitches) were changed to achieve a higher reduction of the self-inductances than the reduction of the mutual inductance, thereby increasing the coupling coefficient k. In the given example, the transmitter and the receiver were set as the same. The number of turns was 3, the pitches p_1 and p_2, shown in Fig. 1-95, were used as the design variables. According to the analytical calculation, when $p_1 = p_2 = 2$ mm, k = 0.0241; when $p_1 = 10$ mm, $p_2 = 25$ mm, k = 0.0292, the improvement is about 21%. However, the maximum achievable coil-to-coil efficiency was not mentioned. In addition, when the pitches are small, there will be significant proximity effect, when the pitches are large, the total AC resistance may still increase instead of decreasing due to the increase of total coil length, which leads to high skin effect loss, even though the proximity effect can be reduced with large pitches. Therefore, it's not wise to only improve k without considering Q.

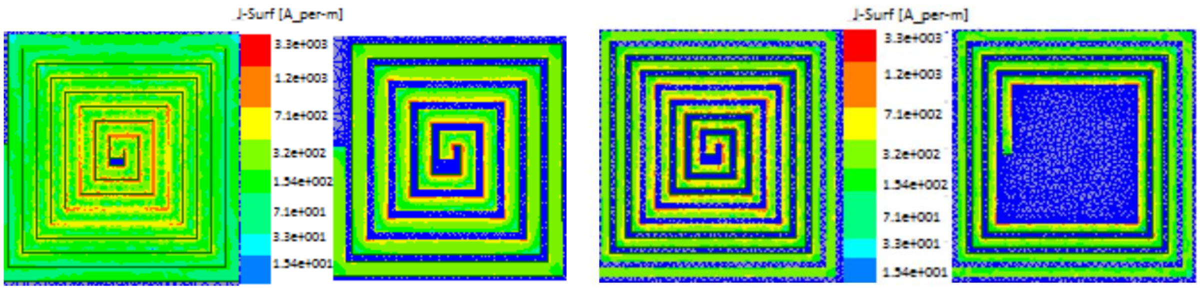

(a) Increasing inter-turn distance (b) Removing inner most turns

Fig. 1-96. Methods to reduce the proximity effect loss

On the other hand, it is believed that improving Q can increase the maximum efficiency [252]. The large inter-turn distance was adopted to reduce the proximity effect loss as shown in Fig. 1-96 (a). However, the mutual inductance reduces as the inter-turn distance increases. Considering the eddy currents are induced in little swirls ("eddies") to create an opposing effect in response to a primary inducing magnetic field. The eddy current will add to the coil current on the inner side and subtract from the coil current on the outer side of the conductor, thus the current density will be higher on the inner side than the outer side, the innermost turns can be removed to reduce the proximity effect loss on the inner side as shown in Fig. 1-96 (b). However, the mutual inductance reduces as the inner turns are removed. When the mutual inductance is reduced, $\eta_{coil,\ max}$ may not be improved even the proximity effect loss is reduced.

In conclusion, improving k and Q independently may not lead to a higher maximum coil-to-coil efficiency due to the cross-coupling caused by the self-inductance. Fundamental terms that determine the maximum achievable coil-to-coil efficiency must be identified.

1.6.5 Power scalability of different coil geometries

In order to scale the magnetic components for higher power level, three factors must be considered in the design process: human body safety limit, misalignment tolerance, and EMI/EMC. It should be noted that safety is the most important factor.

As discussed in the human safety and exposure section, the designed magnetic structure must satisfy the induced current limits and specific absorption rate limits for safety consideration. Although previous designs, such as circular pad, DD pad, DDQ pad, BP pad, TP pad, and double-sided coil operating at kHz frequency can satisfy the magnetic field safety limit at a certain distance from the coil when transferring multi-kW, the magnetic field in the air-gap center region, which is accessible to human beings and animals, is still far above the safety limit. Therefore, these designs can't be scaled to transfer higher power, they shouldn't even be used to transfer multi-kW.

MHz frequency operation has been proposed to reduce the air-gap magnetic field. Since Litz-wire is not effective in MHz frequency due to the irregularities in the fabrication process and parasitic capacitances between the adjacent strands, SSW was proposed to achieve low skin and proximity effect losses when operating at MHz frequency. When transferring 3 kW, the air-gap center magnetic flux density is indeed lower than the magnetic field electrostimulation limit. However, the magnetic field tissue heating safety limit and the electric field safety limit were not considered. Both are much higher than the given safety limit. In addition, the experimental test results showed that the voltage breakdown did happen between the first turn and the end turn when transferring only 1 kW. Therefore, SSW design under MHz frequency also can't be scaled to transfer higher power.

In summary, there is no design methodology that can be scaled to transfer multi-kW and higher power level while maintaining the air-gap center plane magnetic field and electric field within safety limits. No general power scaling laws have been developed to evaluate the maximum transferable power under both magnetic field and electric field safety limits.

1.6.6 Summary and identified research opportunities

In this section, the coil geometric solutions of loosely coupled inductive WPT systems under kHz frequency and MHz frequency have been reviewed. Previous magnetic components have operated dominantly at kHz frequencies. Enhancing the coupling coefficients for high efficiency and high misalignment tolerance is the major focus of the literature. Compared with polarized coils, such as DD pad, DDQ pad, BP pad, and TP pad, and double-sided coils, the circular coil can achieve the highest mutual coupling. Polarized coils and double-sized coils have better lateral misalignment tolerance along the elongated direction. However, the magnetic flux density in the air-gap of these coils operated at kHz in the literature is nearly 5 times higher than required safety limits of the international guidelines. The previous design methodologies in kHz frequency operations are not suitable for large air-gap, kW level power transfer systems.

Operating at MHz frequency can achieve low magnetic flux density in the air-gap. SSW was developed to reduce skin and proximity effect losses. However, the dielectric losses and the spatial voltage stress between the first turn and the end turn were still limiting factors to power transfer efficiency and multi-kW power transfer capability. In addition, the air-gap center electric field of proposed SSW design is nearly 5 times higher than the electric field safety limit. The MHz frequency SSW design is not suitable for large air-gap, kW level power transfer systems.

In the near-field inductive WPT system, lateral and angular misalignments cause coupling coefficient to decrease. The literature has used numerical integration or approximated equations in order to calculate mutual inductance variation depending on the misalignments. The analytical model for mutual inductance calculation under aligned and misaligned conditions is necessary for the system general design methodology.

When the average magnetic flux density over the entire ferrite shielding plate is lower than 0.01 T, the core loss is negligible. In the dominant frequency range of near-field WPT systems, 10 kHz to 10 MHz, the radiation resistance has a trivial impact on the power transfer efficiency. The dielectric loss is critical to achieve high power transfer efficiency when the spatial voltage stress between adjacent turns and the operating frequency are high. Improving k and Q independently may not lead to a higher maximum coil-to-coil efficiency due to the cross-coupling caused by the self-inductance. Fundamental terms the determines the maximum achievable coil-to-coil efficiency must be identified.

Alternative coil geometries with low copper loss and low dielectric loss are required for high coil-to-coil power transfer efficiency and high power scalability. Current coil geometric solutions can't be scaled to transfer multi-kW, a general power scaling law maintaining low air-gap magnetic flux density and low air-gap electric field intensity is required.

1.7 Summary of research opportunities identified

- **Lack of a multi-kW inductive WPT system general design methodology that can inherently achieve low air-gap magnetic and electric fields, and high transfer efficiency**

In the existing literature for kW inductive WPT systems, 41 papers investigated the air-gap magnetic field and only 8 papers paid attention to the air-gap electric field. However, none of them satisfy the IEEE C95.1-2005 magnetic and electric field safety limits. Although designs operating at MHz satisfy the magnetic field electrostimulation limit, they didn't meet magnetic field tissue heating and electric field limits. There has been no design that can satisfy magnetic and electric field tissue heating and electrostimulation safety limits simultaneously in the air-gap center region while transferring kW. A multi-kW inductive WPT system general design methodology, that can inherently achieve low magnetic and electric fields over the air-gap center region, with high efficiency, even under misalignment, has not been developed.

- **Lack of closed-form analytical models for the air-gap center plane magnetic flux density and electric field intensity of the loosely coupled inductive WPT systems**

The magnetic field and electric field analytical methods for a single current loop have been developed. The analytical models for the magnetic flux density at the air-gap center plane central point and measurement point at a certain distance away from the center have been developed. However, the peak air-gap flux density point was not identified. The static electric field analytical methods for a single current loop with a battery excitation does not include the effects of dynamically currents and interactions of the transmitter and the receiver. Therefore, a methodology for analytically calculating the magnetic and electric field distributions in the air-gap center plane for inductive WPT system should be developed to facilitate the design of WPT systems with desired performance, such as low air-gap magnetic and electric fields.

- **Lack of power scaling law with the air-gap center plane magnetic flux density and electric field intensity satisfying the safety standard**

In the literature, power scalability limitations based on voltage-current ratings of power components, coil thermal failure and voltage breakdown have been investigated. Previous designs, such as circular pad, polarized pad, and double-sided pad cannot be used for multi-kW power transfer due to large magnetic fields which exceed the safety limit. The SSW operating at MHz can meet the magnetic field electrostimulation limits, but still cannot be used for multi-kW power transfer due to the magnetic field exceeding the tissue heating safety limit and the electric field exceeding the electrostimulation and tissue heating safety limits. Therefore, a detailed analysis of the degrees of freedom available in the design space to satisfy both safety limits and achieve desirable power transfer is necessary to develop a power scaling law.

- **Lack of shielding technique to maintain low magnetic and electric fields in the whole air-gap region without decaying the power transfer efficiency**

In the literature, magnetic shielding technique has been adopted to shield the magnetic field above the receiver and below the transmitter. Compared with the air-core WPT system, the air-gap center plane peak magnetic field increases after adding magnetic shields due to the concentration of leakage and mutual flux linkages. Active, reactive, and passive shielding techniques were developed to reduce the leakage field in the near-field outside of the winding. However, these techniques have a negligible effect on the air-gap center plane peak magnetic field, and the effect on the air-gap center plane peak electric field was not investigated. No shielding technique has been developed to maintain low magnetic and electric fields in the whole air-gap region without decaying the power transfer efficiency.

- **Absence of methods to deal with change of field distributions under misalignment while maintaining high power transfer efficiency and high output power capacity**

Misalignment is unavoidable in WPT systems. Lateral and angular misalignments cause a change of magnetic and electric field distributions, and the coupling factor and power transfer efficiency to decrease. In the literature, the coupling factor and the power transfer efficiency dependence on the misalignment have been investigated. However, the effects of misalignment on magnetic and electric field distributions have not been quantitatively evaluated. Output power dependence on the misalignment based on safety regulations, and the effects of resonant compensation topologies and coil geometries on magnetic and electric field distributions have not yet been fully explored. Methods to mitigate the change of magnetic and electric field distributions under misalignment while maintaining high power transfer efficiency and high output power capacity have not yet been developed.

Chapter 2 Analytical Modeling of the Air-Gap Center Plane Magnetic and Electric Fields

2.1 Introduction

This chapter begins with comparison of basic winding configurations with respect to coil-to-coil efficiency, air-gap magnetic and electric field distributions, then loosely coupled inductive WPT system equivalent circuit model is developed based on coil geometry and operating frequency, after that, the terms that fundamentally determine the coil-to-coil efficiency are identified, and the system analytical model including the inverter, the coils, and the rectifier is developed. At last, the air-gap center plane magnetic flux density and electric field intensity analytical calculation methods for the loosely coupled inductive WPT system are derived.

2.2 Comparison of basic winding configurations

There are various types of windings used in loosely coupled inductive WPT systems, such as circular winding, square winding, rectangular winding, double-square winding, and double-D winding. A fair comparison of different winding configurations regarding coil-to-coil efficiency, air-gap magnetic field and electric field will be presented in this section.

2.2.1 Illustration of winding configurations and geometries

In order to simplify the comparison, the transmitter and the receiver are set as the same, the number of turns is set as 1, the coil enclosed areas are set as nearly the same to make a fair comparison, the transfer distance between the transmitter and the receiver is set as 300 mm for all configurations, the operating frequency is set at 100 kHz. Copper tubing with outer diameter 3/8" (9.525 mm) and wall thickness 0.032" (0.8128 mm) is used to build the coil due to its low skin effect loss, and easy ability to bend and maintain the structure.

The geometries and current directions (marked with red arrow) of the circular winding (CW), square winding (SW), rectangular winding (RW), double-square winding (DSW), and double-D winding (DDW) are shown in Fig. 2-1.

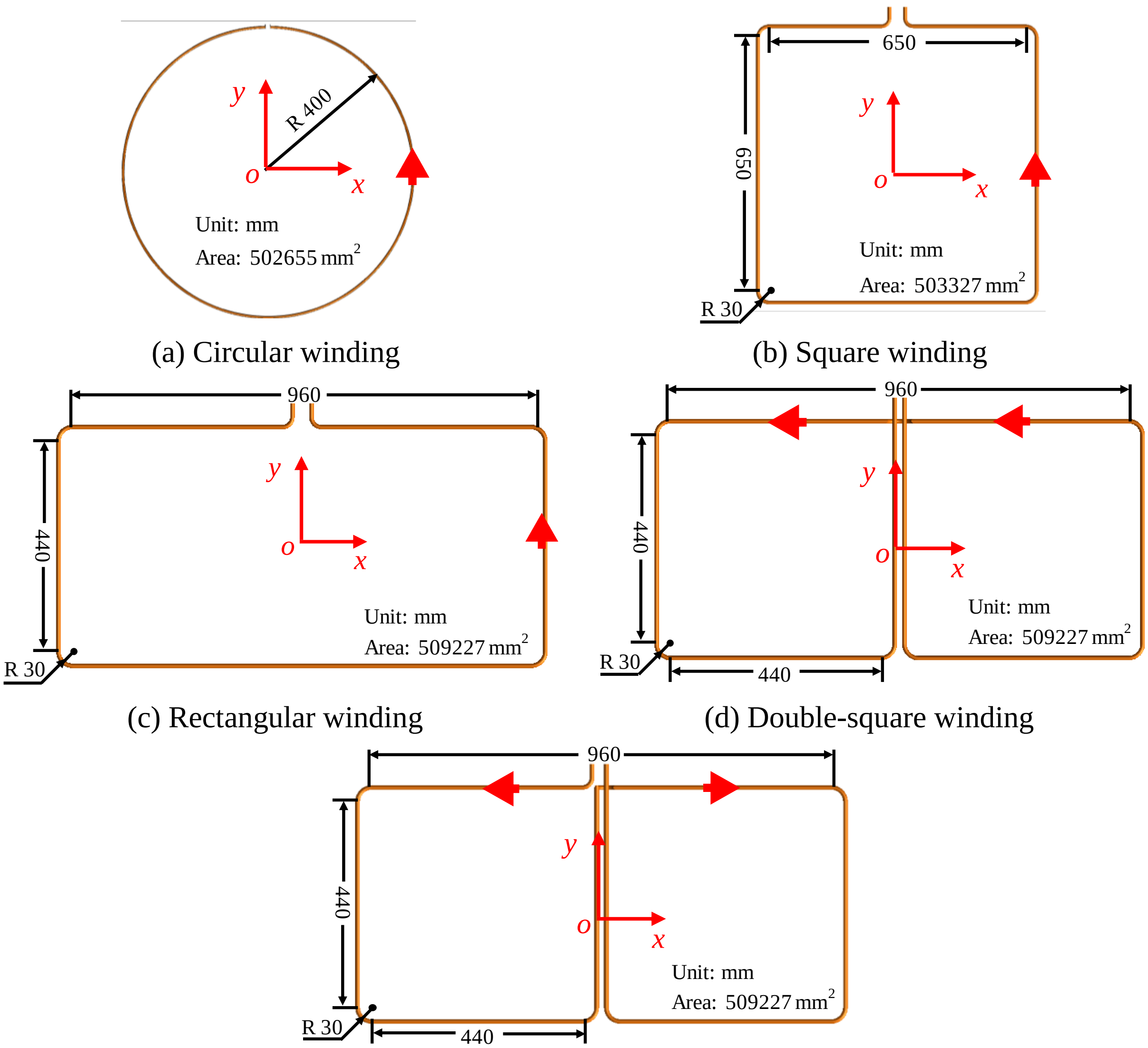

(a) Circular winding (b) Square winding

(c) Rectangular winding (d) Double-square winding

(e) Double-D winding

Fig. 2-1. Coil geometries and current directions

Arc corner is adopted to reduce the field distortion. Y-direction is aligned with the excitation terminal. The enclosed areas of all winding configurations are nearly the same. The RW aspect ratio is set as 2 to ensure the mutual coupling. The DSW emulates the multiple transmitter coil design. According to the double-D winding design methodology shown in [30][31], the receiver is coupled with the horizontal flux generated by the transmitter, and the flux path height, which should be larger than the transfer distance to ensure a good coupling, is proportional to half of the pad length, the DDW design shown in Fig. 2-1 (e) follows the design methodology very well. Half of the pad length 510 mm is 1.7 times the transfer distance 300 mm, which ensures enough mutual coupling.

The magnetic flux patterns of the CW, the SW, the RW, the DSW, and the DDW are compared in Fig. 2-2.

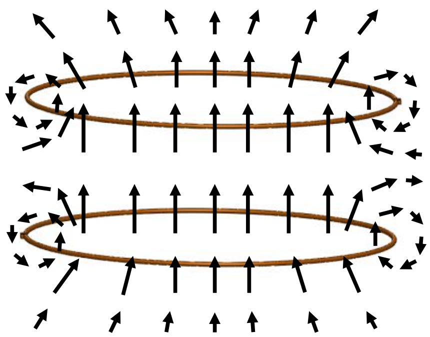

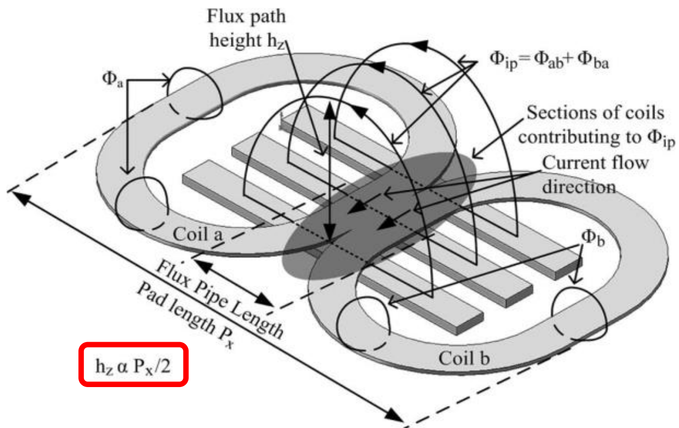

(a) Vertical flux pattern (b) Horizontal flux pattern

Fig. 2-2. Magnetic flux patterns

When using CW, SW, RW, and DSW, the receiver is coupled with the vertical flux generated by the transmitter, the leakage flux decays in the near field, as shown in Fig. 2-2 (a). While the receiver of the DDW is coupled with the horizontal flux generated by the transmitter as shown in Fig. 2-2 (b), which means that the main part of the leakage flux is confined in the air-gap instead of decaying in the near field.

2.2.2 Comparison of the winding parameters and the coil-to-coil efficiencies

During the FEA evaluation of the coil geometries, which are developed in the previous section and have nearly the same coil enclosed area, the receiver is the same as the transmitter, the transfer distance is set as 300 mm, the operating frequency is set at 100 kHz. The coil electrical parameters, such as the transmitter self-inductance L_{tx}, the transmitter equivalent-series-resistance (ESR) R_{tx}, the receiver self-inductance L_{rx}, the receiver ESR R_{rx}, the mutual inductance M, and the maximum achievable coil-to-coil efficiency $\eta_{coil,\ max}$ under perfect aligned condition are compared in Table 2-1.

Table 2-1. Comparison of the coil electrical parameters and the coil-to-coil efficiency

	CW	SW	RW	DSW	DDW
L_{tx} [μH]	2.28	2.43	2.57	2.81	3.43
R_{tx} [mΩ]	6.7	7.5	8.1	11.1	11.1
L_{rx} [μH]	2.28	2.43	2.57	2.81	3.43
R_{rx} [mΩ]	6.7	7.5	8.1	11.1	11.1
M [μH]	0.292	0.286	0.281	0.266	0.230
$\eta_{coil,\ max}$ [%]	92.95	91.99	91.23	87.58	85.86

As shown in Table 2-1, compared with other winding configurations, the CW has the lowest self-inductance, the lowest ESR, and the highest mutual inductance, which leads to the highest coil-to-coil efficiency. For one turn winding, only the skin effect needs to be considered for the ESR. Under the same coil enclosed area, the circular shape has the smallest perimeter, which leads to the lowest ESR. The DSW and the DDW have the same ESR due to the same perimeter. Compared with the square, rectangular, double-square, and double D shapes, the circular shape has no field distortion. The DDW has the lowest mutual coupling due to the horizontal flux coupling pattern, most of the magnetic flux generated by the transmitter is confined within the transmitter instead of coupling to the receiver or decaying outside of the coil.

The coupling coefficient k and the quality factor Q are compared in Table 2-2.

Table 2-2. Comparison of the coupling coefficient and the quality factor

	CW	SW	RW	DSW	DDW
k	0.128	0.118	0.109	0.095	0.067
Q	213.82	203.58	199.36	159.06	194.16

As shown in Table 2-2, the CW has the highest k and Q. Compared with the DSW, the DDW has lower k but higher Q due to the increase of the self-inductance. k and Q are investigated independently to improve the coil-to-coil efficiency in the literature, which may lead to the wrong direction, for example, although the DDW has a higher quality factor, its coil-to-coil efficiency is still lower than the DSW. The factors that fundamentally determine the coil-to-coil efficiency will be analyzed in this thesis.

2.2.3 Comparison of the air-gap magnetic field distribution

When the output power is 1.5 kW, the air-gap magnetic field distributions in the XOZ plane and YOZ plane are compared in Fig. 2-3. X-direction is the coil length direction, and y-direction is the coil width direction, so XOZ plane and YOZ plane can represent the typical magnetic field distribution. However, it should be noted that the air-gap center plane peak magnetic flux density B_{agcppk} may be not located along the x-direction or the y-direction, but along the diagonal direction.

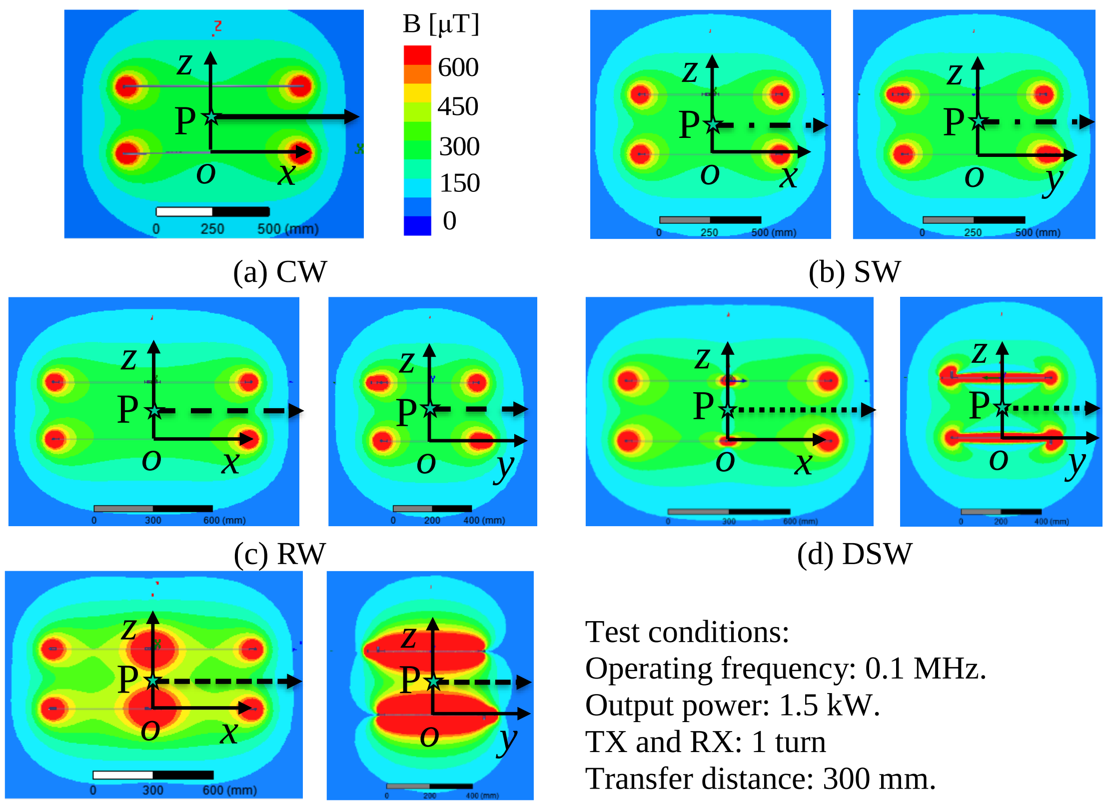

(a) CW (b) SW

(c) RW (d) DSW

(e) DDW

Test conditions:
Operating frequency: 0.1 MHz.
Output power: 1.5 kW.
TX and RX: 1 turn
Transfer distance: 300 mm.

Fig. 2-3. Comparison of magnetic field distributions

The CW magnetic field distributions along any radial directions are the same, therefore, only the magnetic field distribution in the XOZ plane is shown in Fig. 2-3 (a). For the coils coupled with the vertical flux, such as the CW, the SW, the RW, and the DSW, B_{agcppk} is located around the edge of the coils rather than the air-gap center plane central point P as shown in Fig. 2-3 (a) - (d) due to the leakage flux and the coil size. When the coil size is small for vertical flux pattern windings, B_{agcppk} will be located in the air-gap center plane central point P. While B_{agcppk} is always located in the air-gap center plane central point for the horizontal flux pattern windings, such as the DDW as shown in Fig. 2-3 (e).

The magnetic flux densities along the x- and the y-direction measurement lines in the air-gap center plane are plotted in Fig. 2-4.

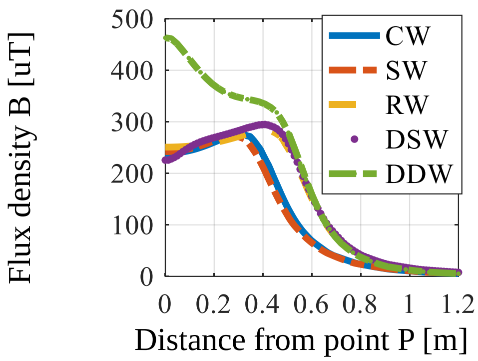

(a) Magnetic flux density in the air-gap center plane along the x-direction

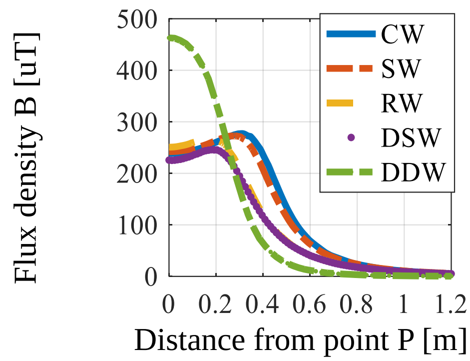

(b) Magnetic flux density in the air-gap center plane along the y-direction

Fig. 2-4. Comparison of magnetic flux densities in the air-gap center plane along the x-direction and the y-direction

As shown in Fig. 2-4, the CW and the SW have similar magnetic field distributions along the x- and y-direction measurement lines, while the RW and the DSW have similar distributions. Along the y-direction, the RW and the DSW magnetic flux densities are much lower than the CW and the SW from 0.25 m due to smaller coil dimension along the y-direction. However, along the x-direction, the peak magnetic flux densities of the RW and the DSW are higher than those of the CW and the SW. The peak magnetic flux densities of the CW, the SW, the RW, and the DSW are all located at the edge of the windings. For the DDW, B_{agcppk} is located in the central point of the air-gap center plane due to the confined leakage flux, which also makes the magnetic field decay much faster along the y-direction.

If the design goal is satisfying the safety standard outside of the winding (or the vehicle), the rectangular shape windings following the shape of the vehicle, such as the RW, the DSW, especially the DDW, are very good candidates, but they are not good designs compared with the CW and the SW if the design goal is meeting the safety standard in the whole air-gap center plane. Based on Fig. 2-4, the peak magnetic flux densities B_{pk} along x- and y-direction measurement lines in the air-gap center plane are compared in Table 2-3.

Table 2-3. Comparison of B_{pk} along x- and y-direction measurement lines in the air-gap center plane

	CW	SW	RW	DSW	DDW
B_{pk} [μT]	277.2	273.3	283.3	294.8	463.0

According to Table 2-3, the SW has the lowest B_{pk} along the x-direction and the y-direction measurement lines in the air-gap center plane. However, the SW B_{pk} along the diagonal direction is 277.6 μT, while the CW B_{pk} is the same along any radial directions, which makes the SW B_{pk} slightly higher than the CW. Due to confined leakage flux, the DDW B_{pk} is about 1.7 times higher than the CW, which is definitely not a good design choice to achieve low air-gap center plane magnetic flux density. Therefore, the CW is a better choice to achieve low air-gap center plane magnetic flux density compared with other winding configurations.

2.2.4 Comparison of the air-gap electric field distribution

The electric field is mainly caused by two terms: the excitation terminal voltage and the AC magnetic field. In order to balance the electric field distribution in the air-gap center plane, the excitation terminals of the transmitter and the receiver should be placed at opposite positions as shown Fig. 2-5. The air-gap center plane measurement line along the y-direction is located right above the transmitter terminal and below the receiver terminal.

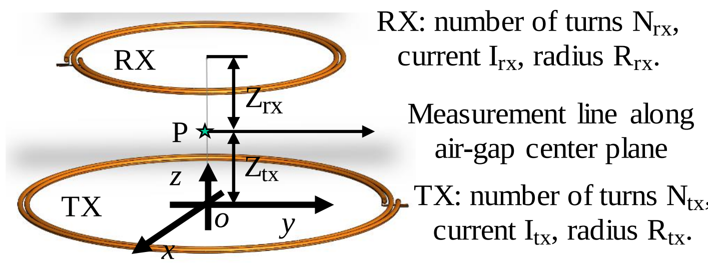

Fig. 2-5. Configuration of WPT coils with inversely placed terminals

According to the FEA result, the air-gap center plane peak electric field intensity E_{agcppk} is located very close to the YOZ plane, therefore, the electric field distribution in the YOZ plane is chosen to compare E_{agcppk} of different winding configurations for simplification purpose.

When the output power is 1.5 kW, the air-gap electric field distributions in the YOZ plane are compared in Fig. 2-6.

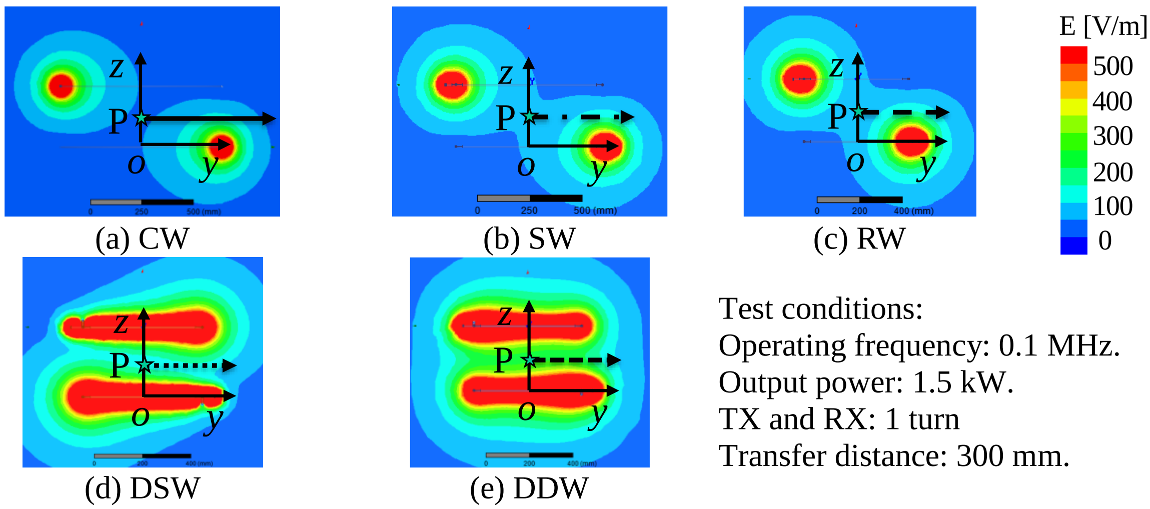

Fig. 2-6. Comparison of electric field distributions

From Fig. 2-6 (a) to (c), it's easy to find that the electric field caused by the excitation terminal is the dominant part. In the DSW, the excitation input conductor and output conductor are in parallel along the y-axis, which forms a strong internal electric field around the y-axis as shown in Fig. 2-6 (d). In the DDW, the excitation input of one square coil is in parallel with the excitation input of another square coil, which also forms a strong internal electric field between two inputs around the y-axis, as shown in Fig. 2-6 (e). It's easy to find that the DSW and the DDW have much higher air-gap center plane electric fields than the CW, the SW, and the RW, one reason is the winding configuration. Another reason is that the coil excitation voltage is proportional to the self-inductance under the excitation current or the same output power. The self-inductances of the DSW and the DDW are much higher than other configurations according to the previous comparison of electrical parameters. The air-gap center plane electric field intensities along the y-direction are plotted in Fig. 2-7.

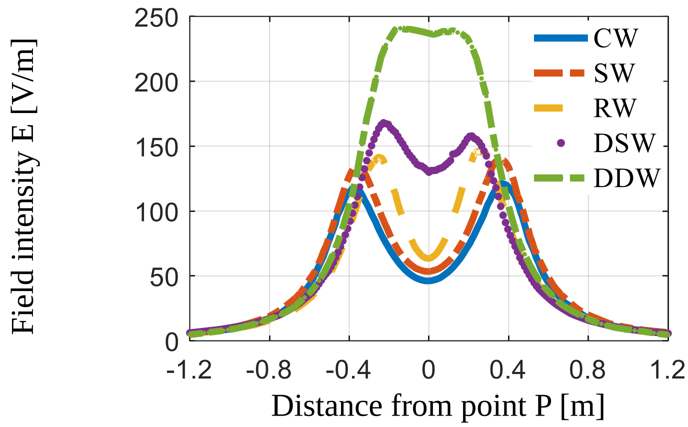

Fig. 2-7. Comparison of electric field intensities in the air-gap center plane along the y-direction

As shown in Fig. 2-7, the air-gap center plane peak electric field intensity locations of the CW, the SW, and the RW are determined by the transmitter terminal location and the receiver terminal location. In addition, the CW has the lowest E_{agcppk}.

Based on Fig. 2-7, the peak electric field intensities E_{pk} along the y-direction measurement line in the air-gap center plane are compared in Table 2-4.

Table 2-4. Comparison of E_{pk} along the y-direction measurement line in the air-gap center plane

	CW	SW	RW	DSW	DDW
E_{pk} [V/m]	121.2	147.2	139.9	168.0	241.2

According to Table 2-4, the CW can achieve the lowest E_{agcppk} under the same test conditions, while the E_{agcppk} of the DDW is about 2 times higher than that of the CW.

Based on the analyses of coil-to-coil power transfer efficiency, magnetic field and electric field distributions, compared with other coil configurations, the CW is a better candidate to help achieve high coil-to-coil efficiency, low air-gap center plane magnetic flux density and electric field intensity, simultaneously.

2.2.5 Effect of the terminal clearance on the air-gap electric field

From previous analyses, the excitation terminal voltage has a significant impact on the air-gap center plane electric field, while the terminal clearance will affect the terminal electric field under the same excitation voltage, therefore, it's necessary to evaluate the effect of terminal clearance on the air-gap center plane electric field.

The test setup is shown in Fig. 2-8, the transfer distance remains as 300 mm, the operating frequency is set at 100 kHz, the evaluated coil radii are 400 mm, 500 mm, and 600 mm, the terminal clearance varies from 10 mm to 30 mm by step 10 mm. There are two measurement lines to evaluate the effect of the terminal clearance: the vertical line along z-direction above the excitation terminal and the horizontal line along y-direction in the air-gap center plane, which goes above the transmitter excitation terminal.

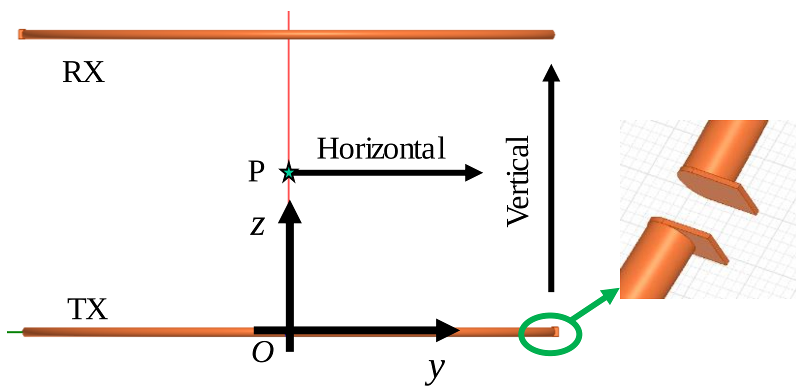

Fig. 2-8. Test setup to evaluate the effect of terminal clearance

When the output power is 3 kW, the electric field intensities along both measurement lines are plotted in Fig. 2-9.

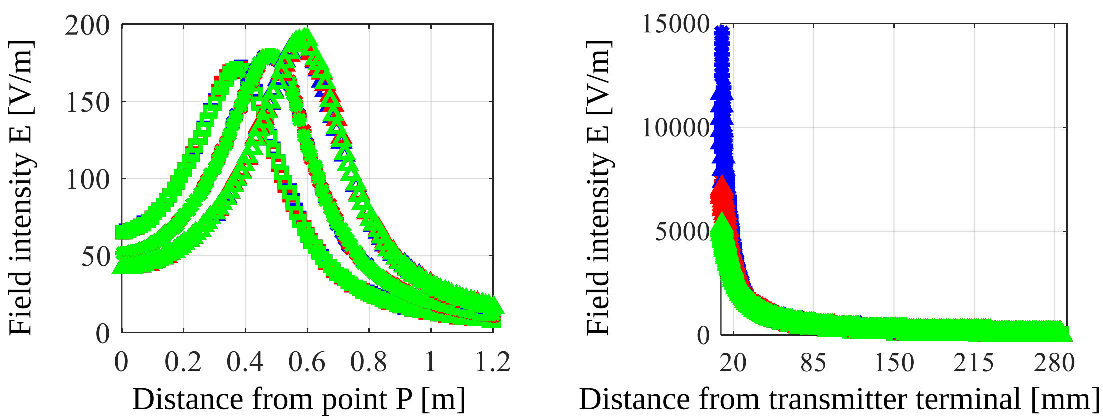

(a) Electric field intensity along the horizontal measurement line

(b) Electric field intensity along the vertical measurement line

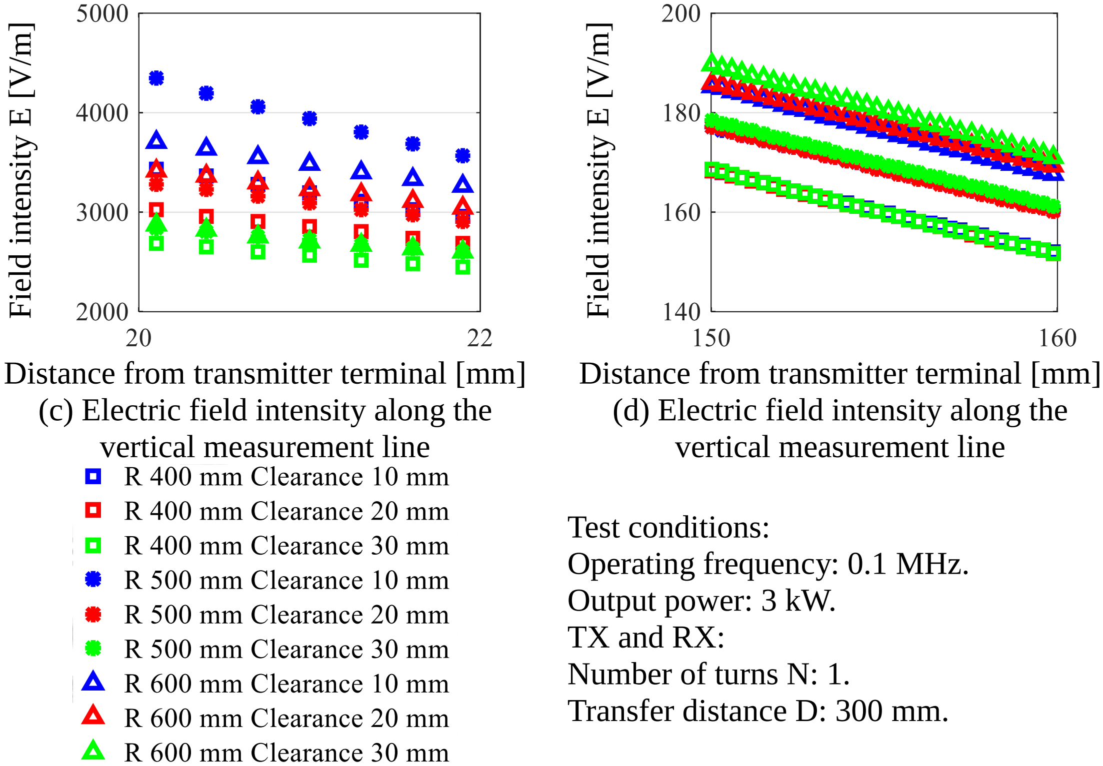

(c) Electric field intensity along the vertical measurement line

(d) Electric field intensity along the vertical measurement line

Fig. 2-9. Evaluation of the effect of the terminal clearance on air-gap electric field

According to the electric field intensity along the horizontal measurement line in the air-gap center plane as shown in Fig. 2-9 (a), different terminal clearances almost do not affect the electric field intensity, which is only affected by the coil radius, since the required excitation voltage changes with the coil radius to provide 3 kW output power.

Based on the electric field intensity along the vertical measurement line above the transmitter excitation terminal as shown in Fig. 2-9 (b), the electric field intensity reduces exponentially as the distance increases. From the zoom in plot Fig. 2-9 (c), the electric field intensity reduces when the terminal clearance increases in the region that is close to the terminal. However, when the distance keeps increasing, the terminal clearance almost has no effect on the electric field intensity as shown in Fig. 2-9 (d).

Therefore, the terminal clearance has a significant impact on the electric field intensity in the region that is very close to the excitation terminal, and it almost has no effect on the electric field intensity that is not close to the excitation terminal. The decay property cancels the effect of the terminal clearance. For the electric field intensity in the air-gap center plane of the loosely coupled inductive WPT system, the effect of the terminal clearance can be neglected.

2.3 Loosely coupled inductive WPT system modeling

Based on the analyses in the previous section, the circular winding is chosen as the research configuration since it can achieve the highest coil-to-coil efficiency, the lowest air-gap center plane peak magnetic flux density, and the lowest air-gap center plane peak electric field intensity. Typical circular windings include planar spiral circular coil, cylindrical spiral circular coil, and surface spiral winding as shown in Fig. 2-10.

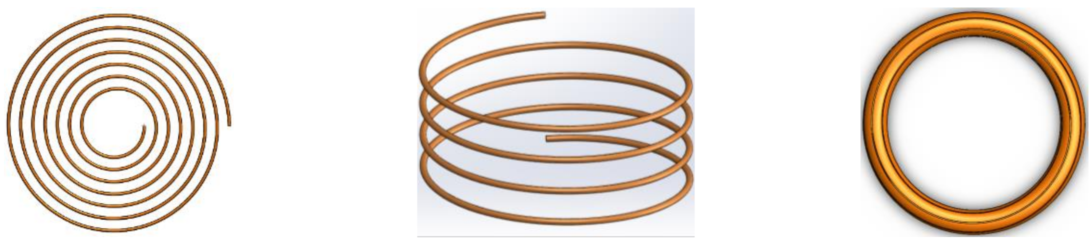

(a) Planar circular spiral coil (b) Cylindrical circular spiral coil (c) Surface spiral winding

Fig. 2-10. Typical types of circular coils

In a planar circular spiral coil, each turn can be represented by a circular loop with an average diameter, the vertical distance between each turn of the primary coil and each turn of the secondary coil are the same. In a cylindrical circular spiral coil, each turn has the same diameter, the vertical distance between each turn of the primary coil and each turn of the secondary coil changes. In a surface spiral winding, each turn has the same diameter, the vertical distance between each turn of the primary coil and each turn of the secondary coil are the same. Coil diameter, number of turns, and inter-turn distance are the main design variables for all three types of circular coils.

Considering the clearance between the vehicle chassis and the ground is small and mostly fixed, the cylindrical circular spiral coil is not a good choice since it requires large vertical distance to install. The surface spiral winding can be treated as a subcategory of the planar circular spiral coil when the inter-turn distance is zero. Therefore, it’s better to choose the planar circular spiral coil as the design example.

The equivalent circuit modeling of a loosely coupled inductive WPT system is required to develop the design methodology. It has been demonstrated that the equivalent transformer model can be used to analyze the system when the diameters of the coils and the transfer distance are smaller than one-tenth of the wavelength. With the equivalent circuit model, the power transfer efficiency, voltages, and currents in each component under the rated power can be derived. After that, the magnetic flux density and the electric field intensity in the air-gap center plane can be analyzed based on coil geometries, coil currents, and the operating frequency.

2.3.1 Analytical calculation of self- and mutual inductances

Self- and mutual inductances are necessary to calculate resonant compensation capacitors and the coupling coefficient between the primary coil and the secondary coil, which are essential to calculate the voltages and currents in each component, and the coil-to-coil power transfer efficiency. A planar circular spiral coil is shown in Fig. 2-11.

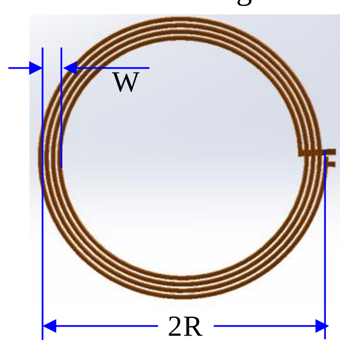

Fig. 2-11. A planar circular spiral coil

The self-inductance of the planar circular spiral coil can be calculated by [254]

$$L_{N=1} = \mu_0 N^2 R\left[\ln\left(\frac{16R}{d}\right) - 2\right] \tag{2.1}$$

$$L_{N>1} = 31.33\,\mu_0 N^2 \frac{R^2}{8R + 11W} \tag{2.2}$$

Where μ_0 is the free space permeability, d is the wire diameter, R is the coil radius, W is the coil width, N is the number of turns.

Misalignment is unavoidable for WPT systems. The mutual inductance calculation method should be able to calculate both perfectly aligned coils and misaligned coils. There are mainly two types of misalignments, lateral misalignment and angular misalignment, which have to be taken into consideration. Lateral misalignment is much more common for electric vehicles due to parking. Angular misalignment is relatively small except flat tire. A laterally misaligned transmitter and receiver configuration is shown in Fig. 2-12.

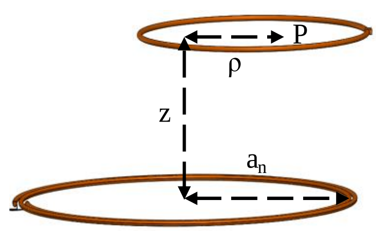

Fig. 2-12. A laterally misaligned transmitter and receiver configuration

In Fig. 2-12, z is the vertical distance between the transmitter and the receiver, a_n is the coil radius of the transmitter turn n, ρ is the lateral distance between the point P within the receiver region and the transmitter center.

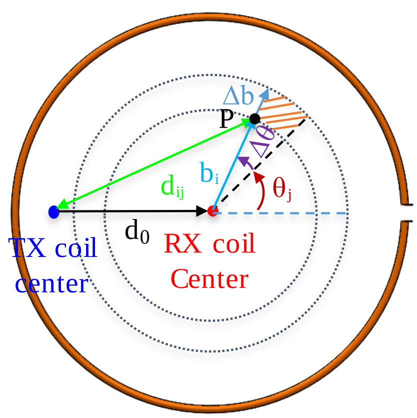

Fig. 2-13. Receiver coil of laterally misaligned coils

The magnetic field generated by the coil with multiple turns can be calculated by adding the field generated by each turn, which can be further simplified by transforming each turn into the circular loop using average coil radius. Using polar coordinates, the area covered by the receiver coil is divided into i elements in the radial direction and j elements in the angular direction as shown in Fig. 2-13. The i*j grids can represent the area covered by the receiver coil when the grid Δb*Δθ is small enough that the flux density at the grid point can be assumed as a constant. Due to the large distance between the transmitter and the receiver, the coupling is relatively small, which is normally smaller than 0.2. It is assumed that only z-direction flux density generated by the transmitter can be coupled with the receiver.

According to Conway [255], the z-direction magnetic flux density at point P generated by the transmitter turn n can be calculated by

$$B_{PnZ_{ij}} = \frac{\mu_0\sqrt{k_{ij}}\ I}{16\pi(a_n{*}d_{ij})^{3/2}} \frac{4a_n\, d_{ij}\,(1-k_{ij})\, K(\sqrt{k_{ij}}) + (a_n^2 - d_{ij}^2 - z^2)\, k_{ij}\, E(\sqrt{k_{ij}})}{1-k_{ij}} \tag{2.3}$$

Where I in the transmitter current, z is the vertical distance between the transmitter and the receiver, a_n is the coil radius of the transmitter turn n, d_0 is the horizontal distance between the transmitter coil center and the receiver coil center, b_i is the distance between the point P and the receiver coil center, d_{ij} is the planar distance between the point P and the transmitter coil center, Δb is the radial length of element ij, $\Delta\theta$ is the incremental angle of element ij, θ_j is the angle of element ij in the polar coordinates, $d_{ij} = \sqrt{d_0^2 + b_i^2 - 2\, d_0\, b_i {*}\cos(\theta_j)}$, $k_{ij} = \dfrac{4a_n d_{ij}}{(a_n+d_{ij})^2 + z^2}$, $K(\sqrt{k_{ij}})$ and $E(\sqrt{k_{ij}})$ are the complete elliptic integrals of the first and second kinds.

The total z-direction magnetic flux density at point P generated by the transmitter can be calculated by

$$B_{PZ_{ij}} = \sum_{n=1}^{N_{TX}} \left[\frac{\mu_0\sqrt{k_{ij}}\ I}{16\pi(a_n{*}d_{ij})^{3/2}} \frac{4a_n\, d_{ij}\,(1-k_{ij})\, K(\sqrt{k_{ij}}) + (a_n^2 - d_{ij}^2 - z^2)\, k_{ij}\, E(\sqrt{k_{ij}})}{1-k_{ij}} \right] \tag{2.4}$$

The total z-direction magnetic flux coupled to the receiver can be calculated by

$$\Phi_Z = MI = \sum_{n=1}^{N_{RX}} \sum_{j=1}^{q} \sum_{i=1}^{p} \left[B_{Z_{ij}}\, \Delta b \times b_i \Delta\theta \right] \tag{2.5}$$

Where p is the total number of elements in the radial direction, $p = R_{rx}/\Delta b$, q in the total number of elements in the angular direction, and $q = 2\pi/\Delta\theta$.

If the receiver has multiple turns N_{rx}, then it can be transformed into N_{rx} individual circular loops, the total z-direction magnetic flux coupled to the receiver can be calculated by adding the z-direction magnetic flux coupled to each individual loop together. The current I in M*I is the same as the current in flux density calculation, they can be canceled out, only the mutual inductance term is left.

When d_0 is zero, the calculated mutual inductance is between aligned transmitter and receiver. When d_0 is non-zero, the calculated mutual inductance is between misaligned transmitter and receiver. The self-inductances of the transmitter and the receiver remain the same for both aligned and misaligned configurations, the coupling between the transmitter and the receiver varies under misalignment, then the required currents in the transmitter and the receiver changes for the rated power level, the magnetic flux density and the electric field intensity in the air-gap region will also change, which require special attention during design.

Compared with Litz wire, the copper tubing has stable characteristics at both low operating frequency and high operating frequency. Therefore, copper tubing is selected to build the transmitter and receiver coils. Typical copper tubing sizes and AC resistances per meter caused by skin effect are listed in Table 2-5.

Table 2-5. Typical copper tubing sizes and AC resistances caused by skin effect

Outside Diameter (O.D.) [Inch]	Inside Diameter (I.D.) [Inch]	Wall Thickness [Inch]	R_{skin} per meter [Ω/m] @ 1 MHz
1/8	0.065	0.030	0.0268
3/16	0.127	0.030	0.0177
1/4	0.190	0.030	0.0133
5/16	0.249	0.032	0.0106
3/8	0.311	0.032	0.0088
1/2	0.436	0.032	0.0066
5/8	0.555	0.035	0.0053
3/4	0.680	0.035	0.0044
7/8	0.785	0.045	0.0038

Under given operating frequency, the skin effect AC resistance R_{skin} decreases when the copper tubing outside diameter increases. A copper tubing with an outside diameter 3/8’’ (9.525 mm) and wall thickness 0.032’’ (0.8128 mm) is selected due to its low skin effect AC resistance, easy ability to bend and maintain the configuration.

A planar circular spiral coil as shown in Fig. 2-11 is evaluated via FEA to verify the analytical model calculation accuracy. The initial distance between the primary coil and the secondary coil is set as 300 mm, which is higher than general electric vehicle ground clearance 200 mm and enough for charging an electric vehicle. The coil radius is initialized as 600 mm, and the inter-turn distance is set as 13.525 mm. The initial operating frequency is set as 0.1 MHz. The transmitter coil and the receiver coil are set as the same. When the primary coil and the secondary coil are perfectly aligned, analytical calculation results and FEA simulation results of the self- and mutual inductances with respect to the number of turns are compared in Fig. 2-14.

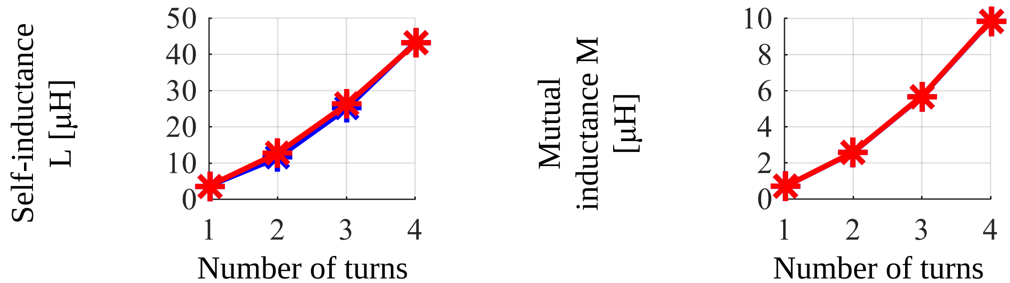

(a) L w.r.t. number of turns (b) M w.r.t. number of turns

Test Conditions: * Analytical, * FEA.

TX and RX radii: 600mm. Inter-turn distance: 13.525mm. TX and RX vertical distance: 300 mm. Copper tubing: outside diameter 9.525 mm, wall thickness 0.8128 mm. Operating frequency: 0.1MHz. Output power: 3kW

Fig. 2-14. Comparison of analytical calculation results and FEA results of the self- and mutual inductances with respect to different number of turns

As shown in Fig. 2-14, the analytical calculation results and the FEA results for the self-inductance, and the mutual inductance with different number of turns perfectly match with each other, which ensure the calculation accuracy of the currents in the primary coil and the secondary coil, and lay a good foundation for the calculation of the air-gap center plane magnetic flux density and electric field intensity. It’s easy to find that the self- and mutual inductances are proportional to the square of the number of turns.

The calculation accuracy of mutual inductance under misalignment is more important since misalignment is unavoidable, and it affects the evaluation of the coil-to-coil power transfer efficiency and the calculation of air-gap center plane magnetic flux density and electric field intensity under misalignment. A planar circular spiral coil, a normal conical spiral coil, and an inverted conical spiral coil, as shown in Fig. 2-15, are used to evaluate the mutual inductance calculation accuracy under misalignment.

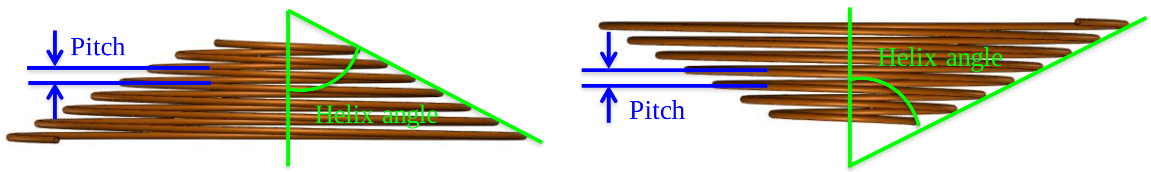

(a) Normal conical spiral coil (b) Inverted conical spiral coil

Fig. 2-15. Normal and inverted conical spiral coils

The secondary coil is set as 1 turn with radius 180 mm. The vertical distance between the top of the normal conical spiral coil and the secondary coil is set as 300 mm. The vertical distance between the top of the inverted conical spiral coil and the secondary coil is also set as 300 mm. All of the primary coils are set as 7 turns, the inside radii for all primary coils are set as 100 mm. The inter-turn distance for planar circular spiral winding (SW) is set as 39.525 mm, the pitches for conical SWs are set as 20 mm, the helix angles are set as 63.156 degrees to keep the total length of three coils the same then the AC resistances caused by skin effect are the same. Surface spiral winding (SSW) reviewed in the first chapter is also evaluated. Each turn of all kinds of transmitters is transformed into a circular loop during the calculation using the analytical method proposed in previous sections. Analytical calculation results and FEA results of the coupling factor with respect to lateral misalignment are compared in Fig. 2-16.

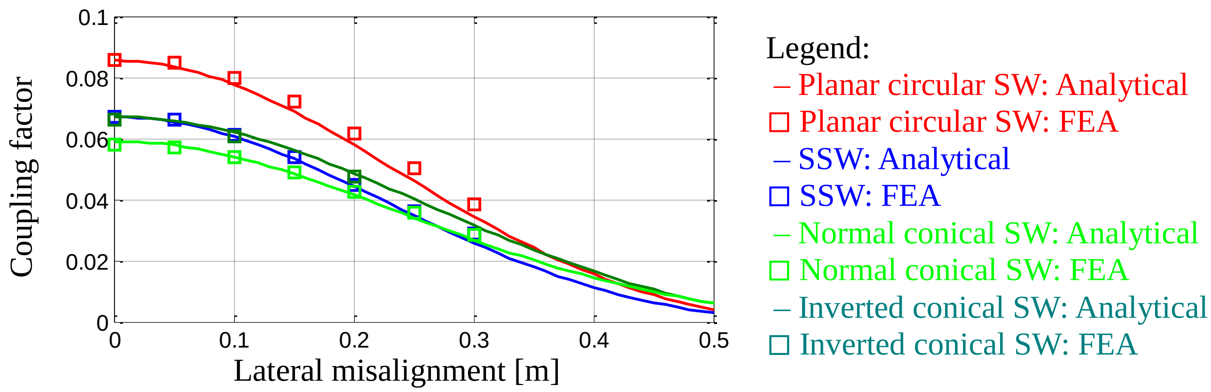

Fig. 2-16. Comparison of analytical calculation results and FEA results of the coupling factor with respect to lateral misalignment

As shown in Fig. 2-16, the errors between the analytical calculation results and the FEA results of the coupling factor for the surface spiral winding, the planar circular spiral winding, the normal conical spiral winding, and the inverted conical spiral winding under lateral misalignment are within 5%, which ensure the accuracy of system evaluation with analytical models under misalignments.

2.3.2 Analytical calculation of the AC resistance

It's necessary to consider the skin effect and the proximity effect when calculating the ESR. Under high operating frequency, the surface eddy currents tend to reduce the net current density in the center of the conductor, and increase the net current density near the surface of the conductor. In addition, the magnetic field generated by the conductor will affect the current distributions in the adjacent conductors. The skin effect and the proximity effect of a conductor are shown in Fig. 2-17.

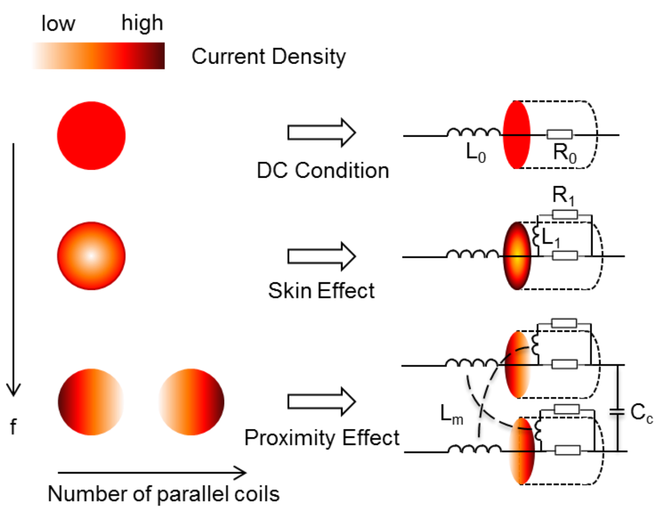

Fig. 2-17. Skin effect and proximity effect of a conductor

As shown in Fig. 2-17, the current will concentrate on the conductor surface when the operating frequency increases. When multiple coils are put close, the current distribution in one conductor will be affected by its adjacent conductors. Between two adjacent conductors, there are flux cross-coupling and parasitic capacitance.

The skin effect AC resistance R_{skin} can be calculated by

$$R_{skin} = \rho \frac{l}{\pi R^2 - \pi (R - \delta)^2} = \rho \frac{l}{2 \pi R \delta - \pi \delta^2} \quad (2.6)$$

Where ρ is electrical resistivity, l is the conductor length, R is the copper tubing outside radius, and δ is the skin depth.

The total AC resistance R_{AC} caused by skin and proximity effects can be calculated by

$$R_{AC} = R_{skin} (1 + G_p) \quad (2.7)$$

Where R_{skin} is the AC resistance caused by skin effect, and G_p is the proximity effect factor.

According to G. S. Smith [232], the relationship between the proximity effect factor and the spacing c/a are plotted in Fig. 1-89 which is repeated in Fig. 2-18 for the convenience.

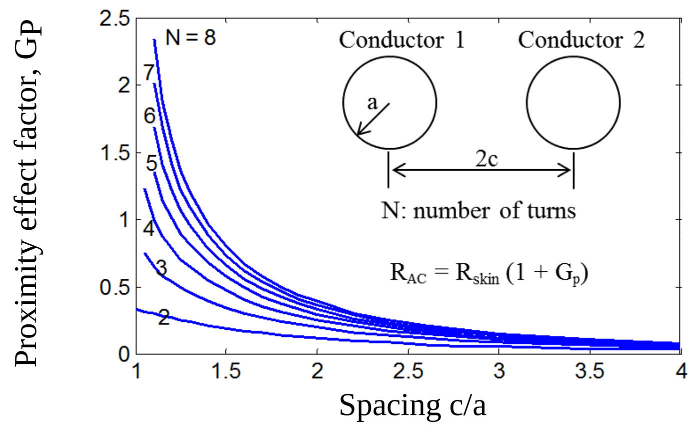

Fig. 2-18. Proximity effect factor dependence on turn-spacing

In Fig. 2-18, N is the number of turns, a is the conductor outer radius, 2c is the inter-turn distance. As the inter-turn distance increase, the AC resistance caused by proximity effect will reduce while the AC resistance caused by skin effect remains the same. In addition, the total AC resistance will be the same no matter if the conductor is a tubing or a solid conductor. However, the wall thickness will affect whether the conductor needs a dielectric substrate or not. In high operating frequency, such as MHz, the dielectric substrate will cause dielectric losses, which may significantly reduce the power transfer efficiency.

A lookup table can be created from Fig. 2-18 to get G_p based on the coil outer diameter, the inter-turn distance, and the number of turns. In the table provided by G. S. Smith, there are only limited number of test cases, the polynomial curve fitting tool can be used to get the values where the spacing case is not tested. The AC resistance due to the skin effect can be calculated using equation (2.5), then the total AC resistance can be calculated using equation (2.6).

Since the proximity effect factor provided by G. S. Smith is based on the experimental test, the calculation accuracy can be guaranteed, and the given number of turns is enough for getting general design guidelines. However, the limitation is that when the number of turns is greater than 8, the test results are not provided, an easy way can be used to extend this method is that using FEA to get the rest proximity effect factor G_p.

A planar circular spiral coil as shown in Fig. 2-11 is evaluated via FEA to verify the analytical model calculation accuracy. All settings are the same as the evaluation of the self- and mutual inductances calculation. The analytical calculation results and FEA simulation results of the total AC resistance with respect to the number of turns are compared in Fig. 2-19.

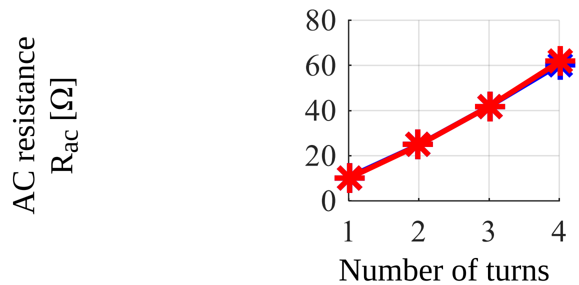

Test Conditions: * Analytical, * FEA.
TX and RX radii: 600mm. Inter-turn distance: 13.525mm. TX and RX vertical distance: 300 mm. Copper tubing: outside diameter 9.525 mm, wall thickness 0.8128 mm. Operating frequency: 0.1MHz. Output power: 3kW

Fig. 2-19. Comparison of analytical calculation results and FEA results of the total AC resistance with respect to different number of turns

As shown in Fig. 2-19, the analytical calculation results match with the FEA results. The total AC resistance increases due to the skin effect and the proximity effect. If only consider the skin effect, the AC resistance incremental rate should reduce as the number of turns increases, since the perimeter incremental rate reduces as the number of turns increases due to the planar configuration. However, the total AC resistance incremental rate increases as the number of turns increases as shown in Fig. 2-19 due to the proximity effect. In addition, as the inter-turn distance reduces, the total AC resistance will be higher than the current value due to the proximity effect.

2.3.3 Loosely coupled inductive WPT system equivalent circuit model

The loosely coupled WPT coils can be transformed into an equivalent transformer model as shown in Fig. 1-36 which is repeated in Fig. 2-20 for the convenience. The transfer ratio *a* of the coupled coils is defined as

$$a = k\sqrt{L_{tx} / L_{rx}} \tag{2.8}$$

Where L_{tx} is the transmitter self-inductance, L_{rx} is the receiver self-inductance, k is the coupling factor between the transmitter and the receiver, $k = M / \sqrt{L_{tx}L_{rx}}$, M is the mutual inductance between the transmitter and the receiver.

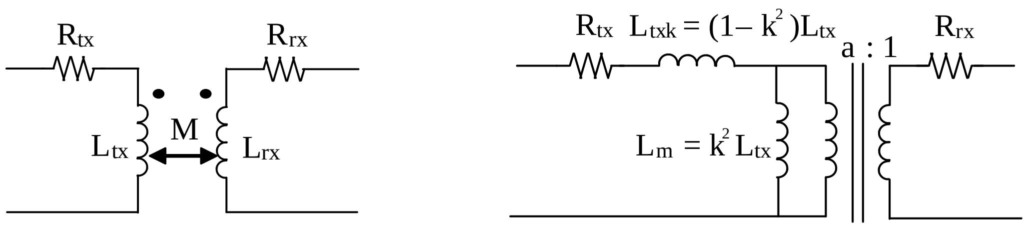

(a) Equivalent lumped circuit model (b) Equivalent transformer model

Fig. 2-20. Equivalent lumped element model of inductive WPT coils

Resonant compensation networks are required to achieve high coil-to-coil efficiency. If the primary is series compensated, a voltage source converter could be directly connected to the coil. If the primary is parallel compensated, an inductor is usually inserted to change the voltage source converter to a current source. A series compensation on the secondary side makes the output like a voltage source, while a parallel compensation makes the output like a current source.

Series-series and series-parallel topologies are widely used in the existing literature to charge the battery. Two steps are required to charge the battery pack: constant current mode to bring up the state-of-charge, and constant voltage mode to meet the battery voltage limit. The constant current mode is generally configured as the series-series type loaded by a diode rectifier and output filter capacitor, as shown in Fig. 2-21 (a), while the constant voltage mode is generally implemented as the series-parallel type loaded by a diode rectifier but with an inductor input filter, as shown in Fig. 2-21 (b).

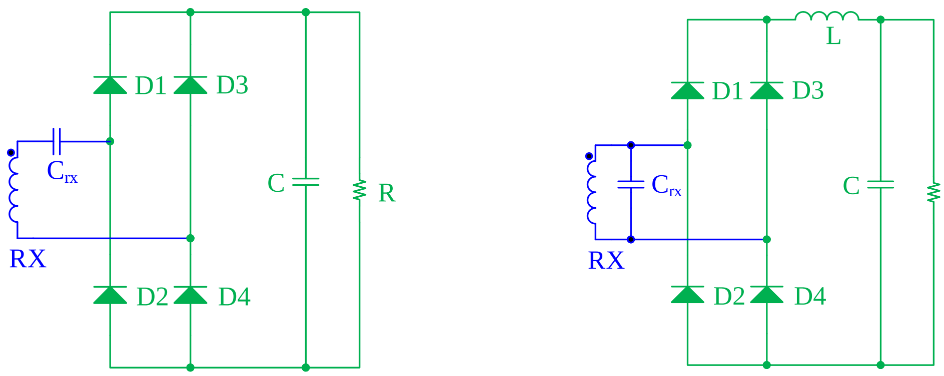

(a) Rectifier with capacitor filter (b) Rectifier with inductor and capacitor filter

Fig. 2-21. Output diode rectifiers and filter networks

When the secondary side is series compensated, the rectifier input voltage is a square wave, the rectifier input current is a sinusoidal wave, the effective load resistance R_e before the rectifier network with the capacitor filter and the load R can be calculated by

$$R_e = \frac{8}{\pi^2} R \tag{2.9}$$

When the secondary side is parallel compensated, the rectifier input voltage is sinusoidal wave, the rectifier input current is square wave, the effective load resistance R_e before the rectifier network with the LC filter and the load R can be calculated by

$$R_e = \frac{\pi^2}{8} R \tag{2.10}$$

The H-bridge resonant inverter is selected since it's easy to control, in addition, the required drain current of the power module can be reduced almost by half, compared with the class E inverter, to transfer the same amount of power.

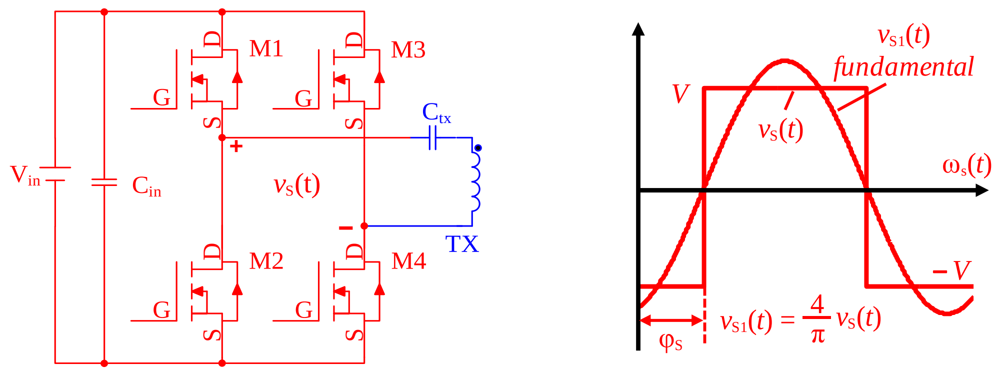

(a) H-bridge resonant inverter (b) Inverter output voltage waveform

Fig. 2-22. H-bridge resonant inverter and output voltage waveform

The primary side is usually series compensated as shown in Fig. 2-22 (a), although the inverter output voltage is square wave, only the fundamental term needs to be considered when analyzing the circuit, since the transmitter side and the receiver side has almost the same resonant frequency, which is the same as the PWM switching frequency, or the voltage fundamental frequency. The power transfer efficiency of the high order harmonics is very low and can be neglected.

The equivalent circuit models for the loosely coupled inductive WPT systems including the input H-bridge inverter, the resonant compensation network, the output rectifier, and the output filter network can be simplified according to above analyses, and are shown in Fig. 2-23.

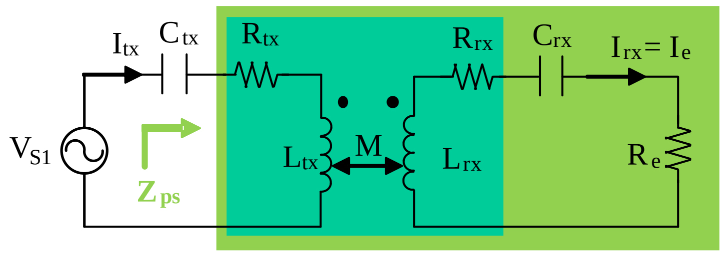

(a) Equivalent circuit model with series-series resonant compensation network

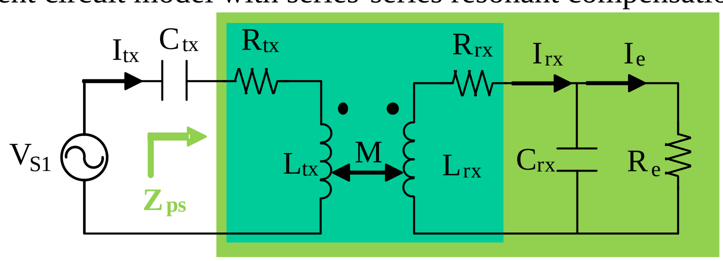

(b) Equivalent circuit model with series-parallel resonant compensation network

Fig. 2-23. Equivalent lumped circuit models of inductive WPT systems

The secondary side resonant capacitance in both series and parallel resonant networks can be calculated by

$$C_{rx} = \frac{1}{L_{rx}\,\omega_0^2} \tag{2.11}$$

The secondary side can be transformed to the primary side using the equivalent transformer model, the equivalent input impedance from the primary side is assigned as Z_{ps}. The primary side resonant capacitance C_{tx} should be designed based on Z_{ps} to achieve power module zero voltage switching (ZVS) to reduce the H-bridge inverter loss.

Assuming the duty ratio is D, C_{tx} can be calculated following

$$L_i = \frac{0.5\ \mathrm{Imag}(Z_{ps})}{\omega_0} \tag{2.12}$$

$$R_i = \frac{0.5\ \mathrm{Real}(Z_{ps})}{\omega_0} \tag{2.13}$$

$$\alpha = 2\ \pi\ (0.5 - D) \tag{2.14}$$

$$\beta = \mathrm{acos}\left(\frac{1 + \cos(\alpha)}{2}\right) \tag{2.15}$$

$$X_i = R_i * \tan(\beta) \tag{2.16}$$

$$X_{ci} = L_i * \omega_0 - X_i \tag{2.17}$$

$$C_i = \frac{1}{\omega_0 * X_{ci}} \tag{2.18}$$

$$C_{tx} = 0.5{*}C_i \tag{2.19}$$

Previous analyses are verified by PLECS simulation with a series-parallel compensated example. Based on Fig. 2-23 (b), the required effective load current I_e for given output power P_{out} can be calculated by

$$I_e = \sqrt{\frac{2{*}P_{out}}{R_e}} \tag{2.20}$$

The receiver coil current I_{rx} can be calculated by

$$I_{rx} = I_e + R_e * I_e * (j{*}\omega_0{*}C_{rx}) \tag{2.21}$$

The transmitter coil current I_{tx} can be calculated by

$$I_{tx} = \frac{I_{rx}{*}(j{*}\omega_0{*}L_{rx} + R_{rx}) + R_e{*}I_e}{j{*}w_0{*}M} \tag{2.22}$$

In the test example, the duty ratio D is set as 0.48, the resonant frequency f_0 is 100 kHz, the output power P_{out} is 3 kW, the load R is 38.11 Ω, L_{tx} = 26.09 µH, R_{tx} = 29.7 mΩ, L_{rx} = 25.91 µH, R_{rx} = 29.9 mΩ, M = 5.39 µH. Following previous analytical analyses, the required resonant capacitances C_{rx} and C_{tx} are 97.75 nF and 103.43 nF, respectively. The transmitter and receiver current amplitudes I_{tx} and I_{rx} are 42.54 A and 42.93 A, respectively, the current phase difference is 78.46°. Using PLECS simulation with the same winding parameters, the gate signal and the transmitter current are compared in Fig. 2-25 (a), the transmitter current and the receiver current are compared in Fig. 2-25 (b).

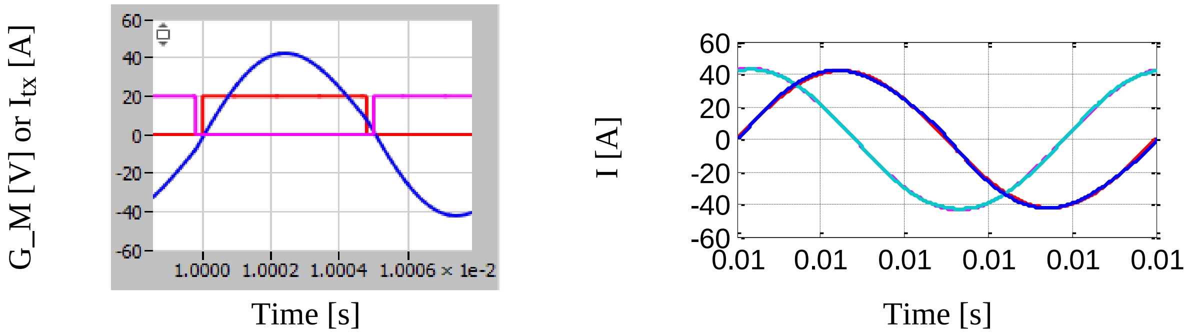

Gate_M1, Gate_M2, I_{tx} PLECS: I_{tx}, I_{rx}. Analytical: I_{tx}, I_{rx}

(a) Gate and transmitter current signals (b) Transmitter and receiver currents

Fig. 2-24. PLECS simulation waveforms and comparison with analytical current waveforms

As shown in Fig. 2-25 (a), when the power module M1 turns on, the current I_{tx} is negative and close to zero, which means the current I_{tx} goes through the diode of the power module M1, and the voltage across M1 is negative, therefore, ZVS is achieved, ZCS can also be achieved by further tuning C_{tx}. According to Fig. 2-25 (b), the maximum values of I_{tx} and I_{rx} from the PLECS simulation are 42.29 A and 42.85 A, respectively, which are almost the same as the analytical results, the current phase difference 75.60° is slightly lower than the analytical result 78.46°. Besides that, the PLECS simulation normally takes about 1 minute, while the analytical calculation only takes several miliseconds. The accurate and fast analytical equivalent model for winding current and voltage provides a quick access to calculate air-gap B&E fields.

2.3.4 Loosely coupled inductive WPT system coil-to-coil efficiency

There are so many methods in the existing literature to improve the coil-to-coil power transfer efficiency, the efficiency factor that fundamentally determines the coil-to-coil power transfer efficiency will be identified in this section based on series-series and series-parallel resonant compensation networks.

The equivalent circuit models for the loosely coupled inductive WPT systems with series-series resonant network can be simplified by an equivalent transformer model, as shown in Fig. 2-25 (a), and the secondary side can be transformed to the primary side as shown in Fig. 2-25 (b).

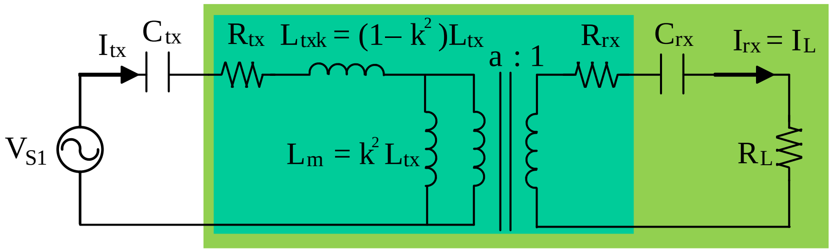

(a) Lumped circuit model using an equivalent transformer

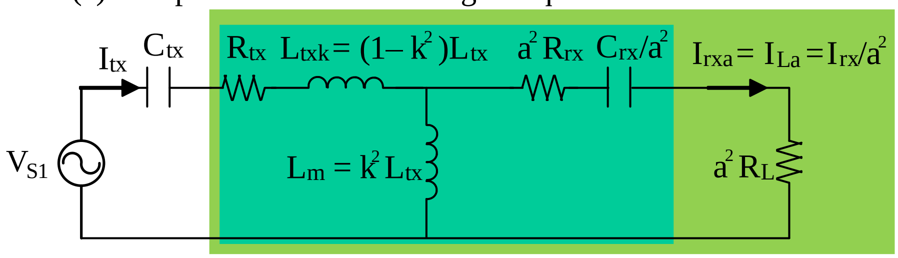

(b) Lumped circuit model transferred to the primary side

Fig. 2-25. Equivalent circuit models of inductive WPT system with series-series resonant compensation network

Using the system equivalent circuit models in Fig. 2-25, the currents and voltages in each component can be calculated based on system parameters, such as the self- and mutual inductances, the ESRs, and the load resistance, when the output power is given. The secondary side resonant capacitance C_{rx} is designed as $1 / (L_{rx}\, \omega_0^2)$ for both series and parallel resonant compensation networks.

Considering the coil radiation loss is negligible, the coil-to-coil power transfer efficiency can be calculated by

$$\eta_{coil} = \frac{P_{load}}{P_{loss\_tx} + P_{loss\_rx} + P_{load}} = \frac{|I_L|^2 R_L}{|I_{tx}|^2 R_{tx} + |I_{rx}|^2 R_{rx} + |I_L|^2 R_L} \tag{2.23}$$

According to Fig. 2-25 (b), η_{coil} can also be calculated by

$$\eta_{coil} = \frac{|I_{rxa}|^2 a^2 R_L}{|I_{tx}|^2 R_{tx} + |I_{rxa}|^2 a^2 R_{rx} + |I_{rxa}|^2 a^2 R_L} = \frac{1}{1 + \frac{R_{rx}}{R_L} + \left|\frac{I_{tx}}{I_{rxa}}\right|^2 \frac{1}{a^2} \frac{R_{tx}}{R_L}} \tag{2.24}$$

Under given output power, the currents I_{tx} and I_{rxa} are independent of the primary resonant capacitance C_{tx}, so is the coil-to-coil efficiency.

Based on Fig. 2-25 (b) and the Kirchhoff's law, the current ratio

$$\frac{I_{tx}}{I_{rxa}} = \frac{a^2 R_{rx} + a^2 R_L + a^2 \dfrac{1}{j\omega_0 C_{rx}}}{ja^2\omega_0 L_{rx} + \dfrac{a^2 L_{rx} / C_{rx}}{R_{rx} + R_L}} = (R_{rx} + R_L)\ \frac{[j\omega_0 L_{rx} + j\omega_0 C_{rx}(R_{rx} + R_L)^2]}{-\omega_0^2 L_{rx}^2 - (R_{rx} + R_L)^2} \quad (2.25)$$

Above current ratio can be further simplified into

$$\left|\frac{I_{tx}}{I_{rxa}}\right|^2 = \left[\frac{R_{rx} + R_L}{\omega_0 L_{rx}}\ \frac{\omega_0^2 L_{rx}^2 + \omega_0^2 L_{rx} C_{rx}(R_{rx} + R_L)^2}{\omega_0^2 L_{rx}^2 + (R_{rx} + R_L)^2}\right]^2 = \left[\frac{R_{rx} + R_L}{\omega_0 L_{rx}}\right]^2 \quad (2.26)$$

Substituting the square of the current ratio into the coil-to-coil efficiency formula, the coil-to-to-coil efficiency can be calculated by

$$\eta = \frac{1}{1 + \dfrac{R_{rx}}{R_L} + \left(\dfrac{R_{rx} + R_L}{\omega_0 L_{rx}}\right)^2 \dfrac{1}{a^2}\dfrac{R_{tx}}{R_L}} = \frac{1}{1 + \dfrac{R_{rx}}{R_L} + \left(\dfrac{R_{rx} + R_L}{\omega_0 M}\right)^2 \dfrac{R_{tx}}{R_L}} \quad (2.27)$$

The maximum coil-to-coil efficiency can be achieved when

$$\left[1 + \frac{R_{rx}}{R_L} + \left(\frac{R_{rx} + R_L}{\omega_0 M}\right)^2 \frac{R_{tx}}{R_L}\right]'\Bigg|_{R_L} = 0 \quad (2.28)$$

The optimal load resistance R_{Lo} satisfying above differential equation is

$$R_{Lo} = \sqrt{R_{rx}^2 + \frac{R_{rx}}{R_{tx}}\omega_0^2 M^2} \quad (2.29)$$

Then, the maximum achievable coil-to-coil efficiency $\eta_{coil,\ max}$ can be calculated by

$$\eta_{coil,\ max} = \frac{1}{1 + \sqrt{\dfrac{R_{tx}R_{rx}}{\omega_0^2 M^2 + R_{tx}R_{rx}}} + \left(\dfrac{\sqrt{R_{tx}R_{rx}} + \sqrt{R_{tx}R_{rx} + \omega_0^2 M^2}}{\omega_0 M}\right)^2 \sqrt{\dfrac{R_{tx}R_{rx}}{\omega_0^2 M^2 + R_{tx}R_{rx}}}}$$

(2.30)

$\eta_{coil,\ max}$ can be simplified into

$$\eta_{coil,\ max} = \frac{1}{1 + 2 \times \dfrac{R_{tx} R_{rx}}{\omega_0^2 M^2} + 2 \times \sqrt{\dfrac{R_{tx}^2 R_{rx}^2}{\omega_0^4 M^4} + \dfrac{R_{tx} R_{rx}}{\omega_0^2 M^2}}} \quad (2.31)$$

According to the expression of the maximum achievable coil-to-coil efficiency $\eta_{coil,\ max}$ for series-series compensated system, it's easy to find out that $\eta_{coil,\ max}$ is fundamentally determined by the efficiency factor $\frac{\omega_0^2 M^2}{R_{tx} R_{rx}}$, which is independent of the self-inductances of the transmitter and the receiver. In addition, $\eta_{coil,\ max}$ increases with the efficiency factor. Various methods, such as increasing the operating frequency and the number of turns, that can increase the efficiency factor will lead to a higher coil-to-coil maximum achievable efficiency.

The equivalent circuit models for the loosely coupled inductive WPT systems with series-parallel resonant compensation network can be re-configured using the receiver coil quality factor $Q_{rx} = \frac{\omega_0 L_{rx}}{R_{rx}}$ as shown in Fig. 2-26 (a), and further simplified by using the equivalent transformer model, as shown in Fig. 2-26 (b), and the secondary side can be transformed to the primary side as shown in Fig. 2-26 (c).

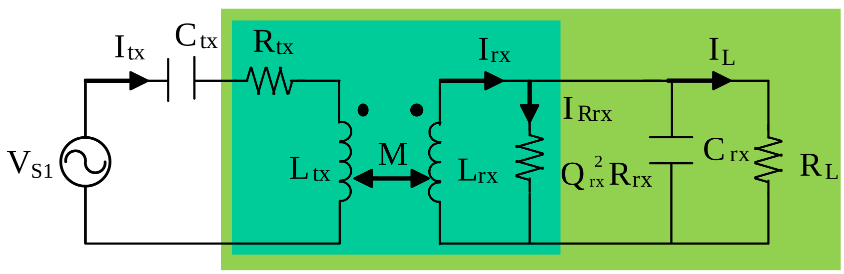

(a) Lumped circuit model reconfigured using the receiver coil quality factor

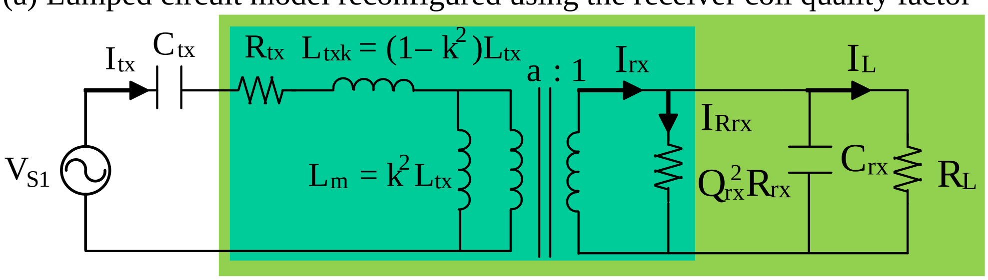

(b) Lumped circuit model using an equivalent transformer

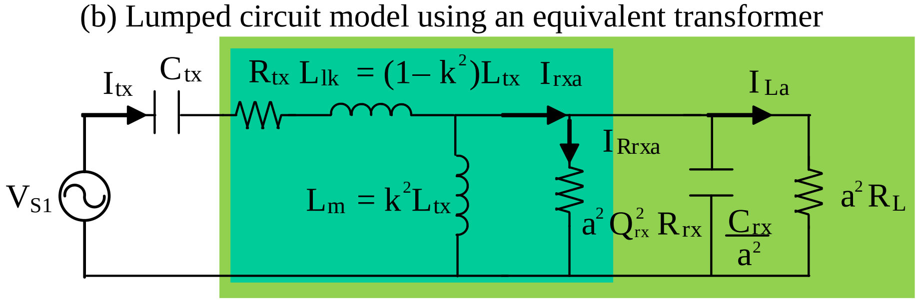

(c) Lumped circuit model transferred to the primary side

Fig. 2-26. Equivalent circuit models of inductive WPT system with series-parallel resonant compensation network

The analysis of the series-parallel compensated network will be based on Fig. 2-26 (c). Considering the secondary side resonant compensation, L_m can be compensated by the resonant capacitor C_{rx} / a^2, the two parallel branches can be neglected.

Following the Kirchhoff's law, the current ratio

$$\frac{I_{Rrxa}}{I_{La}} = \frac{R_L}{Q_{rx}^2 R_{rx}} \tag{2.32}$$

$$\frac{I_{tx}}{I_{La}} = 1 + \frac{R_L}{Q_{rx}^2 R_{rx}} \tag{2.33}$$

The coil-to-coil efficiency can be calculated by

$$\eta = \frac{I_{La}^2 a^2 R_L}{I_{La}^2 a^2 R_L + I_{Rrxa}^2 a^2 Q_{rx}^2 R_{rx} + I_{tx}^2 R_{tx}} = \frac{1}{1 + \frac{R_L}{Q_{rx}^2 R_{rx}} + \left(1 + \frac{R_L}{Q_{rx}^2 R_{rx}}\right)^2 \frac{R_{tx}}{a^2 R_L}} \tag{2.34}$$

It's easy to find that the currents I_{tx}, I_{Rrxa} and I_{La} are independent of the primary resonant capacitance C_{tx} under given output power, so is the coil-to-coil efficiency.

The maximum coil-to-coil efficiency can be achieved when

$$\left[1 + \frac{R_L}{Q_{rx}^2 R_{rx}} + \left(1 + \frac{R_L}{Q_{rx}^2 R_{rx}}\right)^2 \frac{R_{tx}}{a^2 R_L}\right]' \Bigg|_{R_L} = 0 \tag{2.35}$$

The optimal load resistance R_{Lo} satisfying above differential equation is

$$R_{Lo} = \sqrt{\frac{R_{tx}\, R_{rx}^2\, Q_{rx}^4}{a^2\, R_{rx}\, Q_{rx}^2 + R_{tx}}} = \sqrt{\frac{R_{tx}\, \omega_0^4\, L_{rx}^4}{R_{rx}\, M^2\, \omega_0^2 + R_{tx}\, R_{rx}^2}} \tag{2.36}$$

Then, the maximum achievable coil-to-coil efficiency $\eta_{coil,\ max}$ can be calculated by

$$\eta_{coil,\ max} = \frac{1}{1 + \sqrt{\frac{R_{tx}R_{rx}}{\omega_0^2\, M^2 + R_{tx}R_{rx}}} + \left(1 + \sqrt{\frac{R_{tx}R_{rx}}{\omega_0^2\, M^2 + R_{tx}R_{rx}}}\right)^2 \sqrt{\frac{\omega_0^2 M^2 R_{tx} R_{rx} + R_{tx}^2 R_{rx}^2}{\omega_0^4\, M^4}}} \tag{2.37}$$

$\eta_{coil,\ max}$ can be simplified into

$$\eta_{coil,\,max} = \frac{1}{1 + 2 \times \frac{R_{tx}\,R_{rx}}{\omega_0^2\,M^2} + 2 \times \sqrt{\frac{R_{tx}^2\,R_{rx}^2}{\omega_0^4\,M^4} + \frac{R_{tx}\,R_{rx}}{\omega_0^2\,M^2}}} \tag{2.38}$$

According to the expression of the maximum achievable coil-to-coil efficiency $\eta_{coil,\,max}$ for series-parallel compensated system, it's easy to find out that $\eta_{coil,\,max}$ is also fundamentally determined by the efficiency factor $\frac{\omega_0^2\,M^2}{R_{tx}\,R_{rx}}$, which is independent of the self-inductances of the transmitter and the receiver. In addition, $\eta_{coil,\,max}$ increases with the efficiency factor.

In the series-series and series-parallel resonant compensation networks, the primary and secondary coil currents and the coil-to-coil efficiencies are independent of the primary capacitance C_{tx} under given output power. Therefore, the primary resonant compensation type won't affect the currents or the coil-to-coil efficiency. However, the secondary resonant compensation topology affects the currents and the coil-to-coil efficiency. The series-series and parallel-series resonant networks have the same coil-to-coil efficiency when their secondary sides are the same, the series-parallel and parallel-parallel resonant networks have the same coil-to-coil efficiencies when their secondary sides are the same. The coil-to-coil power transfer efficiencies of four basic resonant compensation networks are summarized in Table 2-6.

Table 2-6. The coil-to-coil power transfer efficiency

Type	The coil-to-coil power transfer efficiency
SS and PS	$\frac{1}{1 + \frac{R_{rx}}{R_L} + \left(\frac{R_{rx} + R_L}{\omega_0 M}\right)^2 \frac{R_{tx}}{R_L}}$
SP and PP	$\frac{1}{1 + \frac{R_L}{Q_{rx}^2 R_{rx}} + \left(1 + \frac{R_L}{Q_{rx}^2 R_{rx}}\right)^2 \frac{R_{tx}}{a^2 R_L}}$

As shown in Table 2-6, when the primary coil, the secondary coil, the transfer distance, and the operating frequency are fixed, the mutual inductances, the ESRs and the quality factors are fixed, and the only term that affects the coil-to-coil power transfer efficiency is the load resistance R_L. The optimal loads for the maximum achievable coil-to-coil power transfer efficiencies are summarized in Table 2-7.

Table 2-7. The optimal loads for the maximum coil-to-coil power transfer efficiency

Type	The optimal load
SS and PS	$\sqrt{R_{rx}^2 + \frac{R_{rx}}{R_{tx}} \omega_0^2 M^2}$
SP and PP	$\sqrt{\frac{R_{tx}\, \omega_0^4\, L_{rx}^4}{R_{rx}\, M^2\, \omega_0^2 + R_{tx}\, R_{rx}^2}}$

From Table 2-7, it is easy to find that all optimal loads are independent of the primary coil self-inductance, and all of them increase with the operating frequency. With the optimal loads, the maximum achievable coil-to-coil power transfer efficiencies are summarized as shown in Table 2-8.

Table 2-8. The maximum coil-to-coil power transfer efficiency

Type	The maximum coil-to-coil efficiency
SS and PS	$\frac{1}{1 + 2 \times \frac{R_{tx} R_{rx}}{\omega_0^2 M^2} + 2 \times \sqrt{\frac{R_{tx}^2 R_{rx}^2}{\omega_0^4 M^4} + \frac{R_{tx} R_{rx}}{\omega_0^2 M^2}}}$
SP and PP	$\frac{1}{1 + 2 \times \frac{R_{tx} R_{rx}}{\omega_0^2 M^2} + 2 \times \sqrt{\frac{R_{tx}^2 R_{rx}^2}{\omega_0^4 M^4} + \frac{R_{tx} R_{rx}}{\omega_0^2 M^2}}}$

As shown in Table 2-8, the maximum coil-to-coil power transfer efficiencies are totally the same for all type of resonant topologies, therefore, the maximum achievable coil-to-coil efficiency is independent of the resonant topologies. In addition, it is also independent of the self-inductances of the primary coil and the secondary coil, there are only four factors that can affect the maximum achievable coil-to-coil power transfer efficiency: the primary coil ESR, the secondary coil ESR, the mutual inductance, and the operating frequency.

In conclusion, the maximum achievable coil-to-coil efficiency $\eta_{coil,\ max}$ is fundamentally determined by the efficiency factor $\frac{\omega_0^2 M^2}{R_{tx} R_{rx}}$, and increases with the efficiency factor, which is independent of the self-inductances and is not determined by k or Q independently, since k and Q are cross-coupled due to the self-inductances. Various methods, such as increasing the operating frequency and the number of turns, which can increase the efficiency factor will lead to a higher coil-to-coil maximum achievable efficiency.

A planar circular spiral coil as shown in Fig. 2-11 is evaluated via FEA to verify the coil-to-coil efficiency analytical calculation accuracy. The initial distance between the primary coil and the secondary coil is set as 300 mm. The coil radius is initialized as 600 mm, and the inter-turn distance is set as 13.525 mm. The initial operating frequency is set as 0.1 MHz. The transmitter coil and the receiver coil are set as the same. When the primary coil and the secondary coil are perfectly aligned, analytical calculation results based on the mutual inductance and coil ESRs analytical values, and FEA simulation results of the maximum achievable coil-to-coil efficiency with respect to the number of turns are compared in Fig. 2-27.

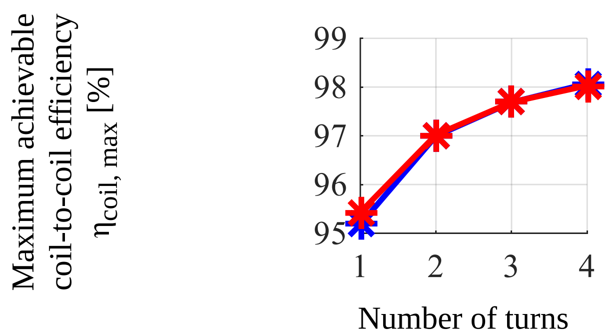

Test Conditions: * Analytical, * FEA.
TX and RX radii: 600mm. Inter-turn distance: 13.525mm. TX and RX vertical distance: 300 mm. Copper tubing: outside diameter 9.525 mm, wall thickness 0.8128 mm. Operating frequency: 0.1MHz. Output power: 3kW

Fig. 2-27. Comparison of analytical calculation results and FEA results of the maximum achievable coil-to-coil efficiency with respect to different number of turns

As shown in Fig. 2-27, the analytical results and the FEA results match with each other very well. The increase rate of $\eta_{coil,\ max}$ reduces as the number of turns increases mainly due to the proximity effect. That can be explained by the efficiency factor.

From previous sections, the primary coil self-inductance L_{tx} and its ESR R_{tx}, the secondary coil self-inductance L_{rx} and its ESR R_{rx}, and the mutual inductance M between the transmitter and receiver coils can be calculated using analytical calculation method under given operating frequency. Then the optimal load and the maximum coil-to-coil power transfer efficiency can be calculated based on Table 2-7 and Table 2-8, respectively. Under given specific output power, the transmitter and receiver coils currents and excitation voltages can be calculated with the system equivalent circuit model, which are necessary to calculate the air-gap center plane magnetic flux density and electric field intensity.

2.4 Analytical modeling of the air-gap center plane magnetic flux density

The magnetic field generated by a planar circular spiral coil with the number of turns N can be calculated by adding the magnetic field generated by each turn as

$$\vec{B}_N = \sum_{n=1}^{N} \vec{B}_n \tag{2.39}$$

The transmission line effect can be neglected since the winding characteristic length is much smaller than the wavelength, the magnetic field generated by each turn has the same phase. The magnetic field $\vec{B}_n$ generated by each turn can be transformed to the magnetic field generated by an equivalent circular current loop with average radius R, as shown in Fig. 2-28, which can be calculated by the magnetic vector potential $\vec{A}$ using [200][201]:

$$\vec{B}_n = \nabla \times \vec{A} \tag{2.40}$$

Where, $A_r = 0$, $A_\theta = 0$, $A_\phi(r, \theta) = \frac{\mu_0 I R}{4\pi} \int_{\varphi'=0}^{2\pi} \frac{\cos \varphi'}{\sqrt{R^2 + r^2 - 2 R r \sin\theta \cos\varphi'}} d\varphi'$, r, θ, and ϕ are spherical coordinates, I is the loop current.

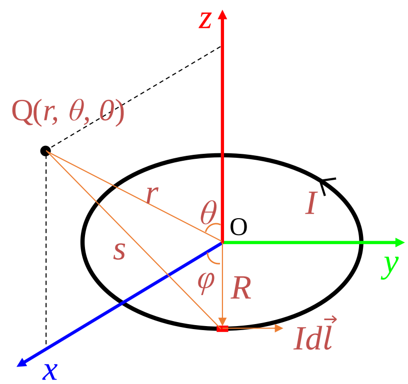

Fig. 2-28. Configuration of a single current loop

The magnetic flux density $\vec{B}$ at an arbitrary point T(r, θ, ϕ) can be calcula d as

$$\begin{bmatrix} B_r \\ B_\theta \\ B_\phi \end{bmatrix} = \begin{bmatrix} \dfrac{\hat{r}}{R^2 \sin\theta} & \dfrac{\hat{\theta}}{R \sin\theta} & \dfrac{\hat{\phi}}{R} \\ \dfrac{\partial}{\partial r} & \dfrac{\partial}{\partial \theta} & \dfrac{\partial}{\partial \phi} \\ A_r & r\,A_\theta & r\,A_\phi \sin\theta \end{bmatrix} = \begin{bmatrix} \dfrac{\cos\theta}{r \sin\theta} A_\phi + \dfrac{1}{r}\dfrac{\partial A_\phi}{\partial \theta} \\ -\dfrac{1}{r} A_\phi - \dfrac{\partial A_\phi}{\partial r} \\ 0 \end{bmatrix} \tag{2.41}$$

The magnetic flux density calculation results in the spherical coordinates can be transformed into the Cartesian coordinates using

$$\begin{bmatrix} B_x \\ B_y \\ B_z \end{bmatrix} = \begin{bmatrix} \sin\theta\cos\phi & \cos\theta\cos\phi & -\sin\phi \\ \sin\theta\sin\phi & \cos\theta\sin\phi & \cos\phi \\ \cos\theta & -\sin\theta & 0 \end{bmatrix} \begin{bmatrix} B_r \\ B_\theta \\ B_\phi \end{bmatrix} \tag{2.42}$$

When the measurement line is along x-direction as shown in Fig. 2-28, $\phi = 0$, $\sin(\phi) = 0$, considering $B_\phi = 0$, it's easy to get $B_y = 0$, which can also be explained by the symmetric property of the circular current loop. Since the circular current loop is symmetry with respect to the x-axis, the magnetic flux density y-components generated by the currents on the positive y-plane and negative y-plane will cancel each other, that leads to the magnetic flux density y-component along the x-direction zero, and the magnetic flux density x-component the same as the radial direction magnetic flux density in the cylindrical coordinates.

The air-gap center plane magnetic flux density is a vector combination of the magnetic fields generated by the transmitter and receiver coils as shown in Fig. 2-29.

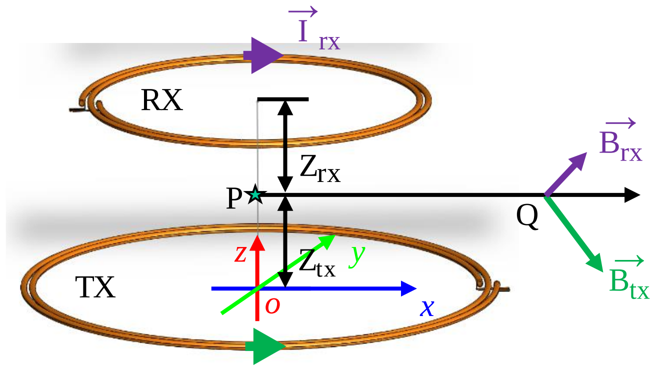

Fig. 2-29. Configuration of air-gap center plane magnetic flux density calculation

At the test point Q in the air-gap center plane along x-direction, the total magnetic flux density can be calculated as

$$\vec{B}_{total} = \vec{B}_{tx} + \vec{B}_{rx} = \begin{bmatrix} B_x \\ B_y \\ B_z \end{bmatrix}_{tx} + \begin{bmatrix} B_x \\ B_y \\ B_z \end{bmatrix}_{rx} = \begin{bmatrix} B_x \\ 0 \\ B_z \end{bmatrix}_{tx} + \begin{bmatrix} B_x \\ 0 \\ B_z \end{bmatrix}_{rx} \quad (2.43)$$

Where, $Z_{tx} = Z_{rx}$, which is half of the transfer distance.

Considering the circular winding magnetic field distributions along any radial directions are the same and the magnetic flux density along x-direction is the same as the radial direction magnetic flux density in the cylindrical coordinates since $B_y = 0$, the total magnetic flux density calculated along x-direction measurement line in the air-gap center plane is actually the magnetic flux density along any radial directions in the air-gap center plane, and the peak magnetic flux density along the calculated x-direction measurement line is the peak magnetic flux density in the whole air-gap center plane.

The magnetic flux density phase is fundamentally determined by the current phase, which should be paid special attention to since the transmitter current phase and the receiver current phase are not the same. In addition, tuning the current phase difference between the transmitter and the receiver provide an access to manipulate the air-gap magnetic field.

The air-gap center plane central point P is a special case since point P is the central symmetric point, which means the magnetic flux density x-component will also be zero at point

P, only the magnetic flux density z-component is nonzero. The magnetic flux density at point P can be calculated by

$$\vec{B}_P = \vec{B}_{z\_tx} + \vec{B}_{z\_rx} = \sum_{n=1}^{N_{tx}} \left[\frac{\mu_0}{2} \frac{\vec{I}_{txn} R_{txn}^2}{\left(Z_{tx}^2 + R_{txn}^2\right)^{3/2}} \right] + \sum_{n=1}^{N_{rx}} \left[\frac{\mu_0}{2} \frac{\vec{I}_{rxn} R_{rxn}^2}{\left(Z_{rx}^2 + R_{rxn}^2\right)^{3/2}} \right] \quad (2.44)$$

Where, N_{tx} is the transmitter number of turns, N_{rx} is the receiver number of turns, Z_{tx} and Z_{rx} are half of the transfer distance, R_{txn} is the average radius of the transmitter coil turn n, R_{rxn} is the average radius of the receiver coil turn n.

Based on the expression to calculate the magnetic flux density at the central point P, it's easy to find that the magnetic flux density at the central point P will reduce when the coil radius increases, then the air-gap center plane peak magnetic flux density may be not located at the central point due to the leakage flux.

The developed analytical method to calculate the air-gap center plane magnetic flux density is verified by FEA simulation. The transmitter and the receiver are set as the same, the number of turns is 1, the coil radius is 600 mm, the transfer distance is 300 mm, and the operating frequency is 0.1 MHz. When the output power is 3 kW under aligned condition, the magnetic field distribution in the XOZ plane is shown in Fig. 2-30 (a), the analytical calculation results of the magnetic flux density along the measurement line is compared with the FEA result in Fig. 2-30 (b).

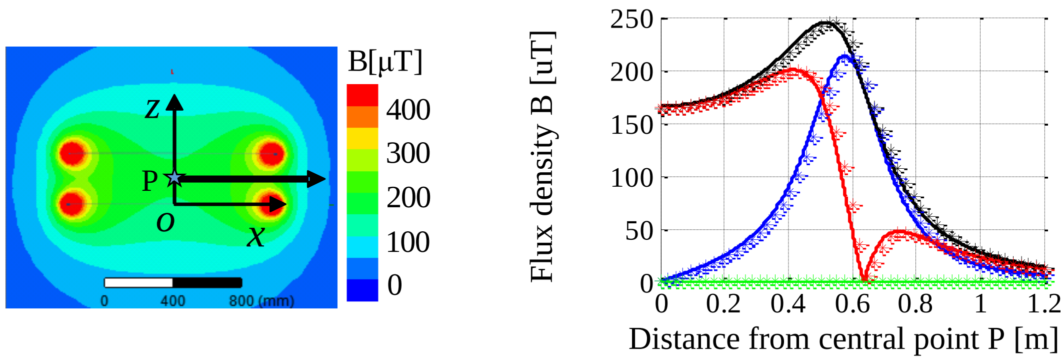

(a) Magnetic field distribution in the XOZ plane

(b) Magnetic flux density along the measurement line

Analytical results: — B_{total}, — B_x, — B_y, — B_z
FEA results: * B_{total}, * B_x, * B_y, * B_z

Test conditions: Operating frequency: 0.1 MHz. Output power: 3 kW. Transmitter and receiver: Number of turns N: 1. Coil radii R: 600 mm. Transfer distance: 300 mm

Fig. 2-30. Comparison of the analytical results and FEA results of the air-gap center plane magnetic flux density

As shown in Fig. 2-30 (a), the peak magnetic flux density is located around the coil edge due to the leakage flux. According to Fig. 2-30 (b), the developed analytical model for the air-gap center plane magnetic flux density agrees with the FEA result. Along the measurement line in the x-direction, the y-component magnetic flux density is zero due to the symmetry along the x-axis. At the central point, the magnetic flux density x-component is also equal to zero since the central point is the central symmetry point of the circular winding. The air-gap center plane peak magnetic flux density is located at a distance almost equal to the coil radius, rather than the central point, due to the leakage flux. When the coil radius is small, the air-gap center plane peak magnetic flux density will be located at the central point.

The effect of the number of turns on the air-gap center plane peak magnetic flux density B_{agcppk} is evaluated, and the analytical results and FEA results are compared in Fig. 2-31.

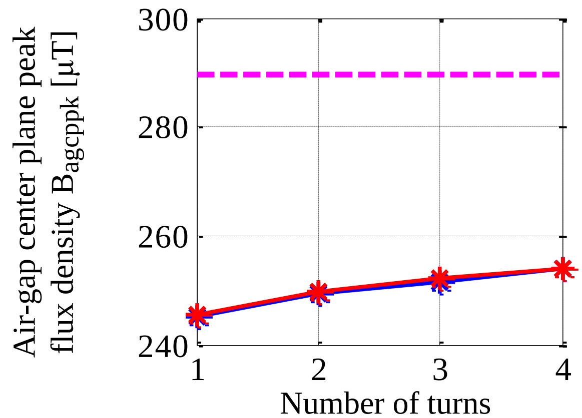

* Analytical, * FEA, - - IEEE C95.1-2005 general public exposure safety limit

Test Conditions: Operating frequency: 0.1 MHz. Transfer distance: 300 mm. TX and RX radii: 600 mm. Inter-turn distance: 13.525 mm. Output power: 3 kW

Fig. 2-31. Effect of the number of turns on the air-gap center plane peak magnetic flux density

As shown in Fig. 2-31, B_{agcppk} increases slightly with the number of turns, although the required coil currents increase with the number of turns, the magnetomotive force (MMF) N*I increases to output 3 kW as shown in Table 2-9, which leads to the higher magnetic flux density even under the same coil configuration.

Table 2-9. The magnetomotive forces of the transmitter and receiver coils

MMF	N = 1	N = 2	N = 3	N = 4
Transmitter coil (N_{tx}*I_{tx}) [A]	120.9178	122.9134	124.1625	125.4332
Receiver coil (N_{rx}*I_{rx}) [A]	118.8909	121.5192	122.8089	124.4424

Besides the increase of the MMF, the coil average radius increases as the number of turns increases, since the winding outer radius remains the same and the inter-turn distance is nonzero. In addition, the winding with small inter-turn distance has much more severe proximity effect loss as shown by the increase of the proximity effect factor, which will reduce the coil-to-coil power transfer efficiency. It's easy to see that the surface spiral winding, that maintains an equal diameter per turn and low proximity effect loss by the special twisting pattern, is a good winding configuration to reduce the effect of the number of turns on B_{agcppk}.

Last but not the least, when the operating frequency increases, the required current to transfer the same amount of power will reduce, and the terminal excitation voltage will increase, then the air-gap magnetic field will reduce, but the air-gap electric field will increase, which needs special attention.

2.5 Analytical modeling of the air-gap center plane electric field intensity

The electric field generated by a planar circular spiral coil is a vector combination of the excitation terminal electric field and the differential of the magnetic vector potential as [200][201]

$$\vec{E} = -\nabla\Phi - \frac{\partial\vec{A}}{\partial t} \tag{2.45}$$

According to the literature review, the electrostatic potential at an arbitrary point T(r, θ, ϕ) in the spherical coordinates for a current loop with an excitation voltage V, as shown in Fig. 2-32, is given by

$$\Phi(r, \theta, \varphi) = \frac{\lambda}{4\pi\varepsilon_0} \int_{\varphi' = 0}^{2\pi} \frac{(\varphi' - \pi)\, d\varphi'}{\sqrt{R^2 + r^2 - 2\, R\, r \sin\theta \cos(\varphi - \varphi')}} \tag{2.46}$$

Where $\lambda = V\, \varepsilon_0\, R / \ln(R/r_0)$, r_0 is the radius of the conductor.

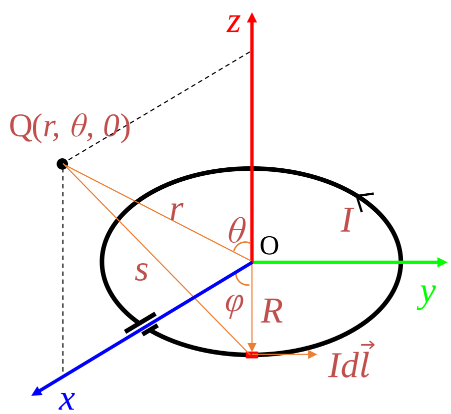

Fig. 2-32. Configuration of a current loop with an excitation voltage

In the Cartesian coordinates, the electrostatic potential can be expressed as

$$\Phi(x, y, z) = \frac{\lambda}{4\pi\varepsilon_0} \int_{\varphi' = 0}^{2\pi} \frac{(\varphi' - \pi)\, d\varphi'}{\sqrt{R^2 + x^2 + y^2 + z^2 - 2\, R\, x \cos\varphi' - 2\, R\, y \sin\varphi'}} \tag{2.47}$$

Then the electric field intensity $\vec{E}_V(x, y, z)$ caused by the excitation terminal can be calculated as

$$\vec{E}_V(x,y,z) = -\nabla\Phi = \frac{\lambda}{4\pi\varepsilon_0} \int_{\varphi' = 0}^{2\pi} \frac{(\varphi' - \pi)\left[(x - R\cos\varphi')\, \hat{x} + (y - R\sin\varphi')\, \hat{y} + z\, \hat{z}\right]}{(R^2 + x^2 + y^2 + z^2 - 2\, R\, x \cos\varphi' - 2\, R\, y \sin\varphi')^{3/2}}\, d\varphi' \tag{2.48}$$

Considering the excitation directions of the transmitter and receiver terminals are along y-direction from the input side to the output side, the terminal electric fields will only have y-component, therefore, the electric field intensity due to the terminal excitation voltage in the air-gap center plane along the measurement line in x-direction will also only have y-component E_{Vy}, $E_{Vx} = E_{Vz} = 0$. In addition, E_{Vy} is proportional to the terminal excitation voltage V.

The induced electric field $\vec{E}_A$ caused by the magnetic vector potential $\vec{A}$ can be calculated by

$$\vec{E}_A = -\frac{\partial \vec{A}}{\partial t} \tag{2.49}$$

Considering that along the measurement line in x-direction as shown in Fig. 2-32, $A_r = 0$, $A_\theta = 0$, and $A_\phi(r, \theta) = \frac{\mu_0 I R}{4\pi} \int_{\varphi'=0}^{2\pi} \frac{\cos \varphi'}{\sqrt{R^2 + r^2 - 2 R r \sin \theta \cos \varphi'}} d\varphi'$, which has only one variable that changes with time, the current I, therefore, $E_{Ar} = 0$, $E_{A\theta} = 0$, $E_{A\phi} = -\omega_0 A_\phi$, which is proportional to the operating frequency.

The electric field intensity calculation results in the spherical coordinates can be transformed into the Cartesian coordinates using

$$\begin{bmatrix} E_{Ax} \\ E_{Ay} \\ E_{Az} \end{bmatrix} = \begin{bmatrix} \sin\theta\cos\phi & \cos\theta\cos\phi & -\sin\phi \\ \sin\theta\sin\phi & \cos\theta\sin\phi & \cos\phi \\ \cos\theta & -\sin\theta & 0 \end{bmatrix} \begin{bmatrix} E_{Ar} \\ E_{A\theta} \\ E_{A\phi} \end{bmatrix} \tag{2.50}$$

When the measurement line is along x-direction as shown in Fig. 2-32, $\phi = 0$, $\sin(\phi) = 0$, considering $E_{Ar} = 0$ and $E_{A\theta} = 0$, therefore, $E_{Ax} = 0$, $E_{Ay} = E_{A\phi}$, and $E_{Az} = 0$.

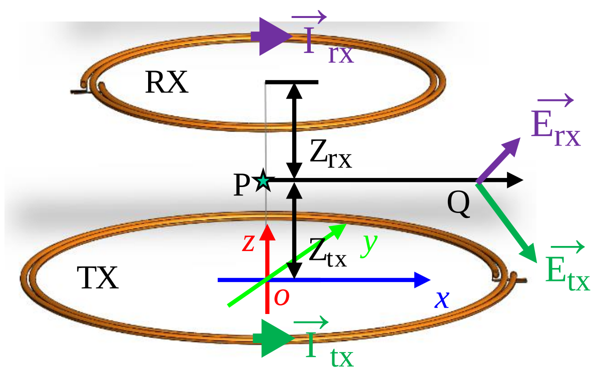

Fig. 2-33. Configuration of air-gap center plane electric field intensity calculation

The air-gap center plane electric field density is a vector combination of the electric fields generated by the transmitter and receiver coils as shown in Fig. 2-33. The transmitter terminal and the receiver terminal are placed at opposite positions to balance the air-gap center plane electric field distribution. At the test point Q in the air-gap center plane along x-direction, the total electric field intensity can be calculated as

$$\vec{E}_{total} = \vec{E}_{tx} + \vec{E}_{rx} = -\nabla\Phi_{tx} - \frac{\partial \vec{A}_{tx}}{\partial t} - \nabla\Phi_{rx} - \frac{\partial \vec{A}_{rx}}{\partial t} \tag{2.51}$$

Considering that $E_{Vx} = E_{Vz} = 0$ and $E_{Ax} = E_{Az} = 0$, the total electric field intensity in the air-gap center plane along the measurement line in x-direction will also only has y-component, which can be simplified into

$$\vec{E}_{total} = \vec{E}_{tx} + \vec{E}_{rx} = \begin{bmatrix} 0 \\ E_{Vy} + E_{Ay} \\ 0 \end{bmatrix}_{tx} + \begin{bmatrix} 0 \\ E_{Vy} + E_{Ay} \\ 0 \end{bmatrix}_{rx} \tag{2.52}$$

In the air-gap center plane, the induced electric field caused by the high frequency AC magnetic field is the same along any radial directions since the magnetic vector potential remains the same along any radial directions, therefore, the electric field caused by the terminal excitation voltage determines the location of the air-gap center plane peak electric field intensity E_{agcppk}. Considering the electric field around the excitation terminal is fundamentally a decay field, the electric field intensity is determined by the distance between the measurement point and the excitation terminal, so the peak electric field intensity along the measurement line going above the transmitter terminal and below the receiver terminal, as shown in Fig. 2-33, can be treated as the air-gap center plane peak electric field intensity E_{agcppk}.

The developed analytical method to calculate the air-gap center plane electric field intensity is verified by FEA simulation. The transmitter and the receiver are set as the same, the number of turns is 1, the coil radius is 600 mm, and the transfer distance is 300 mm, the operating frequency is 0.1 MHz. When the output power is 3 kW under the aligned condition, the electric field distribution in the XOZ plane is shown in Fig. 2-34 (a), the analytical calculation results of the electric field intensity along the measurement line is compared with the FEA result in Fig. 2-34 (b).

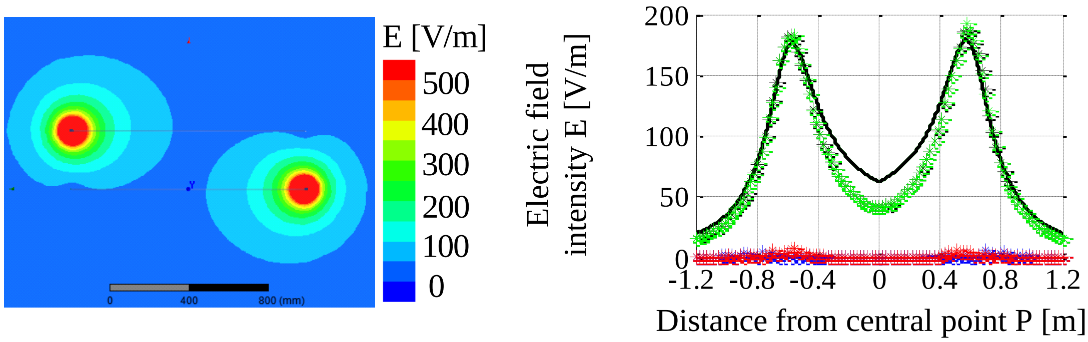

(a) Electric field distribution in the XOZ plane

(b) Electric field intensity along the measurement line

Analytical results: — E_{total}, — E_x, — E_y, — E_z

FEA results: * E_{total}, * E_x, * E_y, * E_z

Test conditions: Operating frequency: 0.1 MHz. Output power: 3 kW. Transmitter and receiver: Number of turns N: 1. Coil radii R: 600 mm. Transfer distance: 300 mm

Fig. 2-34. Comparison of the analytical results and FEA results of the air-gap center plane electric field intensity

As shown in Fig. 2-34 (a), the air-gap electric field is mainly caused by the terminal excitation voltage, placing the transmitter terminal and the receiver terminal at opposite positions are helpful to balance the electric field distribution and reduce the air-gap center plane peak electric field intensity. According to Fig. 2-34 (b), the developed analytical model for the air-gap center plane electric field intensity agrees with the FEA result. Along the measurement line in the x-direction, only the y-component electric field intensity is nonzero, which follows previous theoretical analyses. The air-gap center plane peak electric field intensity is located at a distance almost equal to the coil radius due to the terminal electric field.

The effect of the number of turns on the air-gap center plane peak electric field intensity is evaluated, and the analytical results and FEA results with respect to the number of turns are compared in Fig. 2-35.

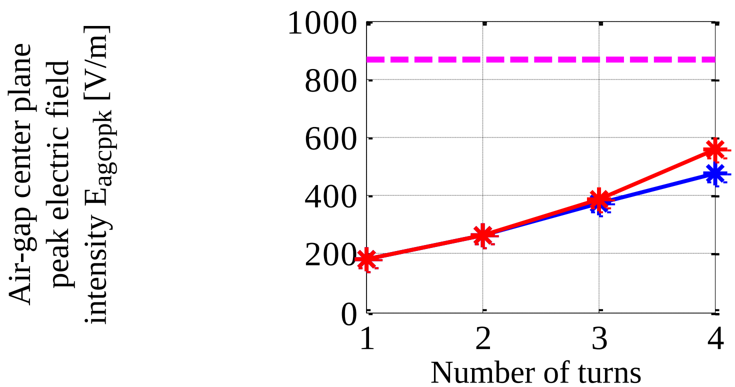

* Analytical, * FEA, - - IEEE C95.1-2005 general public exposure safety limit

Test Conditions: Operating frequency: 0.1 MHz. Transfer distance: 300 mm. TX and RX radii: 600 mm. Inter-turn distance: 13.525 mm. Output power: 3 kW

Fig. 2-35. Effect of the number of turns on the air-gap center plane peak electric field intensity

As shown in Fig. 2-35, E_{agcppk} increases almost linearly with the number of turns N due to the increase of the terminal excitation voltage V, since the self-inductance L is proportional to N^2, and $V \propto \omega_0 \times L \times I \propto \omega_0 \times N^2 \times I \propto \omega_0 \times N \times B$. Even though B remains the same, V still increases linearly with the number of turns N under the same operating frequency. From $V \propto \omega_0 \times N \times B$, it's easy to get the conclusion that E_{agcppk} increases as the operating frequency increases, the number of turns increases, and the magnetic flux density increases.

2.6 Summary

At the beginning, through the fair comparison of circular winding, square winding, rectangular winding, double-square winding, and double-D winding under the same test conditions, the circular winding is identified as the suitable configuration for loosely coupled inductive WPT system which can achieve the lowest air-gap center plane peak magnetic flux density and the lowest air-gap center plane peak electric field intensity while maintaining a high coil-to-coil efficiency. Besides that, the effect of the terminal clearance on the air-gap electric field intensity is also investigated, the terminal clearance affects the electric field that is very close to the excitation terminal and does not affect the air-gap center plane electric field intensity due to large transfer distance.

In the next section, based on the coil geometry and given operating frequency, the analytical methods to calculate the winding electrical parameters, such as the self- and mutual inductances, and the ESRs, are investigated. The loosely coupled inductive WPT system equivalent circuit model including the power converter, the transmitter coil, the receiver coil, and the rectifier is presented. According to the coil-to-coil efficiency analyses, the maximum achievable coil-to-coil efficiency $\eta_{coil,\ max}$ is fundamentally determined by the efficiency factor $\frac{\omega_0^2 M^2}{R_{tx} R_{rx}}$, and increases with the efficiency factor, which is independent of the self-inductances and is not determined by k or Q independently, since k and Q are cross-coupled due to the self-inductances. Various methods, such as increasing the operating frequency and the number of turns, which can increase the efficiency factor can be used to improve the coil-to-coil efficiency.

Furthermore, the analytical methods to calculate the air-gap center plane magnetic flux density and electric field intensity for the loosely coupled inductive WPT system are developed, which are necessary to develop the system general design methodology satisfying the magnetic field and electric field safety limits when transferring multi-kW. The air-gap magnetic field and electric field are vector combination of the magnetic field and electric field generated by the transmitter coil and the receiver coil, respectively.

According to the analysis of the air-gap center plane magnetic field distribution, the air-gap center plane peak magnetic flux density is not always located at the central point due to the leakage flux. When the number of turns increases, the air-gap center plane peak magnetic flux density increases due to the reduction of the average coil radius and the increase of the magneto-motive forces.

From the analysis of the air-gap center plane electric field, the air-gap electric field is caused by two parts: the coil terminal excitation voltage and the AC magnetic field. Placing the transmitter coil terminal and the receiver coil terminal at opposite positions can balance the air-gap electric field distribution. The air-gap center plane peak electric field intensity is located at a distance almost equal to the coil radius due to the coil terminal excitation voltage. In addition, the air-gap center plane peak electric field intensity increases when the operating frequency increases, the number of turns increases, and the magnetic flux density increases due to the increments of the required coil terminal excitation voltage and the induced electric field by the AC magnetic field.

Chapter 3 Multi-kW Loosely Coupled Inductive Wireless Power Transfer System Design Methodologies

3.1 Introduction

This chapter begins with identifying general design variables based on the design requirements, then the multi-kW loosely coupled inductive WPT system general design methodology is developed based on the identified general design variables, the effects of the general design variable are investigated. After that, through emulating the 3D printed SSW, the copper tubing SSW is proposed to reduce the dielectric losses and the spatial voltage stress, surface spiral parallel winding and surface spiral antiparallel winding are proposed to reduce the ESR and equalize the spatial voltage stress. At last, a case study using the proposed design methodology is used to experimentally test the air-gap center plane magnetic field and electric field distributions, and the DC-to-DC efficiency when transferring multi-kW under aligned and misaligned conditions.

3.2 Loosely coupled inductive WPT system general design methodology

In this section, the general design variables are identified based on the design requirements, then the multi-kW loosely coupled WPT system general design methodology is developed to satisfy the air-gap center plane magnetic field and electric field safety limit. After that, the effects of the design variables on the air-gap center plane peak magnetic flux density and peak electric field intensity, and the coil-to-coil power transfer efficiency are investigated.

3.2.1 Design requirements

- **Low magnetic flux density and low electric field intensity**

Since the WPT systems will be used in our daily life, the system must be safe for animals and human beings. In Chapter 1.2, the international regulations for the human body RF exposure are reviewed. The nerve and muscle electro-stimulation and tissue heating are major issues. The level of electrostimulation is critical at below 5 MHz operating frequency, while the tissue heating issue must be taken into consideration when the operating frequency is higher than 100 kHz, since it will have detrimental health effects if the sensitive tissues and organs have more than 1 °C rise in temperature. It should be noted that electrostimulation happens instantly, while tissue and whole-body heating requires time, the human and animal bodies can be treated as a water-cooled system because of the blood circulation. Compared with the IEEE C95.1-2005 safety standard, the ICNIRP standards are widely considered too conservative, in addition, there is no health report saying that the IEEE C95.1-2005 standard is not safe. Even though using the IEEE C95.1-2005 safety standard as the reference, to the best knowledge of the author, there are no multi-kW WPT system designs that satisfy the magnetic field and electric field electrostimulation and tissue heating safety limits simultaneously in the air-gap center region. The air-gap center region magnetic flux density of the existing multi-kW systems operating at a low frequency, such as 20 kHz, is greater than 1 mT, which is much higher than the regulations and doesn’t satisfy the electrostimulation safety limit. Although the air-gap center region magnetic flux density of the existing multi-kW systems operating at MHz frequency, such as 3.7 MHz, satisfies the electrostimulation safety limit, the tissue heating safety limit is not taken into consideration, in addition, the air-gap center region electric field intensity doesn’t satisfy the electrostimulation safety limit. Such high magnetic flux density and electric field intensity will cause severe injuries to human beings and animals. The safety issue must be the primary concern in the design of a loosely coupled inductive wireless EV battery charger. In this research, the design methodologies that can satisfy the magnetic field and electric field electrostimulation and tissue heating safety limits simultaneously when transferring multi-kW are proposed for the loosely coupled inductive WPT system.

- **High efficiency**

It is important that the power transfer efficiency from the grid to the battery must be very high and it must be comparable to the efficiency of the wired (plug-in) chargers. Not only the power converter but also the coil-to-coil efficiency must be as high as possible. The power converter efficiency can be improved by using soft switching techniques. As demonstrated in Chapter 2.3.4, the maximum achievable coil-to-coil efficiency is fundamentally determined by the efficiency factor $\frac{\omega_0^2 M^2}{R_{tx} R_{rx}}$, and increases with the efficiency factor, which is independent of the self-inductances and is not determined by k or Q independently. Under given operating frequency, design methods that can improve the mutual inductance and reduce the winding ESR will improve the maximum coil-to-coil efficiency. Besides that, the effects of the design methods and the operating frequency on the air-gap center plane peak magnetic flux density and peak electric field intensity need special attention.

- **Low voltage-current ratings**

When transferring multi-kW, the voltage-current ratings of the coils will affect the selection of power devices and circuit topologies. Although the transmitted real power is the same in many designs, required reactive power and voltage-current ratings of the coils can be different depending on the circuit topologies. Proposer circuit design can minimize the voltage-current ratings of the coils and the power devices.

- **Low total mass**

Low copper mass and low magnetic shield mass are essential to reduce the manufacturing cost and installation, especially the receiver side installing under the vehicle. The total mass of the WPT systems will be evaluated in the design stage.

3.2.2 Design assumptions

In this research, there are several assumptions that are made to develop the design methodologies. First, the feasible design space for the transmitter coil and the receiver coil is assumed to be given by the application. For stationary EV battery chargers, the circular transmitter and receiver sizes are limited by the width of the vehicle. The maximum diameter of the transmitter and receiver is limited by 1600 mm based on normal vehicle width excluding the wheel space. Second, it is assumed the power transfer distance is given by the target application. In case of stationary EV battery charger, the power transmission distance is from the earth to the bottom of the vehicle. The normal ground clearance is from 150 mm to 250 mm, considering the transmitter can be buried in the ground, the transfer distance between the transmitter and the receiver is assumed as from 150 mm to 300 mm. Third, rated output power and receiver coil voltage are given in the design process, the lithium-ion battery voltage is in 200 V to 500 V in electric vehicles, the rated output power is assumed as 3 kW, which can be extended to higher power level based on the power scaling laws.

3.2.3 Design variables identification

According to the analyses in Chapter 2, the air-gap center plane peak magnetic flux density and peak electric field intensity are determined by the coil radius, the number of turns, the inter-turn distance, the transfer distance, and the operating frequency, therefore, these five variables are selected as the general design variables and must be determined by the design methodology to satisfy the magnetic and electric field safety limits when transferring the desired power, which is selected to 3 kW in this research.

3.2.4 System general design methodology

Using the analytical calculation methods developed in Chapter 2, the loosely coupled inductive WPT system general design methodology is demonstrated via an example using planar circular spiral winding to achieve low air-gap center plane magnetic flux density and low air-gap center plane electric field intensity while maintaining a high power transfer efficiency. The proposed general design methodology flowchart is shown in Fig. 3-1.

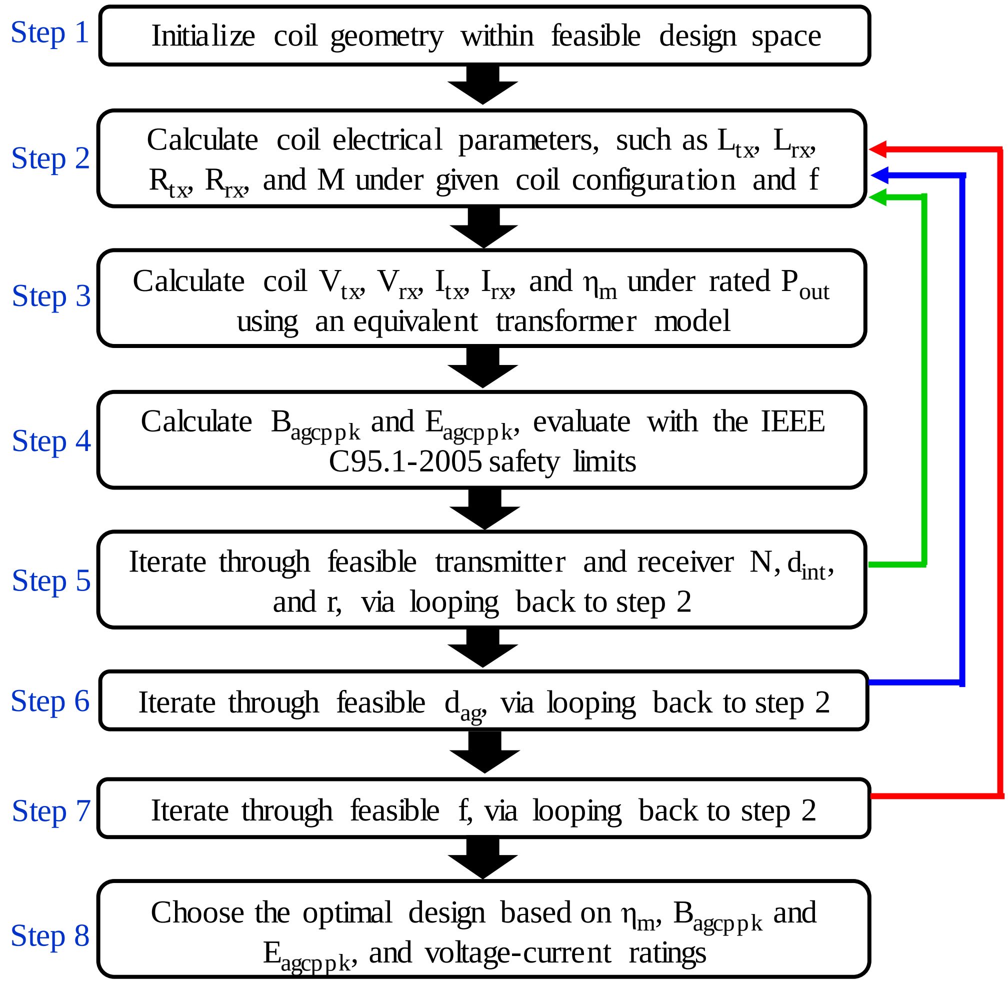

Fig. 3-1. Flow chart for proposed general design methodology

Step 1: Initialize coil geometry within feasible design space

Copper tubing is selected to build the transmitter and the receiver. According to the FEA comparison results, a copper tubing with an outside diameter 3/8'' (9.525 mm) and wall thickness 0.032'' (0.8128 mm) is selected due to its low skin effect AC resistance and easy ability to bend. Using copper tubing can simplify the FEA simulation compared with the Litz-wire. Litz-wire has specific operating frequency range to reduce the skin effect and the proximity effect. When the actual operating frequency is higher than the Litz-wire operation frequency range, its ESR will increase significantly due to the proximity effect. In the general design methodology, the operating frequency is a general design variable, and the characteristics of the copper tubing over a wide operating frequency range are much more stable compared with the

Litz-wire. In the final stage, when the operating frequency is selected, the suitable Litz-wire can be used to improve the power transfer efficiency.

The inter-turn distance 2c is set as 13.525 mm. The transfer distance between the transmitter and the receiver is set as 300 mm. Both numbers of turns are initialized as 1. Initial coil radii are selected as 600 mm, which is much smaller than normal vehicle chassis width. The transmitter and the receiver are set as the same at first to simplify the calculation.

Step 2: Calculate winding electric parameters, such as the self-inductances, the mutual inductances, and the ESRs under given winding configuration and operating frequency

The initial operating frequency is chosen as 0.1 MHz based on the IEEE C95.1-2005 safety standard. Below 0.1 MHz, electrostimulation is the only safety concern. Above 0.1 MHz, tissue heating needs to be taken into consideration in addition to the electrostimulation, and tissue heating safety limit reduces as the operating frequency increases. The self-inductances, mutual inductances, and AC resistances of the transmitter and the receiver can be calculated based on the analytical methods developed in Chapter 2.3.1 and Chapter 2.3.2, respectively.

Step 3: Calculate the coil-to-coil power transfer efficiency, voltages, and currents under rated power using an equivalent transformer model

A resonant compensation network is required for loosely coupled WPT system to achieve high efficiency. According to the analyses in Chapter 2.3.4, the maximum achievable coil-to-coil efficiency is independent of the resonant compensation topologies, only the optimal loads are different under different resonant topologies. Based on the system equivalent models developed in Chapter 2.3.3 and Chapter 2.3.4, the required coil excitation voltages, currents, and the coil-to-coil power transfer efficiency under the rated output power 3 kW and given load can be calculated accurately, which lays a foundation to calculate the air-gap center plane magnetic flux density and electric field intensity in the next step. The power converter loss, the rectifier loss, and the resonant capacitors losses are not taken into consideration in this design methodology due to their nonlinear properties.

Step 4: Calculate the air-gap center plane magnetic flux density and the air-gap center plane electric field intensity, evaluate with the IEEE C95.1-2005 safety standard

Using the required coil currents and excitation voltages calculated from step 3, and the air-gap center plane magnetic flux density and electric field intensity analytical models developed in Chapter 2.4 and 2.5, the air-gap center plane peak magnetic flux density and peak electric field intensity can be calculated accurately.

From the analyses in Chapter 2.4 and 2.5, the air-gap center plane peak magnetic flux density and peak electric field intensity are affected by the general design variables: the coil radius, the number of turns, the inter-turn distance, the transfer distance, and the operating frequency, therefore, it's necessary to iterate through the general design variables to identify the valid design, general design guidelines will be presented in the following sections by analyzing the effects of the general design variables.

Step 5: Iterate through feasible transmitter and receiver coils number of turns, coil radii, and inter-turn distance, via looping back to step 2

During the iteration process, the transmitter and receiver coils number of turns vary from 1 to 7, the coil radii increase from 300 mm to 800 mm with step 50 mm, two inter-turn distances 10.525 mm and 13.525 mm are compared to identify the effects of the inter-turn distance. All iterations are calculated under two operating frequencies: 0.1 MHz and 0.5 MHz. Under 0.5 MHz, the tissue heating magnetic and electric field safety limits must be taken into consideration in addition to the electrostimulation safety limits.

Step 6: Iterate through feasible transfer distance, via looping back to step 2

During the iteration process, the transfer distance between the transmitter and the receiver increases from 150 mm to 400 mm with step 50 mm to identify the effects of the transfer distance on magnetic and electric field distributions, and power transfer efficiency.

Step 7: Iterate through feasible operating frequency, via looping back to step 2

The widely used operating frequencies for inductive WPT systems are 20 kHz, 85 kHz, 100 kHz, 1 MHz, 6.78 MHz, and 13.56 MHz. The feasible operating frequency range is identified as from 0.05 MHz to 10 MHz. During the iteration process, the operating frequency increases from 0.05 MHz to 10 MHz with step 0.05 MHz identify the effects of the operating frequency with respect to the power transfer efficiency, the air-gap center plane peak magnetic flux density and electric field intensity, and the safety standards.

Step 8: Choose the optimal design based on the power transfer efficiency, the air-gap center plane peak magnetic flux density and peak electric field intensity, and voltage-current ratings

After previous steps, feasible designs that satisfy the magnetic field and electric field safety limits, power transfer efficiency, and voltage-current rating requirements could be found, a multi-objective optimal function can be created to balance all considerations with different weighting coefficients, the optimal one can be selected based on practical applications.

3.2.5 Effects of the number of turns and the operating frequency

In the test example to evaluate the effects of the number of turns and the operating frequency, the transmitter and the receiver outer coil radii are chosen as 600 mm, the inter-turn distance is initialized as 13.525 mm, the transfer distance is picked as 300 mm, the number of turns increases from 1 to 7 with step 1, two operating frequencies 0.1 MHz and 0.5 MHz are used to do a simple comparison. When the output power is 3 kW, the effects of the number of turns and the operating frequency on the maximum achievable coil-to-coil efficiency $\eta_{coil,\ max}$, the air-gap center plane peak magnetic flux density B_{agcppk} and peak electric field intensity E_{agcppk} are plotted in Fig. 3-2. The IEEE C95.1-2005 safety limits in rms values are transformed into peak values by multiplying $\sqrt{2}$ considering the currents and the voltages are sinusoidal waves.

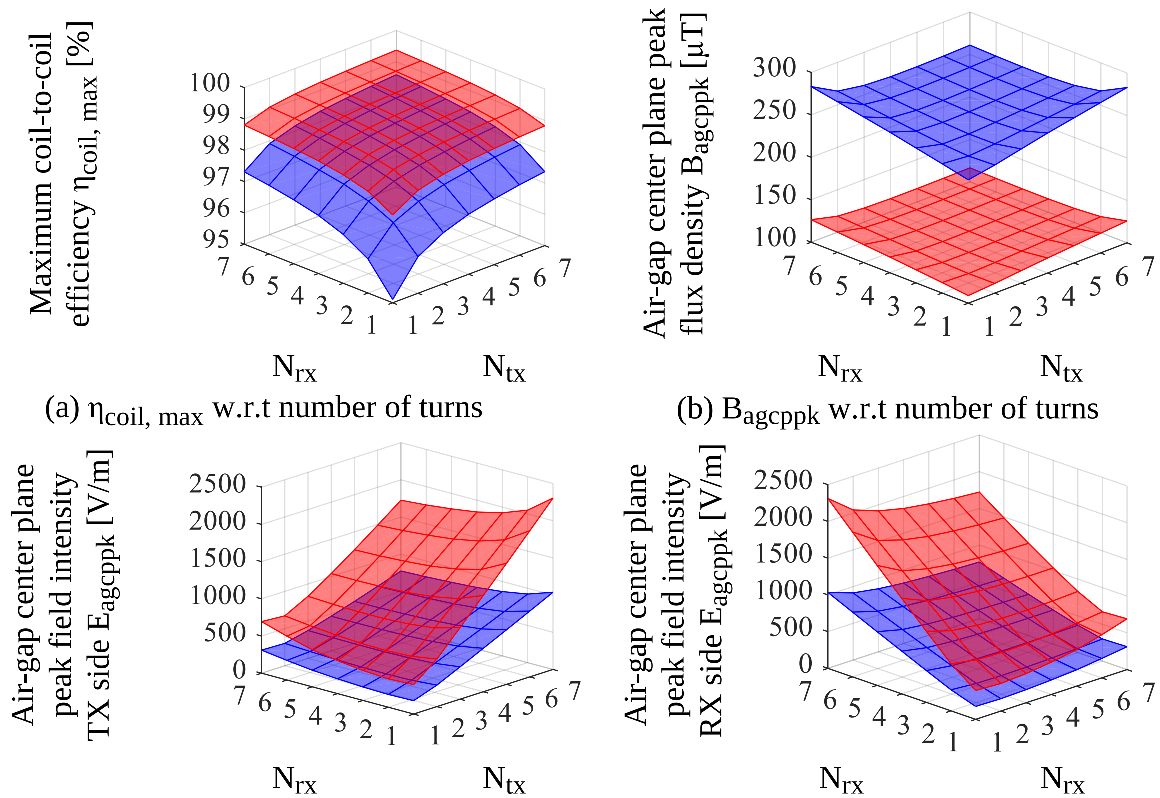

(a) $\eta_{coil,\ max}$ w.r.t number of turns (b) B_{agcppk} w.r.t number of turns

(c) TX side E_{agcppk} w.r.t. number of turns (d) RX side E_{agcppk} w.r.t. number of turns

Test Conditions: output power 3 kW, operating frequency 0.1 MHz and 0.5 MHz.
Transmitter (TX) and receiver (RX): coil outer radius 600 mm, inter-turn distance 13.525 mm, transfer distance 300 mm.
IEEE C95.1-2005 standard: magnetic field electrostimulation safety limit (Peak) 289 μT @ 0.1 MHz and 289 μT @ 0.5 MHz, magnetic field tissue heating safety limit (Peak) 289 μT @ 0.1 MHz and 57 μT @ 0.5 MHz, electric field combined safety limits (Peak): 868 V/m @ 0.1 MHz and 868 V/m @ 0.5 MHz.

Fig. 3-2. Effects of the number of turns and operating frequency on the maximum coil-to-coil efficiency, the air-gap center plane peak magnetic flux density and peak electric field intensity

As shown in Fig. 3-2 (a), under 0.1 MHz and 0.5 MHz, when the number of turns increases, the maximum achievable coil-to-coil efficiency $\eta_{coil,\ max}$ increases, because the mutual inductance increase rate is higher than the ESR increase rate, which lead to the increase of the efficiency factor $\frac{\omega_0^2 M^2}{R_{tx} R_{rx}}$. Besides that, $\eta_{coil,\ max}$ increase rate reduces as the number of turns increases due to the proximity effect, therefore, as the number of turns keeps increasing, $\eta_{coil,\ max}$ may reduce instead of increasing due to the ESR increase caused by the proximity effect. Compared with operating at 0.1 MHz, $\eta_{coil,\ max}$ is higher under 0.5 MHz due to the increase of the efficiency factor caused by the operating frequency.

According to Fig. 3-2 (b), under 0.1 MHz and 0.5 MHz, when the number of turns increases, B_{agcppk} increases due to the increase of the magnetomotive force and the reduction of the average coil radius. Compared with operating at 0.1 MHz, B_{agcppk} is much lower under 0.5 MHz, since the required coil excitation currents are reduced to transfer the same amount of power as the operating frequency increases. When considering the tissue heating safety limit, the magnetic field tissue heating safety limit under 0.5 MHz is 5 times lower than the safety limit under 0.1 MHz. It's easier to satisfy the magnetic field electrostimulation safety limit when increasing the operating frequency, however, it's not easy to satisfy the magnetic field tissue heating and electric field safety limits under high operating frequency.

The transmitter and the receiver terminals are placed at opposite positions to balance the air-gap electric field distribution, so E_{agcppk} is evaluated along the transmitter side and the receiver side as shown in Fig. 3-2 (c) and (d). Under 0.1 MHz and 0.5 MHz, E_{agcppk} increases when the number of turns increases, because the required terminal excitation voltage increases mainly caused by the increase of the self-inductance. Besides that, the induced electric field also increases as the magnetic flux density increases with the number of turns. Compared with operating at 0.1 MHz, E_{agcppk} is much higher under 0.5 MHz, since the required coil excitation voltages increase to transfer the same amount of power as the operating frequency increases and the induced electric field is proportional to the operating frequency. Although the electric field combined safety limits remain the same until 1.34 MHz, it's difficult to satisfy the electric field combined safety limits under high operating frequency with a large number of turns.

When operating at low frequency (below 0.1 MHz) and pushing to transfer higher power level, the air-gap center plane magnetic flux density, rather than the electric field intensity, will first meet the safety limit. When operating at high frequency (above 0.1 MHz), both the magnetic field tissue heating safety limit and electric field safety limit must be taken into consideration. It's a tradeoff between the magnetic field and the electric field to transfer to higher power level.

3.2.6 Effects of the coil radii and the inter-turn distance

In the test example to evaluate the effect of the coil radii on B_{agcppk}, the transmitter and the receiver numbers of turns are set as 1, the transfer distance is picked as 300 mm, the coil radii increase from 300 mm to 800 mm with step 50 mm, two operating frequencies 0.1 MHz and 0.5 MHz are used to do a simple comparison. When the output power is 3 kW, the analytical calculation result is plotted in Fig. 3-3.

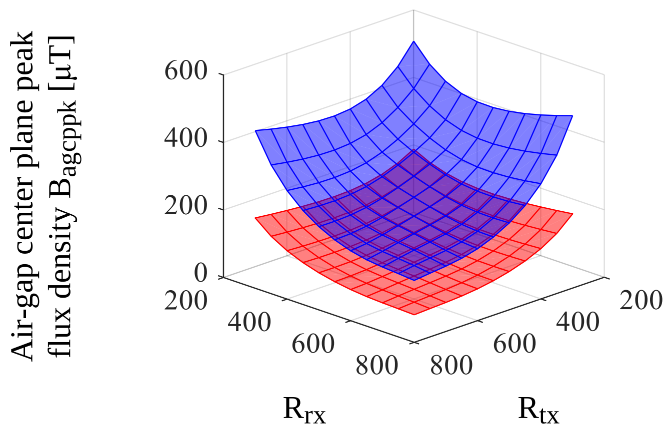

Test Conditions: output power 3 kW, operating frequency 0.1 MHz and 0.5 MHz.
Transmitter (TX) and receiver (RX): number of turns 1, transfer distance 300 mm.
IEEE C95.1-2005 standard: magnetic field electrostimulation safety limit (Peak) 289 µT @ 0.1 MHz and 289 µT @ 0.5 MHz, magnetic field tissue heating safety limit (Peak) 289 µT @ 0.1 MHz and 57 µT @ 0.5 MHz.

Fig. 3-3. Effects of the coil radii on the air-gap center plane peak magnetic flux density via analytical calculation

As shown in Fig. 3-3, under 0.1 MHz and 0.5 MHz, when the coil radii increase, B_{agcppk} reduces. The reduction rate of B_{agcppk} reduces as the coil radii keep increasing. Considering that it's a tradeoff between the magnetic field and the electric field to transfer higher power, it's better to use an equivalent transmitter and receiver coil radii and number of turns to balance the magnetic and electric field distributions.

The reason that the reduction rate of B_{agcppk} reduces as the coil radii increases is investigated through an FEA comparison of coils with radii 200 mm, 400 mm, and 600 mm. The transmitter coil and the receiver coil are set as the same, the number of turns is 1, the transfer distance is 300 mm, and the operating frequency is 0.1 MHz. When the output power is 3 kW, the air-gap magnetic field distributions and the air-gap center plane magnetic flux densities are compared in Fig. 3-4.

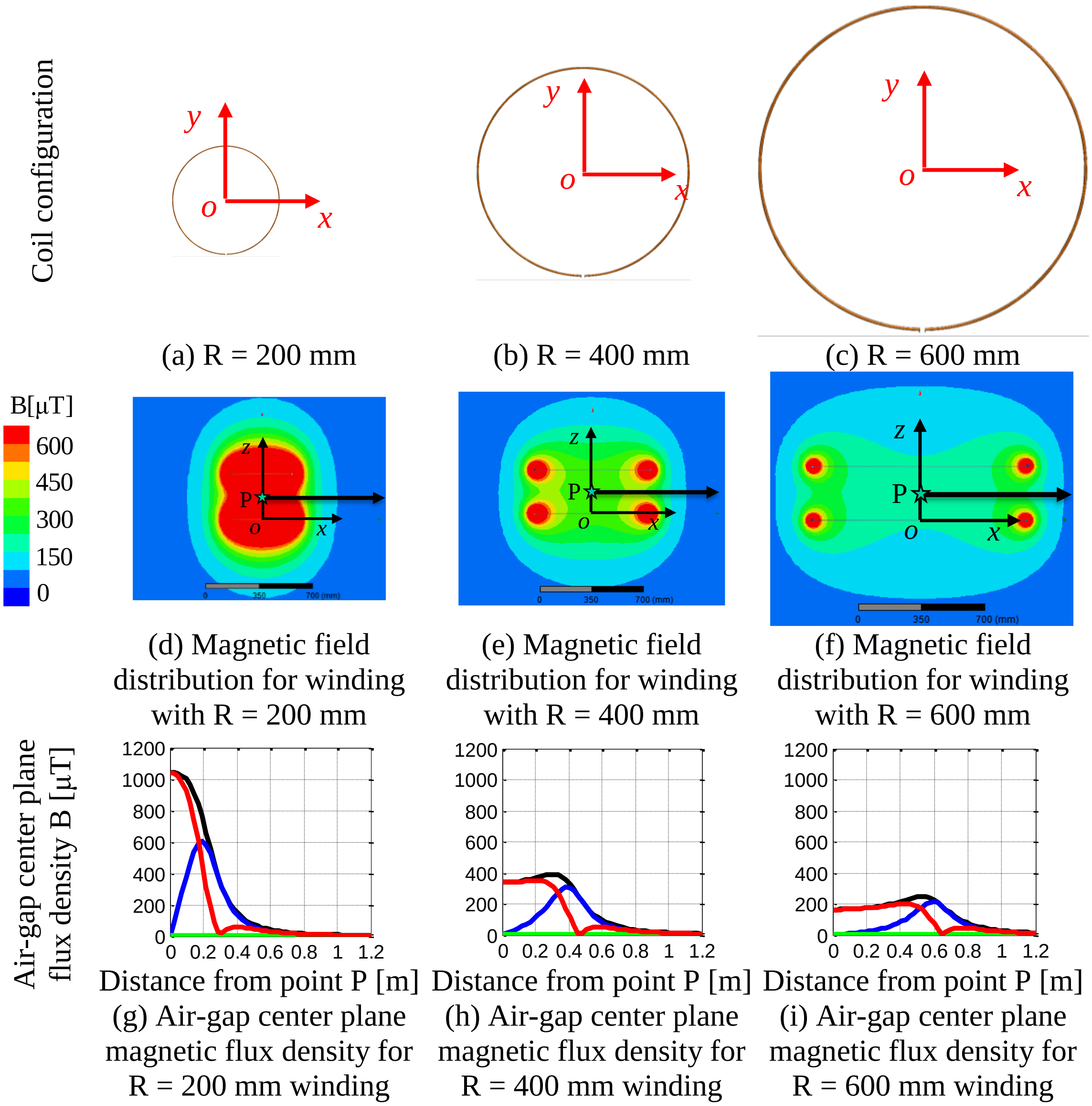

Legend: FEA magnetic flux density B_{total}, B_x, B_y, B_z.

Test Conditions: output power 3 kW, operating frequency 0.1 MHz.

Transmitter (TX) and receiver (RX): number of turns 1, transfer distance 300 mm.

Fig. 3-4. Effects of the coil radii on the air-gap center plane peak magnetic flux density via FEA simulation

As shown in Fig. 3-4, the air-gap center plane peak magnetic flux density and z-direction magnetic flux density keep reducing as the coil radii increase, however, B_{agcppk} is limited by the leakage flux or the radial-direction magnetic flux density when the coil radii are large, therefore, the reason that the reduction rate of B_{agcppk} reduces as the coil radii increases is the leakage flux. In addition, because of the leakage flux, the location of B_{agcppk} is shifted from the central point to the winding edge when the coil radii increase.

In the test example to evaluate the effect of the inter-turn distance on B_{agcppk} and the maximum coil-to-coil efficiency $\eta_{coil,\ max}$, the transfer distance is picked as 300 mm, the number of turns increases from 1 to 7 with step 1 with constant outer radius 600 mm, the operating frequency is 0.1 MHz, B_{agcppk} and $\eta_{coil,\ max}$ under the inter-turn distances 13.525 mm and 10.525 mm are compared in Fig. 3-5.

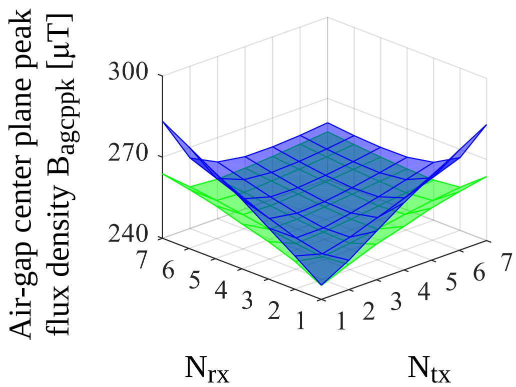

(a) B_{agcppk} w.r.t. number of turns

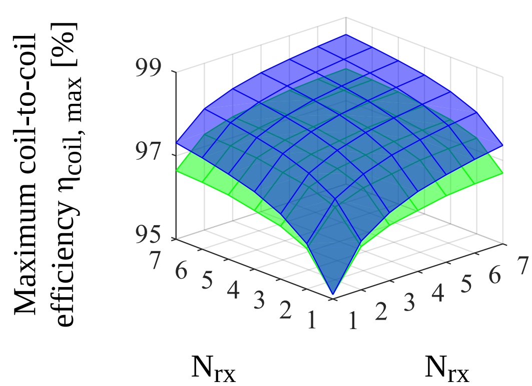

(b) $\eta_{coil,\ max}$ w.r.t. number of turns

Test Conditions: output power 3 kW, operating frequency 0.1 MHz.
Transmitter (TX) and receiver (RX): coil outer radius 600 mm, inter-turn distance 10.525 mm, 13.525 mm, transfer distance 300 mm.

Fig. 3-5. Effects of the inter-turn distance on the air-gap center plane peak magnetic flux density and the maximum achievable coil-to-coil efficiency

As shown in Fig. 3-5, when the inter-turn distance reduces, the coil-to-coil maximum efficiency $\eta_{coil,\ max}$ reduces due to the increase of the ESR caused by the proximity effect, B_{agcppk} also reduces due to the increase of the average coil radius. In addition, it's easy to achieve lower B_{agcppk} when the transmitter and the receiver are the same. Therefore, winding configurations with small inter-turn distance and low ESR can achieve lower B_{agcppk} and higher

$\eta_{coil,\ max}$, such as the surface spiral winding, which maintains equal diameter per turn and low ESR by following the Litz-wire twist pattern to reduce the proximity effect loss; and it's better to make the transmitter the same as the receiver.

3.2.7 Effects of the transfer distance

When the winding radius is large enough, B_{agcppk} is limited by the leakage flux, which fundamentally has the exponential decay property, so does the terminal electric field, therefore, it's necessary to investigate the effects of the transfer distance to identify a better candidate for the practical applications.

During the evaluation, the transmitter and the receiver are both set the same as 1 turn and 500 mm coil radius. The operating frequency is chosen as 0.1 MHz. The transfer distance increases from 150 mm to 400 mm with step 50 mm. The measurement line is along the air-gap center plane as shown in Fig. 3-6.

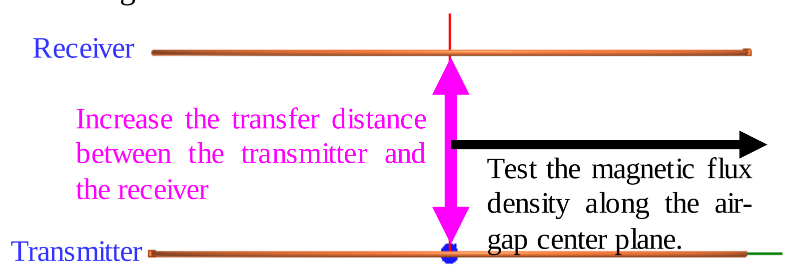

Fig. 3-6. Evaluation configuration for the effects of the transfer distance

When the output power is 3 kW, the air-gap magnetic field distributions with transfer distances 200 mm and 400 mm are compared in Fig. 3-7 (a) and (b). The analytical calculation results and the FEA results of B_{agcppk} and $\eta_{coil,\ max}$ with respect to the transfer distance are compared in Fig. 3-7 (c) and (d). The air-gap electric field distributions with transfer distances 200 mm and 400 mm are compared in Fig. 3-7 (c) and (d). The analytical calculation results and the FEA results of E_{agcppk} at the TX side and the RX side with respect to the transfer distance are compared in Fig. 3-7 (g) and (h).

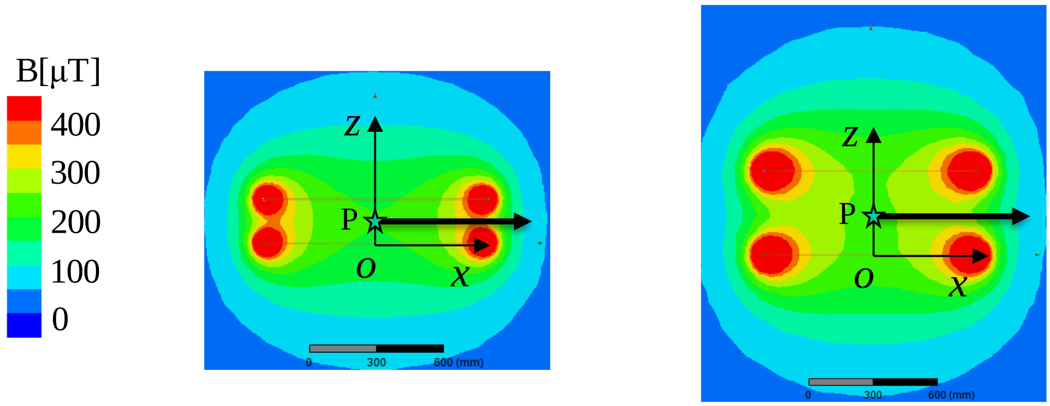

(a) Magnetic field distribution with 200 mm transfer distance

(b) Magnetic field distribution with 400 mm transfer distance

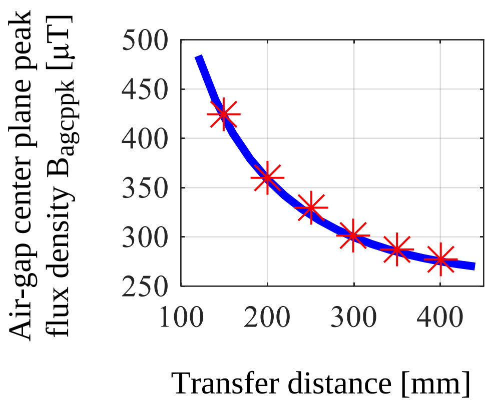

(c) B_{agcppk} w.r.t. transfer distance

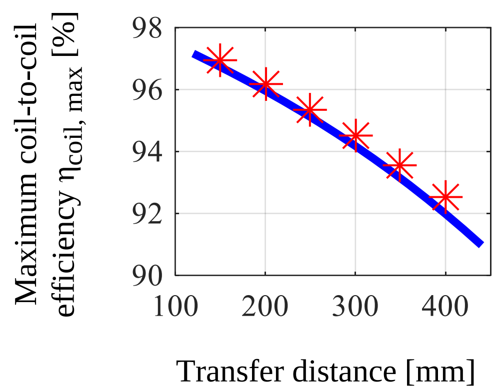

(d) $\eta_{coil, max}$ w.r.t. transfer distance

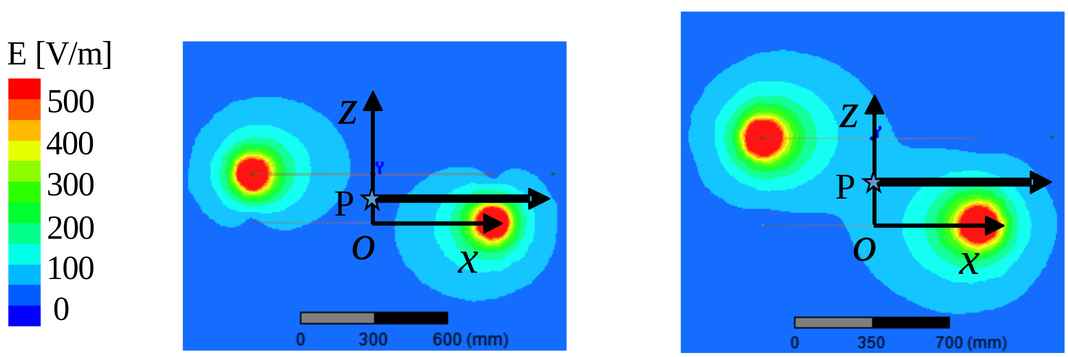

(e) Electric field distribution with 200 mm transfer distance

(f) Electric field distribution with 400 mm transfer distance

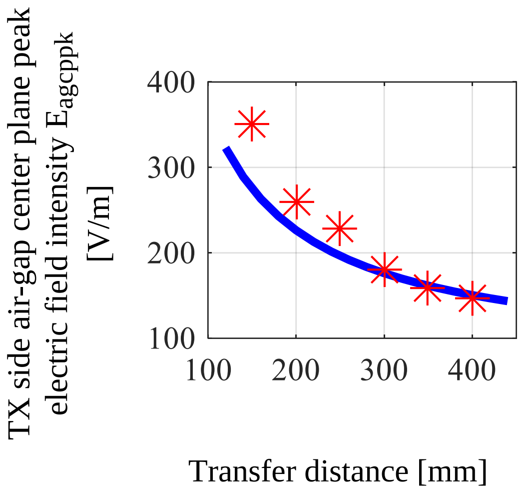

(g) TX side E_{agcppk} w.r.t. transfer distance

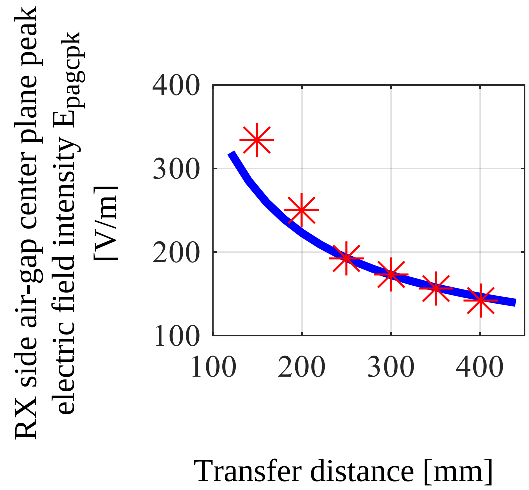

(h) RX side E_{agcppk} w.r.t. transfer distance

Legend: Analytical results, FEA results
Test Conditions: output power 3 kW, operating frequency 0.1 MHz.
Transmitter (TX) and receiver (RX): coil outer radius 500 mm, number of turns 1.

Fig. 3-7. Effects of the transfer distance on the air-gap center plane peak magnetic flux density and peak electric field intensity, and the maximum coil-to-coil efficiency

As shown in Fig. 3-7 (a) and (b), the magnetic fields around the coils are almost the same for the windings with 200 mm transfer distance and the windings with 400 mm transfer distance due to the leakage flux. When the transfer distance increases, the leakage flux density in the air-gap center plane reduces, therefore B_{agcppk} reduces as shown in Fig. 3-7 (c). Besides that, the reduction rate of B_{agcppk} reduces as the transfer distance increases. As the transfer distance increases, $\eta_{coil,\ max}$ reduces due to the reduction of mutual inductance as shown in Fig. 3-7 (d). The required excitation currents will increase in order to transfer the same amount of output power as the transfer distance keeps increasing, which may increase the leakage magnetic flux density around the coil and the z-direction magnetic flux density. According to Fig. 3-7 (e) and (f), the air-gap center plane electric field intensity reduces as the transfer distance increases due to the decay property of the terminal electric field. The air-gap center plane peak electric field intensities at the TX side and the RX side reduce as the transfer distance increases as shown in Fig. 3-7 (g) and (h). The analytical calculation results are not accurate when the transfer distance is small because of the effect of terminal clearance. It's necessary to develop some techniques to make the electric field close to the excitation terminal safe.

Tuning the transfer distance can be treated as a tradeoff between $\eta_{coil,\ max}$, and B_{agcppk} and E_{agcppk}. Considering the electric vehicle ground clearance, 300 mm transfer distance is selected to balance $\eta_{coil,\ max}$, and B_{agcppk} and E_{agcppk}.

3.2.8 Effects of the operating frequency with respect to the safety standard

According to previous analyses under 0.1 MHz and 0.5 MHz, when the operating frequency increases, B_{agcppk} reduces, and E_{agcppk} increases. Above 0.1 MHz, the magnetic field tissue heating safety limit must be taken into consideration. Besides that, the combined electric field intensity reduces above 1 MHz. Therefore, it's necessary to evaluate the operating frequency effects with respect to the safety standard to provide a general guideline when selecting the operating frequency.

During the evaluation, the transmitter and the receiver are set as the same. The number of turns is 1, the transfer distance is set as 300 mm, the coil radii increase from 400 mm to 800 mm with step 100 mm. B_{agcppk} and E_{agcppk}, and $\eta_{coil,\ max}$ are evaluated with respect to the operating frequency as shown in Fig. 3-8.

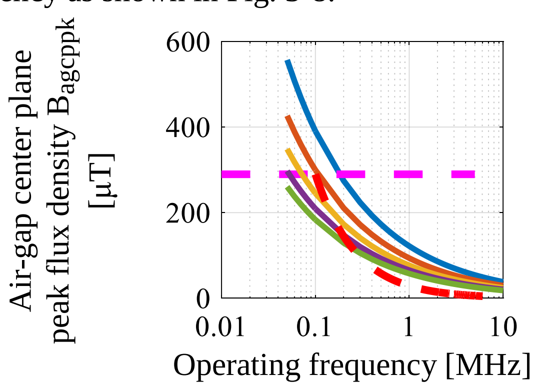

(a) B_{pk} w.r.t. the operating frequency

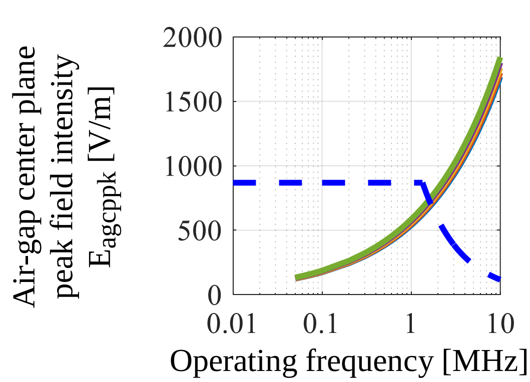

(b) E_{pk} w.r.t. the operating frequency

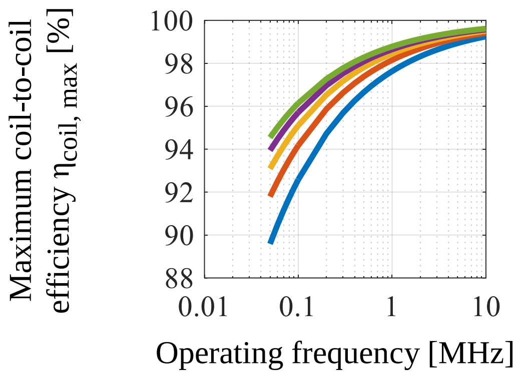

Test Conditions:
Output power: 3 kW.
Transfer distance: 300mm.
TX and RX number of turns: 1.
TX and RX radii [mm]:
— 400, — 500, — 600, — 700, — 800
General public exposure (Peak):
- - IEEE B-field electrostimulation limit
- - IEEE B-field tissue heating limit
- - IEEE combined E-field limit

(c) $\eta_{coil,\ max}$ w.r.t. the operating frequency

Fig. 3-8. Effects of the transfer distance on the air-gap center plane peak magnetic flux density and the maximum achievable coil-to-coil efficiency

As shown in Fig. 3-8 (a), B_{agcppk} reduces as the operating frequency increases, it's easy to satisfy the magnetic field electrostimulation safety limit when operating at above 0.1 MHz. However, the reduction rate of B_{agcppk} is slower than the reduction rate of the tissue heating safety limit, therefore, it’s not recommended to operate at MHz frequency level when the WPT system is required to meet the tissue heating safety limit.

According to Fig. 3-8 (b), E_{agcppk} increases as the operating frequency increases and the coil radius increases, it's easy to satisfy the electric field combined safety limits when operating at below 1.34 MHz. Above 1.34 MHz, the electric field combined safety limits reduce while E_{agcppk} increases as the operating frequency increases. Considering the air-gap center plane electric field intensity is mainly caused by the terminal excitation field, which is determined by the excitation voltage V and the terminal clearance, while $V \propto L*\omega*i \propto N^2*\omega*I$, low number of turns and small coil radius design provides a possible solution to satisfy the electric field safety limit when operating at high frequency.

From Fig. 3-8 (c), $\eta_{coil,\ max}$ increases as the operating frequency increases and the coil radii increase. For the 1 turn coil, only the skin effect AC resistance needs to be considered. The AC resistance can be calculated as

$$R_{skin} = \rho \frac{l}{\pi R^2 - \pi (R - \delta)^2} = \rho \frac{l}{2 \pi R \delta - \pi \delta^2} \tag{3.1}$$

Where ρ is electrical resistivity, l is the conductor length, R is the copper tubing outside radius, δ is the skin depth, $\delta = \sqrt{\frac{2\rho}{\omega_0\mu}}$, μ is the permeability.

When the transmitter and the receiver are set as the same, the efficiency factor can be simplified into

$$\frac{\omega_0^2 M^2}{R_{tx} R_{rx}} = M^2\left[\frac{\omega_0}{R_{skin}}\right]^2 = M^2\left[\frac{\omega_0 (2\pi R \delta - \pi \delta^2)}{\rho l}\right]^2 = M^2\left[\frac{2\pi R}{l}\sqrt{\frac{2\omega_0}{\mu\rho}} - \frac{2\pi\rho}{\mu l}\right]^2 \quad (3.2)$$

It’s easy to find that the efficiency factor increases with the operating frequency and the mutual inductance, which lead to a higher coil-to-coil efficiency. Although increasing the operating frequency can increase the quality factor, it’s not the quality factor that fundamentally determines the maximum achievable coil-to-coil efficiency.

The design goal in this research is satisfying the magnetic field and electric field electrostimulation and tissue heating safety limits in the air-gap center plane when transferring 3 kW and maintaining a high transfer efficiency, based on the design considerations and the analyses in this section, the operating frequency is chosen as 0.1 MHz, the transmitter and the receiver are set as the same, the coil radius is selected as 600 mm, the number of turns is selected as 3 turns, surface spiral winding configuration will be used since it maintains equal diameter per turn to achieve zero inter-turn distance, which is good to achieve low air-gap center plane peak magnetic flux density. Alternative surface spiral winding configurations are required to reduce the spatial voltage stress especially between the first turn and the end turn to avoid voltage breakdown, and to reduce the dielectric losses and the ESR to improve the efficiency.

3.3 Low dielectric losses, low spatial voltage stress, low ESR surface spiral, parallel and antiparallel windings design methodologies

In this section, design methods to reduce the SSW dielectric losses will be presented at first, then alternative dielectric support geometries to withstand higher breakdown voltage will be introduced, after that, copper tubing SSW will be developed to reduce the spatial voltage stress and achieve low dielectric loss simultaneously. At last, surface spiral parallel winding (SSPW) and surface spiral antiparallel winding (SSAPW) design methodologies will be proposed to reduce the ESR and equalize the spatial voltage stress distribution.

3.3.1 Low dielectric losses surface spiral winding designs

The dielectric loss per unit volume of a substrate material can be calculated using (3.3) [250].

$$W_{vol} = \frac{\text{Power loss}}{\text{Volume}} = \omega\, E^2\, \varepsilon_0\, \varepsilon_r\, (\tan\delta) \tag{3.3}$$

In order to reduce the dielectric losses, according to above loss density equation, since the operating frequency can't be changed, there are mainly two methods: one method is reducing relative permittivity (dielectric constant) and dissipation factor, which are determined by materials. Another method is reducing the spatial voltage stress.

- **Low dielectric losses substrate materials**

During selecting appropriate dielectric substrate, not only dielectric constant and dissipation factor should be considered, but heat deflection temperature should also be taken into consideration, since the dielectric substrate for SSW is 3D printed, for example, the dielectric constant of Polytetrafluoroethylene (PTFE) at 1 MHz is 2.1, and its dissipation factor is 0.0002 at 1 MHz, which is a better choice compared with Polycarbonate (PC) or ABS. However, the melting point of PTFE is 330℃, it starts decomposing before melting and releasing toxic fumes above 250℃. Therefore, PTFE is not suitable to use as dielectric substrate material.

Selected materials that are suitable for 3D printing are compared in Table 3-1.

Table 3-1. Selected suitable 3D printing materials

Material	Dielectric constant	Dissipation factor	Heat deflection temperature
Somos_Next (SN) (SSW 1st generation)	3.62 @1 MHz	0.034 @ 4 MHz	56℃ @ 0.46 MPa
Acrylonitrile butadiene styrene (ABS)	3.3 @ 1 MHz	0.02 @ 1 MHz	98℃ @ 0.46 MPa
Polycarbonate (PC) (SSW 2nd generation)	3.0 @1 MHz	0.0063 @ 4 MHz	138 ℃ @ 0.46 MPa

Polytetrafluoroethylene (PTFE)	2.1 @ 1 MHz	0.0002 @ 1 MHz	73℃ @ 0.46 MPa
Perfluoroalkoxy (PFA)	2.1 @ 1 MHz	0.0001 @ 1 MHz	75℃ @ 0.46 MPa
Polyethylene (PE)	2.26 @ 1MHz	0.0002 @ 1 MHz	85℃ @ 0.46 MPa
Fluorinated ethylene propylene (FEP)	2.1 @ 1 MHz	0.0006 @ 1 MHz	77℃ @ 0.46 MPa

According to Table 3-1, PFA and FEP have almost the same heat deflection temperature and dielectric constant which is lower than PE, but the dissipation factor of PFA is much lower. Therefore, PFA is selected to evaluate the effect of dielectric constant and dissipation factor.

Electric field intensity and volume loss density of dielectric bridge cross-section region using PC and PFA are compared in Fig. 3-9.

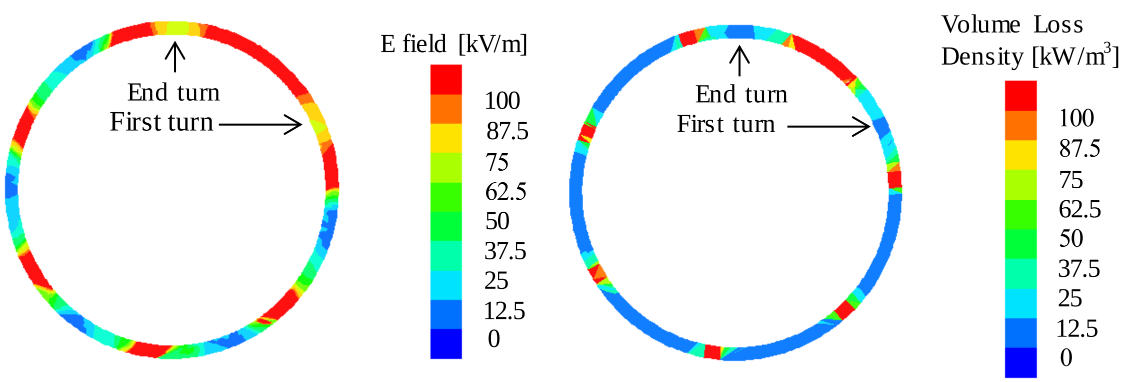

(a) Electric field intensity and volume loss density FEA results using PC

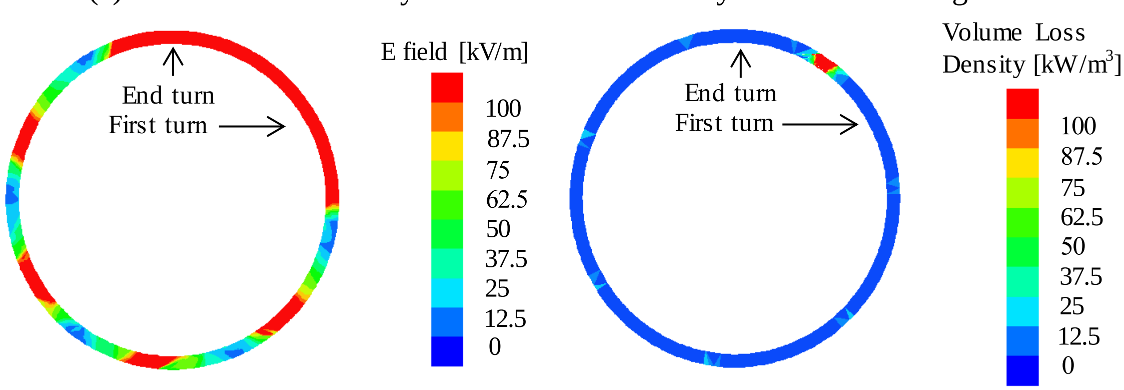

(b) Electric field intensity and volume loss density FEA results using PFA

Fig. 3-9. Comparison of electric field intensity and volume loss density of dielectric bridge cross-section region for SSW using PC and PEA at 3 kW, 3.7 MHz

As shown in Fig. 3-9, since the coil geometry and the test conditions remain the same, the electric field intensity FEA results using PC and PFA are almost the same, however, due to low dissipation factor and low dielectric constant of PFA, a dielectric substrate using PFA has much lower volume loss density. The volume loss density between the first turn and the end turn is still large because the spatial voltage stress between the first turn and the end turn is the maximum location due to SSW geometry limitation as shown in Fig. 1-75.

Loss distribution and coil-to-coil power transfer efficiency of SSW using PC and PFA are compared in Fig. 3-10.

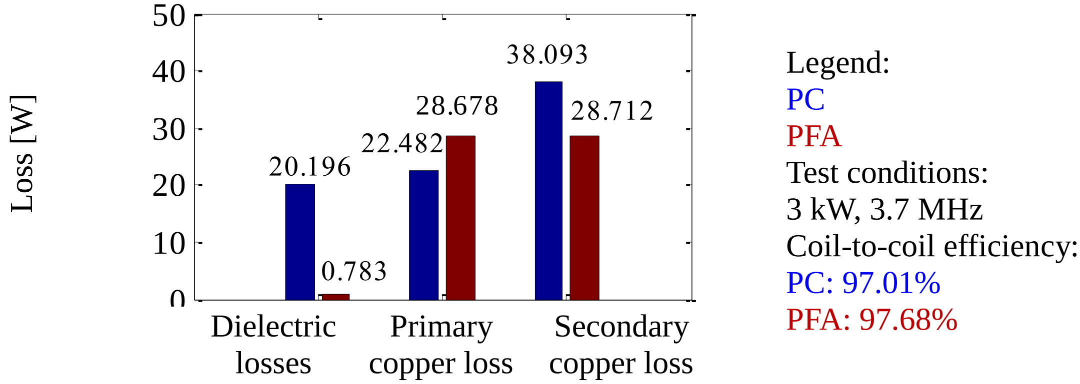

Fig. 3-10. Comparison of loss distribution and coil-to-coil power transfer efficiency using PC and PEA at 3 kW, 3.7 MHz

As shown in Fig. 3-10, the total copper losses using PC and PFA are almost the same, changing dielectric substrate material affects parasitic capacitance, which affects equivalent self-inductance, mutual inductance and optimal load for peak coil-to-coil power transfer efficiency, primary copper loss, and secondary copper loss change a little. However, dielectric losses using PFA reduces from 20.196 W to 0.783 W, which is almost negligible compared with the copper loss, therefore, low dissipation factor and low relative permittivity materials can be used to reduce dielectric losses under same voltage stress. During the selection of dielectric materials, manufacturing technique should also be taken into consideration.

- **Low spatial voltage stress surface spiral parallel winding design**

Although low dielectric constant and low dissipation factor substrate materials could help reducing dielectric losses, there are still limitations due to manufacturing technique. In addition, one material can’t have the best performances in all categories, for example, compared with PC, PFA has much lower dielectric constant and dissipation factor, however, its heat deflection temperature is almost half of PC's heat deflection temperature, higher deflection temperature generally means the higher possibility to transfer higher power. Therefore, it's better to reduce dielectric losses using geometric solutions.

Surface spiral parallel winding (SSPW) is proposed to reduce the voltage stress between adjacent turns. SSPW adds another copper layer within the dielectric substrate as shown in Fig. 3-11.

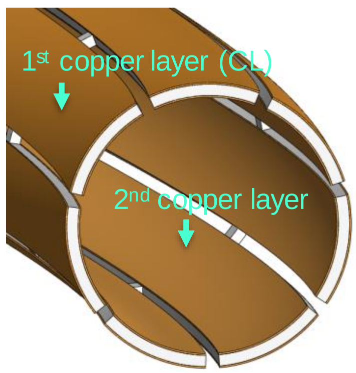

Fig. 3-11. Surface spiral parallel winding geometry

With two copper layers in parallel, the total current will be shared by both copper layers. Since the thickness of the dielectric substrate is just 2 mm, the first copper layer and the second copper layer have almost the same self-inductance and ESR, current in each layer will be equal to half of the total current, the voltage between adjacent turns in each layer will also be reduced to half of the voltage between adjacent turns of SSW. However, the voltage stress across dielectric bridges is not reduced by half since both layers will produce voltage stress across dielectric bridges. The electric field intensity and volume loss density of SSPW and SSW across dielectric bridges and dielectric substrate are compared in Fig. 3-12.

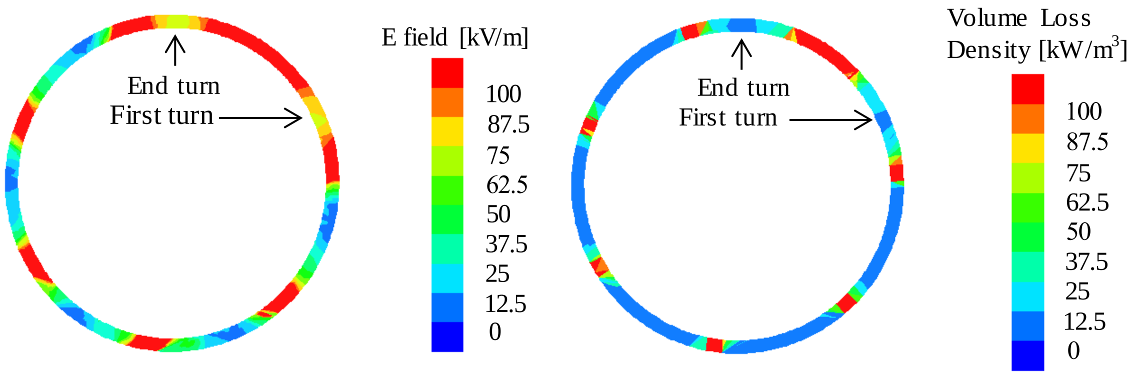

(a) SSW electric field intensity and volume loss density FEA results using PC

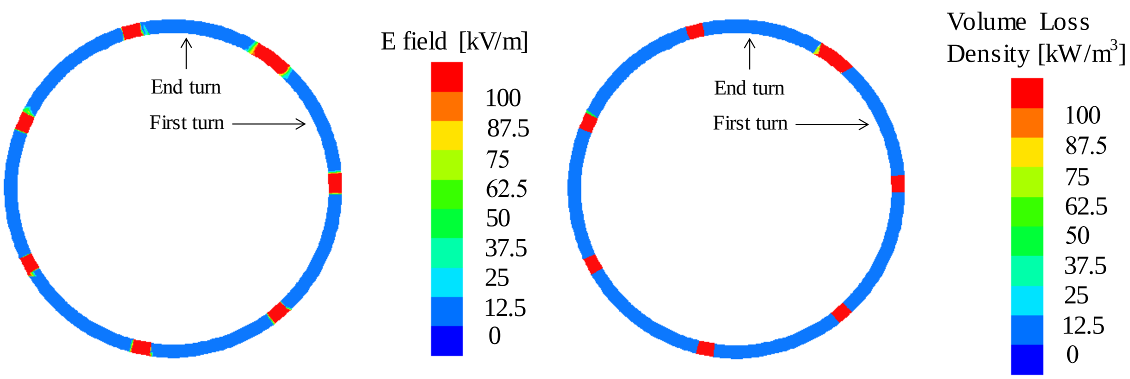

(b) SSPW electric field intensity and volume loss density FEA results using PC

Fig. 3-12. Comparison of electric field intensity and volume loss density of dielectric bridge cross-section region for SSW and SSPW using PC at 3 kW, 3.7 MHz

As shown in Fig. 3-12, compared with SSW geometry, the voltage stress of dielectric substrate in SSPW geometry is reduced to relatively small value since the voltages and currents in the first copper layer and the second copper layer are supposed to be the same along the dielectric substrate due to parallel structure. Compared with SSW geometry, SSPW geometry helps reducing dielectric substrate losses significantly and concentrating dielectric losses within dielectric bridges. The voltage stress and the dielectric losses between the first turn and the end turn are still relatively large even using SSPW geometry. Loss distribution and coil-to-coil power transfer efficiency of SSW using PC and PFA are compared in Fig. 3-13.

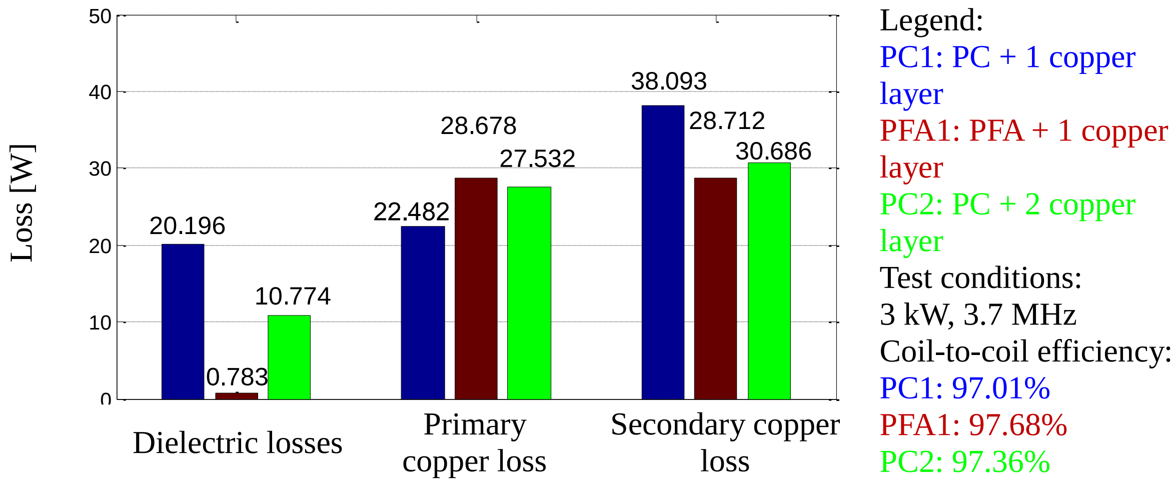

Fig. 3-13. Comparison of loss distribution and coil-to-coil power transfer efficiency for SSW using PC and PEA, and SSPW using PC at 3 kW, 3.7 MHz

As shown in Fig. 3-13, the total copper losses for SSW and SSPW are almost the same. Although using parallel structure, DC resistance can reduce by half. Due to skin effect and proximity effect, AC resistances remain almost the same for 7 turns SSW and SSPW. The total dielectric losses are reduced by 44.5% with SSPW using PC. If SSPW is built with PFA, the coil-to-coil power transfer efficiency can be higher than SSW.

- **Low dielectric losses concave dielectric bridge design**

The voltage or the voltage stress across dielectric bridges of the SSW and the SSPW with copper layer remains almost the same, if the dielectric bridges are treated as resistors, the dielectric losses can be reduced when the resistance increases, it's better to use small short bridges to keep the dielectric losses low, which means that the cross-section area of the dielectric bridges almost couldn't change, therefore, the concave dielectric bridge geometry using long bridges as shown in Fig. 3-14 provides the opportunity to reduce the dielectric losses.

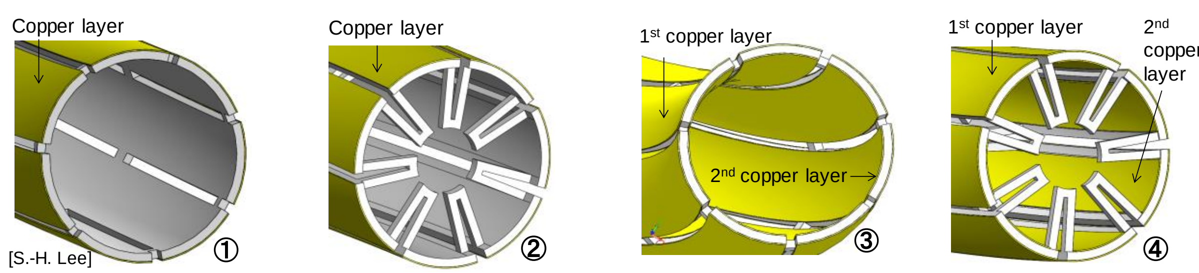

(a) SSW and SSPW with normal dielectric geometry and concave dielectric geometry

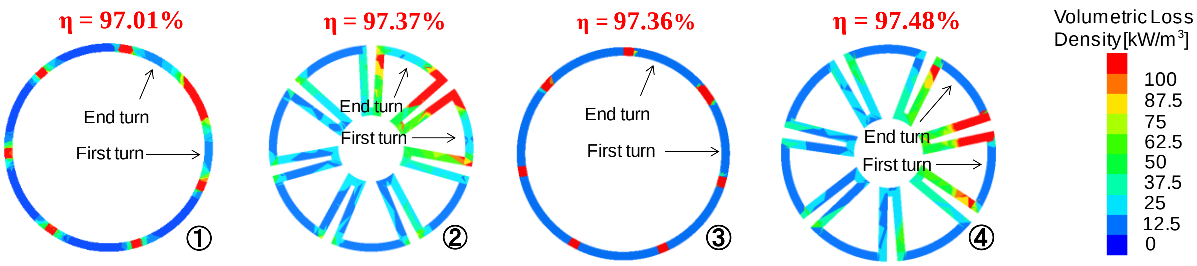

(b) Volume loss density of dielectric bridge cross-section region FEA results using PC

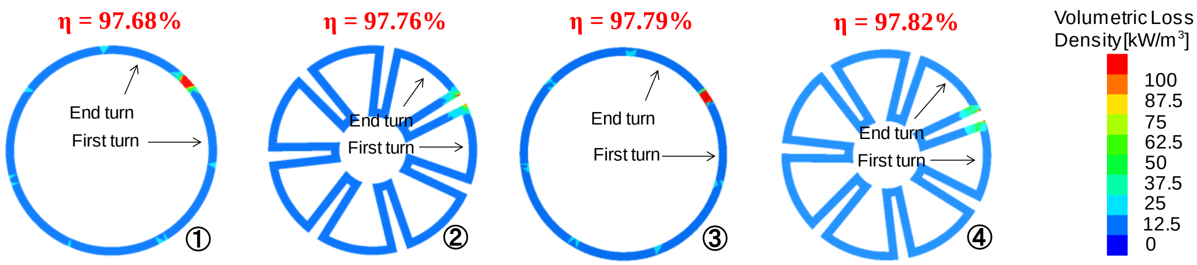

(c) Volume loss density of dielectric bridge cross-section region FEA results using PFA

Fig. 3-14. Comparison of volume loss density of dielectric bridge cross-section region for SSW and SSPW with normal dielectric geometry and concave dielectric geometry using PC and PFA, respectively, at 3 kW, 3.7 MHz

As shown in Fig. 3-14, when using PC and PFA as the dielectric substrate materials, SSW with concave dielectric geometry and SSPW with normal bridges have almost the same coil-to-coil power transfer efficiency, since the total copper losses remain almost the same for SSW and SSPW as shown in the previous section, the dielectric losses with concave geometry can also reduce the dielectric losses by 45% as SSPW. For SSPW with the second copper layer inside, the width of the second copper layer should be reduced compared with the first copper layer due to the concave bridge. However, the SSPW with a concave dielectric bridge using PFA can still achieve the highest coil-to-coil power transfer efficiency of 97.82%.

Although above proposed geometric solutions can effectively reduce the dielectric losses, the spatial voltage stress between the first turn and the end turn is still a potential threat when operating at high power level due to voltage breakdown possibility. The following section will introduce methods to increase dielectric withstand voltage.

3.3.2 High dielectric breakdown voltage surface spiral winding designs

The spacing clearance between components that are required to withstand a given working voltage is specified in terms of clearance and creepage. A visual representation of the distinction between these terms, and their applicability to board-mounted components, is shown in Fig. 3-15 [253].

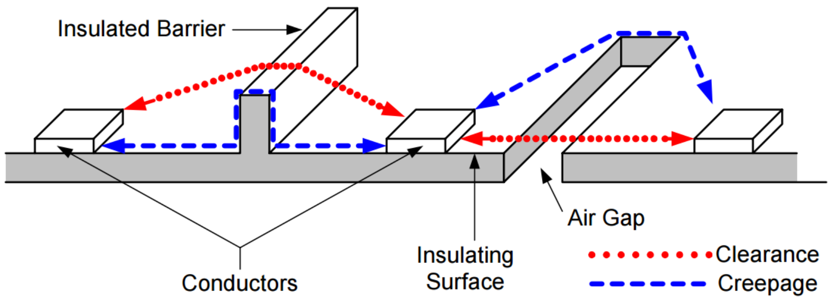

Fig. 3-15. Definitions of Creepage and Clearance

Clearance is defined as the shortest distance through air between two conductive parts. Breakdown along a Clearance path is a fast phenomenon where damage can be caused by a very short duration impulse. Creepage is defined as the shortest distance between two conductive parts along the surface of any insulating material common to both parts. While the path is in the air, it is heavily influenced by the surface condition of the insulation material. Breakdown of the creepage distance is a slow phenomenon determined by dc or RMS voltage levels rather than peak events. Inadequate creepage spacing may last for days, weeks, or months before it fails.

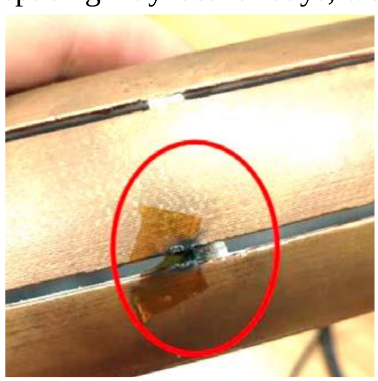

Fig. 3-16. Voltage breakdown region when transferring 1 kW

During the SSW experimental test, the voltage breakdown happens instantly between the first turn and the end turn when pushing to transfer 1 kW as shown in Fig. 3-16, since the spatial clearance between the first turn and the end turn is not large enough to withstand the voltage stress. An insulated barrier can be added between the first turn and the end turn to increase the clearance, or the shortest distance through the air.

When the insulated barrier is added, it should be added along the spatial space between the first turn and end turn. Since the maximum voltage stress is located in the region between the first turn and the end turn, the dielectric losses caused by the solid insulated barrier would be much higher than the traditional design. The coil-to-coil power transfer efficiency, the volume loss density across dielectric bridge region and the dielectric losses are compared in Fig. 3-17.

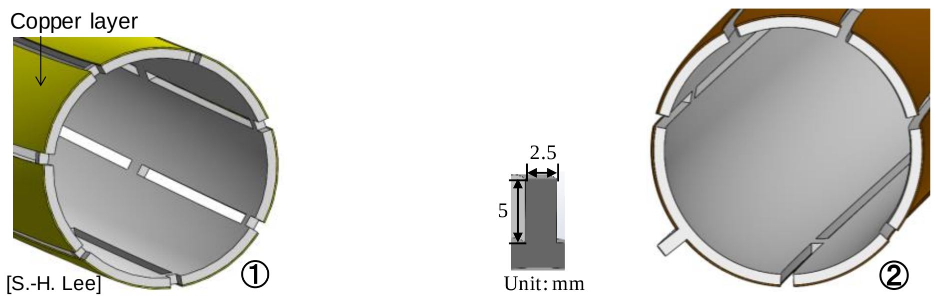

(a) SSW with normal bridge and solid insulted barrier

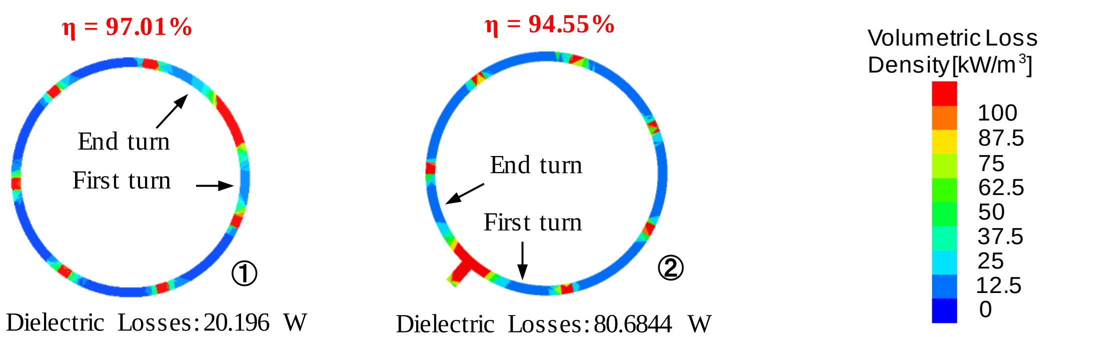

(b) Volume loss density of dielectric bridge cross-section region FEA results using PC

Fig. 3-17. Comparison of dielectric bridge cross-section region for SSW with normal bridge and solid insulated barrier using PC at 3 kW, 3.7 MHz

As shown in Fig. 3-17, the clearance with the normal bridge between the first turn and the end turn is 2.5 mm. The clearance with the solid insulated barrier is increased to 12.5 mm, which is enough to withstand the voltage stress when transferring 3 kW. However, with the solid insulated barrier, the dielectric losses are increased from 20.196 W to 80.6844 W, and the coil-to-coil power transfer efficiency drops from 97.01% to 94.55%. The main dielectric losses are caused by the solid insulated barrier as shown in the volume loss distribution result. Methods to reduce the dielectric losses of the insulated barrier should be developed.

If the insulated barrier is treated as a resistor, the methods that can increase the equivalent resistance are practical to reduce the dielectric losses. The cross-section area of the insulated barrier can be reduced by using a hollow barrier. The length can be increased by increasing the barrier height. The equivalent resistance can also be increased by using open barrier structure. Insulated barrier structures and volumetric loss density FEA results are shown in Fig. 3-18.

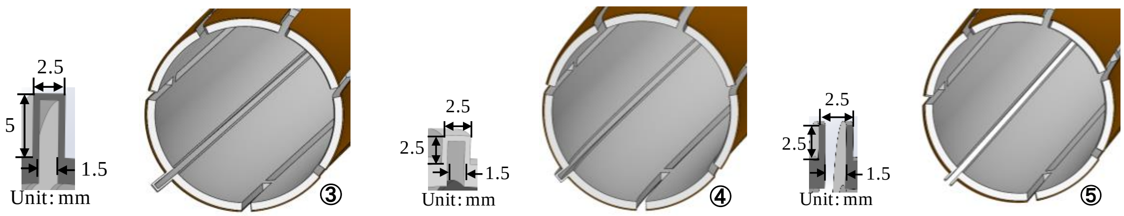

(a) SSW with hollow insulated barrier and open insulated barrier

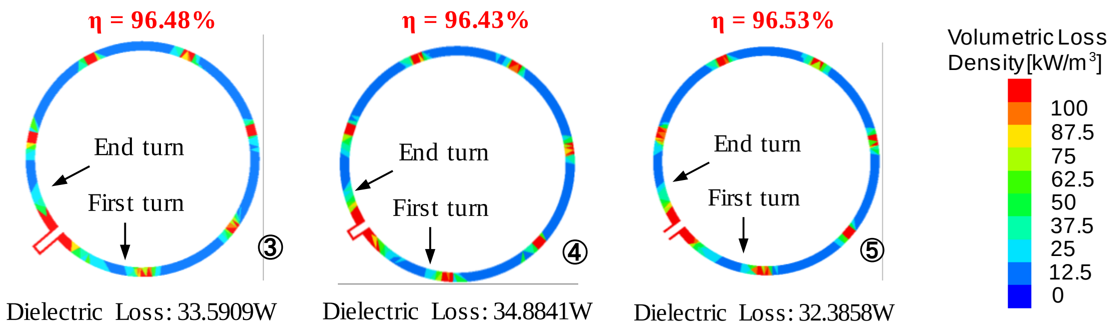

(b) Volume loss density of dielectric bridge cross-section region FEA results using PC

Fig. 3-18. Comparison of volume loss density of dielectric bridge cross-section region for SSW with hollow and open insulated barriers using PC at 3 kW, 3.7 MHz

As shown in Fig. 3-18, when the solid insulated barrier is changed to the hollow insulated barrier with wall thickness 0.5 mm, the dielectric losses are reduced from 80.6844 W to 33.5909 W, the coil-to-coil efficiency increases from 94.55% to 96.48%. When the height of the hollow insulated barrier is reduced by half, the dielectric losses increase about 1.2 W, which verifies that the dielectric losses can be reduced by increasing the barrier equivalent length, namely, the equivalent resistance. When the hollow insulated barrier is changed to the open one, which further increases the equivalent resistance, the dielectric losses are further reduced by 2.5 W, the coil-to-coil efficiency is increased to 96.53%.

Although the hollow insulated barrier and the open insulated barrier structures can reduce the dielectric losses while maintaining high dielectric breakdown voltage compared with the solid insulated barrier structure, the dielectric losses are still high compared with the SSW with the normal bridge. Alternative geometries that can simultaneously reduce dielectric losses and spatial voltage stress are required.

3.3.3 Emulating the 3D printed SSW using copper tubing

In the traditional SSW, the dielectric substrate is necessary to support the thin copper layer since the copper layer is too thin to support themselves. The dielectric losses are mainly located in the dielectric bridge region, and the thin copper layer is practical to reduce the skin effect copper loss. The proximity effect copper loss between adjacent turns is reduced by twisting each turn. The twist factor was optimized as 1. The voltage distribution between adjacent turns is shown in Fig. 3-19.

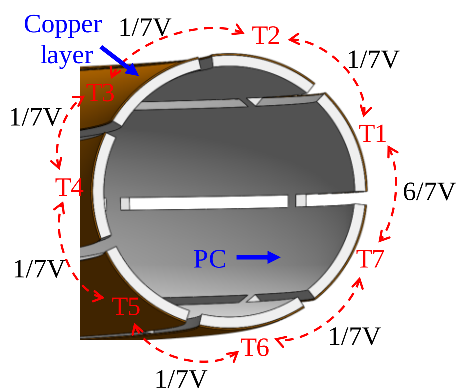

Fig. 3-19. Surface spiral winding voltage distribution

When the twist factor is 1, the spatial voltage between the first turn T1 and the end turn TN is (N – 1) × V/N, where N is the number of turns, and V is the terminal voltage, therefore, the spatial voltage between T1 and T7 as shown in Fig. 3-19 is 6V / 7. It’s easy to find that the spatial air clearance can be increased to increase the breakdown voltage limit and reduce the dielectric losses simultaneously.

When the copper layer is replaced by the thick copper tubing, the dielectric substrate can be removed. The dielectric pad can be used to maintain the twist pattern. Compared with the traditional SSW, the dielectric losses can be reduced. The skin effect copper loss could be the same when the perimeters of the copper layer and the copper tubing are equal even if the thickness is much larger than the skin depth. The proximity effect copper loss can be much lower when the copper tubing twisting pattern emulates the 3D printed SSW twist pattern due to the automatic increase of the spatial clearance between adjacent turns. A copper tubing SSW configuration with dielectric support pads is shown in Fig. 3-20.

(a) Copper tubing SSW (b) Cross-sectional view at support pad

Fig. 3-20. A copper tubing SSW configuration with dielectric support pads

The perimeter of the copper layer for the 3D printed SSW is 40.75 mm, while the perimeter of the copper tubing SSW is 29.92 mm. The skin depth at 3.7 MHz is 33.89 μm, which is smaller than the copper thicknesses for both SSWs. The skin effect AC resistance of the copper tubing SSW is about 4/3 times that of the copper layer SSW. However, the spatial air clearance increases from 2.5 mm of the 3D printed SSW to 12.2 mm of the copper tubing SSW, which increases the breakdown voltage limit by 4.88 times and reduces the copper loss due to the proximity effect. For both SSWs, the receiver winding is a 1 turn copper tubing with a radius of 180 mm, the transfer distance between the transmitter and the receiver is set as 300 mm. The loss distributions and spatial electric fields across dielectric supports of the 3D printed SSW and the copper tubing SSW coil configuration are compared in Fig. 3-21.

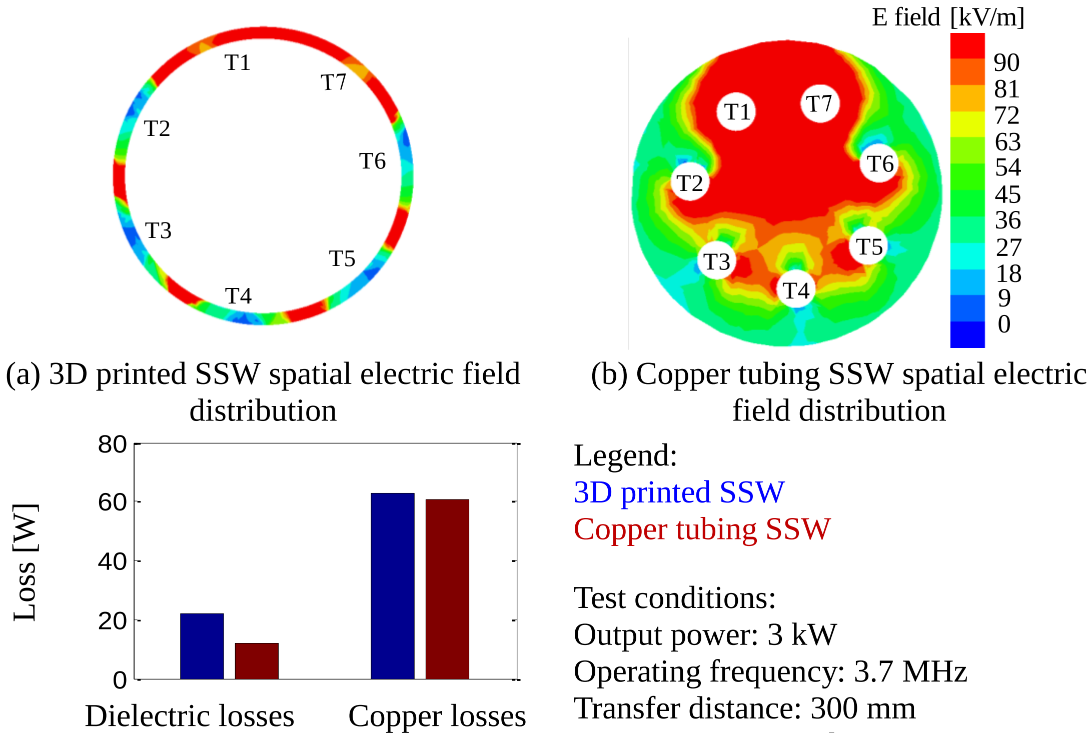

(a) 3D printed SSW spatial electric field distribution

(b) Copper tubing SSW spatial electric field distribution

(c) Comparison of loss distributions

Fig. 3-21. Comparison of spatial electric fields across dielectric supports and loss distributions for 3D printed and copper tubing SSWs operating at 3.7 MHz

As shown in Fig. 3-21 (a) and (b), the spatial region between the first turn T1 and the end turn T7 is the maximum electric field region for the 3D printed SSW and the copper tubing SSW. However, although the spatial voltage distributions are the same for both SSWs, the copper tubing SSW has a much lower electric field in other spatial regions between adjacent turns compared with the 3D printed SSW due to large inter-turn distances. According to Fig. 3-21 (c), the dielectric losses are reduced by 46%, from 21.7 W to 11.7 W, which is still mainly located between the first turn and the end turn. The copper losses are almost the same, since the resistance increased by the skin effect is compensated by the proximity effect, and the 3D printed SSW equivalent mutual inductance between the transmitter and the receiver is higher than the copper tubing SSW due to higher parasitic capacitance, which reduces the required currents in the 3D printed SSW to transfer the same amount of power.

When the operating frequency is reduced from 3.7 MHz to 0.1 MHz due to the magnetic field and electric field safety considerations in the air-gap center plane, loss distributions and spatial electric fields across the dielectric supports for the 3D printed SSW and the copper tubing SSW are compared in Fig. 3-22.

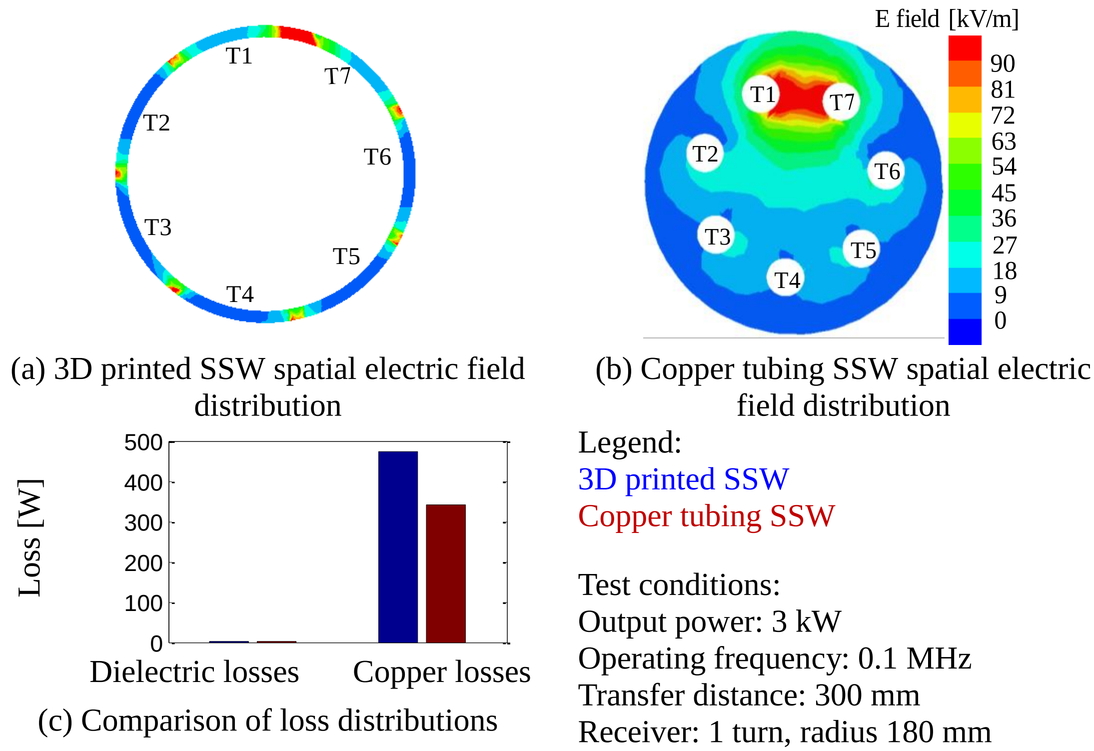

Fig. 3-22. Comparison of spatial electric fields across dielectric supports and loss distributions for 3D printed and copper tubing SSWs operating at 0.1 MHz

When the operating frequency is reduced. The required current increases and the required voltage reduces to transfer the same amount of power, therefore, the spatial voltage stress and the spatial electric field reduce significantly as shown in Fig. 3-22 (a) and (b). According to Fig. 3-22 (c), the dielectric losses of the 3D printed SSW and the copper tubing SSW are reduced to 0.0234 W and 0.0123 W respectively due to the significant reduction of the operating frequency. Compared with the 3D printed SSW, the dielectric losses are still reduced by 47% using the copper tubing SSW. The 3D printed SSW has higher copper losses compared with the copper tubing SSW, because their mutual inductances are almost the same when operating at 0.1 MHz, and the 3D printed SSW has higher ESR due to the proximity effect.

Compared with the copper losses, the dielectric losses are almost negligible. However, the copper tubing should be installed with full dielectric insulation materials in practical application, which may increase the total dielectric losses. Besides that, the copper tubing can also be replaced with the Litz-wire, which has full insulation layers, and needs additional dielectric support material to keep the twist pattern, the design methods developed in previous sections can be used to reduce the total dielectric losses.

3.3.4 Copper tubing-based surface spiral, parallel and antiparallel windings

According to the system design methodology, a 3-turn planar circular spiral winding with 600 mm coil radius and 13.525 mm inter-turn distance can satisfy the air-gap center plane magnetic and electric field safety limits when transferring 3 kW at 0.1 MHz. In order to improve the coil-to-coil efficiency and maintain the same level air-gap center plane magnetic and electric fields, the copper tubing (CT) SSW configuration emulating the SSW configuration, shown in Fig. 3-23, can be used, since it also maintains equal diameter per turn. The twist factor is set as 1 to achieve low proximity effect loss. The spatial region between the first turn and the end turn is the maximum voltage stress location. The voltage between the first turn and the end turn is (N – 1) × V/N, where N is the number of turns, and V is the terminal excitation voltage.

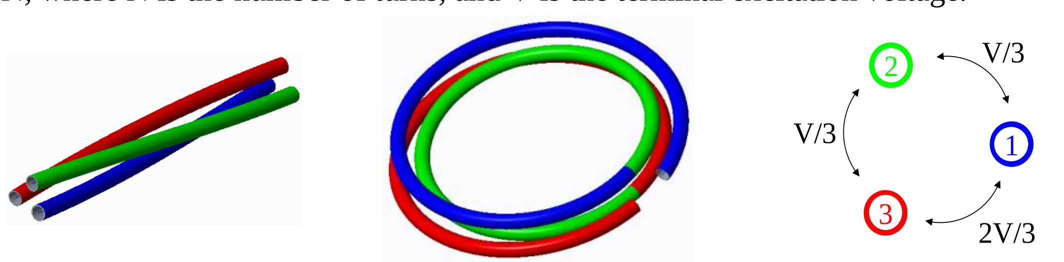

(a) Three-turn twisted coil (b) CT SSW structure (c) Voltage distribution

Fig. 3-23. A copper tubing SSW configuration and its voltage distribution

When operating at 0.1 MHz, the dielectric losses are small compared with the copper losses, alternative winding configurations are required to reduce the copper losses. A copper tubing surface spiral parallel winding (CT SSPW), shown in Fig. 3-24, adds another winding in parallel with the CT SSW. The ESRs can be reduced because of the parallel structure, and the mutual inductance maintains almost the same, therefore, the coil-to-coil efficiency can be improved. However, the ESR will not be reduced by half due to the proximity effect between two parallel windings. In addition, the spatial voltage between the first turn and the end turn is still (N – 1) × V/N.

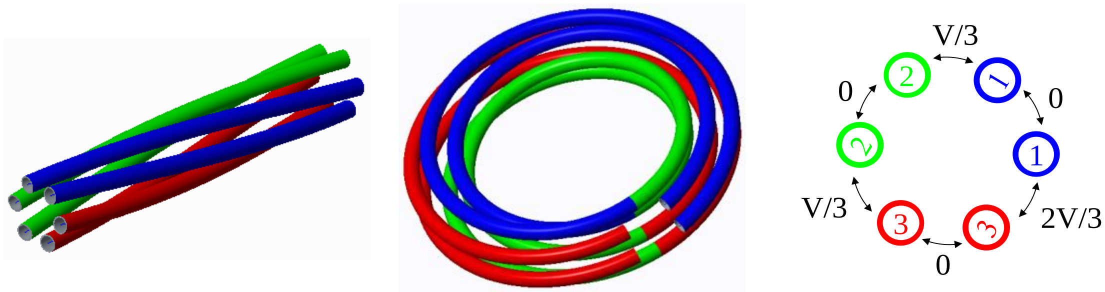

(a) Six-turn twisted coil (b) CT SSPW structure (c) Voltage distribution

Fig. 3-24. A copper tubing SSPW configuration and its voltage distribution

Although the CT SSPW can reduce the ESR, the spatial electric field, especially between the first turn and the end turn, will be increased due to the reduction of the spatial clearance caused by the added parallel winding, while the spatial voltage between two parallel windings is close to zero as shown in Fig. 3-24 (c). Although the spatial clearance between the first turn and the end turn can be increased by reducing the distance between two parallel windings, the ESR will increase due to the proximity effect. Alternative winding configuration is required to reduce the spatial voltage stress while maintaining low ESR.

A copper tubing surface spiral antiparallel winding (CT SSAPW), shown in Fig. 3-25, twists two parallel windings in the opposite direction to separate the first turn and the end turn using twist factor 1, the voltage stress between adjacent turns can be equalized, the maximum voltage between adjacent turns is reduced from (N – 1) × V/N to V/N, which improves the power scalability limitation due to voltage breakdown. In addition, the ESR can be reduced due to the parallel structure. Since the CT SSAPW input and output terminals are not at the same side as the CT SSW and the CT SSPW, the spatial clearance between adjacent turns is slightly smaller.

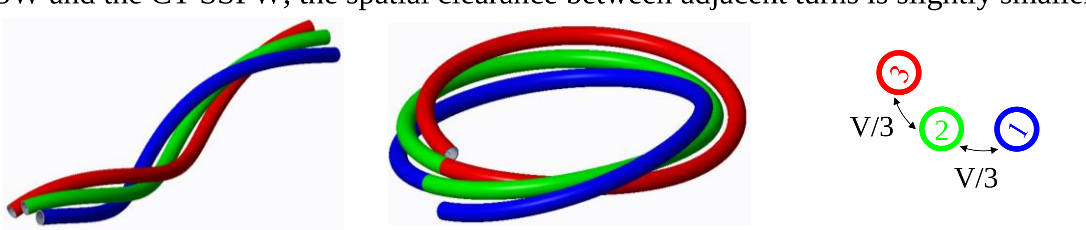

(a) Three-turn twisted coil (b) Half of the CT SSAPW structure (c) Voltage distribution

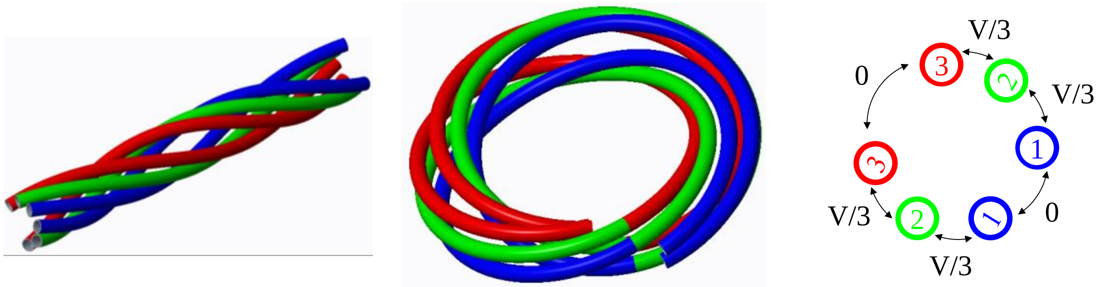

(d) Six-turn twisted coil (e) CT SSAPW structure (f) Voltage distribution

Fig. 3-25. A copper tubing SSAPW configuration and its voltage distribution

The cross-sectional radii are the same for the CT SSW, the CT SSPW, and the CT SSAPW. When transferring 3 kW through 300 mm air-gap at 0.1 MHz, the spatial electric field distributions are compared in Fig. 3-26.

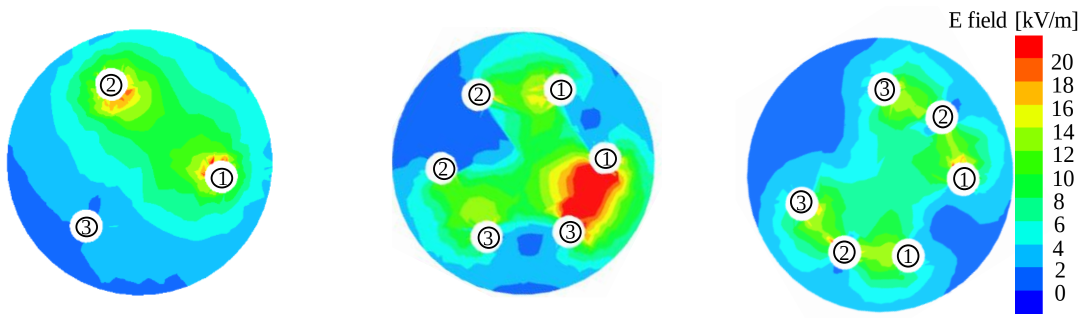

(a) CT SSW (b) CT SSPW (c) CT SSAPW

Test conditions: output power 3 kW, operating frequency 0.1 MHz,
Transmitter and receiver: 3-turn, $R_{winding}$ = 600 mm, $R_{cross\text{-}sectional}$ = 25 mm.

Fig. 3-26. Comparison of spatial electric field distributions

As shown in Fig. 3-26 (a) and (b), the peak electric fields of the CT SSW and the CT SSPW are located in the spatial region between the first turn and the end turn. The CT SSPW has the highest electric field between the first turn and the end turn due to the reduction of spatial air-clearance caused by the added parallel winding. The electric field between two parallel windings is close to zero as shown in Fig. 3-26 (b) and (c). The electric field distribution between adjacent turns of the CT SSAPW is equalized as shown in Fig. 3-26 (c) so that the maximum transferrable power can be pushed to a higher level without worrying about the voltage breakdown between the first turn and the end turn, especially when the number of turns is increased to achieve higher efficiency.

The self- and mutual inductances, the ESRs and the maximum achievable coil-to-coil efficiencies of the CT SSW, the CT SSPW, the CT SSAPW, and the conventional planar circular spiral winding are compared in Table 3-2.

Table 3-2. Comparison of the self- and mutual inductances, the ESRs, and the maximum achievable coil-to-coil efficiencies (N = 3)

	CT SSW	CT SSPW	CT SSAPW	CPSW
L_{tx} [μH]	23.32	21.79	22.13	26.13
R_{tx} [mΩ]	32.2	21.2	22.8	41.8
L_{rx} [μH]	23.32	21.77	22.13	26.12
R_{rx} [mΩ]	32.2	21.5	22.8	41.8
M [μH]	6.07	6.06	6.06	5.70
$\eta_{coil,\ max}$ [%]	98.33	98.89	98.81	97.69

As shown in Table 3-2, the SSW configurations have higher mutual inductances and lower ESRs than the conventional planar circular spiral winding due to large average coil radii and low proximity effect twist pattern. Compared with the CT SSW, the ESRs are reduced 33% for the CT SSPW, and 29% for the CT SSAPW rather than 50% because of the proximity effect between two parallel windings. The mutual inductances are almost the same for the CT SSW, the CT SSPW, and the CT SSAPW. Compared with other windings, the CT SSPW has the highest efficiency factor, therefore, it has the highest maximum achievable coil-to-coil efficiency.

Since the SSW configurations have equal diameter per turn to maintain the air-gap center plane magnetic field, and the air-gap center plane electric field still have safety margins, the number of turns can be increased to achieve higher efficiency. When the number of turns is increased to 5, the voltage and spatial electric field distributions are compared in Fig. 3-27.

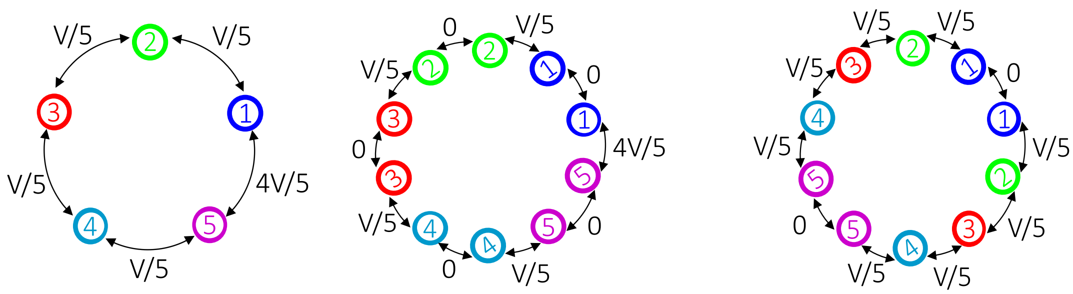

(a) CT SSW voltage distribution

(b) CT SSPW voltage distribution

(c) CT SSAPW voltage distribution

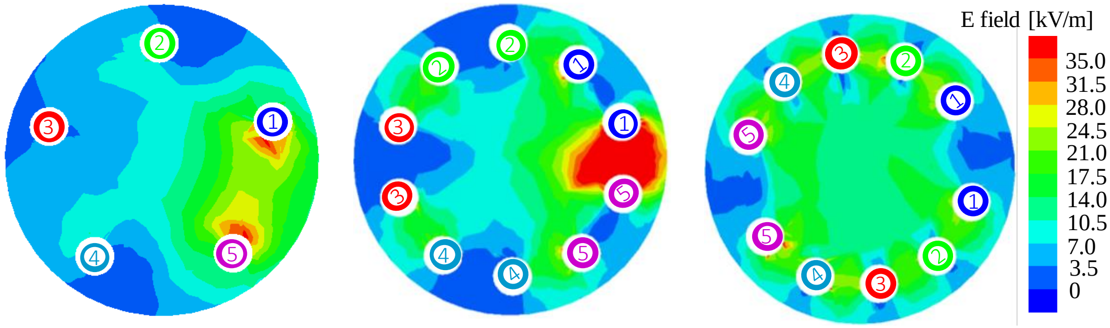

(d) CT SSW electric field distribution

(e) CT SSPW electric field distribution

(f) CT SSAPW electric field distribution

Test conditions: output power 3 kW, operating frequency 0.1 MHz,
Transmitter and receiver: 5-turn, $R_{winding}$ = 600 mm, $R_{cross\text{-}sectional}$ = 25 mm.

Fig. 3-27. Comparison of spatial voltage and spatial electric field distributions

As shown in Fig. 3-27 (a) and (b), the peak electric fields of the CT SSW and the CT SSPW are located in the spatial region between the first turn and the end turn. The CT SSPW has the highest electric field between the first turn and the end turn due to the reduction of spatial air-clearance because of the added parallel winding. The electric field distribution between adjacent turns of the CT SSAPW is equalized as shown in Fig. 3-27 (c). Compared with 3-turn windings, the spatial electric field between adjacent turns increase significantly, especially the CT SSW and the CT SSPW.

The self- and mutual inductances, ESRs and the maximum achievable coil-to-coil efficiencies of CT SSW, CT SSPW, and CT SSAPW are compared in Table 3-3.

Table 3-3. Comparison of the self- and mutual inductances, the ESRs, and the maximum achievable coil-to-coil efficiencies (N = 5)

	CT SSW	CT SSPW	CT SSAPW
L_{tx} [μH]	58.85	56.68	57.03
R_{tx} [mΩ]	61.4	47.3	50.4
L_{rx} [μH]	58.89	56.71	57.05
R_{rx} [mΩ]	61.3	47.2	50.6
M [μH]	17.03	17.02	17.02
$\eta_{coil,\ max}$ [%]	98.86	99.12	99.07

As shown in Table 3-3, the ESR reduction and efficiency improvement follow previous analyses. Compared with 3-turn windings, the improvement of the maximum achievable coil-to-coil efficiencies is limited. Considering the increases of the copper mass and the spatial electric fields between adjacent turns, the 3-turn winding configuration is a better choice to implement in the system.

3.4 Experimental evaluation of power transfer efficiency, and magnetic field and electric field distributions

In this section, the experimental test setup, including the power converter, the rectifier, and the copper tubing surface spiral parallel winding, will be introduced at first. Then the DC-to-DC power transfer efficiencies under aligned and misaligned conditions and the loss distributions will be investigated. After that, the air-gap center plane magnetic flux density and electric field intensity will be measured under 1 kW and 3 kW.

3.4.1 Experiment test setup

A 3-turn copper tubing surface spiral parallel winding (CT SSPW) with twist factor of 1 was built to transfer 3 kW through 300 mm air-gap at 0.1 MHz while maintaining the air-gap center plane magnetic flux density and electric field intensity within the IEEE C95.1-2005 electrostimulation and tissue heating safety limits. The coil prototype is shown in Fig. 3-28.

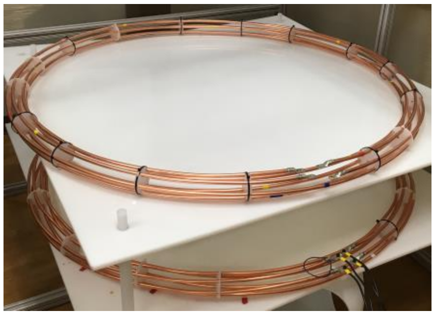

(a) WPT coil prototype

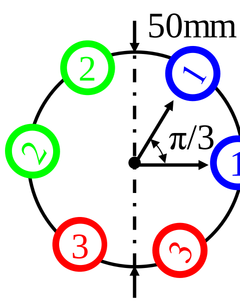

(b) Coil cross-sectional view

Fig. 3-28. WPT coil prototype built with 3-turn copper tubing surface spiral winding

As shown in Fig. 3-28, two parallel windings distribute uniformly around the cross-sectional circle, the winding radius is 600 mm, the cross-sectional radius is 25 mm. Polycarbonate (PC) was used to build the circular dielectric support pad.

When transferring 3 kW at 0.1 MHz, the magnetic and electric field distributions FEA results are shown in Fig. 3-29.

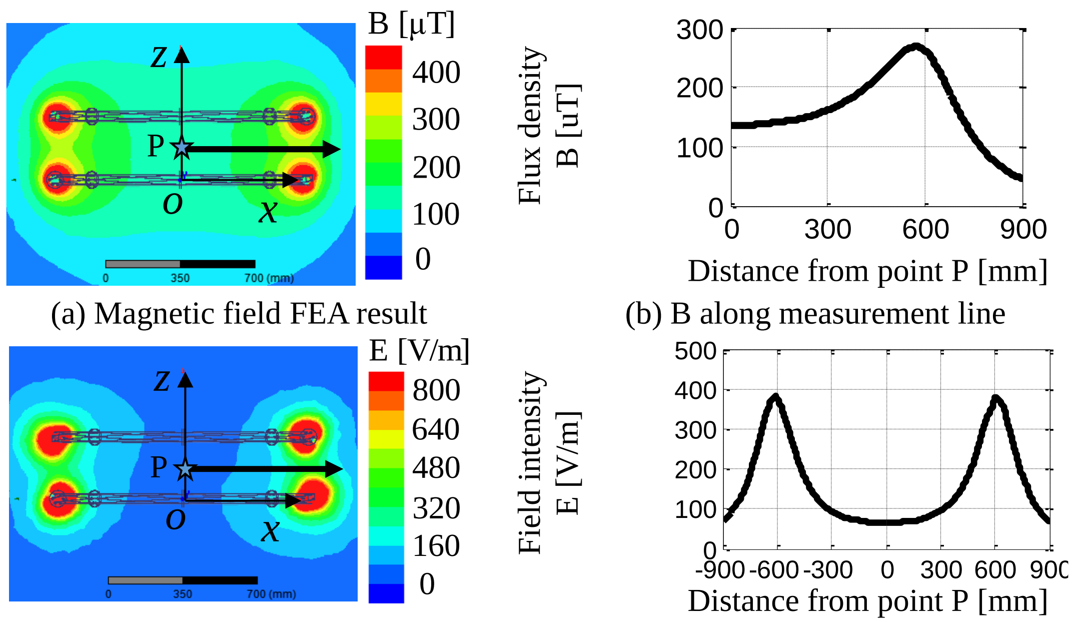

(a) Magnetic field FEA result (b) B along measurement line

(c) Electric field FEA result (d) E along measurement line

Test conditions: Operating frequency: 0.1 MHz. Output power: 3 kW. TX and RX: 3 turns, coil radius 600 mm, cross-sectional radius 25 mm. Transfer distance: 300 mm. Dielectric material: Polycarbonate (PC). Dielectric thickness: 9.525 mm.
IEEE C95.1-2005 @ 0.1 MHz: B_{peak} = 289.67 μT, E_{peak} = 868.32 V/m.

Fig. 3-29. Magnetic field and electric field distributions of a 3-turn CT SSPW

As shown in Fig. 3-29, the air-gap center plane peak magnetic flux density and peak electric field intensity are 268.57 μT and 384.2 V/m, respectively, which are lower than the IEEE C95.1-2005 safety limits 289.67 μT and 868.32 V/m, and provides enough safety margins for the operations under misalignment and pushing to high power level.

The transmitter self-inductance L_{tx} and ESR R_{tx}, the receiver self-inductance L_{rx} and ESR R_{rx}, and the mutual inductance M at 0.1 MHz are measured by WK 6500B impedance analyzer and shown Table 3-4.

Table 3-4. FEA and measured results of the self- and mutual inductances, and the ESRs

	L_{tx} [μH]	R_{tx} [mΩ]	L_{rx} [μH]	R_{rx} [mΩ]	M [μH]
FEA results	21.79	21.2	21.77	21.5	6.06
Measured results	21.3	23.4	21.27	23.6	6.02

As shown in Table 3-4, the measured results are almost the same as the FEA results, which ensure the high coil-to-coil power transfer efficiency. The maximum achievable coil-to-coil power transfer efficiency in the FEA simulation is 98.89%.

An H-bridge inverter using silicon-carbide (SiC) MOSFETs C2M0025120D with 25 mΩ drain-source on-state resistance is built to drive the transmitter and achieve low conduction losses. SiC Schottky diodes IDH20G120C5 are used to build the rectifier to reduce the reverse recovery losses. The series-parallel (S-P) resonant compensated circuit topology and the test setup of the proposed system are shown in Fig. 3-30.

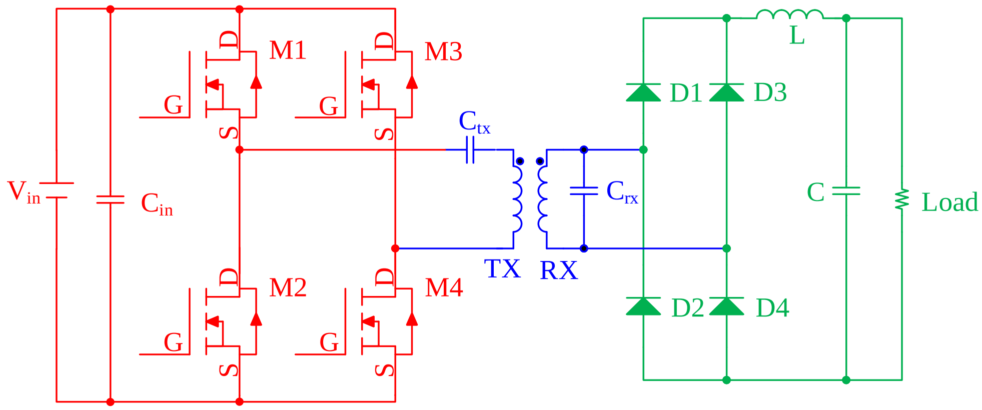

(a) Circuit topology of a S-P compensated inductive WPT system

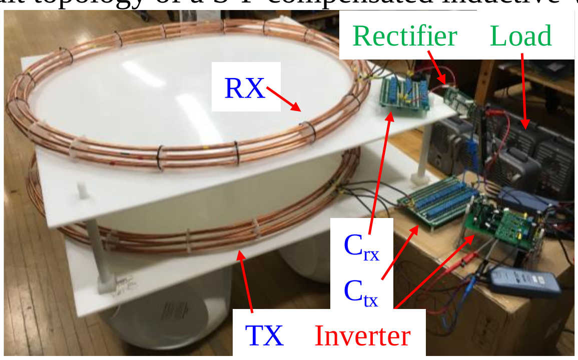

(b) Test setup of a series-parallel compensated inductive WPT system

Fig. 3-30. Topology and test setup of proposed WPT system

As shown in Fig. 3-30, S-P resonant tank is adopted. The switching frequency is set as 100 kHz. The resonant capacitors are calculated and set as C_{tx} = 136.5 nF, C_{rx} = 119.4 nF. PHE450 series film capacitors are used to build the resonant tanks due to low ESR and high rated voltage at 0.1 MHz. The ESRs of the resonant tanks C_{tx} and C_{rx} are measured as 16.3 mΩ and 15.8 mΩ, respectively.

The MOSFET M1 gate PWM signal V_{g_M1} and the primary coil current I_{tx} are measured as shown in Fig. 3-31.

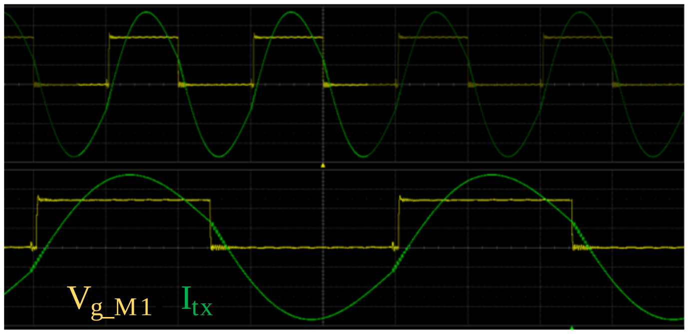

Fig. 3-31. Overlay of gate PWM signal and primary coil current

As shown in Fig. 3-31, the zero-voltage soft switching is achieved, the zero-current soft switching is not achieved, the turn-on current can be further reduced by tuning the primary resonant capacitor.

3.4.2 Analysis of the DC-to-DC power transfer efficiencies under aligned and misaligned conditions

When the transmitter coil and the receiver coil are aligned perfectly, the DC-to-DC power transfer efficiency η is experimentally tested under different power level, the test results are listed in Table 3-5.

Table 3-5. The DC-to-DC power transfer efficiency under different power level

P_{in} [W]	110.48	538.23	1064.4	2121.5	3274.8
P_{out} [W]	103.75	506.97	1004.8	2005.2	3099.2
η [%]	93.91	94.19	94.41	94.52	94.64

As shown in Table 3-5, the DC-to-DC efficiency increases slightly as the power level increases, all DC-to-DC power transfer efficiencies are above 93%. The main efficiency improvement is from the rectifier side and the reverse diode in parallel with the MOSFET, the diode power losses are proportional to the current I due to constant voltage drop, while other sections power losses are proportional to I^2, therefore, as the power level (or the required current) increases, the diode power losses are reduced compared with other sections power losses, which lead to an efficiency improvement.

When transferring 3099.2 W, the input voltage and current, and the output voltage and current waveforms are measured and shown in Fig. 3-32. The input voltage ripple is caused by the reversing current from the transmitter coil, which charges the DC link capacitor and increases the DC link voltage. When the zero-current switching is achieved, or the capacitance of the DC link capacitor is increased, the input voltage ripple can be reduced. The input current, output voltage and current ripples are very small. The average input voltage and current are 138.58 V and 23.631 A, respectively. The average output voltage is 383.3 V, which is located within the EV battery normal voltage range 200 V – 500 V. The average output current is 8.075 A.

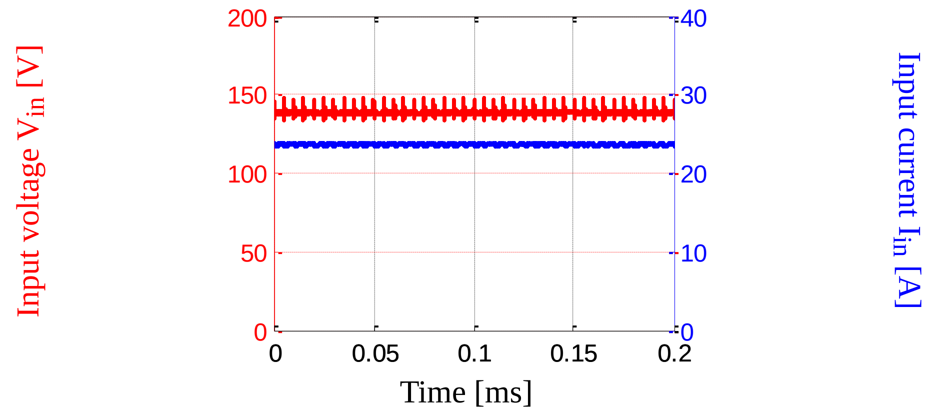

(a) Input voltage and current waveforms

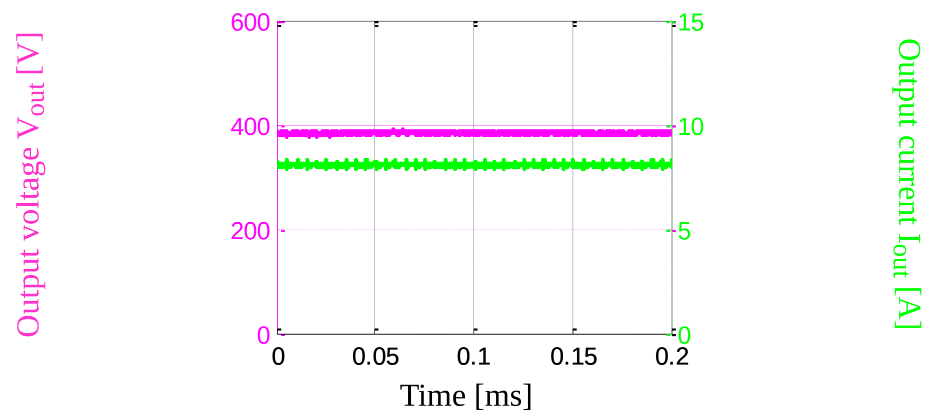

(b) Output voltage and current waveforms

Fig. 3-32. The input and output voltage and current waveforms when transferring 3099.2 W

The voltages and currents of the resonant capacitors are also measured. Using their ESRs, their losses can be calculated. With the output current and the voltage drop of the rectifier diode, the rectifier reverse recovery losses can be calculated. The power converter switching loss is small due to zero-voltage soft switching. The power converter loss can be calculated by adding the conduction losses and the parallel diode reverse recovery losses. When transferring 3099.2 W, the system loss distribution is calculated and shown in Fig. 3-33.

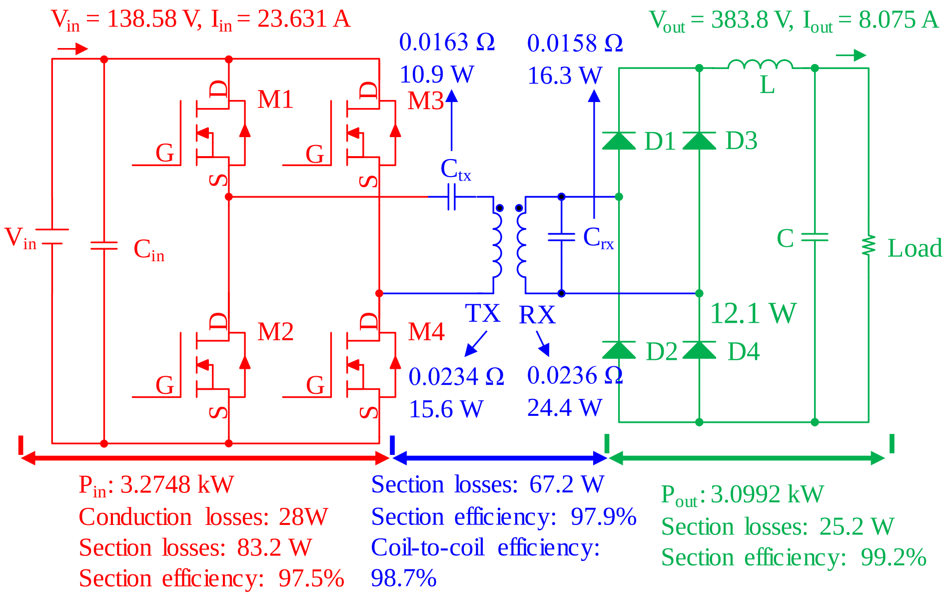

Fig. 3-33. System loss distribution under 3 kW power level

As shown in Fig. 3-33, the coil-to-coil efficiency is 98.7%, which is almost the same as the FEA result 98.89%. The resonant capacitors total loss is 27.2 W, which is comparable with the windings total loss 40.0 W, special attention needs to be paid to the capacitor ESR when trying to improve the DC-to-DC efficiency. In addition, the power converter efficiency can also be improved by further tuning the primary side resonant capacitor to achieve zero-current switching and using devices with lower conduction resistance. Besides that, voltage breakdown between adjacent turns didn't happen when transferring 3 kW, while the 3D printed SSW can only transfer 1 kW.

Considering lateral and angular misalignments are unavoidable in the WPT systems, the DC-to-DC efficiencies are tested under lateral and angular misalignments. The test setups and test results are shown in Fig. 3-34.

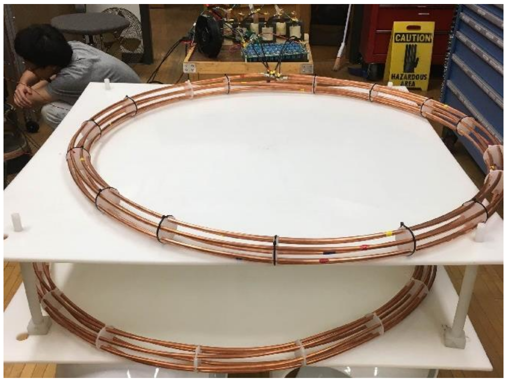

(a) Lateral misalignment test setup

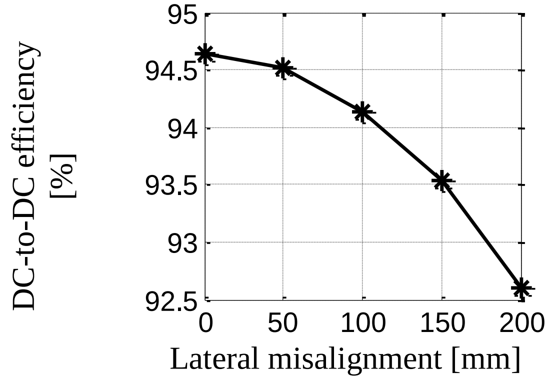

(b) DC-to-DC efficiency under lateral misalignment

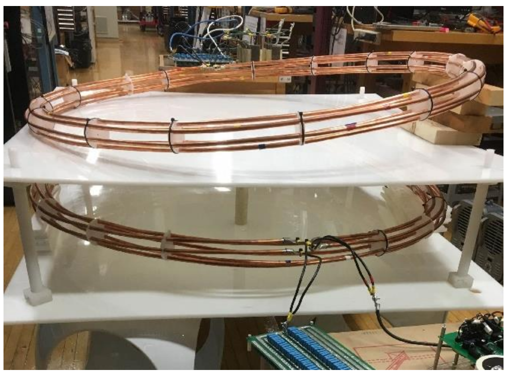

(c) Angular misalignment test setup

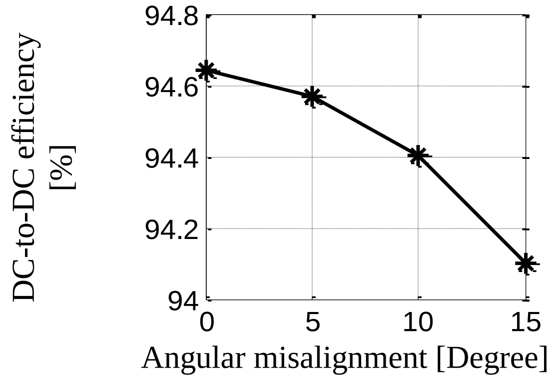

(d) DC-to-DC efficiency under angular misalignment

Fig. 3-34. Test setups and DC-to-DC efficiencies under lateral and angular misalignments

As shown in Fig. 3-34, when the lateral misalignment is within 200 mm, which is only 1/6 of the coil diameter, the DC-to-DC efficiency remains above 92%. When the angular misalignment is within 15-degree, the reduction of the DC-to-DC efficiency is within 1%. The benefit of using a large radius coil is that the mutual inductance remains almost the same within normal lateral and angular misalignments, which ensures that the reduction of the power transfer efficiency under normal misalignment is small.

It's also necessary to investigate the effects of misalignment on output power P_{out}. Compared with angular misalignment, lateral misalignment must be paid more attention since it can cause more efficiency reduction and happen more frequently. The effect of lateral misalignment on mutual inductance M is evaluated analytically using the proposed prototype and compared with FEA results as shown in Fig. 3-35.

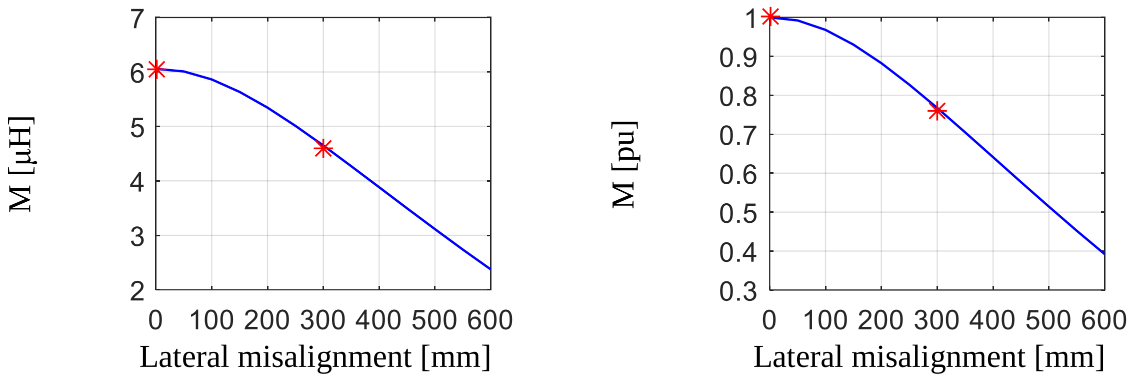

(a) M (μH) vs. Lateral misalignment (b) M (pu) vs. Lateral misalignment

Fig. 3-35. Effects of lateral misalignment on mutual inductance (Analytical, FEA)

According to Fig. 3-35, the analytical calculation result and the FEA result match each other very well. When the lateral misalignment is within winding radius, as the lateral misaligned distance increases, M first reduces slowly then reduces almost linearly. It should also be noted that M is not 0 even when the lateral misaligned distance is equal to winding radius due to the circular winding vertical coupling mode.

SS, SP and LCC-LCC resonant compensation topologies are widely used in WPT area. The effects of lateral misalignment on input impedance Z_{in}, P_{out} (W), P_{out} (pu) and η_{coil} are shown in Fig. 3-36. During the evaluation, the input voltage V_{in} remains the same as $150\sin(\omega_0 t)$ V, the compensation capacitors, winding self-inductances and ESRs, and load also remain the same. Only M reduces with the lateral misaligned distance. M is calculated analytically.

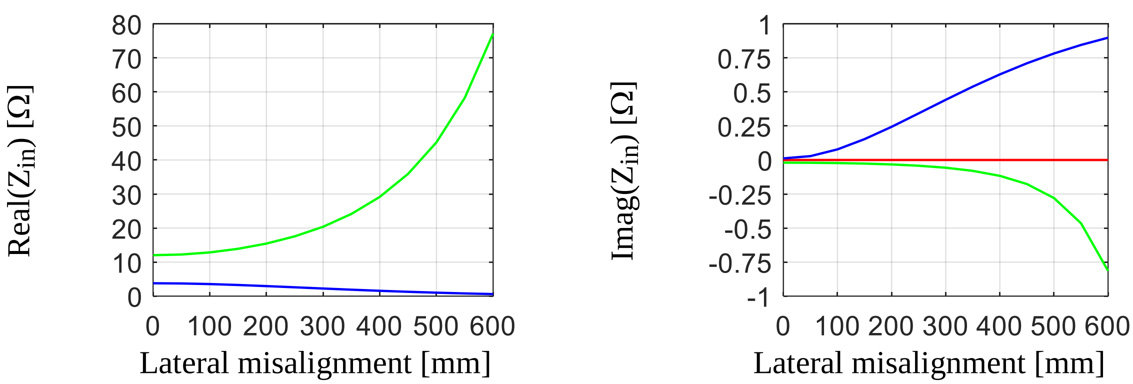

(a) Real(Z_{in}) vs. Lateral misalignment (b) Imag(Z_{in}) vs. Lateral misalignment

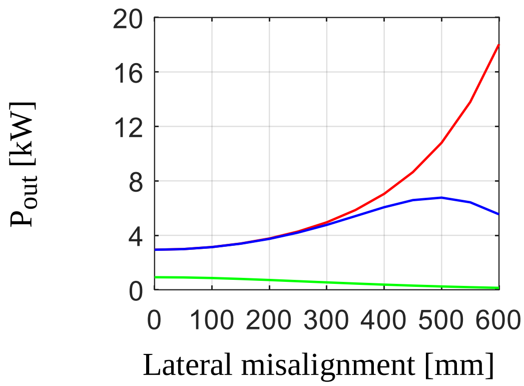

(c) P_{out} (W) vs. Lateral misalignment

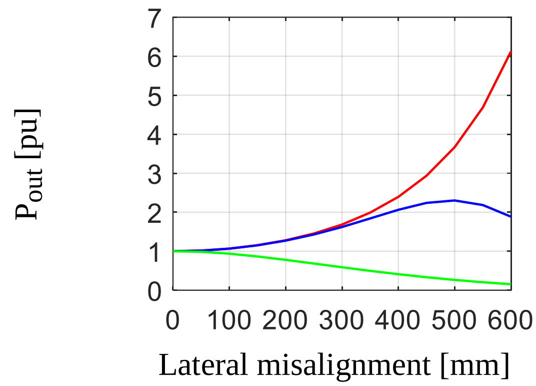

(d) P_{out} (pu) vs. Lateral misalignment

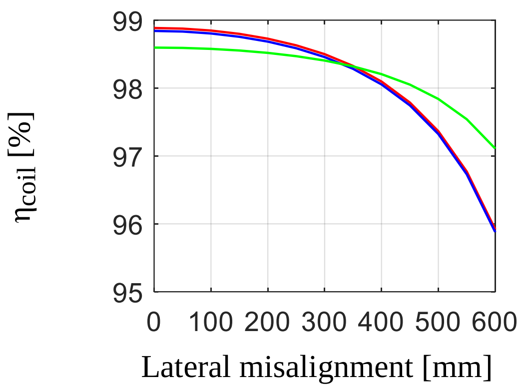

(e) η_{coil} vs. Lateral misalignment

Legend: SS, SP, LCC-LCC
Test conditions:
Winding parameters: L_{tx} = 21.79 µH, R_{tx} = 21.2 mΩ, L_{rx} = 21.77 µH, R_{rx} = 21.5 mΩ
SS: C_{tx} = 116.25 nF, C_{rx} = 116.35 nF
SP: C_{tx} = 125.99 nF, C_{rx} = 116.35 nF
LCC-LCC: L_f = 15.25µH, C_f = 166.07 nF, C_s = 388.66 nF

Fig. 3-36. Effects of lateral misalignment on Z_{in}, P_{out}, and η_{coil}

As shown in Fig. 3-36 (a) and (b), when the lateral misalignment distance increases, or when M reduces, SS and SP topologies Z_{in} reduce, while LCC-LCC topology Z_{in} increase. That leads to the quadratic increase of P_{out} in SS topology, and the linear reduction of P_{out} in LCC-LCC topology, as shown in Fig. 3-36 (c) and (d). In SP topology, P_{out} first increases due to the reduction of Z_{in}, then reduces due to the reactive power at the receiver side. It should also be noted that compared with LCC-LCC topology, SS and SP topologies have higher P_{out} due to lower Z_{in}. Besides that, LCC-LCC topology can achieve higher η_{coil} under lateral misalignment with the sacrifice of peak η_{coil} as shown in Fig. 3-36 (e), while SS and SP topologies can achieve nearly the same η_{coil}. More discussions about impedance matching network design will be presented in chapter 6. In order to regulate the output power at given levels, closed-loop control is recommended. Winding position self-sensing technique combining with the EV auto parking function is beneficial to reduce the lateral misalignment and maintain high transfer efficiency.

3.4.3 Air-gap center plane magnetic flux density and electric field intensity

When transferring 1 kW and 3 kW, the air-gap center plane magnetic flux density and electric field intensity are measured from the central point P along x-direction using NARDA EHP 200 probe and compared with the FEA results as shown in Fig. 3-37. Since the air-gap center plane peak electric field intensity is located above the transmitter terminal when the transmitter terminal and the receiver terminal are placed at opposite positions according to the FEA result, measuring the electric field intensity along the x-direction in the air-gap center plane can capture the air-gap center plane peak electric field intensity.

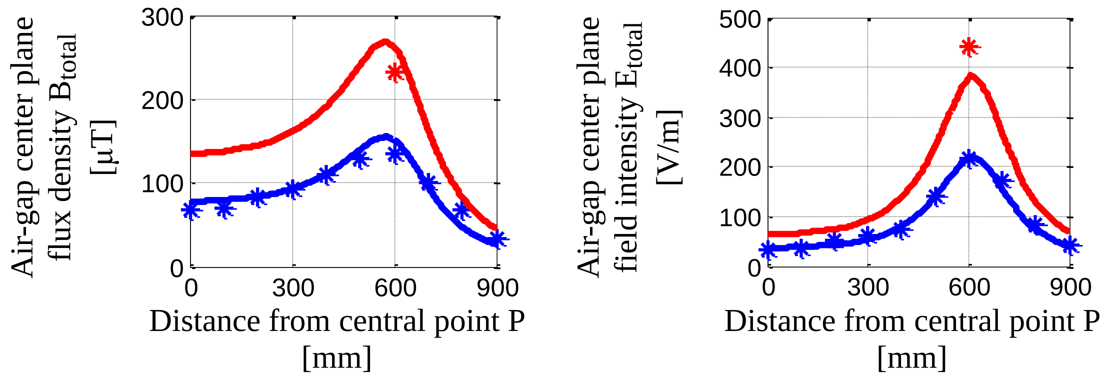

(a) WPT coil prototype (b) Coil cross-sectional view

* Experimental results when P_{out} = 1 kW, - FEA results when P_{out} = 1 kW

* Experimental results when P_{out} = 3 kW, - FEA results when P_{out} = 3 kW

Fig. 3-37. The air-gap center plane magnetic flux density and electric field intensity along the x-direction measurement line

As shown in Fig. 3-37, the test results of the magnetic flux density and the electric field intensity along the x-direction measurement line in the air-gap center plane are close to the FEA results, the peak magnetic flux density and electric field intensity are located almost above the transmitter coil terminal. The maximum magnetic flux density and electric field intensity along the x-direction measurement line in the air-gap center plane, when the output power is 3 kW, are measured as 231.65 μT and 442.31 V/m, respectively, which are lower than the IEEE C95.1-2005 magnetic field safety limit of 289.67 μT and electric field safety limit of 868.42 V/m, there is enough safety margin for operations under misalignment and a potential to push to transfer higher power.

3.5 Summary

In the beginning, the general design variables that affect the air-gap center plane magnetic flux density and electric field intensity are identified as the coil radius, the number of turns, the inter-turn distance, the transfer distance, and the operating frequency. Based on these five general design variables, a loosely coupled inductive WPT system general design methodology using a planar circular spiral winding as design example is developed to achieve low air-gap center plane magnetic flux density, and low air-gap center plane electric field intensity while maintaining a high power transfer efficiency. Through iteration calculations, the effects of the general design variables on air-gap center plane peak magnetic flux density and peak electric field intensity, and maximum achievable coil-to-coil power transfer efficiency are investigated: the air-gap center plane peak magnetic flux density will increase when the coil radius reduces, the number of turns increases due to the increase of the magnetomotive force and the reduction of the average coil radius, the inter-turn distance increases due to the reduction of the average coil radius and the reduction of the mutual inductance, the operating frequency reduces due to the increase of the required current to transfer the same amount of power, and the transfer distance reduces due to the leakage flux. The air-gap center plane peak electric field intensity will increase when the coil radius increases due to the increase of the required excitation voltage, the number of turns increases due to the increase of the required excitation voltage and the increase of the magnetic flux density, the inter-turn distance reduces due to the increase of the required excitation voltage, the operating frequency increases due to the increase of the required excitation voltage. The maximum transferable power under the safety standard is a tradeoff between the magnetic field and the electric field mainly manipulated by the operating frequency, the coil enclosed area, and the transfer distance.

Then, design methods to reduce the dielectric losses, the spatial voltage stress and the ESRs are developed. The dielectric losses can be reduced by using low relative permittivity and low dissipation factor material, by increasing the equivalent dielectric resistance, such as the concave dielectric geometry, and by reducing the spatial voltage stress using alternative coil geometries. Through emulating the 3D printed SSW configuration using copper tubing, large spatial clearance can be obtained to reduce the dielectric losses and the spatial voltage stress, in addition, the ESR increased by the skin effect can be compensated by the reduction of the proximity effect. Surface spiral parallel winding adds another conductor in parallel to reduce the ESR and maintain the same mutual inductance, however, the spatial voltage stress between the first turn and the end turn is still the maximum location. Surface spiral antiparallel winding twists two parallel windings in opposite direction to equalize the spatial voltage stress and achieves low ESR because of the parallel structure. The reduction of the ESR by using parallel structure is less than 50% because of the proximity effect between two parallel windings.

At last, the developed general design methodologies to achieve low air-gap center plane magnetic flux density and electric field intensity, and to improve the coil-to-coil efficiency are evaluated by the experimental tests. The DC-to-DC efficiency of the proposed system under aligned, lateral misalignment within 200 mm, and angular misalignment within 15-degree operating conditions are evaluated experimentally with above 92% efficiency, When transferring 3 kW at 0.1 MHz under the aligned condition, the air-gap center plane peak magnetic flux density and peak electric field intensity are lower than the IEEE C95.1-2005 magnetic field and electric field safety limits with enough safety margin to operate under misaligned conditions.

Chapter 4 Low Air-Gap Magnetic Field, Low Air-Gap Electric Field Shielding Designs

4.1 Introduction

Although winding with 600 mm radius can be installed under the EV chassis, considering that the diameter of the magnetic shield is usually set as 1.5 – 2 times the diameter of the coils to maintain high power transfer efficiency, it's necessary to reduce the coil diameter, which will lead to high air-gap magnetic field. This chapter will begin with investigation of the traditional magnetic shield effects on air-gap magnetic and electric fields. Then active and passive methods will be developed to reduce the air-gap magnetic field. In particular, a new "T" type shielding design will be proposed to reduce the whole air-gap magnetic and electric fields simultaneously without degrading the efficiency. After that, the effects of the vehicle metal chassis on the field distributions and power transfer efficiency will be identified. In the end, the proposed shielding design will be optimized with reduced mass while maintaining the same performance.

4.2 Effects of traditional magnetic shield on air-gap magnetic field and electric field

The proposed winding design from chapter 3 is compared to the normal vehicle design space among four wheels. Tesla Model S is taken as a baseline example. The feasible design space among four wheels is 2426.6 mm (Length) × 1662 mm (Width) considering that the wheel base is 2960 mm, the front track is 1662 mm, and the wheel diameter is 21" (533.4 mm) [256]. The proposed model and the feasible design space are compared in Fig. 4-1 under the same scale.

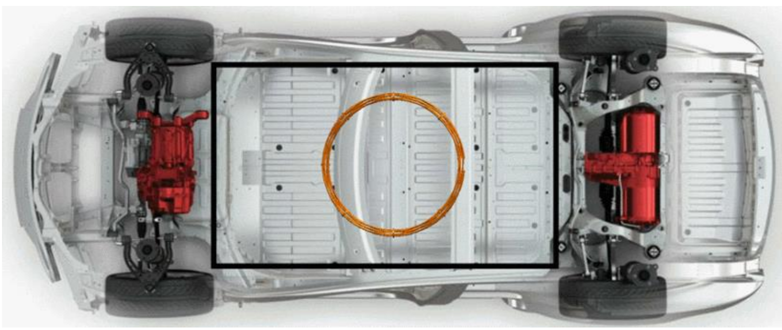

Fig. 4-1. Comparison of proposed coil size and feasible design space

As shown in Fig. 4-1, the design space is still much larger than the proposed design. However, additional magnetic shields below the transmitter and above the receiver, as shown Fig. 4-2, are required to provide a magnetic flux return path to ensure the coil-to-coil power transfer efficiency, since the vehicle aluminum chassis can shield the magnetic flux generated by the coil and reduce the mutual inductance significantly.

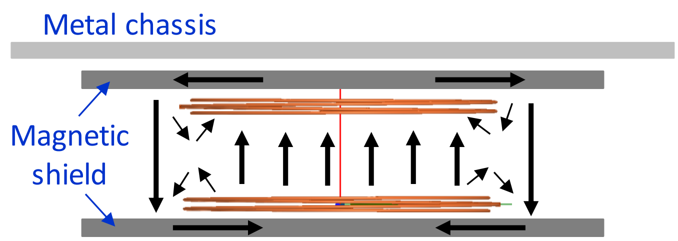

Fig. 4-2. Configuration of inductive WPT windings installed under the vehicle

Assuming the magnetic shield radius is r_m, combining with the air-core winding general design methodology developed in chapter 3, the magnetic design methodology flow chart for low air-gap magnetic and electric fields, and high efficiency is presented in Fig. 4-3.

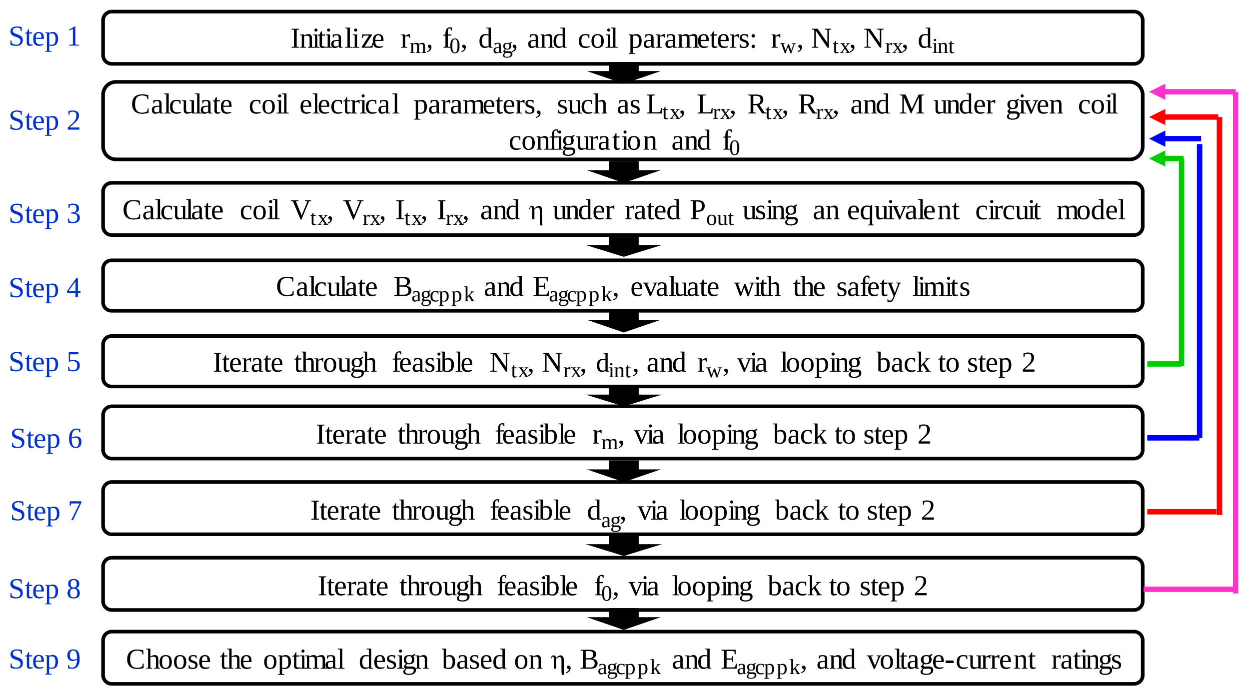

Fig. 4-3. Magnetic design flow chart for low low air-gap magnetic and electric fields, and high efficiency

According to the literature review, the diameter of the magnetic shield is usually set as 1.5 – 2 times the diameter of the winding to maintain high power transfer efficiency. If the coil diameter is 1.2-m as proposed design, after adding magnetic shields, the magnetic shield diameter would be larger than the width requirement in the feasible design space. Therefore, reducing coil diameter is necessary.

Copper tubing surface spiral winding (CT SSW) will be used in the following analyses. When the winding radius is reduced, the mutual inductance will reduce. In order to maintain a high coil-to-coil efficiency, the number of turns can be increased. When the coil radius of a CT SSW is reduced from R_a = 600 mm to R_b = 310 mm, the number of turns N is increased from 3 to 4, the twist angle is changed from 360° + 360/3° when N = 3 to 360° + 360/4° when N = 4, a ferrite material with relative permeability μ_r = 1000 is used to provide the magnetic flux return path below the transmitter and above the receiver, the ferrite shield diameter is set as R_a = 600 mm. The configurations are compared in Fig. 4-4. X-direction goes above the transmitter terminal, the transmitter and the receiver terminals are placed at opposite positions in the FEA simulation to balance the electric field distribution. The system without the vehicle metal frame will be analyzed first. Its effects will be analyzed at the end section of this chapter.

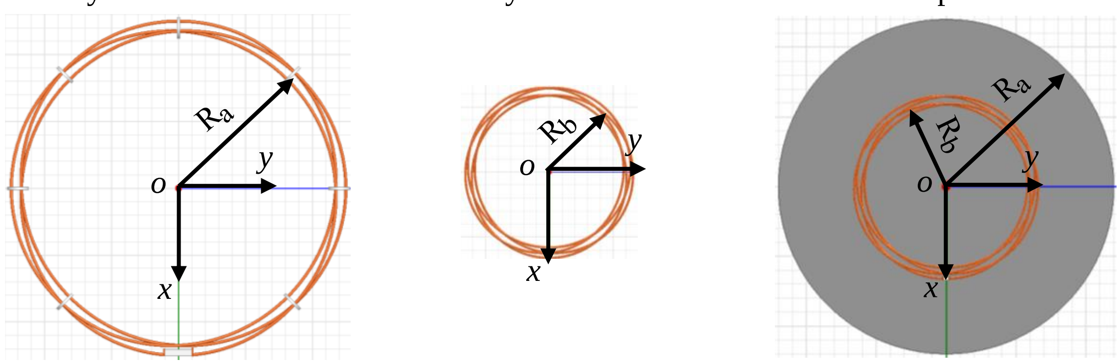

(a) 3-turn CT SSW (Coil radius R_a = 600 mm) (b) 4-turn CT SSW with (Coil radius R_b = 310 mm) (c) 4-turn CT SSW with ferrite shield

Fig. 4-4. Comparison of winding configurations

The self-inductances, mutual inductances, ESRs and maximum coil-to-coil efficiencies are compared in Table 4-1.

Table 4-1. Comparison of the self- and mutual inductances, ESRs, and efficiencies

	L_{tx} [μH]	R_{tx} [mΩ]	L_{rx} [μH]	R_{rx} [mΩ]	M [μH]	$\eta_{coil,\ max}$ [%]
3-turn CT SSW R = 600 mm	23.32	32.2	23.32	32.2	6.07	98.33
4-turn CT SSW R = 300 mm	17.49	25.8	17.49	25.8	2.58	96.87
4-turn CT SSW with ferrite	27.71	31.2	27.71	31.0	6.30	98.44

As shown in Table 4-1, the ESRs are reduced when the coil radius is reduced from 600 mm to 310 mm due to the reduction of the skin effect loss. The mutual inductance reduces significantly when the coil radius is reduced, which leads to lower $\eta_{coil,\ max}$. After adding the ferrite shield, the mutual inductance is improved, since the ferrite shield helps concentrate and re-direct the magnetic flux, the ESRs are increased since the proximity effect is changed due to the change of the magnetic field distribution around the winding, which is caused by the magnetic materials.

When transferring 3 kW through 300 mm air-gap at 0.1 MHz with SP compensated resonant topology, the air-gap electric field distributions and air-gap center plane electric field intensities along the x-direction measurement line are compared in Fig. 4-5.

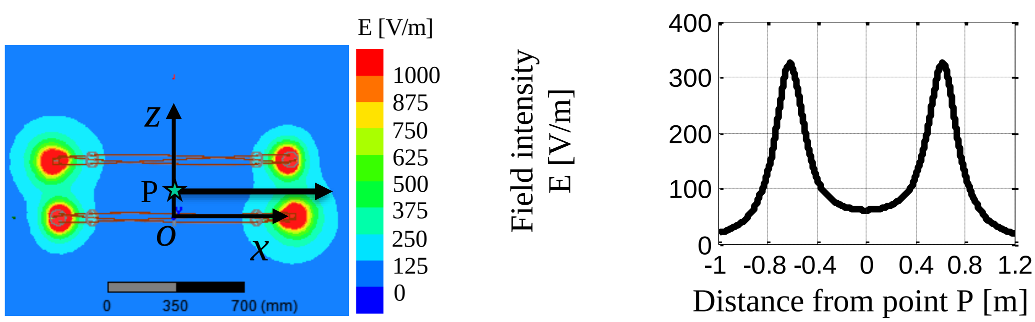

(a) Electric field distribution of 3-turn CT SSW with 600 mm radius

(b) Electric field intensity along measurement line of 3-turn CT SSW with 600 mm radius

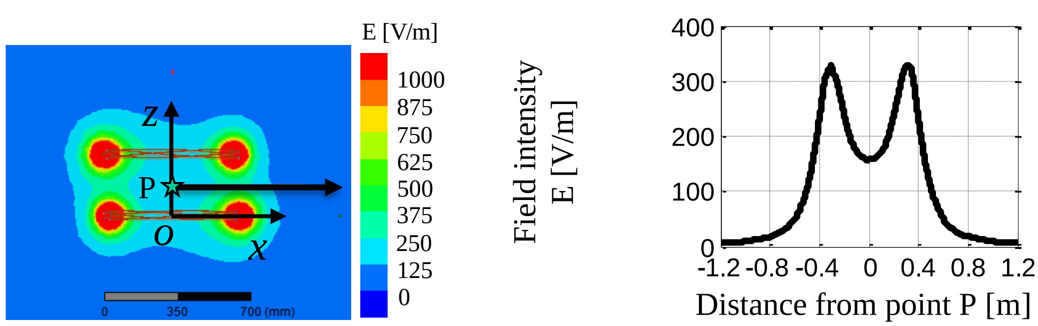

(c) Electric field distribution of 4-turn CT SSW with 300 mm radius

(d) Electric field intensity along measurement line of 4-turn CT SSW with 300 mm radius

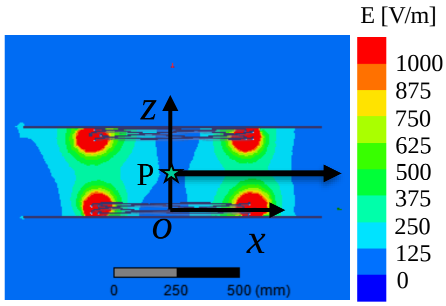

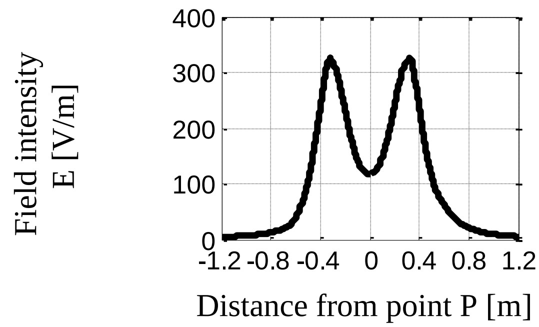

(e) Electric field distribution of 4-turn CT SSW with ferrite shield

(f) Electric field intensity along measurement line of 4-turn CT SSW with ferrite shield

Test conditions: operating frequency 0.1 MHz, output power 3 kW.
TX and RX: (a)(b) 3 turns, coil radius 600 mm. (c)(d) 4 turns, coil radius 300 mm.
(e)(f) 4 turns, ferrite μ_r = 1000, coil radius 300 mm, ferrite radius 600 mm.

Fig. 4-5. Comparison of the air-gap electric field distributions and the air-gap center plane electric field intensities along the measurement line

As shown in Fig. 4-5, E_{agcppk} are all located above the transmitter coil terminals. Using small radius coil is easy to satisfy the electric field intensity safety limit outside of the vehicle. E_{agcppk} are 327.10 V/m, 328.55 V/m and 325.61 V/m for the 3-turn CT SSW, 4-turn CT SSW, and 4-turn CT SSW with ferrite shield, respectively, which are almost the same and have enough safety margin compared with the IEEE C95.1 – 2005 electric field safety limit 868.32 V/m. It's easy to satisfy the electric field safety limit when using low number of turns and placing the transmitter terminal and the receiver terminal at opposite positions.

The air-gap magnetic field distributions and air-gap center plane magnetic flux densities along the x-direction measurement line are compared in Fig. 4-6.

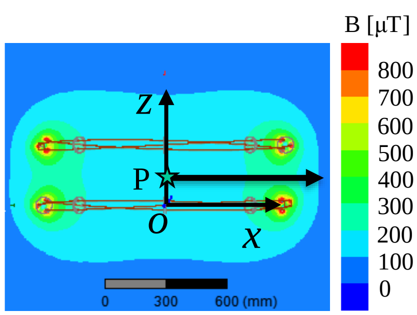

(a) Magnetic field distribution of 3-turn CT SSW with 600 mm radius

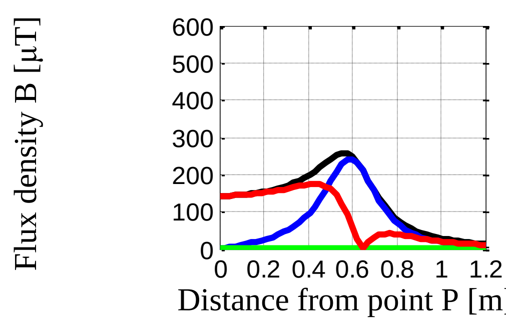

(b) Magnetic flux density along measurement line of 3-turn CT SSW with 600 mm radius

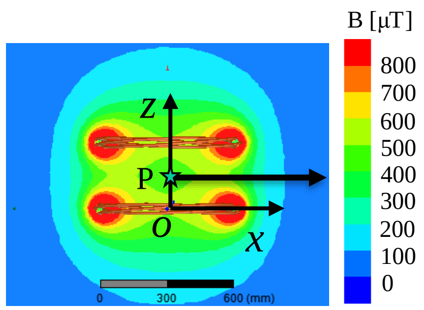

(c) Magnetic field distribution of 4-turn CT SSW with 300 mm radius

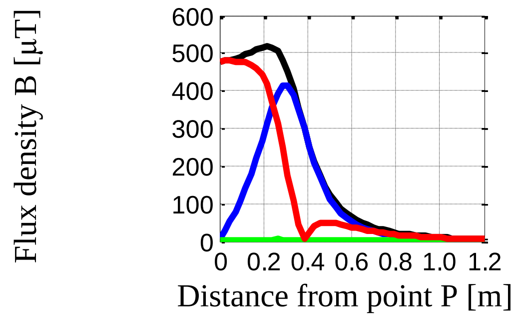

(d) Magnetic flux density along measurement line of 4-turn CT SSW with 300 mm radius

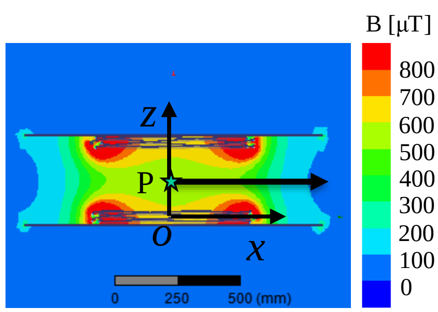

(e) Magnetic field distribution of 4-turn CT SSW with ferrite shield

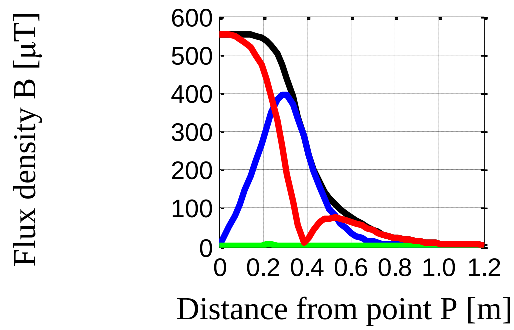

(f) Magnetic flux density along measurement line of 4-turn CT SSW with ferrite shield

Legend: B_{total}, B_x, B_y, B_z

Test conditions: operating frequency 0.1 MHz, output power 3 kW.

TX and RX: (a)(b) 3 turns, coil radius 600 mm. (c)(d) 4 turns, coil radius 310 mm. (e)(f) 4 turns, ferrite $\mu_r = 1000$, coil radius 310 mm, ferrite radius 600 mm.

Fig. 4-6. Comparison of magnetic field distributions and the air-gap center plane magnetic flux densities along the measurement line

As shown in Fig. 4-6, both z-direction and radial direction magnetic flux densities increase when the coil radius reduces, B_{agcppk} increases from 259.06 μT of the 3-turn CT SSW with 600 mm radius to 519.53 μT of the 4-turn CT SSW with 300 mm radius, which is about 1.8 times the IEEE C95.1-2005 magnetic field safety limit. After adding the ferrite shield, the radial direction leakage flux density reduces a little due to the concentrating effect of the magnetic shield, however, B_{agcppk} is increased from 519.53 μT to 553.77 μT, and the peak location is shifted from around coil terminal to the central point. Methods to reduce B_{agcppk} must be developed to satisfy the IEEE C95.1-2005 magnetic field safety limit.

4.3 Active design to reduce air-gap magnetic field

According to the magnetic field distribution analysis for winding with magnetic shielding in previous section, if B_z can be reduced, then B_{agcppk} will be reduced. The air-gap magnetic field is a vector combination of the magnetic fields generated by the transmitter and the receiver. Therefore, the air-gap magnetic field B_{agcp} can be manipulated by tuning the phase difference between the transmitter current and the receiver current. The relationship between the current phase difference θ and B_{agcp} is shown in Fig. 4-7.

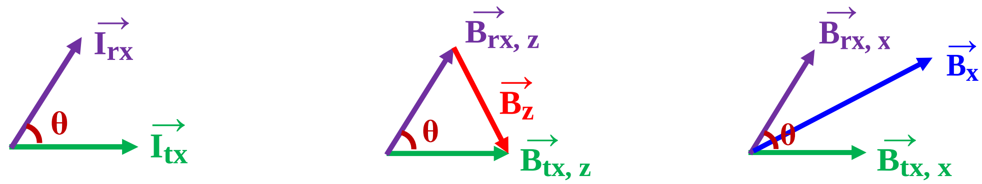

Fig. 4-7. Relationship between current phase difference and air-gap magnetic field

As shown in Fig. 4-7, if θ can be reduced, B_z will be reduced. However, the leakage component B_x will be increased at the same time, which may affect B_{agcppk}.

Before developing techniques to tune θ, it's better to find a resonant circuit topology that inherently has an appropriate θ for lower B_{agcppk}, while maintaining high power transfer efficiency. The equivalent circuit model of a loosely coupled inductive WPT system using SS and SP resonant compensation topologies can be simplified as shown in Fig. 4-8.

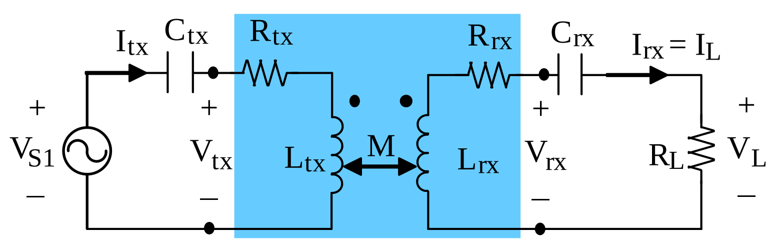

(a) Equivalent circuit model with SS resonant compensation topology

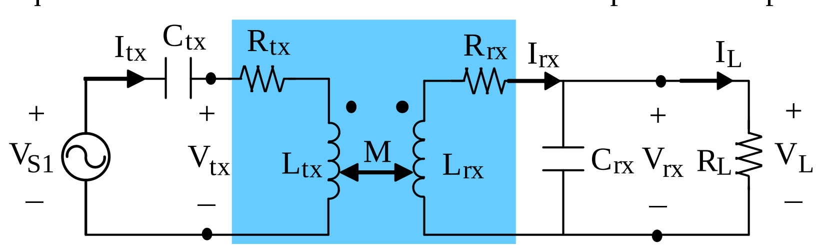

(b) Equivalent circuit model with SP resonant compensation topology

Fig. 4-8. Equivalent circuit model of an inductive WPT system using SS and SP topologies

Based on the resonant compensation conditions

$$\text{SS: } C_{tx} = \frac{1}{L_{tx}\,\omega_0^2},\ C_{rx} = \frac{1}{L_{rx}\,\omega_0^2};\ \text{SP: } C_{tx} = \frac{1}{(1-k^2)\,L_{tx}\,\omega_0^2},\ C_{rx} = \frac{1}{L_{rx}\,\omega_0^2} \tag{4.1}$$

The current ratios can be calculated as

$$\text{SS: } \frac{I_{tx}}{I_{rx}} = \frac{R_{rx}+R_L}{j\omega_0 M};\ \text{SP: } \frac{I_{tx}}{I_{rx}} = \frac{R_{rx}}{j\omega_0 M} + \frac{L_{rx}}{M(1+j\omega_0 C_{rx} R_L)} \tag{4.2}$$

Based on the current ratio expressions, it's easy to find that θ is constantly 90-degree for SS topology. While θ is smaller than 90-degree for SP topology. In addition, both topologies have the same coil-to-coil efficiency. Therefore, SP topology is beneficial for reducing the air-gap magnetic field. The field distributions are compared in Fig. 4-9.

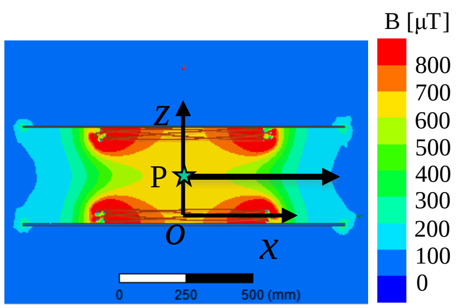

(a) Magnetic field distribution with SS topology

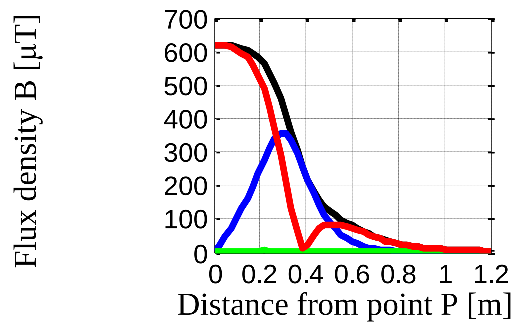

(b) Magnetic flux density along measurement line with SS topology

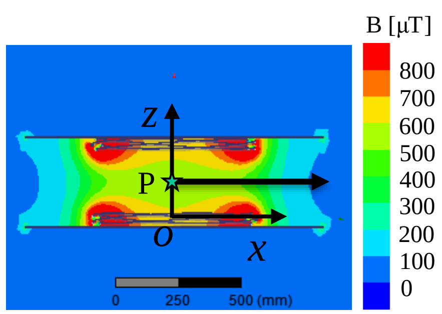

(a) Magnetic field distribution with SP topology

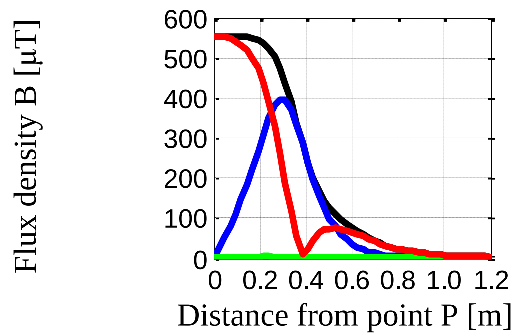

(b) Magnetic flux density along measurement line with SP topology

Legend: B_{total}, B_x, B_y, B_z.

Test conditions: operating frequency 0.1 MHz, output power 3 kW. TX and RX: 4 turns, coil radius 310 mm, ferrite μ_r = 1000, ferrite radius 600 mm.

Fig. 4-9. Comparison of magnetic field distributions and air-gap center plane magnetic flux densities along the measurement line with SS and SP topologies

According to the FEA results, the output power is fixed as 3 kW. When SS topology is used, B_{agcppk} = 619.24 μT, $B_{agcppk,\ x}$ = 357.12 μT, $\eta_{coil,\ max}$ = 98.44%. When SP topology is used, B_{agcppk} = 555.95 μT, $B_{agcppk,\ x}$ = 398.47 μT, $\eta_{coil,\ max}$ = 98.41%. Compared with SS topology, SP topology can reduce B_{agcppk} by 10.22%, while maintaining the power transfer efficiency. Therefore, SP topology is preferred due to inherent smaller current phase difference.

In order to satisfy the IEEE safety standard, B_{agcppk} should be further reduced even with SP topology. One simple way to manipulate the current phase difference is tuning the secondary side resonant capacitor C_{rx}. The primary capacitor C_{tx} is in series with the transmitter coil, so the current phase difference won't be changed by tuning C_{tx}. For the 4-turn CT SSW design with ferrite shield, the secondary side L_{rx} = 27.7132 μH, the required C_{rx} to resonate at 0.1 MHz is 91.402 nF, the current phase difference can be increased when increasing C_{rx}.

When transferring 3 kW through 300 mm air-gap at 0.1 MHz with SP topology, the air-gap magnetic field distributions and the air-gap center plane magnetic flux densities along the x-direction measurement line with different secondary side resonant capacitor C_{rx} of the 4-turn CT SSW with ferrite shield are compared in Fig. 4-10.

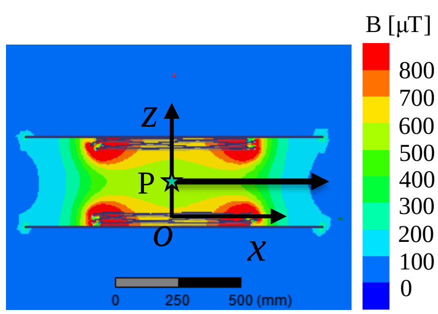

(a) Magnetic field distribution when C_{rx} = 91.402 nF

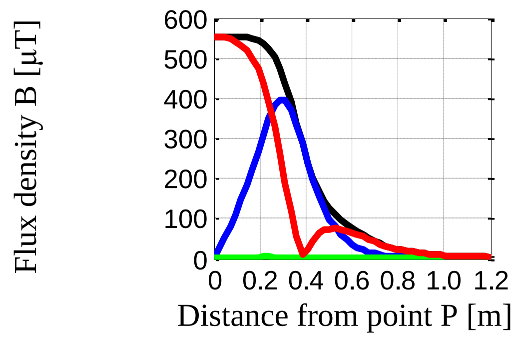

(b) Magnetic flux density along measurement line when C_{rx} = 91.402 nF

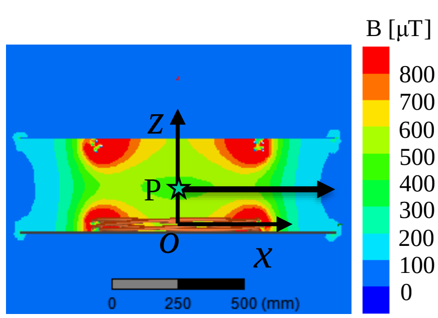

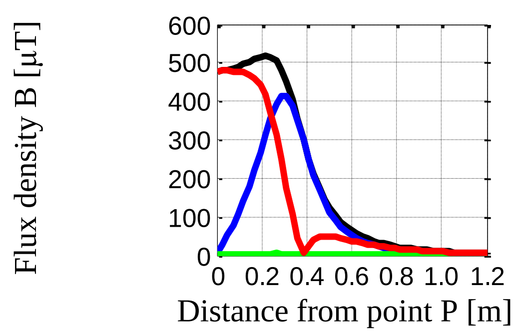

(c) Magnetic field distribution when C_{rx} = 97 nF

(d) Magnetic flux density along measurement line when C_{rx} = 97 nF

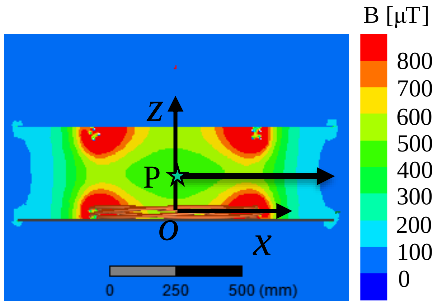

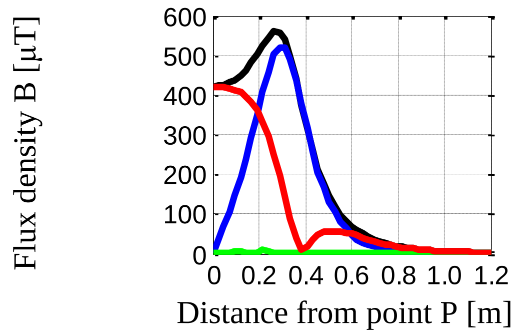

(e) Magnetic field distribution when C_{rx} = 103 nF

(f) Magnetic flux density along measurement line when C_{rx} = 103 nF

Legend: B_{total}, B_x, B_y, B_z.

Test conditions: operating frequency 0.1 MHz, output power 3 kW. TX and RX: 4 turns, coil radius 310 mm, ferrite μ_r = 1000, ferrite radius 600 mm.

Fig. 4-10. Comparison of magnetic field distributions and air-gap center plane magnetic flux densities along the measurement line with different C_{rx}

As shown in Fig. 4-10, when increasing C_{rx} from 91.402 nF to 97 nF, B_{agcppk} is reduced from 555.95 μT to 527.63 μT due to the reduction of B_z, and the location of B_{agcppk} has shifted away from the central point due to the increase of the radial direction leakage flux density. When C_{rx} is further increased to 103 nF, B_z keeps reducing. However, the radial direction leakage flux density increases significantly, which leads to an increase of B_{agcppk} to 562.67 μT. Besides that, η_{coil} are 98.41%, 98.27%, and 97.99% when C_{rx} are 91.402 nF, 97 nF, and 103 nF, respectively. η_{coil} is reduced since the secondary side is shifted away from the resonant point.

In summary, compared with SS topology, SP topology can achieve lower B_z, due to inherent smaller current phase difference, while maintaining the power transfer efficiency. Increasing C_{rx} in SP topology can reduce B_z and η_{coil}, and increase the radial direction leakage flux density, which may result in the increase of B_{agcppk}. In order to reduce B_{agcppk}, methods to reduce the leakage magnetic field must be developed.

4.4 Passive designs to reduce the leakage flux

When zooming in the magnetic field around the transmitter and checking the magnetic field directions, as shown in Fig. 4-11, the magnetic flux close to the transmitter are all leakage field that won't be coupled with the receiver, the leakage field can be reduced by designs that can reduce it from both inside (marked in pink frames) and outside (marked in green frames) of the coil.

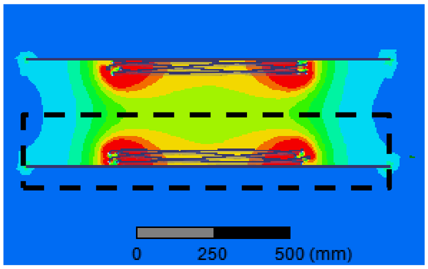

(a) Magnetic field distribution

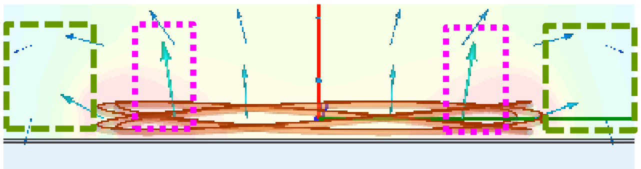

(b) Magnetic field strength direction

Fig. 4-11. Magnetic field distribution and magnetic field strength direction

The general ways to reduce the magnetic flux are canceling (or shielding) the magnetic flux and conducting the magnetic flux to desired directions. Metals, such as aluminum and copper, can be used to shielding the magnetic flux, which will also introduce the eddy current loss at the same time. Magnetic materials can be used to conduct the magnetic flux, which will affect the mutual coupling. In this section, passive methods will be introduced to reduce the outside and inside leakage magnetic fluxes, respectively.

4.4.1 Adding copper rings to reduce the outside leakage flux

The leakage magnetic flux return path outside of the coil can be canceled by using metals, such as aluminum and copper. Compared with aluminum, copper has better conductivity, which means lower loss. Therefore, copper will be used in the following analysis. A copper sheet can be added around the coil to fully cut off the return path. However, this method will also have significant eddy current loss. A copper ring canceling method is developed to cancel the leakage flux in the return path while maintaining a high coil-to-coil efficiency. The configuration with a single copper ring is shown in Fig. 4-12.

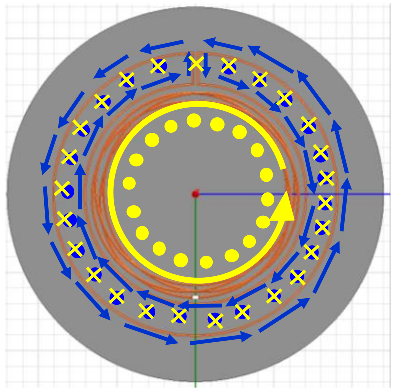

Fig. 4-12. Configuration of a winding with a single copper ring

Assuming the coil current is in counterclockwise direction, as shown in Fig. 4-12, the magnetic field generated by the coil will come out of the paper from the coil inside and go back outside of the coil. That will induce eddy current in the copper ring. The eddy current will generate an opposite direction magnetic field to cancel the magnetic field generated by the coil.

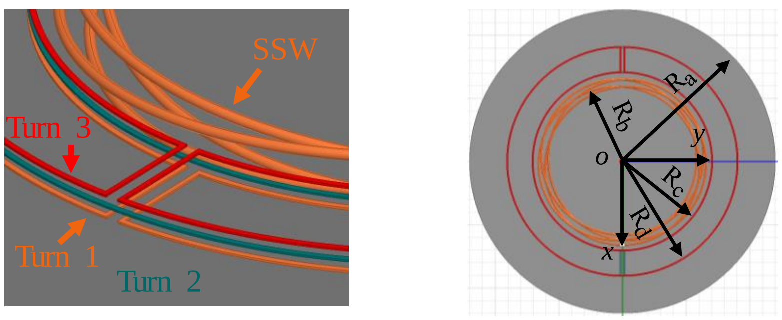

R_a = 600 mm
R_b = 310 mm
R_c = 350 mm
R_d = 450 mm
copper ring width 5 mm,
copper ring thickness 2 mm

(a) Configuration of three copper rings (b) Dimension

Fig. 4-13. Configuration of a winding with three copper rings

There is a gap in the single copper ring to form a current close loop. Two more copper rings are added to cover the gap as shown in Fig. 4-13. When transferring 3 kW through 300 mm air-gap at 0.1 MHz, the magnetic field distributions and the air-gap center plane magnetic flux densities before and after adding three copper rings are compared in Fig. 4-14.

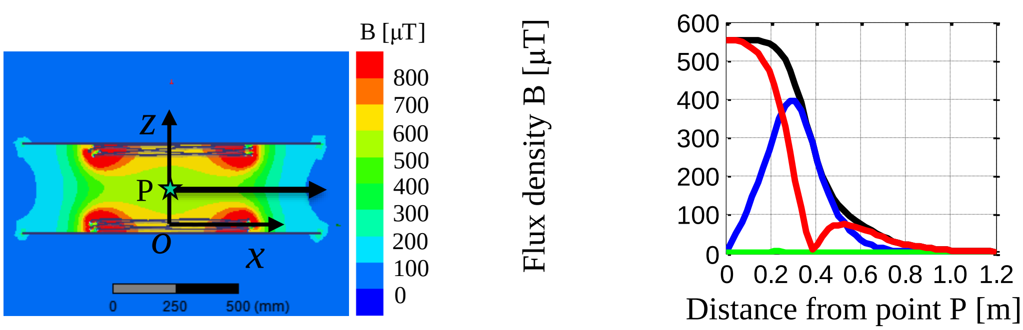

(a) Magnetic field distribution without copper rings

(b) Magnetic flux density along measurement line without copper rings

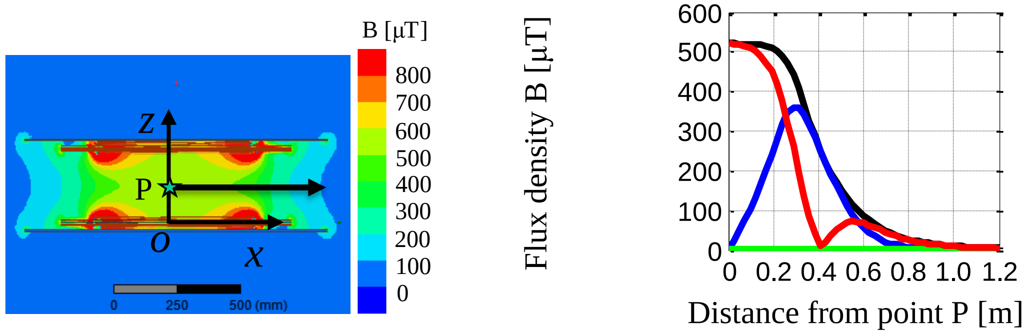

(c) Magnetic field distribution with three copper rings

(d) Magnetic flux density along measurement line with three copper rings

Legend: B_{total}, B_x, B_y, B_z. Test conditions: operating frequency 0.1 MHz, output power 3 kW. TX and RX: (a)(b) no copper rings. (c)(d) three copper rings. (a)(b)(c)(d) 4 turns CT SSW, ferrite μ_r = 1000, coil radius 310 mm, ferrite radius 600 mm.

Fig. 4-14. Comparison of the air-gap magnetic field distributions and the air-gap center plane magnetic flux densities with and without copper rings

As shown in Fig. 4-14, when adding three copper rings, B_{agcppk} is reduced from 555.95 μT to 520.50 μT, and $B_{agcppk,\ x}$ is reduced from 398.47 μT to 361.39 μT by 9.3%. Due to the eddy current losses in the copper rings, $\eta_{coil,\ max}$ is reduced from 98.44% to 98.14%, the efficiency drop is not significant due to the copper ring structure. If the copper sheet was used, the efficiency drop will be much larger. Besides that, the leakage flux within the coil is still large, passive shielding technique will be developed in the next section to reduce it.

4.4.2 Adding center cylindrical magnet to reduce the inside leakage flux

The leakage magnetic flux path inside the coil can't be canceled by adding a copper ring or copper sheet due to the mutual coupling and η_{coil} considerations. The magnetic material can be added inside to conduct the leakage flux path without reducing η_{coil}. A cylindrical ferrite is added inside the coil as shown in Fig. 4-15 (a), dimension details are shown in Fig. 4-15 (b).

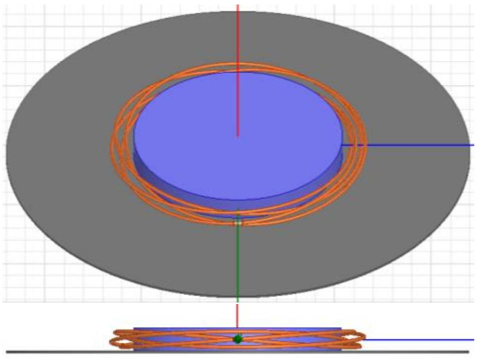

(a) Configuration of added cylindrical ferrite

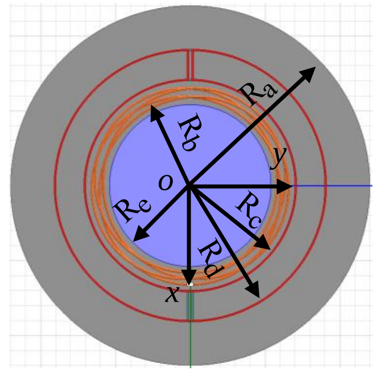

(b) Dimension

Fig. 4-15. Configuration of a winding with three copper rings and a cylindrical ferrite (R_a = 600 mm, R_b = 310 mm, R_c = 350 mm, R_d = 450 mm, R_e = 270 mm, copper ring width 5 mm, copper ring thickness 2 mm)

When transferring 3 kW through 300 mm air-gap at 0.1 MHz, the air-gap magnetic field distribution and the air-gap center plane magnetic flux density along the measurement line of the winding with three copper rings and a cylindrical ferrite are shown in Fig. 4-16.

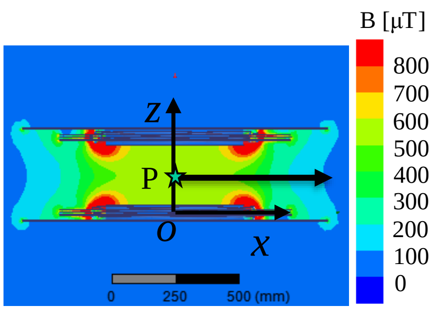

(c) Magnetic field distribution

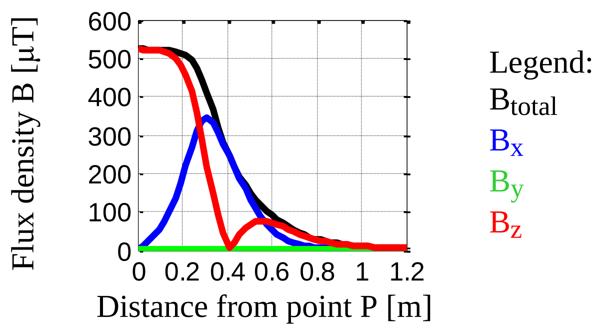

(d) Magnetic flux density along measurement line

Fig. 4-16. The air-gap magnetic field distribution and the air-gap center plane magnetic flux density of the winding with three copper rings and a cylindrical ferrite

As shown in Fig. 4-16, when adding three copper rings and a cylindrical ferrite, B_{agcppk} is reduced to 522.91 μT, and $B_{agcppk,\ x}$ is reduced to 345.20 μT, and η_{coil} is increased to 98.62%. Compared with the traditional shielding design, $B_{agcppk,\ x}$ is reduced from 398.47 μT to 345.20 μT by 13.4%, which is much better than the design with three copper rings. However, B_{agcppk} is still higher than the IEEE C95.1 - 2005 magnetic field safety limit 289.67 μT. In order to satisfy the safety limit, new magnetic shield design must be developed to further reduce the leakage flux.

4.5 New "I" type shielding design

From analyzing the magnetic field strength directions around the coil, in order to achieve low B_{agcppk} and maintain a high η_{coil}, the leakage flux should be confined in the coil side without affecting the mutual flux, the desired magnetic flux paths should follow Fig. 4-17.

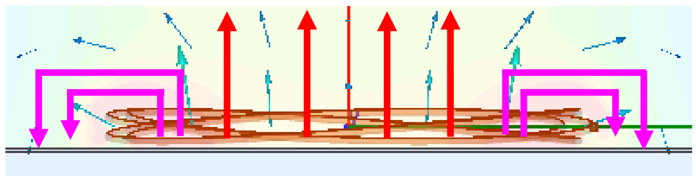

Fig. 4-17. The desired magnetic flux paths

Based on the desired magnetic flux paths, an "I" type passive shield design is proposed as shown in Fig. 4-18.

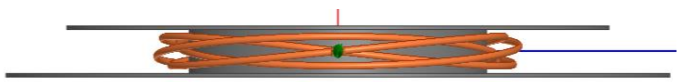

(a) Configuration of an "I" type passive shield

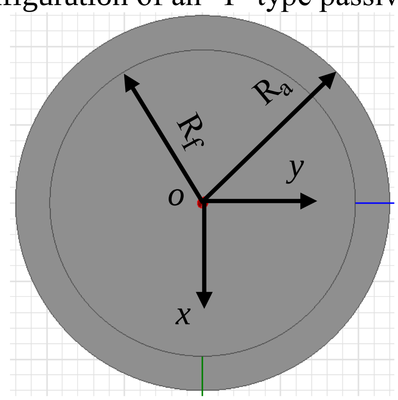

(b) Dimension (R_a = 600 mm, R_f = 490 mm)

Fig. 4-18. Configuration of "I" type passive shield

The added magnetic material above the coil will provide the return path for the leakage flux without affecting the vertical mutual flux. If there is no gap at the ends of the magnetic shield structure above and below the winding, no vertical mutual flux will be coupled to the receiver. The lines of magnetic flux in the inductive WPT system is plotted in Fig. 4-19, the leakage flux at the end of the added center magnetic material is unavoidable.

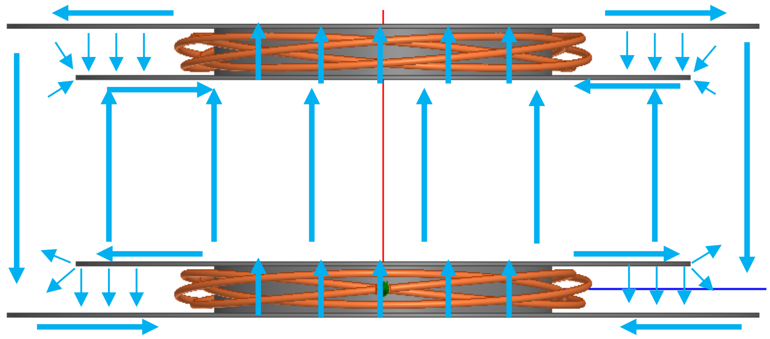

Fig. 4-19. Lines of magnetic flux in the inductive WPT system

When transferring 3 kW through 300 mm air-gap at 0.1 MHz, the air-gap magnetic field distribution and the air-gap center plane magnetic flux density along the measurement line of the winding with "I" type passive shield are shown in Fig. 4-20.

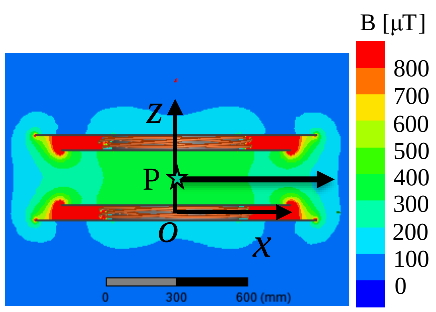

(a) Magnetic field distribution

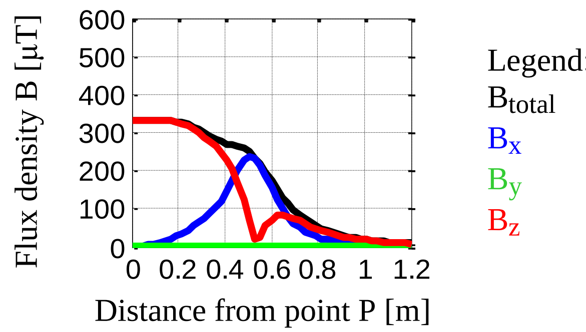

(b) Magnetic flux density along measurement line

Fig. 4-20. The air-gap magnetic field distribution and the air-gap center plane magnetic flux density of the winding with "I" type passive shield

According to Fig. 4-20, compared with the conventional shielding design, B_{agcppk} is reduced from 555.95 μT to 332.51 μT, and $B_{agcppk,\ x}$ is reduced from 398.47 μT to 240.67 μT by 39.6%, and η_{coil} is increased to 98.66%, which is slightly higher than that of the traditional shielding design 98.44%. More importantly, the whole air-gap magnetic field distribution is nearly uniform, and $B_{agcppk,\ x}$ is lower than the IEEE C95.1 - 2005 magnetic field safety limit 289.67 μT. Although B_{agcppk} is still higher than the safety limit, it can be reduced by reducing B_z. It should be noted that the magnetic fields below the transmitter and above the receiver are higher than the conventional shielding design. That means there is a magnetic field return path from the receiver top side to the transmitter bottom side. If the "I" type shielding design is installed under the vehicle, the vehicle metal chassis may affect the power transfer efficiency. It's necessary to evaluate the effects of vehicle chassis.

Considering $B_{agcppk,\ x}$ is lower than the safety limit, active control method can be used to reduce B_z, when C_{rx} is increased from 13.92 nF to 14.25 nF, the magnetic field distribution and the air-gap center plane magnetic flux density when transferring 3 kW are shown in Fig. 4-21.

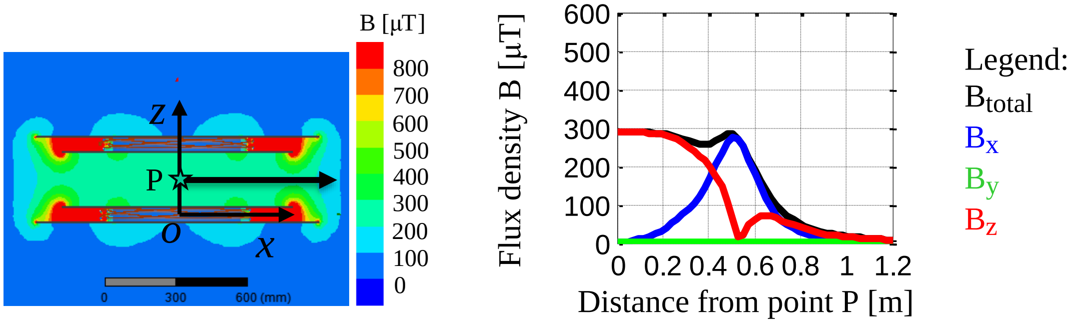

(a) Magnetic field distribution (b) Magnetic flux density along measurement line

Fig. 4-21. The air-gap magnetic field distribution and the air-gap center plane magnetic flux density when C_{rx} = 14.25 nF

As shown in Fig. 4-21, as C_{rx} increases, $B_{agcppk,\ x}$ is increased, and B_z is reduced. Furthermore, B_{agcppk} is reduced to 287.32 μT, which is lower than the IEEE C95.1-2005 magnetic field safety limit. However, η_{coil} is reduced from 98.66% to 98.58% by 0.08%. The electric field distribution and electric field intensity in the air-gap center plane are also evaluated as shown in Fig. 4-22.

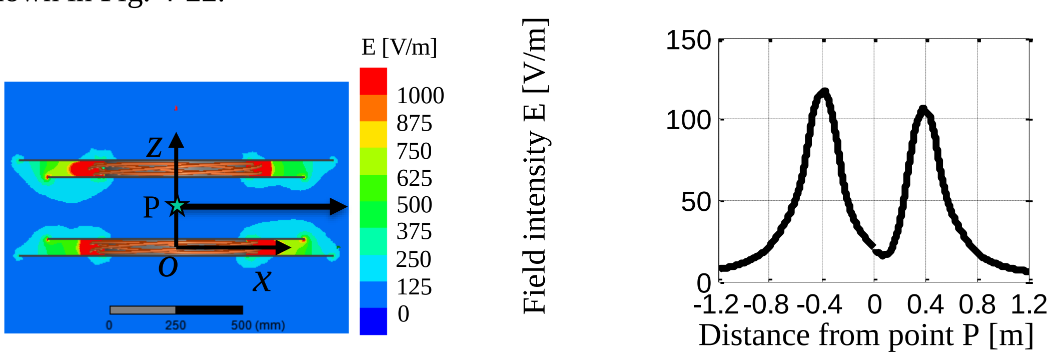

(a) Electric field distribution (b) Electric field intensity along measurement line

Fig. 4-22. The electric field distribution and the air-gap center plane electric field intensity when C_{rx} = 14.25 nF

According to Fig. 4-22, the whole air-gap electric field intensity is lower than the IEEE C95.1-2005 electric field safety limit 868.32 V/m, since the electric field is confined within the

“I” type passive shield. There is no requirement to especially place the transmitter terminal and the receiver terminal. In addition, the nearly uniform air-gap magnetic field provides a large safety region compared to other designs. However, the proposed “I” type design requires more magnetic materials, which means more cost and much heavier. It should be further optimized to reduce the usage of magnetic materials to reduce the total mass and cost.

4.6 Effects of vehicle metal chassis

The main materials of the vehicle chassis are steel or aluminum. In the evaluation of the vehicle chassis effects, the CT circular SSW is used as baseline, a circular metal plate is used to emulate the chassis. The initial FEA test setup for winding with conventional shielding design is shown in Fig. 4-23. For the evaluation of “I” type shield, only the conventional shield will be replaced by the “I” type shield, other settings remain the same.

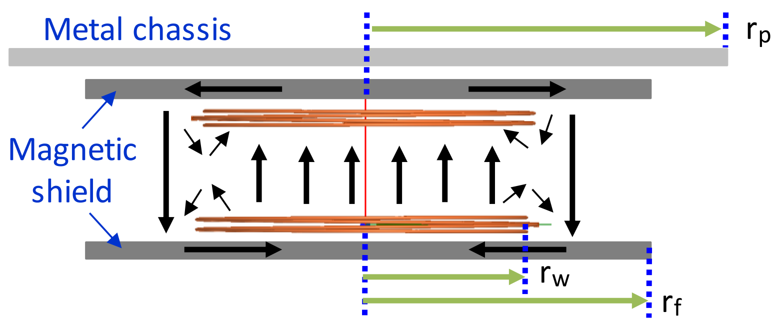

Fig. 4-23. FEA setup for evaluation of vehicle chassis effects

The FEA test cases are air-core, air-core with aluminum plate, winding with magnetic shield and aluminum plate, and winding with magnetic shield and steel plate. The evaluation metrics are winding electrical parameters, coil-to-coil efficiency η_{coil}, and the maximum air-gap transferrable power P_{agm} within the IEEE safety standard. P_{agm} is defined as the power received by the load plus the power consumed by the receiver. The design variable is magnetic shield radius r_f. Metal chassis radius r_p is maintained as a constant 800 mm. 4-turn CT SSW with radius r_w = 300 mm is used as a baseline. The results are summarized in Table 4-2.

Table 4-2. Comparison of winding electrical parameters, η_{coil}, and P_{agm} with and without metal chassis and conventional magnetic shield

	L_{tx} [μH]	R_{tx} [mΩ]	L_{rx} [μH]	R_{rx} [mΩ]	M [μH]	η_{coil} [%]	P_{agm} [W]
Air-core	16.72	24.9	16.73	24.9	2.38	96.7	814.3
W/ Alum.	16.25	24.9	9.23	34.4	0.86	89.8	467.0
W/ Alum. + Ferrite #1	23.80	28.8	22.46	30.0	3.40	97.3	570.7
W/ Steel + Ferrite #1	23.81	30.5	22.48	38.3	3.40	96.9	562.2
W/ Ferrite #2	26.47	29.9	26.47	29.8	5.85	98.4	603.8
W/ Alum. + Ferrite #2	26.09	29.7	25.91	29.9	5.39	98.3	601.9
W/ Steel + Ferrite #2	26.09	31.0	25.92	31.8	5.39	98.2	602.2

FEA conditions: f_0 = 100 kHz, h = 300 mm, B_{agcppk} = 289 μT; TX = RX, r_w = 300 mm, Ferrite μ_r = 1000, σ = 0.01 S/m, #1 r_f = 400 mm, #2 r_f = 600 mm; Aluminum (Alum.) σ = 3.8*1e7 S/m, r_p = 800 mm; Steel σ = 1.1*1e7 S/m, r_p = 800 mm.

As shown in Table 4-2, if the air-core winding is installed under the vehicle without the magnetic shield, η_{coil} will drop from 96.7% to 89.8% by 8.9%, and the power transfer capability within the safety standard drops from 814.3W to 467.0 W by 42.7%. After adding the magnetic shield, η_{coil} can be maintained higher than the air-core winding, since it provides a flux return path to ensure M. When the magnetic shield is large enough, different chassis materials have a negligible effect on η_{coil}. However, compared with air-core winding, P_{agm} is highly reduced after installed under the metal chassis. Even though adding conventional magnetic shields can help to improve P_{agm}, but it's still lower than the air-core winding, since the magnetic field distribution pattern is changed, and adding ferrite shields is equivalent to adding currents that are the mirrored version of the original currents.

According to the analysis in previous section, the proposed "I" type shield can improve P_{agm} by a flux return path for the leakage field. It's necessary to evaluate the effects of metal chassis on the performance of the "I" type shield. The design case winding with aluminum plate and ferrite #2 is used as the baseline. When transferring 2 kW through 300 mm air-gap at 0.1

MHz with SS topology, the winding configurations, magnetic and electric field distributions of conventional shielding design and "I" type design are compared in Fig. 4-24.

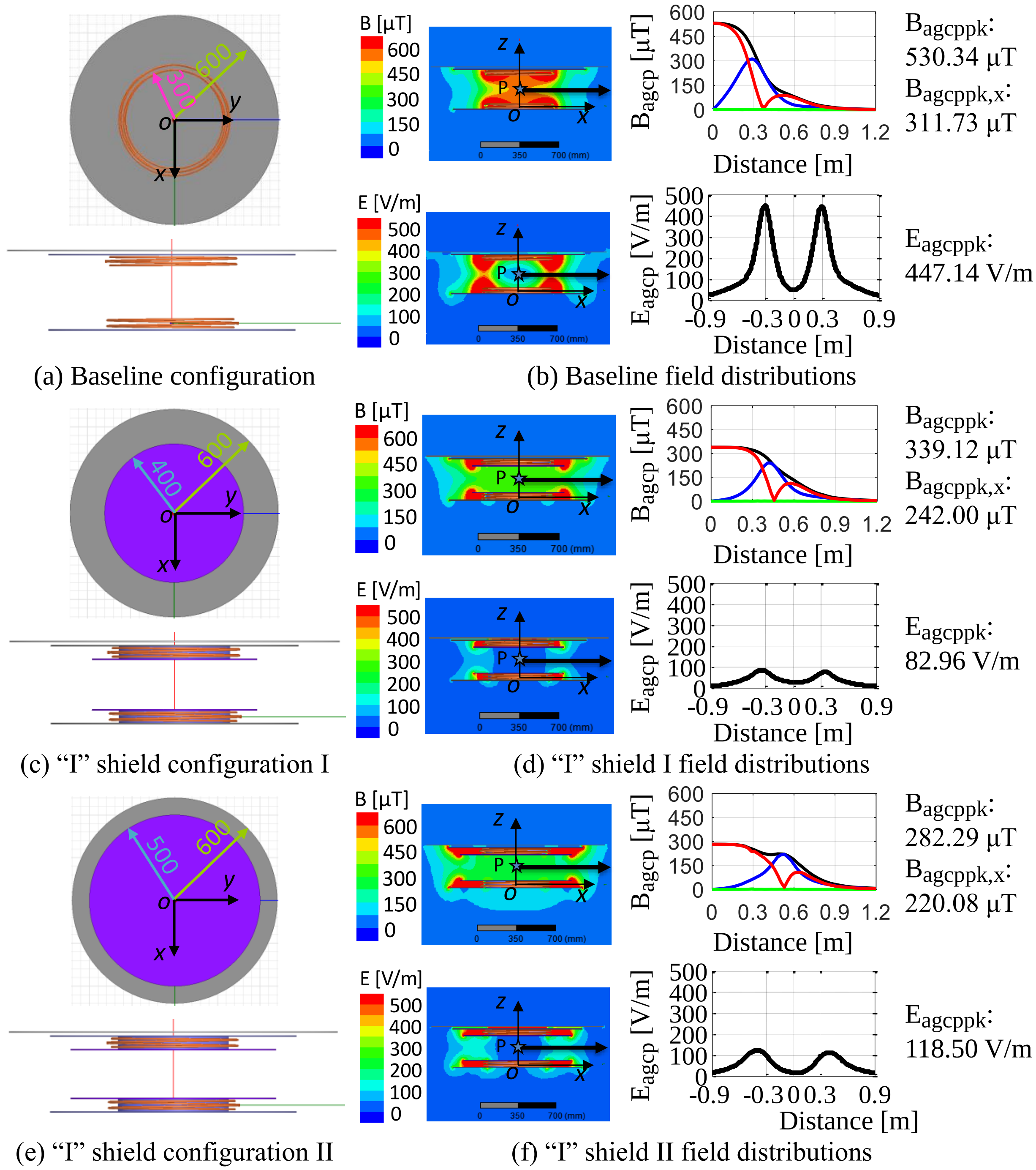

(a) Baseline configuration (b) Baseline field distributions

(c) "I" shield configuration I (d) "I" shield I field distributions

(e) "I" shield configuration II (f) "I" shield II field distributions

Legend: Magnetic field B_{total}, B_x, B_y, B_z. Electric field E_{total}.

Test conditions: SS topology, f_0 = 0.1 MHz, P_{out} = 2 kW. TX and RX: 4 turns SSW, r_w = 300 mm; ferrite μ_r = 1000, σ = 0.01 S/m; Ferrite and aluminum thicknesses = 5 mm.

Fig. 4-24. Comparison of shielding configurations and field distributions

As shown in Fig. 4-24, the “I” type shielding structure can reduce the air-gap magnetic and electric fields significantly. When the inner ferrite radius r_{in} is 400 mm, B_{agcppk} is reduced by 36.06% (from 530.34 μT to 339.12 μT), $B_{agcppk,\,x}$ is reduced by 22.37% (from 311.73 μT to 242.00 μT); E_{agcppk} is reduced by 81.45% (from 447.14 V/m to 82.96 V/m), the whole air-gap electric field E_{ag} is much lower than the IEEE C95.1-2005 general public electric field safety limit 868.3 V//m @ 100 kHz. When r_{in} is 500 mm, B_{agcppk} (282.29 μT) and $B_{agcppk,\,x}$ (220.08 μT) are further reduced to be lower than the IEEE C95.1-2005 general public magnetic field safety limit 289.7 μT @ 100 kHz; E_{ag} also maintains much lower than the safety limit.

The influences on winding performances for conventional magnetic shield and “I” type magnetic shield are compared in Table 4-3.

Table 4-3. Comparison of winding electrical parameters, η_{coil}, and P_{agm} for conventional magnetic shield and “I” type magnetic shield

		L_{tx} [μH]	R_{tx} [mΩ]	L_{rx} [μH]	R_{rx} [mΩ]	M [μH]	η_{coil} [%]	P_{agm} [W]
Air-core		16.72	24.9	16.73	24.9	2.38	96.7	814.3
Baseline: conventional		26.09	29.7	25.91	29.9	5.39	98.3	601.9
“I” type shield	r_{in} = 400 mm	126.26	63.2	124.26	64.9	13.08	98.45	1470.3
	r_{in} = 500 mm	189.92	64.0	184.26	68.3	9.38	97.78	2127.6

According to Table 4-3, when r_{in} is 400 mm, η_{coil} is slightly increased even though more core losses is introduced, because M is increased instead of decreasing. That means redirecting the magnetic field radial component by using “I” type shielding design won’t affect the mutual coupling flux. However, when r_{in} is increased to 500 mm, η_{coil} is slightly reduced due to the reduction of mutual inductance M. When r_{in} is close to r_f, the magnetic field return path is forced to return from the top of the receiver side outer ferrite plate to the bottom of the transmitter side outer ferrite plate as presented in previous section. It’s also verified by the magnetic field below the bottom of the transmitter side outer ferrite plate as shown in Fig. 4-24 (f). This return path can’t be fully utilized due to the aluminum plate, which leads to the reduction of M and η_{coil}. In addition, P_{agm} is reduced compared with previous “I” design with no aluminum plate.

Based on above analysis, it's necessary to investigate the effects of different r_{in} and r_f combinations on η_{coil} and P_{agm} within the IEEE C95.1-2005 field safety limits. Different r_{in} and r_f combinations are evaluated via FEA with given r_f values and compared with the baseline conventional shielding designs, the FEA results are shown in Fig. 4-25.

(a) Baseline conventional shield configuration (b) "I" type shield configuration

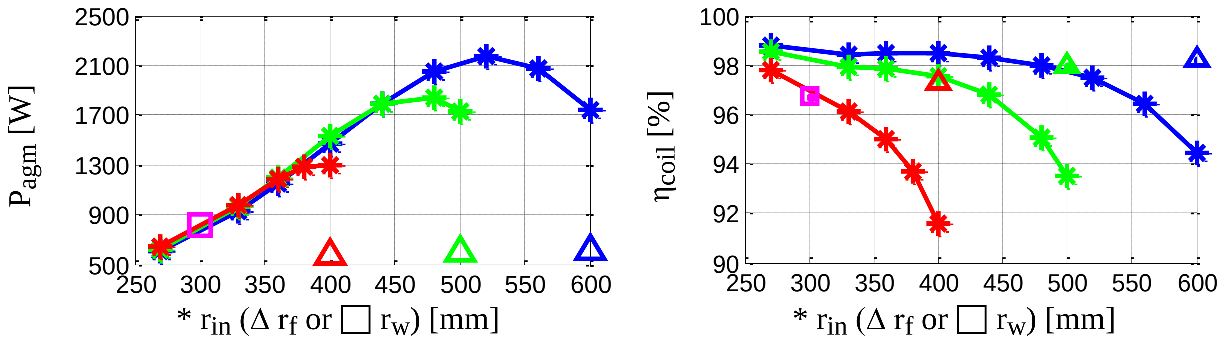

(c) P_{agm} w.r.t. different radii combinations (b) η_{coil} w.r.t. different radii combinations

Legend: □ air-core: r_w = 300 mm, Δ Baseline conventional design: r_f = 400 mm, 500 mm, 600 mm, * "I" type shielding design: r_{out} = 400 mm, 500 mm, 600 mm

FEA conditions: SS topology, f_0 = 100 kHz, TX = RX (SSW), r_w = 300 mm, N = 4, h = 300 mm, B_{agcppk} = 289.7 μT, Ferrite: μ_r = 1000, σ = 0.01 S/m, Aluminum: σ = 3.8*1e7 S/m.

Fig. 4-25. Effects of different radii combinations on P_{agm} and η_{coil}

According to Fig. 4-25, increasing r_f of the conventional shielding design has a nearly negligible effect on P_{agm}, which is about 35% lower than the air-core winding. But η_{coil} can be improved by increasing r_f. It can also be maintained to be higher than the air-core winding η_{coil} even with the aluminum plate. For the "I" type shielding design, P_{agm} first increases as r_{in} increases when r_{in} is much smaller than r_f, then P_{agm} reduces as r_{in} increases when r_{in} is close to r_f. In addition, P_{agm} remains nearly the same for the configurations that have same r_{in} and same r_w even when r_f is not the same, when r_{in} is much smaller than r_f. Besides that, η_{coil} reduces as r_{in} increases. Therefore, r_{in} and r_f must be selected carefully in order to achieve high P_{agm} and high η_{coil} simultaneously. In addition, it's necessary to develop the power scaling laws that can maintain the air-gap magnetic and electric fields within the IEEE safety standard.

4.7 Optimization of "I" type shielding design

According to the winding configuration analysis in chapter 2, the performance of the circular winding and the square winding are nearly the same when their enclosed areas are the same. Besides that, the most common ferrite blocks in the market are square one or rectangular one. Therefore, the optimization process in this section will use the square winding with "I" type square shielding as a baseline design. The optimization process focuses on reducing the total mass, while maintaining nearly the same field distributions and power transfer efficiency. The baseline design configuration and dimension are shown in Fig. 4-26.

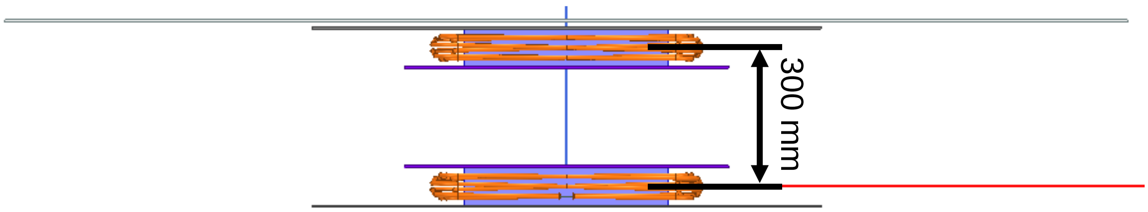

(a) Baseline design FEA configuration

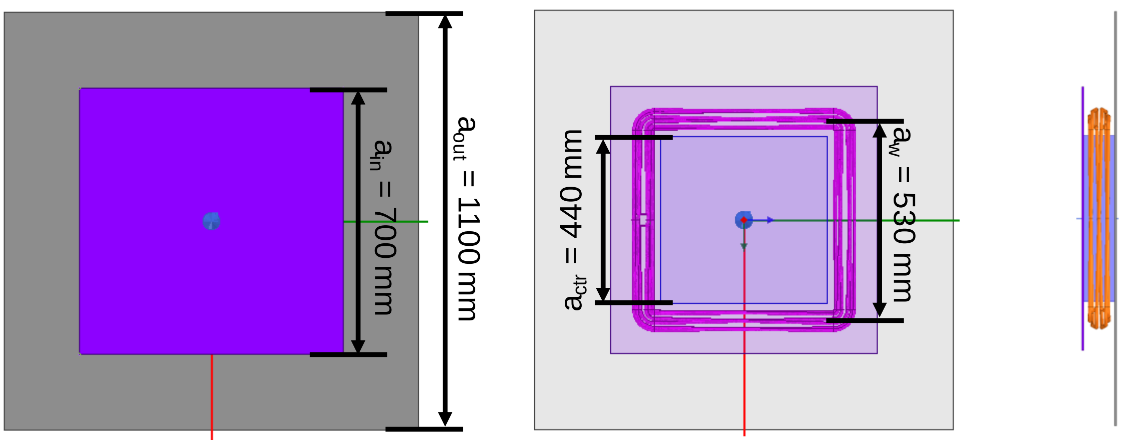

(b) Transmitter (or receiver) dimensions in detail

Fig. 4-26. Illustration of baseline design FEA configuration and dimensions

As shown in Fig. 4-26, the transfer distance is set as 300 mm. The rectangular winding dimensions are transformed from the circular design in previous sections based on same enclosed area. 3-turn SSPW is used to improve the power transfer efficiency. A rectangular aluminum plate (Width: 1662 mm, Length: 2426.6 mm) is used to emulate the vehicle chassis.

When transferring 2 kW at 0.1 MHz with SP resonant compensation topology, magnetic and electric field distributions are shown in Fig. 4-27.

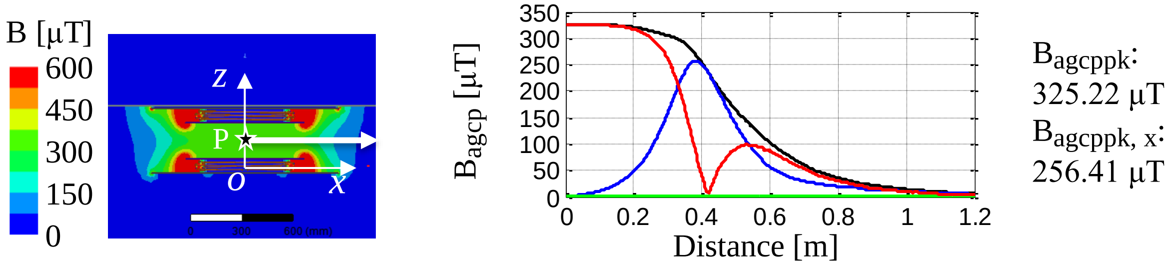

(a) Magnetic field distribution and B along air-gap center plane measurement line

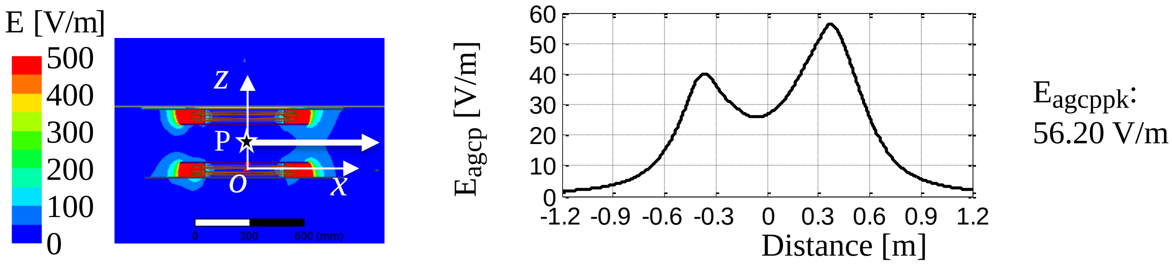

(b) Electric field distribution and E along air-gap center plane measurement line

Legend: Magnetic field B_{total}, B_x, B_y, B_z. Electric field E_{total}.

Test conditions: SP topology, f_0 = 0.1 MHz, P_{out} = 2 kW. TX and RX: 3 turns SSPW, a_w = 530 mm; ferrite μ_r = 1000, σ = 0.01 S/m; Ferrite and aluminum thicknesses = 5 mm.

Fig. 4-27. Baseline design magnetic and electric field distributions

As shown in Fig. 4-27, the main benefits of the "I" type shielding design from the field distribution perspective are listed as follows: (1) It can provide a shorter flux return path for the magnetic leakage field to reduce the air-gap region magnetic field. (2) It can confine the electric field within the shielding structure to reduce the air-gap region electric field. The magnetic materials that can affect above two benefits are the materials that are adjacent to the winding. Therefore, a hollow "I" type shielding design is proposed as shown in Fig. 4-28.

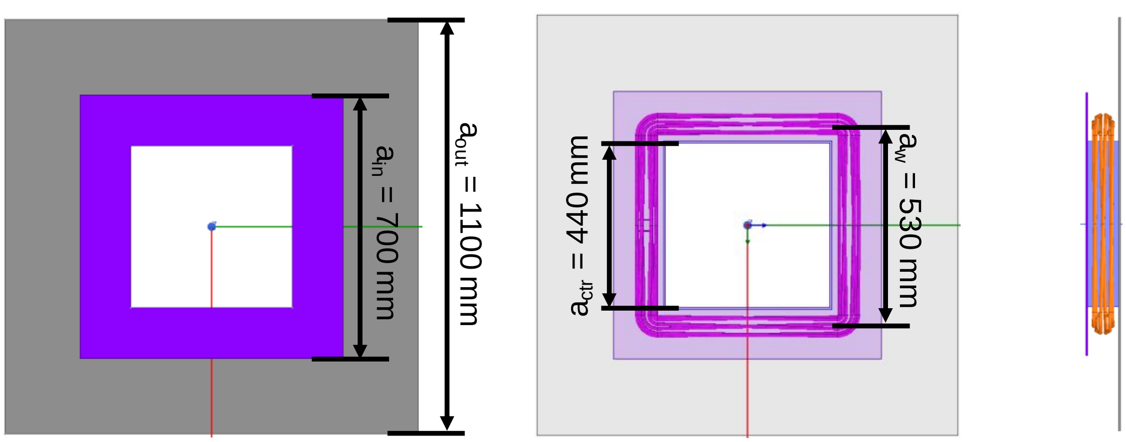

Fig. 4-28. Illustration of hollow "I" type shielding design

As shown in Fig. 4-28, only the ferrite close to the winding is kept, another part is removed. The left ferrite forms a shielding shell to provide a return path for the leakage field and confine the electric field within the shielding shell. The total ferrite material can be reduced by 69.4%. When transferring 2 kW at 0.1 MHz with SP resonant compensation topology, magnetic and electric field distributions of the hollow "I" type shielding design are shown in Fig. 4-29.

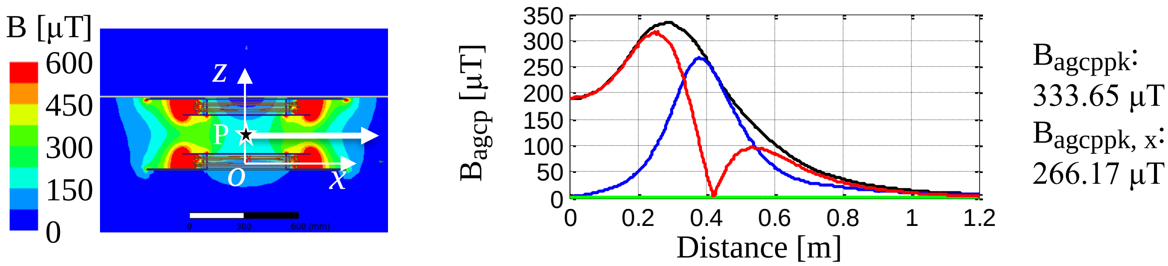

(a) Magnetic field distribution and B along air-gap center plane measurement line

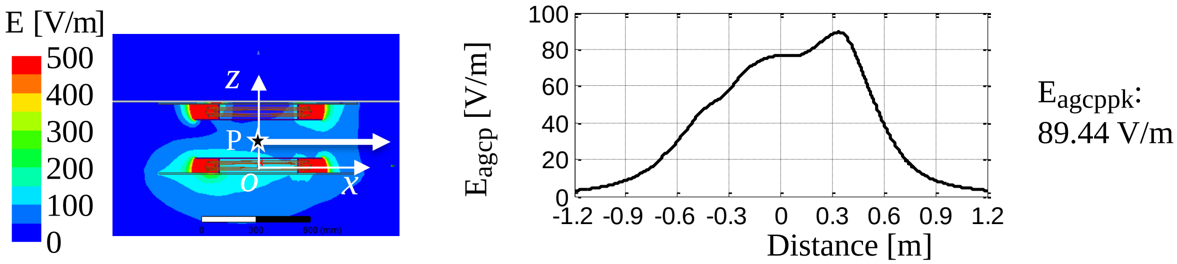

(b) Electric field distribution and E along air-gap center plane measurement line

Legend: Magnetic field B_{total}, B_x, B_y, B_z. Electric field E_{total}.

Test conditions: SP topology, f_0 = 0.1 MHz, P_{out} = 2 kW. TX and RX: 3 turns SSPW, a_w = 530 mm; ferrite μ_r = 1000, σ = 0.01 S/m; Ferrite and aluminum thicknesses = 5 mm.

Fig. 4-29. Field distributions of hollow "I" type shielding design magnetic and electric

As shown in Fig. 4-29, compared with the baseline design, B_{agcppk} is slightly increased from 325.22 μT (baseline) to 333.65 μT by 2.59%, which is nearly negligible. The location of B_{agcppk} has shifted away from the central point, and the magnetic field around the central point is highly reduced. $B_{agcppk,x}$ is slightly increased from 256.41 μT (baseline) to 266.17 μT by 3.81%. E_{ag} is still far below the safety limit as the baseline design. It can be concluded that the proposed hollow "I" type shielding design can maintain the same field distributions as the baseline design, while the total required ferrite material can be reduced by 69.4%.

Considering that it's very difficult to find a large ferrite piece as the proposed designs, square ferrite block, such as 100 mm (width) * 100 mm (length) * 5 mm (thickness), is easy for manufacture. It's necessary to investigate the effect of using ferrite block on field distributions. The hollow "I" type shielding design built by ferrite block is shown in Fig. 4-30. It should be noted that the gap between ferrite blocks should be small enough in order to maintain the mutual coupling. In this proposed design, the gap between ferrite blocks is set as 0.5 mm.

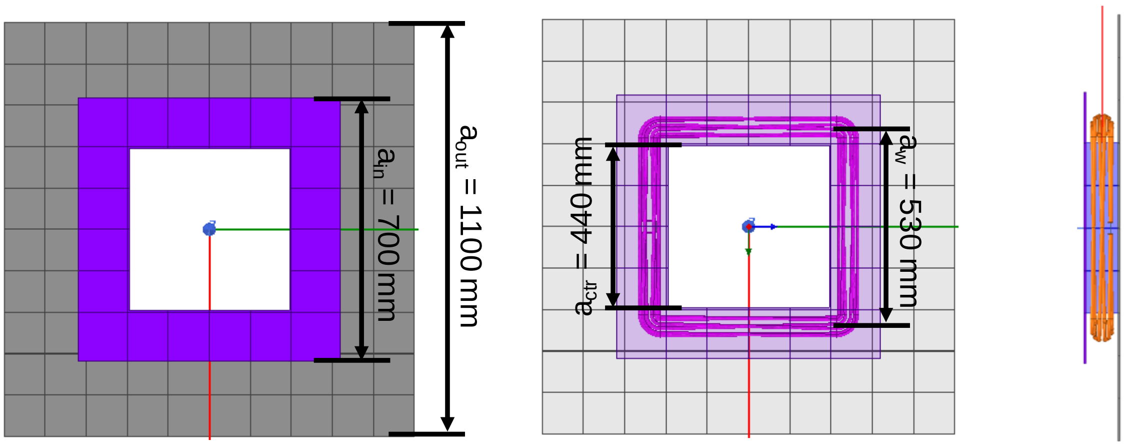

Fig. 4-30. Illustration of hollow "I" type shielding design built by ferrite block

When transferring 2 kW at 0.1 MHz with SP compensation topology, field distributions of the hollow "I" type shielding design built by ferrite block are shown in Fig. 4-31.

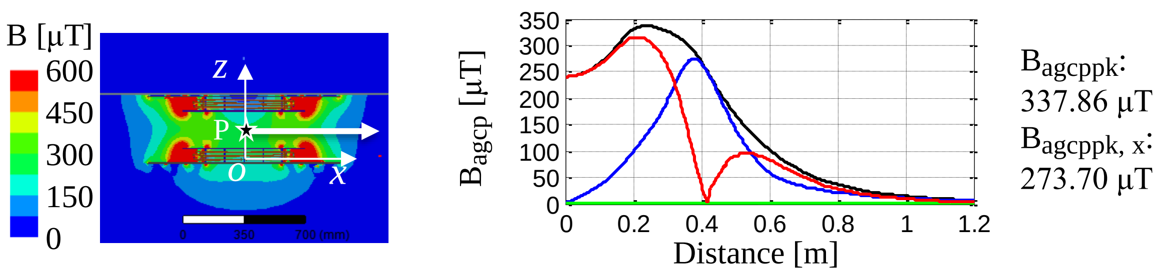

(a) Magnetic field distribution and B along air-gap center plane measurement line

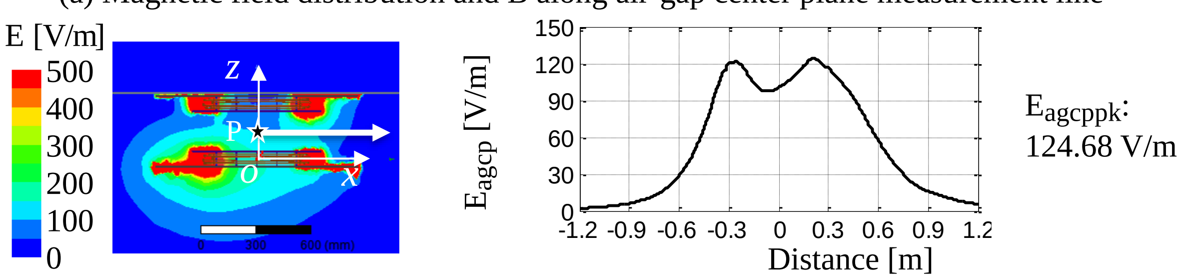

(b) Electric field distribution and E along air-gap center plane measurement line

Legend: Magnetic field B_{total}, B_x, B_y, B_z. Electric field E_{total}.

Test conditions: SP topology, f_0 = 0.1 MHz, P_{out} = 2 kW. TX and RX: 3 turns SSPW, a_w = 530 mm; ferrite μ_r = 1000, σ = 0.01 S/m; Ferrite and aluminum thicknesses = 5 mm.

Fig. 4-31. Field distributions of hollow "I" type shielding design built by ferrite block

As shown in Fig. 4-31, B_{agcppk} is slightly increased from 325.22 μT (baseline) to 337.86 μT by 3.89%, $B_{agcppk,x}$ is slightly increased from 256.41 μT (baseline) to 273.70 μT by 6.47%. The air-gap region magnetic field maintains nearly the same as previous designs. However, the leakage field below the transmitter is increased. The electric field in the air-gap region is still far below the safety limit. However, the electric field close to the ferrite plate increases significantly, since the induced charge in the ferrite plate forms a strong electric field in the 0.5 mm gap between the ferrite blocks. Voltage breakdown may happen when transferring higher power.

An aluminum plate can be added below the transmitter to shield the magnetic and electric fields below the transmitter. The aluminum plate size is set the same as the bottom ferrite plate. The field distributions after adding the aluminum plate are shown in Fig. 4-32.

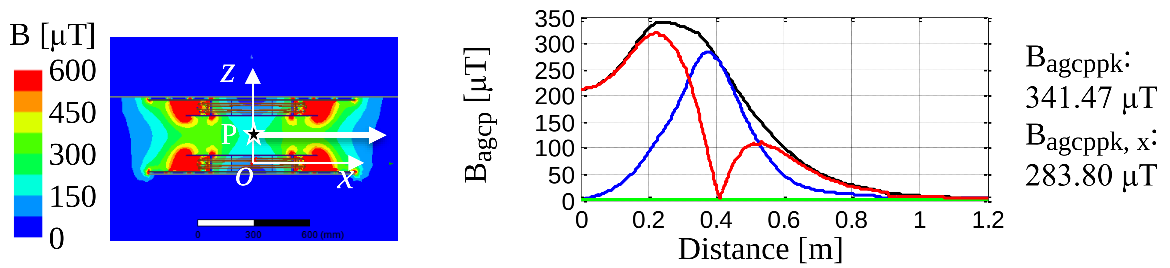

(a) Magnetic field distribution and B along air-gap center plane measurement line

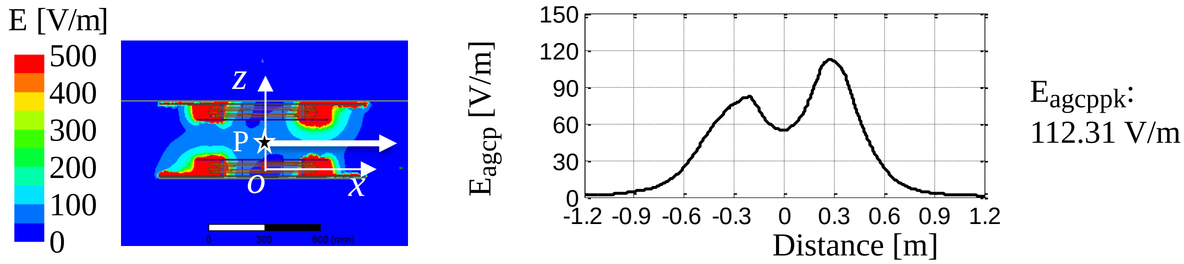

(b) Electric field distribution and E along air-gap center plane measurement line

Legend: Magnetic field B_{total}, B_x, B_y, B_z. Electric field E_{total}.

Test conditions: SP topology, f_0 = 0.1 MHz, P_{out} = 2 kW. TX and RX: 3 turns SSPW, a_w = 530 mm; ferrite μ_r = 1000, σ = 0.01 S/m; Ferrite and aluminum thicknesses = 5 mm.

Fig. 4-32. Field distributions of hollow "I" type shielding design built by ferrite block after adding an aluminum plate below the transmitter

As shown in Fig. 4-32, after adding the aluminum plate below the transmitter bottom ferrite, the magnetic and electric fields below the transmitter is shielded by the aluminum plate. While the air-gap magnetic field is slightly increased. B_{agcppk} is increased from 325.22 μT (baseline) to 341.47 μT by 5.00%, $B_{agcppk,x}$ is slightly increased from 256.41 μT (baseline) to 283.80 μT by 10.68%. Alternative method to reduce the leakage field can be used to reduce B_{agcppk} and $B_{agcppk,\,x}$. The air-gap electric field remains much lower the safety limit.

After further considering the two benefits provided by the “I” type shield, it’s not necessary to fully cover the winding using magnetic material to provide a flux return path for the leakage field. Besides that, the air-gap electric field can be maintained at low level if the air-gap inner magnetic material can be kept. Based on above analysis, parts of the air-gap outer magnetic shields, shown in Fig. 4-33, can be removed without mitigating the benefits of “I” type shield.

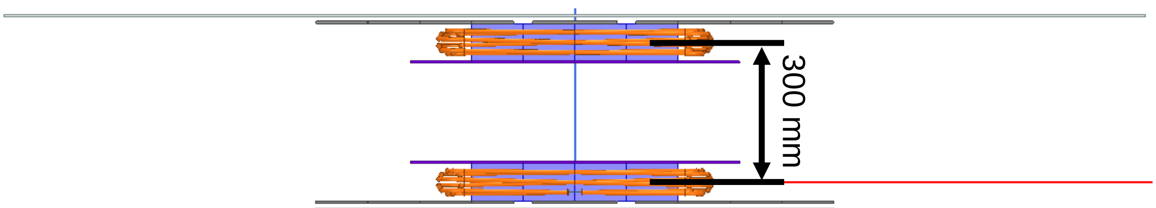

(a) FEA configuration with aluminum plate added below the transmitter bottom ferrite

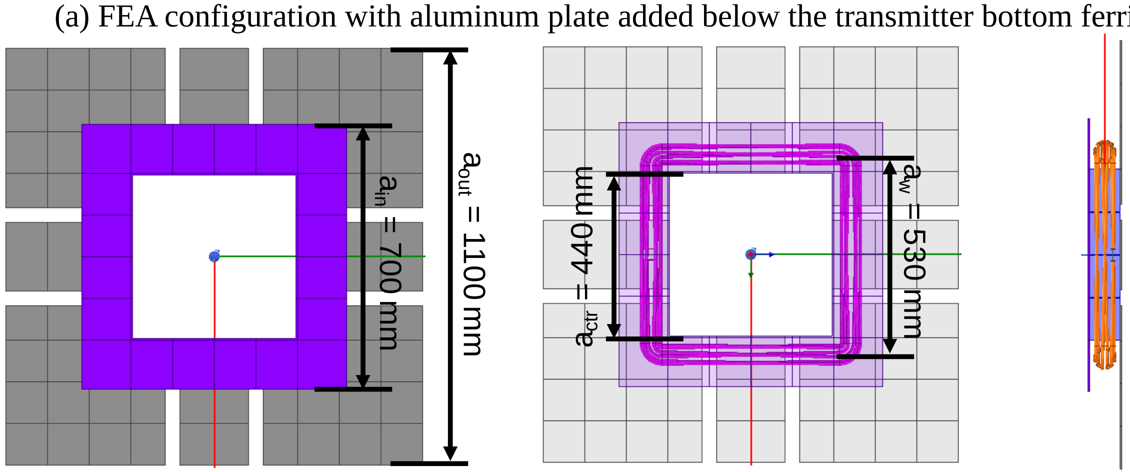

(b) Transmitter (or receiver) dimensions in detail

Fig. 4-33. Illustration of FEA configuration with bottom aluminum plate and hollow “I” type shielding design built by less ferrite block

The aluminum plate below the transmitter bottom ferrite is kept in the FEA analysis. When transferring 2 kW at 0.1 MHz with SP compensation topology, magnetic and electric field distributions are shown in Fig. 4-34.

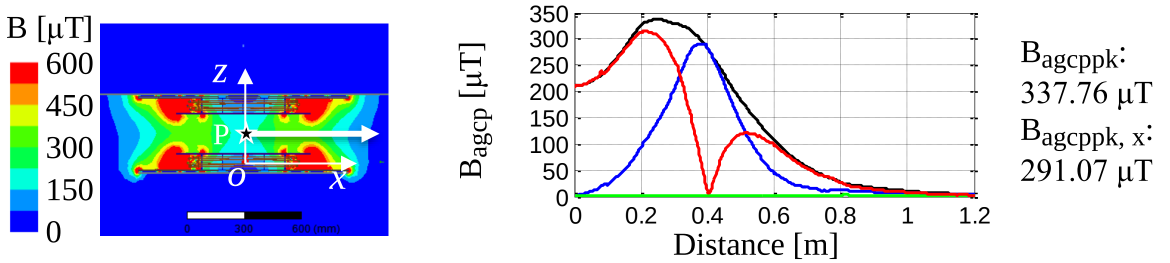

(a) Magnetic field distribution and B along air-gap center plane measurement line

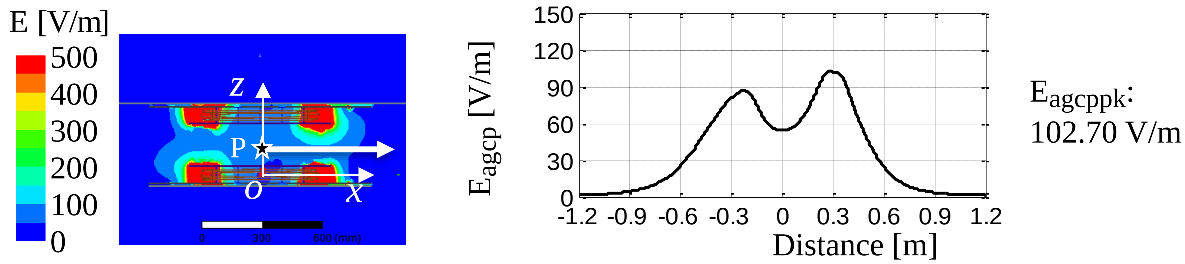

(b) Electric field distribution and E along air-gap center plane measurement line

Legend: Magnetic field B_{total}, B_x, B_y, B_z. Electric field E_{total}.

Test conditions: SP topology, f_0 = 0.1 MHz, P_{out} = 2 kW. TX and RX: 3 turns SSPW, a_w = 530 mm; ferrite μ_r = 1000, σ = 0.01 S/m; Ferrite and aluminum thicknesses = 5 mm.

Fig. 4-34. Field distributions of hollow “I” type shielding design built by less ferrite block with an aluminum plate below the transmitter bottom ferrite

As shown in Fig. 4-34, B_{agcppk} is increased from 325.22 μT (baseline) to 337.76 μT by 3.86%, $B_{agcppk,x}$ is slightly increased from 256.41 μT (baseline) to 291.07 μT by 13.52%. The air-gap electric field remains much lower the safety limit.

It can be concluded that the optimized design can maintain the field distributions in the air-gap region even with less magnetic materials. Another concern regarding the optimized designs is η_{coil}. The winding parameters and η_{coil} are compared in Table 4-4.

Table 4-4. Comparison of winding parameters and η_{coil} for designs in optimization process

	L_{tx} [μH]	R_{tx} [mΩ]	L_{rx} [μH]	R_{rx} [mΩ]	M [μH]	η_{coil} [%]	Ferrite usage
Baseline	60.04	33.3	58.88	34.0	7.97	98.66	Baseline
Hollow “I” type design	56.96	30.2	55.86	30.6	6.70	98.56	↓ 69.37%
Hollow “I” type design built by ferrite block	37.85	18.2	36.14	19.8	3.20	98.12	↓ 69.37%
Hollow “I” type design built by ferrite block + Alum. plate below TX	36.09	20.6	35.97	20.0	2.73	97.66	↓ 69.37%

Hollow "I" type design built by less ferrite block + Alum. plate below TX	34.22	20.5	34.11	20.1	2.38	97.32	↓ 73.96%

As shown in Table 4-4, the final Hollow "I" type design built by less ferrite block and aluminum plate below the transmitter botter ferrite, the ferrite usage can be reduced by 73.96%, while the reduction of η_{coil} is only 1.34%. η_{coil} can be improved by adding the number of turns or changing the copper tubing to high performance Litz wire. It's a tradeoff between ferrite usage and η_{coil}, which should be customized based on application.

4.8 System general design methodology

Through the FEA analysis, it can be identified that the key design variables for the "I" type shielding structure are the outer radius r_{out} and the inner radius r_{in}. Combining with the air-core winding general design methodology for low air-gap magnetic and electric field, and high efficiency developed in chapter 3, the "I" type magnetic design flowchart is shown in Fig. 4-35.

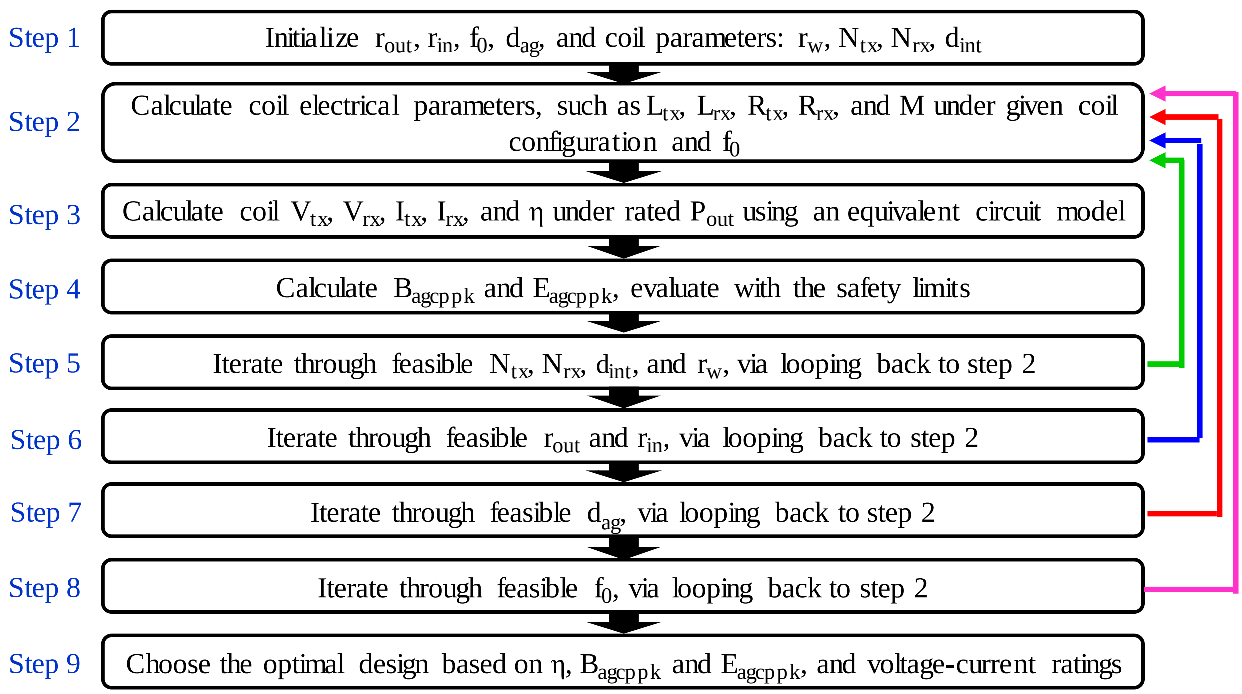

Fig. 4-35. "I" type magnetic design flowchart for low air-gap magnetic and electric field, and high efficiency

In general, following the flowchart of "I" type magnetic design, low air-gap magnetic and electric field, and high efficiency designs can be found. If not, active design and other passive design techniques can be used.

For a general loosely coupled inductive WPT system that can be used in various applications, a systematic general design methology based on conventional magnetic design is summarized based on the developed approaches. The design flowchart is shown in Fig. 4-36.

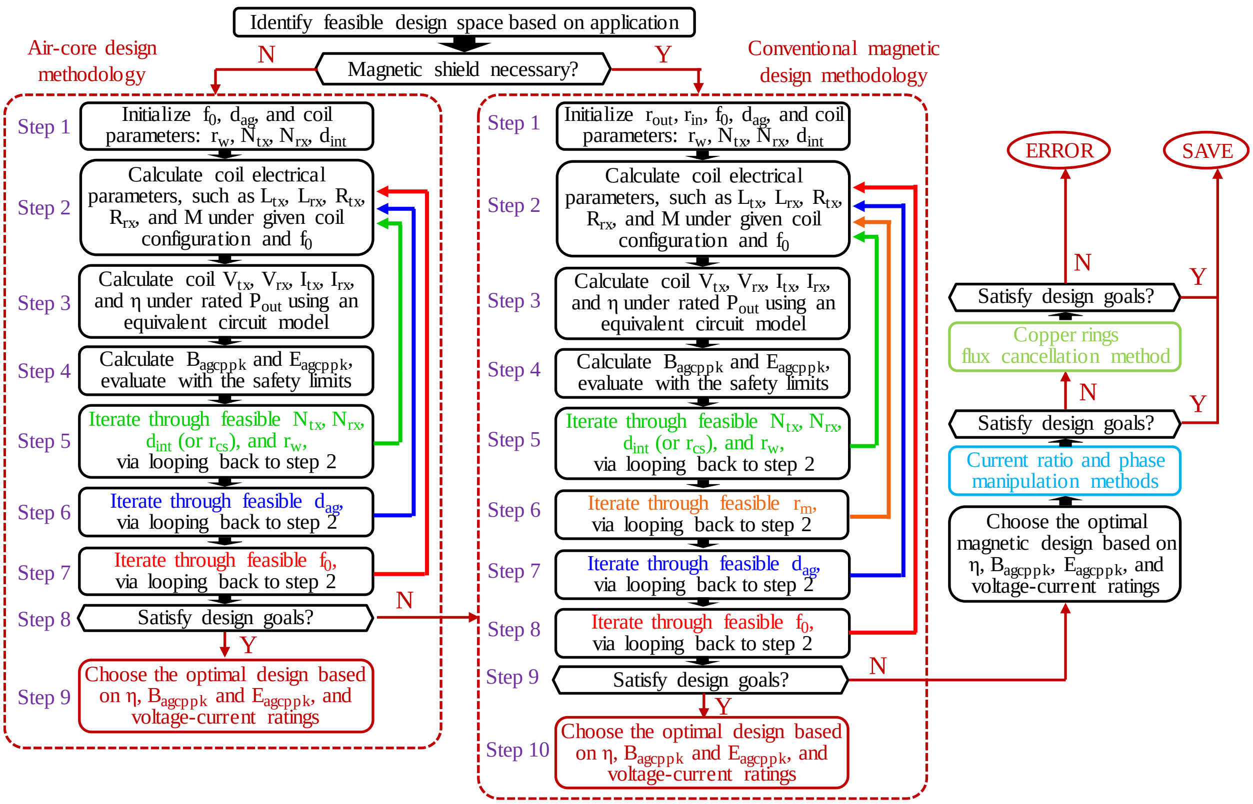

Fig. 4-36. Systematic general design flowchart for low air-gap magnetic and electric field, and high efficiency with conventional magnetic design

Considering after adding the conventional magnetic shields, the air-gap magnetic field normally increases compared with the air-core design. Although the current manipulation, flux cancellation, and flux shaping techniques are very helpful to reduce the air-gap magnetic field, it's possible that a design can't be found to satisfy given goals. In this situation, "I" type magnetic design can be used to replace the conventional magnetic design. The design flowchart with "I" type magnetic design is shown in Fig. 4-37.

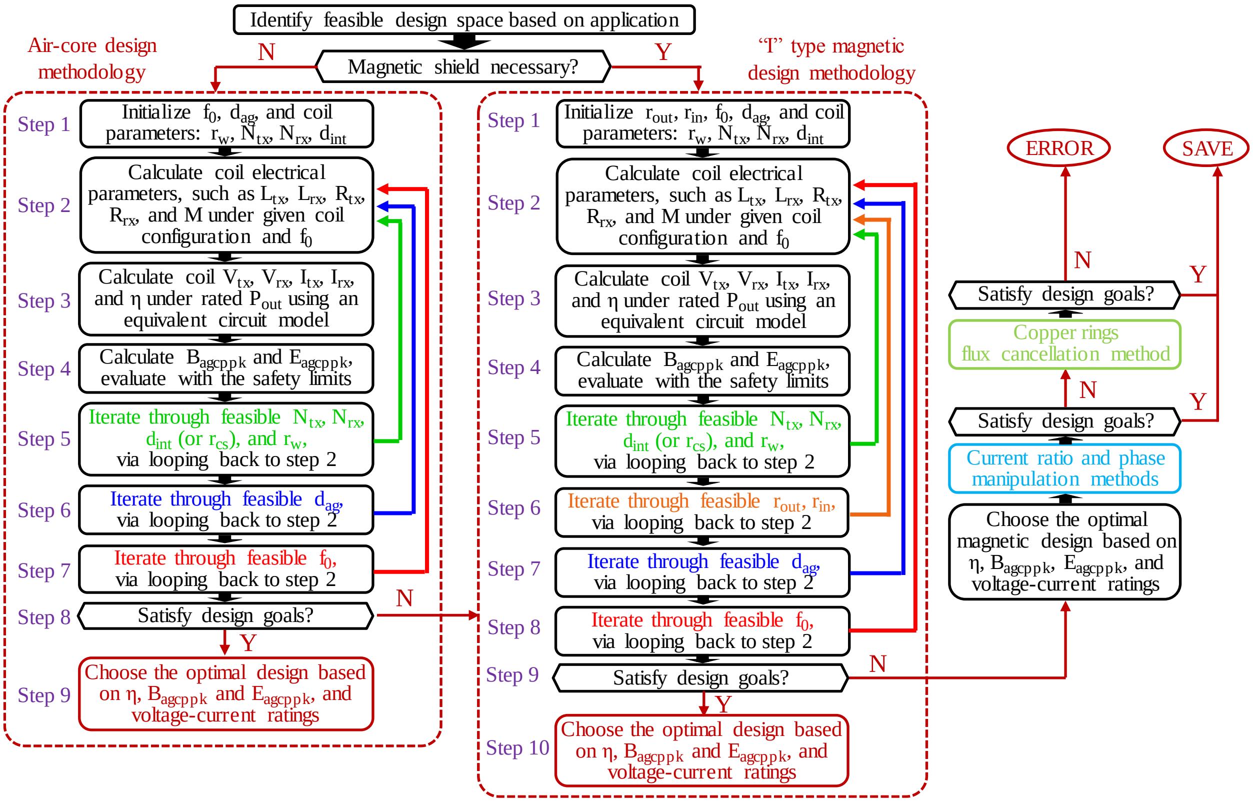

Fig. 4-37. Systematic general design flowchart for low air-gap magnetic and electric field, and high efficiency with "I" type magnetic design

Following the design flowchart for "I" type magnetic design, the design satisfying the low air-gap magnetic and electric field, and high efficiency goal under rated power should be able to find. Otherwise, alternative flux shaping technique has to be developed.

4.9 Summary

At the beginning, the effects of the traditional magnetic shields added below the transmitter and above the receiver on the air-gap magnetic field and electric field distributions are identified. After adding the traditional magnetic shields, B_{agcppk} increases, and the location of B_{agcppk} is shifted to the central point, while E_{agcppk} remains almost the same.

After that, active and passive designs are developed to reduce B_{agcppk}. In active designs, SS and SP topologies are compared systematically. SP topology can achieve lower B_{agcppk} due to inherent smaller current phase difference θ. Furthermore, θ can be manipulated by tuning the receiver side resonant capacitor C_{rx} to adjust the field distribution. θ can be reduced by increasing C_{rx} to reduce B_z. However, the radial direction leakage flux density B_r will increase, which may lead to a higher B_{agcppk}. Anyway, C_{rx} can be tuned to reduce B_{agcppk}. In the passive design methods, copper rings are added along the periphery of the winding to cancel the leakage flux in the return path outside of the winding, which can reduce B_r by 9.5%. But it will also reduce η_{coil} due to the eddy current loss in the copper ring; a cylindrical piece of magnetic material can be added inside the winding to conduct the path of the leakage magnetic flux, which can further reduce B_r by 13.6% with the copper rings outside of the winding. In addition, it can improve η_{coil} since the added center magnet material can increase the mutual inductance.

In particular, an "I" type shielding structure is developed based on the desired magnetic flux paths. It can direct the leakage flux return path without affecting the mutual flux to reduce B_{agcp} without mitigating η_{coil}. The air-gap magnetic field distribution is nearly uniform. Besides that, it can also confine the electric field within the shielding structure instead of decaying in the air-gap to achieve very low electric field in the whole air-gap region. According to the FEA results, the "I" type magnetic shield can reduce B_r by 39.8% and achieve higher η_{coil} compared with the conventional magnetic shield design. With active control method, when transferring 3 kW, B_{agcppk} can meet the IEEE C95.1-2005 magnetic field, and the whole air-gap electric field intensity is much lower than the IEEE C95.1-2005 safety limit.

For the conventional magnetic shield, if the magnetic material size is about 1.5-2 times larger than the winding size, the effect of the vehicle metal chassis on η_{coil} are negligible. However, its power transfer capability P_{agm} within the safety limits is about 35% lower than the air-core winding. For the proposed "I" type shielding design, after adding the vehicle metal chassis, P_{agm} first increases as r_{in} increases when r_{in} is much smaller than r_f, then P_{agm} reduces as r_{in} increases when r_{in} is close to r_f. In addition, P_{agm} remains nearly the same for the configurations that have same r_{in} and same r_w even when r_f is not the same, when r_{in} is much smaller than r_f. Besides that, η_{coil} reduces as r_{in} increases, especially when r_{in} is much close to r_f.

Therefore, r_{in} and r_f must be selected very carefully in order to achieve high P_{agm} and high η_{coil} simultaneously.

The optimized hollow “I” type shielding design can reduce the ferrite usage by nearly 70%, while the field distributions are maintained nearly the same. The reduction of η_{coil} is unavoidable. It can be improved by adding the number of turns or changing the copper tubing to high performance Litz wire. It’s a tradeoff between ferrite usage and η_{coil}, which should be customized based on application.

In the end, general design methodology for various applications is developed based on air-core winding, conventional magnetic design and “I” type mangetic design to achieve low air-gap magnetic and electric field, and high efficiency under rated power. Proposed current manipulation, flux cancellation and flux shaping techniques are also integrated into the general design methodology.

Chapter 5 Power Scaling Laws within Safety Standard

5.1 Introduction

It's necessary to transfer higher power level to charge an electric vehicle faster. When pushing to higher power level, the voltage and current limitations of the power semiconductors can be solved by using multiple devices in series or parallel, the thermal issues can be mitigated by adding cooling system, however, safety is always the first concern, which should be taken into consideration at the beginning. The maximum allowable transfer power of the loosely coupled inductive WPT system should be investigated under the magnetic field and electric field safety limits to understand the limitations. In this chapter, the power scalability limitations will be identified based on the coil enclosed area, the operating frequency, and the transfer distance.

5.2 Air-core winding power scaling law based on feasible design variables

5.2.1 Power scaling law based on winding enclosed area

The winding configurations, such as circular winding, square winding, and rectangular winding as shown in Fig. 5-1, with a single turn, and same transmitter and receiver are used to investigate the power scaling law based on coil enclosed area. The transfer distance is set as 300 mm, the operating frequency is chosen as 0.1 MHz.

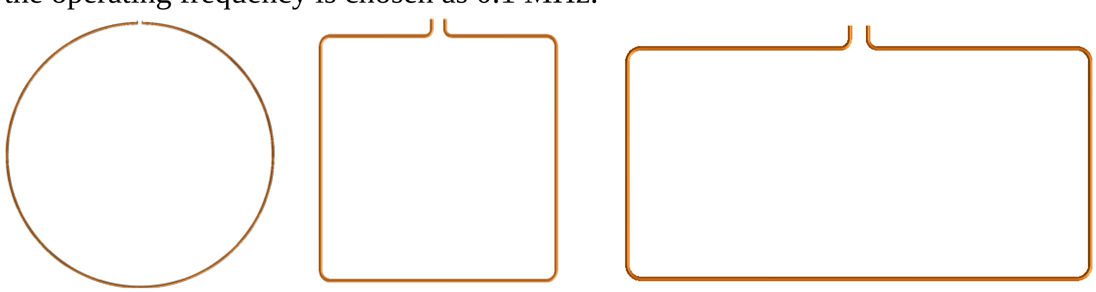

(a) Circular winding (b) Square winding (c) Rectangular winding

Fig. 5-1. Investigated winding configurations

During the FEA evaluation, B_{agcppk} is pushed to the IEEE C95.1-2005 safety limit, the input power P_{in}, the output power P_{out}, and η_{coil} are recorded. Because of the low operating frequency and low number of turns, E_{agcppk} will be lower than the electric field safety limit when B_{agcppk} meets the safety limit. When operating at a higher frequency or with a high number of turns, E_{agcppk} may first meet the safety limit.

When B_{agcppk} meets the safety limit, P_{in}, P_{out}, η_{coil}, coil enclosed area A, P_{in}/A, and P_{out}/A under different winding configurations are compared in Table 5-1.

Table 5-1. Comparison of different winding configurations

Winding dimension		P_{in} [W]	P_{out} [W]	η_{coil} [%]	A [mm^2]	P_{in}/A [W/mm^2]	P_{out}/A [W/mm^2]
Radius [mm]	500	2921	2761	94.52	785398	0.00372	0.00352
	600	4296	4100	95.44	1130973	0.00380	0.00363
	700	5996	5758	96.03	1539380	0.00390	0.00374
	800	7827	7548	96.44	2010619	0.00389	0.00375
Width × Length [mm × mm]	1064×1064	4315	4094	94.88	1132096	0.00382	0.00363
	1064×2128	8664	8316	95.98	2264192	0.00383	0.00368
	1064×2628	10350	9951	96.14	2796192	0.00371	0.00356

According to Table 5-1, the maximum transferable power and the coil-to-coil efficiency increase when the winding enclosed area increases. However, the ratio of the maximum input (or output) power to the coil enclosed area remains almost the same regardless or the coil shape when the coil enclosed area is large enough. The coil enclosed area must be increased to transfer higher power under given operating frequency when satisfying the IEEE C95.1-2005 standard.

Based on the analyses in chapter 3, when the coil is large enough, B_{agcppk} is limited by the radial direction leakage magnetic flux instead of the z-direction mutual flux. One method to reduce the leakage flux is using the shielding techniques developed in chapter 4, however, the improvement is limited. Another method is reducing the required current to transfer the same amount of power, which can be achieved by changing the operating frequency.

5.2.2 Power scaling law based on operating frequency

As the operating frequency increases, the optimal load resistance to achievable η_{coil} also increases, which means the required currents in the transmitter and the receiver to transfer the same amount of power will reduce, therefore, B_{agcppk} can be reduced, however, E_{agcppk} will increase due to the increase of the required terminal excitation voltages. It should be noted that the tissue heating effect should be taken into consideration when the operating frequency is higher than 0.1 MHz, and the magnetic field tissue heating safety limit reduces as the operating frequency increases above 0.1 MHz, the magnetic field electrostimulation safety limit remains the same until 5 MHz, the electric field combined safety limit reduces with the operating frequency when operating above 1.34 MHz.

One-turn circular coil with radii 200 mm, 400 mm, and 600 mm are evaluated with respect to the operating frequency from 20 kHz to 1 MHz. The transfer distance is still set as 300 mm. The maximum allowable output power P_{mo} within the IEEE C95.1-2005 standard is simulated via FEA as shown in Fig. 5-2.

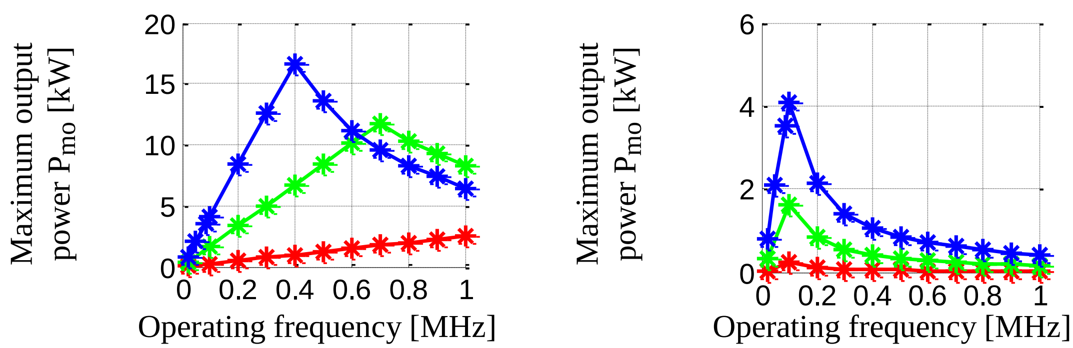

(a) P_{mo} w.r.t. electrostimulation limit (b) P_{mo} w.r.t. tissue heating limit

FEA test conditions: Transfer distance 300 mm. Transmitter and receiver: Number of turns 1, Winding radius (R) 200 mm, 400 mm, 600 mm.

Fig. 5-2. The maximum output power P_{mo} through 300 mm air-gap within the IEEE C95.1-2005 standard under different operating frequency

As shown in Fig. 5-2 (a), P_{mo} first increases linearly with f, since B_{agcppk} reduces as the operating frequency f increases and B_{agcppk} first meet the magnetic field safety limit, and then P_{mo} decreases quadratically with f because E_{agcppk} meets the electric field safety limit. Besides that, the transition frequency is not fixed, the transition frequency of a coil with a small radius is higher than that of a coil with a large radius, since the required excitation voltage and E_{agcppk} increase as the coil radius increase according to the analyses in chapter 2 and chapter 3. Besides that, it can be estimated that the transition frequency will reduce when the number of turns increases, because E_{agcppk} increases as the number of turns increases.

When the number of turns is low, and B_{agcppk} first meets the magnetic field safety limit as the operating frequency increases, above analyses are valid. However, if the coil number of turns is very high, and E_{agcppk} first meets the electric field safety limits even at a low operating frequency, then the maximum transferable power under the safety standard will reduce quadratically as the operating frequency increases, the winding design should be optimized to avoid this situation. It's a tradeoff between the magnetic field and the electric field based on the operating frequency to meet the electrostimulation safety limit.

In Fig. 5-2 (b), P_{mo} reduces as f increases above 0.1 MHz since the tissue heating limit reduction rate is faster than the reduction rate of B_{agcppk}, it's better to operate at 0.1 MHz to achieve higher output power under the electrostimulation and tissue heating safety limits. Below 0.1 MHz, P_{mo} / (A × f) is equal to 0.0363 W/(mm^2×MHz), 0.0326 W/(mm^2×MHz), and 0.0184 W/(mm^2×MHz) with the coil radius 600 mm, 400 mm, and 200 mm, respectively, which provides a direction for general designs.

Based on the analyses in previous section, when the coil enclosed area is larger than the area enclosed by the coil with 600 mm radius, P_{out} / A is relatively stable around 0.0036 ~ 0.0037 W/mm^2 under 0.1 MHz to satisfy the IEEE C95.1-2005 safety limit, therefore P_{mo} / (A × f) will be around 0.036 ~ 0.037 W/(mm^2×MHz) for the coil with enclosed area larger than 1130973 mm^2 when operating under 0.1 MHz.

5.2.3 Power scaling law based on transfer distance

When the transfer distance is reduced, the mutual inductance will increase, which leads to a higher coil-to-coil efficiency. However, B_{agcppk} will increase due to the leakage magnetic flux,

E_{agcppk} will also increase since the air-gap center plane is much closer to the winding terminals. It's necessary to evaluate the maximum allowable output power under different transfer distance with respect to the operating frequency to identify the effects of transfer distance.

Two transfer distances 200 mm and 300 mm are evaluated under different operating frequency from 20 kHz to 1 MHz using a one-turn circular coil with radii 200 mm, 400 mm, and 600 mm. The maximum allowable output powers P_{mo} of different windings within the IEEE C95.1-2005 standard are compared in Fig. 5-3 via FEA.

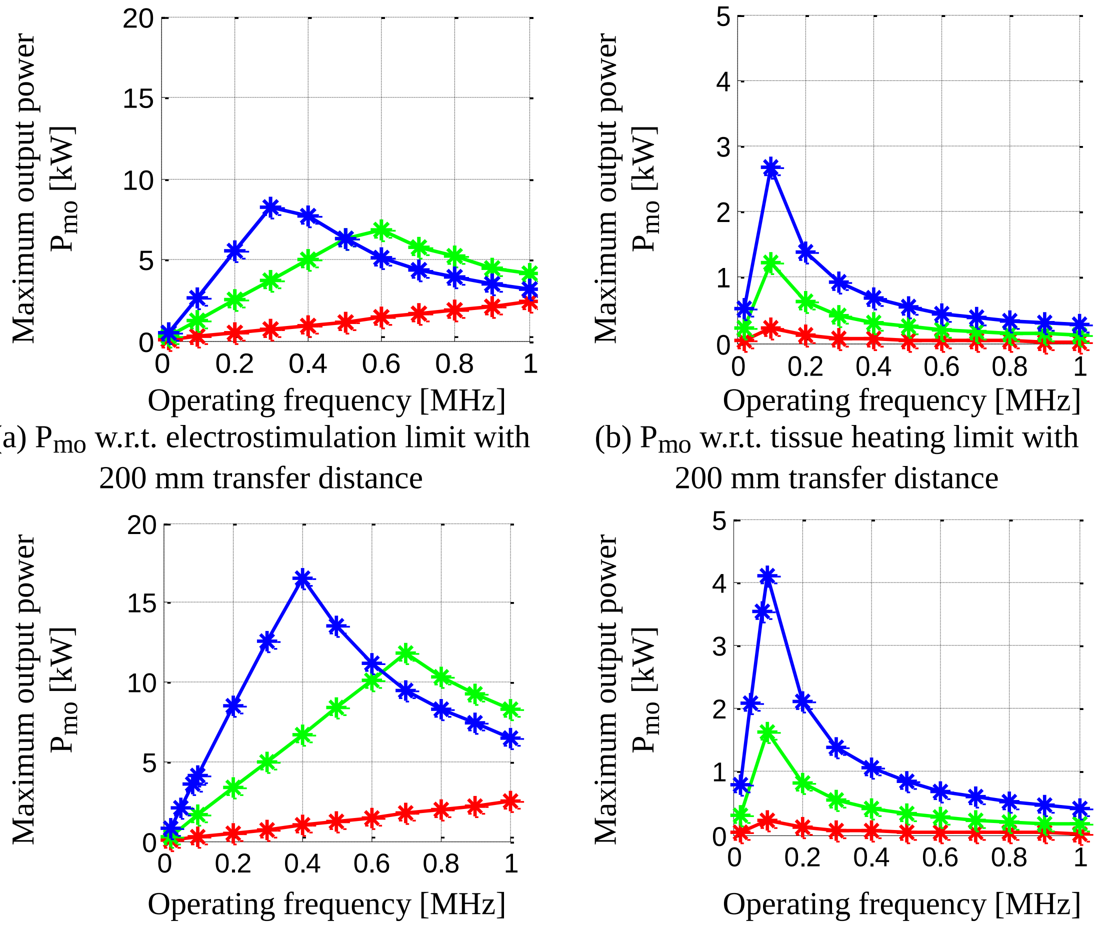

(a) P_{mo} w.r.t. electrostimulation limit with 200 mm transfer distance

(b) P_{mo} w.r.t. tissue heating limit with 200 mm transfer distance

(c) P_{mo} w.r.t. electrostimulation limit with 300 mm transfer distance

(d) P_{mo} w.r.t. tissue heating limit with 300 mm transfer distance

Transmitter and receiver FEA conditions:
number of turns 1, winding radius (R) 200 mm, 400 mm, 600 mm.

Fig. 5-3. The maximum output power P_{mo} through 200 mm and 300 mm air-gap within the IEEE C95.1-2005 standard under different operating frequency

As shown in Fig. 5-3 (a) and (c), under the electrostimulation safety limit, P_{mo} first increases linearly with f limited by B_{agcppk}, then decreases quadratically with f limited by the E_{agcppk} no matter the transfer distance is 200 mm or 300 mm. When the transfer distance is reduced, the transition frequency is also reduced due to E_{agcppk}, since the air-gap center plane is much closer to the excitation terminal, it's possible to push to higher power level with larger transfer distance. According to Fig. 5-3 (b) and (d), P_{mo} reduces as f increases above 0.1 MHz since the tissue heating limit reduction rate is faster than the reduction rate of B_{agcppk}. When the transfer distance is reduced, P_{mo} also reduces because of the leakage magnetic flux density. It's still better to operate at 0.1 MHz to transfer higher power.

5.2.4 Theoretical maximum air-gap power under resonant condition

The power scaling law with respect individual design variables are developed in previous section. In this section, the analytical relationship between air-gap maximum transferrable power P_{agm} and air-gap center plane test point magnetic field H_{agcp} will be developed under SS resonant condition. This can give a physical reference about the power limitation under given field level, although P_{agm} can be slightly improved by phase manipulation method.

The planar circular spiral winding (PCSW) is used as an initial example in the analysis. Its configuration and transformer based equivalent models are shown in Fig. 5-4.

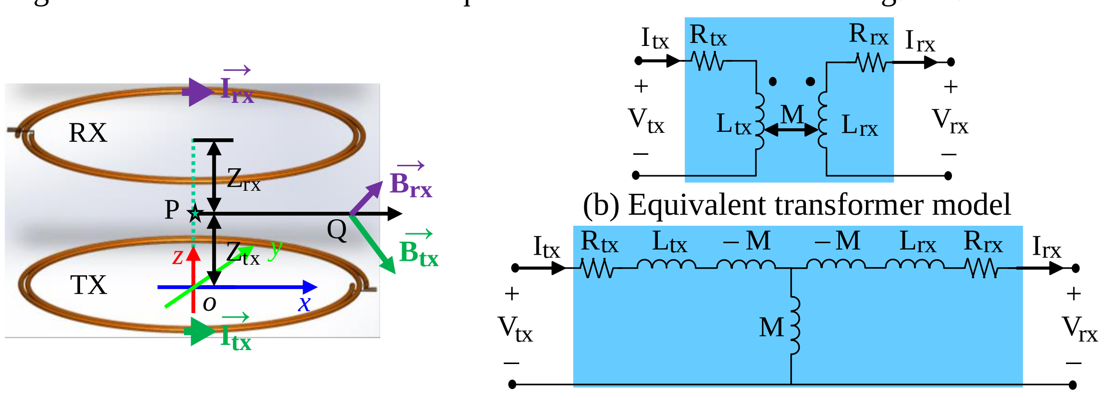

(a) Winding configuration (b) Equivalent transformer model (c) Equivalent transformer "T" model

Fig. 5-4. Winding configuration and equivalent transformer models

Assuming the transmitter and the receiver are the same, the relationship between H_{agcp} at test point Q and the winding excitation currents is

$$H_{agcp} = coef_{xz}\,(N_{tx}\,\overrightarrow{I_{tx}} + N_{rx}\,\overrightarrow{I_{rx}}) \tag{5.1}$$

where, $coef_x = \frac{1}{\pi}\frac{x\,z}{2\alpha^2\beta\rho^2}\left[(r_w^2 + s^2)E(k^2) - \alpha^2 K(k^2)\right]$, $coef_z = \frac{1}{\pi}\frac{1}{2\alpha^2\beta}\left[(r_w^2 - s^2)E(k^2) + \alpha^2 K(k^2)\right]$, $coef_{xz} = \sqrt{coef_x^2 + coef_z^2}$, $\rho^2 = x^2 + y^2$, $s^2 = \rho^2 + z^2$, $\alpha^2 = s^2 + r_w^2 - 2r_w\rho$, $\beta^2 = s^2 + r_w^2 + 2r_w\rho$, $k^2 = 1 - \alpha^2/\beta^2$. N_{tx} and N_{rx} are the number of turns of the transmitter and the receiver, respectively. $K(k^2)$ and $E(k^2)$ are the complete elliptic integrals of the first and second kind, respectively. $z = Z_{tx} = Z_{rx} = h/2$, h is the transfer distance, r_w is winding radius.

When Q is the central point P, $coef_{xz}$ can be simplified as

$$coef_{xz} = \frac{1}{2}\frac{r_w^2}{(z^2 + r_w^2)^{3/2}} \tag{5.2}$$

It's easy to find that $coef_{xz}$ will reduce if z increases or r_w increases.

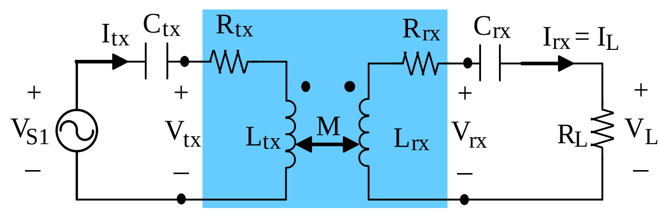

(a) System equivalent circuit model with SS topology based on transformer model

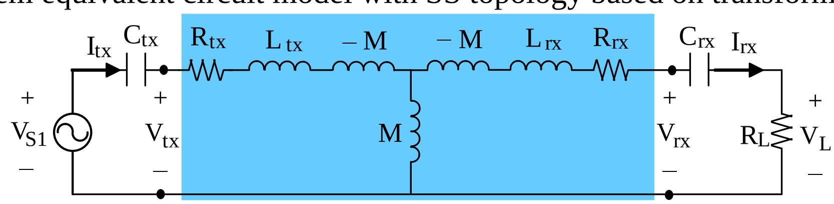

(b) System equivalent circuit model with SS topology based on transformer "T" model

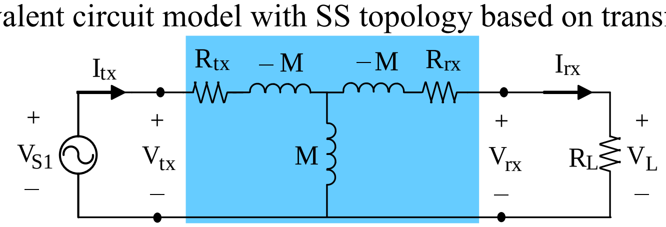

(c) Simplified system equivalent circuit model under resonant condition

Fig. 5-5. System equivalent circuit models

The system equivalent circuit model compensated with SS topology are shown in Fig. 5-5 (a). In order to simplify the calculation, the transformer "T" model can be used to analyze the current and voltage relationships as shown in Fig. 5-5 (b). The equivalent circuit can be further simplified to Fig. 5-5 (c), because the self-inductance terms (L_{tx} and L_{rx}) and the compensation capacitor terms (C_{tx} and C_{rx}) can be canceled under resonant condition

$$\omega_0 L_{tx} = \frac{1}{\omega_0 C_{tx}}, \ \omega_0 L_{rx} = \frac{1}{\omega_0 C_{rx}} \tag{5.3}$$

where, $\omega_0 = 2\pi f_0$, f_0 is the operating frequency.

From Fig. 5-5 (c), the current ratio can be calculated

$$\frac{I_{tx}}{I_{rx}} = \frac{R_{rx} + R_L}{j\omega_0 M} \tag{5.4}$$

Substituting (5.4) into (5.1), H_{agcp} can be expressed by I_{rx} as

$$H_{agcp}^2 = I_{rx}^2 \, coef_{xz}^2 \left\{ N_{tx}^2 \frac{(R_{rx} + R_L)^2}{\omega_0^2 M^2} + N_{rx}^2 \right\} \tag{5.5}$$

The power transferred through the air-gap can be calculated by the power received by the load plus the power consumed by the receiver as

$$P_{ag} = \frac{1}{2} I_{rx}^2 (R_{rx} + R_L) \tag{5.6}$$

Combining (5.5) and (5.6), the relationship between P_{ag} and H_{agcp} can be found

$$P_{ag} = \frac{I_{rx}^2 (R_{rx} + R_L)}{2} = \frac{H_{agcp}^2}{2 \, coef_{xz}^2 \left[N_{tx}^2 \frac{R_{rx} + R_L}{\omega_0^2 M^2} + \frac{N_{rx}^2}{R_{rx} + R_L} \right]} \tag{5.7}$$

The maximum air-gap transferrable power P_{agm} can be achieved when

$$\frac{N_{rx}^2}{R_{rx} + R_L} = N_{tx}^2 \frac{R_{rx} + R_L}{\omega_0^2 M^2}, \ R_L = \omega_0 M \frac{N_{rx}}{N_{tx}} - R_{rx} \tag{5.8}$$

Therefore, P_{agm} can be calculated by

$$P_{agm} = \frac{1}{2} \frac{H_{agcp}^2}{coef_{xz}^2} \frac{\omega_0 M}{2 N_{tx} N_{rx}} = \frac{\pi}{2} \frac{1}{coef_{xz}^2} \frac{M}{N_{tx} N_{rx}} f_0 H_{agcp}^2 \tag{5.9}$$

The air-gap power density P_{agm}/V_{ag} can be calculated by

$$\frac{P_{agm}}{V_{ag}} = \frac{1}{2\pi r_w^2 h} \frac{H_{agcp}^2}{coef_{xz}^2} \frac{\omega_0 M}{2 N_{tx} N_{rx}} = \frac{1}{2 r_w^2 h} \frac{1}{coef_{xz}^2} \frac{M}{N_{tx} N_{rx}} f_0 H_{agcp}^2 \tag{5.10}$$

According to (5.9), within given magnetic field strength H_{agcp}, P_{agm} is proportional to geometric term $(1/coef_{xz})^2$, equivalent mutual inductance $M/(N_{tx}\ N_{rx})$, and operating frequency f_0. The geometric term $(1/coef_{xz})^2$ increases as the winding radius r_w increases or the transfer distance h increases. For given winding configuration and transfer distance, $(1/coef_{xz})^2$ can be treated as a constant value. Therefore, the evaluation will be with respect to $M/(N_{tx}\ N_{rx})$ and f_0.

For the PCSW, when N_{tx}, N_{rx} or d_{int} changes, M and $M/(N_{tx}\ N_{rx})$ are calculated analytically and compared with FEA results as shown in Fig. 5-6.

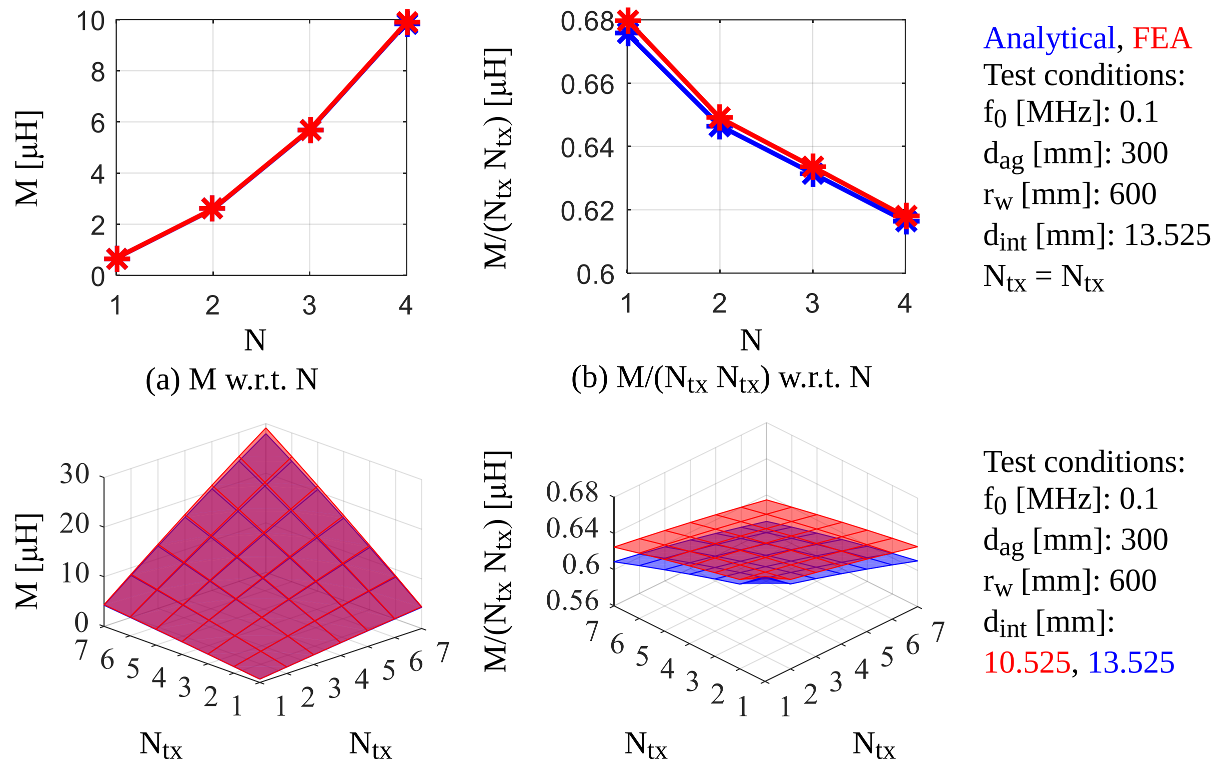

(a) M w.r.t. N

(b) $M/(N_{tx}\ N_{tx})$ w.r.t. N

(c) M w.r.t. N_{tx}, N_{tx}, and d_{int}

(d) $M/(N_{tx}\ N_{tx})$ w.r.t. N_{tx}, N_{tx}, and d_{int}

Fig. 5-6. Effects of N_{tx}, N_{tx}, and d_{int} on M and $M/(N_{tx}\ N_{tx})$

As shown in Fig. 5-6 (a) and (b), the analytical and FEA results match with each other very well. When N increases, M increases, but $M/(N_{tx}N_{rx})$ reduces, which suggests that P_{agm} can achieve higher value when $N_{tx} = N_{rx} = 1$ for PCSW.

According to Fig. 5-6 (c) and (d), when d_{int} reduces, M and $M/(N_{tx}N_{rx})$ increase. However, for the PCSW, d_{int} cannot be reduced to zero. Either N_{tx} or N_{rx} increases, M will increase, but $M/(N_{tx}N_{rx})$ reduces. That means increasing the number of turns will lead to lower P_{agm}, although it can improve η_{coil}. Therefore, in order to ensure P_{agm}, alternative winding configurations that can achieve equal diameter per turn and low proximity effect loss, such as SSW, should be used to maintain the same $M/(N_{tx}N_{rx})$ and η_{coil}. M, $M/(N_{tx}N_{rx})$, η_{coil} and P_{agm} FEA results of the PCSW and the SSW are compared in Fig. 5-7.

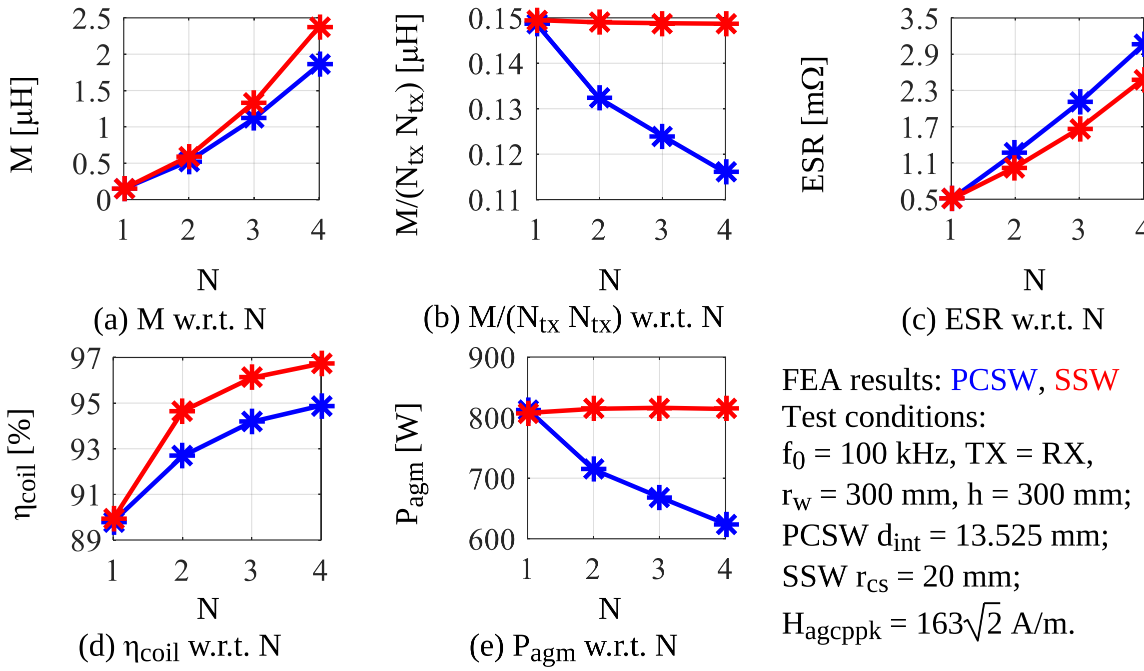

Fig. 5-7. Comparison of the PCSW and the SSW

As shown in Fig. 5-7, when N increases, compared with the PCSW, the SSW can achieve higher M due to equal diameter per turn and lower ESR due to reduced proximity effect. Both lead to higher η_{coil}. In addition, the SSW maintains almost the same $M/(N_{tx}N_{rx})$ and P_{agm}, which also shows that increasing N will not improve P_{agm}. Therefore, using N = 1 is enough to evaluate the power scalability limitation. According to the analysis in chapter 3, E_{agcppk} is much lower than the electric field safety limit at low operating frequency, such as 0.1 MHz, when N = 1, so H_{agcppk} is the power scalability limitation.

Due to the tissue heating issue, H safety limit reduces above 100 kHz, and E safety limit reduces above 1.34 MHz. P_{agm} is calculated with respect to operating frequency f_0 and winding radius r_w as shown in Fig. 5-8 (a) considering the general public exposure magnetic field electrostimulation limit H_{es} below 100 kHz and tissue heating limit H_{th} above 100 kHz. The analytical result is compared with the FEA result in Fig. 5-8 (b).

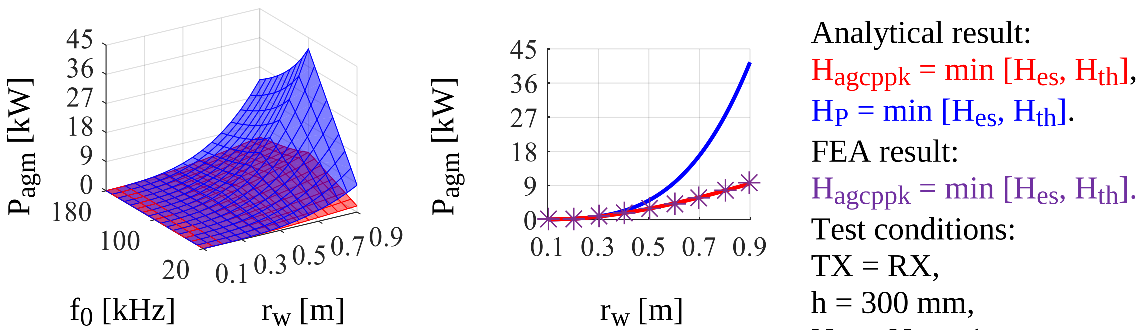

(d) η_{coil} w.r.t. N (e) P_{agm} w.r.t. N

Fig. 5-8. Effects of operating frequency f_0 and winding radius r_w on P_{agm}

As shown in Fig. 5-8 (a), below 100 kHz, P_{agm} increases with f_0, since the required excitation currents reduce as f_0 increases. Above 100 kHz, P_{agm} reduces as f_0 increases due to the tissue heating safety limit. Therefore, it's recommended to operate at 100 kHz from the IEEE safety standard perspective. When r_w increases, P_{agm} following the whole air-gap center plane safety requirement is lower than P_{agm} satisfying the safety limit at central point P, which is verified by the FEA result as shown in Fig. 5-8 (b), because the location of H_{agcppk} is shifted away from point P due to the leakage field.

The relationship between P_{agm}/V_{ag} and r_w at 100 kHz within specific magnetic field limit is calculated and compared with the FEA result as shown in Fig. 5-9.

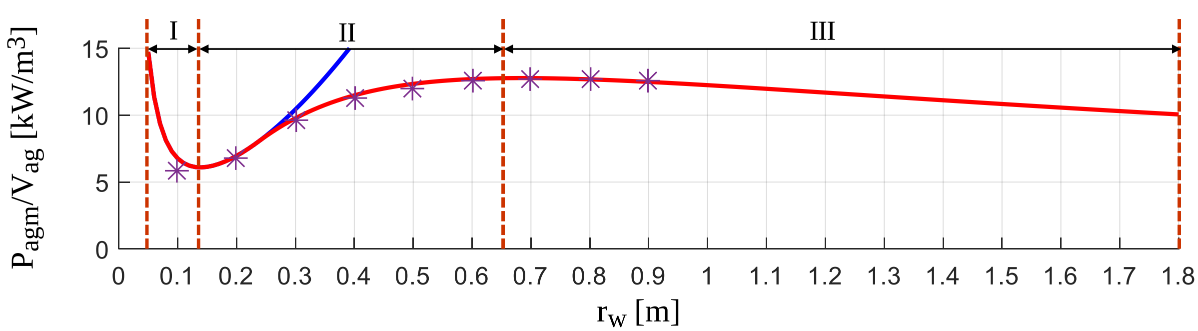

— Analytical maximum limit when considering H_{pk} at central point P, H_{agcppk}
* FEA maximum limit when considering H_{agcppk}
Test conditions: $N_{tx} = N_{rx} = 1$, h = 300 mm.

Fig. 5-9. Relationship between P_{agm}/V_{ag} and r_w at 100 kHz

As shown in Fig. 5-9, when the air-core winding r_w is higher than 0.26 m, the location of H_{agcppk} begins to shift away from the central point. When r_w increases, P_{agm}/V_{ag} first reduces in section I due to the reduction of the air-gap geometry coefficient $coef_{ag} = \frac{1}{r_w^2 h} \frac{1}{coef_{xz}^2}$. Then P_{agm}/V_{ag} increases in section II due to the increase of the mutual inductance coefficient $coef_M = \frac{M}{N_{tx} N_{rx}}$. At the end, P_{agm}/V_{ag} reduces in section III due to the magnetic leakage field. Section I and section II analysis can be verified by the calculation of $coef_{ag}$ and $coef_M$ for the special case at air-gap central point P as shown in Fig. 5-10.

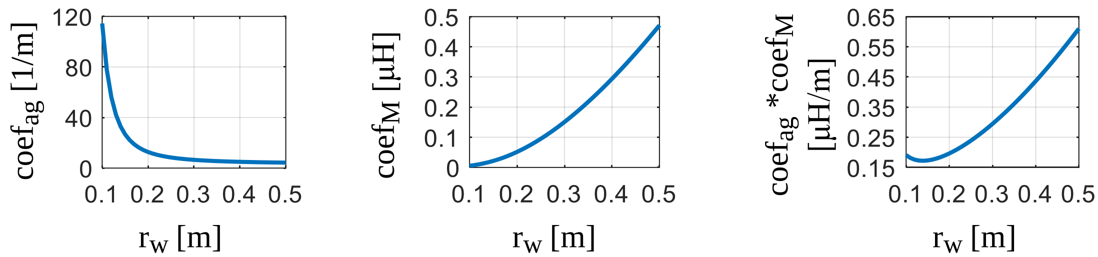

Fig. 5-10. Analysis of $coef_{ag}$ and $coef_M$

As shown in Fig. 5-10, when r_w increases, $coef_{ag}$ keeps reducing, while $coef_M$ keeps increasing. The reduction of $coef_{ag}$ can be compensated by the increase of $coef_M$.

In summary, compared with PCSW, SSW can maintain the equivalent mutual inductance even when the number of turns is increased. SSW η_{coil} can be improved by increasing the number of turns without degrading P_{agm}. For air-core winding design, the winding size must be increased to improve P_{agm}. Flux shaping techniques can be used to improve P_{agm} without increasing the winding size. After adding conventional magnetic shield, P_{agm} will be reduced due to mirrored currents. The proposed “I” type shielding design can improve P_{agm} without mitigating η_{coil}, and achieve higher P_{agm} than the air-core winding.

5.3 “I” type shielding design power scaling law

Before developing high power inductive WPT design with “I” type shielding structure, it’s necessary to identify the relationship between the transferrable power level within the safety standard and the “I” type shielding design dimensions.

According to previous analysis, when transferring power at 100 kHz, the air-gap magnetic field is the limitation to push to higher power level. In the FEA analysis, the power transferred through the air-gap is assigned as P_{agm} when B_{agcppk} meets the IEEE safety limit. A 4-turn circular SSW is used as a baseline. The design variables are winding radius r_w, conventional magnetic shield radius r_f, "I" type magnetic shield inner radius r_{in} and outer radius r_{out}. The winding configurations and P_{agm} are compared in Fig. 5-11.

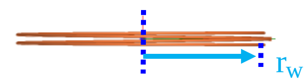

(a) Air-core winding configuration

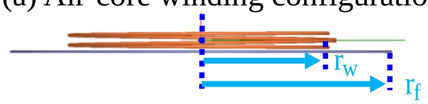

(b) Conventional magnetic design configuration

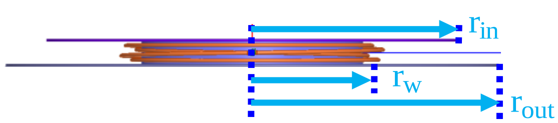

(c) "I" type magnetic design configuration

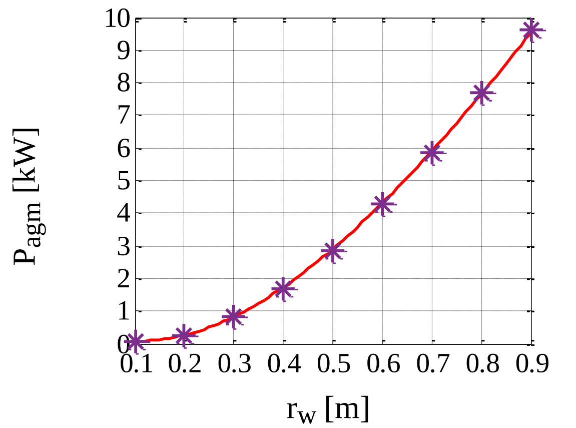

(d) Air-core P_{agm} within IEEE C95.1-2005 safety standard w.r.t. r_w

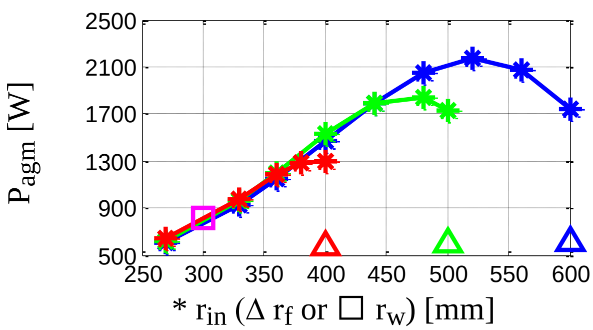

(e) Magnetic designs P_{agm} within IEEE C95.1-2005 safety standard w.r.t. r

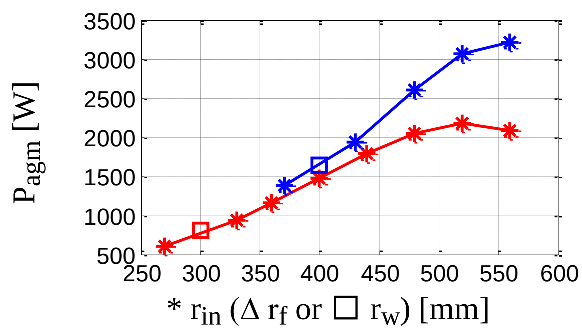

(f) Magnetic designs P_{agm} within IEEE C95.1-2005 safety standard w.r.t. r

FEA conditions: SS topology, TX = RX, f_0 = 100 kHz, h = 300 mm, $B_{agcppk,\ lim}$ = 289 μT, $E_{agcppk,\ lim}$ = 868.3 V/m; Ferrite: μ_r = 1000, σ = 0.01 S/m; Aluminum: σ = 3.8*1e7 S/m.
(d) N_{tx} = N_{rx} = 1, FEA, Analytical. (e) N = 4; □ air-core: r_w = 300 [mm]; Δ Conventional design: r_f = 400, 500, 600 [mm]; * "I" design: r_{out} = 400, 500, 600 [mm]. (f) N = 4; □ air-core: r_w = 300, 400 [mm]; * "I" design: r_{out} = 600 [mm], r_w = 300, 400 [mm].

Fig. 5-11. Comparison of winding configurations and P_{agm} within safety standard

As shown in Fig. 5-11 (d), as r_w increases, the increase rate of P_{agm} changes from quadratic to linear. According to Fig. 5-11 (e), increasing r_f of the conventional magnetic design has a nearly negligible effect on P_{agm}, which is about 35% lower than the air-core winding. However, the "I" type magnetic design can achieve the same P_{agm} when r_{in} is close to winding radius r_w. Besides that, P_{agm} can be increased linearly as r_{in} increases when r_{in} is much smaller than r_{out}. The "I" type magnetic design provides an access to achieve higher P_{agm}, even though P_{agm} reduces as r_{in} increases when r_{in} is close to r_f, it's still higher than the air-core winding. From Fig. 5-11 (f), it can be concluded that when r_{in} isn't very close to r_{out}, the "I" type magnetic design P_{agm} increases linearly as r_{in} increases based on the power capability of air-core winding. The increase rate can be obtained easily by only using two FEA cases with different r_{in} values. It should also be noted that the maximum size of the "I" type magnetic design is still limited by feasible design area beneath the vehicle. Considering that using a larger winding is inherently beneficial to ensure P_{agm} and η_{coil} even under misaligned operating conditions, it's recommended to maintain r_{in} close to r_w, and leave enough margin between r_{in} and r_{out}.

A 3kW design is used to analyze the thermal distribution and check whether additional cooling technique is required. According to the FEA results in Fig. 5-11 (f), in order to satisfy the IEEE C95.1 – 2005 magnetic and electric field safety limits, the winding and "I" type shielding parameters can be selected as listed in Table 5-2.

Table 5-2. A 3kW design winding and "I" type shielding parameters

Winding radius	400 mm	"I" design inner radius	520 mm	"I" design outer radius	600 mm
Number of turns	4	Aluminum plate radius	800 mm	Plate thickness	5 mm

The FEA test setup and loss ditributions are shown in Fig. 5-12.

Output power: 3035.41 W. Transmitter: P_{copper} = 37.24 W, $P_{ferrite}$ = 2.53 W. Receiver: P_{copper} = 33.68 W, $P_{ferrite}$ = 1.98 W. Aluminum plate: P = 5.91 W. Coil-to-coil efficiency: 97.39%.

(a) A 3kW design FEA test setup (b) Loss distributions

Fig. 5-12. A 3kW design FEA test setup and loss distributions

According to Fig. 5-12(b), the ferrite loss is very small, theoretically the temperature increase of ferrite shield should be very small. While the winding copper loss is a relatively bigger concern. The temperature increase of the winding can be calculated by

$$\Delta T = \frac{Q}{hA} \tag{5.11}$$

Where Q is the power loss (W), h is the heat transfer coefficient (W/(m^2×°C)), A is winding surface area (m^2).

In the 3kW design, A can be calculated approximately as 4 × π × 9.525 mm × π × 800 mm = 0.3 m^2. Typical air heat transfer coefficient h = 10 – 100 W/(m^2×°C). If forced air-cooling technique is used, h should be selected as 100 W/(m^2×°C). If no additional cooling technique is used as in this design example, h can be picked as 10 W/(m^2×°C). Then the transmitter winding temperature increase due to copper loss can be calculated as 37.24/10/0.3 °C = 12.4 °C.

Steady-state thermal distribution is simulated via Ansys workbench. The FEA setup and simulation results are shown in Fig. 5-13. The initial temperature is set as 22 °C, the convention coefficient is set as 10 W/(m^2×°C).

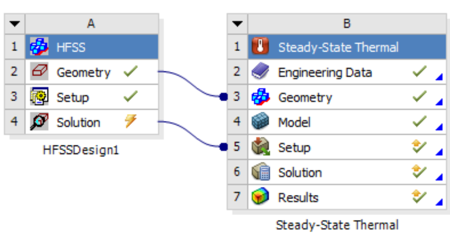

(a) Thermal analysis FEA setup

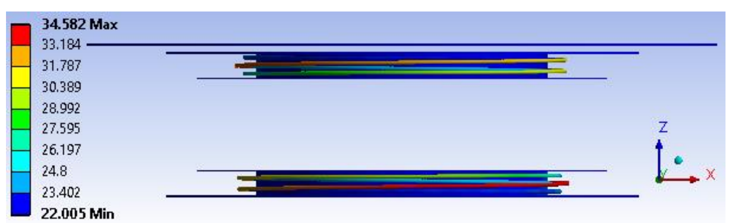

(b) System thermal distribution

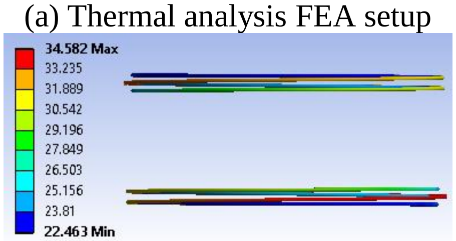

(c) Winding temperature distribution

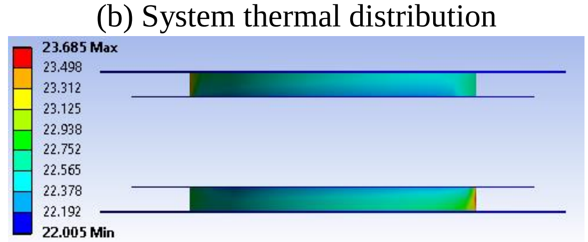

(d) Ferrite temperature distribution

Fig. 5-13. Steady-state thermal distribution FEA setup and simulation results (Unit: °C)

According to Fig. 5-13 (b) and (c), the peak temperature is located in the winding instead of the ferrite shielding. Based on Fig. 5-13 (c), the winding temperature increase due to copper loss is 12.582 °C, which is nearly the same as the analytical calculation result 12.4 °C. As shown in Fig. 5-13 (d), the ferrite shielding temperature increase is only 1.685 °C, which won't affect the performance of the ferrite material. Besides that, considering the low magnetic field around the winding, the ferrite material won't be saturated. Therefore, the performance of the ferrite material, such as permability and permittivity, would remain nearly the same during operation.

In order to find a suitable power level for EV inductive charging, the battery capacity data of full-electric, plugin hybrids, and non-plug-in hybrids are summarized in Table 5-3 [257].

Table 5-3. Summary of battery capacity

Vehicle types	Vehicle	Capacity [kWh]	Vehicle	Capacity [kWh]	Vehicle	Capacity [kWh]
Full-electric	Addax MT	10-15	Hyundai Kona Electric	39.2-64	Renault Twizy	6
	Audi e-tron	95	Hyundai Ioniq Electric	28	Renault Zoe	22 (2012), 41 (2016)
	BMW i3	22-33	Kia Soul EV	27	Smart electric drive II	16.5
	BYD e6	60-82	Kia Niro EV	39.2-64	Smart electric drive III	17.6
	Chevrolet Bolt / Opel Ampera-e	60	Jaguar I-Pace	90	Tesla Model S	60-100
	Citroen C-Zero / Peugeot iOn	14 (2011) / 16 (2012)	Nissan Leaf I	24-30	Tesla Model X	60-100
	Fiat 500e	24	Nissan Leaf II	24-60	Tesla Model 3	50-70
	Ford Focus Electric	23 (2012), 33.5 (2018)	Mitsubishi i-MIEV	16	Toyota RAV4 EV	27.4 (1997), 41.8 (2012)
	Honda Clarity (2018)	25.5	Renault Fluence Z.E.	22	Volkswagen e-Golf Mk7	24-36
Plugin hybrids	Audi A3 e-tron	8.8	Hyundai Ioniq	8.9	Toyota Prius III	4.4
	Audi Q7 e-tron	17	Kia Niro	8.9	Toyota Prius IV	8.8
	BMW i8	7	Koenigsegg Regera	4.5	Volkswagen Golf GTE	8.8
	BMW 2 Series Active Tourer 225xe	6.0	BMW 330e iPerformance	7.6	BMW 530e iPerformance	9.2
	BMW X5 xDrive40e	9.0	Honda Accord PHEV (2013)	6.7	Honda Clarity PHEV (2018)	17
	Chevrolet Volt	16-18	Volkswagen Passat GTE	9.9	Volkswagen XL1	5.5
	Ford Fusion II / Ford C-Max II Energi	7.6	Mitsubishi Outlander PHEV	12	Porsche 918 Spyder	6.8

	Fisker Karma	20	Volvo V60	11.2		
Non-plugin hybrids	Chevrolet Malibu (2016)	1.5	Ford Fusion II / Ford C-Max II	1.4	Hyundai Ioniq Hybrid	1.56
	Kia Niro	1.56	Lexus CT 200h	1.3	Lexus NX 300h	1.6
	Toyota Prius II	1.3	Toyota Prius III	1.3	Toyota Prius C / Toyota Yaris Hybrid	0.9
	Toyota Camry Hybrid (2012)	1.6				

According to Table 5-3, the majority of the battery capacity is less than 60 kWh, which is enough for daily life, not for long distance travel. A 10-kW charging system should be enough for charging the battery overnight to full state-of-charge.

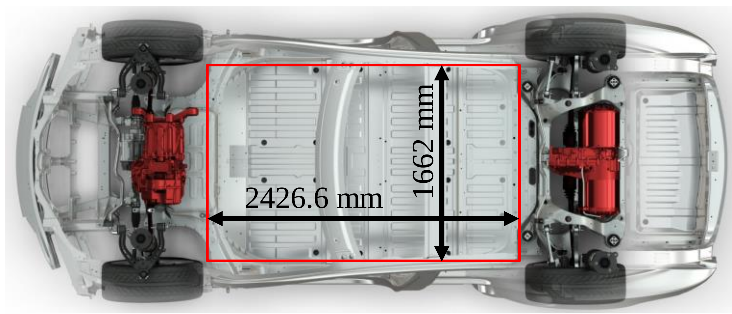

Fig. 5-14. Comparison of winding configurations and P_{agm} within safety standard

A tesla model S is used as a baseline to identify the feasible design space. The space among four wheels (Length 2426.6 mm, Width 1662 mm), as shown in, is selected as the feasible design space. The design space can be transformed in a circle with radius 1133.03 mm to have the enclosed area. It's easy to find that the circular shape winding is not a good choice compared with the rectangular shape, which can achieve larger enclosed area and be located within the design space. According to previous analysis, if the enclosed areas are the same, the circular winding and the rectangular winding have nearly the same field distributions and power transfer efficiency. Therefore, previous power scaling laws are applicable to rectangular winding.

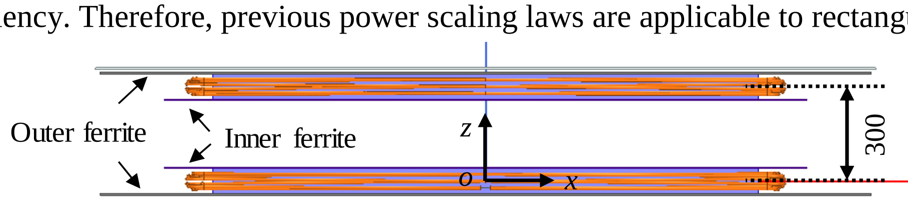

(a) Baseline design FEA configuration

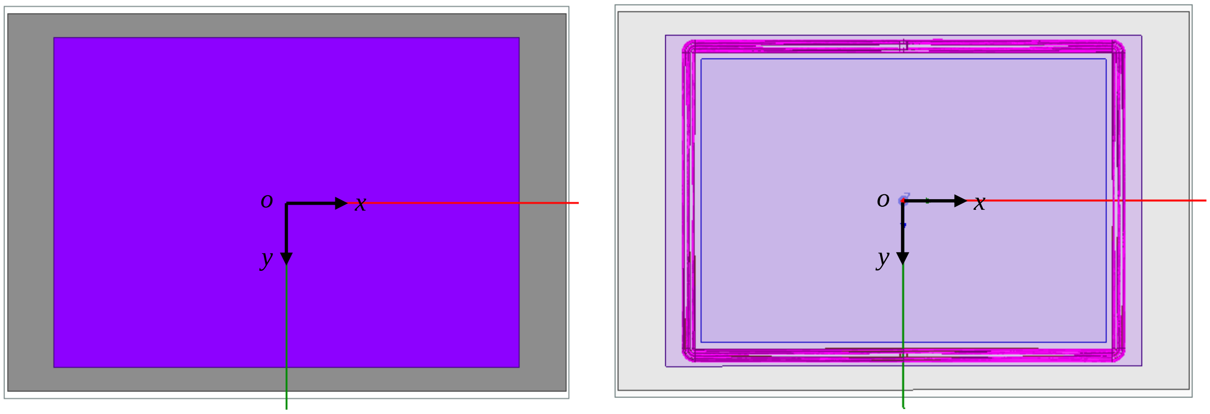

(b) Transmitter (or receiver) configuration in detail

Aluminum plate: length (L) 2426.6 mm × width (W) 1662 mm. Transmitter = Receiver. Winding: L 1810 mm × W 1310 mm. Outer ferrite plate: L 2400 mm × W 1600 mm. Middle ferrite: L 1700 mm × W 1200 mm. Inner ferrite plate: L 2000 mm × W 1400 mm.

Fig. 5-15. Illustration of initial design FEA configuration and dimensions

In the initial design, the aluminum plate to emulate the vehicle chassis is set the same as the design space (Length (L) 2426.6 mm × Width (W) 1662 mm). The “I” type design outer ferrite is set as L 2400 mm × W 1600 mm to leave some space for package and installation. The winding size should be smaller than the outer radius and leave enough space to provide a magnetic field return path. It’s chosen as L 1810 mm × W 1310 mm, which has the same enclosed area as the circular winding with radius 868.76 mm. If the air-core winding is used, 9 kW could be transferred while maintaining the air-gap magnetic and electric fields lower than the IEEE safety limits based on Fig. 5-11 (d). The inner ferrite is selected as L 2000 mm × W 1400 mm to fully cover the winding, but still leave some space for the mutual coupling magnetic flux return path. The winding configuration is presented in Fig. 5-15. The transmitter and the receiver are set as the same initially. The initial design dimensions are summarized in Table 5-4. A 3-turn SSPW is used to ensure the coil-to-coil power transfer efficiency.

Table 5-4. Summary of initial design dimensions (Unit: mm)

Aluminum plate		TX outer ferrite		TX inner ferrite		RX outer ferrite		RX outer ferrite		Winding	
L	W	L	W	L	W	L	W	L	W	L	W
2426.6	1662	2400	1600	2000	1400	2400	1600	2000	1400	1810	1310

When transferring power at 100 kHz using SS topology, B_{agcppk} is pushed to IEEE C95.1 safety limit 289 μT to identify P_{agm}. The winding parameters, power capability and loss distributions are summarized in Table 5-5.

Table 5-5. Summary of initial design parameters, power capability and loss distributions

L_{tx} [μH]	R_{tx} [mΩ]	L_{rx} [μH]	R_{rx} [mΩ]	M [μH]	η_{coil} [%]	P_{agm} [W]	P_{in} [W]	P_{out} [W]
143.74	121.2	135.85	128.1	25.85	98.48	9171.05	9246.02	9105.21

$P_{loss, tx, copper}$ [W]	$P_{loss, tx, ferrite}$ [W]	$P_{loss, rx, copper}$ [W]	$P_{loss, rx, ferrite}$ [W]	$P_{loss, alum.}$ [W]
57.87	6.17	53.19	4.13	18.32

The corresponding field distributions are shown in Fig. 5-16.

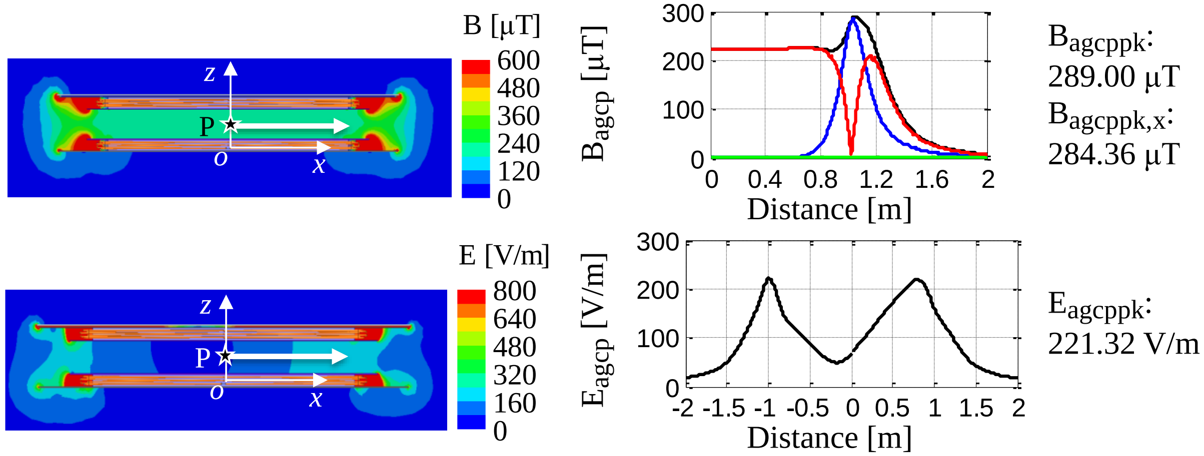

Legend: Magnetic field B_{total}, B_x, B_y, B_z. Electric field E_{total}.

Fig. 5-16. Field distributions when the initial design transferring P_{agm} = 9171.05 W

As shown in Fig. 5-16, B_{agcppk} is still fundamentally limited by the leakage field, the power transfer capability can be improved by optimizing the “I” type shield dimensions to provide a return path for the leakage field. In this case, SS topology is beneficial to achieve higher P_{agm}. The whole air-gap electric field still maintains much lower than the safety limit.

In order to transfer above 10 kW, the “I” type design is optimized to reduce the leakage field. Considering the receiver side is limited by the area beneath the vehicle, there’s less room to modify the receiver side design. The transmitter side is placed on the ground, so it can be slightly increased to provide enough space for magnetic field return path. The optimized design dimensions are summarized and compared with the initial design in Table 5-6.

Table 5-6. Summary of initial and optimized design dimensions (Unit: mm)

Aluminum plate		TX outer ferrite		TX inner ferrite		RX outer ferrite		RX outer ferrite		Winding	
L	W	L	W	L	W	L	W	L	W	L	W
Initial design dimensions											
2426.6	1662	2400	1600	2000	1400	2400	1600	2000	1400	1810	1310
Optimized design dimensions											
2426.6	1662	2400	1700	1950	1400	2400	1660	1950	1400	1810	1310

When transferring power at 100 kHz using SS topology, B_{agcppk} is also pushed to IEEE C95.1 safety limit 289 μT to identify P_{agm}. The winding parameters, power capability and loss distributions are summarized in Table 5-7.

Table 5-7. Summary of initial design parameters, power capability and loss distributions

L_{tx} [μH]	R_{tx} [mΩ]	L_{rx} [μH]	R_{rx} [mΩ]	M [μH]	η_{coil} [%]	P_{agm} [W]	P_{in} [W]	P_{out} [W]
140.23	125.5	134.22	130.7	30.67	98.68	10451.04	10520.96	10382.04

$P_{loss,\ tx,\ copper}$ [W]	$P_{loss,\ tx,\ ferrite}$ [W]	$P_{loss,\ rx,\ copper}$ [W]	$P_{loss,\ rx,\ ferrite}$ [W]	$P_{loss,\ alum.}$ [W]
56.84	5.81	52.84	4.10	18.06

From Table 5-7, it can be seen that above 10 kW output power (10382.04 W) is achieved. The corresponding field distributions are shown in Fig. 5-17.

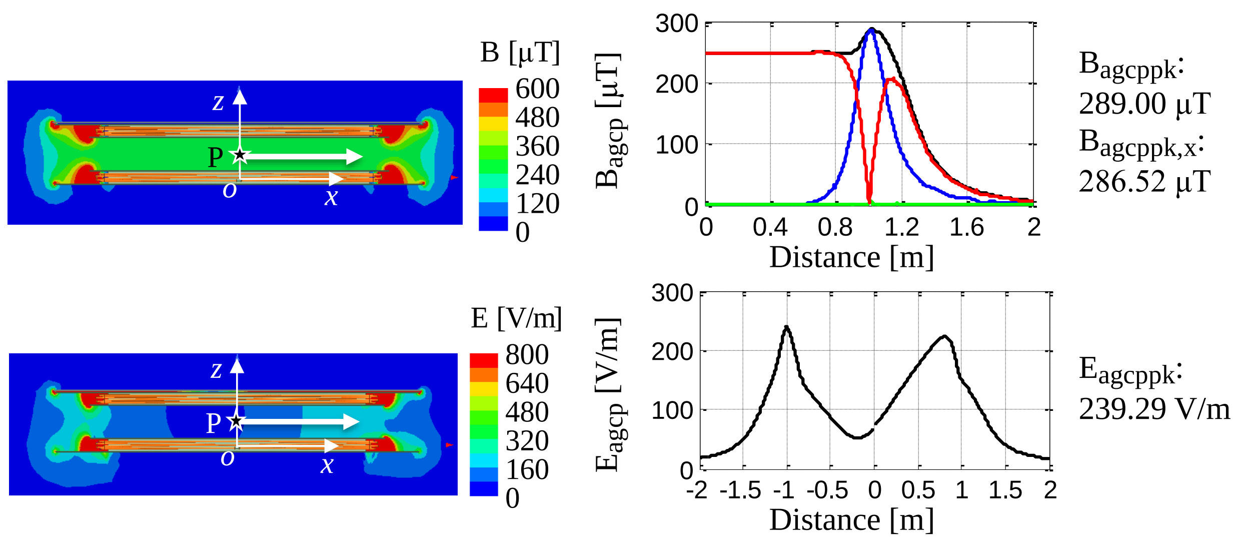

Legend: Magnetic field B_{total}, B_x, B_y, B_z. Electric field E_{total}.

Fig. 5-17. Field distributions when the optimized design transferring P_{agm} = 10451.04 W

As shown in Fig. 5-17, the optimized design magnetic field below the transmitter is highly reduced, compared with the initial design. The improvement of P_{agm} is brought by the additional region for the magnetic flux return path provided by the enlarged transmitter outer ferrite. The whole air-gap electric field is still maintained much lower than the safety limit.

Another concern regarding high power WPT is the thermal distribution. Due to the large size of proposed design, thermal FEA can’t be done due to out of memory error. But from the loss distribution analysis in Table 5-7, the magnet material loss is very small, since the magnetic field in the ferrite material is much lower than the saturation flux density 0.5 T. Therefore, the temperature increase in the ferrite due to core loss can be neglected.

The temperature increase of the winding can be calculated by

$$\Delta T = \frac{Q}{hA} \tag{5.12}$$

Where Q is the power loss (W), h is the heat transfer coefficient (W/(m^2×°C)), A is winding surface area (m^2).

In the optimized design, A can be calculated approximately as 6 × π × 9.525 mm × 2 × (1810 + 1310) mm = 1.12 m^2. Typical air heat transfer coefficient h = 10 – 100 W/(m^2×°C). If forced air-cooling technique is used, h should be selected as 100 W/(m^2×°C). If no additional cooling technique is used as in this design example, h should be picked as 10 W/(m^2×°C). Considering the copper loss in each winding is less than 60 W, the temperature increase due to copper loss is lower than 60/10/1.12 K = 5.4 °C. Therefore, following the developed power scaling law within safety standard, no additional cooling technique is required.

5.4 Summary

At the beginning, the power scaling laws are investigated based on the coil enclosed area, the operating frequency f_0, and the transfer distance for air-core winding. With the IEEE C95.1-2005 magnetic field and electric field safety limits, the maximum allowable transfer power P_m increases when the coil enclosed area increases. The ratio of P_m to the coil enclosed area is nearly the same for circular, square, and rectangular winding configurations. Under the electrostimulation safety limit for coils with low number of turns, when f_0 increases, P_m first increases limited by the magnetic field safety limit, then decreases limited by the electric field safety limit. The transition frequency reduces when the coil radius and the number of turns increase due to the increase of required terminal excitation voltage, and the transfer distance reduces due to the coil terminal electric field. P_m can be pushed to a higher power level when the coil radius increases, the transfer distance increases, and the number of turns reduces. Under the tissue heating safety limit for coils with a low number of turns, since the reduction rate of B_{agcppk} is lower than the reduction rate of the tissue heating safety limit, P_m is always limited by the magnetic field safety limit as f_0 increases. 100 kHz is a recommended operating frequency to transfer higher power due to magnetic field tissue heating safety limit.

After that, theoretical P_{agm} is derived under resonant condition. P_{agm} is proportional to the equivalent mutual inductance $M/(N_{tx}\ N_{rx})$ and f_0. In PCSW, increasing the number of turns leads to the reduction of $M/(N_{tx}\ N_{rx})$ and lower P_{agm}. While SSW can maintain the same $M/(N_{tx}\ N_{rx})$, which provides an access to improve the power transfer efficiency without degrading P_{agm}.

At the end, the power scaling law for “I” type shield is developed. Compared with air-core winding, the conventional magnetic design can reduce P_{agm} about 35%. While the “I” type magnetic design can achieve the same P_{agm} as air-core winding when r_{in} is close to winding radius r_w. Besides that, P_{agm} can be increased linearly as r_{in} increases when r_{in} is much smaller than r_{out}. The “I” type magnetic design provides an access to achieve higher P_{agm}. The “I” type magnetic design P_{agm} increases linearly as r_{in} increases based on the power capability of air-core winding. The increase rate can be obtained easily by only two FEA cases with different r_{in}. A 10 kW design example is developed and optimized based on proposed power scaling law. Additional cooling techniques are not necessary for the magnetic part developed based on proposed power scaling law. The winding temperature increase is less than 5.4 °C, and the ferrite temperature increase is negligible.

Chapter 6 Active Tuning Methods for Operation under Misalignment

6.1 Introduction

Misalignment is unavoidable in WPT systems. It will cause a change of magnetic and electric field distributions, and the reduction of coupling factor and power transfer efficiency. In this chapter, the effects of misalignment on winding parameters, power transfer efficiency, and reactive power will be first analyzed. Then the limitations of conventional active tuning method will be identified. After that, low loss active tuning methods will be developed. In the end, active compensation designs to manipulate the field distribution will be developed.

6.2 Performance analysis under misalignment operation

According to the efficiency experimental test results under lateral and angular misaligned conditions in chapter 3, the efficiency reduction due to angular misalignment is less than 0.5%, which is very small compared with 2% efficiency reduction due to lateral misalignment. Therefore, this chapter will mainly focus on the lateral misalignment.

The FEA configurations for the conventional magnetic design and "I" type magnetic design under no misaligned condition are shown in Fig. 6-1. The aluminum plate is used to emulate the effects of vehicle chassis. A 4-turn SSW is selected as the winding. The transmitter and the receiver are set as the same. During the evaluation of lateral misalignment, both the receiver and the aluminum plate are shifted laterally.

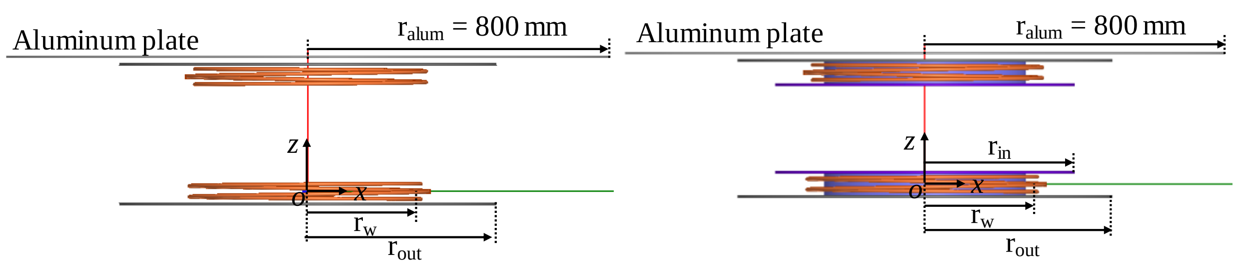

(a) Conventional magnetic design (b) "I" type magnetic design

FEA conditions: r_{out} = 600 mm, f_0 = 100 kHz, d_{ag} = 300 mm, r_{alum} = 800 mm. TX = RX, N = 4, r_w = 300 mm. Ferrite: μ_r = 1000, σ = 0.01 S/, Aluminum: σ = 3.8*1e7 S/m

Fig. 6-1. FEA configurations of conventional and "I" type magnetic designs

When the lateral misalignment is 200 mm, the change of winding parameters for both designs is compared in Fig. 6-2.

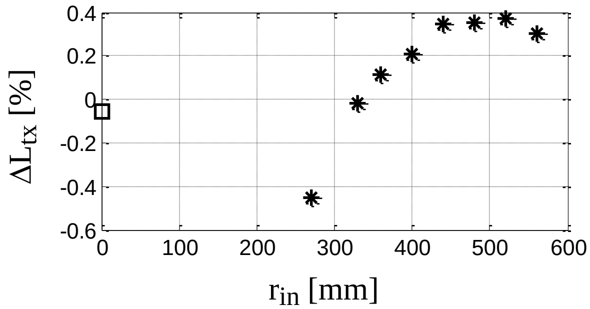

(a) ΔL_{tx} w.r.t. r_{in}

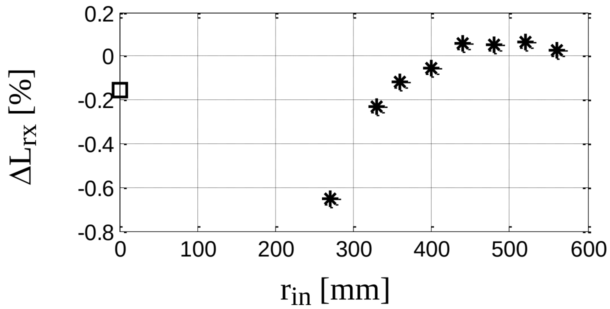

(b) ΔL_{rx} w.r.t. r_{in}

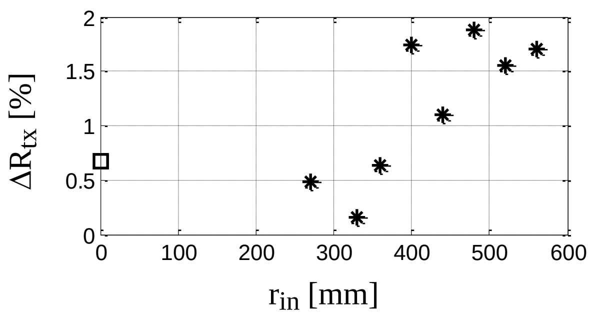

(c) ΔR_{tx} w.r.t. r_{in}

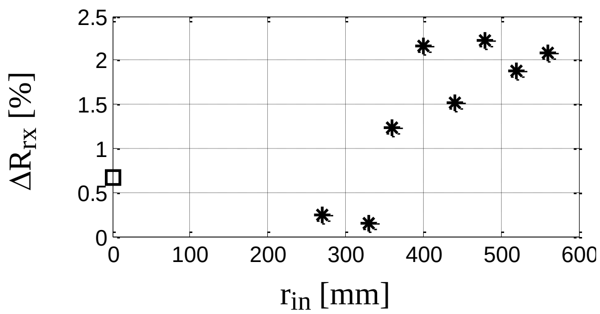

(d) ΔR_{rx} w.r.t. r_{in}

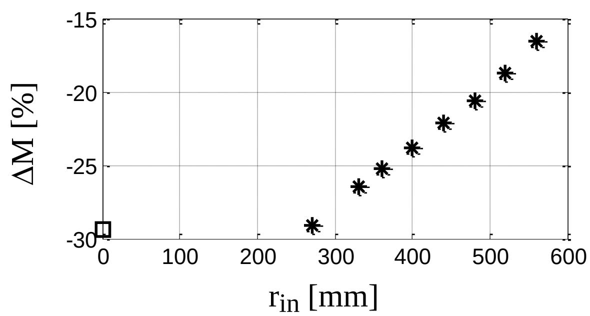

(c) ΔR_{tx} w.r.t. r_{in}

□ Conv. shielding * "I" type shielding

FEA conditions: r_{out} = 600 mm, f_0 = 100 kHz, d_{ag} = 300 mm, r_{alum} = 800 mm. TX = RX, N = 4, r_w = 300 mm. Lateral misalignment: 200 mm. Ferrite: μ_r = 1000, σ = 0.01 S/, Aluminum: σ = 3.8*1e7 S/m.

Fig. 6-2. Effects of lateral misalignment on winding parameters

As shown in Fig. 6-2, the variation of self-inductances and winding resistances for both magnetic designs are relatively small, which may affect the resonant operating frequency. But more attention should be paid to the reduction of M, which leads to the reduction of η_{coil}. Although the reduction of M can be reduced by using "I" type shielding design as r_{in} increases, it may be not true for η_{coil}, because it's the absolute value that matters. The absolute values of L_{tx}, R_{tx}, M, and η_{coil} are compared in Fig. 6-3.

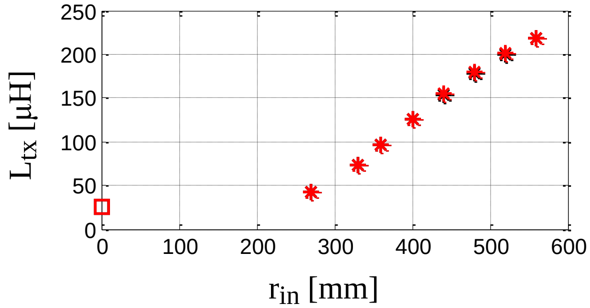

(a) ΔL_{tx} w.r.t. r_{in}

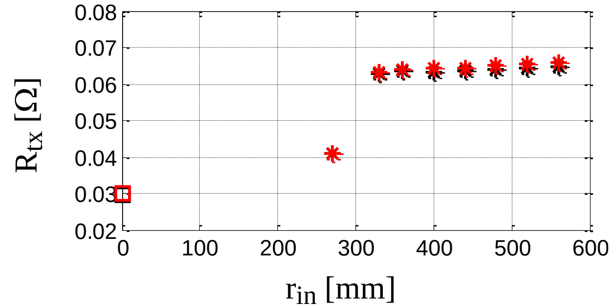

(b) ΔL_{rx} w.r.t. r_{in}

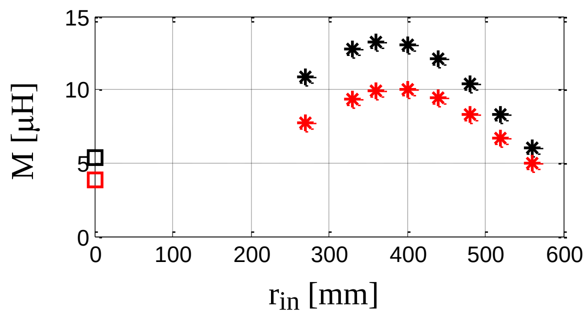

(c) ΔR_{tx} w.r.t. r_{in}

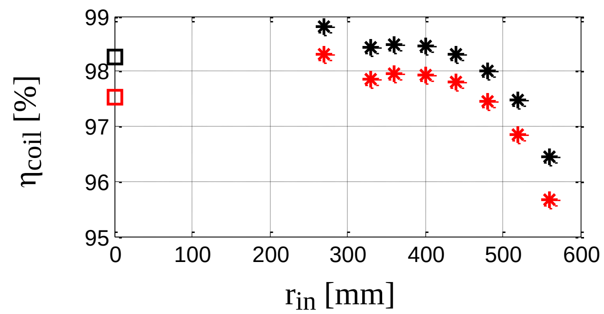

(d) ΔR_{rx} w.r.t. r_{in}

No misalignment, Lateral misalignment: 200 mm. □ Conv. Shielding, * “I” type shielding.
FEA conditions: r_{out} = 600 mm, f_0 = 100 kHz, d_{ag} = 300 mm, r_{alum} = 800 mm. TX = RX, N = 4, r_w = 300 mm. Ferrite: μ_r = 1000, σ = 0.01 S/, Aluminum: σ = 3.8*1e7 S/m.

Fig. 6-3. Effects of lateral misalignment on winding parameters and coil-to-coil efficiency

As shown in Fig. 6-3, the self-inductance, winding resistance and mutual inductance of the “I” type magnetic design are all higher than the conventional magnetic design, even under lateral misaligned condition. However, η_{coil} of the “I” type design is only higher than that of the conventional design within certain range of r_{in} (r_{in} < 480mm). Out of this range, the increase of M can’t compensate the increase of ESR, which leads to the reduction of efficiency factor $\omega^2M^2/(R_{tx}R_{rx})$ and η_{coil}. It should also be noted that the reduction of coil-to-coil power transfer efficiency due to lateral misalignment can’t be compensated by any circuit topologies or resonant compensation techniques. The efficiency reduction that can be compensated is the power conversion efficiency, such as DC-to-AC inverter efficiency, and AC-to-DC rectifier efficiency.

Compared with SS topology, the inherent smaller current phase difference of SP topology is beneficial to improve P_{agm} within the safety limits without mitigating η_{coil}. η_{coil} and P_{agm} of SS and SP topologies under no misalignment are compared in Fig. 6-4.

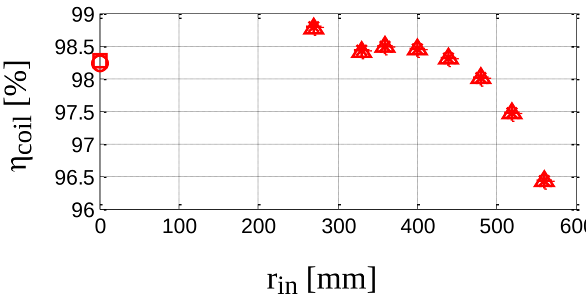

(a) η_{coil} w.r.t. r_{in}

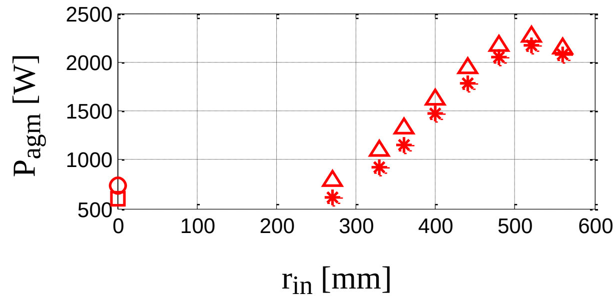

(b) P_{agm} w.r.t. r_{in}

□ Conventional design + SS, ○ Conventional design + SP, * "I" type design + SS, Δ "I" type design + SP. FEA conditions: r_{out} = 600 mm, f_0 = 100 kHz, d_{ag} = 300 mm, r_{alum} = 800 mm. TX = RX, N = 4, r_w = 300 mm. Ferrite: μ_r = 1000, σ = 0.01 S/, Aluminum: σ = 3.8*1e7 S/m.

Fig. 6-4. Comparison of η_{coil} and P_{agm} for SS and SP topologies under no misalignment

As shown in Fig. 6-4, SP topology has the same η_{coil} as SS topology. While SP topology has higher P_{agm} for both conventional design and "I" type design. In most of the magnetic designs for indutive WPT, B_{agcppk} is dominated by B_z, not the leakage field B_r, smaller current phase difference topologies, such as SP topology, is beneficial to achieve higher P_{agm}.

On the other hand, reactive power during misaligned operation is unavoidable for all compensation topologies. It can be caused by the compensation techniques or the migration of winding parameters. SP topology is taken as an example to analyze the reactive power. The circuit topology, and waveforms under aligned and misaligned conditions are shown in Fig. 6-5. In order to simplify the analysis, only M is reduced from aligned operating condition to misaligned operating condition, all other parameters are remained the same.

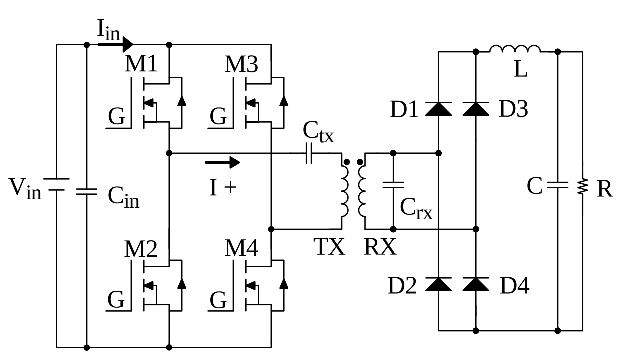

(a) SP compensated circuit topology

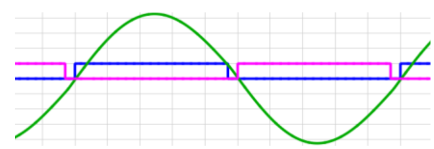

(b) Waveforms under aligned condition

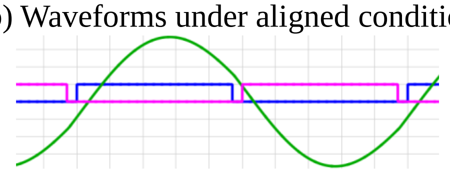

(c) Waveforms under misaligned condition

M1&M4 G, M2&M3 G, Current I

Fig. 6-5. SP circuit topology and waveforms under aligned and misaligned conditions

As shown in Fig. 6-5, under no misalignment operation, zero-voltage soft switching is achieved, and the turn-on current is very close to zero; MOSFET turn-on loss can be neglected, its conduction loss and turn-off loss will contribute the inverter total loss. However, current phase lag is introduced during misaligned condition. After M2 and M3 are turned off, and before current I reaches zero (or after M1 and M4 are turned off, and before I reaches zero), I will go back to the power supply or the DC link capacitor, which will also lead to the increase of MOSFET turn-off loss. This part of reactive power will not be transferred to the receiver side, the power transfer capability under the same input voltage will be reduced. In addition, the reactive power will reduce the capacitor life and affect the performance of the power supply.

The power module switching loss events corresponding to current polarity and gate signals are summarized in Table 6-1.

Table 6-1. Summary of switching loss events corresponding to current polarity and gate signals

Circuit configuration	Current Polarity	G +			G –			D +	D –
		Initial State	Final State	Loss Mode	Initial State	Final State	Loss Mode	Loss Mode	Loss Mode
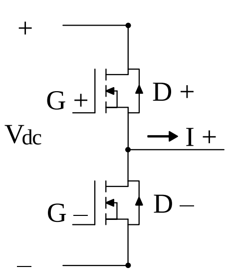	+	0	1	Eon	0	0	0	0	Err
	+	1	0	Eoff	0	0	0	0	0
	+	0	0	0	0	1	0	0	0
	+	0	0	0	1	0	0	0	0
	–	0	1	0	0	0	0	0	0
	–	1	0	0	0	0	0	0	0
	–	0	0	0	0	1	Eon	Err	0
	–	0	0	0	1	0	Eoff	0	0

As shown in Table 6-1, when zero-voltage switching is achieved, only Eoff needs to be considered for power inverter switching loss.

In the PLECS simulation, SiC MOSFET C2M0025120D is used for the high frequency inverter. Only winding loss and inverter loss are evaluated during the simulation. Resonant capacitor and rectifier losses are not included, since they can always be optimized, and it’s not easy to give a good baseline. C2M0025120D model was created by Cree with switching loss and conduction loss under different operating temperature and current [258]. Its turn-on loss, turn-off loss, and conduction loss are shown in Fig. 6-6. The initial ambient temperature was set at 25 °C.

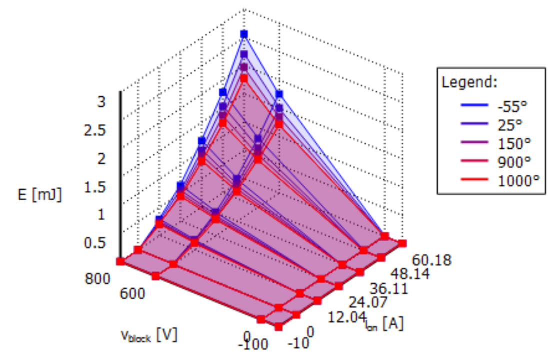

(a) C2M0025120D turn-on loss

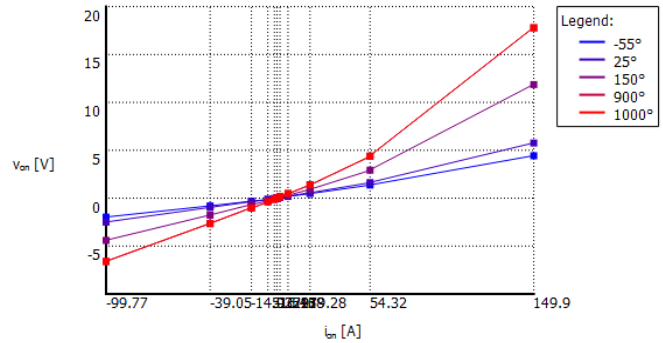

(b) C2M0025120D conduction loss

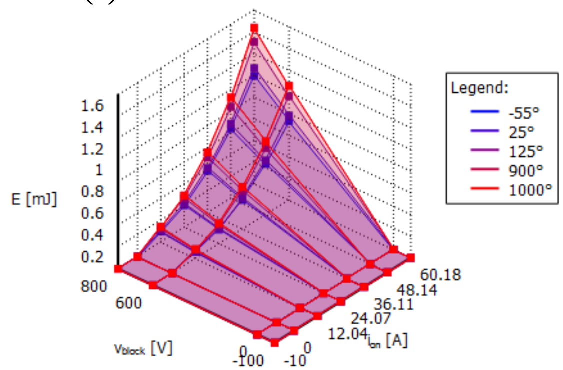

(c) C2M0025120D turn-off loss

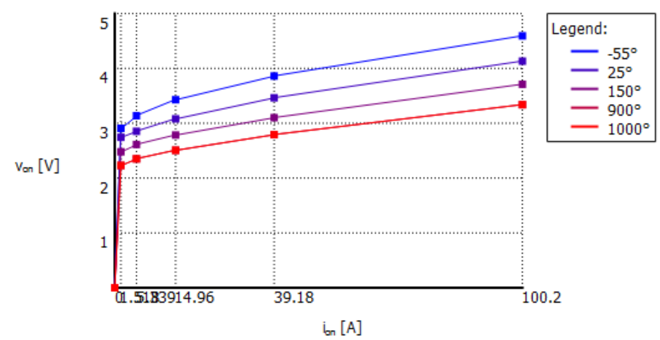

(d) C2M0025120D body diode conduction loss

Fig. 6-6. C2M0025120D switching loss and conduction loss, and its body diode conduction loss

The winding parameters and compensation capacitors are summarized in Table 6-2.

Table 6-2. Summary of winding parameters and compensation capacitors

L_{tx} [μH]	R_{tx} [mΩ]	L_{rx} [μH]	R_{rx} [mΩ]	M [μH]	C_{tx} [nF]	C_{rx} [nF]	R_{load} [Ω]
26.09	29.7	25.91	29.9	5.39	104.44	97.75	63.25

The input voltage V_{in} is set as 116.57 V to ensure that the power delivered to the load P_{out} is 3 kW. For SP topology, under misaligned condition, M will reduce, which leads the reduction of input impedance. Then P_{out} will be higher than 3 kW. The loss distribution will also change. In order to do a fair comparison, the switching loss energy is calculated in Watts using moving average. The averaging time is 1 ms, and the buffer size is 1024. Under no misalignment condition, the waveforms and loss distribution are presented in Fig. 6-7. The coil-to-coil efficiency η_{coil} is calculated by P_{out} divided by P_{out} plus winding losses. The DC-to-DC efficiency η_{dc} is simplified as P_{out} divided by P_{out} plus winding losses and inverter losses.

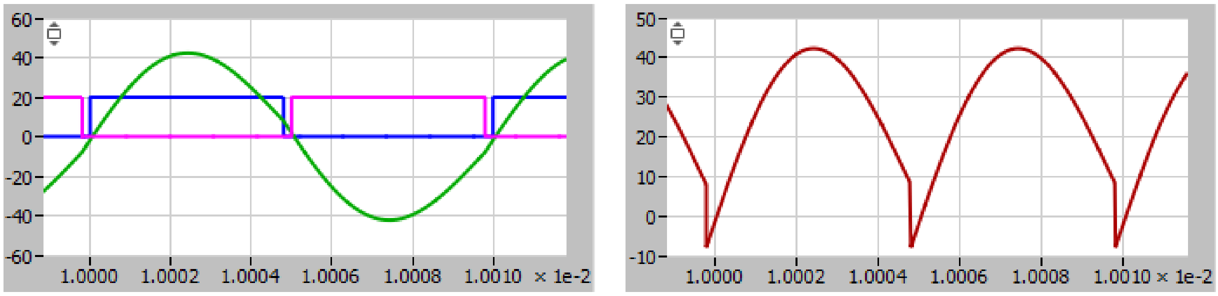

M1&M4 G, M2&M3 G, Current I [A] Input current I_{in} [A]

M = 5.39µH, V_{in} = 116.57V, P_{out} = 3000W, η_{coil} = 98.20%, η_{dc} = 96.40%

Winding loss: P_{tx} = 26.80W, P_{rx} = 28.07W.

Inverter loss (each module): $P_{condution\_M}$ = 13.80W, P_{switch_M} = 0.19W, $P_{condution\_D}$ = 0.28W.

Fig. 6-7. Waveforms and loss distributions under aligned condition

As shown in Fig. 6-7, conduction loss is the dominant term of MOSFET losses, switching loss is very low compared with the conduction loss due to soft switching. The negative input current I_{in} is the reactive current charging back to the capacitor. It is caused by the PWM dead time, which is acceptable and can be further reduced by reducing the PWM dead time.

Assuming M is reduced by 30% to 3.78 µH under misaligned condition, the waveforms and loss distribution are shown in Fig. 6-8.

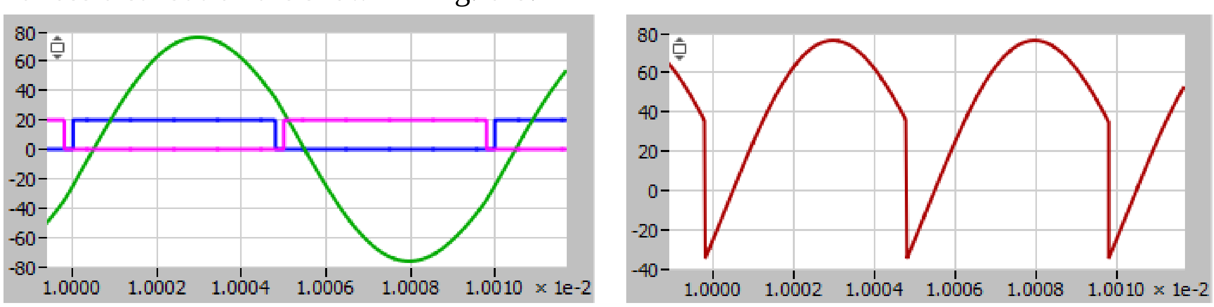

M1&M4 G, M2&M3 G, Current I [A] Input current I_{in} [A]

M = 3.78µH, V_{in} = 116.57V, P_{out} = 4878.8W (↑ 62.6%), η_{coil} = 97.33%, η_{dc} = 93.25%

Winding loss: P_{tx} = 88.50W (↑ 230.2%), P_{rx} = 45.46W (↑ 62.0%).

Inverter loss (each module): $P_{condution\_M}$ = 51.07W (↑ 270.1%), P_{switch_M} = 1.28W (↑ 573.7%), $P_{condution\_D}$ = 2.01W (↑ 617.9%).

Fig. 6-8. Waveforms and loss distributions under misaligned condition

As shown in Fig. 6-8, under the misaligned condition, P_{out} is increased due to the reduction of input impedance. η_{coil} is reduced by 0.87%. η_{dc} is reduced by 3.15%, one part is caused by the reduction of η_{coil}, another part is caused by the increase of transmitter winding loss and MOSFET losses, especially the conduction loss. From the loss distribution analysis, the increase percentage of P_{rx} is almost the same as the increase percentage of P_{out}. Therefore, P_{rx} won't bring the reduction of η_{coil} or η_{dc}. However, the increase percentages of P_{tx} and inverter loss components are much higher due to the reactive power. Compared with aligned condition, the negative I_{in} charging back to the capacitor is increased significantly under misalignment.

Through simulation, it's identified that the current phase lag under misaligned condition can be pulled back by reducing the transmitter side resonant compensation capacitor C_{tx}. Active tuning methods have been developed to tune C_{tx}. The limitations of conventional active tuning methods will be investigated in next section.

6.3 Limitations of conventional active tuning methods

Additional tunable capacitor can be added in series with C_{tx} to reduce the total equivalent transmitter side compensation capacitance. There are mainly two ways to tune the capacitance as shown in Fig. 6-9. Adding multiple discrete bulky capacitors in parallel can't tune the effective capacitance C_{eff} continuously. In addition, the conduction loss in the switching devices will reduce the power transfer efficiency. While using the switch-controlled capacitor (SCC) can tune C_{eff} continuously. The circuit is much simpler. The only concern is the additional loss.

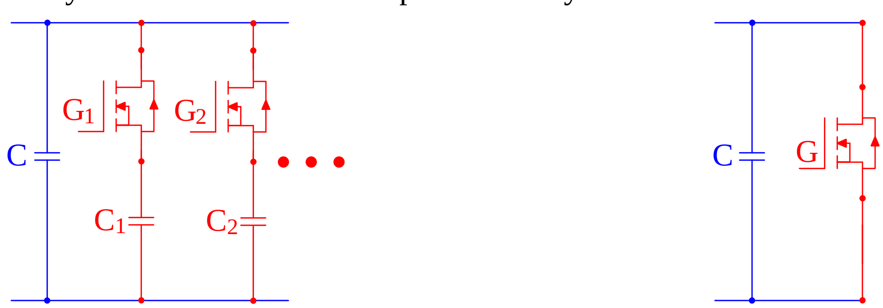

(a) Adding discrete capacitors in parallel (b) Switch-controlled capacitor

Fig. 6-9. Circuit topologies to tune capacitance

Assuming the input current I_{eff} is a sinusoidal wave $I_0 \sin(\omega_0 t)$. The effective capacitance C_{eff} can be manipulated by tuning α. The SCC circuit topology and operation waveforms are presented in Fig. 6-10.

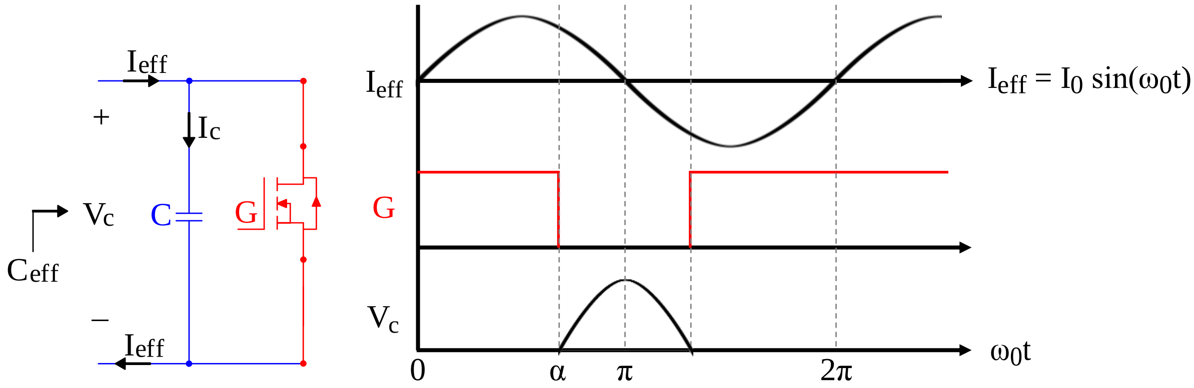

(a) SCC topology (b) Waveforms

Fig. 6-10. SCC circuit topology and operation waveforms

When G is on, C will be shorted, $V_c = 0$, $I_c = 0$. When G is off, $I_c = I_{eff}$. When G is off and I_{eff} is positive, C will be charged. When G is off and I_{eff} is negative, C will be discharged. The effective capacitance C_{eff} can be calculated as [194]

$$C_{eff} = \frac{\pi C}{\pi - \alpha + \sin(\alpha)\cos(\alpha)} \tag{6.1}$$

In order to achieve low switching loss, G should always be turned on when I_{eff} is negative to avoid turn-on loss. In addition, α should be close to π to achieve low turn-off loss. This conventional capacitor tuning method can be concluded as $\alpha \rightarrow \pi$ method.

The system circuit topology with capacitor active tuning part is shown in Fig. 6-11. When M0 duty cycle is 100%, C_0 is shorted, $C_{eq} = C_{tx}$. When M0 duty cycle is α/π, the transmitter side equivalent compensation capacitance $C_{eq} = C_{eff} C_{tx} / (C_{eff} + C_{tx})$. It should be noted that C_{eq} should be smaller than C_{tx} in order to correct the current phase lag during misaligned condition.

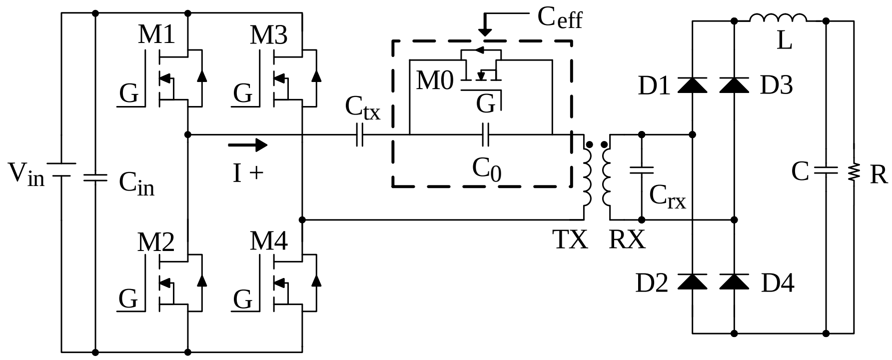

Fig. 6-11. System circuit topology with active tuning capacitor

Reducing α in feasible steps can limit M1 turn-on current I within a given range (e.g. [– 4A, – 1A]). If I ∈ [– 4A, – 1A], then α = π, M0 duty cycle = 100%. If I < – 4A, then α = π – π/1000, M0 duty cycle = α / π (Step π/1000 is a configurable parameter based on requirement). It should also be noted that the control angle α is aligned with current I_{eff}, which is the transmitter excitation current I in the system. Although I is very close to a sinusoidal wave, it's not practical to lock M0 gate signal G with current I, especially when there is current phase delay during misaligned operating condition.

The last thing is selecting the initial value of C_0 to achieve low Eoff of M0 and low voltage stress across C_0 simultaneously. Assume that $C_{eq} = 0.9\ C_{tx}$ under misaligned condition, it's easy to get $C_{eff} = 9\ C_{tx}$ based on $C_{eq} = C_{eff} C_{tx} / (C_{eff} + C_{tx})$. Following the conventional α → π capacitor active tuning method, α is selected as higher than $\frac{8\pi}{9}$. According to (6.1), $C_{eff} = \frac{C_0 * \pi}{\pi - \alpha + \sin(\alpha)\cos(\alpha)} = 9\ C_{tx} > \frac{C_0 * \pi}{0.0277}$, therefore $C_0 < 0.08\ C_{tx}$. In addition, C_0 can't be too small to avoid very high voltage V_{c_amp} across M0 and C_0. V_{c_amp} can be calculated by

$$V_{c\_amp} = \frac{1}{C_0} \int_{t=t_\alpha}^{t_\pi} I_0 \sin(\omega_0 t)\, dt = \frac{I_0}{C_0}\left(\frac{-\cos(\pi)}{\omega_0} - \frac{-\cos(\alpha)}{\omega_0}\right) = \frac{I_0}{C_0}\,\frac{1+\cos(\alpha)}{\omega_0} \tag{6.2}$$

In the end, C_0 is selected as $0.06\ C_{tx}$ in the PLECS simulation. The MOSFET for C_0 active tuning circuit is the same as the inverter SiC MOSFET. During the simulation, before 0.01 s, M0 duty cycle is set as 100%, C_0 is shorted by M0. After 0.01 s, the active tuning circuit begins to work, M0 duty cycle is adjusted to tune C_{eq} online to reduce the current phase lag. The waveforms and loss distribution are shown in Fig. 6-12.

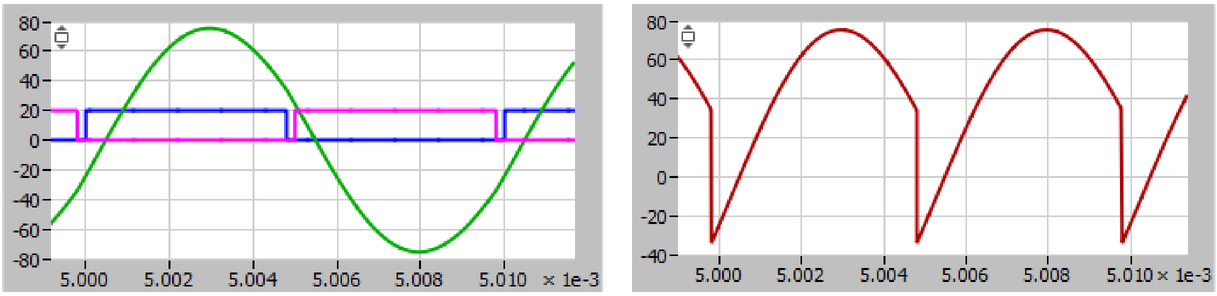

M1&M4 G, M2&M3 G, Current I [A] Input current I_{in} [A]

(a) Waveforms before capacitor active tuning

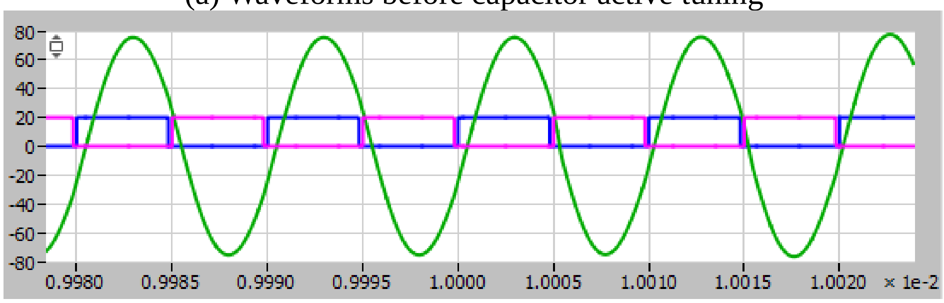

(b) Waveforms during capacitor active tuning (M1&M4 G, M2&M3 G, Current I [A])

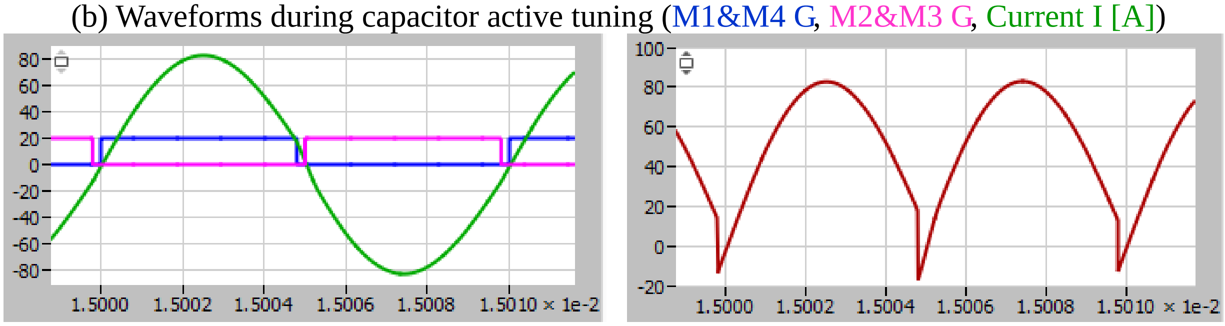

M1&M4 G, M2&M3 G, Current I [A] Input current I_{in} [A]

(c) Waveforms after capacitor active tuning

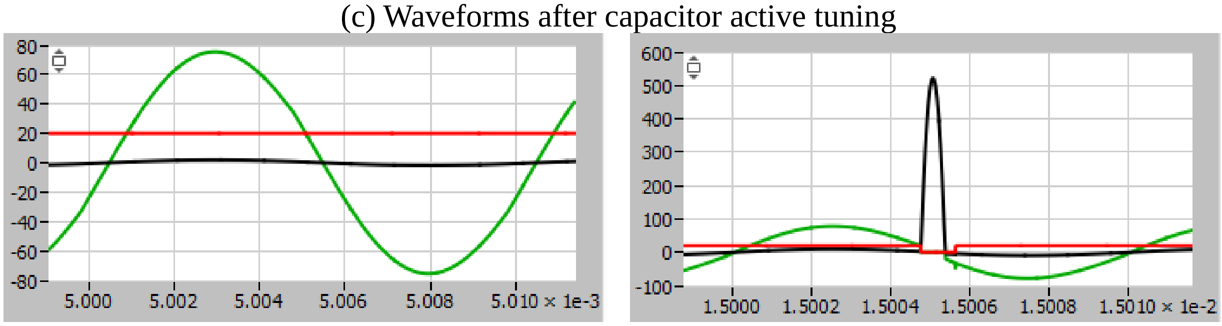

V_{C0}, M0 G, Current I through G [A] V_{C0}, M0 G, Current I through G [A]

(d) SCC circuit waveforms before and after capacitor active tuning

Before C_0 active tuning (baseline):
M = 3.78μH, V_{in} = 116.57V, P_{out} = 4768.2W, η_{coil} = 97.33%, η_{dc} = 91.77%
Winding loss: P_{tx} = 86.47W, P_{rx} = 44.42W.
Inverter loss (each module): $P_{condution\_M}$ = 48.5W, P_{switch_M} = 1.23W, $P_{condution\_D}$ = 1.96W.
M0 loss: $P_{condution\_M}$ = 87.0W, P_{switch} = 0W, $P_{condution\_D}$ = 2.15W.
After C_0 active tuning:
M = 3.78μH, V_{in} = 116.57V, P_{out} = 5740.5W (↑ 20.4%), η_{coil} = 97.33%, η_{dc} = 91.70% (↓ 0.07 %)
Winding loss: P_{tx} = 104.23W (↑ 20.5%), P_{rx} = 53.45W (↑ 20.3%).
Inverter loss (each module): $P_{condution\_M}$ = 64.0W (↑ 32.0%), P_{switch_M} = 0.46W (↓ 62.6%), $P_{condution\_D}$ = 0.43W (↓ 78.1%).
M0 loss: $P_{condution\_M}$ = 117.2W (↑ 34.7%), P_{switch} = 0W, $P_{condution\_D}$ = 6.78W (↑ 215.3%).

Fig. 6-12. Waveforms and loss distributions with conventional α → π capacitor active tuning technique under misaligned condition

As shown in Fig. 6-12 (b), the conventional α → π capacitor active tuning method can pull the current phase delay back to reduce the reactive power and improve P_{out} by 20.4%. The negative current I charging back to the DC link capacitor is highly reduced. The conduction loss in all power modules is the dominant term. The conduction loss of M0 is nearly 2 times the conduction loss of each module in the inverter, which leads to the reduction of η_{dc}, even before the active tuning of C_0. The voltage stress across C_0 and the required current rating, shown in Fig. 6-12(d), demonstrates that conventional capacitor active tuning method is practical for high power operation. After C_0 active tuning, the increase of winding losses is close to the increase of P_{out}. Inverter switching loss and body diode conduction loss can be reduced by more than 60% even with higher P_{out}. However, η_{dc} is further reduced due to the increase of power module conduction loss. Therefore, low conduction loss active tuning method must be developed to ensure η_{dc}. Besides that, new gate signal generation method for active tuning technique is necessary to implement this technique easily without degrading the performance.

6.4 Low loss active tuning method

6.4.1 Low loss capacitor active tuning method

In order to maintain low conduction loss for M0, the conduction period of M0 should be very small. In addition, the current goes through the device should be close to zero during the switching event to maintain low switching loss. The device should be turned on when the current is negative to achieve zero-voltage soft switching. $\alpha \rightarrow 0$ capacitor active tuning method can be used to achieve above goals simultaneously. The waveforms are shown in Fig. 6-13.

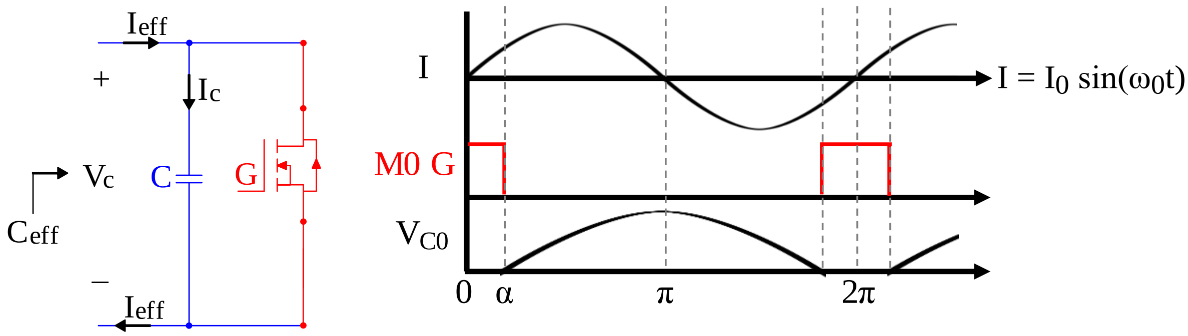

(a) SCC topology (b) Waveforms

Fig. 6-13. SCC circuit topology and $\alpha \rightarrow 0$ tuning method operation waveforms

In conventional $\alpha \rightarrow \pi$ tuning method, when α increases, the conduction loss will increase due to the increase of conduction time, and the switching loss will reduce due to the reduction of switching current. However, in $\alpha \rightarrow 0$ tuning method, when α increases, both conduction and switching losses will increase. Therefore, the initial tunable capacitor value should be selected very carefully to achieve low conduction loss and low switching loss simultaneously.

If the SCC gate signal M0 G generation method is locked with the current phase, it's relatively easy to implement when there is no misalignment, since current zero-crossing events are almost the same as the inverter gate signal switching events, as shown in Fig. 6-14 (b). However, during misaligned condition, M0 G must be phase shifted due to current phase delay, as shown in Fig. 6-14 (c), which increases the implementation difficulty. In order to make it easy for implementation, M0 G is proposed to be aligned with the inverter gate signal M1&M4 G, instead of the current zero-crossing event, as shown in Fig. 6-14 (d).

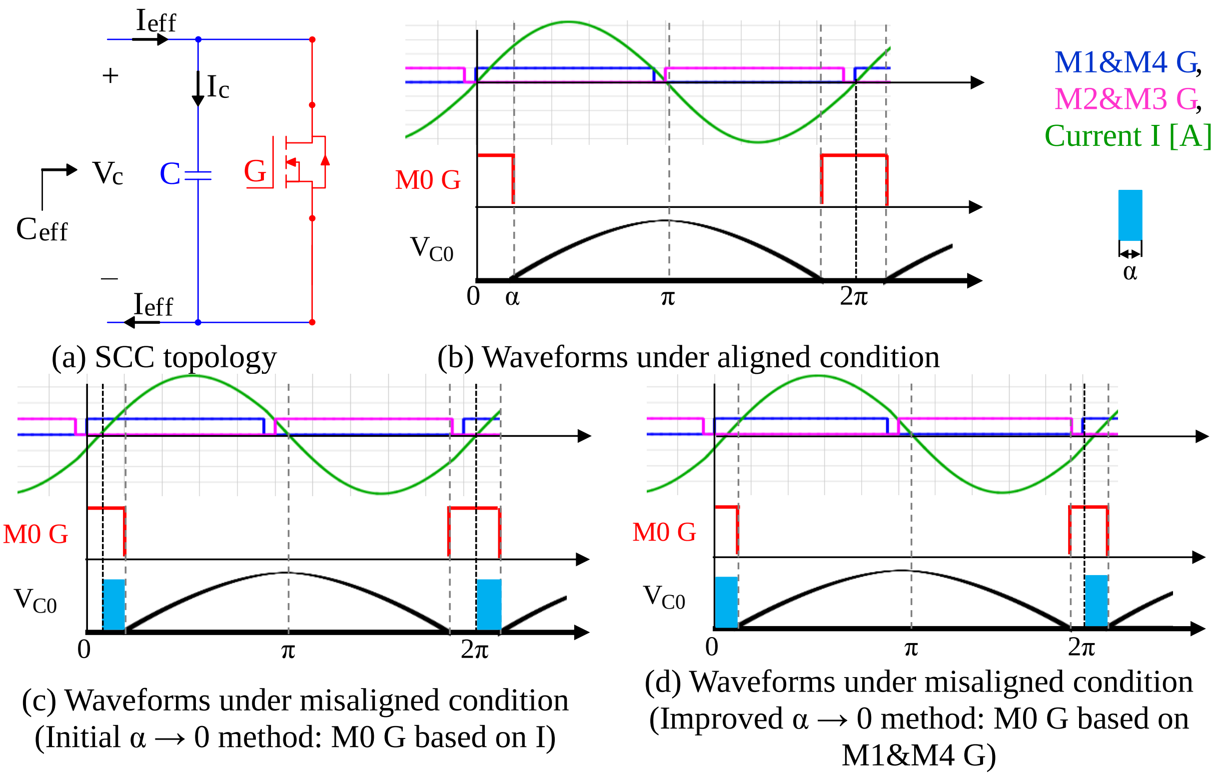

(a) SCC topology

(b) Waveforms under aligned condition

(c) Waveforms under misaligned condition (Initial α → 0 method: M0 G based on I)

(d) Waveforms under misaligned condition (Improved α → 0 method: M0 G based on M1&M4 G)

Fig. 6-14. SCC topology and operation waveforms under aligned and misaligned conditions

Compared with the initial $\alpha \rightarrow 0$ tuning method, the improved $\alpha \rightarrow 0$ tuning method has slightly longer charging time for the switch-controlled capacitor C, which is equivalent to reduce the effective capacitance C_{eff}. This property can bring automatic impedance correction for transmitter side compensation network during misaligned operation condition.

The next thing is determining C_0 initial value. In order to achieve low conduction of M0 over the whole operating range, C_0 can't be shorted by M0 anytime. Therefore, the original C_{tx} must be adjusted to provide the required compensation during aligned condition. C_{tx} is increased to $2C_{tx} = \dfrac{2}{(1-k^2)\, L_{tx}\, \omega_0^2}$. If M0 duty cycle is 0, then the minimum transmitter side resonant compensation capacitance $C_{eq,\,min}$ can be calculated as $C_{eq,\,min} = \dfrac{C_0 * 2C_{tx}}{C_0 + 2C_{tx}}$. Assume $C_{eq,\,min} = 0.95\ C_{tx}$ is enough to compensate operation under misaligned condition, C_0 is chosen as $1.8\ C_{tx}$. The system circuit topology, related waveforms and loss distribution are shown in Fig. 6-15.

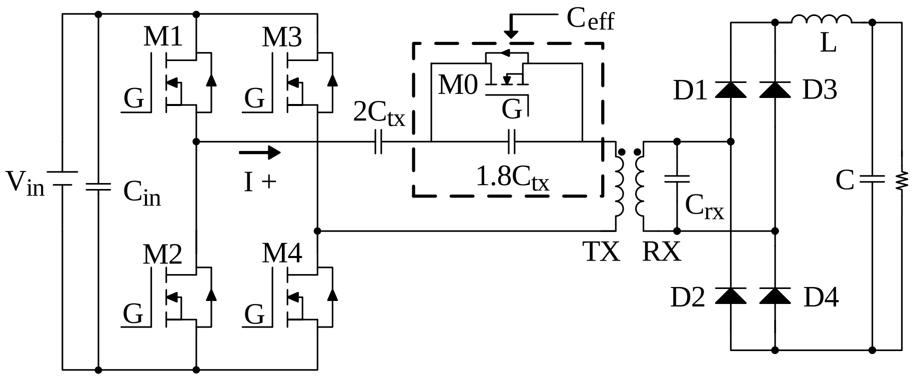

(a) System circuit topology

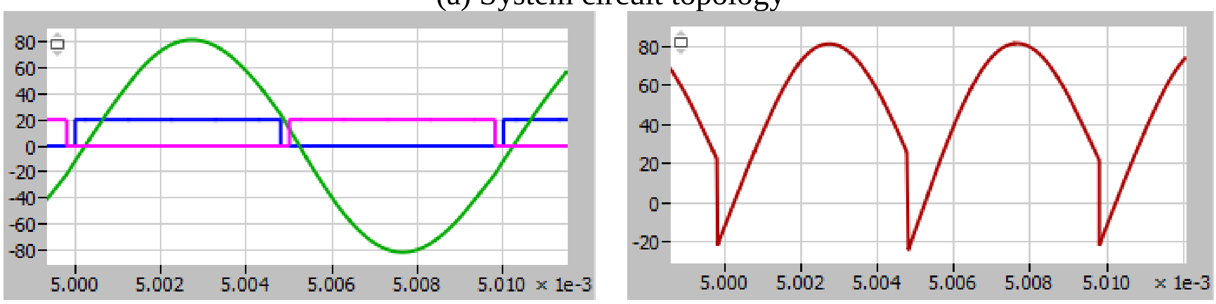

M1&M4 G, M2&M3 G, Current I [A]   Input current I_{in} [A]

(b) Waveforms before capacitor active tuning

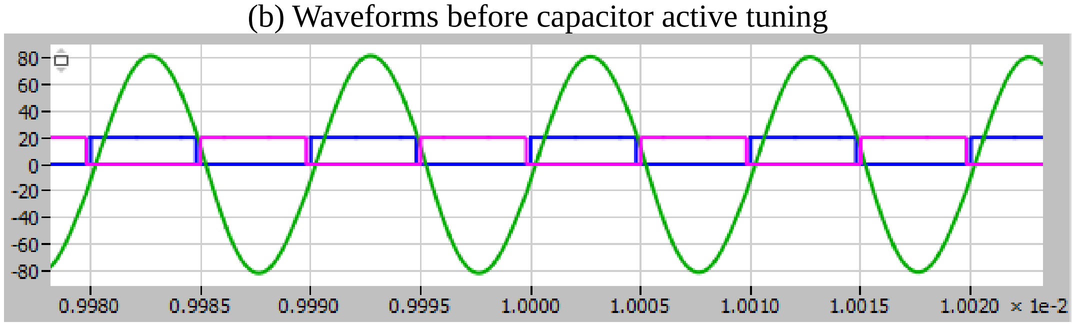

(c) Waveforms during capacitor active tuning (M1&M4 G, M2&M3 G, Current I [A])

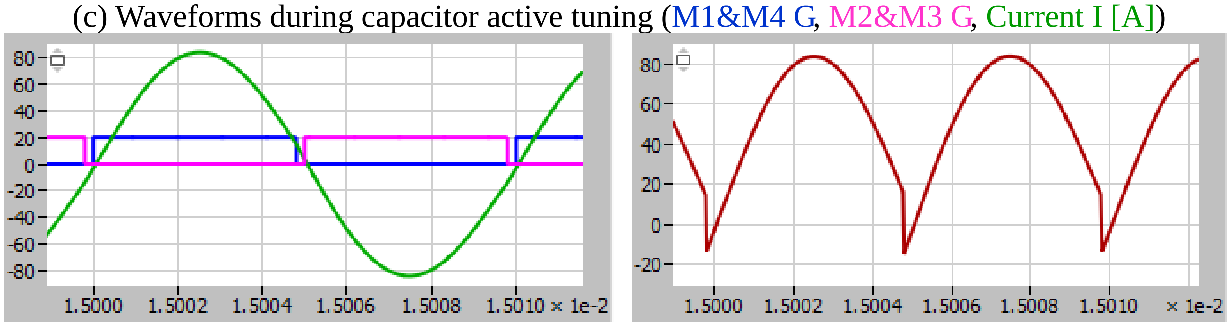

M1&M4 G, M2&M3 G, Current I [A]   Input current I_{in} [A]

(d) Waveforms after capacitor active tuning

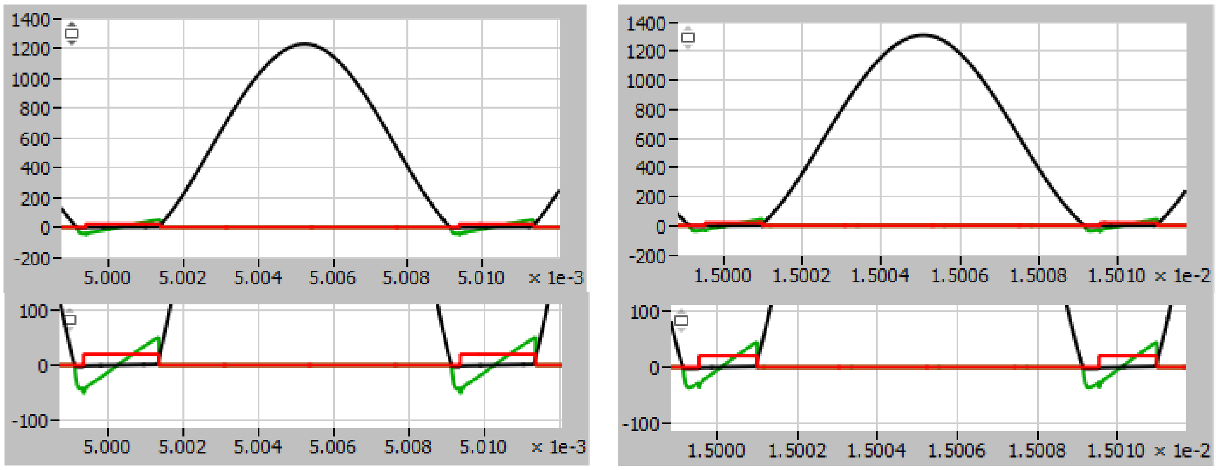

V_{C0}, M0 G, Current I through G [A] V_{C0}, M0 G, Current I through G [A]

(e) SCC circuit waveforms before and after capacitor active tuning

Before C_0 active tuning (Improved $\alpha \rightarrow 0$ method) (baseline):

M = 3.78μH, V_{in} = 116.57V, P_{out} = 5428.9W, η_{coil} = 97.33%, η_{dc} = 93.20%

Winding loss: P_{tx} = 98.45W, P_{rx} = 50.58W.

Inverter loss (each module): $P_{condution\_M}$ = 57.8W, P_{switch_M} = 0.66W, $P_{condution\_D}$ = 1.06W.

M0 loss: $P_{condution\_M}$ = 4.46W, P_{switch} = 0.25W, $P_{condution\_D}$ = 2.99W.

After C_0 active tuning (Improved $\alpha \rightarrow 0$ method):

M = 3.78μH, V_{in} = 116.57V, P_{out} = 5738.4W (↑ 5.7%), η_{coil} = 97.33%, η_{dc} = 93.07% (↓ 0.03%)

Winding loss: P_{tx} = 104.06W (↑ 5.7%), P_{rx} = 53.47W (↑ 5.7%).

Inverter loss (each module): $P_{condution\_M}$ = 65.5W (↑ 13.3%), P_{switch_M} = 0.39W (↓ 40.9%), $P_{condution\_D}$ = 0.49W (↓ 53.8%).

M0 loss: $P_{condution\_M}$ = 2.36W (↓ 47.1%), P_{switch} = 0.17W (↓ 32.0%), $P_{condution\_D}$ = 4.09W (↑ 36.8%).

Fig. 6-15. Waveforms and loss distributions with improved $\alpha \rightarrow 0$ capacitor active tuning technique under misaligned condition

Compared with conventional $\alpha \rightarrow \pi$ method, the improved $\alpha \rightarrow 0$ method can inherently correct the current phase delay and reduce the reactive power, as shown in Fig. 6-15 (b). Before C_0 active tuning, P_{out} is increased from 4768.2 W of the conventional $\alpha \rightarrow \pi$ method to 5428.9 W of the improved $\alpha \rightarrow 0$ method. After C_0 active tuning, P_{out} is further improved. Besides that, M0 conduction loss is reduced significantly in the whole operating range compared with the conventional $\alpha \rightarrow \pi$ method. That leads to an increase of η_{dc}.

The loss distribution and efficiency under aligned and misaligned conditions for capacitor active tuning method are summarized in Table 6-3.

Table 6-3. Summary of loss distribution and efficiency for capacitor active tuning techniques

Inverter loss (each module)			Winding loss		Output power & efficiency		
Under aligned condition							
$P_{condution\_M}$ [W]	P_{switch_M} [W]	$P_{condution\_D}$ [W]	P_{tx} [W]	P_{rx} [W]	P_{out} [W]	η_{coil} [%]	η_{dc} [%]
13.80	0.19	0.28	26.80	28.07	3000	98.20	96.40
Under misaligned condition (No regulation)							
$P_{condution\_M}$ [W]	P_{switch_M} [W]	$P_{condution\_D}$ [W]	P_{tx} [W]	P_{rx} [W]	P_{out} [W]	η_{coil} [%]	η_{dc} [%]
51.07	1.28	2.01	88.50	45.46	4878.8	97.33	93.25
Under misaligned condition (Before C_0 active tuning: conventional $\alpha \to \pi$ method)							
$P_{condution\_M}$ [W]	P_{switch_M} [W]	$P_{condution\_D}$ [W]	P_{tx} [W]	P_{rx} [W]	P_{out} [W]	η_{coil} [%]	η_{dc} [%]
48.5	1.23	1.96	86.47	44.42	4768.2	97.33	91.77
M0	$P_{condution\_M}$ = 87.0W	P_{switch} = 0W		$P_{condution\_D}$ = 2.15W			
Under misaligned condition (After C_0 active tuning: conventional $\alpha \to \pi$ method)							
$P_{condution\_M}$ [W]	P_{switch_M} [W]	$P_{condution\_D}$ [W]	P_{tx} [W]	P_{rx} [W]	P_{out} [W]	η_{coil} [%]	η_{dc} [%]
64.0	0.46	0.43	104.23	53.45	5740.5	97.33	91.70
M0	$P_{condution\_M}$ = 117.2W	P_{switch} = 0W		$P_{condution\_D}$ = 6.78W			
Under misaligned condition (Before C_0 active tuning: improved $\alpha \to 0$ method)							
$P_{condution\_M}$ [W]	P_{switch_M} [W]	$P_{condution\_D}$ [W]	P_{tx} [W]	P_{rx} [W]	P_{out} [W]	η_{coil} [%]	η_{dc} [%]
57.8	0.66	1.06	98.45	50.58	5428.9	97.33	93.20
M0	$P_{condution\_M}$ = 4.46W	P_{switch} = 0.25W		$P_{condution\_D}$ = 2.99W			
Under misaligned condition (After C_0 active tuning: improved $\alpha \to 0$ method)							
$P_{condution\_M}$ [W]	P_{switch_M} [W]	$P_{condution\_D}$ [W]	P_{tx} [W]	P_{rx} [W]	P_{out} [W]	η_{coil} [%]	η_{dc} [%]
65.5	0.39	0.49	104.06	53.47	5738.4	97.33	93.07
M0	$P_{condution\_M}$ = 2.36W	P_{switch} = 0.17W		$P_{condution\_D}$ = 4.09W			

From Table 6-3, it's easy to find that the improved $\alpha \to 0$ capacitor tuning method can maintain high output power and reduce the reactive power during misaligned condition with a very small sacrifice of the power transfer efficiency. Its automatic tuning property due to special designed gate signal generation technique can inherently maintain low reactive power even before the active tuning of the switched capacitor.

6.4.2 Low loss inductor active tuning method

The reliability of the capacitor active tuning method is affected by the switched capacitor voltage and current ratings under high operating frequency. If the inductor can be used in the active tuning circuit, there is no need to worry about the device reliability. The switch-controlled inductor (SCI) circuit topology and operation waveforms are shown in Fig. 6-16.

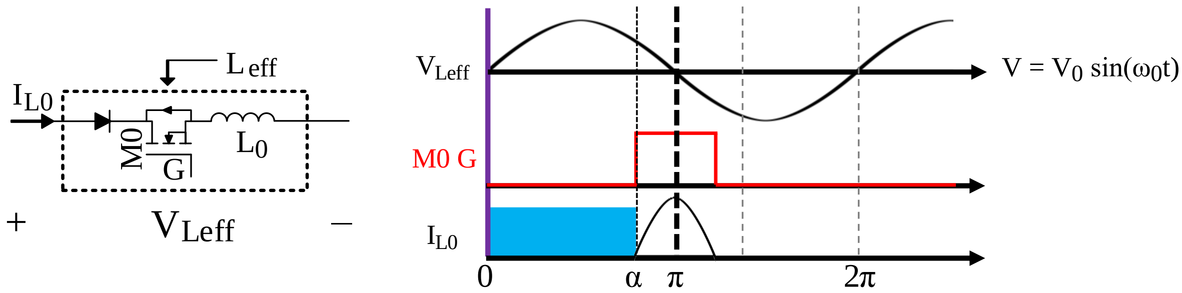

(a) SCI topology (b) Waveforms

Fig. 6-16. SCI circuit topology and operation waveforms

Different from SCC, SCI is driven by a voltage source instead of a current source. In addition, an additional diode is necessary to avoid the inductor current I_{L0} going negative. Otherwise, the effective inductance L_{eff} can't be manipulated. Conventional SCI switch gate signal M0 G is aligned with the applied voltage V_{Leff}. When M0 is turned on with positive V_{Leff}, the inductor L_0 will be charged, and it will be discharged when V_{Leff} goes negative. When M0 is turned off, there is no current going through L_0. The control angle α should be close to π to ensure low switching loss, low conduction loss can also be achieved at the same time. L_{eff} can be calculated as [194]

$$L_{eff} = \frac{\pi\, L_0}{\pi - \alpha + \sin(\alpha)\cos(\alpha)} \tag{6.3}$$

Double checking the SP compensated system topology, the voltage of C_{tx} can be treated as a sinusoidal voltage source. Therefore, the SCI circuit can be added in parallel with C_{tx}, as shown in Fig. 6-17 (a). It should be noted that the voltage V_{Leff} across C_{tx} is lagging the current I 90-degree. Under aligned condition, M0 can be turned off, as shown in Fig. 6-17 (b). However, there will be current phase delay when operating under misaligned condition, that will also lead to V_{Leff} phase delay. Using conventional M0 gate signal generation method is not practical.

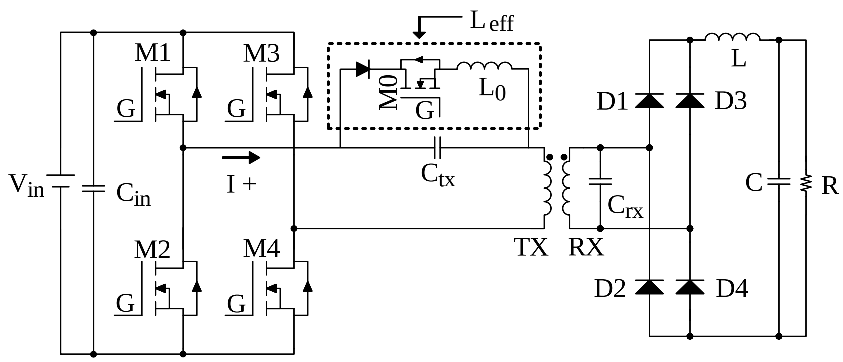

(a) SP compensated system topology with SCI circuit

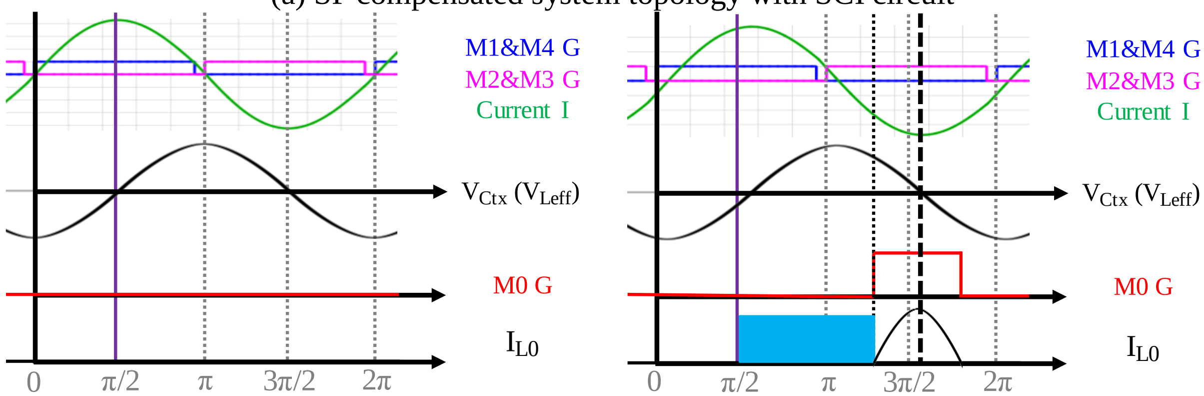

(b) Waveforms under aligned condition (b) Waveforms under misaligned condition

Fig. 6-17. SP compensated system topology with SCI circuit and its operation waveforms

Instead of locking M0 G signal with V_{Leff}, M0 G can be aligned with M1&M4 G with 90-degree phase shift, as shown in Fig. 6-17 (c). This M0 G generation method also has the automatic phase correction property as the improved $\alpha \rightarrow 0$ capacitor tuning method. α tuning method for SCI circuit can still be based on M1 turn-on current as the method used for capacitor active tuning control.

Another thing left is the selection of L_0 initial value. The transmitter side compensation capacitance C_{tx} can be calculated as

$$j\omega_0 C_{eq} = j\omega_0 C_{tx} + \frac{1}{j\omega_0 L_{eff}} \tag{6.4}$$

$$C_{eq} = C_{tx} - \frac{1}{\omega_0^2 L_{eff}} = C_{tx} - \frac{\pi - \alpha + \sin(\alpha)\cos(\alpha)}{\omega_0^2 \, \pi \, L_0} \tag{6.5}$$

Assume $C_{eq} = 0.95C_{tx}$ and $\alpha = \frac{8\pi}{9}$ is enough for active tuning during misalignment, C_{tx} = 104.44 nF, then L_0 = 4.27 μH.

Waveforms and loss distribution under misaligned condition are shown in Fig. 6-18.

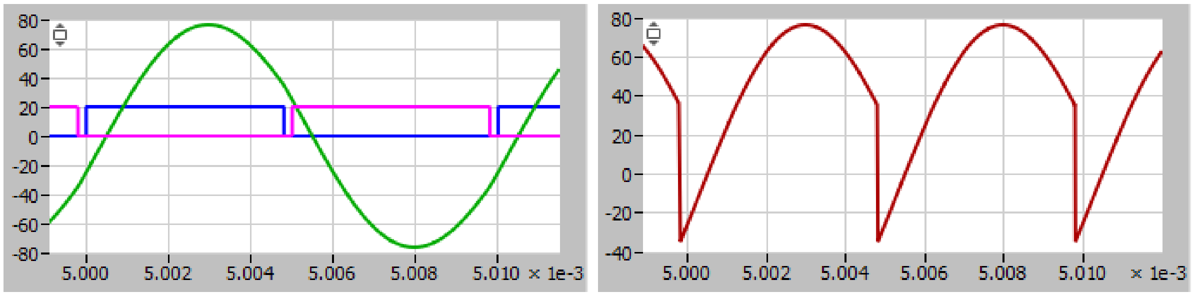

M1&M4 G, M2&M3 G, Current I [A]　　Input current I_{in} [A]

(a) Waveforms before inductor active tuning

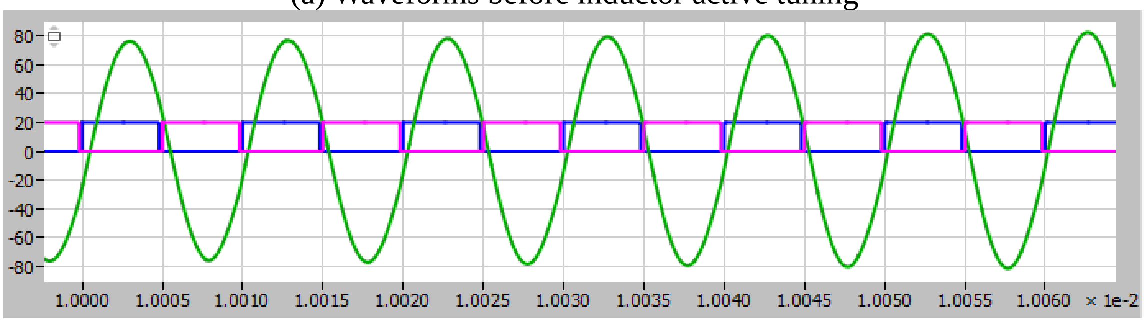

(b) Waveforms during inductor active tuning (M1&M4 G, M2&M3 G, Current I [A])

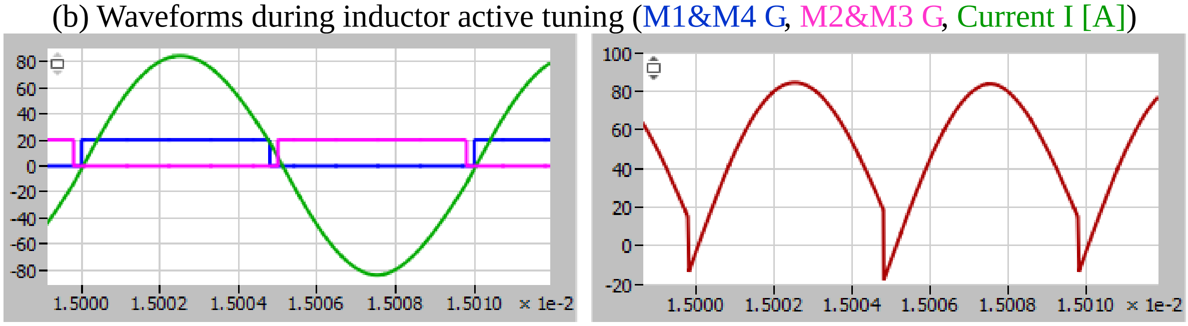

M1&M4 G, M2&M3 G, Current I [A]　　Input current I_{in} [A]

(c) Waveforms after inductor active tuning

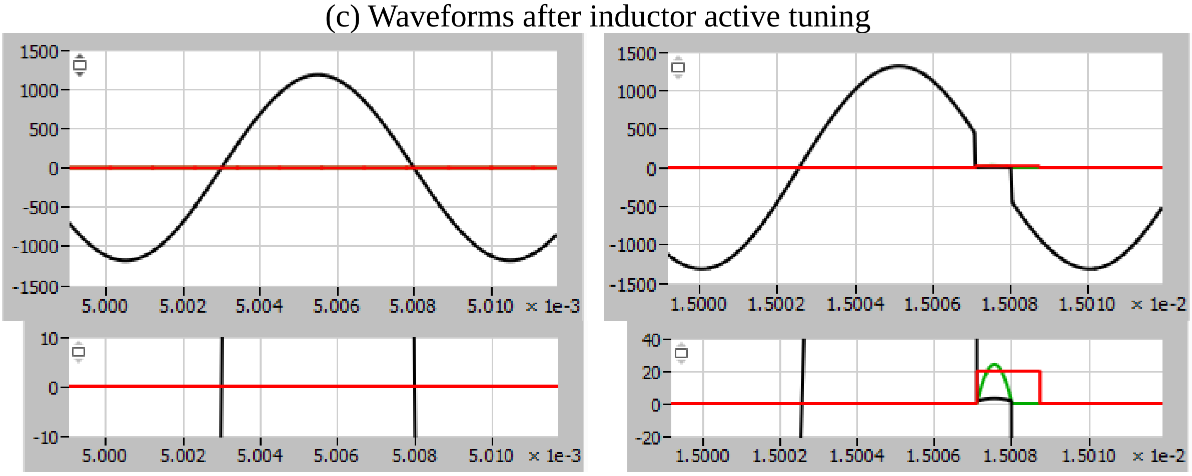

V_{M0}, M0 G, Current I through G [A]　　V_{M0}, M0 G, Current I through G [A]

(d) SCI circuit waveforms before and after inductor active tuning

Before L_0 active tuning (Improved $\alpha \rightarrow \pi$ method):
M = 3.78μH, V_{in} = 116.57V, P_{out} = 4879.5W, η_{coil} = 97.33%, η_{dc} = 93.35%
Winding loss: P_{tx} = 88.50W, P_{rx} = 45.45W.
Inverter loss (each module): $P_{condution\_M}$ = 50.0W, P_{switch_M} = 1.28W, $P_{condution\_D}$ = 2.02W.
M0 loss: $P_{condution\_M}$ = 0W, P_{switch} = 0W, $P_{condution\_D}$ = 0W.
After L_0 active tuning (Improved $\alpha \rightarrow \pi$ method):
M = 3.78μH, V_{in} = 116.57V, P_{out} = 5767.5W (↑ 18.2%), η_{coil} = 97.33%, η_{dc} = 93.16% (↓ 0.19%)
Winding loss: P_{tx} = 104.65W (↑ 18.2%), P_{rx} = 53.73W (↑ 18.2%).
Inverter loss (each module): $P_{condution\_M}$ = 67.5W (↑ 35.0%), P_{switch_M} = 0.48W (↓ 62.5%), $P_{condution\_D}$ = 0.47W (↓ 76.7%).
M0 loss: $P_{condution\_M}$ = 0.87W, P_{switch} = 0W, $P_{condution\_D}$ = 0W.

Fig. 6-18. Waveforms and loss distributions with improved $\alpha \rightarrow \pi$ inductor active tuning technique under misaligned condition

As shown in Fig. 6-18, the improved $\alpha \rightarrow \pi$ inductor active tuning can maintain very low condition and switching losses of M0 over the whole operating range. P_{out} can be improved by 18.2% after L_0 active tuning with the sacrifice of 0.19% η_{dc}. The inverter switching loss can by reduced by more than 60% even within higher P_{out}. However, its conduction loss is the dominant term, which leads to the reduction of η_{dc}. According to voltage and current rating requirements from Fig. 6-18 (d), there is no worry for device voltage breakdown.

The loss distribution and efficiency under aligned and misaligned conditions for both capacitor and inductor active tuning techniques are summarized in Table 6-4.

Table 6-4. Summary of loss distribution and efficiency for active tuning techniques

Inverter loss (each module)			Winding loss		Output power & efficiency		
Under aligned condition							
$P_{condution\_M}$ [W]	P_{switch_M} [W]	$P_{condution\_D}$ [W]	P_{tx} [W]	P_{rx} [W]	P_{out} [W]	η_{coil} [%]	η_{dc} [%]
13.80	0.19	0.28	26.80	28.07	3000	98.20	96.40
Under misaligned condition (No regulation)							
$P_{condution\_M}$ [W]	P_{switch_M} [W]	$P_{condution\_D}$ [W]	P_{tx} [W]	P_{rx} [W]	P_{out} [W]	η_{coil} [%]	η_{dc} [%]
51.07	1.28	2.01	88.50	45.46	4878.8	97.33	93.25
Under misaligned condition (Before C_0 active tuning: conventional $\alpha \rightarrow \pi$ method)							
$P_{condution\_M}$ [W]	P_{switch_M} [W]	$P_{condution\_D}$ [W]	P_{tx} [W]	P_{rx} [W]	P_{out} [W]	η_{coil} [%]	η_{dc} [%]
48.5	1.23	1.96	86.47	44.42	4768.2	97.33	91.77
M0	$P_{condution\_M}$ = 87.0W	P_{switch} = 0W		$P_{condution\_D}$ = 2.15W			
Under misaligned condition (After C_0 active tuning: conventional $\alpha \rightarrow \pi$ method)							

<table>
<tr><td colspan="2">$P_{condution\_M}$ [W]</td><td>P_{switch_M} [W]</td><td>$P_{condution\_D}$ [W]</td><td>P_{tx} [W]</td><td>P_{rx} [W]</td><td>P_{out} [W]</td><td>η_{coil} [%]</td><td>η_{dc} [%]</td></tr>
<tr><td colspan="2">64.0</td><td>0.46</td><td>0.43</td><td>104.23</td><td>53.45</td><td>5740.5</td><td>97.33</td><td>91.70</td></tr>
<tr><td>M0</td><td colspan="2">$P_{condution\_M}$ = 117.2W</td><td colspan="2">P_{switch} = 0W</td><td colspan="3">$P_{condution\_D}$ = 6.78W</td><td></td></tr>
<tr><td colspan="9">Under misaligned condition (Before C_0 active tuning: improved $\alpha \rightarrow 0$ method)</td></tr>
<tr><td colspan="2">$P_{condution\_M}$ [W]</td><td>P_{switch_M} [W]</td><td>$P_{condution\_D}$ [W]</td><td>P_{tx} [W]</td><td>P_{rx} [W]</td><td>P_{out} [W]</td><td>η_{coil} [%]</td><td>η_{dc} [%]</td></tr>
<tr><td colspan="2">57.8</td><td>0.66</td><td>1.06</td><td>98.45</td><td>50.58</td><td>5428.9</td><td>97.33</td><td>93.20</td></tr>
<tr><td>M0</td><td colspan="2">$P_{condution\_M}$ = 4.46W</td><td colspan="2">P_{switch} = 0.25W</td><td colspan="3">$P_{condution\_D}$ = 2.99W</td><td></td></tr>
<tr><td colspan="9">Under misaligned condition (After C_0 active tuning: improved $\alpha \rightarrow 0$ method)</td></tr>
<tr><td colspan="2">$P_{condution\_M}$ [W]</td><td>P_{switch_M} [W]</td><td>$P_{condution\_D}$ [W]</td><td>P_{tx} [W]</td><td>P_{rx} [W]</td><td>P_{out} [W]</td><td>η_{coil} [%]</td><td>η_{dc} [%]</td></tr>
<tr><td colspan="2">65.5</td><td>0.39</td><td>0.49</td><td>104.06</td><td>53.47</td><td>5738.4</td><td>97.33</td><td>93.07</td></tr>
<tr><td>M0</td><td colspan="2">$P_{condution\_M}$ = 2.36W</td><td colspan="2">P_{switch} = 0.17W</td><td colspan="3">$P_{condution\_D}$ = 4.09W</td><td></td></tr>
<tr><td colspan="9">Under misaligned condition (Before L_0 active tuning: improved $\alpha \rightarrow \pi$ method)</td></tr>
<tr><td colspan="2">$P_{condution\_M}$ [W]</td><td>P_{switch_M} [W]</td><td>$P_{condution\_D}$ [W]</td><td>P_{tx} [W]</td><td>P_{rx} [W]</td><td>P_{out} [W]</td><td>η_{coil} [%]</td><td>η_{dc} [%]</td></tr>
<tr><td colspan="2">50.0</td><td>1.28</td><td>2.02</td><td>88.50</td><td>45.45</td><td>4879.5</td><td>97.33</td><td>93.35</td></tr>
<tr><td>M0</td><td colspan="2">$P_{condution\_M}$ = 0W</td><td colspan="2">P_{switch} = 0W</td><td colspan="3">$P_{condution\_D}$ = 0W</td><td></td></tr>
<tr><td colspan="9">Under misaligned condition (After L_0 active tuning: improved $\alpha \rightarrow \pi$ method)</td></tr>
<tr><td colspan="2">$P_{condution\_M}$ [W]</td><td>P_{switch_M} [W]</td><td>$P_{condution\_D}$ [W]</td><td>P_{tx} [W]</td><td>P_{rx} [W]</td><td>P_{out} [W]</td><td>η_{coil} [%]</td><td>η_{dc} [%]</td></tr>
<tr><td colspan="2">67.5</td><td>0.48</td><td>0.47</td><td>104.65</td><td>53.73</td><td>5767.5</td><td>97.33</td><td>93.16</td></tr>
<tr><td>M0</td><td colspan="2">$P_{condution\_M}$ = 0.87W</td><td colspan="2">P_{switch} = 0W</td><td colspan="3">$P_{condution\_D}$ = 0W</td><td></td></tr>
</table>

In summary, improved capacitor and inductor active tuning techniques can reduce the reactive power and improve the output power capacity significantly with very little sacrifice of η_{dc}. Besides that, the improved $\alpha \rightarrow 0$ capacitor active tuning method can automatically correct the current phase delay to reduce the reactive power. It should be noted that η_{coil} maintains the same under misaligned condition with and without the proposed active tuning methods.

Compared with aligned condition, the transmitter and receiver winding loss ratio is increased with and without active tuning methods during misaligned condition, because the transmitter current has to be increased to achieve the same amount of output power due to the reduction of mutual coupling. The increase of transmitter current leads to the increase of transmitter side magnetic field. According to chapter 4 section 3, the magnetic field distribution can be tuned by adjusting the current phase difference, which will lead to the reduction of power transfer efficiency. The limitation of the phase manipulation method has not been evaluated quantatively. In addition, the root cause for the reduction of power transfer efficiency has not been identified. Besides that, it’s beneficial to develop a compensation topology that can adjust the transmitter and receiver current ratio and current phase difference to manipulate the air-gap magnetic field distribution without degrading the power transfer efficiency.

6.5 Active compensation design method to manipulate field distribution

A parallel resonant compensation circuit with resistive load, shown in Fig. 6-19 (a), can be transformed into the series one, shown in Fig. 6-19 (b).

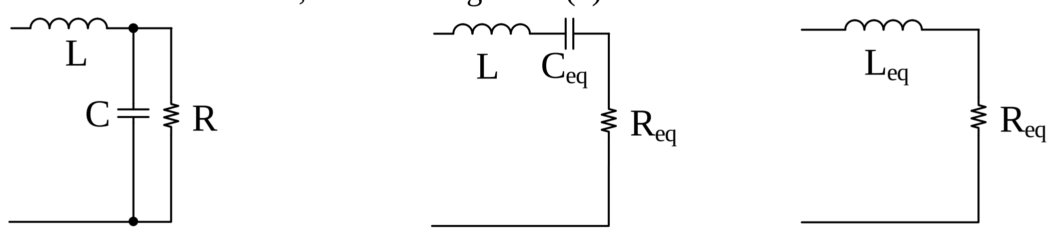

(a) Parallel resonant circuit (b) Equivalent series circuit (c) Simplified circuit

Fig. 6-19. Parallel resonant compensation circuit and its equivalent series version

Assuming the resonant angular frequency is ω_0, the relationship between L and C is $\omega_0^2 LC = 1$, then the relationship between parallel resonant circuit and equivalent series version is

$$R_{eq} = \frac{R}{1 + \omega_0^2 C^2 R^2},\ C_{eq} = C + \frac{1}{\omega_0^2 CR^2} = C + \Delta C,\ \Delta C = \frac{1}{\omega_0^2 CR^2} \tag{6.6}$$

From above expression, it's easy to find that the parallel resonant circuit is equivalent to increase C by ΔC of the conventional LC series resonant circuit. In addition, increasing C in the parallel LC resonant circuit is equivalent to increase C in the series LC resonant circuit. This can also explain that increasing the receiver side resonant compensation capacitor C_{rx} in SP topology is equivalent to increasing C_{rx} in SS topology. Besides that, the inherent smaller current phase difference of SP topology can also be achieved by SS topology through increasing C_{rx} by ΔC with little sacrifice of the coil-to-coil efficiency η_{coil}. The equivalent impedance Z_{eq} of the equivalent series version shown in Fig. 6-19 (b) can be calculated as

$$Z_{eq} = j\omega_0 L + \frac{1}{j\omega_0(C + \Delta C)} + R_{eq} = j\omega_0 \frac{L\Delta C}{C + \Delta C} + R_{eq} = j\omega_0 L_{eq} + R_{eq} \tag{6.7}$$

Where $L_{eq} = \frac{L\Delta C}{C + \Delta C} = \frac{L}{1 + \omega_0^2 C^2 R^2}$.

Therefore, the equivalent series version shown in Fig. 6-19 (b) can be further simplified into Fig. 6-19 (c) under resonant operating frequency.

If C_{rx} is increased by δC_{rx} and the variation of M is ΔM, inductive WPT system with series and parallel resonant compensated receivers under resonant operating frequency f_0 can be simplied into Fig. 6-20 using transformer T-model.

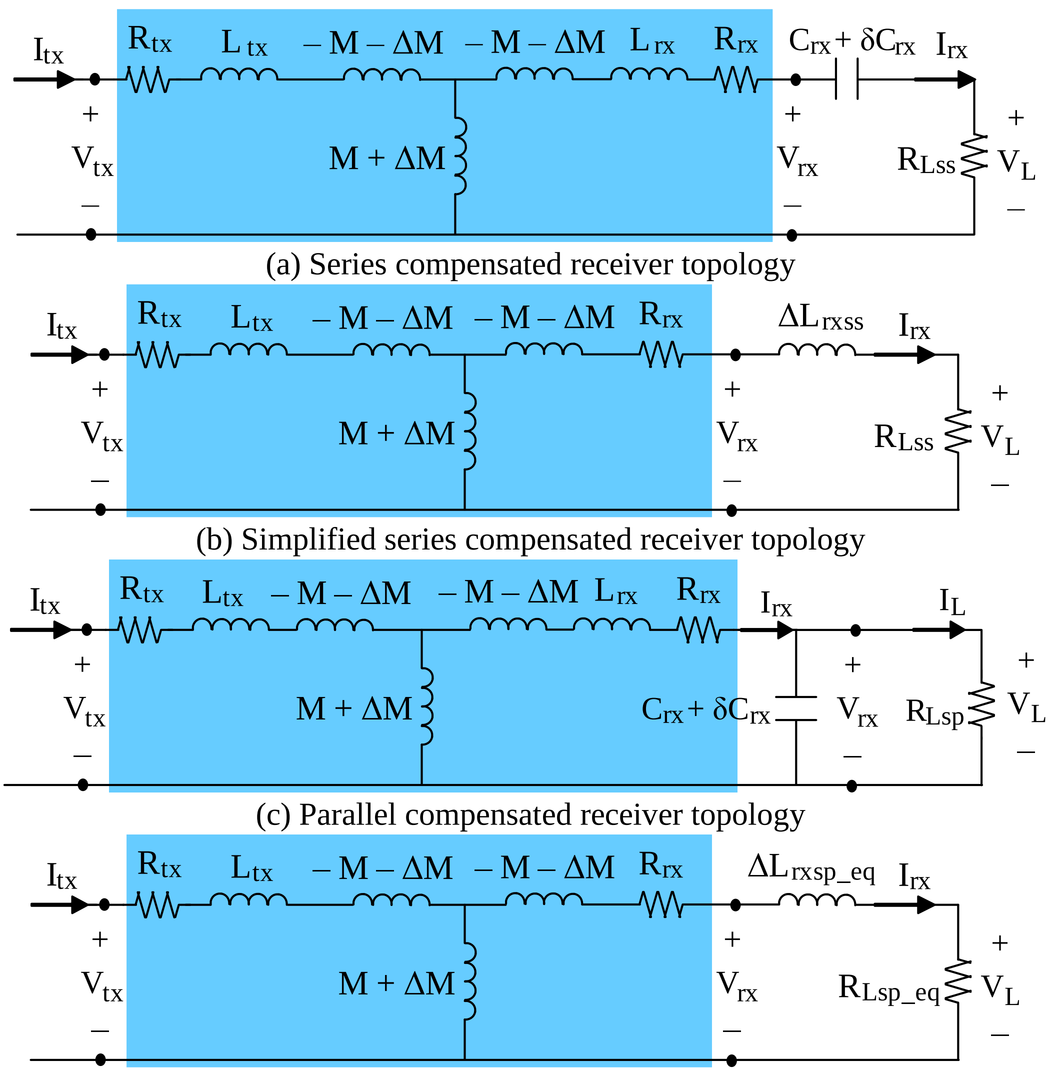

Fig. 6-20. Series and parallel compensated receiver topologies using transformer T-model

Assuming that the loads R_{Lss} and R_{Lsp} are the optimal loads for maximum η_{coil}.

$$R_{Lss} = \sqrt{R_{rx}^2 + \frac{R_{rx}}{R_{tx}} \omega_0^2 M^2}\ , \ R_{Lsp} = \sqrt{\frac{R_{tx}\,\omega_0^4 L_{rx}^4}{R_{rx} M^2 \omega_0^2 + R_{tx} R_{rx}^2}} \tag{6.8}$$

The equivalent parameters R_{Lsp_eq} in SP topology can be calculated

$$R_{Lsp\_eq} = \frac{R_{Lsp}}{1 + \omega_0^2 (C_{rx} + \delta C_{rx})^2 R_{Lsp}^2} \tag{6.9}$$

In SS topology, ΔL_{rxss} is caused by the increase of C_{rx} and can be calculated as

$$\Delta L_{rxss} = \frac{L_{rx}\, \delta C_{rx}}{C_{rx} + \delta C_{rx}} \tag{6.10}$$

In SP topology, ΔL_{rxsp} is caused by the increase of C_{rx} and the transformation from SP topology to SS topology, ΔL_{rxsp_eq} can be calculated as

$$\Delta L_{rxsp\_eq} = \frac{1 + \omega_0^2\, R_{Lsp}^2\, (C_{rx} + \delta C_{rx})\, \delta C_{rx}}{1 + \omega_0^2\, R_{Lsp}^2\, (C_{rx} + \delta C_{rx})^2} L_{rx} \tag{6.11}$$

$$\Delta L_{rxsp\_eq} = \left[1 - \frac{\omega_0^2\, R_{Lsp}^2\, (C_{rx} + \delta C_{rx})\, C_{rx}}{1 + \omega_0^2\, R_{Lsp}^2\, (C_{rx} + \delta C_{rx})^2} \right] L_{rx} \tag{6.12}$$

From (6.10) and (6.12), it’s easy to find that both ΔL_{rxss} and ΔL_{rxsp_eq} increase when δC_{rx} increases, which means the receive and transmitter current phase differences of both SS and SP topologies will reduce when the receiver side resonant compensation capacitor C_{rx} increases. That can help reduce the z-direction magnetic flux density and provides an access to reduce the air-gap region magnetic field.

Under misaligned condition, when M changes to $M + \Delta M$, the receiver and transmitter current ratio can be calculated by

$$\left. \frac{I_{rx}}{I_{tx}} \right|_{ss} = \frac{j\omega_0 (M + \Delta M)}{R_{rx} + R_{Lss} + j\omega_0 \Delta L_{rxss}} \tag{6.13}$$

$$\left. \frac{I_{rx}}{I_{tx}} \right|_{sp} = \frac{j\omega_0 (M + \Delta M)}{R_{rx} + R_{Lsp\_eq} + j\omega_0 \Delta L_{rxsp\_eq}} \tag{6.14}$$

Due to the variation of M, and additional ΔL_{rxss} and ΔL_{rxsp_eq}, the current ratio will also change under misaligned condition. However, it should be noticed that the current phase differnece is not affected by the variation of M.

A design example with conventional magnetic shield is evaluated. The winding radius is 300 mm, the ferrite shield radius is 600 mm, a circular aluminum plate with radius 800 mm is used to emulate the vehicle metal chassis. When the lateral misalignment is 200 mm, the reduction of M is 30%. The winding parameters are summerized in Table 6-5

Table 6-5. Summary of winding parameters with conventional shield

L_{tx} [μH]	R_{tx} [mΩ]	L_{rx} [μH]	R_{rx} [mΩ]	M [μH] (Aligned)	M_{mis} [μH] (Lateral misalign: 200 mm)
26.09	29.7	25.91	29.9	5.39	3.80

Whether using series or parallel resonant compensation topologies at the receiver side, the required receiver side resonant compensation capacitor C_{rx} is the same as $1/(\omega_0^2 L_{rx})$. When $C_{rx} + \delta C_{rx}$ varies from $1/(\omega_0^2 L_{rx})$ to $2/(\omega_0^2 L_{rx})$, the current ratio abs(I_{tx}/I_{rx}), I_{rx}, current phase difference θ, and η_{coil} with the same output power P_{out} = 3 kW are compared in Fig. 6-21.

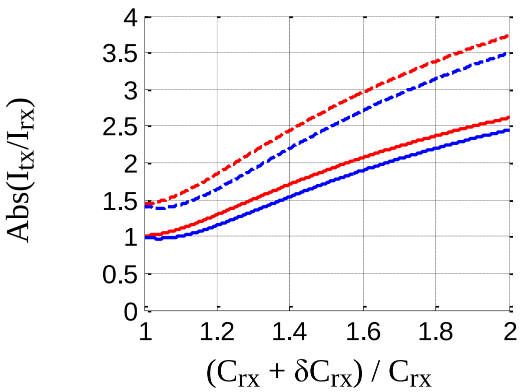

(a) Abs(I_{tx}/I_{rx}) vs. ($C_{rx} + \delta C_{rx}$) / C_{rx}

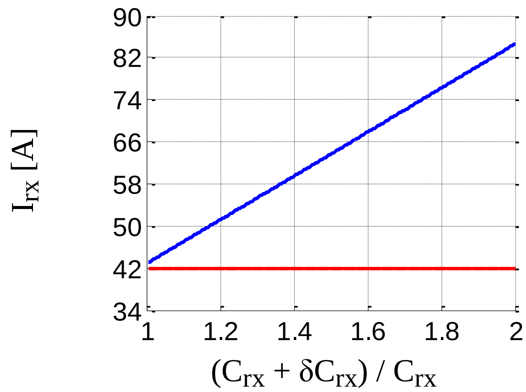

(b) I_{rx} vs. ($C_{rx} + \delta C_{rx}$) / C_{rx}

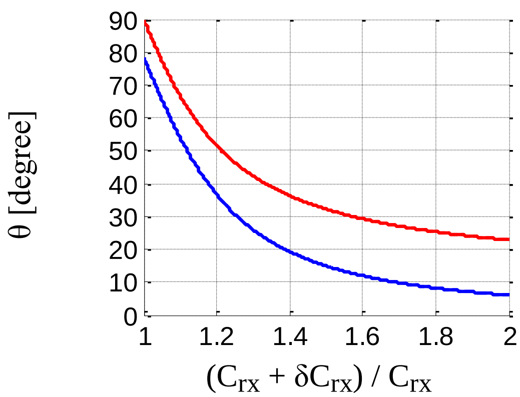

(c) θ vs. ($C_{rx} + \delta C_{rx}$) / C_{rx}

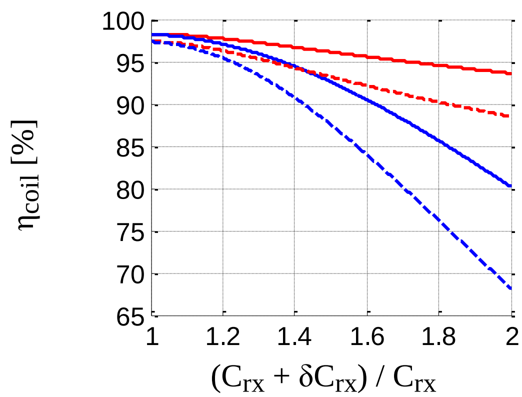

(d) η_{coil} vs. ($C_{rx} + \delta C_{rx}$) / C_{rx}

Legend: aligned condition — S, — P. Misaligned condition - - - S, - - - P

Fig. 6-21. Current and efficiency comparison with different $C_{rx} + \delta C_{rx}$

As shown in Fig. 6-21 (a), when $C_{rx} + \delta C_{rx}$ increases, the current ratio abs(I_{tx}/I_{rx}) increases for both compensation topologies, and the current ratio under misaligned condition is about 50% higher than the aligned condition, which means the transmitter has to generate high magnetic field to support the same P_{out}. Besides that, abs(I_{tx}/I_{rx}) of the series topology is higher than that of the parallel topology when δC_{rx} is above 0.

According to Fig. 6-21 (b), when $C_{rx} + \delta C_{rx}$ increases, I_{rx} remains constant with series topolgogy since it's the same as the load current, while I_{rx} increases linearly with parallel topology. Besides that, there is no difference under aligned and misaligned conditions.

Based on Fig. 6-21 (c), the parallel topology has wider current phase difference range, and θ remains the same for aligned and misaligned conditions. In Fig. 6-21 (d), the parallel topology η_{coil} reduces faster than the series topology. However, it should be noted that it's θ that affects the air-gap field distribution. When analyzing η_{coil}, it should be corresponded to θ. The relationship between η_{coil} and θ is plotted in Fig. 6-22.

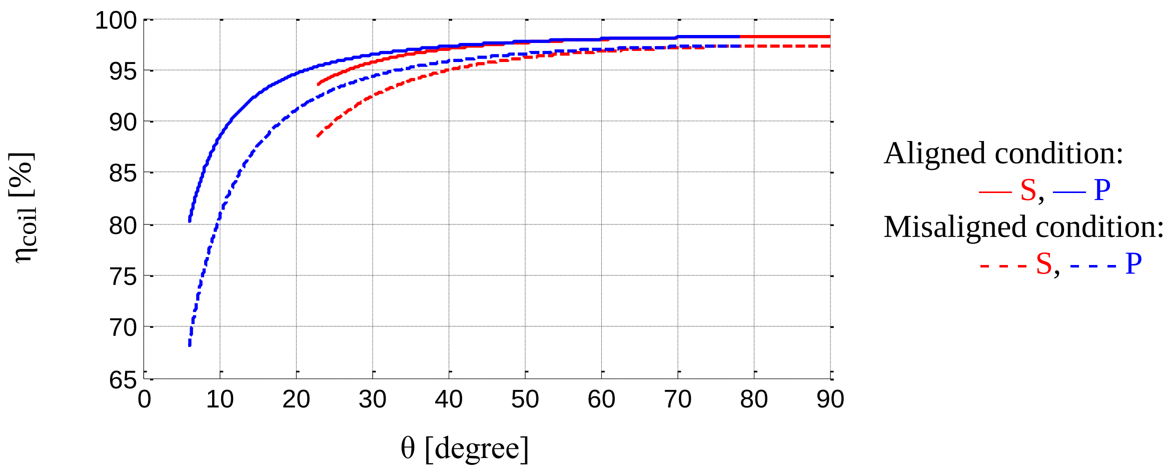

Fig. 6-22. The relationship between η_{coil} and θ

As shown in Fig. 6-22, with the same θ, the parallel topology η_{coil} is not lower than the series topology η_{coil} even under misaligned condition. Therefore, parallel resonant compensation topolog at the receiver side is better to maintain high η_{coil} and low air-gap magnetic field even under misaligned condition.

Under aligned condition, when P_{out} = 3kW, the air-gap magnetic field distributions are compared in Fig. 6-23 with different δC_{rx} using SS and SP compensation topologies.

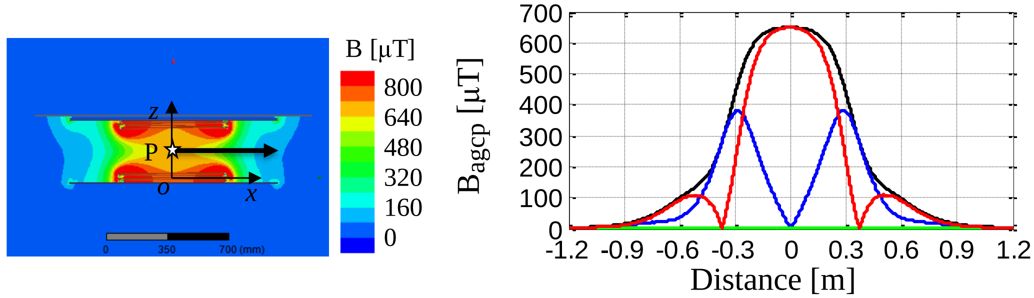

Legend: B_x, B_y, B_z, B_{total}
B_{agcppk}: 649.54 μT
$B_{agcppk,x}$: 381.72 μT
η_{coil}: 98.26%

(a) Air-gap magnetic field distribution using SS topology ($\delta C_{rx} = 0$)

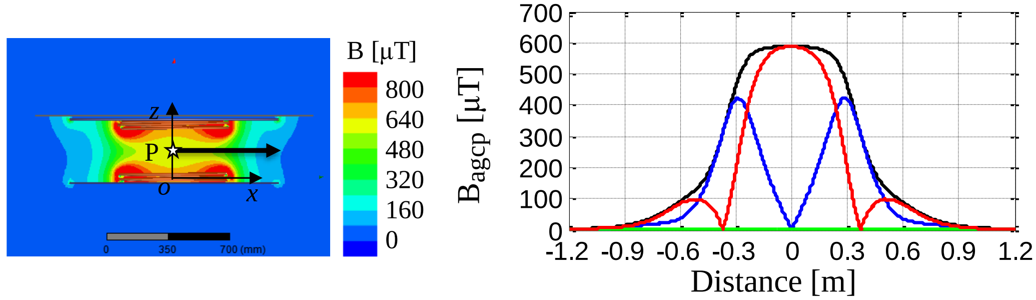

Legend: B_x, B_y, B_z, B_{total}
B_{agcppk}: 587.63 μT
$B_{agcppk,x}$: 422.14 μT
η_{coil}: 98.23%

(b) Air-gap magnetic field distribution using SP topology ($\delta C_{rx} = 0$)

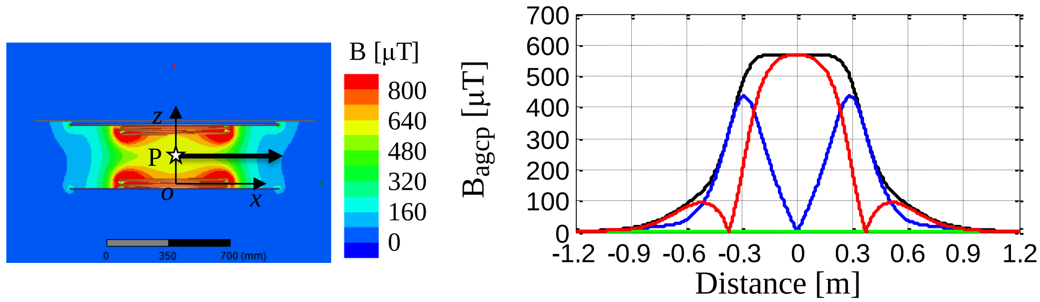

Legend: B_x, B_y, B_z, B_{total}
B_{agcppk}: 569.19 μT
$B_{agcppk,x}$: 436.21 μT
η_{coil}: 98.21%

(c) Air-gap magnetic field distribution using SS topology ($\delta C_{rx} = 0.06C_{rx}$)

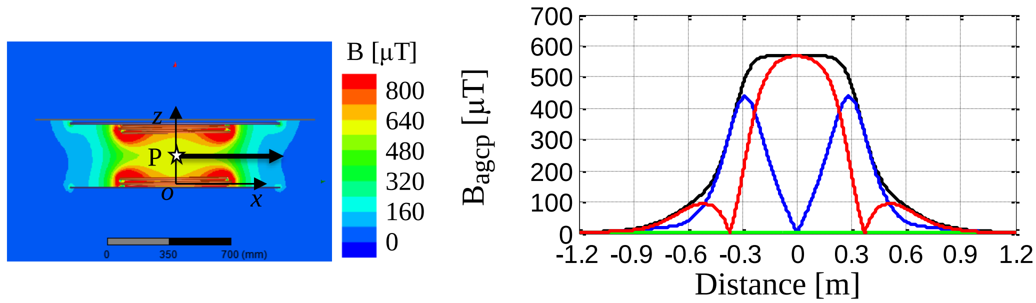

Legend: B_x, B_y, B_z, B_{total}
B_{agcppk}: 567.48 μT
$B_{agcppk,x}$: 437.65 μT
η_{coil}: 98.20%

(d) Air-gap magnetic field distribution using SP topology ($\delta C_{rx} = 0.015C_{rx}$)

Fig. 6-23. Air-gap magnetic field distributions using SS and SP topologies (Aligned condition)

As shown in Fig. 6-23 (a) and (b), when $\delta C_{rx} = 0$, compared with SS topology, SP topology can reduce B_{agcppk} from 649.54 μT to 587.63 μT by 9.5% with only a sacrifice of 0.03% η_{coil}. This result verified previous theoretical analysis. B_{agcppk} can be further reduced by increasing δC_{rx} as shown in Fig. 6-23 (c) and (d). δC_{rx} is tuned to $0.06C_{rx}$ for SS topology and

$0.015C_{rx}$ for SP topology to achieve the minimum B_{agcppk}. If δC_{rx} is further increased, the increase of B_x will lead to higher B_{agcppk}. Although after tuning δC_{rx}, SS topology can achieve nearly the same B_{agcppk} as SP topology, the reduction of η_{coil} in SS topology is 0.05% higher than the SP topology. This result verified that η_{coil} with the receiver side parallel compensation is not lower than η_{coil} with the receiver side series compensation, when θ is the same.

Under 200 mm lateral misalignment condition, when P_{out} = 3kW, the air-gap magnetic field distributions are compared in Fig. 6-24 with different δC_{rx} using SS and SP topologies. δC_{rx} is the same as the aligned condition to achieve the minimum B_{agcppk}.

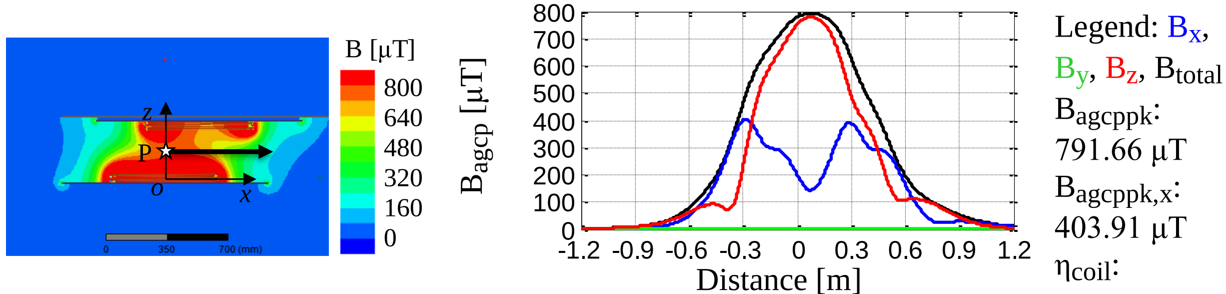

(a) Air-gap magnetic field distribution using SS topology (δC_{rx} = 0)

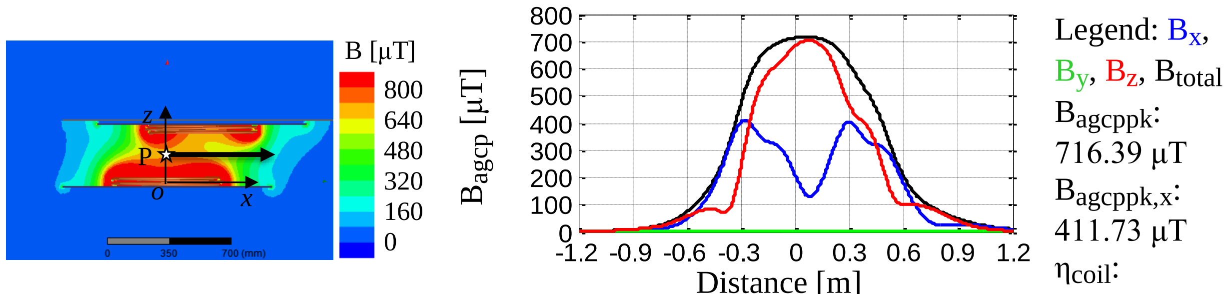

(b) Air-gap magnetic field distribution using SP topology (δC_{rx} = 0)

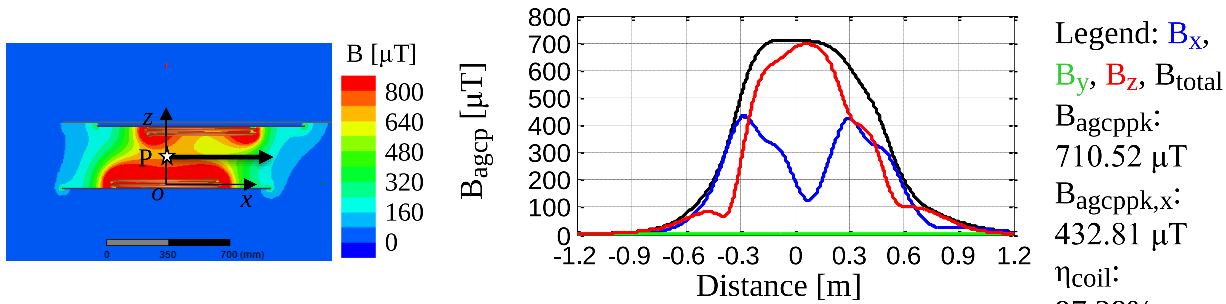

(c) Air-gap magnetic field distribution using SS topology ($\delta C_{rx} = 0.06C_{rx}$)

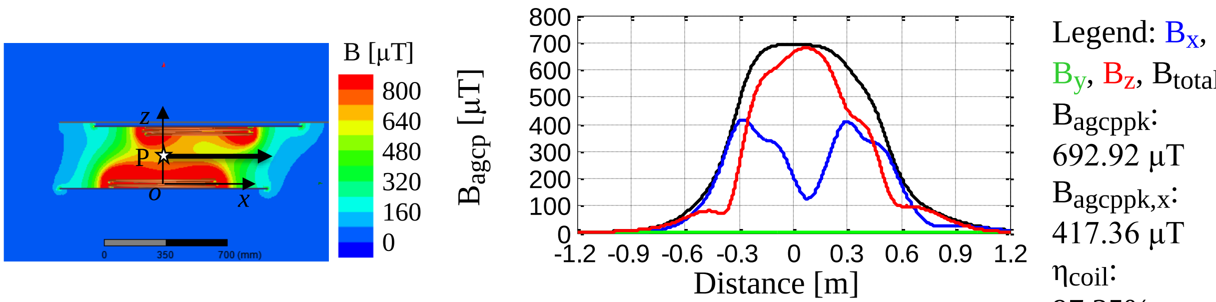

(d) Air-gap magnetic field distribution using SP topology ($\delta C_{rx} = 0.015C_{rx}$)

Fig. 6-24. Air-gap magnetic field distributions using SS and SP topologies (200 mm lateral misalignment)

As shown in Fig. 6-24, through increasing δC_{rx}, B_{agcppk} of the receiver side series compensation can be very close to B_{agcppk} of the receiver side parallel compensation. However, the reduction of η_{coil} in SS topology is higher than the SP topology. Therefore, SP topology is recommended due to low air-gap magentic field and low η_{coil} reduction during active tuning.

Compared with aligned condition, the minimum achievable B_{agcppk} under 200 mm lateral misalignment is 692.92 μT, which is 22.1% higher than the minimum achievable B_{agcppk} under aligned condition (567.48 μT). One reason is that the current ratio abs(I_{tx}/I_{rx}) increases nearly 50% using SS and SP topologies, which leads to high magnetic field at the transmitter side. If the current ratio can be maintained close to 1 under misalignment, the transmitter side magnetic field can be reduced. It is a possible way to reduce the air-gap magnetic field.

Impedance transformation network is necessary to transform the receiver side impedance to manipulate the current ratio, η_{coil} may be reduced due to the migration from optimal load. LCC network is selected as an example. The system topology using LCC compensation network and its equivalent circuits are shown in Fig. 6-25.

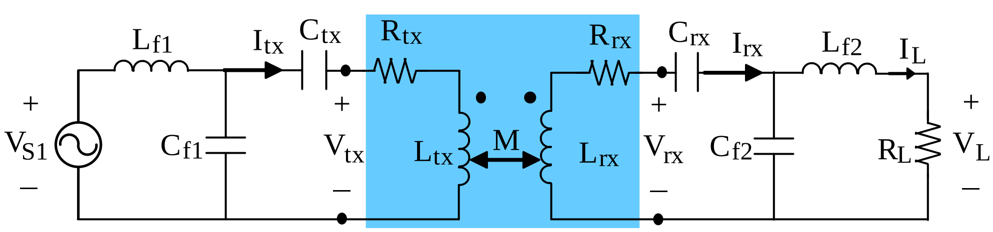

(a) System toplogy using LCC compensation network

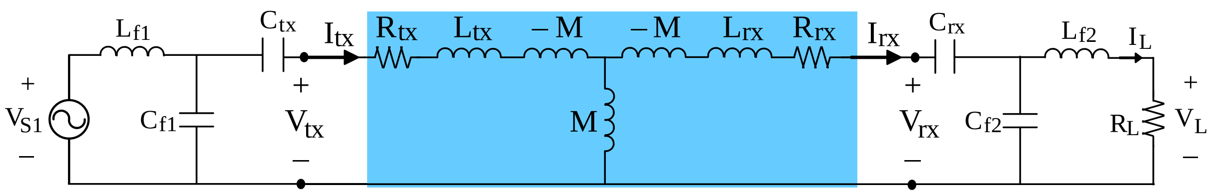

(b) Equivalent system toplogy using transformer T-model

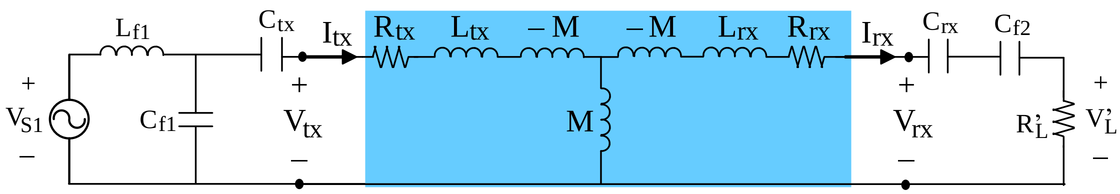

(c) Simplified equivalent system toplogy using transformer T-model

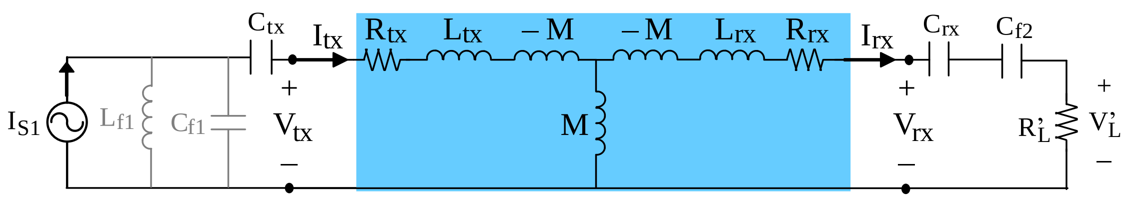

(d) Equivalent system toplogy using transformer T-model and Norton conversion

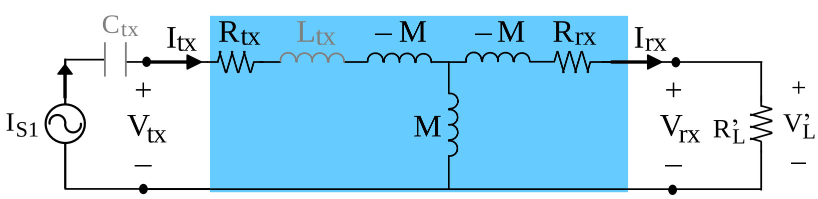

(e) Simplified equivalent system toplogy using transformer T-model and Norton conversion

Fig. 6-25. System topology using LCC network and its equivalent circuits

The resonant relationships in LCC network are

$$L_{f1} = \frac{1}{C_{f1}\,\omega_0^2},\ L_{tx} = \frac{1}{C_{tx}\,\omega_0^2} + \frac{1}{C_{f1}\,\omega_0^2},\ L_{f2} = \frac{1}{C_{f2}\,\omega_0^2},\ L_{rx} = \frac{1}{C_{rx}\,\omega_0^2} + \frac{1}{C_{f2}\,\omega_0^2} \tag{6.15}$$

The load R_L can be transformed into R_L' by

$$R_L' = \frac{L_{f2}}{C_{f2}\,R_L} = \frac{\omega_0^2 L_{f2}^2}{R_L} \tag{6.16}$$

From the load transformation relationship, when R_L is 0, R_L' is ∞, which acts like open circuit. When R_L is ∞, R_L' is 0, which acts like short circuit. It should also be noted that the LCC network can be transformed into series compensation as shown in Fig. 6-25 (c). R_L' can be optimized to the optimal load R_{Lss} of SS toplogy to achieve higher η_{coil} with the same R_L, such as the optimal load R_{Lsp} of SP toplogy.

The transmitter and reciver current ratio can be calculated as

$$\frac{I_{tx}}{I_{rx}} = \frac{R_{rx} + R_L^{'}}{j\omega_0 M} \tag{6.17}$$

It's well-known that there can't be no load (R_L can't be 0 or ∞) in SS and SP topologies. Otherwise, the transmitter side will act like short circuit, the inverter is shorted by the transmitter winding and its compensation capacitor. However, when LCC compensation network is used, there can be no load due to the current source input property.

Following above analysis, two design directions can be adopted to achieve low air-gap magnetic field and high η_{coil}. One desgin direction is manipulating the transmitter and reciver current ratio, another design direction is regulating the value $R_L^{'}$ close to R_{Lss}.

If the transmitter and reciver current ratio abs(I_{tx}/I_{rx}) is set as 1 under 200 mm lateral misalignment (M_{mis} = 0.7M), then the required $R_L^{'}$ can be calculated from (6.17) as

$$\mathrm{abs}(I_{tx}/I_{rx}) = \left|\frac{I_{tx}}{I_{rx}}\right| = \left|\frac{R_{rx} + R_L^{'}}{j\omega_0 M_{mis}}\right| = 1,\ R_L^{'} = \frac{\omega_0^2 L_{f2}^2}{R_L} = \omega_0 M_{mis} - R_{rx} \tag{6.18}$$

The load R_L is maintained as R_{Lsp} under aligned condition

$$R_L = R_{Lsp} = \sqrt{\frac{R_{tx}\,\omega_0^4\,L_{rx}^4}{R_{rx}\,M^2\,\omega_0^2 + R_{tx}\,R_{rx}^2}} \tag{6.19}$$

Combining (6.18) and (6.19), the required L_{f2} can be calculated as

$$L_{f2} = \frac{\sqrt{(\omega_0 M_{mis} - R_{rx})\,R_{Lsp}}}{\omega_0} \tag{6.20}$$

In order to achieve high η_{coil} under misaligned condition, the required $R_L^{'}$ can also be set as the optimal R_{Lss} under misalignment

$$R_L^{'} = \frac{\omega_0^2 L_{f2}^2}{R_L} = R_{Lss\_mis} = \sqrt{R_{rx}^2 + \frac{R_{rx}}{R_{tx}}\,\omega_0^2\,M_{mis}^2} \tag{6.21}$$

If R_L is also maintained as R_{Lsp} under aligned condition, then the required L_{f2} is

$$L_{f2} = \frac{\sqrt{R_{Lss\_mis}\,R_{Lsp}}}{\omega_0} \tag{6.22}$$

Comparing (6.20) and (6.22), there is no big difference between these two design directions if $\omega_0 M_{mis} - R_{rx}$ is very close to R_{Lss_mis}, which is ture for the given design example. In the given design example $\omega_0 M_{mis} - R_{rx} = 2.36\ \Omega$, while $R_{Lss\_mis} = 2.40\ \Omega$.

In the following analysis, higher η_{coil} is selected as priority. (6.22) is used to calculate L_{f2}. Then the required C_{f2} and C_{rx} can be calculated based on (6.15). The transmitter side compensation components are set the same as the receiver side to simplify the design effort. The component parameters for LCC network are summarized in Table 6-6.

Table 6-6. Summary of parameters for LCC compensation network

L_{f1} [μH]	C_{f1} [nF]	C_{tx} [nF]	L_{f2} [μH]	C_{f2} [nF]	C_{rx} [nF]
21.68	116.83	598.51	21.68	116.83	598.51

According to Fig. 6-25 (d), the receiver side L_{rx} is compensated by series connected C_{f2} and C_{rx} together. The required capacitance to compensate L_{rx} is 97.75 nF. Increasing C_{rx} can reduce the current phase difference as SS topology. Compared with SS topology, the benefit using LCC network is that the resonant frequency will be shifted smaller with the same increment of C_{rx}, which can bring smaller reduction of η_{coil}. It's easier for implementation.

Under 200 mm lateral misalignment condition, when P_{out} = 3kW, the air-gap magnetic field distribution using LCC network is shown in Fig. 6-26.

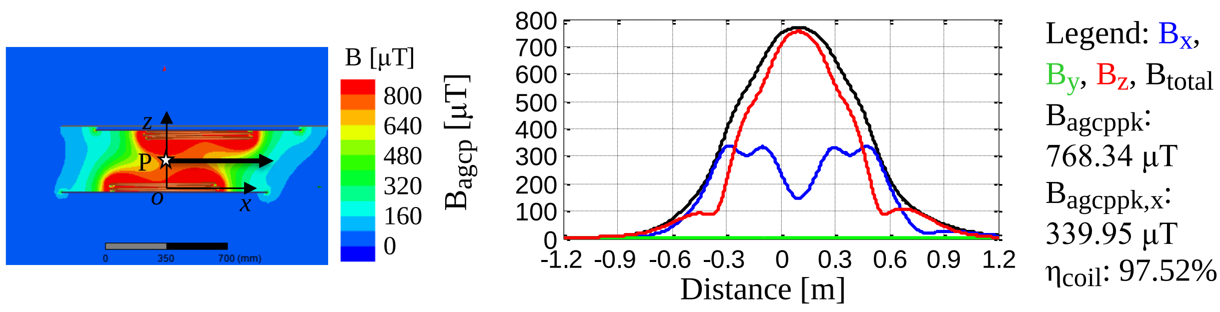

Fig. 6-26. Air-gap magnetic field distribution using LCC network when $\delta C_{rx} = 0$

As shown in Fig. 6-26, the magnetic field distribution around the transmitter and receiver windings are nearly the same due to the current ratio manipulation using LCC network. However, compared with SP topology, B_{agcppk} is increased from 716.39 μT to 768.34 μT by 7.3%. Fortunately, $B_{agcppk,x}$ is reduced from 411.73 μT to 339.95 μT by 17.4%, which gives access to reduce by B_{agcppk} tuning C_{rx}. In addition, η_{coil} is increased to 97.52%. When C_{rx} + δC_{rx} is increased to 1.5 C_{rx} and P_{out} = 3kW, the air-gap magnetic field distribution under 200 mm lateral misalignment is shown in Fig. 6-27.

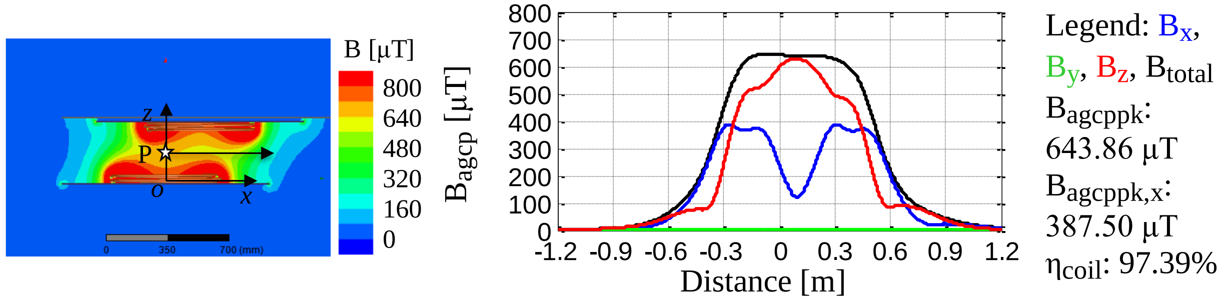

Fig. 6-27. Air-gap magnetic field distribution using LCC network when δC_{rx} = 0.5 C_{rx}

As shown in Fig. 6-27, after increasing δC_{rx} to 0.5 C_{rx}, B_{agcppk} is reduced from to 768.34 μT to 643.86 μT by 16.2%, which is nearly the same as SS topology under aligned condition. Besides that, η_{coil} is maintained higher than SS and SP topologies under misalignment.

The magnetic field distribution and η_{coil} under SS, SP and LCC-LCC with different δC_{rx} under 200 mm lateral misalignment are compared and summarized in Table 6-7.

Table 6-7. Magnetic field distribution and η_{coil} under SS, SP and LCC-LCC with different δC_{rx}

	SS		SP		LCC-LCC	
δC_{rx} / C_{rx}	0	0.06	0	0.015	0	0.5
B_{agcppk} [μT]	791.66	710.52	716.39	692.92	768.34	643.86
$B_{agcppk,x}$ [μT]	403.91	432.81	411.73	417.36	339.95	387.5
η_{coil} [%]	97.37	97.28	97.37	97.35	97.52	97.39

From Table 6-7, using LCC resonant compensation topology can achieve the lowest B_{agcppk} while maintaining high η_{coil}.

6.6 Summary

In this chapter, the performance under misaligned condition is first analyzed. Reactive power at the transmitter side reduces the output power capability due to primary current phase delay. The output power capability can be improved by reducing the primary side resonant compensation capacitance using capacitor and inductor active tuning methods. Conventional capacitor active tuning method leads to lower DC-to-DC efficiency due to high switch conduction loss. Developed low loss capacitor and inductor active tuning methods can highly reduce the switch conduction loss and improve the DC-to-DC efficiency. Improved gate signal generation method can correct the current phase delay automatically.

Although the transmitter side reactive power can be compensated, SS and SP topologies will lead to the increase of transmitter side magnetic field and the whole air-gap magnetic field. The air-gap magnetic field can be reduced by using current phase difference θ manipulation method and tuning the transmitter and receiver current ratio. The receiver side resonant compensation capacitor can be increased to reduce θ and the air-gap magnetic field with a little sacrifice of the coil-to-coil efficiency η_{coil}. It is also found that with the same θ, the parallel topology η_{coil} is not lower than the series topology η_{coil} even under misaligned condition. However, the transmitter and receiver current ratio can't be manipulated by SS or Sp topologies. Through tuning the compensation parameters in LCC network, the current ratio can be configured. Combining with the phase manipulation method, the air-gap magnetic field can be reduced while maintaining high η_{coil}.

Chapter 7 Conclusions, Contributions, and Proposed Remaining Work

7.1 Research conclusions

The following list summarizes the key new conclusions reached via this research.

7.1.1 Analytical modeling of the air-gap magnetic and electric fields

- Compared with rectangular, square, double-square, and double-D windings, circular winding can achieve the lowest air-gap magnetic and electric fields, and highest efficiency.
- The air-gap center plane peak magnetic flux density (B_{agcppk}) of aligned air-core WPT coils is not always located at the air-gap center plane central point due to the leakage flux.
- The air-gap center plane peak electric field intensity (E_{agcppk}) is independent of the coil terminal clearance in loosely coupled inductive WPT system.
- Placing the transmitter coil terminal and the receiver coil terminal at opposite positions can balance the air-gap electric field distribution.

7.1.2 Multi-kW loosely coupled inductive WPT system design methodologies

- The maximum achievable coil-to-coil efficiency (η_{coil}) is fundamentally determined by the efficiency factor $\omega^2M^2/(R_{tx}R_{rx})$.
- The general design variables are identified in sequence as operating frequency f_0, transfer distance d_{ag}, winding radius r_w, number of turns N_{tx} & N_{rx}, and inter-turn distance d_{int}.
- η_{coil} can be improved by increasing f_0, reducing d_{ag}, increasing r_w, increasing N_{tx} or N_{rx}, or reducing d_{int} (within a finite range where the skin and proximity effects are not dominant).
- B_{agcppk} can be reduced by increasing f_0, increasing d_{ag}, increasing r_w, reducing N_{tx} or N_{rx}, or reducing d_{int}.
- E_{agcppk} can be reduced by reducing f_0, increasing d_{ag}, reducing r_w, reducing N_{tx} or N_{rx}, or increasing d_{int}.

- η_{coil} can be improved by using winding configurations with low copper and dielectric losses.
- B_{agcppk} can be reduced by flux shaping techniques and current phase manipulation method.
- B_{agcppk} and E_{agcppk} can be reduced simultaneously with "I" type shielding technique while maintaining η_{coil}.

7.1.3 Low copper loss, low dielectric loss, and low spatial voltage stress winding configurations

- The dielectric losses can be reduced by using low loss materials, by increasing the equivalent dielectric resistance, and by reducing the spatial voltage stress.
- Emulating the 3D printed SSW by using copper tubing, a large spatial clearance can be obtained to reduce the copper loss, the dielectric loss, and the spatial voltage stress.
- By adding another conductor in parallel, the surface spiral parallel winding can be designed to reduce ESR and maintain mutual inductance, thereby improving the efficiency.
- By twisting two parallel windings in opposite direction, the surface spiral antiparallel winding can be designed to equalize the spatial voltage stress and maintain low ESR.

7.1.4 Magnetic shielding design methodologies for low air-gap B&E fields

- Adding magnetic shields below the transmitter and above the receiver has a negligible effect on E_{agcppk}, but increases B_{agcppk} by around 7%.
- Adding copper rings along the winding periphery can reduce the leakage flux nearly 9% by canceling it in the return path, with close to 0.3% reduction of η_{coil} due to eddy current loss.
- Adding a soft magnetic piece at the winding center can reduce the leakage flux nearly 14% by providing a shorter flux return path and maintain η_{coil} due to improved mutual coupling.
- The "I" type magnetic shield can shape the magnetic flux path to reduce B_{agcppk} up to 60% without degrading the mutual coupling and η_{coil}.
- The "I" type magnetic shield can effectively reduce the air-gap electric field up to 60% by confining the electric field within the shielding structure instead of decaying in the air-gap.

- The “I” type shielding structure general design variables are identified in sequence as initial winding parameters, especially r_w, outer ferrite radius r_{out}, and inner ferrite radius r_{in}.
- The “I” type shielding structure performance metrics are identified as η_{coil} and maximum power transferred through the air-gap within safety standard P_{agm}.
- With “I” type magnetic design, η_{coil} can be improved by increasing r_{out}, or reducing r_{in}.
- When r_{in} is smaller than r_{out}, the “I” type magnetic design P_{agm} increases linearly as the r_{in} increases. In addition, P_{agm} is nearly the same for designs that have same r_{in} and r_w.
- When r_{in} is close to r_{out}, the “I” type magnetic design P_{agm} reduces slightly as r_{in} increases.
- The “I” type magnetic shield can be optimized with reduced mass by only keeping the important shielding part that can shape the magnetic flux and confine the electric field.
- Hollow “I” type magnetic shield can be used to reduce the ferrite usage by nearly 70% without degrading the air-gap B&E field distributions, and η_{coil}.
- Ferrite blocks with a small gap between each block can be used to replace the ferrite plate with very little sacrifice of air-gap field distributions and η_{coil}.
- The inner ferrite above the winding should be kept to maintain the air-gap field distributions, while segments of the ferrite below the winding can be removed to reduce ferrite usage.

7.1.5 Power scaling law within safety standard

- The maximum output power within safety limits P_{mout} is dominated by f_0, the area enclosed by the coil A_0, and d_{ag}.
- P_{mout} is proportional to equivalent mutual inductance $(M/(N_{tx}\ N_{rx}))$ and f_0.
- The ratio of P_{mout} to A_0 is nearly the same for the circular, square, and rectangular windings.
- When f_0 increases, P_{mout} within electrostimulation safety limit first increases, limited by the magnetic field, then it decreases limited by the electric field.
- The reduction rate of B_{agcppk} due to the increase of f_0 is lower than the reduction rate of the tissue heating safety limit.

- Higher P_{mout} can be achieved through increasing r_w, reducing N, or increasing d_{ag}.
- When the number of turns increases, planar spiral winding P_{mout} reduces due to the reduction of equivalent mutual inductance.
- When the number of turns increases, SSW can maintain the equivalent mutual inductance and P_{mout} with higher η_{coil} due to low copper loss.
- When r_w increases, the air-core winding P_{mout} first increases quadratically, then increases linearly.
- Increasing the magnetic shield size of the conventional magnetic design has negligible effect on P_{mout}, which is about 35% lower than air-core winding.
- The "I" type magnetic design P_{mout} can be improved by increasing r_w, r_{in}, or r_{out} within a finite range.
- When r_{in} is smaller than r_{out}, the "I" type magnetic design P_{mout} increases linearly as the r_{in} increases. In addition, P_{mout} is nearly the same for designs that have same r_{in} and r_w.
- When r_{in} is close to r_{out}, the "I" type magnetic design P_{mout} reduces slightly as r_{in} increases.
- When r_{in} is close to r_w, the "I" type magnetic design can achieve the same P_{mout} as the air-core winding.
- No additional cooling is required, since the temperature increase is less than 6 °C with "I" type shielding design when transferring 10 kW based on the developed power scaling law.

7.1.6 Tunable matching network for operation under misalignment

- Under misalignment, the transmitter current has phase delay, which reduces the output power capability and can be compensated by reducing the transmitter compensation capacitance.
- Conventional $\alpha \rightarrow \pi$ capacitor tuning method can pull the current phase delay back to reduce the reactive power and improve the output power capability by more than 10%.
- Conventional $\alpha \rightarrow \pi$ capacitor tuning method can reduce the DC-to-DC efficiency due to high conduction loss in the tuning switch, that is almost equal to the inverter conduction loss.

- In the conventional $\alpha \rightarrow \pi$ capacitor tuning method, the tuning switch gate signal is aligned with current, which is difficult to implement under misalignment due to current phase delay.
- In the improved $\alpha \rightarrow 0$ capacitor tuning method, the tuning switch gate signal is aligned with inverter gate signal, which can automatically correct the current phase delay.
- The improved $\alpha \rightarrow 0$ capacitor tuning method can improve the output power capability to be the same as the conventional one with ultra-low tuning switch conduction loss.
- In the conventional $\alpha \rightarrow \pi$ inductor tuning method, the tuning switch gate signal is aligned with voltage, which is difficult to implement under misalignment due to voltage phase delay.
- In the improved $\alpha \rightarrow \pi$ inductor tuning method, the switch gate signal is aligned with the inverter gate signal with a 90° phase delay, which is easy to implement and has a current phase delay automatic correction property.
- The improved $\alpha \rightarrow \pi$ inductor tuning method can achieve the lowest tuning switch losses with high reliability due to inductor high voltage and current ratings.

7.1.7 Active compensation design method to manipulate the air-gap magnetic field

- Reducing the transmitter and receiver current phase difference θ can reduce the z-axis flux density B_z, but increase the radial-axis flux density B_r.
- Through reducing θ, B_{agcppk} can be reduced by nearly 10%, with less than 0.05% reduction of η_{coil} under aligned and misaligned conditions.
- θ can be reduced by increasing the receiver side resonant compensation capacitor C_{rx} for SS and SP topologies.
- Compared with SS topology, SP topology can achieve lower B_z due to inherently smaller θ.
- With the same θ, SP topology η_{coil} is not lower than SS topology η_{coil} under aligned and misaligned conditions.
- Under aligned and misaligned conditions, θ remains the same if other settings are the same.

- During misalignment with SS and SP topologies, the transmitter and receiver current ratio increases, which leads to the increase of transmitter side magnetic field.
- Using LCC compensation network at the receiver side, the transmitter and receiver current ratio can be reduced by decreasing L in the LCC network to control the air-gap B-field.
- Using LCC compensation network at the receiver side, θ can be reduced by increasing the capacitor in series with receiver winding to control the air-gap B-field.
- Using LCC compensation network at the receiver side to regulate the current ratio and phase difference, B_{agcppk} can be reduced by ~16% under aligned condition while maintaining η_{coil}.

7.2 Research contributions

The following list summarizes the key contributions made by this research.

7.2.1 Developed a general, scalable loosely coupled inductive WPT system design methodology

- Developed fast converging air-gap magnetic (B) and electric (E) fields analytical models and verified using FEA.
- Developed a closed-form system analytical model that captures the effects of general design variables on air-gap B&E fields and power transfer efficiency and verified using simulation.
- Identified the trends between relevant performance metrics and loosely coupled inductive WPT system key design variables to give general design guidelines.
- Developed low copper loss and low dielectric loss winding configurations and verified using FEA and experimental tests.
- Developed low loss active and passive shielding design methodologies to achieve low air-gap B&E fields while maintaining high power transfer efficiency and verified using FEA.
- Developed power scaling laws with air-gap B&E fields satisfying the safety standard.
- Developed inherently low air-gap B&E fields, and high efficiency design even under misalignment conditions using the design methodology developed in this research.

7.2.2 Developed low copper and dielectric losses winding configurations

- Developed a copper tubing SSW winding design to simultaneously achieve low spatial electric field, low skin effect and proximity effect copper losses, and low dielectric loss.
- Developed a surface spiral parallel winding configuration to further reduce the copper loss and the dielectric loss, thereby increasing the coil-to-coil transfer efficiency.
- Developed a surface spiral antiparallel winding configuration to equalize the spatial voltage stress between adjacent turns, thereby improve the power scalability, while maintaining low dielectric loss and low copper loss.

7.2.3 Developed low loss passive shielding design methodologies

- Developed low eddy current loss copper ring shielding structure to reduce the leakage flux by canceling it in the return path.
- Developed a flux shaping design by adding a soft magnetic piece at the coil center to reduce the leakage flux by providing a shorter flux return path and improve the mutual coupling.
- Developed an "I" type magnetic shield configuration to shape the leakage flux return path and confine the electric field to effectively reduce the whole air-gap region B&E fields.
- Identified the relation between performance metrics, such as air-gap B&E fields and power transfer efficiency, and key design variables of the "I" type shielding.
- Developed "I" type shielding structure optimized design with nearly 70% reduction of ferrite usage without degrading the air-gap B&E field distributions and efficiency.
- Developed "I" type shielding structure power scaling law within safety standard and demonstrated with a 10kW design example.

7.2.4 Developed low loss tunable matching network

- Identified the limitations of conventional $\alpha \rightarrow \pi$ capacitor active tuning method.
- Developed $\alpha \rightarrow 0$ capacitor active tuning technique to reduce the reactive power and improve output power capability during misaligned condition with a very small sacrifice of efficiency.

- Developed $\alpha \rightarrow \pi$ inductor active tuning technique to reduce the reactive power and improve output power capability during misaligned condition with a very small sacrifice of efficiency.
- Developed easy-to-implement tuning switch gate signal generation methods for capacitor and inductor active tuning techniques, which can automatically correct the current phase delay.

7.2.5 Developed active transmitter and receiver current phase difference and current ratio tuning methods to manipulate the air-gap magnetic field

- Identified the relationship between the transmitter and receiver current phase difference and performance metrics, such as air-gap B&E fields and efficiency, and verified using FEA.
- Developed receiver side compensation capacitor tuning method to manipulate the current phase difference and reduce the air-gap magnetic field even under misaligned condition.
- Developed LCC compensation network parameter tuning method to adjust the current ratio to manipulate the air-gap magnetic field distribution.
- Developed LCC compensation network parameter tuning method to adjust the current phase difference to manipulate the air-gap magnetic field distribution.

7.3 Recommended future work

Following the research that has been done, the recommended future work is presented.

- Investigation of closed-loop control strategies with high Q tunable matching network

In this research, low loss active tuning method is developed to compensate reactive power and manipulate current phase differnence. Reducing the total loss of the active tuning method can further improve the quality factor of the tunable matching network.

In the real world, the winding parameters, such as self-inductance and ESR, and the compensation capacitors can change due to various reasons. That can cause the migration of the resonant frequency and operating point, then reactive power and field distribution change are unavoidable. High Q tunable matching network is beneficial for high power transfer efficiency and closed-loop control design. It’s recommended to investigate method to improve the quality factor of the tunable matching network and develop closed-loop control strategies to ensure output power capability, power transfer efficiency, and air-gap B&E fields within safety standard even under misaligned condition.

- Experimental evaluation of "I" type field shaping design

In this research, "I" type field shaping design is developed to reduce air-gap B&E-fields significantly without mitigating the power transfer efficiency. Loss and thermal distribution FEA analysis showed that no additional cooling technique is required for the winding and ferrite shielding due to relatively small temperature increase. In addition, following the developed power scaling law, low magnetic and electric fields can be achieved inherently. That won't cause magnetic saturation. Magnetic material performance, such as permeability and permittivity, will remain nearly the same during operation. It's recommended to evaluate the magnetic material properties and the performance of "I" type field shaping design experimentally.

- Investigation of winding position self-sensing technique

In this research, methods to mitigating the reactive power and variations of magnetic field distribution and amplitude during unavoidable misalignment are developed. In order to maintain high power transfer efficiency, high output power capability, low reactive power and low air-gap B&E-fields, it's recommended to develop winding position self-sensing technique, which can be combined with EV auto-parking function to reduce misalignment.

- Investigation of low loss online tunable LCC compensation network

In this research, it's identified that through tuning the LCC compensation network parameters, the load equivalent impedance can be regulated, and the air-gap magnetic field can be manipulated, even under misaligned condition. Low loss online tunable LCC compensation network will provide an access to regulate the load equivalent impedance and the air-gap field distributions without interruption.

- Investigation of system control strategies with well-behaved transient field distributions

There is power overshoot when the system starts very quickly from low power level to high power level. A feasible transient trajectory is necessary to ensure that the transient magnetic and electric field distributions are within the safety limit during the startup process.

- Investigation of alternative flux shaping magnetic shield structures

The proposed “I” type shielding structure is very effective to shape the magnetic flux path. However, it would be beneficial to have alternative flux shaping techniques to further reduce the leakage field and improve the output power capability within the safety limits.

References

[1] C.A. Balanis, *Antenna Theory: Analysis and Design*. New York: Harper & Row, 1982.

[2] Y. Rahmat-Samii, L.I. Williams, R.G. Yaccarino, "The Ucla Bi-Polar Planarnear-Field Antenna-Measurement and Diagnostics Range," *Antennas and Propagation Magazine, IEEE*, vol. 37, pp. 16-35, 1995.

[3] A. Yaghjian, "An Overview of near-Field Antenna Measurements," *IEEE Trans. on Antennas and Propagation*, vol. 34, pp. 30-45, 1986.

[4] H. Gao, M.K. Matters-Kammerer, P. Harpe, D. Milosevic, A.v. Roermund, J. Linnartz, P. G.M. Baltus, "A 60-GHz energy harvesting module with on-chip antenna and switch for co-integration with ULP radios in 65-nm CMOS with fully wireless mm-wave power transfer measurement," in *International Symposium on Circuits and Systems (ISCAS), 2014 IEEE*, 2014, pp. 1640-1643.

[5] J.O. McSpadden, J.C. Mankins, "Space Solar Power Programs and Microwave Wireless Power Transmission Technology," *Microwave Magazine, IEEE*, vol. 3, pp. 46-57, 2002.

[6] ICNIRP, "Guidelines for Limiting Exposure to Time-Varying Electric, Magnetic and Electromagnetic Fields (up to 300 GHz)," ed: Health Physics, 1998, pp. 494-522.

[7] IEEE, "IEEE Standard for Safety Levels with Respect to Human Exposure to Radio Frequency Electromagnetic Fields, 3 kHz to 300 GHz," in *IEEE Std C95.1-2005 (Revision of IEEE Std C95.1-1991)*, ed, 2006.

[8] G.A. Landis, "Space Power by Ground-Based Laser Illumination," *Aerospace and Electronic Systems Magazine, IEEE*, vol. 6, pp. 3-7, 1991.

[9] T.J. Nugent, T.K. Jordin, "Laser power for uavs." *Laser Motive White Paper-Power Beaming for UAVs, NWEN* 2010.

[10] S. Sood, S. Kullanthasamy, M. Shahidehpour, "Solar Power Transmission: From Space to Earth," in *Power Engineering Society General Meeting, 2005. IEEE*, 2005, pp. 605-610 vol. 1.

[11] J.T. Kare, F. Mitlitsky, A. Weisberg, "Preliminary Demonstration of Power Beaming with Non-Coherent Laser Diode Arrays," in *Space Technology & Applications International Forum (STAIF-99)*, 1999, pp. 1641-1646.

[12] B.J. Comaskey, R. Beach, G. Albrecht, W.J. Benett, B.L. Freitas, C. Petty, D. VanLue, D. Mundinger, R.W. Solarz, "High Average Powers Diode Pumped Slab Laser," *IEEE Journal of Quantum Electronics*, vol. 28, pp. 992-996, 1992.

[13] U.S. Inan, A.S. Inan, *Engineering Electromagnetics and Waves*: Pearson Custom Publishing, 2000.

[14] M. Stratmann, P. Trawinski, "Rechargeable Toothbrushes with Charging Stations," ed: Google Patents, 2004.

[15] S.Y.R. Hui, W.W.C. Ho, "A New Generation of Universal Contactless Battery Charging Platform for Portable Consumer Electronic Equipment," *IEEE Trans. on Power Electronics*, vol. 20, pp. 620-627, 2005.

[16] B. Choi, J. Nho, H. Cha, T. Ahn, S. Choi, "Design and Implementation of Low Profile Contactless Battery Charger Using Planar Printed Circuit Board Windings as Energy Transfer Device," *IEEE Trans. on Industrial Electronics*, vol. 51, pp. 140-147, 2004.

[17] Z. Li, D. Li, L. Lin, Y. Chen, "Design Considerations for Electromagnetic Couplers in Contactless Power Transmission Systems for Deep-Sea Applications," *Journal of Zhejiang University-Science C,* vol. 11, pp. 824-834, 2010.

[18] J.J. Casanova, Z.N. Low, J. Lin, "A Loosely Coupled Planar Wireless Power System for Multiple Receivers," *IEEE Trans. on Industrial Electronics*, vol. 56, pp. 3060-3068, 2009.

[19] C.S. Wang, G.A. Covic, O.H. Stielau, "Power Transfer Capability and Bifurcation Phenomena of Loosely Coupled Inductive Power Transfer Systems," *IEEE Trans. on Industrial Electronics*, vol. 51, pp. 148-157, 2004.

[20] Z.N. Low, R.A. Chinga, R. Tseng, J. Lin, "Design and Test of a High-Power High-Efficiency Loosely Coupled Planar Wireless Power Transfer System," *IEEE Trans. on Industrial Electronics*, vol. 56, pp. 1801-1812, 2009.

[21] K. Fotopoulou, B.W. Flynn, "Wireless Power Transfer in Loosely Coupled Links: Coil Misalignment Model," *IEEE Trans. on Magnetics,* vol. 47, pp. 416-430, 2011.

[22] O.H. Stielau, G.A. Covic, "Design of Loosely Coupled Inductive Power Transfer Systems," *PowerCon 2000, 2000 International Conference on Power System Technology, Proceedings*, 2000, pp. 85-90 vol. 1.

[23] P. Si, A.P. Hu, S. Malpas, D. Budgett, "A Frequency Control Method for Regulating Wireless Power to Implantable Devices," *IEEE Trans. on Biomedical Circuits and Systems*, vol. 2, pp. 22-29, 2008.

[24] A.K. RamRakhyani, S. Mirabbasi, M. Chiao, "Design and Optimization of Resonance-Based Efficient Wireless Power Delivery Systems for Biomedical Implants," *IEEE Trans. on Biomedical Circuits and Systems*, vol. 5, pp. 48-63, 2011.

[25] Z. Yang, W. Liu, E. Basham, "Inductor Modeling in Wireless Links for Implantable Electronics," *IEEE Trans. on Magnetics*, vol. 43, pp. 3851-3860, 2007.

[26] M. Soma, D.C. Galbraith, R.L. White, "Radio-Frequency Coils in Implantable Devices: Misalignment Analysis and Design Procedure," *IEEE Trans. on Biomedical Engineering*, pp. 276-282, 1987.

[27] C.S. Wang, O.H. Stielau, G.A. Covic, "Design Considerations for a Contactless Electric Vehicle Battery Charger," *IEEE Trans. on Industrial Electronics*, vol. 52, pp. 1308-1314, 2005.

[28] J. Sallán, J.L. Villa, A. Llombart, J.F. Sanz, "Optimal Design of ICPT Systems Applied to Electric Vehicle Battery Charge," *IEEE Trans. on Industrial Electronics*, vol. 56, pp. 2140-2149, 2009.

[29] H.H. Wu, A. Gilchrist, K. Sealy, P. Israelsen, J. Muhs, "A Review on Inductive Charging for Electric Vehicles," in *Electric Machines & Drives Conference (IEMDC), 2011 IEEE International*, 2011, pp. 143-147.

[30] M. Budhia, G.A. Covic, J.T. Boys, C.Y. Huang, "Development and Evaluation of Single Sided Flux Couplers for Contactless Electric Vehicle Charging," in *Energy Conversion Congress and Exposition (ECCE), 2011 IEEE*, 2011, pp. 614-621.

[31] M. Budhia, J.T. Boys, G.A. Covic, C.Y. Huang, "Development of a Single-Sided Flux Magnetic Coupler for Electric Vehicle IPT Charging Systems," *IEEE Trans. on Industrial Electronics*, vol. 60, pp. 318-328, 2013.

[32] L. Huang, A.P. Hu, A.K. Swain, Y. Su, "Z-Impedance Compensation for Wireless Power Transfer Based on Electric Field," *IEEE Trans. on Power Electronics*, vol. 31, pp. 7556-7563, 2016.

[33] J. Kim, F. Bien, “Electric field coupling technique of wireless power transfer for electric vehicles,” in *TENCON Spring Conference, 2013 IEEE*, 2013, pp. 267-271.

[34] J. Dai, D.C. Ludois, "Capacitive Power Transfer Through a Conformal Bumper for Electric Vehicle Charging," *IEEE Journal of Emerging and Selected Topics in Power Electronics*, vol. 4, pp. 1015-1025, 2016.

[35] C. Liu, A.P. Hu, N.K.C. Nair, "Coupling Study of a Rotary Capacitive Power Transfer System," in *Industrial Technology, 2009. ICIT 2009. IEEE International Conference on*, 2009, pp. 1-6.

[36] J. Dai, D.C. Ludois, "A Survey of Wireless Power Transfer and a Critical Comparison of Inductive and Capacitive Coupling for Small Gap Applications," *IEEE Trans. on Power Electronics*, vol. 30, pp. 6017-6029, 2015.

[37] H. Zhang, F. Lu, H. Hofmann, W. Liu, C.C. Mi, "A Four-Plate Compact Capacitive Coupler Design and LCL-Compensated Topology for Capacitive Power Transfer in Electric Vehicle Charging Application," *IEEE Trans. on Power Electronics*, vol. 31, pp. 8541-8551, 2016.

[38] J. Deng, F. Lu, S. Li, T.D. Nguyen, C.C. Mi, "Development of a high efficiency primary side controlled 7kW wireless power charger," *Electric Vehicle Conference (IEVC), 2014 IEEE International*, 2014, pp. 1-6.

[39] H. Zhang, F. Lu, H. Hofmann, W. Liu, C.C. Mi, "A Six-Plate Capacitive Coupler to Reduce Electric Field Emission in Large Air-Gap Capacitive Power Transfer," *IEEE Trans. on Power Electronics*, vol. PP, no.99, pp.1-10, 2017.

[40] C. Liu, A.P. Hu, N.K.C. Nair, G.A. Covic, "2-D Alignment Analysis of Capacitively Coupled Contactless Power Transfer Systems," in *Energy Conversion Congress and Exposition (ECCE), 2010 IEEE*, 2010, pp. 652-657.

[41] E. Litvak, K.R. Foster, M.H. Repacholi, "Health and Safety Implications of Exposure to Electromagnetic Fields in the Frequency Range 300 Hz to 10 Mhz," *Bioelectromagnetics*, vol. 23, pp. 68-82, 2002.

[42] K. Shiba, M. Nukaya, T. Tsuji, K. Koshiji, "Analysis of Current Density and Specific Absorption Rate in Biological Tissue Surrounding an Air-Core Type of Transcutaneous Transformer for an Artificial Heart," *2006 International Conference of the IEEE Engineering in Medicine and Biology Society*, 2006, pp. 5392-5395.

[43] D.C. Ng, X. Wang, G.K. Felic, S. Bai, C.S. Boyd, M. Halpern, E. Skafidas, "Specific Absorption Rate Distribution on a Human Head Model from Inductive Power Coils," in *EMC Europe 2011 York*, 2011, pp. 79-83.

[44] N. Kuster, Q. Balzano, "Energy absorption mechanism by biological bodies in the near field of dipole antennas above 300 MHz," *IEEE Trans. on Vehicular Technology*, vol. 41, pp. 17-23, 1992.

[45] A. Christ, M.G. Douglas, J.M. Roman, E.B. Cooper, A.P. Sample, B.H. Waters, J.R. Smith, N. Kuster, "Evaluation of Wireless Resonant Power Transfer Systems with Human Electromagnetic Exposure Limits," *IEEE Trans. on Electromagnetic Compatibility*, vol. 55, pp. 265-274, 2013.

[46] S. Judek, K. Karwowski, "Supply of Electric Vehicles Via Magnetically Coupled Air Coils," in *Power Electronics and Motion Control Conference, 2008. EPE-PEMC 2008. 13th*, 2008, pp. 1497-1504.

[47] J.L. Villa, J. Sallán, A. Llombart, J. F. Sanz, "Design of a High Frequency Inductively Coupled Power Transfer System for Electric Vehicle Battery Charge," *Applied Energy*, vol. 86, pp. 355-363, 2009.

[48] C.Y. Huang, J.T. Boys, G.A. Covic, M. Budhia, "Practical Considerations for Designing IPT System for Ev Battery Charging," in *Vehicle Power and Propulsion Conference, 2009. VPPC '09. IEEE*, 2009, pp. 402-407.

[49] Y. Nagatsuka, N. Ehara, Y. Kaneko, S. Abe, T. Yasuda, "Compact Contactless Power Transfer System for Electric Vehicles," in *Power Electronics Conference (IPEC), 2010 International*, 2010, pp. 807-813.

[50] S.H. Lee, R.D. Lorenz, "Development and validation of model for 95% efficiency, 220 W wireless power transfer over a 30cm air-gap," *in Energy Conversion Congress and Exposition (ECCE), 2010 IEEE*, 2010, pp. 885-892.

[51] M. Scudiere, J. McKeever, “Wireless power transfer for electric vehicles,” *SAE Technical Paper*, 2011.

[52] M. Budhia, G.A. Covic, J.T. Boys, "Design and Optimization of Circular Magnetic Structures for Lumped Inductive Power Transfer Systems," *IEEE Trans. on Power Electronics*, vol. 26, pp. 3096-3108, 2011.

[53] G.A. Covic, M.L.G. Kissin, D. Kacprzak, N. Clausen, H. Hao, "A bipolar primary pad topology for EV stationary charging and highway power by inductive coupling," in *Energy Conversion Congress and Exposition (ECCE), 2011 IEEE*, 2011, pp. 1832-1838.

[54] A. Zaheer, G.A. Covic, D. Kacprzak, "A Bipolar Pad in a 10-kHz 300-W Distributed IPT System for AGV Applications," *IEEE Trans. on Industrial Electronics*, vol. 61, pp. 3288-3301, 2014.

[55] S. Kim, A. Zaheer, G. Covic, J. Boys, "Tripolar pad for inductive power transfer systems," in *40th Annual Conference of the IEEE Industrial Electronics Society, 2014 IECON*, 2014, pp. 3066-3072.

[56] S. Kim, G.A. Covic, J.T. Boys, "Analysis on Tripolar Pad for Inductive Power Transfer systems," *Emerging Technologies: Wireless Power Transfer (WoW), 2016 IEEE PELS Workshop on*, 2016, pp. 15-20.

[57] S. Kim, G.A. Covic, J.T. Boys, "Tripolar Pad for Inductive Power Transfer Systems for EV Charging," *IEEE Trans. on Power Electronics*, vol. 32, no. 7, pp. 5045-5057, 2017.

[58] H. Takanashi, Y. Sato, Y. Kaneko, S. Abe, T. Yasuda, "A large air gap 3 kW wireless power transfer system for electric vehicles," *Energy Conversion Congress and Exposition* (*ECCE*), *2012 IEEE*, 2012, pp. 269-274.

[59] S. Li, C.C. Mi, "Wireless Power Transfer for Electric Vehicle Applications," in *IEEE Journal of Emerging and Selected Topics in Power Electronics*, vol. 3, no. 1, pp. 4-17, March 2015.

[60] W. Zhang, J.C. White, A.M. Abraham, C.C. Mi, "Loosely Coupled Transformer Structure and Interoperability Study for EV Wireless Charging Systems," *IEEE Trans. on Power Electronics*, vol. 30, no. 11, pp. 6356-6367, Nov. 2015.

[61] H.J. Song, H. Shin, H.B. Lee, J.H. Yoon, J.K. Byun, "Induced Current Calculation in Detailed 3-D Adult and Child Model for the Wireless Power Transfer Frequency Range," in *IEEE Trans. on Magnetics*, vol. 50, no. 2, pp. 1041-1044, Feb. 2014.

[62] F. Wen, X. Huang, "Human Exposure to Electromagnetic Fields from Parallel Wireless Power Transfer Systems," *Int. J. Environ. Res. Public Health*, vol. 14, no. 157, pp. 1-15, 2017.

[63] X.L. Chen, A.E. Umenei, D.W. Baarman, N. Chavannes, V.D. Santis, J.R. Mosig, N. Kuster, "Human Exposure to Close-Range Resonant Wireless Power Transfer Systems as a Function of Design Parameters," *IEEE Trans. on Electromagnetic Compatibility*, vol. 56, no. 5, pp. 1027-1034, Oct. 2014.

[64] Y. Kitano, H. Omori, T. Morizane, N. Kimura, M. Nakaoka, "A new shielding method for magnetic fields of a wireless EV charger with regard to human exposure by eddy current and magnetic path," *2014 International Power Electronics and Application Conference and Exposition*, Shanghai, 2014, pp. 778-781.

[65] T. Sunohara, I. Laakso, K.H. Chan, A. Hirata, "Compliance of induced quantities in human model for wireless power transfer system at 10 MHz," *2013 International Symposium on Electromagnetic Theory*, Hiroshima, 2013, pp. 831-833.

[66] W.G. Kang, H.Y. Jun, Y.H. Park, J.K. Pack, "Investigation of the assessment method for human exposure from a wireless power transfer system," *2013 Asia-Pacific Microwave Conference Proceedings (APMC)*, Seoul, 2013, pp. 836-838.

[67] T. Iwamoto, T. Arima, T. Uno, T. Iwamoto, K. Wake, K. Fujii, S. Watanabe, "Measurement of electromagnetic field in the vicinity of wireless power transfer system for evaluation of human-body exposure," *2014 International Symposium on Electromagnetic Compatibility, Tokyo*, Tokyo, 2014, pp. 529-532.

[68] T. Sunohara, I. Laakso, A. Hirata, T. Onishi, "Induced field and SAR in human body model due to wireless power transfer system with induction coupling," *2014 International Symposium on Electromagnetic Compatibility, Tokyo*, Tokyo, 2014, pp. 449-452.

[69] A. Hirata, S. Tsuchida, I. Laakso, "Variability of SAR in different human models due to wireless power transfer with magnetic resonance," *2013 International Symposium on Electromagnetic Compatibility*, Brugge, 2013, pp. 89-92.

[70] S.M. Kim, S.W. Kim, J.I. Moon, I.K. Cho, "A 100W wireless charging system with a human protection function from EM field exposure," *2016 IEEE Transportation Electrification Conference and Expo, Asia-Pacific (ITEC Asia-Pacific)*, Busan, 2016, pp. 684-688.

[71] M. Koohestani, M. Zhadobov, M. Ettorre, "Design Methodology of a Printed WPT System for HF-Band Mid-Range Applications Considering Human Safety Regulations," *IEEE Trans. on Microwave Theory and Techniques*, vol. 65, no. 1, pp. 270-279, Jan. 2017.

[72] J. Jin, Y. Yashima, H. Omori, N. Kimura, T. Morizane, M. Nakaoka, "Reduction of magnetic fields to human exposure from a wireless EV charger by a new cancelling method," *2015 IEEE International Telecommunications Energy Conference (INTELEC)*, Osaka, 2015, pp. 1-4.

[73] S.E. Hong, I.k. Cho, H.D. Choi, J.K. Pack, "Numerical anlaysis of human exposure to electromagnetic fields from wireless power transfer systems," *2014 IEEE Wireless Power Transfer Conference*, Jeju, 2014, pp. 216-219.

[74] A. Christ, M.G. Douglas, J.M. Roman, E.B. Cooper, A.P. Sample, B.H. Waters, J.R. Smith, N. Kuster, "Evaluation of Wireless Resonant Power Transfer Systems with Human Electromagnetic Exposure Limits," *IEEE Trans. on Electromagnetic Compatibility*, vol. 55, no. 2, pp. 265-274, April 2013.

[75] A. Christ, M. Douglas, J. Nadakuduti, N. Kuster, "Assessing Human Exposure to Electromagnetic Fields from Wireless Power Transmission Systems," in *Proceedings of the IEEE*, vol. 101, no. 6, pp. 1482-1493, June 2013.

[76] I.K. Cho, S.M. Kim, J.I. Moon, J.H. Yoon, W.J. Byun, J.I. Choi, "Wireless energy transfer by using 1.8 MHz magnetic resonance coils considering limiting human exposure to EM fields," *2012 15 International Symposium on Antenna Technology and Applied Electromagnetics*, Toulouse, 2012, pp. 1-2.

[77] I. Laakso, S. Tsuchida, A. Hirata, Y. Kamimura, "Analysis of in situ electric field and specific absorption rate in human models for wireless power transfer system with induction coupling," *Phys. Med. Biol.*, vol. 57, no. 15, pp. 4991-5002, 2012.

[78] T. Sunohara, A. Hirata, I. Laakso, T. Onishi, "Evaluation of SAR in a human body model due to wireless power transmission in the 10 MHz band," *Phys. Med. Biol.*, vol. 59, no. 14, pp. 3721-3735, 2014.

[79] S.H. Lee, R.D. Lorenz, "Surface spiral coil design methodologies for high efficiency, high power, low flux density, large air-gap wireless power transfer systems," *Applied Power Electronics Conference and Exposition (APEC), 2013 Twenty-Eighth Annual IEEE*, 2013, pp. 1783-1790.

[80] S.H. Lee, R. D. Lorenz, "A design methodology for multi-kW, large air-gap, MHz frequency, wireless power transfer systems," in *Energy Conversion Congress and Exposition (ECCE), 2011 IEEE*, 2011, pp. 3503-3510.

[81] S.H. Lee, "Design Methodologies for Low Flux Density, High Efficiency, kW Level Wireless Power Transfer Systems with Large Air Gaps," Ph.D. dissertation, University of Wisconsin-Madison, 2013.

[82] S.H. Lee, R.D. Lorenz, "Development and Validation of Model for 95%- Efficiency 220-W Wireless Power Transfer over a 30-cm Air Gap," *IEEE Trans. on Industry Applications*, vol. 47, pp. 2495-2504, 2011.

[83] C. Deng, G. Zhu, R. D. Lorenz, "MHz frequencies, kW, 30 cm gap wireless power transfer with low air gap flux density and high efficiency using surface spiral winding coils," *2017 IEEE Applied Power Electronics Conference and Exposition (APEC)*, Tampa, FL, 2017, pp. 1606-1613.

[84] S.H. Lee *et al*., "A new design methodology for a 300 kW, low flux density, large air-gap, on-line wireless power transfer system," *2015 IEEE Transportation Electrification Conference and Expo (ITEC)*, Dearborn, MI, 2015, pp. 1-7.

[85] "Wireless Power Transfer for Light-Duty Plug-In/Electric Vehicles and Alignment Methodology," ed: SAE TIR J2954_201605, 2016.

[86] H. Kim, C. Song, J. Kim, D.H. Jung, E. Song, S. Kim, J. Kim, J. Kim, "Design of magnetic shielding for reduction of magnetic near field from wireless power transfer system for electric vehicle," *2014 International Symposium on Electromagnetic Compatibility*, Gothenburg, 2014, pp. 53-58.

[87] S. Ahn *et al*., "Low frequency electromagnetic field reduction techniques for the On-Line Electric Vehicle (OLEV)," *2010 IEEE International Symposium on Electromagnetic Compatibility*, Fort Lauderdale, FL, 2010, pp. 625-630.

[88] S. Ahn, J. Kim, "Magnetic field design for high efficient and low EMF wireless power transfer in on-line electric vehicle," *Proceedings of the 5th European Conference on Antennas and Propagation (EUCAP)*, Rome, 2011, pp. 3979-3982.

[89] J. Shin, S. Shin, Y. Kim, S. Ahn, S. Lee, G. Jung, S.J. Jeon, D.H. Cho, "Design and Implementation of Shaped Magnetic-Resonance-Based Wireless Power Transfer System for Roadway-Powered Moving Electric Vehicles," *IEEE Trans. on Industrial Electronics*, vol. 61, no. 3, pp. 1179-1192, March 2014.

[90] S. Kim, H.H. Park, J. Kim, J. Kim, S. Ahn, "Design and Analysis of a Resonant Reactive Shield for a Wireless Power Electric Vehicle," *IEEE Trans. on Microwave Theory and Techniques*, vol. 62, no. 4, pp. 1057-1066, April 2014.

[91] H. Moon, S. Ahn, Y. Chun, "Design of a novel resonant reactive shield for wireless charging system in electric vehicle," *2014 IEEE Wireless Power Transfer Conference*, Jeju, 2014, pp. 220-223.

[92] H. Moon, S. Kim, H.H. Park, S. Ahn, "Design of a Resonant Reactive Shield with Double Coils and a Phase Shifter for Wireless Charging of Electric Vehicles," *IEEE Trans. on Magnetics*, vol. 51, no. 3, pp. 1-4, March 2015.

[93] S. Cruciani, T. Campi, M. Feliziani, F. Maradei, "Optimum coil configuration of wireless power transfer system in presence of shields," *2015 IEEE International Symposium on Electromagnetic Compatibility (EMC)*, Dresden, 2015, pp. 720-725.

[94] J. Zhang, Y. Guo, C. Liao, "FEM simulation and experiment of a novel shielding structure of wireless power transfer system," *2014 IEEE Conference and Expo Transportation Electrification Asia-Pacific (ITEC Asia-Pacific)*, Beijing, 2014, pp. 1-4.

[95] M. Masuda, M. Kusunoki, H. Umegami, F. Hattori, M. Yamamoto, "Reduce of electric ner-field intensity by a shield box in wireless power transfer via field resinance coupling," *2015 IEEE International Telecommunications Energy Conference (INTELEC)*, Osaka, 2015, pp. 1-4.

[96] M. Kim, S. Kim, S. Ahn, Y. Chun, S. Park, "Low frequency electromagnetic compatibility of wirelessly powered electric vehicles," *2014 International Symposium on Electromagnetic Compatibility, Tokyo*, Tokyo, 2014, pp. 426-429.

[97] T. Yilmaz, N. Hasan, R. Zane, Z. Pantic, "Multi-Objective Optimization of Circular Magnetic Couplers for Wireless Power Transfer Applications," *IEEE Trans. on Magnetics*, vol. PP, no.99, pp.1-14, 2017.

[98] A. Hariri, M.E. Hariri, A.E. Sayyed, O.A. Mohammed, "An Iterative Design Approach for Shielding of WPT Systems in Electric Vehicle Charging Applications," *2016 IEEE Vehicle Power and Propulsion Conference (VPPC)*, Hangzhou, 2016, pp. 1-4.

[99] Y. Yashima, H. Omori, T. Morizane, N. Kimura, M. Nakaoka, "Leakage magnetic field reduction from Wireless Power Transfer system embedding new eddy current-based shielding method," *2015 International Conference on Electrical Drives and Power Electronics (EDPE)*, Tatranska Lomnica, 2015, pp. 241-245.

[100] M. Feliziani, S. Cruciani, "Mitigation of the magnetic field generated by a wireless power transfer (WPT) system without reducing the WPT efficiency," *2013 International Symposium on Electromagnetic Compatibility*, Brugge, 2013, pp. 610-615.

[101] M. Lu, K.D.T. Ngo, "Pareto fronts for coils' efficiency versus stray magnetic field in inductive power transfer," *2016 IEEE PELS Workshop on Emerging Technologies: Wireless Power Transfer (WoW)*, Knoxville, TN, 2016, pp. 140-144.

[102] M. Lu, K.D.T. Ngo, "Synergetic optimization of efficiency and stray magnetic field for planar coils in inductive power transfer using matrix calculation," *2017 IEEE Applied Power Electronics Conference and Exposition (APEC)*, Tampa, FL, 2017, pp. 3654-3660.

[103] M. Lu, K.D.T. Ngo, "Field attenuation around inductive-power-transfer coils with dual-side-controlled converter," *2017 IEEE Energy Conversion Congress and Exposition (ECCE)*, Cincinnati, OH, 2017, pp. 126-132.

[104] M. Lu, K.D.T. Ngo, "A Fast Method to Optimize Efficiency and Stray Magnetic Field for Inductive-Power-Transfer Coils Using Lumped-Loops Model," *IEEE Trans. on Power Electronics*, vol. 33, no. 4, pp. 3065-3075, April 2018.

[105] M. Lu, K.D.T. Ngo, "Comparison of passive shields for coils in inductive power transfer," *2017 IEEE Applied Power Electronics Conference and Exposition (APEC)*, Tampa, FL, 2017, pp. 1419-1424.

[106] M. Lu, K.D.T. Ngo, "Attenuation of Stray Magnetic Field in Inductive Power Transfer by Controlling Phases of Windings' Currents," *IEEE Trans. on Magnetics*, vol. 53, no. 9, pp. 1-8, Sept. 2017.

[107] A. Brencher, D. Arthur, *Review and evaluation of wireless power transfer (WPT) for electric transit applications*. FTA Report No. 0060, Aug., 2014.

[108] PLUGLESSTM Level 2 EV Charging System (3.3 kW) by Evatran Group Inc.. Idaho national laboratory test report, Jan., 2015. Available online: https://avt.inl.gov/sites/default/files/pdf/evse/PLUGLESSEvatranChevyVoltTestResultsFactSheet.pdf.

[109] Y. Hori, "Application of Electric Motor, Supercapacitor, and Wireless Power Transfer to enhance operation of future vehicles," *Industrial Electronics, 2010 IEEE International Symposium on*, 2010, pp. 3633-3635.

[110] J.M. Miller, O.C. Onar, C. White, S. Campbell, C. Coomer, L. Seiber, R. Sepe, A. Steyerl, "Demonstrating Dynamic Wireless Charging of an Electric Vehicle: The Benefit of Electrochemical Capacitor Smoothing," *IEEE Power Electronics Magazine*, vol. 1, pp. 12-24, 2014.

[111] L. Chen, G.R. Nagendra, J.T. Boys, G.A. Covic, "Double-Coupled Systems for IPT Roadway Applications," in *IEEE Journal of Emerging and Selected Topics in Power Electronics*, vol. 3, no. 1, pp. 37-49, March 2015.

[112] G.R. Nagendra, G.A. Covic, J.T. Boys, "Sizing of Inductive Power Pads for Dynamic Charging of EVs on IPT Highways," *IEEE Trans. on Transportation Electrification*, vol. 3, no. 2, pp. 405-417, June 2017.

[113] A. Zaheer, M. Neath, H.Z.Z. Beh, G.A. Covic, "A Dynamic EV Charging System for Slow Moving Traffic Applications," *IEEE Trans. on Transportation Electrification*, vol. 3, no. 2, pp. 354-369, June 2017.

[114] J. Huh, S.W. Lee, W.Y. Lee, G.H. Cho, C.T. Rim, "Narrow-Width Inductive Power Transfer System for Online Electrical Vehicles," *IEEE Trans. on Power Electronics*, vol. 26, no. 12, pp. 3666-3679, Dec. 2011.

[115] S. Lee, J. Huh, C. Park, N.S. Choi, G.H. Cho, C.T. Rim, "On-Line Electric Vehicle Using Inductive Power Transfer System," in *Energy Conversion Congress and Exposition (ECCE), 2010 IEEE*, 2010, pp. 1598-1601

[116] M. Kim, H. Kim, D. Kim, Y. Jeong, H.H. Park, S. Ahn, "A Three-Phase Wireless-Power-Transfer System for Online Electric Vehicles with Reduction of Leakage Magnetic Fields," *IEEE Trans. on Microwave Theory and Techniques*, vol. 63, no. 11, pp. 3806-3813, Nov. 2015.

[117] F. Lu, H. Zhang, H. Hofmann, C.C. Mi, "A Dynamic Charging System with Reduced Output Power Pulsation for Electric Vehicles," *IEEE Trans. on Industrial Electronics*, vol. 63, pp. 6580-6590, 2016.

[118] F. Lu, H. Zhang, H. Hofmann, Y. Mei, C.C. Mi, "A dynamic capacitive power transfer system with reduced power pulsation," *2016 IEEE PELS Workshop on Emerging Technologies: Wireless Power Transfer (WoW)*, Knoxville, TN, 2016, pp. 60-64.

[119] I.S. Suh, J. Kim, "Electric vehicle on-road dynamic charging system with wireless power transfer technology," *2013 International Electric Machines & Drives Conference*, Chicago, IL, 2013, pp. 234-240.

[120] J. Huh, S. Lee, C. Park, G.H. Cho, C.T. Rim, "High Performance Inductive Power Transfer System with Narrow Rail Width for on-Line Electric Vehicles," in *Energy Conversion Congress and Exposition (ECCE), 2010 IEEE*, 2010, pp. 647-651.

[121] N.P. Suh, D.H. Cho, C.T. Rim. "Design of on-line electric vehicle (OLEV)." *Global Product Development*. Springer Berlin Heidelberg, 2011. 3-8.

[122] J.H. Kim, B.S. Lee, J.H. Lee, S.H. Lee, C.B. Park, S.M. Jung, S.G. Lee, K.P. Yi, J. Baek, "Development of 1-MW Inductive Power Transfer System for a High-Speed Train," *IEEE Trans. on Industrial Electronics*, vol. 62, pp. 6242-6250, 2015.

[123] *Electric and Magnetic Field Levels Generated by AC Power Systems - Measurement Procedures with Regard to Public Exposure*, IEC62110, International Electrotechnical Commission, 2015.

[124] S.H. Lee, B.S. Lee, J.H. Lee, "A New Design Methodology for a 300-kW, Low Flux Density, Large Air Gap, Online Wireless Power Transfer System," *IEEE Trans. on Industry Applications*, vol. 52, pp. 4234-4242, 2016.

[125] H. Kim, C. Song, D.H. Kim, J. Kim, "Design of conductive shield for wireless power transfer system for electric vehicle considering automotive body," *2015 IEEE International Symposium on Electromagnetic Compatibility (EMC)*, Dresden, 2015, pp. 1369-1374.

[126] S.Y. Choi, J. Huh, W.Y. Lee, C.T. Rim, "Asymmetric Coil Sets for Wireless Stationary EV Chargers with Large Lateral Tolerance by Dominant Field Analysis," *IEEE Trans. on Power Electronics*, vol. 29, no. 12, pp. 6406-6420, Dec. 2014.

[127] J.M. Miller, O.C. Onar, M. Chinthavali, "Primary-Side Power Flow Control of Wireless Power Transfer for Electric Vehicle Charging," in *IEEE Journal of Emerging and Selected Topics in Power Electronics*, vol. 3, no. 1, pp. 147-162, March 2015.

[128] F. Lu, H. Zhang, H. Hofmann, C. C. Mi, "An Inductive and Capacitive Combined Wireless Power Transfer System with LC-Compensated Topology," *IEEE Trans. on Power Electronics*, vol. 31, pp. 8471-8482, 2016.

[129] H. Kim, C. Song, J. Kim, "Coil design for high efficiency and low magnetic field leakage of wireless charging system for electric vehicle," *2015 IEEE Wireless Power Transfer Conference (WPTC)*, Boulder, CO, 2015, pp. 1-3.

[130] H. Kim *et al*., "Coil Design and Measurements of Automotive Magnetic Resonant Wireless Charging System for High-Efficiency and Low Magnetic Field Leakage," in *IEEE Trans. on Microwave Theory and Techniques*, vol. 64, no. 2, pp. 383-400, Feb. 2016.

[131] M. Jo, Y. Sato, Y. Kaneko, S. Abe, "Methods for reducing leakage electric field of a wireless power transfer system for electric vehicles," *2014 IEEE Energy Conversion Congress and Exposition (ECCE)*, Pittsburgh, PA, 2014, pp. 1762-1769.

[132] T. Batra, E. Schaltz, "Magnetic field emission comparison at different quality factors with series-series compensation network for inductive power transfer to vehicles," *2014 IEEE Wireless Power Transfer Conference*, Jeju, 2014, pp. 13-16.

[133] T. Batra, E. Schaltz, S. Ahn, "Reduction of magnetic emission by increasing secondary side capacitor for ferrite geometry based series-series topology for wireless power transfer to vehicles," *2014 16th European Conference on Power Electronics and Applications*, Lappeenranta, 2014, pp. 1-11.

[134] T. Batra, E. Schaltz, "Magnetic field emission comparison at different quality factors with series-parallel compensation network for wireless power transfer to vehicles," *2014 4th International Electric Drives Production Conference (EDPC)*, Nuremberg, 2014, pp. 1-4.

[135] Y. Gao, K.B. Farley, Z.T.H. Tse, "Investigating safety issues related to Electric Vehicle wireless charging technology," *2014 IEEE Transportation Electrification Conference and Expo (ITEC)*, Dearborn, MI, 2014, pp. 1-4.

[136] R. Haldi, K. Schenk, I. Nam, E. Santi, "Finite-element-simulation-assisted optimized design of an asymmetrical high-power inductive coupler with a large air gap for EV charging," *2013 IEEE Energy Conversion Congress and Exposition*, Denver, CO, 2013, pp. 3635-3642.

[137] H. Fujibe, K. Kesamaru, "Magnetic field analysis of wireless power transfer via magnetic resonant coupling for electric vehicle," *2013 International Conference on Electrical Machines and Systems (ICEMS)*, Busan, 2013, pp. 884-887.

[138] A. Tejeda, C. Carretero, J.T. Boys, G.A. Covic, "Core-less Circular Pad with Controlled Flux Cancellation for EV Wireless Charging," *IEEE Trans. on Power Electronics*, vol. 32, no. 11, pp. 8349-8359, Nov. 2017.

[139] J. Zhang, X. Yuan, C. Wang, Y. He, "Comparative Analysis of Two-Coil and Three-Coil Structures for Wireless Power Transfer," *IEEE Trans. on Power Electronics*, vol. 32, no. 1, pp. 341-352, Jan. 2017.

[140] O. Simon, T. Krempel, W. Schnurbusch, A. Hoppe, F. Turki, "Proposal of a power source definition to provide interoperable use of wireless power transfer systems," *2014 IEEE International Electric Vehicle Conference (IEVC)*, Florence, 2014, pp. 1-7.

[141] L. Tan, X. Huang, C. Chen, W. Wang, C. Yan, "Design and magnetic properties of electric vehicle wireless charging system," *2015 IEEE Magnetics Conference (INTERMAG)*, Beijing, 2015, pp. 1-1.

[142] S. Bandyopadhyay, V. Prasanth, P. Bauer, J.A. Ferreira, "Multi-objective optimisation of a 1-kW wireless IPT systems for charging of electric vehicles," *2016 IEEE Transportation Electrification Conference and Expo (ITEC)*, Dearborn, MI, 2016, pp. 1-7.

[143] R. Pinto *et al*., "Exposure assessment of stray electromagnetic fields generated by a wireless power transfer system," *2015 9th European Conference on Antennas and Propagation (EuCAP)*, Lisbon, 2015, pp. 1-4.

[144] H. Jiang, W. Li, M. Tabaddor, C. Mi, "Optimization and safety evaluation of a 3.3 kW wireless EV charger," *2015 IEEE Transportation Electrification Conference and Expo (ITEC)*, Dearborn, MI, 2015, pp. 1-5.

[145] J. McLean, A. Medina, R. Sutton, "Magnetostimulation by inductive power transfer systems," *2013 IEEE Radio and Wireless Symposium*, Austin, TX, 2013, pp. 298-300.

[146] H. Hirayama, T. Amano, N. Kikuma, K. Sakakibara, "Undesired emission and biological effect of open-end and short-end antennas for coupled-resonant wireless power transfer," *2013 Asia-Pacific Symposium on Electromagnetic Compatibility (APEMC)*, Melbourne, VIC, 2013, pp. 1-4.

[147] C. Zhang, D. Lin, N. Tang, S.Y. Hui, "A Novel Electric Insulation String Structure with High-Voltage Insulation and Wireless Power Transfer Capabilities," *IEEE Trans. on Power Electronics*, May 2017.

[148] J. McLean, R. Sutton, "Electric field breakdown in Wireless Power Transfer systems due to ferrite dielectric polarizability," *2016 IEEE Wireless Power Transfer Conference (WPTC)*, Aveiro, 2016, pp. 1-4.

[149] K. Wada *et al*., "Development of an exposure system for 85 kHz magnetic field for the evaluation biological effects," *2016 IEEE PELS Workshop on Emerging Technologies: Wireless Power Transfer (WoW)*, Knoxville, TN, 2016, pp. 158-161.

[150] F. Lu, H. Zhang, H. Hofmann, C. Mi, "An inductive and capacitive integrated coupler and its LCL compensation circuit design for wireless power transfer," *IEEE Trans. on Industry Applications*, April 2017.

[151] T. Campi, S. Cruciani, F. Maradei, M. Feliziani, "Near-Field Reduction in a Wireless Power Transfer System Using LCC Compensation," *IEEE Trans. on Electromagnetic Compatibility*, vol. 59, no. 2, pp. 686-694, April 2017.

[152] A.A.S. Mohamed, A. Berzoy, O.A. Mohammed, "Physics-Based Co-Simulation Platform for EMC Analysis of Two-Way Inductive WPT System in EV Applications," *2016 IEEE Vehicle Power and Propulsion Conference (VPPC)*, Hangzhou, 2016, pp. 1-6.

[153] A.O. Hariri, T. Youssef, A. Elsayed, O. Mohammed, "A Computational Approach for a Wireless Power Transfer Link Design Optimization Considering Electromagnetic Compatibility," *IEEE Trans. on Magnetics*, vol. 52, no. 3, pp. 1-4, March 2016.

[154] K. Kim, J. Kim, H. Kim, J. Ahn, H.H. Park, S. Ahn, "Evaluation of electromagnetic field radiation from wireless power transfer electric vehicle," *2016 International Symposium on Antennas and Propagation (ISAP)*, Okinawa, 2016, pp. 40-41.

[155] M. Budhia, G.A. Covic, J.T. Boys, "Design and optimisation of magnetic structures for lumped Inductive Power Transfer systems," *2009 IEEE Energy Conversion Congress and Exposition*, San Jose, CA, 2009, pp. 2081-2088.

[156] A. Zaheer, H. Hao, G.A. Covic, D. Kacprzak, "Investigation of Multiple Decoupled Coil Primary Pad Topologies in Lumped IPT Systems for Interoperable Electric Vehicle Charging," *IEEE Trans. on Power Electronics*, vol. 30, no. 4, pp. 1937-1955, April 2015.

[157] A. Tejeda, G.A. Covic, J.T. Boys, "Novel single-sided ferrite-less magnetic coupler for roadway EV charging," *2015 IEEE Energy Conversion Congress and Exposition (ECCE)*, Montreal, QC, 2015, pp. 3148-3153.

[158] C. Qiu, K.T. Chau, C. Liu, W. Li, F. Lin, "Quantitative comparison of dynamic flux distribution of magnetic couplers for roadway electric vehicle wireless charging system," *Journal of Applied Physics*, vol. 115, issue 17, pp. 1-4, 2014.

[159] R. Bosshard, J.W. Kolar, J. Mühlethaler, I. Stevanović, B. Wunsch, F. Canales, "Modeling and eta - alpha - Pareto Optimization of Inductive Power Transfer Coils for Electric Vehicles," in *IEEE Journal of Emerging and Selected Topics in Power Electronics*, vol. 3, no. 1, pp. 50-64, March 2015.

[160] R. Bosshard, “Multi-objective optimization of inductive power transfer systems for EV charging,” Ph.D. dissertation, Dept. Inf. Technol. Elect. Eng., ETH Zürich, Zürich, Switzerland, 2015.

[161] R. Bosshard, J.W. Kolar, "Multi-Objective Optimization of 50 kW/85 kHz IPT System for Public Transport," in *IEEE Journal of Emerging and Selected Topics in Power Electronics*, vol. 4, no. 4, pp. 1370-1382, Dec. 2016.

[162] C.S. Wang, G.A. Covic, O.H. Stielau, "Investigating an LCL load resonant inverter for inductive power transfer applications," *IEEE Trans. on Power Electronics*, vol. 19, pp. 995-1002, 2004.

[163] Y. Su, C. Tang, S. Wu, Y. Sun, "Research of LCL Resonant Inverter in Wireless Power Transfer System," *2006 International Conference on Power System Technology*, 2006, pp. 1-6.

[164] M.L.G. Kissin, C.Y. Huang, G.A. Covic, J. T. Boys, "Detection of the Tuned Point of a Fixed-Frequency LCL Resonant Power Supply," *IEEE Trans. on Power Electronics*, vol. 24, pp. 1140-1143, 2009.

[165] H.H. Wu, A. Gilchrist, K. Sealy, D. Bronson, “A 90 percent efficient 5 kW inductive charger for EVs,” in *Energy Conversion Congress and Exposition (ECCE), 2012 IEEE*, 2012, pp. 275–282.

[166] S. Li, W. Li, J. Deng, T.D. Nguyen, C.C. Mi, "A Double-Sided LCC Compensation Network and Its Tuning Method for Wireless Power Transfer," *IEEE Trans. on Vehicular Technology*, vol. 64, pp. 2261-2273, 2015.

[167] R.W. Erickson, D. Maksimovic, *Fundamentals of Power Electronics*, 2nd ed. Norwell, Mass.: Kluwer Academic, 2001.

[168] C.A. Desoer, E.S. Kuh, *Basic Circuit Theory*: Tata McGraw-Hill Education, 1984.

[169] T.H. Lee, *The Design of Cmos Radio-Frequency Integrated Circuits*: Cambridge Univ Pr., 2004.

[170] W. Zhang, C.C. Mi, "Compensation Topologies of High-Power Wireless Power Transfer Systems," *IEEE Trans. on Vehicular Technology*, vol. 65, pp. 4768-4778, 2016.

[171] C.S. Wang, O.H. Stielau, G.A. Covic, "Design considerations for a contactless electric vehicle battery charger," *IEEE Trans. on Industrial Electronics*, vol. 52, no. 5, pp. 1308-1314, Oct. 2005.

[172] J.M. Miller, B. Long, “What All Technology Adoptors Should Know About WPT for High Power Charging,” *IEEE Workshop on Wireless* (WOW2016), Knoxville, TN, 4-6 October 2016.

[173] J.M. Miller, P.C. Schrafel, B.R. Long, A. Daga, "The WPT dilemma — High K or high Q?", *2016 IEEE PELS Workshop on Emerging Technologies: Wireless Power Transfer (WoW)*, Knoxville, TN, 2016, pp. 128-134.

[174] G.A. Kendir, L. Wentai, W. Guoxing, M. Sivaprakasam, R. Bashirullah, M.S. Humayun, and J. D. Weiland, "An Optimal Design Methodology for Inductive Power Link with Class-E Amplifier," *IEEE Trans. on Circuits and Systems I: Regular Papers*, vol. 52, pp. 857-866, 2005.

[175] R. Mecke, C. Rathge, "High Frequency Resonant Inverter for Contactless Energy Transmission over Large Air Gap," in *Power Electronics Specialists Conference, 2004. PESC 04. 2004 IEEE 35th Annual*, 2004, pp. 1737-1743.

[176] P. Meyer, P. Germano, Y. Perriard, "Modelling and Design of a Contactless Energy Transfer System for a Notebook Battery Charger," in *Electrical Machines (ICEM), 2010 XIX International Conference on*, 2010, pp. 1-6.

[177] X. Liu, S. Hui, "Optimal Design of a Hybrid Winding Structure for Planar Contactless Battery Charging Platform," *IEEE Trans. on Power Electronics*, vol. 23, pp. 455-463, 2008.

[178] H.L. Li, A.P. Hu, G.A. Covic, C.S. Tang, "A New Primary Power Regulation Method for Contactless Power Transfer," in *Industrial Technology, 2009. ICIT 2009. IEEE International Conference on*, 2009, pp. 1-5.

[179] A.J. Moradewicz, M.P. Kazmierkowski, "Contactless Energy Transfer System with Fpga-Controlled Resonant Converter," *IEEE Trans. on Industrial Electronics*, vol. 57, pp. 3181-3190, 2010.

[180] F. Lu, H. Hofmann, J. Deng, C. Mi, "Output power and efficiency sensitivity to circuit parameter variations in double-sided LCC-compensated wireless power transfer system," *Applied Power Electronics Conference and Exposition (APEC), 2015 IEEE*, 2015, pp. 597-601.

[181] W. Li, H. Zhao, J. Deng, S. Li, C. C. Mi, "Comparison Study on SS and Double-Sided LCC Compensation Topologies for EV/PHEV Wireless Chargers," *IEEE Trans. on Vehicular Technology*, vol. 65, no. 6, pp. 4429-4439, June 2016.

[182] S. Cruciani, T. Campi, M. Feliziani, "Parametric analysis of load variation in WPT systems applied to AIMDs," *2016 46th European Microwave Conference (EuMC)*, London, 2016, pp. 703-706.

[183] G. Bacelli, J.V. Ringwood, P. Iordanov, “Impedance matching controller for an inductively coupled plasma chamber: L-type matching network automatic controller,” *4th International Conference on Information in Control, Automation and Robotics (ICNICO)*, Angers, France, 2007, pp. 202-207.

[184] W.C.E. Neo, et. al., “Adaptive multi-band multi-mode power amplifier using integrated Varactor-based tunable matching networks,” *IEEE Journal of Solid-State Circuits*, vol. 41, pp. 2166-2176, 2006.

[185] Q. Shen, N.S. Barker, “Distributed MEMS tunable matching network using minimal-contact RF-MEMS varactors,” *IEEE Trans. on Microwave Theory and Technology*, vol. 54, pp. 2646-2658, 2006.

[186] M.T. Arnous, Z. Zhang, S.E. Barbin, G. Boeck, "Characterization of high voltage varactors for load modulation of GaN-HEMT power amplifier," *2015 17th International Conference on Transparent Optical Networks (ICTON)*, Budapest, 2015, pp. 1-4.

[187] P. Sjoblom, H. Sjoland, “Measured CMOS switched high-quality capacitors in a reconfigurable matching network,” *IEEE Trans. on Circuits and Systems II*, vol. 54, pp. 858-862, 2007.

[188] A. van Bezooijen, et. al., “A GSM/EDGE/WCDMA adaptive series-LC matching network using RF-MEMS switches,” *IEEE Journal of Soli-State Circuits*, vol. 43, pp. 2259-2268, 2008.

[189] C. Sánchez-Pérez, J. de Mingo, P.L. Carro, P. García-Dúcar, "Design and Applications of a 300–800 MHz Tunable Matching Network," *IEEE Journal on Emerging and Selected Topics in Circuits and Systems*, vol. 3, pp. 531-540, 2013.

[190] B. Guo *et al.*, "Resonant filter based buck converters with tunable capacitor," in *Energy Conversion Congress and Exposition (ECCE), 2017 IEEE*, 2017, pp. 2036-2042.

[191] B. Guo, S. Dwari, S. Priya, K. Ngo, R. Burgos, C. Nies, "Novel Actively Tuned Resonant Filter Based Buck Converter Using Tunable Capacitor," in *Energy Conversion Congress and Exposition (ECCE), 2018 IEEE*, 2018, pp. 149-154.

[192] H. Zeng, F.Z. Peng, "Non-linear capacitor based variable capacitor for self-tuning resonant converter in wireless power transfer," in *Applied Power Electronics Conference and Exposition (APEC), 2018 IEEE*, 2018, pp. 1375-1379.

[193] Y. Lim, H. Tang, S. Lim and J. Park, "An Adaptive Impedance-Matching Network Based on a Novel Capacitor Matrix for Wireless Power Transfer," *IEEE Trans. on Power Electronics*, vol. 29, pp. 4403-4413, 2014.

[194] W.-J. Gu, K. Harada, "A new method to regulate resonant converters," *IEEE Trans. on Power Electronics*, vol. 3, pp. 430-439, 1988.

[195] D.J. Perreault, A.S. Jurkov, "Tunable matching network with phase-switched elements." U.S. Patent 9,755,576 B2, issued Sept. 5, 2017.

[196] A.S. Jurkov, A. Radomski, D.J. Perreault, "Tunable impedance matching networks based on phase-switched impedance modulation," *2017 IEEE Energy Conversion Congress and Exposition (ECCE)*, Cincinnati, OH, 2017, pp. 947-954.

[197] C.S. Wang, G.A. Covic, O.H. Stielau, "General Stability Criterions for Zero Phase Angle Controlled Loosely Coupled Inductive Power Transfer Systems," in *Industrial Electronics Society, 2001. IECON '01. The 27th Annual Conference of the IEEE*, 2001, pp. 1049-1054.

[198] C.S. Wang, O.H. Stielau, G.A. Covic, "Load Models and Their Application in the Design of Loosely Coupled Inductive Power Transfer Systems," in *Power System Technology, 2000. Proceedings. PowerCon 2000. International Conference on*, 2000, pp. 1053-1058.

[199] A. Kurs, A. Karalis, R. Moffatt, J.D. Joannopoulos, P. Fisher, M. Soljacic, “Wireless power transfer via strongly coupled magnetic resonances,” *Science*, vol. 317, pp. 83-86, 2007.

[200] J.D. Jackson, *Classical Electrodynamics*, 3rd Edition, John Wiley & Sons, 1998.

[201] R.P. Feynman, R.B. Leighton, M. Sands, *The Feynman Lectures on Physics Volume 2*, Addison-Wesley, 1963.

[202] J. Simpson, J. Lane, C. Immer, R. Youngquist, "Simple analytic expressions for the magnetic field of a circular current loop", *Proc. NASA Tech. Document Collect.*, pp. 1-3, 2001.

[203] S. Kong *et al.*, "Analytical model for predicting the electromagnetic fields intensity in wireless power transfer systems," *2011 IEEE Electrical Design of Advanced Packaging and Systems Symposium (EDAPS)*, Hanzhou, 2011, pp. 1-4.

[204] C. Capps, "Near Field or Far Field," EDN, August 16, 2001, pp. 95-102. Online at: http://m.eet.com/media/1140931/19213-150828.pdf

[205] J. Li, P.W. Neurath, "Electric and Magnetic Fields Near a Circular Loop at 27 MHz," *IEEE Trans. on Biomedical Engineering*, vol. BME-16, no. 1, pp. 96-98, Jan. 1969.

[206] B.S. Davis, L. Kaplan, “Poynting vector flow in a circular circuit,” *Am. J. Phys.*, vol. 79, no. 11, pp. 1155-1162, 2011.

[207] C.W.T. McLyman, *Transformer and Inductor Design Handbook* vol. 121: CRC press, 2004.

[208] S. Ahn, H.H. Park, C.S. Choi, J. Kim, E. Song, H.B. Park, H. Kim, J. Kim, "Reduction of electromagnetic field (EMF) of wireless power transfer system using quadruple coil for

laptop applications," *Microwave Workshop Series on Innovative Wireless Power Transmission: Technologies, Systems, and Applications (IMWS), 2012 IEEE MTT-S International*, 2012, pp. 65-68.

[209] F. Nakao, Y. Matsuo, M. Kitaoka, H. Sakamoto, "Ferrite Core Couplers for Inductive Chargers," in *Power Conversion Conference, 2002. PCC Osaka 2002. Proceedings of the*, 2002, pp. 850-854 vol.2.

[210] R. Laouamer, M. Brunello, J.P. Ferrieux, O. Normand, N. Buchheit, "A Multi-Resonant Converter for Non-Contact Charging with Electromagnetic Coupling," in *Industrial Electronics, Control and Instrumentation, 1997. IECON 97. 23rd International Conference on*, 1997, pp. 792-797 vol.2.

[211] C.R. Sullivan, L. Beghou, "Design methodology for a high-Q self-resonant coil for medical and wireless-power applications," *Control and Modeling for Power Electronics (COMPEL), 2013 IEEE 14th Workshop on*, 2013, pp. 1-8.

[212] F. Lu, H. Zhang, H. Hofmann, C. Mi, "A high efficiency 3.3 kW loosely-coupled wireless power transfer system without magnetic material," in *Energy Conversion Congress and Exposition (ECCE), 2015 IEEE*, 2015, pp. 2282-2286.

[213] A.P. Sample, D.A. Meyer, J.R. Smith, "Analysis, Experimental Results, and Range Adaptation of Magnetically Coupled Resonators for Wireless Power Transfer," *IEEE Trans. on Industrial Electronics,* vol. 58, pp. 544-554, 2011.

[214] K. Knaisch, P. Gratzfeld, "Comparison of magnetic couplers for inductive electric vehicle charging using accurate numerical simulation and statistical methods," *2015 5th International Electric Drives Production Conference (EDPC)*, Nuremberg, 2015, pp. 1-10.

[215] K. Knaisch, M. Springmann, P. Gratzfeld, "Comparison of coil topologies for inductive power transfer under the influence of ferrite and aluminum," *2016 Eleventh International Conference on Ecological Vehicles and Renewable Energies (EVER)*, Monte Carlo, 2016, pp. 1-9.

[216] F.B.J. Leferink, "Inductance Calculations; Methods and Equations," in *Electromagnetic Compatibility, 1995. Symposium Record. 1995 IEEE International Symposium on*, 1995, pp. 16-22.

[217] B. Noureddine, M. Mohamed, D. Lies, "Attenuation in Transferred Rf Power to a Biomedical Implant Due to the Misalignment Coils," *IEEE Trans. on Computing and Technology*, vol. 10, pp. 161-164, 2005.

[218] S.I. Babic, C. Akyel, "Calculating Mutual Inductance between Circular Coils with Inclined Axes in Air," *IEEE Trans. on Magnetics,* vol. 44, pp. 1743-1750, 2008.

[219] F.C. Flack, E.D. James, D.M. Schlapp, "Mutual Inductance of Air-Cored Coils: Effect on Design of Radio-Frequency Coupled Implants," *Med Biol Eng,* vol. 9, pp. 79-85, Mar 1971.

[220] E.S. Hochmair, "System Optimization for Improved Accuracy in Transcutaneous Signal and Power Transmission," *IEEE Trans. on Biomedical Engineering,* vol. 31, pp. 177-86, 1984.

[221] K.B. Kim, E. Levi, Z. Zabar, L. Birenbaum, "Mutual Inductance of Noncoaxial Circular Coils with Constant Current Density," *IEEE Trans. on Magnetics,* vol. 33, pp. 4303-4309, 1997.

[222] D.C. Galbraith, M. Soma, R.L. White, "A Wide-Band Efficient Inductive Transdennal Power and Data Link with Coupling Insensitive Gain," *IEEE Trans. on Biomedical Engineering,* vol. BME-34, pp. 265-275, 1987.

[223] J.C. Maxwell, *A Treatise on Electricity and Magnetism* vol. 1: Clarendon Press, 1873.

[224] W.G. Hurley, M.C. Duffy, "Calculation of Self and Mutual Impedances in Planar Magnetic Structures," *IEEE Trans. on Magnetics,* vol. 31, pp. 2416-2422, 1995.

[225] H.C. Miller, "Inductance Formula for a Single-Layer Circular Coil," *Proceedings of the IEEE,* vol. 75, pp. 256-257, 1987.

[226] Y.P. Su, L. Xun, S.Y.R. Hui, "Mutual Inductance Calculation of Movable Planar Coils on Parallel Surfaces," *IEEE Trans. on Power Electronics,* vol. 24, pp. 1115-1123, 2009.

[227] C. Akyel, S.I. Babic, M.M. Mahmoudi, "Mutual Inductance Calculation for Non-Coaxial Circular Air Coils with Parallel Axes," *Progress in Electromagnetics Research,* vol. 91, pp. 287-301, 2009.

[228] T. Ishimine, A. Watanabe, T. Ueno, T. Maeda, T. Tokuoka, "Development of Low-Iron-Loss Powder Magnetic Core Material for High-Frequency Applications." *SEI Technical Review*, vol. 72, pp. 1-6, 2011.

[229] R. Bosshard, J. Mühlethaler, J.W. Kolar, I. Stevanović, "Optimized magnetic design for inductive power transfer coils," *2013 Twenty-Eighth Annual IEEE Applied Power Electronics Conference and Exposition (APEC)*, Long Beach, CA, USA, 2013, pp. 1812-1819.

[230] Design of Planar Power Transformers. Application Note. Ferroxcube. Link: http://ferroxcube.home.pl/appl/info/plandesi.htm

[231] S.A. Mulder, Loss formulas for power ferrites and their use in transformer design, Philips Components, 1994.

[232] G.S. Smith, "Proximity Effect in Systems of Parallel Conductors," *Journal of Applied Physics*, vol. 43, pp. 2196-2203, 1972.

[233] M. P. Perry, *Low Frequency Electromagnetic Design*: M. Dekker, 1985.

[234] S. Butterworth, "Eddy-Current Losses in Cylindrical Conductors, with Special Applications to the Alternating Current Resistances of Short Coils," *Philosophical Trans. of the Royal Society of London. Series A, Containing Papers of a Mathematical or Physical Character,* vol. 222, pp. 57-100, 1922.

[235] H.B. Dwight, "Skin Effect and Proximity Effect in Tubular Conductors," *American Institute of Electrical Engineers, Trans. of the,* vol. 41, pp. 189-198, 1922.

[236] A. Arnold, "The Alternating-Current Resistance of Tubular Conductors," *Electrical Engineers, Journal of the Institution of,* vol. 78, pp. 580-596, 1936.

[237] A. Arnold, "The Alternating-Current Resistance of Parallel Conductors of Circular Cross-Section," *Electrical Engineers, Journal of the Institution of,* vol. 77, pp. 49-58, 1935.

[238] A. Lotfi, F.C. Lee, "Two-Dimensional Skin Effect in Power Foils for High Frequency Applications," *IEEE Trans. on Magnetics,* vol. 31, pp. 1003-1006, 1995.

[239] P.L. Dowell, "Effects of eddy currents in transformer windings", *Proceedings of the IEEE*, vol. 113, pp. 1387–1394, 1966.

[240] J.A. Ferreira, "Analytical computation of ac resistance of round and rectangular litz wire windings", *IEEE Proceedings-B Electric Power Applications*, vol. 139, pp. 21–25, 1992.

[241] J.A. Ferreira, "Improved analytical modeling of conductive losses in magnetic components", *IEEE Trans. on Power Electronics*, vol. 9, pp. 127–131, Jan. 1994.

[242] N. Xi, C.R. Sullivan, "An Improved Calculation of Proximity-Effect Loss in High-Frequency Windings of Round Conductors," in *Power Electronics Specialist Conference, 2003. PESC '03. 2003 IEEE 34th Annual*, 2003, pp. 853-860 vol.2.
[243] M.K. Kazimierczuk, *High-Frequency Magnetic Components (Second Edition)*: Wiley, 2014.
[244] J.A. Ferreira, "Analytical Computation of Ac Resistance of Round and Rectangular Litz Wire Windings," *Electric Power Applications, IEE Proceedings B*, vol. 139, pp. 21-25, 1992.
[245] A.W. Lotfi, F.C. Lee, "A High Frequency Model for Litz Wire for Switch Mode Magnetics," in *Industry Applications Society Annual Meeting, 1993., Conference Record of the 1993 IEEE*, 1993, pp. 1169-1175.
[246] T. Bieler, M. Perrottet, V. Nguyen, Y. Perriard, "Contactless Power and Information Transmission," *IEEE Trans. on Industry Applications*, vol. 38, pp. 1266-1272, 2002.
[247] J. Acero, R. Alonso, J.M. Burdio, L.A. Barragan, D. Puyal, "Frequency Dependent Resistance in Litz-Wire Planar Windings for Domestic Induction Heating Appliances," *IEEE Trans. on Power Electronics*, vol. 21, pp. 856-866, 2006.
[248] F E. Terman, *Radio Engineers' Handbook* vol. 2: McGraw-Hill New York, 1943.
[249] I. HSM Wire International. (2012). *Litz Wire Technical Information*. Available: www.litz-wire.com/technical.html
[250] S. Kasap, *Principles of Electronic Materials and Devices*: McGraw Hill Higher Education, 2005.
[251] H. Li, K. Wang, L. Huang, J. Li, X. Yang, "Coil structure optimization method for improving coupling coefficient of wireless power transfer," *2015 IEEE Applied Power Electronics Conference and Exposition (APEC)*, Charlotte, NC, 2015, pp. 2518-2521.
[252] S. Mehri, A.C. Ammari, J. Slama, M. Sawan, "Minimizing printed spiral coil losses for inductive link wireless power transfer," *2016 IEEE Wireless Power Transfer Conference (WPTC)*, Aveiro, 2016, pp. 1-4.
[253] B. Mammano, L. Bahra, "Safety Considerations in Power Supply Design." Texas Instruments, 2004.
[254] F.W. Grover, Inductance Calculations, Dover Publications, Mineola, 2004.
[255] J.T. Conway, "New exact solution procedure for the near fields of the general thin circular loop antenna," *IEEE Trans. on Anten. Prop.*, vol. 53, pp. 509-517, 2005.
[256] Tesla Model S Owner's Manual, pp. 161-166, link: https://www.tesla.com/sites/default/files/model_s_owners_manual_north_america_en_us.pdf.
[257] Example vehicles and their battery capacity, link: https://en.wikipedia.org/wiki/Electric_vehicle_battery.
[258] SiC MOSFET PLECS C2M0025120D model, link: https://www.wolfspeed.com/c2m0025120d